Oliver Buß

Photon- and Pion-induced Nuclear Reactions in a Transport Approach

Inaugural-Dissertation zur Erlangung des Doktorgrades der
naturwissenschaftlichen Fachbereiche der Justus-Liebig-Universität Gießen

Gießen, 26. August 2008

JUSTUS-LIEBIG-
UNIVERSITÄT
GIESSEN

Fachbereich 07 - Mathematik und Informatik, Physik, Geographie

Dekan: Prof. Dr. Bernd Baumann
1. Berichterstatter: Prof. Dr. Ulrich Mosel
2. Berichterstatter: Prof. Dr. Volker Metag

Preface

During my PhD time, many collaborations and friendships developed and I thank everyone involved in making this project a success. Already in this place I apologize to all those people I might not have place to mention explicitly in the following lines and express my gratitude for their help – in particular for their moral support, for cheering me up while, e.g., having a pot of coffee or an after-work swimming or running exercise together, for interested questions and most of all for their time discussing some of my (stupid) ideas.

First of all I am deeply indebted to my scientific supervisor *Prof. Dr. Ulrich Mosel* for his experienced guidance, support and enduring interest during the course of my PhD years. I have especially appreciated the opportunity to present my results at various international conferences. His great scientific intuition, and his open-minded and friendly nature made this project an outstanding experience for me.

My very special thanks go to my room mate *Tina Leitner*, whom I am grateful for our numerous scientific joint-ventures and also for our great office atmosphere. Furthermore, I am grateful to *Dr. Luis Alvarez-Ruso* for our lively discussions, his guidance and refreshing direct nature. Thanks also to *Dr. Pascal Mühlich* for the fruitful physics collaboration and non-physics discussions. I am indebted to *Dr. Alexei Larionov* for our collaboration during the rewriting of the transport code and for all our physics discussions. Thanks to *Dr. Kai Gallmeister* for his superior hacking skills from which I greatly benefited. Thanks also to my short-time room mate *Dr. Thomas Falter* for participating in the rewriting of the simulation and for his Getränkekassen legacy. Furthermore, I am grateful to all present and former members of the GiBUU team, which have not been mentioned yet (in alphabetical order): *Dr. Theodoros Gaitanos, David Kalok, Dr. Murat Kaskulov, Dr. Olga Lalakulich, Birger Steinmüller and Janus Weil.* I am also indebted to all the *Giessen BUU alumni*, which put a lot of effort in the development of the predecessor BUU code. Special thanks to *Janus, Kai, Olga and Tina* for pointing out typos and complicated notations while proof reading this thesis.

As computing administrator of the institute, I wish to thank my predecessor *Dr. Frank Frömel* and my successor *Fabian Eichstädt* for the good & bad times we shared resolving software and hardware issues and *Prof. Dr. Horst Lenske* for backing us up. All three of them have contributed to a very nice and friendly working atmosphere. Thanks also to our nice institute's secretary *Elke Jung* for all the administrative work and her fight with bureaucracy, which I gladly never needed to enter myself.

I thank my experimental physics colleagues *Ralf Gregor, Dr. Igal Jaegle, Dr. Martin Kotulla, Prof. Dr. Bernd Krusche, Stefan Lugert, Prof. Dr. Volker Metag, Prof. Dr. Paolo Pedroni and Dr. David Trnka* for numerous constructive discussions. Furthermore, I acknowledge the friendly support by *Dr. Lothar Tiator* during the implementation of the MAID model within our transport model.

I benefited greatly from the friendly and also competitive atmosphere at our institute. Especially the shared experiences on several of our graduate school trips, the nice summer BBQs, the great gatherings at the Christmas and PhD parties, our weekly meetings of the institute's running team and last but not least the daily coffee chats made my life at the institute and in Giessen very enjoyable and entertaining. Thanks to all of you!

Special thanks and gratitude go out to *my family* for supporting me during all my studies and for giving me this great feeling of freedom and security no matter what the future might bring. And last but not least I thank *Ada* for the joy she is bringing into my life and her help during the proof reading procedure.

Contents

Chapter 1

Introduction

1.1 Survey and motivation

Within the last century our picture of matter changed drastically and has undergone several revolutionary steps in understanding. At the beginning of the 20th century one believed that atoms, which are the fundamental building blocks for solid-state physics, chemistry and biology, consisted of a homogeneous bulk of positively charged particles and therein embedded electrons having a size of roughly 10^{-10}m. This picture, proposed by Thomson in 1903, is also known as the ‘raisin-cake’ model. Then the ground-breaking experiments performed by E. Rutherford in 1911 led to the discovery of the atomic nucleus and made the physicists realize, that in fact most of the volume of a piece of ordinary matter is almost as empty as the outer space, and the atomic nucleus has only the size of several femtometers (10^{-15}m). Based upon innovative detection techniques, e.g. cloud chambers, the neutron was discovered by J. Chadwick in 1932, and both the muon (1937 by C.D. Anderson) and the pion (1947 by C.F. Powell) were detected within the cosmic radiation. Novel accelerator-driven experiments then led to the discovery of a whole zoo of particles, which could be understood and categorized in terms of composite particles built out of so-called quarks. Mesons, which are the lightest of such particles, are made up of a quark and an anti-quark, whereas the heavier baryons – such as the proton and the neutron – are composed of three quarks. These quarks could first be resolved in high energy electron scattering of protons, where one could infer their multiplicity within the proton from the measured form factors. Nowadays, one knows about three different elementary building blocks of matter. First there are the *quarks* which are confined within the hadrons and can not be isolated. The *leptons*, e.g. the electron and the neutrino, do not couple to the strong force, which binds the quarks, and interact only electromagnetically or via the weak force. The interactions themselves are mediated by *gauge bosons*: the strong one by the gluons, the weak one by the exchange of $W^{\pm}$ and Z^0 bosons and the electromagnetic interaction by the photon. The standard model of particles explains all performed measurements and ”stands triumphant” according to the Nobel prize winner F. Wilczek [Wil07]. However, there are several yet unresolved puzzles. Besides the major problem that astro-physical observations lead to the conclusion that only roughly 4% of all the energy density of the universe is given by baryonic matter and the rest by an unknown form of matter and energy, called dark energy ($\approx 76\%$) and dark matter ($\approx 20\%$) [Yao06], there are also major unknowns within the baryonic sector itself.

The standard model part dealing with the strong interaction of quarks, which are the building blocks of baryons, is the theory of Quantum-Chromo-Dynamics (QCD). While the interaction is weak for high momentum transfer, it is very strong for low momentum transfer such that standard perturbation theory does not succeed. Within the last decades, the speed-up of computer hardware opened a window to the strong coupling regime via the so-called lattice QCD (LQCD), which evaluates expectation values of QCD-operators on a space-time lattice. Another approach to the strong coupling regime is the so-called chiral perturbation theory (χPT), which may be

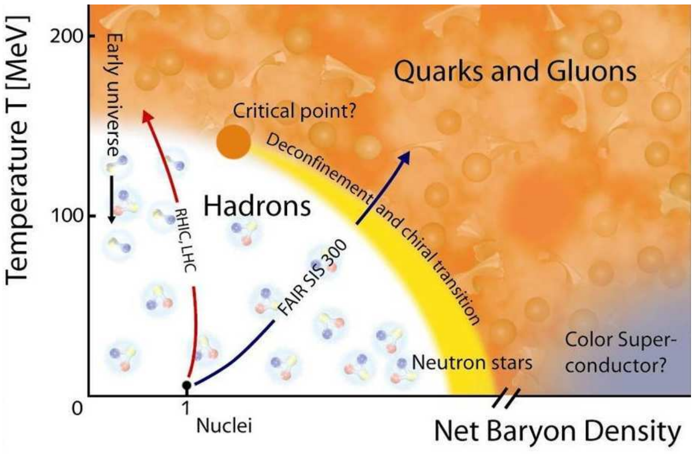

Figure 1.1: An artistic view of the QCD phase-diagram taken from [CBM08].

applied to low-momentum processes. For instance, the origin of hadron masses and the origin of the nucleon-nucleon force is presently addressed within both schemes[1].

Another line of research program is addressing the QCD phase diagram being sketched in fig. 1.1. At large temperature one expects a phase transition from the hadronic phase, in which quarks are confined in hadrons, to a deconfined phase where the quarks and gluons are liberated within a so-called Quark-Gluon-Plasma (QGP). To investigate this phase transition one collides heavy-ions, e.g. at RHIC [RHI08] or the upcoming LHC [LHC08] and FAIR [FAI08] facilities, to produce a dense and hot system of hadronic matter, which is expected to become so hot and dense that it enters the QGP phase. However, the complicated time dependence of the single-particle phase-space densities during these collisions complicates the disentanglement of different phenomena, such that the discovery of a QGP is still under debate. Besides the confinement-deconfinement phase transition one also expects a restoration of the so-called chiral symmetry within a hot and dense medium. In vacuum, this symmetry is both explicitly broken by the finite quark masses and spontaneously broken due to a non-vanishing expectation value of the $\langle \bar{q}q \rangle$ condensate. This $\langle \bar{q}q \rangle$ expectation value represents an order parameter for the spontaneous symmetry breaking and is expected to decrease by about 30% already at normal nuclear matter density [Dru90, Coh92, Bro96]. Thus signals for partial chiral symmetry restoration should be observable in nuclear reaction experiments and, in particular, photon induced processes are highly suited due to two key reasons. First, the reaction leaves the nucleus close to its ground state, so that it takes place under well-defined conditions. And as a second point, the photon penetrates deeply into the nucleus, giving rise to a high effective density. Especially the modification of the so-called σ or $f_0(600)$ meson inside the nuclear medium was proposed as a signal for such a partial symmetry restoration. Theoretical models predict a shift of its spectral strength to lower masses and a more narrow width due to the onset of the restoration [Ber87, Hat99]. The σ-meson is a very short-lived state with a width of roughly $600 - 1000$ MeV [Yao06], decaying predominantly into a $\pi\pi$ final state in S-wave. Hence the experimental aim has been to find modifications of this state in $\pi\pi$ production reactions in finite nuclear systems close to threshold. Such experiments have been performed with incident pions by the CHAOS collaboration [Bon96, Bon00] and with photons by the TAPS collaboration [Mes02, Blo07]. Both experiments have shown an accumulation of strength near the $\pi\pi$

---

[1] More details can be found in the recent review by W. Weise [Wei08b].

threshold in the decay channel of the σ in large nuclei. A possible interpretation of this effect is the in-medium modification of this resonance due to partial symmetry restoration, but also conventional final state interactions (FSI) must be treated properly. In general, final state effects play a major role in nuclear reactions. Particles being produced in nuclei, e.g. in $\gamma A \to \pi A'$ reactions, must transverse the nuclear medium on their way to the detector. Given the sizable interaction rates with the medium, the distortion of the particle tracks and also the absorption and charge exchange reactions lead to important modifications of the finally measured particle yields.

Within the exact QCD approximations of LQCD or χPT it is at present not feasible to address complex many-body reactions such as $\pi\pi$ production off nuclei or heavy-ion collisions, which leaves room for model building. In general, one must distinguish between processes which have a simple time-evolution of the involved phase-space densities, as for example a γA-reaction at low energies where the nucleus stays close to its ground state, from processes where the phase-space densities evolve rapidly in time as for the case of heavy ion-collisions. The first class of reactions can still be approximated within fully-quantum frameworks such as, e.g., distorted-wave (DWIA) or plain-wave impulse-approximations (PWIA) although these models generally lack coupled-channels features. In particular the commonly used DWIA and PWIA methods do usually not incorporate side-feeding from one channel to the other channel due to the complex implementation.

As an example for the second class of reactions, fig. 1.2 shows a typical time development for an almost central, high-energetic (40 A GeV) Calcium-Calcium collision. Besides the production of numerous new particles, one also notes that the initial nuclei undergo an almost complete break-up during the reaction. For such reactions involving rapidly changing phase-space densities far from equilibrium, the most general description in terms of quantum field theory is given by the so-called Kadanoff-Baym equation [Kad94], which simplifies under special assumptions (in particular small, slowly varying disturbances and Born approximation for the self energies) to the so-called Boltzmann-Uehling-Uhlenbeck (BUU) equation [Kad94, cf. especially section 9.2 therein]. The BUU equation is of semi-classical nature and describes the time-development of the so-called Wigner transform [Wig32], which represents a generalized phase-space density. Thus simulating the BUU equation one obtains a full space-time picture of the whole reaction process, and in particular one gets the phase-space densities of all involved particles as a function of time. Such BUU models were introduced for the simulations of heavy-ion collisions [Ber84, Ber88] starting in the beginning of the 1980's. In parallel also quantum-molecular-dynamics (QMD) models have been established, which propagate the particles in the simulations based on two-body and three-body forces instead of introducing mean fields like the BUU models. Nowadays, several groups are still actively developing new or improving well-known highly-complex transport models, some of the more prominent ones are e.g. the *Dubna/Moscow INC* [Ili97], *HSD* [Cas99, HSD08], *LAQGSM* [Mas05], *MCMC/MCEF* [Dep02], *RELDIS* [Psh05], *RQMD* [Fuc96, Gai05] and *URQMD* [Bas98, URQ08] models. The models differ in the included reaction mechanisms, in the multiplicity of particle species and, last but not least, in the numerical realization.

In 1986, the Giessen theory group started with the development of a first BUU-type model. Based on a rewrite of the original *Bertsch code* [Ber88], the rate for photon production in heavy-ion collisions was predicted [Bau86, Bau89]. While the code was originally designed for heavy-ion collisions [Cas90, Tei96, Hom98, Lar05], it was within the last decade also extended to become a state-of-the-art model for electron- and photon-induced reactions [Eff99a, Leh03, Fal04a, Gal05, Mü07]. For such rather elementary reactions, transport models compete with fully-quantum DWIA and PWIA calculations. However, transport models comprise the important full-coupled

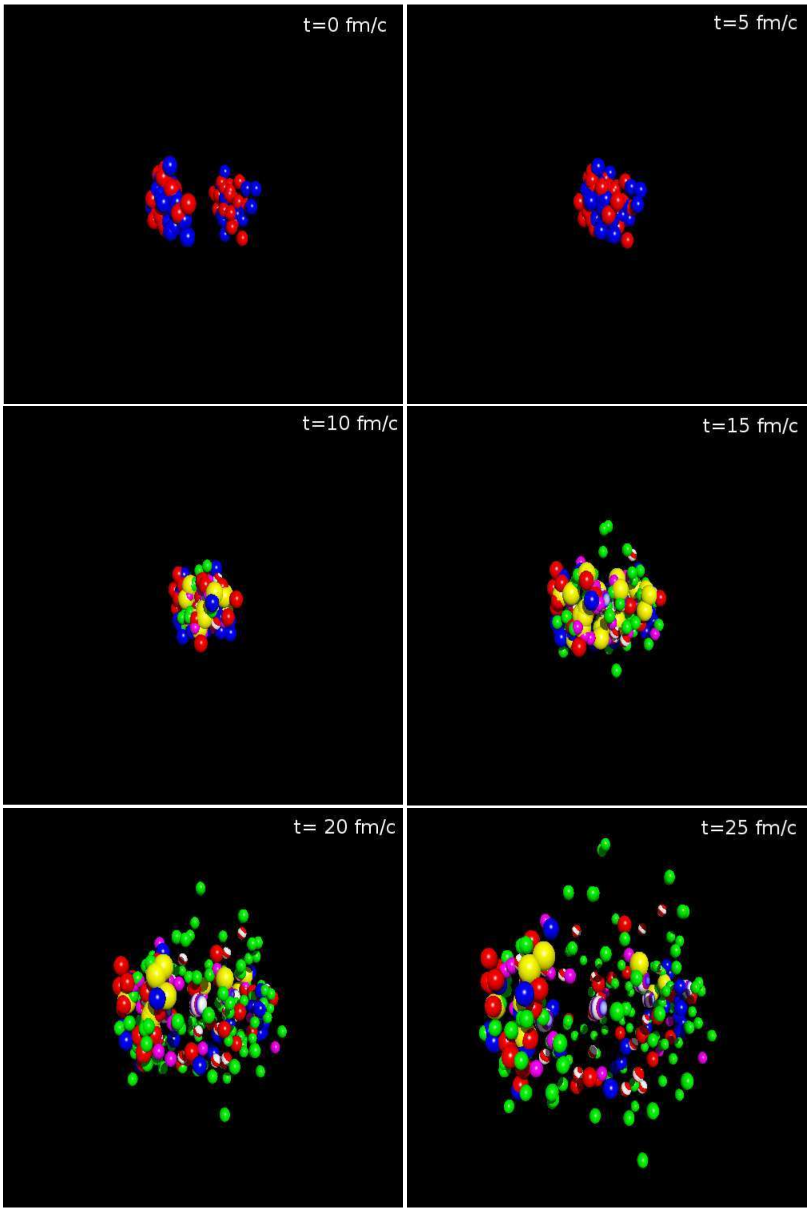

Figure 1.2: Time development of a Calcium-Calcium collision in a simplified simulation where each physical particle is represented by one sphere. The kinetic energy of the projectile is 40 A GeV. All pictures are taken in the CM-frame of the collision and the first time slice shows both Lorentz-contracted nuclei before the collision, the next time slices are given after 5 fm/*c*, 10 fm/*c*, 15 fm/*c*, 20 fm/*c* and 25 fm/*c*. Protons are depicted in blue, neutrons in red, non-exotic baryon resonances in yellow, exotic baryon resonances in white with blue/violet stripes, pions in green, exotic mesons in white with red stripes.

channel FSI-treatment which is not feasible in the other frameworks. Extending the BUU model to such reactions resulted in an universal field of application and the additional fact that the model has both been used for the description of very high-energy, e.g. [Lar05, Fal04c, Gal05], and low-energy processes, e.g. [Eng94, Mü04a], made it an outstanding model. Unfortunately, the fast development speed of the model was not accompanied by a change of the code infrastructure. So in 2004 several parallel branches of the source code co-existed and the source code structure had become highly involved hindering further developments. As a consequence, the GiBUU project was launched with the main intention to restructure and rewrite the original source code based on a modern multi-user software development environment, which guarantees an unified main branch, version control, proper documentation and multi-compiler compatibility.

The intention of this work comprises two major aspects. First it introduces to the new GiBUU model framework, emphasizing the physical inputs, the numerical realization and the new code management structure. Compared to the predecessor model version, major improvements have been realized. We enhanced the underlying resonance model by obtaining the real parts of the self-energies via a once-subtracted dispersion relation out of the imaginary parts, which leads to analytical self energies and restores the normalization of the spectral functions. The imaginary parts are now consistently obtained from the underlying collision rates as a function of four-momentum and density. The refined resonance model together with readjusted non-resonant background cross sections lead also to better elementary cross sections, which are needed as input for the BUU equations. Also the connection of the region of high-energies, which is described in the model based on Pythia [pyt07], to the low-energy region, where the cross sections are based on the resonance model, has been enhanced by implementing event-mixing of both the string and the resonance model in a cross-over energy regime. Concerning algorithm development, we implemented for the first time the local-ensemble-algorithm [Lan93] such that this work presents mostly results obtained in a full-ensemble test-particle scheme. All results obtained with the predecessor model relied on the parallel-ensemble approximation, which introduces large non-localities in the scattering processes. Both the dependence on the time-step and the dependence on the position grid, which stores the densities for the mean fields, have been reconsidered and improved. Thanks to the new code management, it is now possible that at present eight physicists (five Post-Doc's, two Phd- and one Diploma-student[2]) work in parallel on the project boosting its development speed and its reliability. After improving the code structure and supplemented with a proper documentation, we also published the model source code under the GPL license on our website [GiB08b].

The second major aspect of this thesis is the analysis of photon, electron and pion induced nuclear reactions in the resonance-energy region. Based on the work presented in [Mü06a], an improved analysis of the $\pi\pi$ experiment by the TAPS collaboration [Mes02, Blo07] is performed. Simulating this reaction involves the treatment of low-energy pions with kinetic energies down to 20 MeV. Therefore, one first needs to validate the treatment of such pions having a long wavelength in a semi-classical transport picture. This key question is addressed by a comparison to quantum calculations and experimental data on pion-nucleus scattering, and the model treatment of the $\pi\pi$ final state is thereby evaluated. In the course of these studies major approximations on the numerical realization and their impact on observables are investigated. We find a very good description of available data on pion absorption, pion single-charge exchange and double-charge exchange (DCX) in the kinetic energy regime of $30 - 200$ MeV. Thereby our work extends and improves the work of Engel *et al.* [Eng94] for lower pion energies. The DCX process is found to have high sensitivity on model details and represents a strong model benchmark.

---

[2] cf. our website [GiB08b] for a complete list of project members

We achieved considerable improvements compared to earlier microscopic works [Hüf79, Vic89]. The physics of DCX shows also surprises: according to our model it is a interesting cancellation of Coulomb effects and neutron skins, which allows for a scaling of the cross section according to naive expectations [Gra89]. A comparison of full and parallel ensemble runs shows visible differences in the physical results, such that we conclude that the parallel ensemble approximation should be avoided in future works. For the photon-induced $\pi\pi$-production we investigate closely the present situation on the elementary data, before analyzing the nuclear data. We show that the process is highly influenced by final-state processes which lead to rescattering, absorption and charge exchange of the pions. It is concluded that, given the present data and theory uncertainties, the influence of final-state processes and the influence of chiral symmetry restoration can not be disentangled. We also present a new treatment of electron and photon scattering off nuclei. The initial $\gamma^\star$N vertex is treated with full in-medium kinematics and we investigate the impact of in-medium potentials and in-medium spectral functions on inclusive and single-π-production experiments. The importance of a momentum-dependent nucleon potential is emphasized and we obtain good results for inclusive electron scattering off nuclei. Adressing neutral pion production in the energy regime of $0.25 - 0.8$ GeV, we achieve a proper description for the quasi-free production mechanism. Beyond its general interest, these studies serve as a benchmark for ν-induced processes, which are performed using the very same model basis by Leitner *et al.* [Lei06b, Lei06a]. Last but not least, the description of elementary reactions serves as a testing-ground of model details important also for the complex heavy-ion reactions.

1.2 Overview and chapter abstracts

This work is structured into two major parts. Part I, which comprises chapters 2-5, deals with the Giessen Boltzmann-Uehling-Uhlenbeck transport model and details the treatment of electron- and photon-induced processes within the model. Thereafter, we present results on pion–, electron– and photon–induced reactions. The following list of abstracts gives a short summary for each of the sections and emphasizes its scope. Technical details have partially been shifted to the appendix to facilitate the readability - especially the details on the source code structure and management can be found there.

Chapter 2: Transport theory The theoretical basis for the non-equilibrium processes is summarized and the concept of the BUU approximation is introduced. This chapter emphasizes the numerical solution of the BUU equation and is especially intended to give a comprehensive overview on the derivation of the algorithms. In particular, it is intended for those readers, which later also want to work on the source code and which are interested in the foundation of the algorithms therein. Different methods for the implementation of the collisions among particles are presented and their pros and cons are discussed.

Chapter 3: GiBUU model This chapter introduces the reader to details specific to the GiBUU model. After a short historical detour, the implemented particle species and their couplings are discussed. The resulting imaginary parts of the self-energies and the derivation of the real parts via dispersion relations are detailed. In the end, we present benchmarks for off-shell propagation of resonances.

Chapter 4: Interaction of electrons and photons with nucleons Based on the MAID model for photon-nucleon interactions, we introduce pion and resonance production in electron- and photon-nucleon scattering. The elastic scattering of virtual photons and nucleons is treated using the latest form factor parametrizations based on recent Jefferson-Lab data.

Chapter 5: Interaction of electrons and photons with nuclei This chapter generalizes the elementary cross sections presented in chapter 4 to the case that the target nucleon is embedded in a nuclear medium. Therefore, the kinematics are revisited and the modeling of in-medium form factors is addressed. Finally, the nuclear cross sections and the implementation in the GiBUU framework are specified.

Chapter 6: Pion induced reactions Results on pion scattering off nuclei are presented. After discussing the pion mean free path within our model and comparing simulations for pion absorption to data, we primarily address the double-charge exchange process, which serves as a strict model benchmark. In the course of this chapter we investigate numerical approximations to the collision term and evaluate their impact on the observables. Thereby it is shown that the full ensemble method is superior to the parallel ensemble method. We achieve good agreement with the available data in the regime of $30 - 200$ MeV kinetic energy.

Chapter 7: Electron and photon induced reactions Inclusive electron and photon scattering off nuclei is addressed and a good description of existing data is obtained. The role of a momentum-dependent mean field is emphasized and the impact of different model ingredients is investigated. Finally, we present simulations for photon-induced pion production.

Chapter 8: Double pion photo-production This chapter is devoted to photon-induced $\pi\pi$ production off nucleons and nuclei. After a survey on the available data for the elementary reaction, we analyze the implications of nuclear corrections on the extraction of the neutron data from the deuteron data. It is concluded that only a minor impact of such corrections has to be expected. Finally, we address $\pi\pi$ production off complex nuclei and outline the dominant role of final-state interactions on the resulting spectra.

Appendices Appendix A and B comprise explicit details, parameters and cross section parametrizations used in the GiBUU model. Appendix C focuses on technical details related to the source code infrastructure, e.g. directory structure, version control, license issues and the documentation style. Appendix D gives explicit cross sections for quasi-elastic electron-nucleon scattering, Appendix E details the derivation of the resonance form-factors out of the helicity amplitudes. In Appendix F the connection of hadron tensor and virtual photon cross sections for pion production is summarized. Appendix G contains useful formulas concerning the kinematics of electron-nucleon scattering.

1.3 Units and conventions

Throughout this thesis, a unit system in which $\hbar = c = 1$ is used. Time and length, energy and momentum, respectively, share the same units. The energy/momentum unit is given by the inverse of the length/time unit,

$$[time] = [length] = [energy]^{-1} = [momentum]^{-1} \quad .$$

For our applications, it is customary to choose electron charge times Volt (eV) as a measure of energy, especially MeV $= 10^6$ eV and GeV $= 10^9$ eV. For conversion to the SI system, the following relations are most useful [Yao06]:

$$\begin{aligned} 0.1973269631(49)\ \text{GeV fm} = 197.3269631(49)\ \text{MeV fm} \approx \quad \hbar c &= 1 \quad , \\ 299.792458 \times 10^{21}\ \text{fm/s} = \quad c &= 1 \end{aligned}$$

with 1 fm = 10^{-15} m. Cross sections are conventionally measured in units of barns where

$$1 \text{ barn} = 1 \text{ b} = 10^{-28} \text{ m}^2 = 100 \text{ fm}^2 \Rightarrow 1 \text{ fm}^2 = 10 \text{ mb} \quad .$$

The definitions of the γ-matrices and the Dirac spinors are chosen according to Bjorken and Drell [Bjo93], i.e. the normalization condition for a Dirac-spinor u is given by

$$\bar{u}(p,s)u(p,s) = 1 \quad . \tag{1.1}$$

Three-vectors are in general denoted with a vector sign, e.g. $\vec{r}$, while four-vectors are given by $r = (r_0, \vec{r})$.

1.4 Constants

The following constants are frequently used throughout this work:

	Value			
nuclear matter density	ρ_0	=	0.168 fm^{-3}	
charge averaged nucleon mass	m_N	=	0.938 GeV	
electron charge	e	=	$1.602176487(40) \times 10^{-19}$ C	[Yao06]
electron mass	m_e	=	0.510998910(13) MeV	[Yao06]

Part I

The GiBUU transport model

Chapter 2

Transport theory

OVERVIEW: This chapter introduces the concept of non-equilibrium transport comprising details on the Boltzmann-Uehling-Uhlenbeck (BUU) equation and its numerical realization in terms of test-particles.

2.1 Introduction

In the most general context, the theory of transport describes non-equilibrium processes. There are various applications for such a theory which vary both in time and length scales, e.g. bursts of super-novas, traffic jams on highways or nucleus-nucleus collisions. Such transport processes are classified according to the mean free paths of the participating scattering centers and the extension of their wave packages relative to the inter-particle spacings. The flow of classical particles, which have a negligible wave-length, can be successfully described applying either the *Boltzmann equation* in case of a finite mean free path (e.g. gas particles within a neon bulb) or the *Navier-Stokes equations*[1] for negligible mean free path (e.g. within classical fluids). At short length scales, one must, additionally, consider quantum mechanical effects. In the language of quantum field theory (QFT), the most general description is given by the *Kadanoff-Baym equation* which simplifies under special assumptions (in particular small, slowly varying disturbances and Born approximation for the self energies) to the *Boltzmann-Uehling-Uhlenbeck (BUU) equation* [Kad94, cf. especially section 9.2 therein]. In this work we want to describe nuclear reactions based on BUU and want to simulate within this framework the flow of hadronic phase-space densities, i.e. the transport of hadrons, through space and time. For such a treatment, which has a quite some tradition since already in the 1980's one started solving the BUU equation for hadronic flows [Ber84, Bau86, Ber88], there exist within the hadron physics community two widely used numerical schemes: the *parallel ensemble method* employed in the BUU models [Aic85, Bau86, Ber88, Cas90] and in the Vlasov-Uehling-Uhlenbeck model [Mol85]; and the *full ensemble method* used in the Landau-Vlasov [Gre87], Boltzmann-Nordheim-Vlasov [Bon89, Bon94] and Relativistic BUU [Fuc96, Gai05] models. Both schemes are based on the so-called test-particle representation of the single-particle phase space density, but they differ in the locality of the scattering processes (cf. discussion in [Wel89, Lan93]).

The major topic of this chapter is the BUU equation. Since there exists already a wealth of literature concerning BUU (e.g. [Ueh33, Ber84, Ber88, Kad94, Eff99a, Leu00, Juc03]), we will only emphasize the most relevant issues. Hereby we will mainly focus on the test-particle ansatz as a method to numerically solve the BUU equation and the primary intention is to clarify the links between the *real* BUU equation and the test-particle algorithms. We address mean field propagation, simulation of decay processes, two- and three-body reactions using this ansatz.

---

[1] cf. discussion of Uhlenbeck in [Coh73] and references therein for the connection of the Boltzmann and Navier-Stokes equation via the Chapman-Enskog expansion

In the discussion of the two-body reactions, both the full ensemble and the parallel ensemble schemes are introduced and their limiting behaviors are investigated.

2.2 BUU equation

A detailed derivation of the BUU equation based on non-equilibrium QFT is given, e.g., in the didactic book by Kadanoff and Baym [Kad94]. Concerning the subtle issue of transporting resonances, i.e. unstable particles, one finds in [Eff99a, Leu00, Juc03] the derivation of the generalized BUU equation which also holds for particles with non-vanishing widths. Lehr [Leh03] confronts the rigorous results of Leupold [Leu00] with the so-called *off-shell potential* (OSP) ansatz introduced by Effenberger *et al.* [Eff99b, Eff99a]. It is shown that the OSP ansatz is within low-density approximation ($\Gamma \sim \rho$) in good agreement with the full solution according to [Leu00]. Furthermore, Lehr performed an explicit comparison of particle trajectories, evaluated within OSP and using the relativistic BUU version derived by Juchem *et al.* [Cas00, Juc03], which show for our practical purposes only negligible differences. As a pragmatic approach, we start out directly with the formulation of BUU according to the OSP ansatz. Hence the term 'BUU equation' will in the following always refer to the generalized off-shell version as presented by Effenberger [Eff99b, Eff99a]. The BUU equation comprises a series of coupled differential equations, which describe the time evolution of the Wigner transforms [Wig32] of the real time Green's functions

$$\bar{g}_i^<(r,p) = \pm i \int d^4y e^{ipy} \underbrace{\pm \frac{1}{i} \left\langle \Psi_i^\dagger(r - \frac{y}{2}) \Psi_i(r + \frac{y}{2}) \right\rangle}_{=g_i^<(r+\frac{y}{2}, r-\frac{y}{2})} \tag{2.1}$$

and

$$\bar{g}_i^>(r,p) = i \int d^4y e^{ipy} \underbrace{\left\langle \frac{1}{i} \Psi_i(r + \frac{y}{2}) \Psi_i^\dagger(r - \frac{y}{2}) \right\rangle}_{=g_i^>(r+\frac{y}{2}, r-\frac{y}{2})} \quad , \tag{2.2}$$

which depend on the 8-dimensional phase space point (r, p). In the definitions above, Ψ_i denotes the field operator of the ith particle species. Here and in the following the upper sign corresponds to bosons, the lower sign to fermions. The factors in front of the integrals are chosen such that $\bar{g}_i^>(r,p)$ and $\bar{g}_i^>(r,p)$ are real non-negative quantities. The quantity $\bar{g}_i^<$ has the interpretation of a generalized particle phase-space density, whereas $\bar{g}_i^>$ represents a generalized density of holes in phase-space. The time evolution of these quantities is governed by the BUU equation

$$\left[p_0 - H_i, \bar{g}_i^<\right]_P + \underbrace{\left[\mathrm{Re}(g_i), \Sigma_i^<\right]_P}_{=\mathrm{A}_{\text{off-shell}}} = \underbrace{-\Sigma^> \bar{g}_i^< + \Sigma_i^< \bar{g}_i^>}_{=\mathrm{I}_{\text{coll}}} \quad , \tag{2.3}$$

where we have used the Poisson brackets

$$[a, b]_P = \frac{\partial a}{\partial p_\mu} \frac{\partial b}{\partial x^\mu} - \frac{\partial a}{\partial x_\mu} \frac{\partial b}{\partial p^\mu} \quad . \tag{2.4}$$

The $\Sigma^{\lessgtr}$ stand for loss and gain terms of the phase space densities and H_i represents the Hamilton function of the ith particle species. The variable g_i in eq. 2.3 denotes the retarded Green's function. Its imaginary part is given by

$$\mathrm{Im}(g_i) = \frac{1}{2}\left(\bar{g}_i^{>} \mp \bar{g}_i^{<}\right) \quad . \tag{2.5}$$

Since g_i is analytic, its real part can be reconstructed out of the imaginary part by dispersion relations. However, $\mathrm{Re}(g_i)$ has not to be evaluated since the second term on the LHS of eq. 2.3, which we denote $A_{\text{off-shell}}$, is neglected within the OSP ansatz. Its effects are simulated by an extra-term in the equations of motion for the test-particles, which will be detailed in section 2.4 (for further details see also [Leh03]). For later usage, we also want to define the *Vlasov equation*, which is a limiting case of the BUU equation in which $\Sigma_i^{>} = \Sigma_i^{<} = 0$:

$$\left[p_0 - H_i, \bar{g}_i^{<}\right]_P = 0 \quad . \tag{2.6}$$

The single-particle Hamilton function for the ith particle species is chosen in relativistic form and given by

$$H_i = \sqrt{(m_i + U_i(r,p))^2 + (\vec{p} - \vec{A}_i(r,p))^2} + A_i^0 \quad , \tag{2.7}$$

where m_i denotes the pole mass of the i-th particle species. It must be emphasized that the Hamilton function of the particle species and the phase space variable p_0 are distinct entities, in particular it is important to note that the Hamilton function may also explicitly depend on p_0. The function $U_i(r,p)$ denotes a scalar and $A_i^{\mu}(r,p)$ a vector Hartree-Fock-like mean-field potential, which are in the general both functions of r and p, i.e. position, time, momentum and energy. These mean fields may in principle depend upon the phase-space densities of all other particle species, such that the differential equations 2.3 are already coupled through the mean fields. Besides the Hamilton function, a further coupling of the particle species comes in through the so-called *collision term*

$$I_{\text{coll}}(r,p) = -\Sigma_i^{>}(r,p)\bar{g}_i^{<}(r,p) + \Sigma_i^{<}(r,p)\bar{g}_i^{>}(r,p) \quad , \tag{2.8}$$

which includes all kind of scattering processes. For this we consider resonance decays, two-body and three-body interactions (e.g. $NN\pi \to NN$), but higher correlations with more than three involved particles (e.g. $NNN\pi \to NNN$) are neglected. While the first term in I_{coll} represents a loss of particles at the generalized phase space point $(\vec{r},p)$ at time t, the second term is a gain term due to strength being scattered into this generalized phase space element. As we will see in the upcoming sections, the evaluation of this collision term is the most demanding task in the numerical realization of the model.

2.2.1 Initial conditions

The BUU differential equation is a first order differential equation in time, so we need as initial conditions the distribution functions $\bar{g}_i^{<}(\vec{r},t=0,p)$ and $\bar{g}_i^{>}(\vec{r},t=0,p)$ for all species i at time t=0. In our approach, we rewrite the whole problem with the help of the *spectral function*

$$\mathcal{A}_i(r,p) = \bar{g}_i^{>}(r,p) \mp \bar{g}_i^{<}(r,p) \quad . \tag{2.9}$$

We assume that there is a function $f(\vec{r},t,\vec{p})$ which can be considered as a phase space distribution function and fulfills

$$\begin{aligned} \bar{g}_i^{<}(r,p) &= f_i(\vec{r},t,\vec{p})\mathcal{A}_i(r,p) & (2.10)\\ \bar{g}_i^{>}(r,p) &= \left(1 \pm f_i(\vec{r},t,\vec{p})\right)\mathcal{A}_i(r,p) \quad . & (2.11) \end{aligned}$$

Within this assumption, the problem is fully solvable if the initial conditions $f_i(\vec{r},t=0,\vec{p})$ and $\mathcal{A}_i(\vec{r},t=0,p)$ are known.

The spectral function In [Leu00, Leu05] it has been shown that for the BUU equation the spectral function of a particle with four-momentum p is given by[2]

$$\mathcal{A}_i(p,r) = \frac{1}{\pi} \frac{-\mathrm{Im}\Pi_i(p)}{(p^2 - m_i^2 - \mathrm{Re}\Pi_i(p))^2 + (\mathrm{Im}\Pi_i(p))^2} \quad , \tag{2.12}$$

with the self energy $\Pi_i(E,\vec{p})$. The imaginary part of the self-energy is induced by the collision term

$$\mathrm{Im}\left[\Pi_i\right] = -\sqrt{p^\mu p_\mu}\left(\Sigma_i^> - \Sigma_i^<\right) \quad , \tag{2.13}$$

and the real part Re $\left[\Sigma_i^{coll}\right]$ can be derived via dispersion relations. Using a subtraction constant, also mean field contributions can be incorporated – this topic will be addressed in detail in sec. 3.7. The spectral function is normalized by the following integral relation

$$\int_0^\infty dp^0 \left\{2p^0 \mathcal{A}(p^0,\vec{p})\right\} = 1 \quad . \tag{2.14}$$

2.3 Test-particle ansatz

For simplicity and the virtue of a shorter notation, we consider in the following only one particle species. Therefore, the corresponding index i denoting the species is suppressed. The generalization to a finite number of particle species is however straightforward. The BUU equation can be solved numerically using the so-called test-particle ansatz. The phase-space density is expressed in terms of δ-functions

$$\bar{g}^<(\vec{r},t,p) = \lim_{n(t)\to\infty} \frac{(2\pi)^4}{N} \sum_{j=1}^{n(t)} w_j \;\; \delta(\vec{r}-\vec{r}_j(t))\delta(\vec{p}-\vec{p}_j(t))\delta(p^0 - p_j^0(t)) \quad , \tag{2.15}$$

with the weights w_j (while w_j may in general have arbitrary values we will later restrict it to the integer values $\{-1,0,1\}$). The function $n(t)$ denotes the number of test-particles at time t. This number varies in time due to collisions which lead to loss or gain in the phase space densities which is reflected by fluctuating number of test-particles. At starting time one sets $w_j = 1 \;\forall\; i$ and $n(0) = A \times N$ where A denotes the number of physical particles and N is the number of ensembles, i.e. the number of test-particles per physical particle. Thus the single-particle phase-space distribution is interpreted as a sum of all test-particle densities. Note, that we allow for a fluctuating number of test particles per time and changing positions and momenta of these test-particles. However, we restrict our distribution function to a sum of δ function products.

2.3.1 Solving the BUU equation via test-particles

To solve the BUU equation we first isolate the time dependence in eq. 2.3 with $A_{\text{off-shell}} = 0$ according to the OSP ansatz

$$\begin{aligned} -\Sigma^>\bar{g}^< + \Sigma^<\bar{g}^> &= \left[p_0 - H, \bar{g}^<\right]_P \\ &= \frac{\partial(p_0 - H)}{\partial p_\mu}\frac{\partial \bar{g}^<}{\partial x^\mu} - \frac{\partial(p_0 - H)}{\partial x_\mu}\frac{\partial \bar{g}^<}{\partial p^\mu} \\ &= \left(1 - \frac{\partial H}{\partial p_0}\right)\frac{\partial \bar{g}^<}{\partial t} + \frac{\partial H}{\partial \vec{p}}\frac{\partial \bar{g}^<}{\partial \vec{x}} - \frac{\partial H}{\partial \vec{x}}\frac{\partial \bar{g}^<}{\partial \vec{p}} + \frac{\partial H}{\partial t}\frac{\partial \bar{g}^<}{\partial p^0} \quad . \end{aligned} \tag{2.16}$$

---

[2] We prefer to have the factor π in the definition to simplify the normalization condition.

We get

$$\frac{\partial \bar{g}^<}{\partial t} = \frac{1}{1-\frac{\partial H}{\partial p_0}}\left(-\frac{\partial H}{\partial \vec{p}}\frac{\partial \bar{g}^<}{\partial \vec{x}} + \frac{\partial H}{\partial \vec{x}}\frac{\partial \bar{g}^<}{\partial \vec{p}} - \frac{\partial H}{\partial t}\frac{\partial \bar{g}^<}{\partial p^0} - \Sigma^>\bar{g}^< + \Sigma^<\bar{g}^>\right) \quad . \tag{2.17}$$

Let us now assume that $n(t) > n(t')$ for $t > t'$ [3]. We discretize the problem introducing a finite time step size Δt

$$\begin{aligned}
\frac{\partial \bar{g}^<}{\partial t} &= \frac{\bar{g}^<(t+\Delta t,\vec{r},\vec{p}) - \bar{g}^<(t,\vec{r},\vec{p})}{\Delta t} && (2.18)\\
&= \frac{1}{\Delta t}\frac{(2\pi)^4}{N}\sum_{j=n(t)+1}^{n(t+\Delta t)} w_j\,\delta(\vec{r}-\vec{r}_j(t+\Delta t))\delta(\vec{p}-\vec{p}_j(t+\Delta t))\delta(p^0-p^0_j(t+\Delta t)) \\
&\quad +\frac{(2\pi)^4}{N}\sum_{j=1}^{n(t)}\frac{1}{\Delta t}\left[w_j\,\delta(\vec{r}-\vec{r}_j(t+\Delta t))\delta(\vec{p}-\vec{p}_j(t+\Delta t))\delta(p^0-p^0_j(t+\Delta t))\right. \\
&\quad \left. -w_j\,\delta(\vec{r}-\vec{r}_j(t))\delta(\vec{p}-\vec{p}_j(t))\delta(p^0-p^0_j(t))\right] && (2.19)\\
&= \frac{1}{\Delta t}\frac{(2\pi)^4}{N}\sum_{j=n(t)+1}^{n(t+\Delta t)} w_j\,\delta(\vec{r}-\vec{r}_j(t))\delta(\vec{p}-\vec{p}_j(t))\delta(p^0-p^0_j(t)) \\
&\quad +\frac{(2\pi)^4}{N}\sum_{j=1}^{n(t)}\frac{\partial}{\partial t}\left[w_j\,\delta(\vec{r}-\vec{r}_j(t))\delta(\vec{p}-\vec{p}_j(t))\delta(p^0-p^0_j(t))\right] \quad . && (2.20)
\end{aligned}$$

If the test-particles $1\ldots n(t)$ obey the equations of motion

$$\begin{aligned}
\frac{\partial \vec{r}_j}{\partial t} &= \frac{1}{1-\frac{\partial H}{\partial p_0}}\frac{\partial H}{\partial \vec{p}} \quad , && (2.21)\\
\frac{\partial \vec{p}_j}{\partial t} &= -\frac{1}{1-\frac{\partial H}{\partial p_0}}\frac{\partial H}{\partial \vec{r}} \quad , && (2.22)\\
\frac{\partial p^0_j}{\partial t} &= \frac{1}{1-\frac{\partial H}{\partial p_0}}\frac{\partial H}{\partial t} \quad , && (2.23)
\end{aligned}$$

then we obtain

$$\begin{aligned}
&\frac{(2\pi)^4}{N}\sum_{j=1}^{n(t)}\frac{\partial}{\partial t}\left[w_j\,\delta(\vec{r}-\vec{r}_j(t))\delta(\vec{p}-\vec{p}_j(t))\delta(p^0-p^0(t))\right] \\
&= \frac{1}{1-\frac{\partial H}{\partial p_0}}\left(-\frac{\partial H}{\partial \vec{p}}\frac{\partial \bar{g}^<(t,\vec{r},\vec{p})}{\partial \vec{x}} + \frac{\partial H}{\partial \vec{x}}\frac{\partial \bar{g}^<(t,\vec{r},\vec{p})}{\partial \vec{p}} - \frac{\partial H}{\partial t}\frac{\partial \bar{g}^<}{\partial p^0}\right) \quad . && (2.24)
\end{aligned}$$

It has to be emphasized that the position, time and energy dependence of the Hamiltonian

---

[3] This is no limitation to the general case since one might also introduce new test-particles with a negative weight ($w_j = -1$) to cancel old test-particles. In this way the effective number of test-particles may still stay constant or even decrease.

introduced in eq. 2.7 is fully given by the potentials $U(r,p)$ and $A(r,p)$. Using the latter identity 2.24 and eq. 2.20 within eq. 2.17, we get an expression for the newly produced test-particles

$$\begin{aligned}
&\frac{1}{\Delta t}\frac{(2\pi)^4}{N}\sum_{j=n(t)+1}^{n(t+\Delta t)} w_j\, \delta(\vec{r}-\vec{r}_j(t+\Delta t))\delta(\vec{p}-\vec{p}_j(t+\Delta t))\delta(p^0-p^0_j(t+\Delta t)) \\
&= -\Sigma^{>}\bar{g}^{<}(\vec{r},t,\vec{p}) + \Sigma^{<}\bar{g}^{>}(\vec{r},t,\vec{p}) \quad . \qquad (2.25)
\end{aligned}$$

Henceforth the collision term is considered as a source and sink term for new test-particles. In other words, the loss term generates test-particles with negative weight and the gain term generates test-particles with positive weight. We introduce the abbreviation

$$\begin{aligned}
\bar{g}^{>,\Delta t}(\vec{r},t,\vec{p}) &= \left.\bar{g}^{>}(\vec{r},t,\vec{p})\right|_{\text{test-particles propagated for}\Delta t \text{ according to 2.21-2.23}} \\
&= \frac{(2\pi)^4}{N}\sum_{j=1}^{n(t)} w_j\, \delta(\vec{r}-\vec{r}_j(t+\Delta t))\delta(\vec{p}-\vec{p}_j(t+\Delta t))\delta(p^0-p^0_j(t+\Delta t)) \qquad (2.26)
\end{aligned}$$

Let us summarize the above considerations: if we know the distribution function at time t, then we can construct the distribution function at a later time $t+\Delta t$ via

$$\begin{aligned}
&\bar{g}^{>}(t+\Delta t,\vec{r},\vec{p}) \\
&= \bar{g}^{>,\Delta t}(t,\vec{r},\vec{p}) + \Delta t\left(-\Sigma^{>}\bar{g}^{<}(t,\vec{r},\vec{p}) + \Sigma^{<}\bar{g}^{>}(t,\vec{r},\vec{p})\right) + \mathcal{O}((\Delta t)^2) \\
&= \bar{g}^{>,\Delta t}(t,\vec{r},\vec{p}) + \Delta t\left(-\Sigma^{>}\bar{g}^{<,\Delta t}(t,\vec{r},\vec{p}) + \Sigma^{<}\bar{g}^{>,\Delta t}(t,\vec{r},\vec{p})\right) + \mathcal{O}((\Delta t)^2) \quad . \qquad (2.27)
\end{aligned}$$

The last two lines differ only by terms proportional $\mathcal{O}((\Delta t)^2)$, which we neglect anyhow. The equation 2.27 basically defines the algorithm to be used: propagate the test-particles according to the equations of motions and introduce new test-particles or delete old test-particles (via new test-particles with negative weight) according to the collision term.

2.4 Simulating the off-shell term

Fig. 2.1 visualizes our understanding of a so-called *broad* particle: a broad particle has a finite lifetime caused either by collisions or decay of the particle; the non-vanishing probability for such collisions or decays leads to a non-vanishing imaginary part of the self-energy Π. Consequently the spectral function $\mathcal{A}(r,p)$ introduced in eq. 2.12 (depicted by the dashed line in fig. 2.1) has not only strength at the pole of the denominator of eq. 2.12

$$p^2 = m^2_{\text{pole}} = m^2 + \mathrm{Re}\Pi(p) \quad , \qquad (2.28)$$

but also at other values of p^2 (m is the vacuum pole mass of the particle species). This strength, which is not situated at the pole-mass, is called off-shell strength, or *off-shellness*, of the particle. Contrary to the broad particle, a *stable* particle has infinite lifetime and the imaginary part of its self-energy vanishes. Its spectral function is, consequently, a δ-function diverging at the pole-mass as shown by the solid line in fig. 2.1.

The relation

$$f_i(\vec{r},t,\vec{p})\mathcal{A}_i(r,p) \quad = \bar{g}^{<}_i(r,p) = \lim_{n(t)\to\infty}\tfrac{(2\pi)^4}{N}\textstyle\sum_{j=1}^{n(t)} w_j \;\; \delta(\vec{r}-\vec{r}_j(t))\delta(\vec{p}-\vec{p}_j(t))\delta(p^0-p^0_j(t))$$

connects a spread of the spectral function $\mathcal{A}$ as a function of $(p^\mu p_\mu)^{1/2}$ to the fact that the test-particles must also have different $((p_j)^\mu(p_j)_\mu)^{1/2} = ((p^0_j)^2-(\vec{p}_j)^2)^{1/2}$. The broadness of a

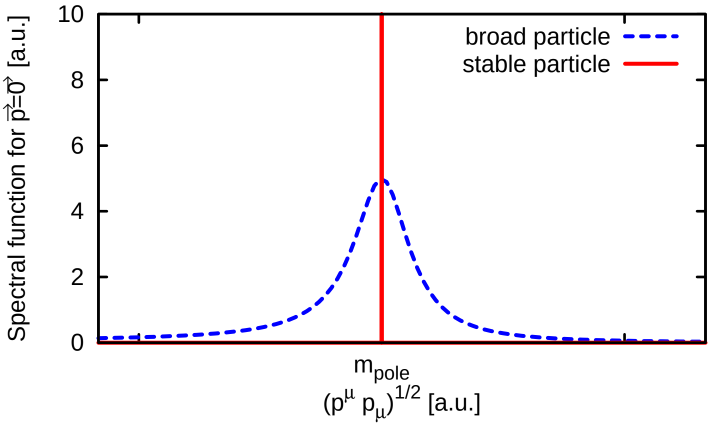

Figure 2.1: Spectral function of a *broad* and *stable* particle with same pole mass $m_{\text{pole}} = m^2 + \text{Re}\Pi(p)$, where m is the vacuum pole mass, as a function of $\sqrt{p^\mu p_\mu}$ at fixed momentum $\vec{p} = 0$.

spectral function, i.e. the value of ImΠ, varies when, e.g., a particle travels from high to low density since at low densities the collision rate is different and, therefore, the imaginary part of the self-energy is modified. This change in the spectral function must be accommodated by a change of the test-particle $((p_j)_\mu (p_j)^\mu)^{1/2}$ in time. However, in eqs. 2.21-2.23 the test-particle motion is so far only influenced by the mean fields U and A but not by a change of ImΠ. To include this effect, we introduce the off-shell potential ansatz. It is used throughout this work and was developed by Mosel and Effenberger [Eff99a]. In their formalism the Hamiltonian is first reformulated (cf. eq 2.7) in terms of a scalar potential V which may depend on position and momentum

$$H = \sqrt{(m+U)^2 + (\vec{p} - \vec{A})^2} + A^0 \equiv \sqrt{(m+V)^2 + \vec{p}^2} \quad . \tag{2.29}$$

Let us consider the jth test-particle for which a so-called off-shellness $\Delta\mu_j$ is defined which fulfills

$$\sqrt{p_j^2} = \underbrace{V + m}_{\text{In medium pole mass}} + \Delta\mu_j \quad . \tag{2.30}$$

Note that the scalar potential at the pole mass can also be connected to the self energy via eq. 2.28

$$(V + m)^2 = m^2 + \text{Re}\Pi \quad . \tag{2.31}$$

Since $\sqrt{p_j^2}$ is the full mass of the test-particle, the *off-shellness* is basically the difference between the in-medium pole mass of the particle species and the test-particle mass. According to this definition, the energy of the test-particle is given by [4]

$$p_j^0 = \sqrt{(V + m + \Delta\mu_j)^2 + \vec{p}^{\,2}} \quad . \tag{2.32}$$

In the full Kadanoff-Baym approach, the term $A_{\text{off-shell}}$, which was introduced in eq. 2.3, has a profound impact on the time development of the off-shellness. Since we neglected this

---

[4] Note that $p_j^0 = H$ only if $(p_j)^\mu (p_j)_\mu = m_{\text{pole}}^2$, but in general $p_j^0 \neq H$.

term, we must regulate the off-shellness by hand. In particular, we want the mass of an in-vacuum stable particle to be driven back to its vacuum value as soon as the particle leaves the nucleus. Such a behavior could be achieved, if the off-shellness depended linearly on the width $\Gamma_{\text{tot}} = -\text{Im}\Pi/(2p^0)$ of the represented particle

$$\Delta\mu_j(\vec{r},p) = \frac{\Delta\mu_j(\vec{r}_j(t_0),p_j(t_0))}{\Gamma_{tot}(\vec{r}_j(t_0),p_j(t_0))}\Gamma_{tot}(\vec{r},p) \quad , \tag{2.33}$$

where $\vec{r}_j(t_0)$ and $p_j(t_0)$ denote the position and 4-momentum of the test-particle at its production time. The Γ_{tot}'s are evaluated in the calculation frame, which corresponds to the center-of-mass frame for heavy-ion reaction simulations and to the lab frame for all other reaction types[5].

For broad states there are two different possible scenarios. Either the width is larger in the medium (especially due to collisional broadening), in which case the off-shellness should get reduced while the particle travels to the vacuum. The other possibility is that the Pauli blocking of the free width dominates in the medium such that the width is eventually decreased. In the latter case, the off-shellness should be enhanced, when the particle propagates out of the nuclear medium. To include all this in the test-particle propagation, one defines for each test-particle a separate Hamilton function. One replaces the particle mass by $m + \Delta\mu_j$, such that the off-shellness can be interpreted as a momentum and position dependent scalar potential as defined in eq. 2.33,

$$H = \sqrt{(m+V)^2 + \vec{p}^2} \to H_j = \sqrt{(m+\Delta\mu_j+V)^2+\vec{p}^2} \quad . \tag{2.37}$$

Since $H_j(t_o) = p_j^0(t_0)$ and $\partial_t H = 0$, we have $H_j(t) = p_j^0(t)\ \forall t$.

In principle, the particle is driven back to its mass shell due to interactions with all other test-particles. Therefore, the off-shell potential must also induce a potential on all other particles (actio=reactio). Such a back-coupling term due to the off-shellness has been implemented in earlier works [Leh03, Eff99a], which then also restores the overall momentum conservation. Since in our applications the ground state will be on-shell and only a few final-state particles will be propagated off-shell, we neglect this momentum-non-conservation problem and the somewhat involved implementation of the back-coupling term[6].

---

[5] To understand why we take the width in the calculation frame,let us analyze the transformation properties of $\Delta\mu_j$. The term $\Delta\mu_j(\vec{r},p)$ must be a Lorentz-scalar since $\sqrt{p^\mu p_\mu}$ is a scalar and also $m+V$ are scalars. Henceforth

$$\frac{\Delta\mu_j(\vec{r}_j(t_0),p_j(t_0))}{\Gamma_{tot}(\vec{r}_j(t_0),p_j(t_0))}\Gamma_{tot}(\vec{r},p) \tag{2.34}$$

must be a scalar. Since $\Delta\mu_j$ must be a scalar for all times, the fraction

$$\frac{\Gamma_{tot}(\vec{r}_j(t_0),p_j(t_0))}{\Gamma_{tot}(\vec{r},p)} \tag{2.35}$$

must be a scalar as well. This is fulfilled if both Γ's are being defined within the very same inertial system - so we choose the calculation frame as our reference frame. Note that the term

$$\frac{\Gamma_{tot,RF}(\vec{r}_j(t_0),p_j(t_0))}{\Gamma_{tot,RF}(\vec{r},p)} \quad , \tag{2.36}$$

where the $\Gamma_{tot,RF}$'s are being evaluated in the rest-frames of the particle, is not a Lorentz scalar! This is caused by the fact that $p(t)$ is in general not identical to $p(t_0)$, and as a consequence the rest-frames defined by $p(t)$ and $p(t_0)$ are in general different. So the numerator and denominator are not defined in the same frame, hence the fraction is no scalar.

[6] See e.g. [Leh03] for the problem of choosing the proper mass initialization in the presence of the back-coupling term.

In the original work of Effenberger [Eff99a], the off-shell potential was assumed to be

$$\Delta\mu_j^{\text{Effenberger}}(\vec{r},p) = \frac{\Delta\mu_j(\vec{r}_j(t_0),p_j(t_0))}{\rho(\vec{r}_j(t_0))}\rho\left(\vec{r}\right) \quad , \tag{2.38}$$

which included already the assumption $\Gamma_{\text{tot}} \sim \rho$. However, even in a $\Gamma = \sigma\rho v$ ansatz, the width may depend in a non-linear fashion on the density if the cross section itself becomes density-dependent. So the implementation according to eq. 2.33 is more general and, therefore, favored in this work. Since the off-shell potential according to eq. 2.33 is dependent on the width, it is important to note that we have introduced for the first time an energy dependent width in the GiBUU model. As a consequence, the term $\partial H/\partial p_0$ in eq. 2.21-2.23 is explicitly non-zero since H depends on $\Delta\mu$ (cf. eq. 2.37), which depends itself on Γ_{tot}. In practice, we determine the width $\Gamma_{\text{tot}}\left(\vec{r},p\right)$ not for all possible values of p and $\vec{r}$ but only on a grid in momentum- and position-space in order to save computation time. Thereafter, we use an interpolation of this tabulation in our calculations. This tabulation must be smooth and should not include numerical fluctuations, e.g. due to a low numerical accuracy. Otherwise the gradients $\partial\Gamma_{\text{tot}}/\partial p_0$ might get large due to these fluctuations and one generates test-particle velocities larger than the speed of light. Altogether, the inclusion of the $\partial H/\partial p_0$ term complicates the numerical treatment considerably, since the width must be determined with high accuracy[7].

Annotation. The replacement $m \to m + \Delta\mu_j$ introduces a test-particle dependent Hamiltonian. First, this modification was only an educated guess by U. Mosel and M. Effenberger [Eff99a]. However, as has been shown later by Lehr [Leh03], it implements most features of the more complicated derivations including $A_{\text{off-shell}}$, as, e.g., in [Leu00, Juc03]. Nevertheless, there remains one subtlety: it has not yet been shown how to construct out of the given test-particle dependent Hamiltonian H_j a Hamiltonian H for the non-test-particle representation. The OSP ansatz as sketched above is a very efficient way of implementing off-shell effects as caused by the term $A_{\text{off-shell}}$. Though this approach might not be particularly aesthetic, it is being preferred due its efficiency aspects.

2.5 Simulating the collision term

The scope of this section, which is dealing with the collision term, is two-fold. First, the collision term is expressed in terms of resonance decay rates and cross sections. Then it is rewritten in terms of the test-particle basis to evaluate eq. 2.25.

The collision term can be split into terms having different initial-state multiplicities. We include in our model processes with just one particle (=resonance decays), two and three particles in the initial state; any higher correlations are neglected. So the loss term $\Sigma^>$ reads

$$\Sigma^> = \Sigma^{>,1} + \Sigma^{>,2} + \Sigma^{>,3} \quad , \tag{2.39}$$

where the indices $1, 2, 3$ define the initial-state multiplicities. This section deals first with the one-body processes, then with two- and three-body interactions and will be rather general. So it does not particularly depend on details of cross sections or involved particle species which are postponed to sec. 3.2.1 and sec. 3.3. As it will be shown in the forthcoming paragraphs, the loss term describes events, where test-particles get annihilated. For each annihilation event, a Monte-Carlo decision is performed to retrieve the final state particles. To conserve all quantum

---

[7] For numerical results see sec. 3.9.

numbers, new test-particles corresponding to the final-state particles of such an annihilation event are added to the simulation and the initial state particles are deleted. These additional test-particles are then interpreted as the test-particles which represent the gain term. So we focus in the following paragraphs on this loss term and the implementation of the gain term will then be obvious.

2.5.1 Resonance decays

We assume a dependence of the resonance lifetime τ on the resonance decay width Γ, which is given by the standard formula

$$\tau = \frac{1}{\Gamma} \quad . \tag{2.40}$$

In [Leu01], another lifetime definition was presented, which is based on the original Kadanoff-Baym formalism. When one averages this latter lifetime and the $1/\Gamma$-lifetime over the spectral functions then the averages are identical. Additionally, it was shown in [Lar02] that introducing the different lifetime prescription is mostly counter-balanced by a related renormalization of the 2-body interactions, which was also proposed in [Leu01]. So we neglect in this work for simplicity both the renormalization and the modification in the lifetime definition. However, it might be interesting for the future to include both the lifetime prescription according to [Leu01] and the renormalization terms in the 2-body interactions, and to perform a comparison as in [Lar02] also for more exclusive channels.

The loss term. The one-body loss term represents basically the rate with which particles decay, in particular $\Sigma^{>,1} = -1/\tau$ where τ is the life time of the particle. Choosing $\tau = \frac{1}{\Gamma}$, the loss term due to resonance decays is given by

$$\begin{aligned} I^1_{\text{loss}}(\vec{r},t,p) &= \Sigma^{>,1}(\vec{r},t,p)\bar{g}^{<}(\vec{r},t,p) && (2.41) \\ &= \Gamma(\vec{r},t,p)\bar{g}^{<}(\vec{r},t,p) \quad . && (2.42) \end{aligned}$$

The decay width of the particle within the calculation frame is connected to the one in the resonance rest-frame via

$$\Gamma(\vec{r},t,p) = \frac{\sqrt{p_\mu p^\mu}}{p_0}\left[\Gamma(\vec{r},t,p)\right]_{\text{Res. rest-frame}} \quad , \tag{2.43}$$

where the prefactor $\frac{\sqrt{p_\mu p^\mu}}{p_0}$ takes care of the proper time to resonance eigentime transformation. In the rest-frame, the decay width is given by

$$\begin{aligned} \left[\Gamma(\vec{r},t,p)\right]_{\text{Res. rest-frame}} = {} & \frac{1}{2M}\sum_{n=1}^{\infty} \sum_{\substack{\text{all combinations}\{j_1,\dots j_n\} \\ \text{with } j_1 \leqq j_2 \leqq \dots}} \prod_{k=1}^{n} \left\{ \int \frac{dp_k^4}{2\pi^4} 2\pi \mathcal{A}_{j_k}(\vec{r},t,p_k) \right. \\ & \left. \times \left(1 \pm f_{j_k}(\vec{r},t,\vec{p}_k)\right)\right\} (2\pi)^4\, \delta^4\left(\sum_{j=1}^{n} p_k - p\right) \left|M^2_{\to j_1,\dots j_n}\right| \quad , \end{aligned} \tag{2.44}$$

where the sum over n denotes the sum over all possible numbers of final states and j_k denotes the particle species of the kth final state particle. The momenta p_k denote the momenta of the final state particles. Note that besides the additional Pauli-blocking/Bose-enhancement factors

$1 \pm f_{j_k}(\vec{r}, t, \vec{p})$ this corresponds just to the standard decay width definition taking into account broad final state particles[8].

In terms of test particles, we can now write down the first contribution to eq. 2.25

$$
\begin{aligned}
&\frac{1}{N}\sum_{i=n(t)+1}^{n(t+\Delta t)} w_i\,\delta(\vec{r}-\vec{r}_i(t+\Delta t))\delta(\vec{p}-\vec{p}_i(t+\Delta t))\delta(p^0-p_i^0(t+\Delta t)) && (2.45)\\
&= \frac{\Delta t}{(2\pi)^4}\left(\Sigma^{>,1}\bar{g}^<(\vec{r},t,\vec{p})+\Sigma^{>,2}\bar{g}^<(\vec{r},t,\vec{p})+\Sigma^{>,3}\bar{g}^<(\vec{r},t,\vec{p})\right) && (2.46)\\
&= \frac{\Delta t}{(2\pi)^4}\left(\Gamma(\vec{r},t,p)\bar{g}^<(\vec{r},t,\vec{p})+\ldots\right) && (2.47)\\
&= \frac{\Delta t}{(2\pi)^4}\left(\Gamma(\vec{r},t,p)\bar{g}^<(\vec{r},t+\Delta t,\vec{p})+\ldots\right)+\mathcal{O}\left(\Delta t)^2\right) && (2.48)\\
&= -\frac{1}{N}\sum_{i=1}^{n(t)}\Gamma(\vec{r}_i,t,p_i)\Delta t\ w_i\ \delta(\vec{r}-\vec{r}_i(t+\Delta t))\delta(\vec{p}-\vec{p}_i(t+\Delta t))\delta(p^0-p_i^0(t+\Delta t))\\
&\quad +\ldots+\mathcal{O}\left((\Delta t)^2\right) \quad . && (2.49)
\end{aligned}
$$

The dots stand for the contributions of 2- and 3-particle loss terms; the term $\mathcal{O}\left((\Delta t)^2\right)$ is neglected in the limit $\Delta t \to 0$. To simulate the loss of strength through resonance decay one now interprets $\Gamma(\vec{r}_i, t, p_i)\Delta t$ as the probability for the decay of the ith test-particle. This corresponds to substituting $p = \Gamma(\vec{r}_i, t, p_i)\Delta t$ by a Bernoulli distributed random number $1_{p=\Gamma(\vec{r}_i,t,p_i)\Delta t}$ with probability $p = \Gamma(\vec{r}_i, t, p_i)\Delta t$[9]. In the simulation, we then decide by a Monte-Carlo method whether $1_{p=\Gamma_i(\vec{r}_i,t,p_i)\Delta t} = 1$ or 0. If the value is 1, then we get a negative test-particle at the position of an original one and the test-particle is basically removed from the simulation. If it is 0 then the test-particle remains. Since $1_{p=\gamma(\vec{r}_i,t,p_i)\Delta t}$ is being evaluated separately for each test-particle, the above described substitution is appropriate in the limit of many test-particles when the loss term approaches the expectation value.

The gain term. For each event where a test-particle is absorbed due to the loss term, we choose by a Monte-Carlo method a possible final state and its kinematics. Test-particles representing this final state are thereafter added to the simulation. This procedure conserves quantum numbers within such an absorption event and simulates the gain term.

2.5.2 Two-body collisions

For the sake of simplicity, let us consider a model with only one fermionic particle species which has no degeneracy, allowing only for binary scattering processes

$$A(p_A)\ B(p_B) \longrightarrow a(p_a)\ b(p_b) \quad . \tag{2.50}$$

If such a scattering event occurs at point $\vec{r}$, then the single-particle phase-space density decreases in the vicinity of the phase space points $(\vec{r}, p_A)$ and $(\vec{r}, p_B)$ and increases in the vicinity of $(\vec{r}, p_a)$ and $(\vec{r}, p_b)$. In each phase space point, the two-body contribution to the collision term consists

---

[8] Note that the decay width is not identical to the full width of the particle. The full width also includes scattering processes.

[9] For small Δt this corresponds to the well known decay probability $\lim_{\Delta t\to 0} p = 1 - e^{-\Gamma(\vec{r}_i,t,p_i)\Delta t}$.

of a gain term due to particles which are scattered into this phase space point and a loss term due to particles which are scattered out. The loss and gain terms are given by

$$
\begin{aligned}
I^2_{\text{loss}}(\vec{r},t,p_A) &= \Sigma^{>,2}(\vec{r},t,p_A)g^{<}(\vec{r},t,p_A) &(2.51)\\
&= \int \frac{d^4p_B}{(2\pi)^4} \int d\Omega_{CM} \frac{d\sigma_{AB\to ab}}{d\Omega_{CM}} v_{AB} \;\; g^{<}(\vec{r},t,p_B)g^{<}(\vec{r},t,p_A)\mathcal{P}_a\mathcal{P}_b \quad , &(2.52)
\end{aligned}
$$

and

$$
\begin{aligned}
I^2_{\text{gain}}(\vec{r},t,p_A) &= \Sigma^{<,2}(\vec{r},t,p_A)g^{>}(\vec{r},t,p_A) &(2.53)\\
&= \int \frac{d^4p_a}{(2\pi)^4}\frac{d^4p_b}{(2\pi)^4}(2\pi)^3 \frac{d\sigma_{ab\to AB}}{d^4p_A} v_{ab} \; g^{<}(\vec{r},t,p_a)\; g^{<}(\vec{r},t,p_b)\mathcal{P}_A\mathcal{P}_B \quad , &(2.54)
\end{aligned}
$$

where $d\sigma_{AB\to ab}/d\Omega_{CM}$ and $d\sigma_{ab\to AB}/d^4p_A$ are the angular and momentum differential cross sections for the reactions $AB \to ab$ and $ab \to AB$, respectively. v_{AB} and v_{ab} are the relative velocities of the collision partners AB and ab. The terms $\mathcal{P}_X = 1-f(\vec{r},\vec{p_X},t)$ with $X = A,B,a,b$ correspond to the Pauli blocking of the final states. The momenta of the particles in loss and gain term satisfy the condition of energy and momentum conservation.

To point out the connection between our numerical implementation and the underlying BUU equation, we focus on the loss term of BUU. Therefore, we will not elaborate on the gain term I_{gain}, which describes the production of particles. However, its numerical implementation is analogous to the loss term since both are related by detailed balance.

In terms of the test-particle ansatz the loss term reads

$$
\begin{aligned}
\Delta t\; I^2_{\text{loss}}(\vec{r},t,\vec{p_A}) &= \lim_{N\to\infty} \frac{(2\pi)^4}{N} \sum_{i=1}^{n(t)} \sum_{\substack{j=1\\ j\neq i}}^{n(t)} w_i w_j\, \delta(p_A^0 - p_i^0)\delta(\vec{p}_A - \vec{p}_i)\delta(\vec{r}-\vec{r}_i)\\
&\times \lim_{N\to\infty} \underbrace{\frac{1}{\sigma_{ij}} \int d\Omega_{CM}\; \mathcal{P}_a\mathcal{P}_b \frac{d\sigma_{ij\to ab}}{d\Omega_{CM}}}_{=\overline{\mathcal{P}_a\mathcal{P}_b}} \underbrace{\sigma_{ij}\Delta t\, v_{ij}\frac{1}{N}}_{=\Delta V_{ij}} \delta(\vec{r}-\vec{r}_j) &(2.55)\\
&= \lim_{N\to\infty} \left(\frac{(2\pi)^4}{N} \sum_{i=1}^{n(t)} \sum_{\substack{j=1\\ j\neq i}}^{n(t)} w_i w_j\, \delta(p_A - p_i)\delta(\vec{r}-\vec{r}_i)\overline{\mathcal{P}_a\mathcal{P}_b} \int_{\Delta V_{ij}} \delta(\vec{r}\,'-\vec{r}_j)d^3r' \right) &(2.56)
\end{aligned}
$$

where σ_{ij} and v_{ij} are the total interaction cross section and the relative velocity of the test-particles i,j; $\Delta V_{ij} = \sigma_{ij}\Delta t\, v_{ij}/N$ is an infinitesimal volume in the vicinity of $\vec{r}_i$. Note that this volume defines the locality of the scattering process of two test-particles. The term $\overline{\mathcal{P}_a\mathcal{P}_b}$ denotes the blocking of the final state averaged over its angular distribution. We excluded self-interactions – therefore a test-particle cannot scatter with itself.

Numerical implementation

In a real calculation the number of test-particles N is chosen finite, for our purposes usually of the order of 300-1500. The time step Δt is chosen such that the average distance traveled by the particles during Δt is less than their mean free path. Therefore, ΔV_{ij} is small enough such that a particle has no more than one scattering partner at a given time step. The algorithm proceeds as a sequence of the following steps:

- The loss term is implemented according to eq. 2.56. We consider therefore each term in eq. 2.56 separately. For simplicity let us just consider one summand describing the loss of the ith test-particle due to a collision with the jth test-particle.
  1. The term $\int_{\Delta V_{ij}} \delta(\vec{r}\,' - \vec{r}_j) d^3 r'$ gives 1 or 0 depending on the fact whether j is within ΔV_{ij}. The volume ΔV_{ij} is chosen to be a cylinder of height $\Delta t v_{ij}$ with a circle basis σ_{ij}/N; the symmetry axis is chosen along $\vec{v}_{ij}$ and the basis is centered at $\vec{r}_i$. This corresponds to the usual minimum distance concept [Cug81].
  2. If the result of the integral is 1, then we evaluate

     $$\overline{\mathcal{P}_a \mathcal{P}_b} = \frac{1}{\sigma_{ij}} \int d\Omega_{CM}\ \mathcal{P}_a \mathcal{P}_b \frac{d\sigma_{ij\to ab}}{d\Omega_{CM}} \quad . \tag{2.57}$$

     For this we perform a Monte-Carlo integration with only one integration point. This is a good approximation in the large N limit since then a lot of collisions occur such that, effectively, the above integral is evaluated to a good precision. This one point Ω^{CM} is chosen in the center of mass (CM) frame randomly according to the weight $\frac{1}{\sigma_{ij}} \frac{d\sigma_{ij\to ab}}{d\Omega_{CM}}$. Since $\sqrt{s}$ is fixed, Ω^{CM} defines the random momentum $\vec{p}_a^{\ \mathrm{CM}}$. Furthermore,

     $$\vec{p}_b^{\ \mathrm{CM}} = -\vec{p}_a^{\ \mathrm{CM}} \quad . \tag{2.58}$$

     Finally, by boosting the momenta to the computational frame[10], we obtain

     $$\overline{\mathcal{P}_a \mathcal{P}_b} = (1 - f(\vec{r}, \vec{p}_a, t))(1 - f(\vec{r}, \vec{p}_b, t)) \quad . \tag{2.59}$$

  3. Now we interpret $\overline{\mathcal{P}_a \mathcal{P}_b}$ as a probability that the reaction takes place. A second Monte-Carlo decision is being performed in which one decides whether the reaction is accepted or not. This corresponds to substituting $\overline{\mathcal{P}_a \mathcal{P}_b}$ by a Bernoulli distributed random number with $p = \overline{\mathcal{P}_a \mathcal{P}_b}$. With this substitution, the expectation value of the summand is equal to the original summand. In the limit of many ensembles N, i.e. many summands, this yields the right loss term.
  4. If the reaction is accepted, then we get for this event where i is scattering with j the loss contribution

     $$w_i w_j\, \delta(p_A - p_i) \delta(\vec{r} - \vec{r}_i) \quad , \tag{2.60}$$

     which corresponds to the destruction of the ith test-particle if $w_j = 1$, if $w_j < 1$ then it is contribution to $g^{<}$ is only decreased. Due to the double sum in eq. 2.62, we get also the contribution

     $$w_i w_j\, \delta(p_A - p_j) \delta(\vec{r} - \vec{r}_j) \quad . \tag{2.61}$$

     This latter term corresponds to the full or partial destruction of the jth test-particle. Note that we do not evaluate $\overline{\mathcal{P}_a \mathcal{P}_b}$ for this case, but take the same value which leads to the destruction of i. This reflects that energy is conserved on an event-by-event basis.

---

[10] For our simulations of πA, γA and $e^- A$ collisions the computational frame is chosen to be the laboratory frame. Note that for heavy-ion simulations in GiBUU, the computational frame is usually the CM-frame of the two colliding ions.

5. In our simulation, the final states with momenta $\vec{p_b}^{\,\mathrm{CM}}$ and $\vec{p_a}^{\,\mathrm{CM}}$ contribute to the gain term. New test particles with those momenta are therefore added to the simulation.

A generalization to 2 → 3 and 3 → 2 processes and to finite particle species including degeneracies is straight-forward.

Note that we will always have $w_i = w_j = 1$ in our simulation: all test-particles are initialized with $w_i = 1$ and $\partial w_i/\partial t = 0$; test-particles which are added due to decays just compensate others and therefore these two test-particles can then be removed from the simulation (cf. discussion on page 20). Hence we only need to consider particles with $w_i = w_j = 1$ in the two-particle loss term which leads in case that the collision is accepted during the Monte-Carlo procedure to a full destruction of the scattering particles (i.e. $w_i w_j = 1$ in eqs. 2.60-2.61).

Since the elementary cross sections are based on the fact that the final states are asymptotic, we have to deter that two final state particles scatter among each other before undergoing a collision with a third particle. Therefore, we demand as an extra condition that a test-particle representing a particle labeled as A is not allowed to scatter off more than one member of a particle labeled as B before undergoing interactions with another particle labeled C with $C \neq A$ and $C \neq B$. This is meant to preserve the limit when going to elementary scattering processes, e.g. there are no double charge exchange processes in elementary πN collisions.

Approximations

Full and parallel ensembles. The kind of simulation for the 2-body processes we described in the last paragraph, is called a *full ensemble* calculation. There exists a common simplification to this method: *the parallel ensemble method* [Ber88]. In this scheme one performs in parallel $\tilde{N}$ calculations which all include only one single ensemble ($N = 1$). The densities used in each parallel run are the averaged densities of all $\tilde{N}$ parallel runs. Therefore the propagation part basically stays the same, whereas the collision term gets very much simplified.

Note that the only justification for this simplification is a great gain in computation time. In a full ensemble method, the propagation part scales according to the number of test-particles per nucleon N, whereas the two-body collision term scales with N^2 - therefore the computation time is $\mathcal{O}(N^2)$. In a parallel ensemble method $\tilde{N}$ runs are performed, which results in $\mathcal{O}(\tilde{N})$ computation time. Thus there is a linear scaling in a parallel ensemble run, but a quadratic one in a full ensemble run.

The major drawback of the parallel ensemble scheme is the non-locality in the collisions. As a showcase, let us consider the pion-nucleon interaction. There the maximum cross section amounts to roughly 200 mb. This leads to a maximal impact parameter of two test-particles which is given by $\sqrt{200\mathrm{mb}/\pi} \simeq 2.52$ fm. Hence the parallel ensemble scheme may lead to large non-localities whereas the underlying BUU collision term is strictly local.

In pioneering works, it was shown by Welke et al. [Wel89] and Lang et al. [Lan93], that the parallel ensemble scheme is a good approximation to the full ensemble scheme under the conditions of high-energy heavy ion collisions. However, it is still an open question whether this also applies to more surface sensitive processes such as, e.g., pion double charge exchange in nuclei. We will discuss this problem together with our numerical results.

The local ensemble method. The so-called *local ensemble method*, which was first applied to heavy ion collisions by Lang et al. [Lan93], is a method allowing for a full-ensemble run which is less time consuming than the standard algorithm. Here one divides the position space into small cubical boxes V_i with equal volumes ΔV. The loss term is then represented by

$$\Delta t \; I^2_{\text{loss}}(\vec{r},t,\vec{p_A}) = \lim_{N\to\infty}\left(\frac{(2\pi)^4}{N}\sum_{i=1}^{n(t)}\sum_{\substack{j=1\\ j\neq i}}^{n(t)} w_i w_j\,\delta(p_A-p_i)\delta(\vec{r}-\vec{r}_i)\right.$$
$$\left.\times\,\overline{\mathcal{P}_a\mathcal{P}_b}\Delta V_{ij}\frac{1}{\Delta V}\int_{V_A}\delta(\vec{r}\,'-\vec{r}_j)d^3r'\right) \quad , \tag{2.62}$$

where V_A is the box, in which the particle A is situated. Now the whole expression $\overline{\mathcal{P}_a\mathcal{P}_b}\Delta V_{ij}\frac{1}{\Delta V}$ is interpreted as the probability that an interaction takes place. If there are n test-particles within one box, then there are $n(n-1)/2$ possible scattering events. One now chooses randomly only $n/2$ collision pairs out of the possible pairs. To conserve the overall reaction rate one must rescale the collision probability by the factor

$$\frac{\text{number of possible collisions}}{\text{number of collisions}} = \frac{n(n-1)/2}{n/2} \quad . \tag{2.63}$$

Finally, we obtain the probability that a chosen collision takes place

$$p = \frac{n(n-1)/2}{n/2}\overline{\mathcal{P}_a\mathcal{P}_b}\Delta V_{ij}\frac{1}{\Delta V} \quad . \tag{2.64}$$

This method is faster than the original full-ensemble method, since one can effectively order all test-particles into the cells before one simulates the collision term. Afterwards only such test-particles must be correlated/compared which are within one cell. In the limit of $\Delta V \to 0$ and $N \to \infty$ this corresponds to a full-ensemble calculation. The only drawback is that one must adjust beforehand the parameters ΔV and Δt such that $p < 1$ for all boxes. Therefore, one must roughly estimate the mean value of n by the nuclear matter density ($\bar{n} \approx \rho\Delta V N$) and the cross section by some meaningful average value. Larger numbers of N lead to better estimates of n, while low N can lead to huge fluctuations in n. Typical volumes for $N \approx 300-1500$ are[11] $\Delta V = (0.25-1.0\text{ fm})^3$.

We implemented all three algorithms (parallel, full, local ensemble) within our model and we will later explicitly compare them.

We emphasize, that the gain term is in our approach given by test-particles representing the final-state particles determined by the loss term (cf. item *5.* on page 24).

2.5.3 Three-body collisions

The rates for three-body collisions are experimentally not accessible, hence one estimates the matrix elements for such a process via detailed balance. The whole procedure is detailed in [Eff99a] and in section 3.3.2.

Numerical implementation In the following, we sketch the numerical implementation. To get the probability for one test-particle to collide with two others, one must in principle consider all three-particle combinations which are possible. Since this is rather time consuming, one picks

---

[11] The default in our code is chosen to be $(0.5\text{ fm})^3$. If events occur in which $p > 1$, then the calculation must be repeated with smaller time step size Δt.

randomly two test-particles out of a given vicinity with radius r of a regarded test-particle. This is again considered to be a one-point Monte-Carlo integration. As argued for the 2-body collisions, we get in the limit of many test-particles the right mean value for the three body rate. The vicinity is chosen such that it is large enough to find two scattering partners within this vicinity. This means, one must adjust this parameter to the test particle densities[12], hence the radius of this volume scales like $1/\sqrt[3]{N}$. Intuitively, one might want to choose the closest pair in the vicinity. However, this again implies a sorting of the particles within the vicinity which is time-consuming. Furthermore, in the limit of large N locality is restored anyhow. As a speed-up, we use the sorting of the particles into the volume boxes (which is being done for the local collision criteria) to find the scattering partners. Having defined a pair to scatter with, the rate Γ_3 for this process is calculated and then all three particles are annihilated with the probability $\Delta t \Gamma_3$. Annihilating all three particles means that we implicitly also evaluated the three-body loss term for the other involved particle species, e.g. for the nucleons in the $\pi NN \to NN$ process. As gain term we represent the final state particles by new test-particles which are added to the simulation.

---

[12] E.g. for $NN\pi \to NN$, we choose the radius $r = 2.8$ fm$/\sqrt[3]{N}$ to define the vicinity in which we search for two nucleons as scattering partners for a given pion.

Chapter 3

The GiBUU model

Overview: This chapter introduces the Giessen Boltzmann-Uehling-Uhlenbeck (GiBUU) transport model, and details the included particle species, interaction rates, medium modifications, self-energies and the resulting in-medium spectral functions.

3.1 Introduction

Over the last two decades, the Giessen theory group has been developing a Boltzmann-Uehling-Uhlenbeck (BUU) transport model to describe heavy ion collisions, photon-, electron-, pion- and neutrino-induced reactions within one unified transport framework. The simulation of transport processes comes hand-in-hand with an elaborated piece of computer code. We therefore want to structure the following historical overview giving some key dates concerning the actual code development and the most significant physics topics which have been addressed.

The code history. First simulations have been undertaken with a modified version of the original *Bertsch code* [Ber88]. Starting in 1986, this resulted in predictions for photon production in heavy-ion collisions [Bau86, Bau89]. The code was undergoing several major development steps during the following years[1]. In the mid 90's, Effenberger [Eff99a] and Teis [Tei96] rewrote large parts of it. Besides the original field of application, which were heavy ion collisions, the code was then already applied to the prediction of photon- and pion-induced reactions. In the years 2000-2005, T. Falter worked on the description of high-energy non-resonant electron-induced reactions. Together with K. Gallmeister a picture for the time-dependence of fragmentation was established [Fal04b, Gal05]. A. Larionov has been working on the description of heavy ion collisions in the SIS energy region and above; as a major topic, he studied the influence of medium-dependent cross sections (see e.g. [Lar03, Lar05]). Together with M. Wagner [Wag05], he investigated strangeness production in heavy ion collisions. J. Lehr (see [Leh03] and references therein) included off-shell nucleons in his code version and worked on both photon- and electron-induced processes in the resonance region. The last results based on the the original Effenberger-Teis version were published by P. Mühlich [Mü07]. He worked on pion and photon induced processes both in the resonance and high energy region, thereby focusing on possible signals for changes of meson properties within the medium [Mü04b, Mü06b, Mü06a].

The rewriting of the code - the GiBUU project. In 2004, we launched the GiBUU project. The main intention of this project was the restructuring and rewriting of the original source code using FORTRAN 2003 as a programming language. FORTRAN was chosen since the included libraries, in particular FRITIOF and PYTHIA, have also been programmed in FORTRAN.

---

[1] More details concerning the *ancient* days can be found in [GiB08a].

In the beginning, I took the responsibility for the basic framework - especially type definitions, array structure and code management. Thereafter I implemented the propagation of the test-particles, potentials, evaluation of the densities based on the test-particles and the baryon-meson cross sections. In the meantime, T. Falter also joined the project and rewrote his version of the high-energy part, implementing it in the new code structure. Later, also A. Larionov and K. Gallmeister joined the initiative. A. Larionov took care of the implementation of strangeness production and improved the baryon-baryon cross sections. Furthermore, he included a relativistic mean field in the propagation which can now be used alternatively to the Skyrme mean field. K. Gallmeister revised the Makefile and in a joined effort, together we implemented the local ensemble method. This algorithm was not included in the precursor Effenberger-Teis version and improved the speed of the full ensemble simulations. K. Gallmeister was also a major player in the speed-up of the core routines. Furthermore, he managed to replace FRITIOF by a modified PYTHIA [pyt07] version. In 2006, T. Leitner joined the project and implemented in the following her model [Lei06a, Lei06b] for neutrino-nucleon interactions and shared the work-load in the implementation of the off-shell potential. Lately, also T. Gaitanos (nuclear fragmentation), D. Kalok [Kal07] (nucleon spectral functions), B. Steinmüller [Ste07](ground state properties) and J. Weil [Wei08a] (dileptons and vector meson production, gfortran compatibility) contributed to the new code. In April 2008, the first source-code release was published on our website [GiB08b] under the GPL [gpl07] license.

From a programmers point of view, the most remarkable successes of the new code version are the following:

- *The structure of the code is now completely modular.* Henceforth each fragment can be tested independently. This was not possible with the old Effenberger-Teis version.

- All GiBUU users *work in parallel* on one code. Without the prerequisite of a modular code this would not be possible. Within the old structure, one could rarely exchange small code pieces but very often a lot of pieces had to be modified at once. So each member of the group had his own code version. There existed also a so-called *standard version*, where every user was supposed to implement important changes to the code. However, this code has never been used for real calculations and, therefore, the *standard* implementation was not fully reliable.

- The code is based on a version control system (SUBVERSION[2]).
  - The *standard version* is *fully reliable* and always up-to-date.
  - The full code history can be analyzed and published results can be 100% recalculated at any later stage.
  - No source code can get lost, although there are large fluctuations among the group members.

- No proprietary software is used. All ”imported” code fragments, i.e. fragments which are not coded by the GiBUU group, are under the GPL license[3]. The former code version included proprietary software, e.g. *Numerical Recipes*, which impeded open-source publishing.

---

[2] See Appendix C.2 for details.

[3] See Appendix C.3 for details.

- The code is running successfully with all so-far tested FORTRAN 2003 compatible compilers: Intel[4], Absoft[5], gfortran[6] and g95[7].

More details on technical issues concerning the code management, documentation and code structure can be found in appendix C.

From now on, we will focus on the physics input to the model. First, the list of implemented particle species and their properties is detailed. Then the hadronic cross sections, the medium modifications and potentials are addressed. In the following, we investigate the spectral functions of the baryons. Finally, we deal with ground state properties of nuclei and present numerical results for off-shell transport of baryons.

3.2 Degrees of freedom: The implemented particle species

3.2.1 Introduction

The relevant degrees of freedom in our model are baryons, mesons, leptons, their anti-particles and the gauge bosons. Within the hadronic sector, the model rests upon two main pillars. The πN scattering phase shift analysis performed by Manley and Saleski [Man92] serves as input for all parameters of hadrons built out of up and down quarks - the so-called non exotic hadronic matter. For the exotic hadronic matter, we use the parameters collected by the particle data group [Hag02].

Baryons. There are 31 resonances made up of up- and down-quarks implemented according to Manley *et al.*. These resonances are listed in table 3.1 together with their quantum numbers and ratings according to the Manley analysis. Additionally, 30 resonances with non-zero strangeness and/or charm content have been included. Their properties are listed in table 3.2. Besides the nucleon, also the Λ, Σ, Ξ, Ω, Λ_C, Σ_C, Ξ_c and Ω_C are assumed to be stable due to their long lifetimes which are much longer than the usual timescales for nuclear reactions. The decay branching ratios at the resonance pole mass are given in table A.1. In this work, we neglect the very small branching ratios into dileptons[8].

Mesons. There are 21 mesonic states implemented (for details cf. table 3.3). We treat the lowest-lying state - the π-meson - and also the η, J/Ψ, K, $\overline{K}$, D, $\overline{D}$, D_s^+ and D_s^- mesons as stable particles due to their long lifetimes. The decay branching ratios at the resonance pole masses are given in table A.2.

Leptons and gauge bosons. Neither the leptons nor the electro-weak gauge bosons (γ, $W^{\pm}$, Z^0) are explicitly propagated in the simulation. We assume that they decouple due to the small coupling strength from the hadronic matter after production (e.g. in $\eta \to \gamma\gamma$), or after the first interaction vertex (e.g. in $eA \to eX$). Gluons are also not propagated, but so-called strings or pre-hadrons which carry information about gluonic excitations (for details cf. [Gal05, Fal04b]).

---

[4] Intel: all versions ≥ 9.1. Note that Intel frequently provides bug-fix patches.

[5] Absoft version 10.0 with the latest bug-fix patch

[6] gfortran version 4.3, revision ≥ 127750

[7] g95 version ≥ 0.91

[8] In 2007, J. Weil [Wei08a] implemented also the dilepton branching ratios according to Mühlich [Mü07] in the GiBUU code.

Name	**Index**	**Mass** [GeV]	**Width** [GeV]	**Spin**	**Rating**	**Isospin**	**Strangeness**	**Charm**
N	1	0.938	0.000	1/2	****	1/2	0	0
Δ	2	1.232	0.118	3/2	****	3/2	0	0
P$_{11}$(1440)	3	1.462	0.4591	1/2	****	1/2	0	0
S$_{11}$(1535)	4	1.534	0.151	1/2	***	1/2	0	0
S$_{11}$(1650)	5	1.659	0.173	1/2	****	1/2	0	0
S$_{11}$(2090)	6	1.928	0.414	1/2	*	1/2	0	0
D$_{13}$(1520)	7	1.524	0.124	3/2	****	1/2	0	0
D$_{13}$(1700)	8	1.737	0.249	3/2	*	1/2	0	0
D$_{13}$(2080)	9	1.804	0.447	3/2	*	1/2	0	0
D$_{15}$(1675)	10	1.676	0.159	5/2	****	1/2	0	0
G$_{17}$(2190)	11	2.127	0.547	7/2	****	1/2	0	0
P$_{11}$(1710)	12	1.717	0.478	1/2	*	1/2	0	0
P$_{11}$(2100)	13	1.885	0.113	1/2	*	1/2	0	0
P$_{13}$(1720)	14	1.717	0.4583	3/2	*	1/2	0	0
P$_{13}$	15	1.879	0.498	3/2	***	1/2	0	0
F$_{15}$(1680)	16	1.684	0.139	5/2	****	1/2	0	0
F$_{15}$(2000)	17	1.903	0.494	5/2	*	1/2	0	0
F$_{17}$(1990)	18	2.086	0.535	7/2	**	1/2	0	0
S$_{31}$(1620)	19	1.672	0.154	1/2	**	3/2	0	0
S$_{31}$(1900)	20	1.920	0.263	1/2	***	3/2	0	0
D$_{33}$(1700)	21	1.762	0.599	3/2	*	3/2	0	0
D$_{33}$(1940)	22	2.057	0.460	3/2	*	3/2	0	0
D$_{35}$(1930)	23	1.956	0.526	5/2	**	3/2	0	0
D$_{35}$(2350)	24	2.171	0.264	5/2	**	3/2	0	0
P$_{31}$	25	1.744	0.299	1/2	*	3/2	0	0
P$_{31}$(1910)	26	1.882	0.239	1/2	****	3/2	0	0
P$_{33}$(1600)	27	1.706	0.430	3/2	***	3/2	0	0
P$_{33}$(1920)	28	2.014	0.152	3/2	*	3/2	0	0
F$_{35}$	29	1.752	0.251	5/2	*	3/2	0	0
F$_{35}$(1905)	30	1.881	0.4527	5/2	***	3/2	0	0
F$_{37}$(1950)	31	1.945	0.4500	7/2	****	3/2	0	0

Table 3.1: Properties of non-exotic baryons in GiBUU. The parameters are chosen according to the πN scattering analysis by Manley and Saleski [Man92]. The *index* is used in the code as an identifier.

Name	**Index**	**Mass** [GeV]	**Width** [GeV]	**Spin**	**Rating**	**Isospin**	**Strangeness**	**Charm**
Λ	32	1.116	0.000	1/2	****	0	-1	0
Σ	33	1.189	0.000	1/2	****	1	-1	0
$\Sigma(1385)$	34	1.385	0.036	3/2	****	1	-1	0
$\Lambda(1405)$	35	1.405	0.050	1/2	****	0	-1	0
$\Lambda(1520)$	36	1.520	0.016	3/2	****	0	-1	0
$\Lambda(1600)$	37	1.600	0.150	1/2	***	0	-1	0
$\Lambda(1670)$	38	1.670	0.035	1/2	****	0	-1	0
$\Lambda(1690)$	39	1.690	0.060	3/2	****	0	-1	0
$\Lambda(1810)$	40	1.810	0.150	1/2	***	0	-1	0
$\Lambda(1820)$	41	1.820	0.080	5/2	****	0	-1	0
$\Lambda(1830)$	42	1.830	0.095	5/2	****	0	-1	0
$\Sigma(1670)$	43	1.670	0.060	3/2	****	1	-1	0
$\Sigma(1775)$	44	1.775	0.120	5/2	****	1	-1	0
$\Sigma(2030)$	45	2.030	0.180	7/2	****	1	-1	0
$\Lambda(1800)$	46	1.800	0.4500	1/2	***	0	-1	0
$\Lambda(1890)$	47	1.890	0.100	3/2	****	0	-1	0
$\Lambda(2100)$	48	2.100	0.200	7/2	****	0	-1	0
$\Lambda(2110)$	49	2.110	0.200	5/2	***	0	-1	0
$\Sigma(1660)$	50	1.660	0.100	1/2	***	1	-1	0
$\Sigma(1750)$	51	1.750	0.090	1/2	***	1	-1	0
$\Sigma(1915)$	52	1.915	0.120	5/2	****	1	-1	0
Ξ	53	1.315	0.000	1/2	****	1/2	-2	0
Ξ^*	54	1.530	0.009	3/2	****	1/2	-2	0
Ω	55	1.672	0.000	3/2	****	0	-3	0
Λ_c	56	2.285	0.000	1/2	****	0	0	1
Σ_c	57	2.452	0.000	1/2	****	1	0	1
Σ_c^*	58	2.520	0.015	3/2	****	1	0	1
Ξ_c	59	2.466	0.000	1/2	****	1/2	-1	1
Ξ_c^*	60	2.645	0.004	3/2	****	1/2	-1	1
Ω_c	61	2.697	0.000	1/2	****	0	-2	1

Table 3.2: Properties of exotic baryons in GiBUU. The parameters are taken from the PDG database [Hag02]. The *index* is used in the code as an identifier.

Name	**Index**	**Mass** [GeV]	**Width** [GeV]	**Spin**	**Isospin**	**Strangeness**	**Charm**
π	101	0.1380	0.0000	0	1	0	0
η	102	0.5474	0.0000	0	0	0	0
ρ	103	0.7700	0.1510	1	1	0	0
σ	104	0.8000	0.8000	0	0	0	0
ω	105	0.7820	0.0084	1	0	0	0
η'	106	0.9580	0.0002	0	0	0	0
ϕ	107	1.0200	0.0044	1	0	0	0
η_c	108	2.9800	0.0130	0	0	0	0
J/ψ	109	3.0970	0.0000	1	0	0	0
K	110	0.4960	0.0000	0	1/2	1	0
$\overline{K}$	111	0.4960	0.0000	0	1/2	-1	0
$K^\star$	112	0.8920	0.0500	1	1/2	1	0
$\overline{K}^\star$	113	0.8920	0.0500	1	1/2	-1	0
D	114	1.8670	0.0000	0	1/2	0	1
$\overline{D}$	115	1.8670	0.0000	0	1/2	0	-1
$D^\star$	116	2.0070	$(D^\star)^0$: .0020 $(D^\star)^+$: 96×10^{-6}	1	1/2	0	1
$\overline{D}^\star$	117	2.0070	$(\overline{D}^\star)^0$: .0020 $(\overline{D}^\star)^+$: 96×10^{-6}	1	1/2	0	-1
D_s^+	118	1.9690	0.0000	0	0	1	1
D_s^-	119	1.9690	0.0000	0	0	-1	-1
$(D_s^*)^+$	120	2.1120	0.0010	1	0	1	1
$(D_s^*)^-$	121	2.1120	0.0010	1	0	-1	-1

Table 3.3: Properties of mesons in GiBUU. The parameters are taken from the Manley analysis [Man92] and the PDG database [Hag02]. The *index* is used in the code as an identifier.

3.2.2 Vacuum decay widths of the baryonic resonances

Our model allows the baryonic resonances to decay only into two-body final states. Overall, there are 19 different decay channels: πN, ηN, ωN, $K\Lambda$, $\pi\Delta$, ρN, σN, $\pi P_{11}(1440)$, $\rho\Delta$, $\pi\Lambda$, $\overline{K}N$, $\pi\Sigma$, $\pi\Sigma(1385)$, $\eta\Lambda$, $\overline{K}^\star N$, $\pi\Lambda(1520)$, $\pi\Xi$, $\pi\Lambda_c$, $\pi\Xi_c$. The angular momenta L for the final state particles depend on the resonance and are listed in table A.1. Following Manley *et al.*, we assume that the decay width off the resonance pole is given by

$$\Gamma_{R\to ab}(m) = \Gamma^0_{R\to ab}\frac{\rho_{ab}(m)}{\rho_{ab}(M^0)} \quad , \tag{3.1}$$

where $m = \sqrt{p^\mu p_\mu}$ is the mass of the resonance, M^0 its pole mass and $\Gamma^0_{R\to ab}$ its decay width into a final state consisting of particles a and b at the pole mass. The function ρ is given by

$$\rho_{ab}(m) = \int dp_a^2 dp_b^2 \mathcal{A}_a(p_a^2)\mathcal{A}_b(p_b^2)\frac{p_{ab}}{m}B^2_{L_{ab}}(p_{ab}R)\mathcal{F}^2_{ab}(m) \ . \tag{3.2}$$

In vacuum, the spectral functions $\mathcal{A}$ depend only on the square of the four momentum. The term p_{ab} denotes the CM-momentum of the final state products. The Blatt-Weisskopf functions $B_{L_{ab}}$ depend on the the angular momentum L_{ab} of the final state particles a and b, on the so-called interaction radius $R = 1$ fm and on the CM momentum p_{ab}. The $B_{L_{ab}}$ are given by

$$\begin{aligned}
B_0(x) &= 1 && (3.3)\\
B_1(x) &= \frac{x}{\sqrt{1+x^2}} && (3.4)\\
B_2(x) &= \frac{x^2}{\sqrt{9+3x^2+x^4}} && (3.5)\\
B_4(x) &= \frac{x^3}{\sqrt{225+45x^2+6x^4+x^6}} && (3.6)\\
B_4(x) &= \frac{x^4}{\sqrt{11025+1575x^2+135x^4+10x^6+x^8}} \quad . && (3.7)
\end{aligned}$$

Compared to Manley [Man92] and the Effenberger [Eff99a] implementation, we modified the large-m behavior by a cut-off function $\mathcal{F}_{ab}(m)$. This became necessary since in some channels the width grew too fast with increasing mass to be used in a dispersion analysis. If the decay channel included only stable final state particles, this modification was not necessary ($\Rightarrow \mathcal{F}_{ab}(m) = 1$); for all other decay channels we have chosen a form factor according to Post [Pos04, eq. 3.22 on page 35]

$$\mathcal{F}_{ab}(m) = \frac{\lambda_{ab}^4 + \frac{1}{4}(s_0 - M_0^2)^2}{\lambda_{ab}^4 + \left(m^2 - \frac{1}{2}(s_0 + M_0^2)\right)^2} \quad , \tag{3.8}$$

where s_0 is the Mandelstam s for the threshold of the regarded process. The parameter λ has been tuned to pion scattering and is chosen to be

$$\lambda = \begin{cases} 0.85 & \text{GeV} \quad \text{for the } \Delta\rho \text{ channel} \\ 1.6 & \text{GeV} \quad \text{if there is an unstable meson, but no unstable baryon} \\ 2.0 & \text{GeV} \quad \text{if there is an unstable baryon, but no unstable meson} \end{cases} \quad . \tag{3.9}$$

The $\Delta\rho$ plays a special role, since it is the only channel with two unstable final state particles. The impact of this cut-off function is discussed in sec. 3.7.

3.2.3 Vacuum decay widths of the mesonic resonances

The mesonic resonances can decay into 16 different two-body decay channels ($\pi\pi$, $\pi\rho$, $K\overline{K}$, $K\pi$, $\rho\gamma$, $\pi\gamma$, $\gamma\gamma$, $D_s^+\gamma$, $D_s^-\gamma$, πD_s^+, πD_s^-, $\overline{K}\pi$, $D\gamma$, $\overline{D}\gamma$, πD, $\pi\overline{D}$) and 4 distinct three-body channels ($\pi^0\pi^0\eta$, $\pi^0\pi^-\pi^+$, $\pi^0\pi^0\pi^0$, $\pi^+\pi^-\eta$). For channels with two scalar final-state mesons with parity $P = -1$ (i.e. the dominant 2π, $K\overline{K}$, πK, $\pi\overline{K}$ channels), the angular momentum of the two final states must equal the spin of the parent resonance. Given this angular momentum, we can implement for those channels a mass-dependent partial width according to eq. 3.1. The widths of the other decay channels are assumed to be mass independent.

3.3 Elementary processes

In the following, we address the elementary reaction processes of the GiBUU collision term. In the previous sections, we already discussed the vacuum decay modes of the resonances. Additionally to these decay reactions, there are reactions implemented with two or three initial state particles. Higher correlations, e.g. four particle interactions, are neglected based on the assumption that the nuclear matter density does not reach too high values during the reactions. Such multi-particle correlations are only expected to become important at very high nuclear densities as they may be accessed within high-energy heavy-ion collisions [Lar07].

3.3.1 Two-body interactions

For the two-body interactions, we distinguish a *low-energy* and a *high-energy* region. The low-energy region is dominated by resonance contributions and small non-resonant background terms. In the high energy region, perturbative QCD becomes relevant and interaction mechanisms as, e.g., the Pomeron exchange are used to model the cross sections. According to the importance for this thesis, we will first discuss the low-energy processes. Thereafter we briefly introduce, for completeness, the high-energy processes. Finally, we discuss the matching of the low-energy and high-energy regions.

Resonant and non-resonant processes in the low-energy region

Baryon-meson processes. The implemented resonance model is reliable for baryon-meson interactions from pion-threshold up to roughly 2.3 GeV center of mass energy. The resonance production cross sections for $a\ b \to R$ itself are given by (cf. [Tei96, Eff99a] for details and derivation)

$$\begin{aligned}\sigma_{a\,b\to R}(s) &= \sum_f F_I \frac{2J_R+1}{(2J_a+1)\,(2J_b+1)} \frac{1}{\mathcal{S}_{ab}} \frac{4\pi}{p_{ab}^2(s)} \frac{s\,\Gamma_{ab\to R}(s)\,\Gamma_{R\to f}(s)}{\left(s-m_R^2-\mathrm{Re}\Pi(s)\right)^2+\underbrace{s\Gamma_{tot}^2(s)}_{=(\mathrm{Im}\Pi(s))^2}} \\ &= F_I \frac{2J_R+1}{(2J_a+1)\,(2J_b+1)} \frac{1}{\mathcal{S}_{ab}} \frac{4\pi}{p_{ab}^2(s)} \frac{s\,\Gamma_{ab\to R}(s)\,\Gamma_{tot}(s)}{\left(s-m_R^2-\mathrm{Re}\Pi(s)\right)^2+s\Gamma_{tot}^2(s)} \qquad (3.10)\end{aligned}$$

with

$$\mathcal{S}_{ab} = \begin{cases} 1 \text{ if a,b not identical} \\ \frac{1}{2} \text{ if a,b identical} \end{cases} \qquad (3.11)$$

being the symmetry factor of a and b. The term p_{ab} denotes the CM-momentum of particles a and b, the J_i's define the total spin of the particles and

$$F_I = \left\langle I^a\, I^b; i_z^a\, i_z^b | I^R\, i_z^a + i_z^b \right\rangle^2 \tag{3.12}$$

incorporates the Clebsch-Gordan coefficients due to isospin. The term $\Gamma_{ab\to R}$ denotes the so-called in-width. It is for stable particles a and b identical to the out-width $\Gamma_{R\to ab}$; for unstable particles the final result is given in [Eff99a, eq. 2.77].

In this energy region, we implemented additional *non-resonant background processes* to improve the comparison with experimental data and/or trustworthy model calculations. These background processes are point-like: while the two vertexes of , e.g., $\pi N \to R \to \pi N$ may be separated in space-time, the background process $\pi N \to \pi N$ has only one vertex and is therefore point-like. Such background processes are defined for several channels, see Appendix A.3 for details.

Baryon-baryon processes. For the baryon-baryon cross sections, matrix elements have been fitted to π, $\pi\pi$ and ρ^0 and strangeness production up to a CM-energy of ca. 2.6 GeV [Tei97]. The following processes are implemented: $NN \leftrightarrow NN$, $NN \leftrightarrow NR$, $NN \leftrightarrow \Delta\Delta$ and the background point-like contribution $NN \to NN\pi$. Details can be found in Appendix A.2.

Meson-meson processes. The impact of meson-meson interactions are negligible for the purpose of this thesis. However, such processes are implemented in the code. Besides the relevant resonance production channels, e.g. $\pi\pi \to \rho$, also non-resonant background channels are implemented for $\pi\pi \to X$, $K\overline{K} \to X$, $K^\star\overline{K} \to X$ and $K\overline{K}^\star \to X$. We refer the interested reader for details to the works of Larionov and Wagner [Wag03, Wag05].

High energy processes

The implemented PYTHIA model [pyt07], based on the LUND string model (for details see [Fal04a] and the references therein), can be used for high center-of-mass energies above ca. 2 GeV for baryon-meson collisions and ca. 2.6 GeV for baryon-baryon collisions. The total and elastic cross sections in the high-energy region are fitted to available data. The total interaction rates are fixed via these cross sections and the final state decision is then performed by PYTHIA. In former code versions, PYTHIA could not be applied in the energy region defining the upper energy boundary for the resonance model (ca. 2.6 GeV for baryon-baryon scattering, and 2.3 GeV for meson-baryon scattering). So FRITIOF was used to bridge the gap in between the PYTHIA energy region and the resonance-model region. Nowadays, this is not necessary anymore due to a modification of PYTHIA by K. Gallmeister [Gal07] which just forbids the creation of diffractive events, when kinematics and parameter settings are in conflict (before the modification these situations lead to configurations, where PYTHIA entered infinite loops).

Matching the high energy processes and the resonance region

Altogether, we have two models (PYTHIA and resonances+non-resonant background) for two different energy regimes with a small overlap region. Finally, we must match both models in this overlap region. Therefore, we use a CM-energy interval with length 2Δ and center point $\sqrt{s_0}$ in which we mix both types of events. The probability for a high energy event is then given by

$$p_{\text{high energy}}(s) = \begin{cases} 0 & \text{for } \sqrt{s} < \sqrt{s_0} - \Delta \\ \frac{\sqrt{s}-(\sqrt{s_0}-\Delta))}{2\Delta} & \text{for } \sqrt{s_0} - \Delta < \sqrt{s} < \sqrt{s_0} + \Delta \\ 1 & \text{for } \sqrt{s} > \sqrt{s_0} + \Delta \end{cases} \quad , \tag{3.13}$$

where $\sqrt{s}$ is the CM-energy and the probability for a low-energy events is consequently $1 - p_{\text{high energy}}$. We have chosen $\Delta = 0.2$ GeV and $\sqrt{s_0} = 2.2$ GeV for baryon-meson and $\sqrt{s_0} = 2.6$ GeV for baryon-baryon reactions. This procedure yields a smooth transition also after modifications of individual cross sections in the low- or high-energy region.

3.3.2 Three-body interactions

Two distinct three-body channels are incorporated: the $NN\pi \to NN$ and the $NN\Delta \to NNN$ processes[9]. In 2.5.3 the numerical realization was pointed out, however the rates have not yet been defined.

$\mathbf{NN\pi \to NN}$. The process $NN \to NN\pi$ has been extensively studied in several experiments over the last twenty years [Lan88, And88, Dau02, Har97a, Tsu88, Shi82, Bon95]. We can therefore construct well defined background cross sections on top of our resonance contributions for all possible isospin channels. In fig. A.5 we show the relevant cross sections.

The $\pi NN \to NN$ process is described by the two-step process $\pi N \to R$ followed by $RN \to NN$, and a direct background contribution. One defines the pion absorption rate as

$$\Gamma_{N_A N_B \pi \to N_a N_b} = S_{ab} S_{AB} \frac{|\vec{p}_{ab}|}{4\pi\sqrt{s}} \frac{|\mathcal{M}|^2}{2E_\pi} \frac{\rho_{N_A}}{2E_A} \frac{\rho_{N_B}}{2E_B} \quad . \tag{3.14}$$

This rate depends on the densities ρ_{N_A} and ρ_{N_B} of the nucleons in the initial state. The symmetry factors are given by

$$S_{AB} = \begin{cases} \frac{1}{2} & \text{if particles A and B are identical} \\ 1 & \text{otherwise} \end{cases} \quad .$$

The matrix element $\mathcal{M}$ can be calculated by detailed balance, assuming that it only depends on the Mandelstam variable s.

$$|\mathcal{M}(s)| = |\mathcal{M}_{N_a N_b \to N_A N_B \pi}(s)| = |\mathcal{M}_{N_A N_B \pi \to N_a N_b}(s)| \quad . \tag{3.15}$$

To obtain this matrix element we consider more closely the $NN \to NN\pi$ process. The cross section for this process is given by

$$\begin{aligned} \sigma_{N_a N_b \to N_A N_B \pi} &= S_{AB} \int \frac{(2\pi)^4}{4\,|\vec{p}_{ab}|\,\sqrt{s}} \delta^4\left(p_a + p_b - p_A - p_B - p_\pi\right) |\mathcal{M}_{N_a N_b \to N_A N_B \pi}|^2 \\ &\quad \times \frac{d^3 p_A}{(2\pi)^3\; 2E_A} \frac{d^3 p_B}{(2\pi)^3 2E_B} \frac{d^3 p_\pi}{(2\pi)^3 2E_\pi} \end{aligned} \tag{3.16}$$

$$\cong S_{AB} \frac{1}{(2\pi)^3 64\,|\vec{p}_{ab}|\,\sqrt{s}^3} |\mathcal{M}|^2 \int_{(m^2_{AB})_{min}}^{(m^2_{AB})_{max}} dm^2_{AB} \int_{(m^2_{A\pi})_{min}}^{(m^2_{A\pi})_{max}} dm^2_{A\pi} \tag{3.17}$$

---

[9] A more general approach to three-body interactions in heavy-ion collisions using GiBUU has been studied in in [Lar07].

with

$$
\begin{aligned}
m_{xy}^2 &= (p_x + p_y)^2 && (3.18)\\
(m_{AB}^2)_{min} &= (m_A + m_B)^2 && (3.19)\\
(m_{AB}^2)_{max} &= (\sqrt{s} - m_\pi)^2 && (3.20)\\
(m_{A\pi}^2)_{min/max} &= (E_A^\star + E_\pi^\star)^2 - \left(\sqrt{(E_A^\star)^2 - m_A^2} \pm \sqrt{(E_\pi^\star)^2 - m_\pi^2}\right)^2 && (3.21)\\
E_\pi^\star &= \frac{s - m_{AB}^2 - m_\pi^2}{2m_{AB}} && (3.22)\\
E_A^\star &= \frac{m_{AB}^2 + m_A^2 - m_B^2}{2m_{AB}} \quad , && (3.23)
\end{aligned}
$$

where $\vec{p}_{ab}$ denotes the momentum of the particles a and b in their center of mass frame. Equation 3.17 holds under the assumption that the matrix element is only dependent on the Mandelstam s. We therefore obtain

$$
|\mathcal{M}(s)|^2 = \left(S_{AB}\frac{1}{64(2\pi)^3\,|\vec{p}_{ab}|\,\sqrt{s}^3}\int dm_{AB}^2 dm_{A\pi}^2\right)^{-1} \sigma_{N_aN_b\to N_AN_B\pi}\ . \tag{3.24}
$$

After inserting this result for $|\mathcal{M}(s)|^2$ into eq. 3.14 we find that $\Gamma_{N_AN_B\pi\to N_aN_b}$ depends linearly on $\sigma_{N_aN_b\to N_AN_B\pi}$. This cross section $\sigma_{N_aN_b\to N_AN_B\pi}$ is, according to eq. A.31, a sum of background and resonance contributions. Therefore, $\Gamma_{N_AN_B\pi\to N_aN_b}$ can also be split into a resonance and a background contribution.

$$
\Gamma_{N_AN_B\pi\to N_aN_b} = \Gamma^{\mathrm{BG}}_{N_AN_B\pi\to N_aN_b} + \Gamma^{\text{resonance contribution}}_{N_AN_B\pi\to N_aN_b} \tag{3.25}
$$

with

$$
\begin{aligned}
\Gamma^{\mathrm{BG}}_{N_AN_B\pi\to N_aN_b} &\sim \sigma^{\mathrm{BG}}_{NN\to NN\pi} && (3.26)\\
\Gamma^{\text{resonance contribution}}_{N_AN_B\pi\to N_aN_b} &\sim \sigma^{\text{resonance contribution}}_{NN\to NN\pi} \quad . && (3.27)
\end{aligned}
$$

More details concerning this absorption rate can be found in [Bus04]. The resonance absorption part is included in the collision term for the resonances, which are propagated explicitly. The background absorption rate $\Gamma^{\mathrm{BG}}_{N_AN_B\pi\to N_aN_b}$ is shown in fig. 3.1 for symmetric nuclear matter at $\rho = \rho_0$ with $\rho_0 = 0.168\ \mathrm{fm}^{-3}$ being the normal nuclear matter density. For positive pions we get the same results as for negative ones due to isospin symmetry. Notice that in-medium modifications are not accounted for so far.

NN$\boldsymbol{\Delta}$ → NNN. The rate for the $NN\Delta \to NNN$ process is based on the model of Oset *et al.* [Ose87]. We will come back to this in the discussion of the Δ in-medium width in sec. 3.6.1.

3.4 Medium effects

As medium modifications, we include Pauli-blocking and Fermi-motion of the nucleons, Coulomb forces and hadronic potentials. After discussing these features, we address the cross-section modifications within the nuclear medium.

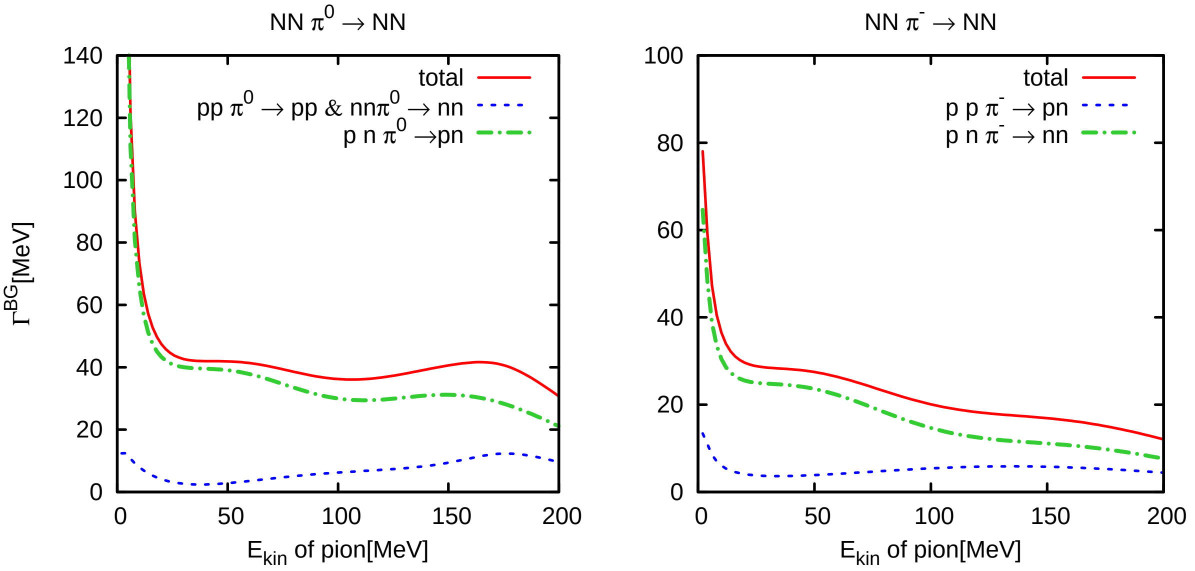

Figure 3.1: The $NN\pi \rightarrow NN$ background absorption rate for symmetric nuclear matter at $\rho = \rho_0$. In-medium-modifications are not included in these decay widths. The rate for π^0 is shown on the left and for π^- on the right panel.

3.4.1 The electromagnetic forces

The electromagnetic potential is implemented according to the fast *ADI* algorithm presented in [Tei96, appendix B]. After the reimplementation in the new code, this algorithm has been successfully cross checked by the slower integral representation of the potential

$$\Phi(\vec{r}) = \int d^3r' \frac{\rho(r')}{|\vec{r} - \vec{r}\,'|} \quad . \tag{3.28}$$

By default, the electromagnetic potential is considered in the propagation of the test-particles. However, it is a long-ranging smooth potential which does not fluctuate much within typical reaction volumes. We assume therefore that it does not influence particle reaction rates, i.e. it is not considered in the collision term.

3.4.2 Hadronic potentials

The hadronic potentials are introduced as time-like components of vector potentials in the local rest-frame (LRF)[10] [Tei97]. For our purposes the most important mean field potentials are those acting on the nucleon and the resonances. The nucleon mean-field potential is parametrized by Welke et al. [Wel88] as a sum of a Skyrme term depending only on the density and a momentum-dependent contribution

$$A_N^0 = a\frac{\rho(\vec{r})}{\rho_0} + b\left(\frac{\rho(\vec{r})}{\rho_0}\right)^\tau + \frac{2c}{\rho_0}g\int \frac{d^3p\,'}{(2\pi)^3}\frac{f(\vec{r},\vec{p}\,')}{1+\left(\frac{\vec{p}\,'-\vec{p}}{\Lambda}\right)^2} \tag{3.29}$$

with $\rho_0 = 0.168 fm^{-3}$ and $g = 4$ is the nucleon degeneracy. Five distinct standard parameter sets, which differ in the nuclear matter compressibility, were adjusted to nuclear matter properties

---

[10] The *local rest frame* is defined to be the frame in which the baryonic currents vanish.

Type of parameter set	$C[MeV]$	a[MeV]	b[MeV]	c[MeV]	τ	Λ[1/ fm]
Soft mom.-dep. (EQS 1)	215	-108.6	136.8	-63.6	1.26	2.13
Hard mom.-dep. (EQS 2)	380	-10.0	38.0	-63.6	2.4	2.13
Soft (EQS 3)	215	-287.0	233.7	0	1.23	-
Hard (EQS 4)	380	-124.3	71.0	0	2.0	-
Medium mom.-dep. (EQS 5)	290	-29.3	57.2	-63.6	1.76	2.13

Table 3.4: Parameter sets for the nuclear potential presented in eq. 3.29. The five sets differ only in the nuclear matter compressibility C which is listed in the second column. Those sets have been obtained by Teis [Tei96] assuming a nuclear matter saturation density $\rho_0 = 0.168\ \text{fm}^{-3}$, a binding energy of 16 MeV and the momentum-dependent (mom.-dep.) parameter sets fulfill $A^0_N(\rho = \rho_0, p = 0) = -75$ MeV and $A^0_N(\rho = \rho_0, p = 800\ \text{MeV}) = 0$ MeV. Cf. appendix A.4.1 for details on the fixing procedure.

by Teis [Tei97] and are listed in table 3.4. By default, the parameter set *medium momentum-dependent* (EQS 5) is being used for all calculations. Details on the parameter fixing procedure are given in appendix A.4.

Phenomenology tells us that the Δ potential has a depth of about -30 MeV at ρ_0 [Eri88, Pet98]. Compared to a momentum independent nucleon potential, which is approximately -50 MeV deep, the Δ potential is assumed to be

$$A^0_\Delta(\vec{r}, \vec{p}) = \frac{2}{3}\ A^0_N(\vec{r}, \vec{p}) \quad , \tag{3.30}$$

This incorporates the assumption that there is a common momentum dependence for the nucleon and the Δ potentials. For all spin 3/2 resonances the same potential as for the Δ is used; for all other non-exotic resonances, we use the same potential as for the nucleon. The strange resonances with $S = -1$ get 2/3 of the nucleon potential according to the number of the light up- and down-quarks. The more exotic nuclei ($S < -1$ or $C \neq 0$) are propagated without potential. Since these potentials are only well defined within the LRF, we must first boost to the LRF before we evaluate the single test-particle energy or before we convert the potential A^0 to the scalar V as shown in eq. 2.29.[11]

A low-energy potential for the pion up to kinetic energies of 150 MeV is included according to [Bus04]. However, whenever it is not explicitly stated otherwise then it is not used for the calculations.

3.4.3 Pauli blocking and Bose enhancement

Within our calculations, Pauli blocking is approximated by the condition that each momentum state below the Fermi momentum is Pauli blocked. The default implementation is given by the following procedure:

1. In the test-particle representation, the phase-space density of particles is a sum of δ-functions. For the Pauli blocking, the δ functions are smeared in position space by a Gaussian of width $\sigma = 1$ fm [12] to get a smoother distribution. We emphasize, that this

---

[11] Note there is also an alternative Yukawa potential implemented in the code. However, it was not used for any calculations.

[12] This value is tuned to a number of ensembles N greater than 200. Using larger N one could even reduce the width.

procedure is just a numerical trick to compensate for the finite number of test-particles and has nothing to do with a wave-packet interpretation for the test-particles.

2. Then, we define the integral

$$I(\vec{r},\vec{p}) = \sum_{i\in\{1,N(t)\}\ \text{with}\ \vec{p}_i\in V_p} \frac{1}{\sqrt{2\pi\sigma}^3} \int_{V_r} d^3r\ e^{-\frac{(\vec{r}-\vec{r_i}')^2}{\sigma^2}} . \tag{3.31}$$

   This integral basically measures the number of test-particles which are in momentum space within a volume V_p around $\vec{p}$ and at the same time also close to the volume V_r around $\vec{r}$.

3. Due to spin statistics, only 2 fermionic states can be accommodated in a phase space cell of size $1/\left(2\pi\right)^3$. Therefore, the probability for Pauli blocking is given by

$$p(\vec{r},\vec{p}) = \frac{I(\vec{r},\vec{p})}{\Delta V_r \Delta V_p \frac{2}{(2\pi)^3} \times \text{ number of ensembles}} . \tag{3.32}$$

   The volumes ΔV_r and ΔV_p are chosen with radii $r_r = 1.86$ fm and $r_p = 0.08$ fm, respectively. The size of these boxes is chosen to minimize statistical fluctuations so far, such that the Pauli blocking condition is well fulfilled for ground state nuclei.

4. Via a Monte-Carlo decision one now decides whether a given phase space point $(\vec{r},\vec{p})$ is Pauli blocked or not.

The Bose enhancement factors are neglected due to the low phase-space density of bosons (e.g. pions, kaons) in the regarded reactions.

3.5 Reactions in the medium

Besides the modification of the collision rate via the Pauli blocking term, the presence of potentials modifies the in-medium kinematics and should be considered in the collision term. For resonance production, we will also include the width modification. After addressing general aspects, we deal with resonance production and discuss the non-resonant direct processes where the medium dependence of the cross section is a major unknown.

3.5.1 Preliminaries

In general, the cross section for a process $a+b \to 1+\ldots+N$ is given by

$$d\sigma = \underbrace{\frac{1}{v_{rel}}}_{I_{\text{flux}}} \times \underbrace{\frac{n_a n_b n_1 \ldots n_N |\mathcal{M}|^2}{2p_a^0 2p_b^0}}_{I_{\mathcal{M}}} \times \underbrace{\prod_{i=1}^{N} \frac{d^4p_i}{(2\pi)^4} \mathcal{A}(p_i) (2\pi)^4 \delta^4 \left(p_a + p_b - \sum_{i=1}^{N} p_i \right)}_{I_{\Phi}} \tag{3.33}$$

where the field normalization factors n_i are given by

$$n_i = \left\{ \begin{array}{ll} 1 & \text{for bosons} \\ 2m_i & \text{for fermions} \end{array} \right. . \tag{3.34}$$

The function $\mathcal{A}$ denotes the spectral function and $\mathcal{M}$ is the matrix element. In a coupled-channel model like GiBUU, one must consider cross sections for various processes. To evaluate for each of the various channels the proper in-medium cross section, e.g. including RPA in-medium resummations in the matrix elements and a full modification of the final-state phase-space, has not yet been achieved in any hadronic transport model. Thus approximations have to be applied when evaluating the in-medium cross section. In eq. 3.33 the cross section is split into three different terms: the flux I_{flux}, matrix element $I_{\mathcal{M}}$ and phase space I_{Φ} terms. While the I_{flux} term can easily be modified in the medium, the phase space term and especially the matrix element term usually have to be approximated.

A commonly used approximation is the following. Assuming that the amount of potential energy of incoming resonance and outgoing final states would be the exactly the same, then one could view the potential as a background field which is assumed not to influence the reaction rates. E.g. let us consider a momentum independent potential and an elastic $NN \to NN$ scattering process. In this case the potential energy is exactly conserved during the reaction. One defines a potential-corrected, so-called 'free', center of mass energy

$$s_{\text{free}} = (p_{\text{a,free}} + p_{\text{b,free}})^2 \tag{3.35}$$

where

$$p_{\text{free}} = (\sqrt{m^2 + \vec{p}^{\,2}}, \vec{p}) \quad . \tag{3.36}$$

With the help of this free CM-energy, the in-medium cross section is approximated by

$$\sigma \approx \sigma_1 = I_{\text{flux}} \frac{\sigma_{\text{vac}}(s_{\text{free}})}{I_{\text{flux,vac}}} \quad . \tag{3.37}$$

Within this method only the flux factor is explicitly evaluated in the medium, the product of the two other terms $I_{\mathcal{M}} I_{\Phi}$ is approximated by the vacuum values shifted in the center of mass energy to s_{free}. The problem with this approximation starts as soon as the outgoing and incoming potential energy differs, which is the case for momentum-dependent potentials and for in-elastic processes where there are different particles in the incoming and outgoing states. Henceforth a next step of sophistication would give

$$\sigma \approx \sigma_2 = I_{\text{flux}} \frac{\sigma_{\text{vac}}(s_{\text{free}})}{I_{\text{flux,vac}} I_{\Phi,\text{vac}}} I_{\Phi} \quad , \tag{3.38}$$

where one additionally implements a modification of the outgoing phase space. Our model for in-medium hadron-hadron collisions is mostly based on the assumption $\sigma \approx \sigma_1$ and $\sigma \approx \sigma_2$; for electron and photon induced processes we use a more involved treatment which is presented in chapter 5 (pages 91 ff.) and includes also explicit modifications of $I_{\mathcal{M}}$. In the following, we first consider the hadron-hadron reactions.

3.5.2 Resonance production

In the works of Lehr [Leh03] and Effenberger [Eff99a], the resonance production cross section has been modeled without taking into account the real part of the self energy. In the following, we first detail their model, focusing then on the present implementation.

The Lehr and Effenberger ansatz. The ansatz is overall very similar to $\sigma \approx \sigma_2$ with σ_2 defined in eq. 3.38. First the mass μ of the produced resonance without the potential contributions is evaluated and hereafter the process is treated like a vacuum collision at $s = \mu$. In the process $ab \to R$, energy and momentum conservation yield

$$\begin{aligned} \vec{p}_a + \vec{p}_b &= \vec{p}_R && (3.39) \\ E_a + E_b &= E_R = \sqrt{\vec{p}_R^{\,2} + (\mu + V(p_R, \rho))^2} \quad . && (3.40) \end{aligned}$$

The bare mass μ of the resonance is therefore given by the energy and momentum of the incoming particles[13]

$$\mu = \sqrt{E_R^2 - \vec{p}_R^2} - V(p_R, \rho) \quad . \tag{3.41}$$

Now, we replace in a first step in the vacuum cross section (cf. eq. 3.10) s by μ,

$$\sigma_{a\,b \to R}(s) \sim \frac{1}{p_{ab}^2(\mu)} \frac{\mu^2\,\Gamma_{ab\to R}(\mu)\,\Gamma_{\text{tot}}(\mu)}{\left(\mu^2 - M_R^2\right)^2 + \mu^2 \Gamma_{\text{tot}}^2(\mu)} \quad . \tag{3.42}$$

As a next step we need to consider a correction due to the relative velocities of the colliding particles which was introduced by Effenberger [Eff99a, cf. especially eq. 3.45]. According to our preliminary considerations this gives the $\sigma \approx \sigma_1$ approximation scheme

$$\sigma(s) = I_{\text{flux}} \frac{\sigma\,(\mu)}{I_{\text{flux,vac}}} \quad . \tag{3.43}$$

Hence the cross section in the case of a resonance produced in a potential is given by

$$\begin{aligned} \sigma_{a\,b \to R}(s) = \quad & \frac{v_{\text{rel,vac}}^{ab}}{v_{\text{rel}}^{ab}} F_I \frac{2J_R + 1}{(2J_a + 1)\,(2J_b + 1)} \frac{1}{\mathcal{S}_{ab}} \\ & \times \frac{4\pi}{p_{ab}^2(\mu)} \frac{\mu^2\,\Gamma_{ab\to R}(\mu)\,\Gamma_{\text{tot}}(\mu)}{\left(\mu^2 - M_R^2\right)^2 + \mu^2 \Gamma_{\text{tot}}^2(\mu)} \quad . \end{aligned} \tag{3.44}$$

In the medium the widths of the resonances will be modified. Either there might be Pauli-blocking of final states in the medium, or new decay channels may open in the medium. The Δ resonance, for example, has a much smaller $\Delta \to \pi N$ partial width due to the Pauli-Blocking of the nucleons, but gains a collisional width due to $\Delta NN \to NNN$ and $\Delta N \to NN$ processes. Therefore, we have to take these modified widths and new final state scenarios into account, replacing in eq. 3.44

$$\Gamma_{\text{tot}}^{\text{vacuum}}(s) \to \Gamma_{\text{tot}}^{\text{medium}}(s, \vec{p}) \tag{3.45}$$

in the propagator and in the numerator. The so called in-width $\Gamma_{ab\to R}$ [Eff99a, eq. 2.77] is not to be modified since we do not assume a modification of the couplings. The Pauli-blocking of the resonances could have an influence on the in-width but generally it does not, since the resonance-densities are too low.

In terms of our preliminary considerations this means nothing else than setting

$$I_{\mathcal{M}}(s) = v_{\text{rel,vac}}^{ab} F_I \frac{2J_R + 1}{(2J_a + 1)\,(2J_b + 1)} \frac{1}{\mathcal{S}_{ab}} \frac{4\pi\mu\Gamma_{ab\to R}(\mu)}{p_{ab}^2(\mu)} = I_{\mathcal{M},\text{vac}}(\mu) \tag{3.46}$$

---

[13] Note that eq. 3.41 must be evaluated in the local rest frame, since only there the potential is well defined. This is a technical complication of the procedure, because one needs to boost all variables to this system.

and

$$I_\Phi = \frac{\mu \Gamma_{\text{tot}}^{\text{medium}}(\mu)}{\left(\mu^2 - M_R^2\right)^2 + \mu^2 (\Gamma_{\text{tot}}^{\text{medium}})^2(\mu)} = I_{\Phi,\text{vac}}(\mu, \Gamma \to \Gamma^{\text{medium}}) \quad . \tag{3.47}$$

However, especially the last term I_Φ which is nothing else then the resonance spectral function ($I_\Phi = \mathcal{A}_R$) can be evaluated exactly given that the in-medium self-energies of the resonances have been determined.

The new ansatz Thus in our new ansatz, we still evaluate μ and set

$$I_{\mathcal{M}}(s) = I_{\mathcal{M},\text{vac}}(\mu) \quad , \tag{3.48}$$

but we use the proper phase space factor $I_\Phi = \mathcal{A}_R(p_R)$. Thus the cross section is given by

$$\begin{aligned} \sigma_{a\,b\to R}(s, p_R) &= I_{\text{flux}} I_{\mathcal{M},\text{vac}}(\mu) I_\Phi & (3.49)\\ &= I_{\text{flux}} I_{\mathcal{M},\text{vac}}(\mu) \mathcal{A}_R(p_R) \quad , & (3.50)\end{aligned}$$

which exactly corresponds to the $\sigma \approx \sigma_2$ scheme introduced in eq. 3.38. The real and imaginary part of the self energy Π will be evaluated in the medium and the resonances will be dressed resonances. We will address the self energies in sec. 3.7.

3.5.3 Resonance decays

For the decays of the resonances we make the assumption that in the medium

$$\Gamma_{R\to ab}(s) = \begin{cases} \Gamma_{R\to ab,vac}(\mu) & \text{if there is a solution to } p_R = p_a + p_b \\ 0 & \text{else} \end{cases} \quad , \tag{3.51}$$

where μ is again the bare mass of the resonance. Within this assumption we do not include modifications of the final state phase space, except that we reject decay events where we can not fulfill energy and momentum conservation given the intial momentum p_R. E.g. if μ is greater than the sum of the vacuum masses of particles a and b, then $\Gamma_{R\to ab}(s)$ is non-zero. But if the in-medium mass s of the resonance is smaller than the in-medium masses m_a and m_b, then the event must be rejected. This basically corresponds for two-body reactions to a slightly modified $\sigma \approx \sigma_1$ scheme.

3.5.4 Direct processes

Besides resonance contributions, there are also direct contributions (e.g. $\pi N \to \eta N$). The cross section and/or matrix element parametrizations for these contributions are obtained from vacuum kinematics, either measured in elementary processes or determined in calculations which do not take any potentials into account. As an approximation, we assume that the in-medium cross sections depend – as the vacuum ones – only on s and use the $\sigma \approx \sigma_1$ scheme in which the in-medium cross section is given by

$$\sigma(s) = \frac{v_{\text{rel,vac}}}{v_{\text{rel}}} \sigma\left(s_{\text{free}}\right) \quad , \tag{3.52}$$

including the flux factor correction. For the evaluation of s_{free} we choose the CM-frame of both particles as a preferred frame of reference. Therefore we boost with the full kinematics to this frame and evaluate there s_{free}. The decision for the final state momenta is performed according to the algorithm presented in appendix B.2.

3.6 Self energies

3.6.1 Imaginary part of the self energy

In our ansatz, the imaginary part of the self energy Π is given by

$$\mathrm{Im}\Pi = -\sqrt{p^\mu p_\mu}\,(\Gamma_{\mathrm{coll}}(p,\vec{r},t) + \Gamma_{\mathrm{free,P.b.}}(p,\vec{r},t)) \tag{3.53}$$

where $\Gamma_{\mathrm{free,P.b.}}$ denotes the Pauli-blocked free decay width of the regarded particle and Γ_{coll} denotes the collisional broadening of the considered particle due to 2- and 3-body scattering processes. For calculations at low density and in the approximation that the nucleus stays close to its ground state, one can approximate the collisional broadening by

$$\Gamma_{\mathrm{coll}}(p,\vec{r},t) = \int_{\text{Fermi sea at } \vec{r}} \sigma(p,p')\ v_{\mathrm{rel}}(p,p')\ \frac{d\vec{p}\,'}{(2\pi)^3} \quad , \tag{3.54}$$

where $\sigma(p,p')$ are vacuum cross sections and the dispersion relation for the particles in the Fermi sphere is the vacuum one, i.e. $p_0' = (\vec{p}\,'^{\,2} + m_N^2)^{1/2}$. This approximation for Γ_{coll} is first order in density since the cross sections are not density dependent. To get a self-consistent result, one could now reinsert our first-order result for Γ_{coll} into the cross section evaluation of eq. 3.54 and iterate the procedure until a self-consistent width was generated. Such an effort has been performed for simpler systems with less reaction channels by, e.g., Frömel *et al.* [Fro07] for quark matter and Lehr *et al.* [Leh02] for nuclear matter. However, this task is at present too demanding within our model given the large number of possible channels and the large number of involved particle species.

Cut-Off. If the mass of the resonance is smaller than the mass of its lightest decay channel, then the contribution of the Pauli-blocked free width is vanishing $\Gamma_{\mathrm{free,P.b.}} = 0$. For numerical reasons [14], we neglect also the collisional width Γ_{coll} below this threshold[15]. This is justified since the collisional broadening is anyhow small, especially at low masses.

The nucleon. For the nucleon, we have no information on the off-shell cross sections. Therefore, we assume that the interaction cross sections with other particles are independent of the nucleon mass; cf. appendix A.2 for details on the implemented cross sections. Henceforth, the collisional broadening is also mass independent. In fig. 3.2, we show this mass-independent collisional width for different nuclear densities. At low momentum ($\lesssim 0.5$ GeV) the curves show different slopes and different threshold behaviors. In the region where the momentum is smaller than the specific Fermi momentum ($p_f \sim \rho^{2/3}$), Pauli blocking does not allow for any scattering process to occur. Increasing the momentum, one slowly overcomes Pauli blocking and arrives in the regime where the width is proportional to the number of scattering partners, i.e. proportional to ρ. At 1 GeV momentum, one observes that the slopes of all four curves become already very similar and the regime of $\Gamma \sim \rho$ is almost reached. Note, that according to our ansatz, the width should vanish below the Fermi momentum and the spectral function should be proportional to a δ function. However, we represent the δ-function in the numerical implementation by a Gaussian

---

[14] We want to avoid that resonances leave the nucleus with a mass lower than the mass of its lightest vacuum decay channel. The resonance would then be stable in vacuum. This may occur if one performs simulations which neglect the off-shell potential.

[15] As an example, let us consider the Δ resonance: we set $\Gamma = 0$ for $\sqrt{(\sqrt{m^2+\vec{p}^{\,2}},\vec{p})^2} < m_N + m_\pi$.

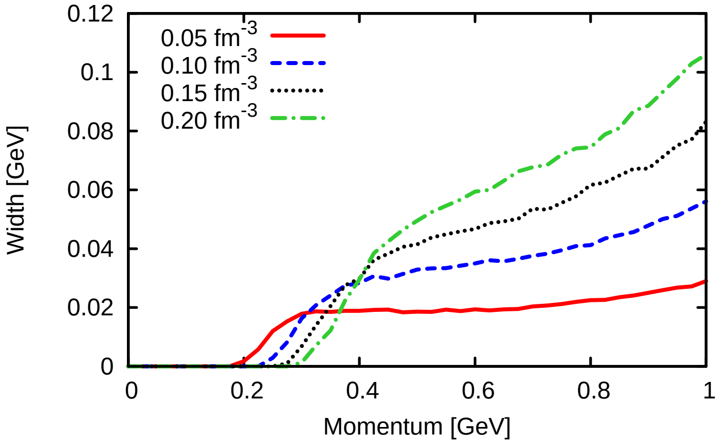

Figure 3.2: Collisional width of the nucleon in symmetric nuclear matter of density $\rho = 0.05, 0.10, 0.15, 0.20\ \mathrm{fm}^{-3}$ as a function of the nucleon momentum.

of 1 MeV width. Thus in fig. 3.2, the width does not go to 0 MeV but to 1 MeV below the Fermi momentum.

D. Kalok [Kal07, cf. especially fig. 5.5] compared the width discussed above with the width obtained with a self-consistent Hartree-Fock method. He shows that both models yield similar results for momenta larger than the Fermi momentum. However, the more sophisticated model generates also a width below the Fermi momentum since it also includes the gain contribution to the width. This leads to a smearing of the Fermi sphere and to a high-momentum tail in the momentum distribution. The high-momentum tail is not generated in our simplified approach.

The baryon resonances. As already pointed out by Effenberger [Eff99a], the collisional width of the Δ within a $\sigma\rho v$ ansatz differs from the results of Oset *et al.* [Ose87]. Analogous to fig. 12 of [Ose87], we choose a special kinematical situation for our study. In an isotropic medium, the width is a function of both E_Δ and $|p_\Delta|$. However, we now want to assume that the Δ has been excited by a pion colliding with a nucleon out of the Fermi sea. Due to this, an average E_Δ and $|p_\Delta|$ can be evaluated as soon as we fix the pion energy. Varying the energy of the pion, we henceforth follow a special cut in the $(E_\Delta, |p_\Delta|)$ plane. This cut is given by

$$|\vec{p}_\Delta| \quad = \quad < \sqrt{(\vec{p}_\pi + \vec{p}_N)^2} >_{\text{Fermi sea}} = \sqrt{p_\pi^2 + \frac{3}{5}p_{\mathrm{F}}^2} = \sqrt{E_\pi^2 - m_\pi^2 + \frac{3}{5}p_{\mathrm{F}}^2} \quad , \tag{3.55}$$

$$E_\Delta \quad = \quad < E_\pi + E_N >_{\text{Fermi sea}} = E_\pi + \frac{3}{5}\frac{p_{\mathrm{F}}^2}{2m_N} + m_N \quad , \tag{3.56}$$

where p_F denotes the Fermi momentum. For the $\Delta N \to \Delta N$ and $\Delta N \to NN$ reactions Effenberger [Eff99a] proposed a single-pion exchange model as detailed in appendix A.2.1 where also plots of the resulting cross sections are shown. In fig. 3.3 we compare our result including this single tree-graph model to the results of Oset *et al.*. The total width obtained within our model is represented by the double dashed line and must be compared to the result of Oset and Salcedo (solid curve) which is phenomenologically consistent. Obviously, our model underestimates the collisional width considerably at low pion energies and predicts considerably larger width at high pion energies. Note that the Oset model should not be used for too high energies[16]. While

---

[16] We assume a validity range given by the plot ranges in [Ose87]: $T_\pi \lessapprox 0.35$ GeV

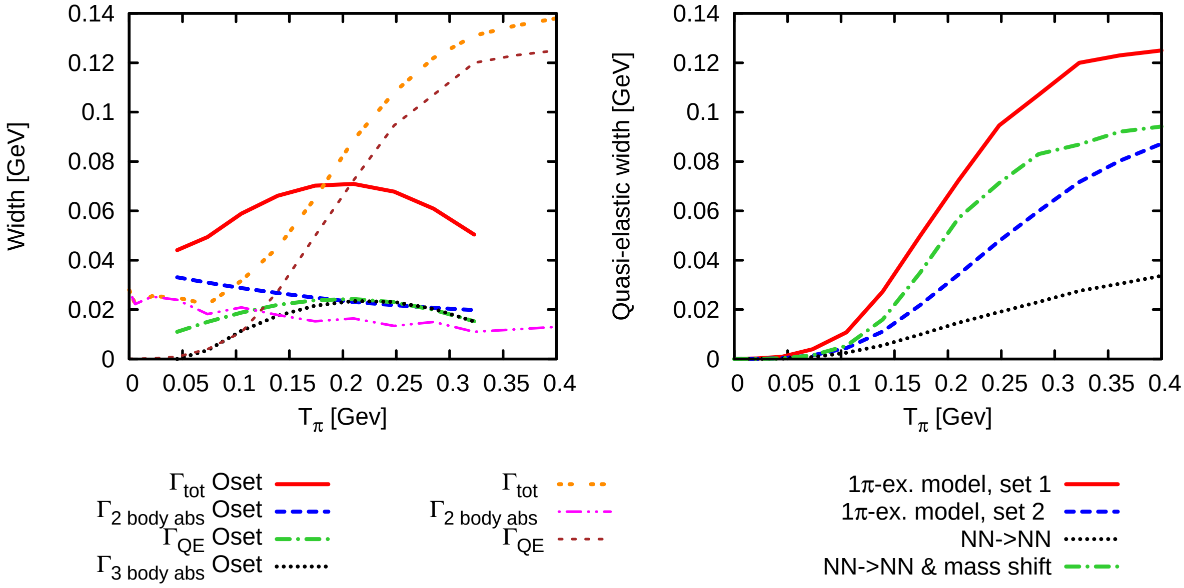

Figure 3.3: [color online] The left panel shows a comparison of the collisional width of the Δ in comparison to the result of Oset and Salcedo [Ose87] at $\rho = 0.75\rho_0$ fm^{-3}. We choose analogous kinematics to fig. 12 of [Ose87]. We assume that the Δ was excited by a πN collision. The energy of the Δ is then a function of the kinetic energy of the pion T_π. On the right panel, we show only the quasi-elastic width for different model approaches.

there is at least qualitative agreement for the 2-body absorption contributions (dashed and dashed-double-dotted), the quasi-elastic contribution (dashed-dotted vs. short-dashed) shows differences in shape and absolute magnitude. To investigate this QE-width further we have compared in the right panel of fig. 3.3 different approaches to estimate this width. The solid and dashed lines show the result of the 1π-exchange model as presented in appendix A.2.1 for the two parameter sets:

$$\begin{array}{lll} \text{set } \#\ 1: & \Lambda = 0.6\ \text{GeV}, & f_{\Delta\Delta\pi} = 4/5 f_{NN\pi} \quad , \\ \text{set } \#\ 2: & \Lambda = 1.2\ \text{GeV}, & f_{\Delta\Delta\pi} = 9/5 f_{NN\pi} \quad . \end{array}$$

Both show the same qualitative behavior, but differ in the absolute magnitude. In former code versions, the elastic $\Delta N \to \Delta N$ cross section was assumed to be same as the $NN \to NN$ one. The dotted curve shows the result within this assumption where the $NN \to NN$ cross section has been charge averaged. However, the center of mass energy in $NR \to NR$ scattering is shifted by $m_R - m_N$ in comparison to $NN \to NN$ scattering. As an educated guess one might therefore assume

$$\sigma_{NR\to NR}(\sqrt{s}) = \sigma_{NN\to NN}(\sqrt{s} - m_R + m_N) \quad , \tag{3.57}$$

where m_R is the mass of the incoming resonance. The qualitative behavior and absolute magnitude of this educated guess (dashed-dotted curve) is similar to the 1π exchange model (dashed and solid curves). Note that the $\Delta N \to \Delta N$ cross section and especially the coupling constants including two Δ's are basically unknown and not accessible for a direct measurement. The comparison with NN elastic scattering shows that our estimate looks reasonable. However, one might ask why there is such a discrepancy, both qualitatively and quantitatively, to the

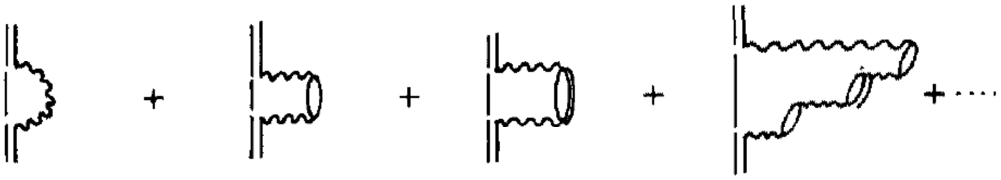

Figure 3.4: The upper figure shows schematically the type of diagrams being included in the work of Oset and Salcedo [Ose87]. The double-lines represent Δ propagators, the solid ones nucleon propagators and the wavy ones pion propagators. This picture is taken from the work of Oset and Salcedo [Ose87, fig. 2].

result obtained by Oset and Salcedo who focused on so-called RPA-ladder-diagrams as shown in fig. 3.4. They accounted for loop contributions and short-range correlations but not for a direct $\pi\Delta\Delta$ coupling. However, this direct $\pi\Delta\Delta$ coupling is in our estimate found to be sizable. We emphasize that the simple tree-graph model for $N\Delta \to N\Delta$ as detailed in appendix A.2.1 should not be taken too serious before one really evaluates the impact of this tree-graph in a unitary coupled channel scheme. Nevertheless, the two approaches presented here – the Oset/Salcedo RPA-approach and the 1π-exchange model approach according to appendix A.2.1 – include complementary model ingredients. In future, it might be interesting to include the $\pi\Delta\Delta$ vertex in the Oset-and-Salcedo approach which is, however, out of scope for the present work. Finally, we will have to compare the implications of our estimate to the ones of the Oset model when analyzing πA and $\gamma^\star A$ experiments to evaluate the quality of our assumptions.

The Oset/Salcedo model gives, additionally, a non-negligible 3-body contribution (solid green curve), which has not been included in our approach. Note that the Oset/Salcedo model is not applicable for energies higher than $T_\pi \simeq 350$ MeV - so we can not use this model for a dispersion analysis. Whenever there is a curve including this width, the real part is just given by the mean field. Due to this we get a normalization error of the order of ±5%.

For all other resonances we include the inelastic cross sections detailed in appendix A.2.1.

In the following will use three different models to perform our calculations and evaluate the influence of the in-medium change of the Δ and other resonances on our observables. To summarize the options:

mass-shift option. For the Δ and other baryons, we use the implemented baryon-baryon reaction channels ($NR \to NR$, $NR \to NN$, $NR \to NR'$) and the ordinary vacuum decays to determine the width. In this case we do not incorporate any explicit $NN\Delta \to NNN$ processes.

no mass-shift option. As the first option, but we use $\sigma_{NR\to NR}(\sqrt{s}) = \sigma_{NN\to NN}(\sqrt{s})$.

mass-shift+Oset option. As the first option, but we use different cross sections for the Δ resonance. The Oset/Salcedo model [Ose87] gives probabilities for a quasi-elastic Δ collision, a 2-body or 3-body absorption. These probabilities are then included as reaction rates in the collision term[17].

In fig. 3.5 and-3.6, we compare the collisional width of the four most prominent resonances in γN scattering ($P_{33}(1232)$, $S_{11}(1535)$, $D_{13}(1520)$, $F_{15}(1680)$) using the three different prescriptions. The left panels of fig. 3.5 and 3.6 show the result for the collisional broadening including

---

[17] See appendix A.2.1 for details.

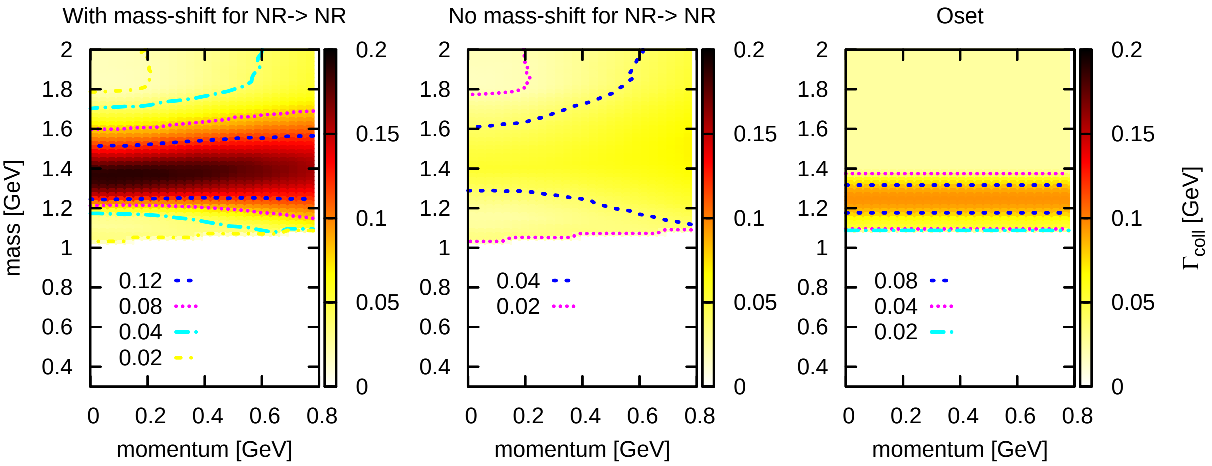

Figure 3.5: The collisional width of the $P_{33}(1232)$ resonance in symmetric nuclear matter of density $\rho = 0.168$ fm^{-3} as a function of resonance momentum and mass. The left panel shows the result according to the mass-shift scenario, the middle panel shows the no-mass-shift result and the right panel shows our adaptation of the collisional broadening according to Oset *et al.* [Ose87].

the mass-shift, whereas the middle panel in fig. 3.5 and the right panels in fig. 3.6 show the no-mass-shift result. One observes that the shifted cross section leads to more collisional broadening, especially at low resonance momentum. For the Δ, the right panel of fig. 3.5 shows also our adaptation of the collisional broadening according to Oset *et al.* [Ose87] which we assume to be momentum independent and only mass-dependent.

Numerical implementation

As detailed before we assume that the nuclear matter is mostly undisturbed by the reaction process such that we can treat the nuclear phase-space density as constant in time. Additionally, we approximate the nuclear phase space density by a Fermi sphere at position $\vec{r}$. With this prerequisites, the width $\Gamma(\vec{r}, p)$ according to eq. 3.54 depends only on the neutron- and proton-density at position $\vec{r}$, the mass and the absolute three-momentum of the resonance. To save CPU-time, we tabulate the width for each resonance as a function of these four variables with a grid size of

$$\Delta|\vec{p}| = 40 \text{ MeV} \tag{3.58}$$

$$\Delta m \simeq 15 \text{ MeV} \tag{3.59}$$

$$\Delta\rho_{\rm proton} = \Delta\rho_{\rm neutron} = 0.025 \text{ fm}^{-3} \tag{3.60}$$

Since we later want to use the width for a dispersion relation analysis we need a very large grid size in m (400 grid points) and we need a large grid size in $|\vec{p}|$ (75 grid points) for high resonance momenta. For the density dependence only a few grid points (5 points) are needed since the collisional width is anyhow close to linear in the density. Altogether we need for each of the 31 non-strange resonances a grid of size $400 \times 75 \times 5^2$. On this grid we store both the collisional width and the Pauli blocked free width. Even in single precision, this array causes roughly 180 MB memory usage. To evaluate $\Gamma(\vec{r}, p)$ we use a Monte Carlo algorithm with 2000 integration points. The tabulation of the width takes roughly 1.5 CPU days per resonance on a *Dual-Core AMD Opteron 3.0 GHz*.

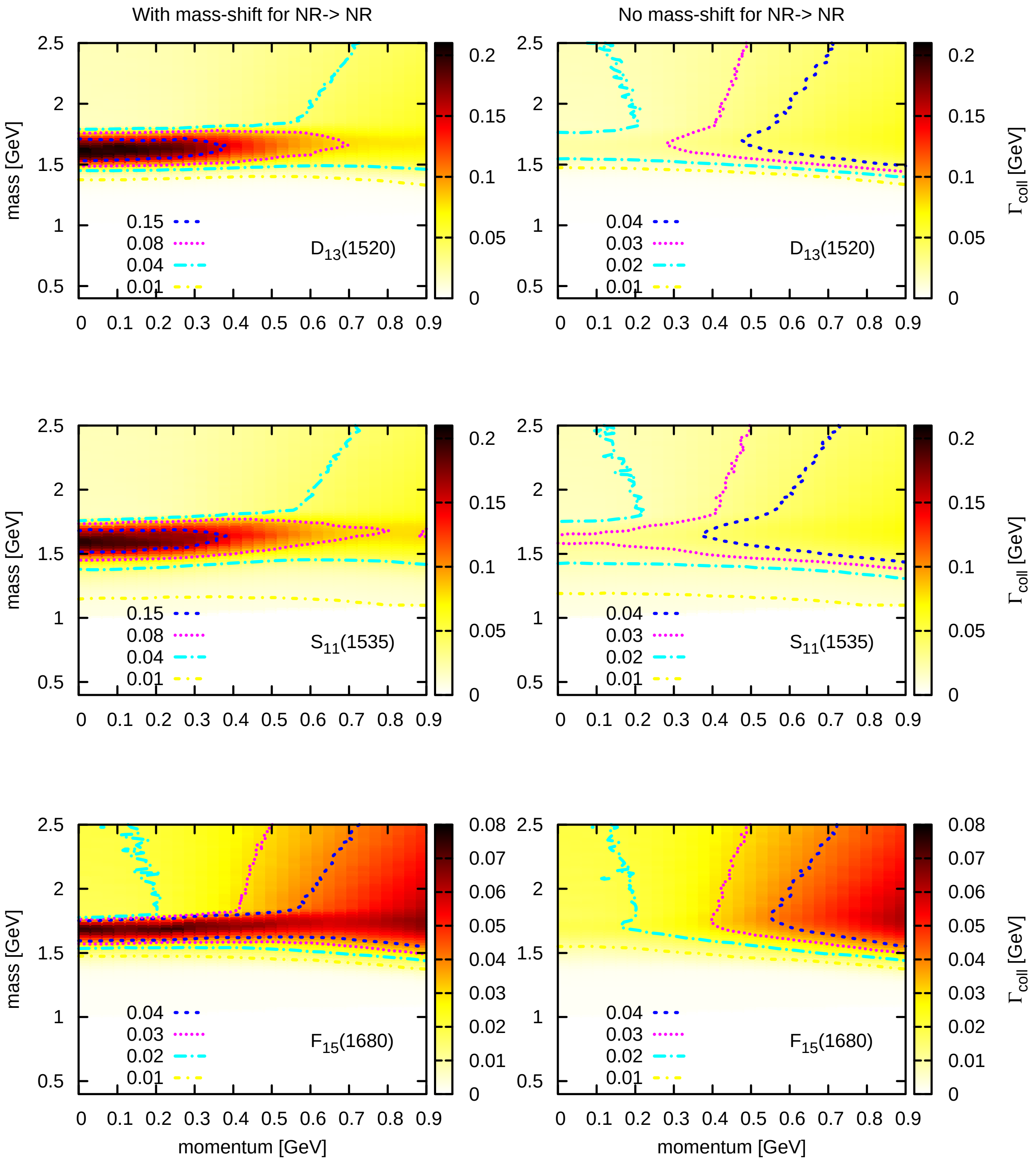

Figure 3.6: The collisional width of the $D_{13}(1520)$, $S_{11}(1535)$ and $F_{15}(1680)$ resonances in symmetric nuclear matter of density $\rho = 0.168\ \mathrm{fm}^{-3}$ as a function of resonance momentum and mass. The left panels show the result according to the mass-shift scenario, whereas the right panels show the no-mass-shift result.

Given this large cost for the numerical implementation, one must raise the question whether this effort pays off or whether we could also use a more simplified prescription, as e.g. using an average σ to evaluate the collisional broadening. We will address this issue in sec. 7.2.2, where we compare the results of quasi-elastic electron scattering obtained using the full model for Γ_{coll} to the results obtained in a more approximate model.

3.6.2 Real part of the self energies

In the same line as J. Lehr [Leh03, cf. chapter 3] we demand that at the pole energy, the off-shellness is given by the mean-fields. Henceforth, we demand that at the pole

$$p_0^{\text{pole}} = \sqrt{\vec{p}^{\,2} + (m_0 + U_{mf}(\vec{p}))^2} \quad . \tag{3.61}$$

such that

$$\text{Re}\Pi(p_0^{\text{pole}}, \vec{p}) = 2m_0 U_{mf}(\vec{p}) + U_{mf}(\vec{p})^2 \quad . \tag{3.62}$$

In the following, we construct the off-shell behavior of this real part via dispersion relations.

Dispersion relations

Demanding that the self energy is an analytic function of p_0, we can connect the real part of the self energy to its imaginary part. To fix the real part of the self energy at the pole, we choose a once-subtracted dispersion relation which is based on Cauchy's relation[18]. We choose a contour C_ϵ as depicted in figure 3.7 to express the self energy as a contour integral

$$\frac{\Pi(p)}{p_0 - p_0^{\text{pole}}(p)} = \lim_{\epsilon\to 0} \frac{1}{2\pi i} \oint_{C_\epsilon} dp_0' \frac{\Pi(p_0', \vec{p})}{(p_0' - p_0^{\text{pole}})(p_0' - p_0)} \quad . \tag{3.63}$$

Applying complex calculus, we get in the limit of $\epsilon \to 0$

$$\Pi(p) = \frac{\Pi(p_0^{\text{pole}}, \vec{p})}{2} + \frac{p_0 - p_0^{\text{pole}}}{\pi i} \wp \int_{-\infty}^{\infty} dp_0' \frac{\Pi(p_0', \vec{p})}{(p_0' - p_0^{\text{pole}})(p_0' - p_0)} + C_\infty \quad , \tag{3.64}$$

where C_∞ denotes the contribution of the semi-circle at ∞ and $\wp$ denotes a principle value integral. The real and imaginary parts of the self energy are given by

$$\begin{aligned} \text{Re}\Pi(p) &= \text{Re}\Pi(p_0^{\text{pole}}, \vec{p}) + \frac{p_0 - p_0^{\text{pole}}}{\pi} \wp \int_{-\infty}^{\infty} dE' \frac{\text{Im}\Pi(p_0', \vec{p})}{(p_0' - p_0^{\text{pole}})(p_0' - p_0)} \\ &\quad + \text{Re}C_\infty \end{aligned} \tag{3.65}$$

$$\begin{aligned} \text{Im}\Pi(p) &= \text{Im}\Pi(p_0^{\text{pole}}, \vec{p}) - \frac{p_0 - p_0^{\text{pole}}}{\pi} \wp \int_{-\infty}^{\infty} dp_0' \frac{\text{Re}\Pi(p_0', \vec{p})}{(p_0' - p_0^{\text{pole}})(p_0' - p_0)} \\ &\quad + \text{Im}C_\infty \, . \end{aligned} \tag{3.66}$$

In the numerical realization, we approximate the dispersion integral for ReΠ by

$$\begin{aligned} \text{Re}\Pi(p) &= \text{Re}\Pi(p_0^{\text{pole}}, \vec{p}) + \frac{p_0 - p_0^{\text{pole}}}{\pi} \wp \left(\int_{E_{\min}}^{E_1} dp_0' \frac{\text{Im}\Pi(p_0', \vec{p})}{(p_0' - p_0^{\text{pole}})(p_0' - p_0)} \right. \\ &+ \left. \int_{E_1}^{E_2} dp_0' \frac{\text{Im}\Pi(p_0', \vec{p})}{(p_0' - p_0^{\text{pole}})(p_0' - p_0)} \frac{E_2 - p_0'}{E_2 - E_1} \right) \end{aligned} \tag{3.67}$$

---

[18] for details see in particular [Bjo93, chapter 18.1].

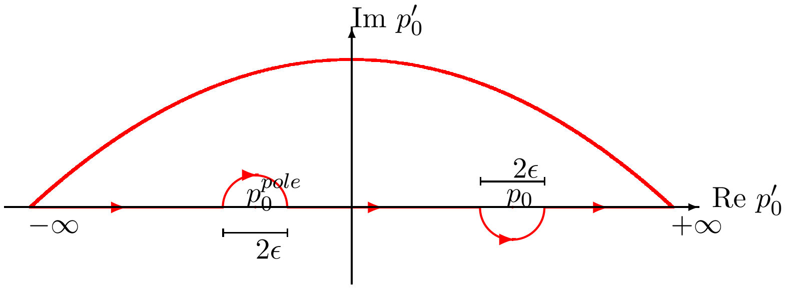

Figure 3.7: The contour C_ϵ which is stretching along the Re p_0' axis and closing at infinity.

with the cut off parameters $E_1 = 5$ GeV and $E_2 = 7$ GeV. The value of E_{min} is chosen such that it corresponds to the cut-off's for the width.

3.7 Spectral functions

Given the information about the real and imaginary parts of Π, the spectral function can be readily evaluated and is given by

$$\mathcal{A}(p) = \frac{1}{\pi} \frac{-\text{Im}\Pi(p)}{(p^2 - m_0^2 - \text{Re}\Pi(p))^2 + (\text{Im}\Pi(p))^2} \,. \tag{3.68}$$

This spectral function is normalized to

$$\int_{-\infty}^{\infty} A(p) d(p_0)^2 = 1 \,. \tag{3.69}$$

Since we demand $\Gamma = 0$ for $p_0 < E_{\text{min}}$, the normalization integral can be written as

$$\int_{E_{\text{min}}}^{\infty} A(p) 2p_0 dp_0 = 1 \,. \tag{3.70}$$

3.7.1 Numerical results for the nucleon

In fig. 3.8, we show the normalization of the spectral function as function of the nucleon momentum at a sample density of $\rho = 0.15$ fm^{-3}. It is fulfilled up to a 1% level. Fig. 3.9 demonstrates the shape of the spectral function for different momentum cuts. Obviously, the spectral functions is broadened due to the larger width when going to larger momenta. Note that we introduced a lower cutoff for the nucleon mass at $m_{min} = 0.4$ GeV - this is needed to prevent nucleons being propagated to negative masses during the time evolution. Also for a width of 0.15 GeV, this cut has only a minor influence.

3.7.2 Numerical results for the baryonic resonances

Normalization

In fig. 3.10, the normalizations of the spectral functions of the baryonic resonances are shown on the interval $p_0 \in [0, 6.5]$ GeV and at vanishing density (upper panel) and finite density $\rho = 0.15$ fm^{-3} (lower panel). In the upper panel, the solid line shows the result for the full calculation. The dotted curve does not include the real parts of the spectral functions, and in the dashed one also the additional cut-of function $\mathcal{F}_{ab}$ has been neglected. Obviously, the

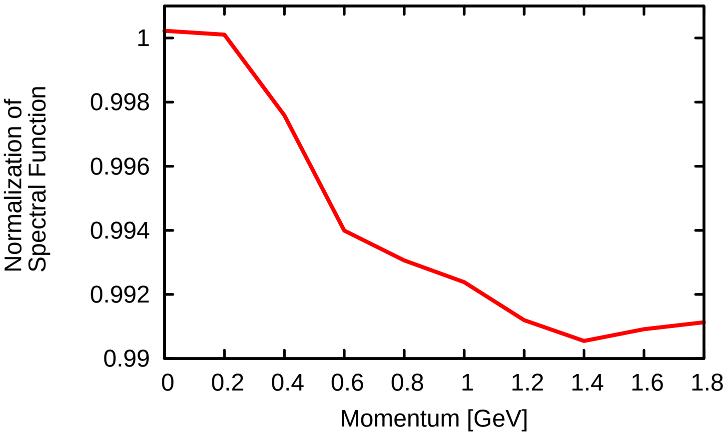

Figure 3.8: The normalization of the spectral function of the nucleon in symmetric nuclear matter of density $\rho = 0.15$ fm^{-3} as a function of the nucleon momentum.

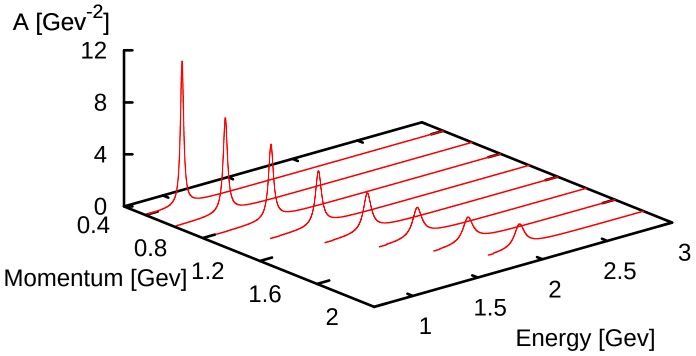

Figure 3.9: The spectral function of the nucleon in symmetric nuclear matter of density $\rho = 0.15$ as a function of energy for different momentum cuts $p = 0.4, \ldots, 1.8$ GeV.

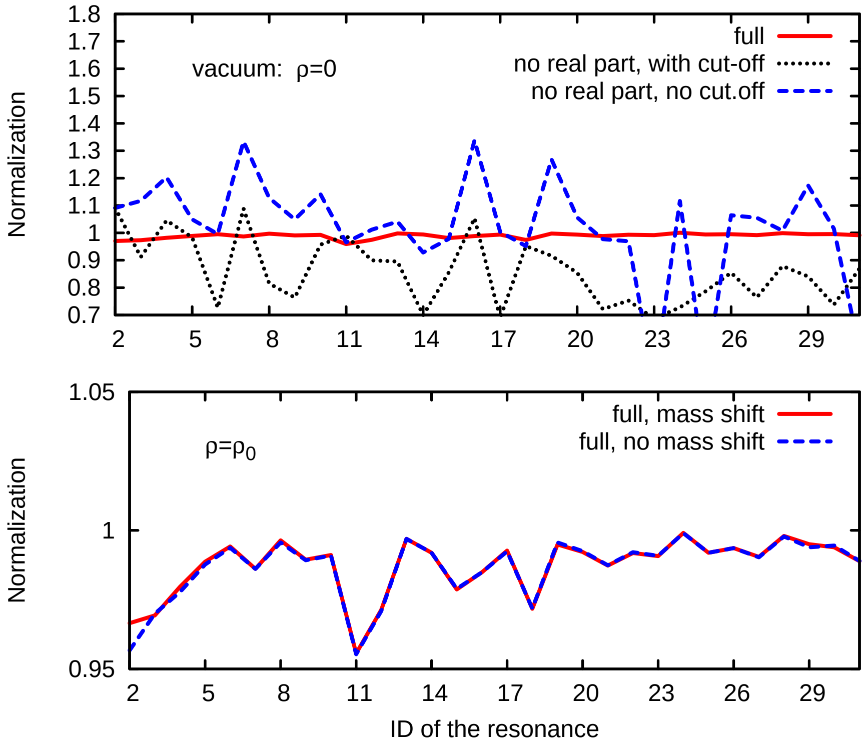

Figure 3.10: The upper panels show the normalization of the spectral function of non-strange baryons for the full model (solid), without a consistent real part (dotted), and additionally without the additional cut-off $\mathcal{F}_{ab}$ (dotted line) for a resonance momentum of $|\vec{p}| = 0.6$ GeV. The upper plot shows the result for density $\rho = 0$ and the lower one for $\rho = 0.15$ fm^3. The resonances are labeled by their ID as given in table 3.1 on page 30.

normalization condition is considerably improved by the inclusion of a proper real part for the self energy Π. In this case the normalization is fulfilled up to a 2% level; the missing 2% may also be due to our finite integration interval. When one neglects the real part of Π in the spectral function, very large normalization errors occur: Note that normalizations larger than 1 hint to errors, normalizations smaller than 1 may in principle also be due to the finite integration range. However, resonance strengths of more than 20% at masses higher than 6 GeV are rather unexpected and not very physical. We emphasize that in the previous calculations (in particular in [Eff99a] and [Leh03]), the real parts of the resonance self energies have not been included for the resonance states.

In the lower panel, we see that the spectral functions for both the *mass-shift* and the *no-mass-shift* scenario are properly normalized up to a $2\% - 5\%$ level.

Spectral shape

Let us now come back to the additional cut-off $\mathcal{F}_{ab}$ which was introduced in the preceding section 3.2.2. We study the dependence of the resonance spectral function on this cut-off at a fixed resonance momentum of 0.4 GeV. In figures 3.11-3.12, we show the spectral functions of six sample resonances for both $\rho = 0$ and $\rho = 0.15$ fm^{-3}.

Let us focus on the zero-density case which is shown in figure 3.11. The dotted line denotes the result without cut-off, the dashed the one with cut-off. Both do not include a real part for the

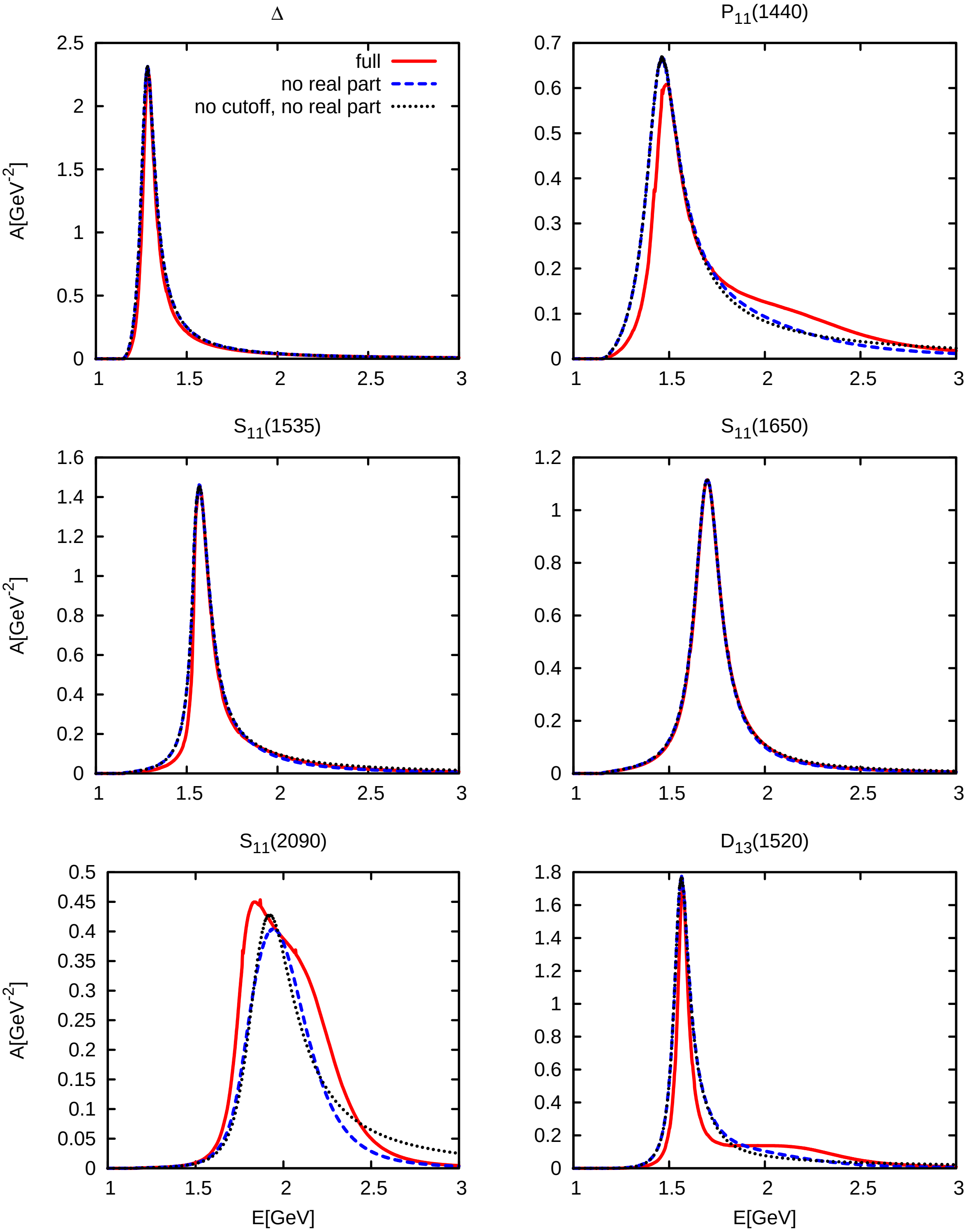

Figure 3.11: Spectral functions of the baryonic resonances for three different scenarios at $\rho = 0$: with the full model (solid curve), with $\mathrm{Re}\Pi$ excluded (dashed curve), with $\mathrm{Re}\Pi$ excluded and without $\mathcal{F}_{ab}$ (dotted curve). The absolute momentum is chosen to be $|\vec{p}| = 0.4$ GeV.

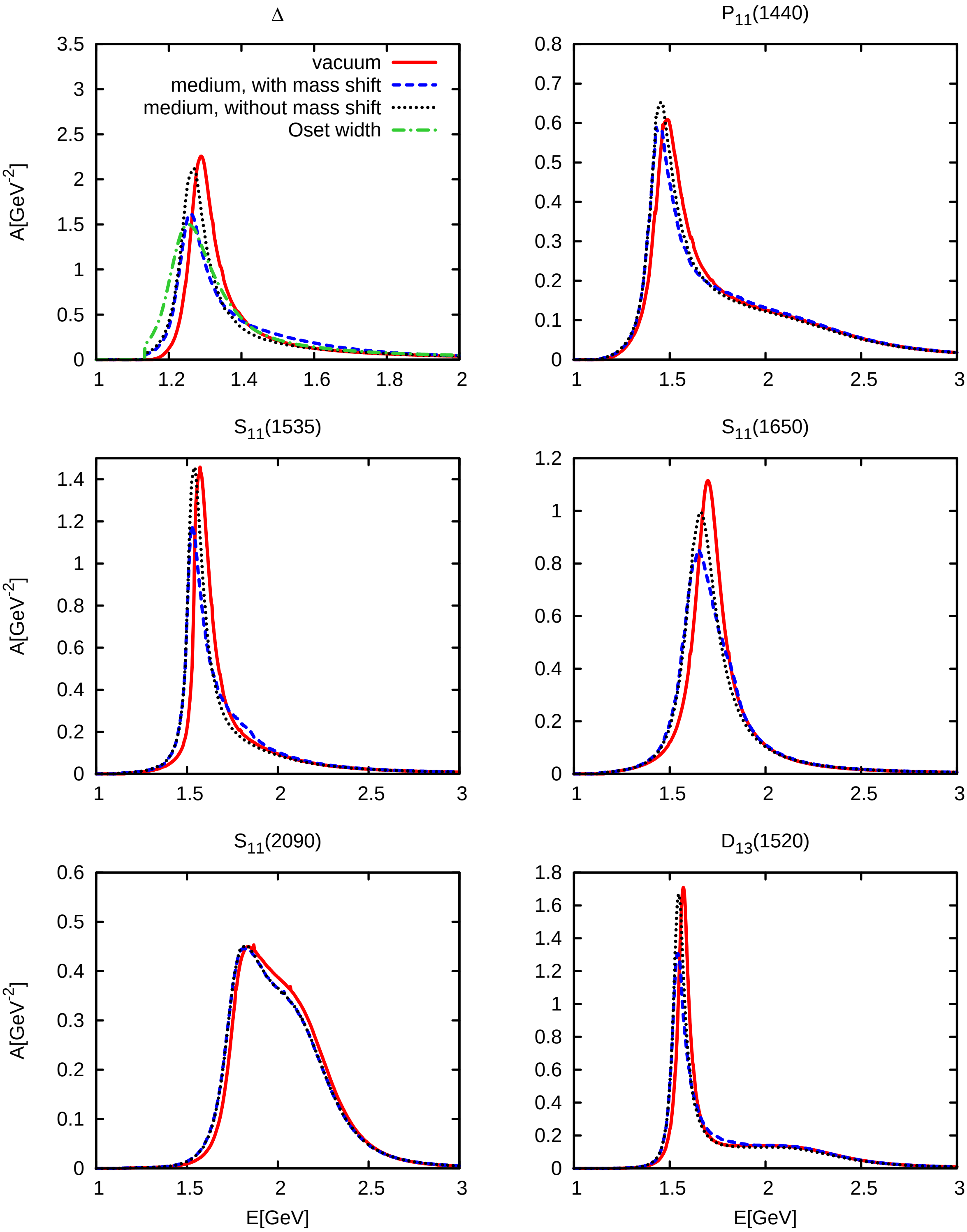

Figure 3.12: Spectral function with the full model at $\rho = 0.0\ \mathrm{fm}^{-3}$ (solid curve) and at $\rho = 0.15\ \mathrm{fm}^{-3}$ for the *mass-shift* (dashed curve), *no mass-shift* (dashed) and *mass-shift+Oset* (dashed-dotted) options of the in-medium self-energies. The absolute momentum is chosen to be $|\vec{p}| = 0.4$ GeV.

self energy. One observes that the cut-off itself has only a minor influence on the spectral shape, except for the $S_{11}(2090)$ resonance which has a large ρN branching ratio. For this resonance, the old width parametrizations resulted in extraordinary unphysical values of more than 1 GeV at large off-shell masses. We therefore had to regulate this width in order to perform the dispersion integrals. The solid curve denotes the result with the proper real part included. Here one observes larger differences than the ones induced by the cut-off. Obviously, the area under the curves, which corresponds to the integral strength of the spectral functions, is modified.

In figure 3.12, we compare the different scenarios for the in-medium modifications of the width to the vacuum spectral function (solid line). For all scenarios (mass shift, no mass shift, mass-shift+Oset model), the spectral shape is shifted towards lower energies due to the slightly attractive potential at $|\vec{p}| = 0.4$ GeV. Additionally, the peak height is decreased due to a larger width caused by the collisional broadening. Including the mass shift of eq. 3.57, the resonances are broadened and the peak height is decreased as compared to the no-mass-shift case. For the Δ we show also the non-normalized spectral function which results when using the Oset model for the Δ width. As compared to the other two scenarios, the spectral shape is broader. Especially at low masses, there is more strength due to the stronger $ND \to NN$ absorption and due to the three-body absorption channel.

Impact of the cut-off parameters

Finally, we want to discuss the cut-off parameters which have been introduced in eq. 3.67 to cut the dispersion integrals. And the question arises: how sensitive are our results on the cut-off parameters $E_1 = 5$ GeV and $E_2 = 7$ GeV? We choose the Δ resonance as a show-case and study the real part while varying the parameters. In fig. 3.13, we show the difference of the results for the parameters $E_1 = 3$ GeV, $E_2 = 5$ GeV and $E_1 = 4$ GeV, $E_2 = 6$ GeV to the standard result normalized to the standard result. We conclude that in the most relevant region ($m \approx 1.1 - 1.4$) the deviation is within an acceptable level. We note that the variation obtained with the $E_1 = 4$ GeV, $E_2 = 6$ GeV set is almost everywhere only ca. 8%, the sensitivity being thus rather moderate.

3.7.3 Exotic baryons and mesons

For the mesons and baryons with strange or charm quark content, the real parts of the self energy have been neglected and no collisional broadening has been included.

3.8 Nuclear ground state

The target nucleus is treated within a local Thomas-Fermi approximation as a Fermi gas of nucleons bound by a mean-field. In position space the nucleons are distributed according to a given density distribution. In momentum space, we assume that the nucleons occupy a sphere of radius p_f. The local Fermi momentum $p_f(\vec{r})$ for neutrons and protons is given by

$$p_f^{n,p}(\vec{r}) = \sqrt[3]{3\pi^2 \rho^{n,p}(\vec{r})} \quad . \tag{3.71}$$

Density profiles For ${}^{16}_{8}$O, ${}^{18}_{8}$O, ${}^{27}_{13}$Al, ${}^{40}_{20}$Ca, ${}^{44}_{20}$Ca, ${}^{197}_{79}$Au and ${}^{207}_{82}$Pb we have implemented density profiles $\rho(r)$ according to the parametrizations collected in ref. [Nie93b], which are of Woods-Saxon type for heavier nuclei and of harmonic-oscillator type for lighter ones. The

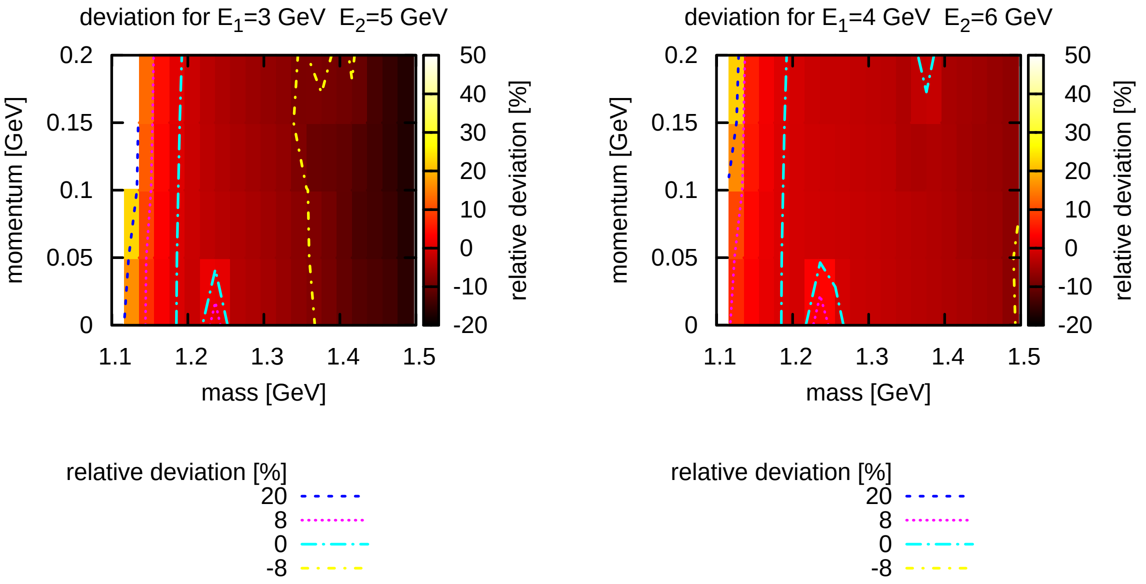

Figure 3.13: The impact of the cut off parameters E_1 and E_2 on the evaluation of the real part of the Δ self energy at density $\rho = 0.15$ fm^{-3}. The two different panels show the relative difference for the results obtained with $E_1 = 3$ GeV, $E_2 = 5$ GeV (left panel) and $E_1 = 4$ GeV,$E_2 = 6$ GeV (right panel) when compared to the result obtained with the standard cut-off.

proton densities are based on the compilation of ref. [De 74] from electron scattering. The neutron densities are provided by Hartree-Fock calculations.

Additionally, we implemented for comparison Woods-Saxon density distributions

$$\rho_n(r) = \frac{\rho_n^0}{1+\exp((r-R_n)/a_n)} \tag{3.72}$$

$$\rho_p(r) = \frac{\rho_p^0}{1+\exp((r-R_p)/a_p)} \quad , \tag{3.73}$$

with the parameters given in table 3.5 [Len05]. As will be shown in sec. 6.4, the larger neutron radii of heavy nuclei play a relevant role in the double charge exchange (DCX) of pions in the interaction with a nuclear target. For the deuteron we implemented special momentum and density distributions which will be addressed in sec. 8.4.1.

Evaluation of the baryon densities based on the test-particle densities The real density must be evaluated out of the test-particle density. As a numerical trick, we convolute the test-particles with a Gaussian, i.e. we smear the test-particle, to get a smooth density distribution. The smearing vector $\vec{\sigma} = (\sigma_x, \sigma_y, \sigma_z)$ is chosen such that it equals the grid-spacings. The density

nucleus	$\rho_p^0[fm^{-3}]$	$\rho_n^0[fm^{-3}]$	$R_p[fm]$	$R_n[fm]$	$a_p[fm]$	$a_n[fm]$
${}^{16}_{8}$O	0.080	0.081	2.607	2.615	0.490	0.469
${}^{40}_{20}$Ca	0.079	0.081	3.731	3.707	0.490	0.469
${}^{56}_{26}$Fe	0.076	0.082	4.170	4.263	0.481	0.474
${}^{103}_{45}$Rh	0.071	0.083	5.194	5.358	0.474	0.478
${}^{197}_{79}$Au	0.064	0.086	6.538	6.794	0.465	0.483
${}^{207}_{82}$Pb	0.064	0.086	6.649	6.920	0.464	0.484

Table 3.5: Parameters of the Woods-Saxon parametrizations presented in eq. 3.73 which are obtained within the Hartree-Fock calculations of Lenske [Len05]. In principle, parameters for all stable nuclei are included in the GiBUU code. We present here only those ones which are being addressed in this thesis.

at $\vec{r} = (x, y, z)$ is then given by a sum over all test-particles [19]

$$\rho(\vec{r}) = \sum_i \frac{1}{\sqrt{2\pi\sigma_x^2}\sqrt{2\pi\sigma_y^2}\sqrt{2\pi\sigma_z^2}} e^{-\left(\frac{(x_i-x)^2}{2\sigma_x^2}+\frac{(y_i-y)^2}{2\sigma_y^2}+\frac{(z_i-z)^2}{2\sigma_z^2}\right)} . \tag{3.75}$$

Consequently, the density profile depends on the value of σ. This value must be chosen such that there are only minor fluctuations within the density profile. To decrease σ, one must therefore increase the statistics by choosing large numbers of ensembles (> 1000). As an example, we show in fig. 3.14 the density profile of a ${}^{16}_{8}$O-nucleus with two different values of σ and two different numbers of test-particles. In this figure, it becomes obvious that the size of σ has a definite impact on the density profile of the light Oxygen nucleus. For $\sigma = 0.4$ fm, the number of ensembles used for the dotted curve is obviously too small - the fluctuations are too high. For $\sigma = 0.8$ fm, both the curve with 5000 ensembles (dashed) and the one with 500 ensembles (dashed-dotted) have very little fluctuations. However, the smearing width is now so large that the surface of the nucleus is washed out. Obviously, the result with many ensembles and small smearing width (solid line) represents the best approximation to the underlying density parametrization (open squares) according to eq. 3.73. In the following, we choose the smearing width to be of the order of 0.4 fm.

Binding energies. The binding energies depend on the density, therefore also on the smearing width σ. The larger the smearing, the smaller the binding energy since the average density decreases. However, for the above example of an Oxygen nucleus the difference is only of the order of 0.8 MeV.

The binding energy is obtained by representing a nucleus of atomic mass A by $A \times N$ (N is the number of ensembles) test-particles. Then the binding energy is given by a sum over the test-particle energies taking into account the so-called *rearrangement terms* R (cf. [Tei96, pages

---

[19] Note, that we use in the actual numerical implementation an additional cut-off for the Gaussians ($C = \sqrt{5}$ fm) such that

$$\frac{1}{\sqrt{2\pi\sigma^2}} e^{-\frac{(x_i-x)^2}{2\sigma^2}} \to \frac{1}{\mathcal{N}} \Theta\left(C - |x_i - x|\right) e^{-\frac{(x_i-x)^2}{2\sigma^2}} . \tag{3.74}$$

The factor $\mathcal{N}$ represents the proper normalization.

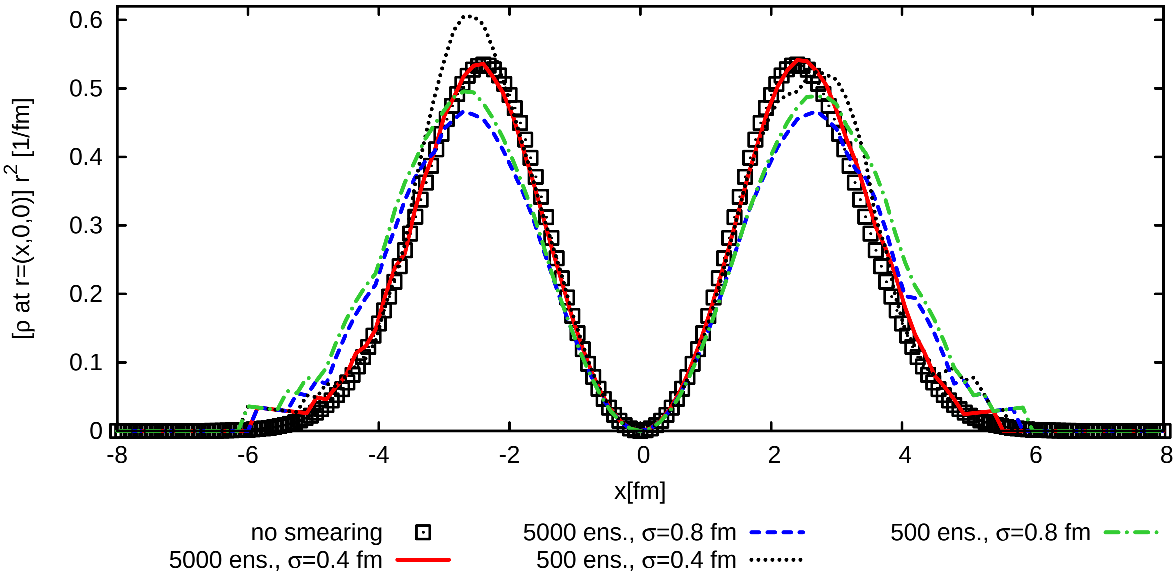

Figure 3.14: The density of a $^{16}_{8}$O nucleus weighted by r^2 along the x-axis. The solid and dashed curves represent calculations with 5000 ensembles, the dashed-dotted and dotted ones are produced with only 500 ensembles. Concerning the size of the smearing width, the solid and the dotted ones represent $\sigma = 0.4$ fm, the other two $\sigma = 0.8$ fm. The open squares represent the underlying density parametrization according to eq. 3.73.

76ff.]) [20]

$$\frac{E_{\text{bind}}}{A} = \frac{1}{A \times N} \sum_{i}^{A \times N} \left(p_i^0 + R(p_i) \right) - m_N \quad . \tag{3.76}$$

Note that the contribution due to the Coulomb potential is not included in the binding energy. In fig. 3.15, we compare the results obtained with $\sigma = 0.4$ fm, 5000 ensembles and the *EQS 5* potential to the sum of the Bethe-Weizsäcker volume and surface term. The asymmetry energy and pairing energy are neglected. Our results show an over-binding by ca. 1.5 MeV for all nuclei. Performing a fit to our data with the Bethe-Weizäcker parametrization

$$E_{\text{bind}} = a_v A - a_s A^{\frac{2}{3}} \quad , \tag{3.77}$$

we find

$$a_v = 15.8 \pm 0.1 \text{ MeV} \quad , \tag{3.78}$$

$$a_s = 13.5 \pm 0.4 \text{ MeV} \quad . \tag{3.79}$$

The resulting volume term a_v is in accordance to the standard value (e.g. [MK94, page 49]), but the surface term a_s comes out too low by approximately 5 MeV which explains the too strong binding energies. However, for our needs this level of agreement is sufficient given the generally large energy transfers to the target nucleons[21]. Comparing to Effenberger's results [Eff99a, fig. 3.8] for the binding energy obtained with the former numerical implementation, we find satisfying quantitative agreement.

---

[20] Confer *subroutine evaluateBindingEnergy_theiss* in *module checks.f90* for the numerical implementation.

[21] An improvement to this has recently been implemented by B. Steinmüller [Ste07].

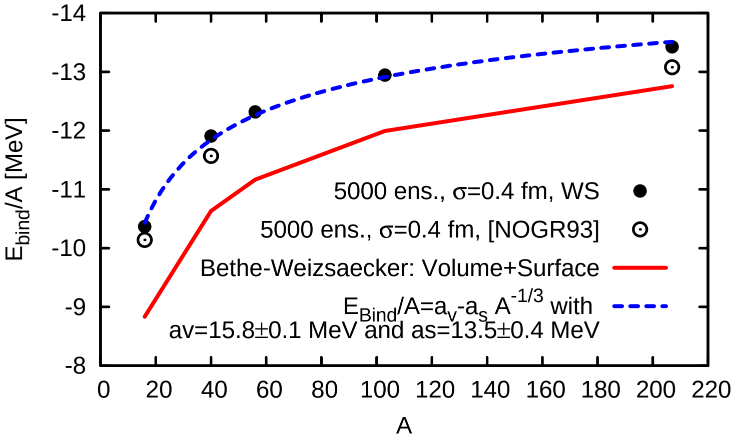

Figure 3.15: The binding energies per nucleon of ${}^{16}_{8}$O, ${}^{40}_{20}$Ca, ${}^{56}_{26}$Fe, ${}^{103}_{45}$Rh and ${}^{207}_{82}$Pb for the Wood Saxon density distribution (full circles) and the density distributions according to the ones collected in ref. [Nie93b] (open circles). The solid line represent the sum of volume and surface term of the Bethe-Weizäcker formula [Pov99]. The dashed curve represents a Bethe-Weizäcker fit ($E_{\text{bind}} = a_v A + a_s A^{\frac{2}{3}}$) to our result for the Wood-Saxon density, which gives $a_v = 15.8 \pm 0.1$ MeV and $a_s = 13.5 \pm 0.4$ MeV.

Ground state stability. A problem already addressed by Effenberger [Eff99a] is the stability of the ground state. The density distributions discussed above do not represent the ground state density distributions according to the implemented potentials. The potentials are local – therefore, the ground state according to the potentials must be perfect spheres of constant density. Already in [Eff99a], an oscillation of the root-mean-square (RMS) radius in time was observed. Stable oscillations show that no energy loss due to numerical friction occurs and this is, therefore, a good signature for stable numerics. We repeated the oscillation measurements and the results are shown on the upper panel of fig. 3.16. The oscillation frequency depends on the smearing width σ, and amounts to ca. 22 fm/c. In the case of $\sigma = 0.4$ fm and 5000 ensembles, the RMS-radius returns to its initial value within an accuracy better than 0.025 fm/c. On the lower panel of fig. 3.16, the binding energy is shown as a function of time during the oscillation period. We observe that the energy conservation is fulfilled within the order of $0.6 - 1.1$ MeV. This accuracy is acceptable for our needs since we usually deal with several hundred MeV's energy transfers during the reactions. After one oscillation, the binding energy comes very close to its initial value. We conclude that the numerics behaves properly and very similar to what has been shown for the previous code version in [Eff99a]. Furthermore, the oscillating behavior can not be much improved by smaller values of σ. The oscillations may, however, lead to improper results. E.g. for π absorption on nuclei, the size of the nucleus is crucial. Henceforth, the oscillations will have a definite impact on the total absorption cross sections.

In order to suppress the undesirable oscillations, we can within the ground state assumption - in particular within the *perturbative mode*[22]- freeze the test-particles which represent the nucleus and thus kill the oscillations hereby.

---

[22] cf. sec. B.1 for the definition of *real* and *perturbative* particles and an explanation of the *perturbative mode.*

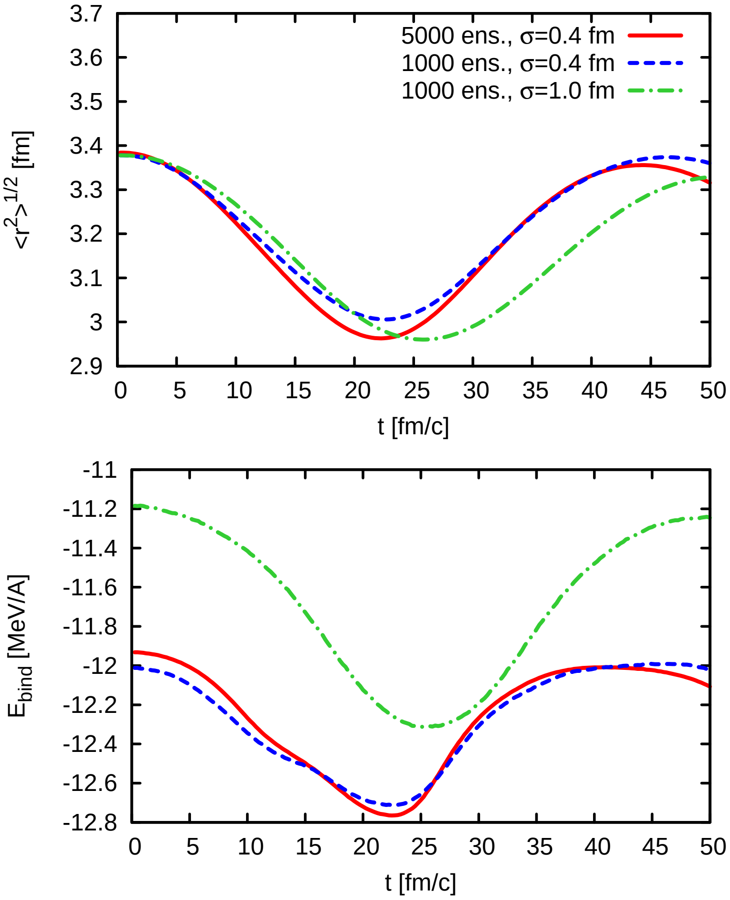

Figure 3.16: The upper panel shows the RMS radius $\sqrt{(\sum_{i=1}^{N} r_i^2)/N}$ of $^{40}_{20}$Ca as a function of time. The lower panel shows the binding energy per nucleon of $^{40}_{20}$Ca as a function of time. In both panels, three different calculations are shown: 5000 ensembles and $\sigma = 0.4$ fm (solid lines), 1000 ensembles and and $\sigma = 0.4$ fm (dashed line), 1000 ensembles and and $\sigma = 1$ fm (dashed-dotted line). For the initialization, the Wood-Saxon density distribution was used.

3.9 Details on the off-shell transport

In sec. 2.4, we introduced the concept of transporting broad particles. Each test-particle is being propagated under the influence of the so-called off-shell potential. For the i-th test-particle it is defined by eq. 2.33

$$\Delta\mu_i(\vec{r},p) = \frac{\Delta\mu_i(\vec{r}_i(t_0),p_i(t_0))}{\Gamma_{tot}(\vec{r}_i(t_0),p_i(t_0))}\Gamma_{tot}(\vec{r},p) \ . \tag{3.80}$$

At production time of the i-th test-particle, we store the parameter

$$\alpha_i = \frac{\Delta\mu_i(\vec{r}_i(t_0),p_i(t_0))}{\Gamma_{tot}(\vec{r}_i(t_0),p_i(t_0))} \tag{3.81}$$

representing its offshellness at production time divided by the width of the particle at production time. To propagate the test-particle according to eq. 2.21-2.23, we need to evaluate the four-momentum and spatial derivatives of the Hamilton-function. The Hamilton function defined in eq. 2.37 depends on the off-shell potential:

$$H_i = \sqrt{(m + \Delta\mu_i + V)^2 + \vec{p}^2} \ . \tag{3.82}$$

Hence derivatives acting on $\Delta\mu_i$ have to be performed

$$\begin{aligned} \frac{\partial\Delta\mu_i(\vec{r},p)}{\partial p^\mu} &= \alpha_i \frac{\partial\Gamma(\vec{r},p)}{\partial p^\mu} \ , & (3.83)\\ \frac{\partial\Delta\mu_i(\vec{r},p)}{\partial\vec{r}} &= \alpha_i \frac{\partial\Gamma(\vec{r},p)}{\partial\vec{r}} \ . & (3.84)\end{aligned}$$

Eventually, the resulting gradients acting on the width create major difficulties. As pointed out in the end of sec. 3.6.1, the tabulation of the width for all non-strange baryons costs roughly 50 CPU days. This long computation time is mainly needed to achieve high enough statistics in the Monte-Carlo integrations, such that we get a smooth tabulation which can then be used for the derivatives. Large fluctuations, i.e. errors of the Monte-Carlo integration, in the width tabulation lead to large derivatives of the width. Finally, this yields test-particles which are accelerated to velocities greater than the speed of light. Additionally we get some test-particles which become tachyons since the off-shell potential becomes too stiff for large off-shell parameters α_i. To prevent this feature, we additionally introduce a maximum off-shellness by demanding $|\alpha_i| < 5$, which translates into a maximal and minimal mass at production time. However, this cut should not have any impact on any observable since the spectral function is anyhow small at 5Γ away from the pole mass. Additionally, we cut on the resonance spectral functions demanding that $m_{\text{pole}} + \Delta\mu_i(\vec{r}_i(t_0),p_i(t_0))$ is larger than the masses of the lightest resonance decay products in vacuum. E.g. for a Δ we get

$$\begin{aligned} m_\Delta + \Delta\mu_i(\vec{r}_i(t_0),p_i(t_0)) &> m_\pi + m_N & (3.85)\\ \Rightarrow \Delta\mu_i(\vec{r}_i(t_0),p_i(t_0)) &> m_\pi + m_N - m_\Delta \ . & (3.86)\end{aligned}$$

For the nucleons we choose 700 MeV as a minimal mass. These cuts simplify our numerics and are justified by the smallness of the resonance and nucleon spectral functions below the cuts.

The implementation of an off-shell potential would be very much simplified if the in-medium widths of the particles were constant in momentum and mass. Then there would be no problem due to tachyons, since the offshell potential would not give any contribution to $\dot{r} = \partial H/\partial p$. In sec. 7.2.2 we compare the consequences of a simplified collisional broadening on quasi-elastic electron scattering, and conclude that a simplified procedure must go hand-in-hand with a fine-tuning of a free-parameter which in the worst case must even be readjusted for each specific reaction. Hence a simplified collisional broadening does not represent a good approximation to be used. The right questions to be asked, are the following: 'How large is the impact of the off-shell-potential on our results? Is it negligible?' Given that the interaction rates are high, then the time in-between collisions would be short. Hence there would also be a small mass change in-between collisions and neglecting the off-shell potential might even be a good approximation. We will address this question in sec. 7.4.1, were we study the impact of the off-shell potential on photon induced pion production.

Numerical results As a test of the off-shell propagation we want to consider six different scenarios:

test #1 A Δ is produced in the center of a Calcium nucleus with momentum $\vec{p} = 0.5$ GeV $\vec{e}_x$.

test #2 Same as test #1 but at a higher momentum of 1.5 GeV.

test #3 A Δ is initialized at position $\vec{r} = (-8, 1, 0)$ fm with momentum $\vec{p} = (0.5, 0, 0)$ GeV and starting to propagate through the nucleus.

test #4 Same as test #3 but at a higher momentum of 1.5 GeV.

test #5 A nucleon is produced at the center of a Calcium nucleus with momentum 0.5 GeV.

test #6 Same as test #5 but at a higher momentum of 1.5 GeV.

For the initialization, we distribute the test-particle masses according to the full spectral function. Thereafter, we propagate the test-particles according to their equations of motion, in particular including the off-shell potential. The collision term is switched off during the propagation to focus on the change of the mass-distribution of the test-particles due to the off-shell potential. Fig. 3.17 shows the results for those six test scenarios[23]. The two top panels show the tests #1 and #2 where Δ test-particles propagate out of the nucleus. One observes that the spectral functions are deformed during the propagation such that the final spectra (solid curves) resemble the vacuum spectral functions (dotted curves). Note that the initial spectral functions for 0.5 and 1.5 GeV momentum differ quite considerably due to the momentum-dependent in-medium width, however the final ones are almost identical since the vacuum width is momentum-independent. Especially in the top left panel, the influence of the low-mass cut-off on the initial spectral function at $m_\pi + m_N$ becomes visible. Since the test-particles, which are initiated at this low-mass cut-off, all propagate to higher masses, the cut-off reappears in the final spectra at roughly 1.15 GeV - a slightly higher mass than the sum of pion and nucleon mass. The middle panel depicts tests #3 and #4 where Δ test-particles propagate through the nucleus. During this propagation, the spectral functions are completely deformed (dotted curves). But when all test-particles have finally left the nucleus, then the original spectral function is restored which proves the correct numerical implementation. The lower panels show tests #5 and #6: the propagation of a nucleon with 0.5 GeV (lower left panel) and 1.5 GeV (lower right panel) out of Calcium. Obviously most of the nucleon test-particles propagate back to mass-shell. However, there is also a tiny contribution of test-particles which get caught in the nucleus due to the attractive nature of the off-shell potential for very negative

---

[23] Movies of the whole process can be found on http://gibuu.physik.uni-giessen.de/GiBUU/wiki/testOffshell.

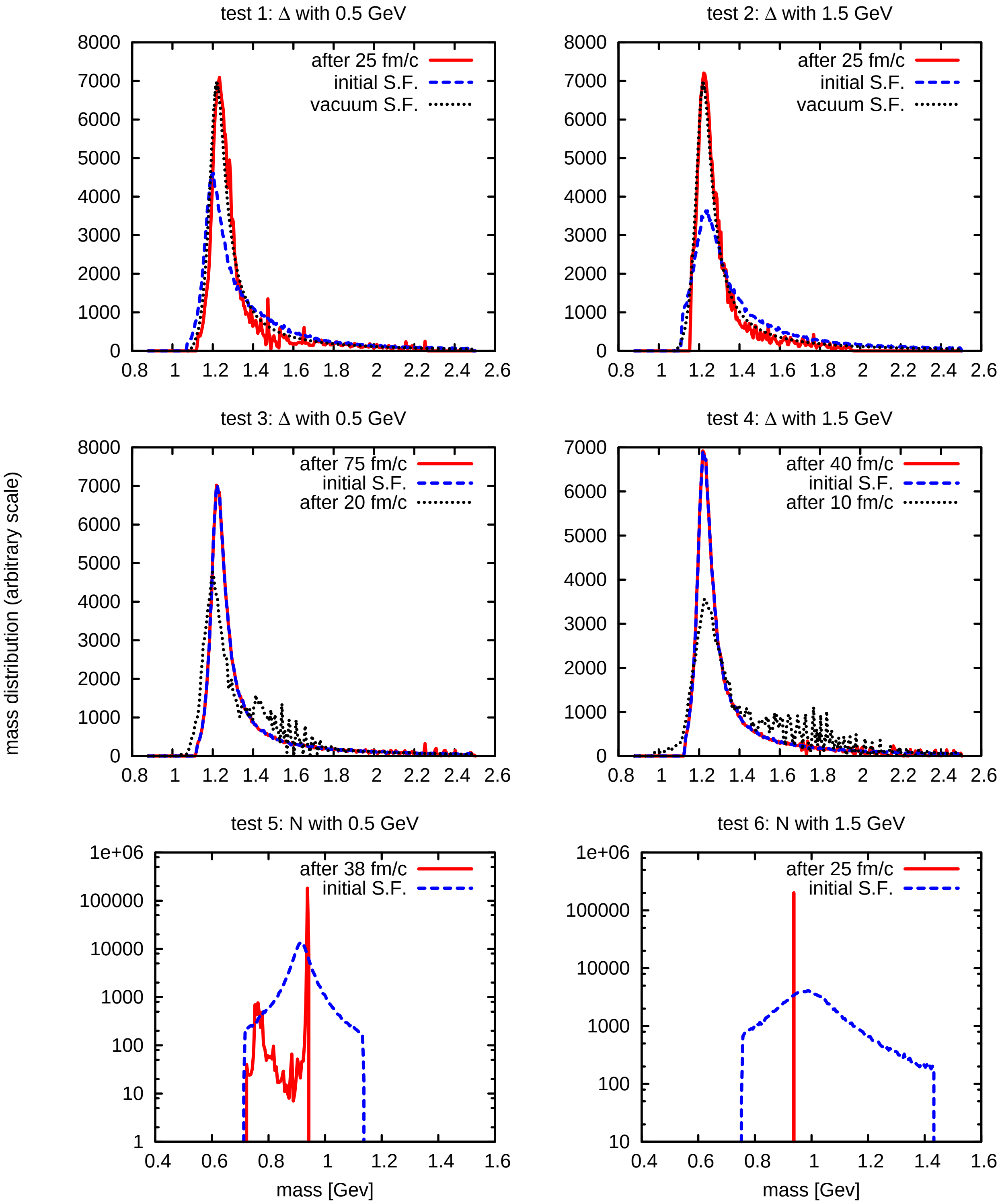

Figure 3.17: The upper panels show the results of the off-shell tests as described in this section. The dashed curves represent the initial spectral functions, the full ones the final spectral functions after propagation for a time of 40 fm/c. The dotted curve in the top panels depict the vacuum spectral function of the Δ resonance, whereas the dotted curve in the middle panel show the spectra 20 fm/c, respectively 10 fm/c, after initialization.

α_i. These test-particles then propagate for all times within the nucleus (if the collision term is switched off) and produce the low mass shoulder in the lower left panel.

	CPU time per time-step [s]
Propagating 200.000 Δ test-particles without off-shell potential	29.5
Propagating 200.000 Δ test-particles with off-shell potential	68.3
Propagating 200.000 nucleon test-particles with off-shell potential	69.4

Table 3.6: Average CPU time for one time-steps with 200.000 test-particles on a *Single-Core AMD Opteron* 2.2*GHz*. For the above time measurements, the collision term has been switched off.

Table 3.6 shows the average CPU-time being used for one time-step using 200.000 test-particles representing the off-shell particle. Switching the off-shell potential on, we observe a slow-down by roughly a factor 2.4 since we need to evaluate the derivatives of the width for the propagation step. Therefore, we need to interpolate the 4-dimensional tabulation in all dimensions which costs CPU time. Since the off-shell potential may become stiff, we also need to reduce the time-step sizes from 0.25 to 0.05 fm/c, if the off-shell potential is switched on. This causes a factor of 5 more time steps. Altogether the off-shell potential causes a slow-down of the propagation step by approximately a factor of 12 both due to the increase in time steps and the increased CPU time per time-step.

Chapter 4

Interaction of electrons and photons with nucleons

OVERVIEW: This chapter introduces a model for the electron- and photon-nucleon interaction. The elastic scattering of virtual photons and nucleons is treated using the latest form factor parametrizations based on recent Jefferson-Lab data, pion production and resonance excitation rates are based on the MAID model.

4.1 Introduction

In the last preceding chapter, we have only addressed hadron-hadron interactions and hadron decays. The topic of this chapter is the so-far untouched interaction of photons and electrons with hadrons, in particular with nucleons. This sets the stage for the study of photons and electrons interacting with nuclei, which will be addressed in the next chapter.

Due to the smallness of the electromagnetic coupling, we assume a dominance of one-photon exchange (OPE) mechanisms in the electron-nucleon scattering. This assumption is also known as *Born approximation*. Fig. 4.1 shows typical Feynman graphs for photon-nucleon scattering and electron-nucleon scattering within OPE approximation visualizing the similar nature of both processes. Both, electron scattering in OPE approximation and photon scattering would be fully understood if it was possible to calculate the so-called *hadronic current* j_μ, denoted by the ovals in both graphs, from first principles. However, this is a formidable task within non-perturbative QCD. A full understanding via *ab initio* calculations, e.g. via Lattice QCD, is not available so far[1]. Alternatively, the experimental data have been interpreted in terms of hadronic degrees of

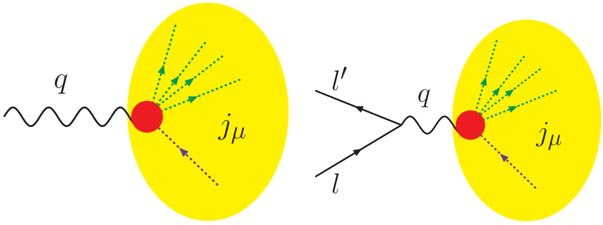

Figure 4.1: The upper figure shows photon-nucleon scattering (left panel) and electron-nucleon scattering in OPE approximation (right panel). Both processes share the same photon-nucleon interaction vertex. However, for the electron scattering process the $Q^2 = -q^\mu q_\mu$, i.e. the virtuality, of the exchanged photon is non-vanishing. The yellow blobs within the panels represent the hadronic current which is denoted by j_μ.

---

[1] For an introduction into the description of electromagnetic couplings to baryons within Lattice QCD see, e.g.,

freedom. The idea of *resonance excitations* interfering with so-called *background processes* is the most common model basis (for a recent review cf. [Bur05]). Also in our approach, we assume a dominant contribution of the nucleon resonances and an additional background contribution, which together add up to generate the hadronic current. Eventually we are interested in the modification of this current within the nuclear medium. Recently, it was observed that the extraction of nucleon form factors in electron-nucleon scattering via the so-called Rosenbluth extraction method and via a method based on polarization transfer yield different results for high four-momentum transfers ($Q^2 > 1.0$ GeV^2) [Jon00]. To solve this puzzle, also the influence of two-photon exchange (TPE) processes is studied with increasing interest - see, e.g., the recent articles [Kon06, Bra06, Arr07] and references therein. As we want to deal with rather low-Q^2 processes, the effects of two-photon processes are neglected in this work.

This chapter is organized as follows. First, the matrix elements for the $e^- N$ and γN scattering processes are introduced. In earlier BUU works performed by Falter [Fal04a] and Lehr [Leh03], the so-called Hand convention [Han63] was exploited to connect electron and photon scattering. After introducing this method, we will motivate why we follow a different procedure. Thereafter, the different contributions to the hadronic current are addressed: quasi-elastic scattering, single-pion production and, closely-connected, the excitation of baryon resonances. In the final discussion of the total cross sections for photon and electron scattering off nucleons, the issue of background extraction is being addressed. Prohibiting double-counting, we there have to account for the resonance contribution to pion production. Finally, we also discuss a non-resonant 2π contribution to photon induced reactions.

This chapter is meant to introduce the formalism for scattering of photons with free nucleons. In the forthcoming chapter 5, we will then, based on the vacuum case, address the scattering of nucleons being embedded in a nuclear environment.

4.2 Matrix elements

The matrix elements defined by the diagrams of fig. 4.1 are given by

$$\begin{aligned}
\mathcal{M}_{e^-\text{-induced}} &= \text{hadronic current} \times \text{photon propagator} \times \text{ electromagnetic coupling} \\
&\quad \times \text{electromagnetic current of electron} \\
&= j_\mu \frac{-i\, g_{\mu\nu}}{q^2}(-ie)\overline{v}(l\,', t_f)\gamma^\nu v(l, t_i) \quad , && (4.1) \\
\mathcal{M}_{\gamma\text{-induced}} &= \text{hadronic current} \times \text{photon polarization vector} \times \text{ electromagnetic coupling} \\
&= j_\mu \epsilon^\mu (-ie) \, . && (4.2)
\end{aligned}$$

Our notation is chosen according to fig. 4.1. The incoming and outgoing lepton momenta are denoted l and $l\,'$ and its spins t_i and t_f, the spins of the incoming nucleon and the outgoing hadrons are s_i and s_f. The electron charge is denoted e, q is the photon momentum.

In the following, polarized nucleons or photons will not be considered. Thus one can sum and average over all incoming and outgoing spins and polarizations. With this prerequisite, the

---

[Lei93] and for recent progress on the $\gamma N \rightarrow \Delta$ process see [Ale07].

squared matrix elements are given by

$$\begin{aligned}
|\mathcal{M}_{e^-\text{-induced}}|^2 &= \underbrace{\frac{1}{2}\sum_{s_i,s_f}\left[j_\mu(s_i,s_f)j^\star_\nu(s_i,s_f)\right]}_{=\text{hadronic tensor } H_{\mu\nu}} \\
&\quad\times\frac{1}{q^4}\underbrace{\frac{1}{2}\sum_{s_i,s_f}\left[\overline{v}(l',t_f)\gamma^\mu v(l,t_i)\left(\overline{v}(l',t_f)\gamma^\mu v(l,t_i)\right)^\star\right]e^2}_{=\text{leptonic tensor } L_{\mu\nu}} \quad , \qquad (4.3)\\
|\mathcal{M}_{\gamma\text{-induced}}|^2 &= \underbrace{\frac{1}{2}\sum_{s_i,s_f}\left[j_\mu(s_i,s_f)j^\star_\nu(s_i,s_f)\right]}_{=\text{hadron tensor } H_{\mu\nu}}\frac{1}{2}\underbrace{\sum_{\lambda}\left[\epsilon^\mu(\lambda)(\epsilon^\nu(\lambda))^\star\right]e^2}_{=-g_{\mu\nu}} \quad . \qquad (4.4)
\end{aligned}$$

In the equations above, we introduced the so-called *hadronic tensor* $H_{\mu\nu}$ and *leptonic tensor* $L_{\mu\nu}$. The latter can be simplified to[2]

$$\begin{aligned}
L_{\mu\nu} &= e^2\frac{1}{2}\sum_{s_i,s_f}\overline{v}(l',s_f)\gamma^\mu v(l,s_i)\ \left(\overline{v}(l's_f)\gamma^\nu v(l,s_i)\right)^\star \\
&= e^2\frac{1}{2}Tr\left[\frac{\not{l}'+m_e}{2m_e}\gamma^\mu\frac{\not{l}+m_e}{2m_e}\gamma^\nu\right] = \frac{e^2}{8m_e^2}\left(m_e^2Tr[\gamma^\mu\gamma^\nu]+Tr[\not{l}'\gamma^\mu\not{l}\gamma^\nu]\right) \\
&= \frac{e^2}{q^4\ 2m_e^2}\left(m_e^2g^{\mu\nu}+l^\mu l'^\nu+l^\nu l'^\mu-g^{\mu\nu}l'\cdot l\right) \quad , \qquad (4.5)
\end{aligned}$$

where m_e denotes the electron mass. Furthermore, we can simplify the polarization sum of eq. 4.4 by means of the QED Ward-identity[3]

$$\sum_{\lambda}\left[\epsilon^\mu(\lambda)(\epsilon^\nu(\lambda))^\star\right] = -g_{\mu\nu} \ . \qquad (4.6)$$

4.3 Photon flux and virtual photon cross sections

As has been shown in the previous section, e^-N and γN scattering processes share an identical hadron tensor. To evaluate the cross section for one of these processes, this hadron tensor is contracted with either the lepton tensor or the polarization vectors, multiplied by the corresponding flux factor and integrated over the corresponding finale-state phase-space. In this approach, it is just the hadron tensor which reflects the similar nature of both processes.

However, there is also a method to connect directly the electron cross-section to the photon cross-section. Hereby one defines a flux of photons, which is sent out by the incoming electron and then the electron cross section is defined to be a product of this flux and the photon-nucleon cross section. How to split the electron cross section into flux and virtual photon cross section is a matter of convention. One of the most prominent conventions is the so-called *Hand convention (HC)* [Han63], in which the differential cross section for electron scattering is given by

$$\frac{d^2\sigma}{dl'^0 d\Omega_{l'}} = \Gamma_v(\sigma_T+\epsilon\sigma_L) \quad , \qquad (4.7)$$

---

[2] For numerical implementation see leptonTensor.f90.

[3] For details see e.g. [Pes, chapter 5.5].

where

$$\Gamma_v = \frac{\alpha}{2\pi^2}\frac{l'^0}{l^0}\frac{K}{Q^2}\frac{1}{1-\epsilon} \quad , \tag{4.8}$$

with $K=(s-M_n)/(2\,M_n)$, denotes the flux of virtual photons. The variable s is the Mandelstam s and $Q^2=-q^2$, with q being the photon four momentum.

The quantity

$$\epsilon = \left(1+2\frac{\vec{q}^{\,2}}{Q^2}\tan^2\left(\frac{\theta_l{}'}{2}\right)\right)^{-1} \tag{4.9}$$

represents a measure for the longitudinal and transverse polarization of the virtual photon. It is zero for $Q^2=0$, i.e. for a real photon. The factors σ_T/σ_L in eq. 4.7 denote the cross section for the scattering of a transversely/longitudinally polarized photon with a nucleon. So the cross-section for electron-induced processes is directly proportional to the photon-induced one.

HC has been used in the precursor works of Falter [Fal04a] and Lehr [Leh03]. It is a very convenient method, if one starts out with a known parametrization of the photon cross section at $Q^2=0$. Then one can parametrize the additional Q^2 dependence to model $\sigma_T(Q^2)$, the small σ_L can often be neglected. Finally, one obtains the electron cross section by multiplying with the corresponding flux.

As a major drawback, HC is defined in the nucleon rest frame (NRF). Therefore, the electron cross section must be constructed in this very frame and only there $\sigma_v=\sigma_T+\epsilon\sigma_L$ can be isolated. In the lab, the nucleon may have arbitrary momentum, e.g. due to Fermi motion within a nucleus. Thus the cross section is not invariant and we obtain in the lab frame (for details cf. appendix G.1)

$$\sigma = \sigma^{\text{NRF}}\frac{\sqrt{p_\mu p^\mu}\ \left|\vec{q}^{\,\text{NRF}}\right|}{\left|\vec{p}\,q_0-p_0\vec{q}\,\right|} \quad , \tag{4.10}$$

where q and p are the photon and nucleon four-momenta in the lab frame, q^{NRF} is the photon momentum and σ^{NRF} the cross section in the nucleon rest frame.

However, the whole procedure of boosting momenta from lab to nucleon rest frame is numerically intensive and the potentials are all defined in the lab frame. Therefore, the direct calculation of the matrix elements in the lab frame based on eq. 4.4 is for our needs more appropriate and, most important, faster. Additionally, we aim to modify the hadronic tensors, the flux and the phase space elements in the medium. So we anyhow have to evaluate the full cross-section in the medium, instead of working with pre-parametrized σ_T and σ_L.

4.4 (Quasi-)elastic scattering

We start discussing the different reaction channels for $\gamma^\star N$ scattering considering first the most trivial case of the nucleon-photon interaction: the elastic scattering. In this process the photon is simply absorbed by a nucleon. Due to kinematics, for a real photon this process can only occur when scattering off a bound nucleon. If the target nucleon is bound, one, traditionally, calls this a quasi-elastic scattering process since there is some energy loss involved owing to binding effects. In later sections we will then also address resonance excitations, single-π and double-π production.

Our notation for the $\gamma^\star N\to N$ process is chosen according to fig. 4.2: the in- and outgoing nucleon momenta are denoted p and p', the photon momentum q and the masses of the in-

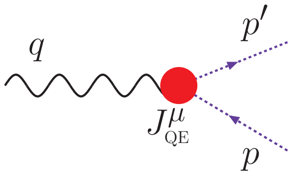

Figure 4.2: This Feynman diagram shows the absorption of a photon by a nucleon. The photon momentum is denoted q, the in- and outgoing nucleon momenta p and p'. The vertex is parametrized by the functional J^μ_{QE}.

and outgoing nucleons m and m'. In vacuum the masses of in- and outgoing particles are identical, in the medium the masses may differ due to momentum-dependent potentials and collisional broadening of the spectral function. Although this chapter deals primarily with the vacuum case, we will keep the m and m' dependence explicitly to simplify the generalization to the medium-case as presented in chapter 5. Our spinor normalization is chosen according to Bjorken and Drell [Bjo93] ($\bar{u}(p)u(p) = 1$).

4.4.1 Construction of the vertex operator

In the following, we will mainly repeat the derivation of the vertex operator as has been presented in standard textbooks[4]. However, in contrast to the standard derivation, we will for a later generalization keep track of the incoming and outgoing nucleon masses, although they are identical in vacuum and given by $m = m' = m_N$.

The hadronic current

$$j^\mu = \overline{u}(p', s_f) J^\mu_{\mathrm{QE}} u(p, s_i) \tag{4.11}$$

must be a Lorentz-vector, therefore also the operator J_{QE} must transform as a Lorentz vector. We start by constructing the most general form of the vertex. There are two independent four-momenta which can be constructed out of the available three momenta q, p and p' – let us choose $q = p' - p$ and $P = p' + p$ as our basis. The most general form of a parity-conserving vertex is then given by

$$J^\mu_{\mathrm{QE}} = a\, q^\mu + b\, P^\mu + c\, \gamma^\mu + d\, \sigma^{\mu\nu} q_\nu + e\, \sigma^{\mu\nu} P_\nu \tag{4.12}$$

with the scalar functions $a(q,P), b(q,P), \ldots, e(q,P)$ and

$$\sigma^{\mu\nu} = \frac{i}{2}[\gamma^\mu, \gamma^\nu] \quad . \tag{4.13}$$

The term $\sigma^{\mu\nu} P_\nu$ can also be expressed as a linear combination of q^μ and γ^μ terms:

$$\begin{aligned}
&\overline{u}(p', s_f)\sigma^{\mu\nu} P_\nu u(p, s_i) = \frac{i}{2}\overline{u}(p', s_f)[\gamma^\mu, P_\nu \gamma^\nu] u(p, s_i) \\
&= \frac{i}{2}\overline{u}(p', s_f)[\gamma^\mu, (p' + p)_\nu \gamma^\nu] u(p, s_i) = \frac{i}{2}\overline{u}(p', s_f)\left(\gamma^\mu(\not{p}' + m) - (m' + \not{p})\gamma^\mu\right) u(p, s_i) \\
&= \frac{i}{2}\overline{u}(p', s_f)\left(2p'^\mu - 2p^\mu - 2\gamma^\mu(m' - m))\right) u(p, s_i) \\
&= i\, \overline{u}(p', s_f)\ \left[q^\mu - \gamma^\mu(m' - m)\right]\ u(p, s_i) \quad .
\end{aligned} \tag{4.14}$$

---

[4] cf., for example, Steve Ellis' excellent lecture notes about particle physics [Ell08]

As a next step the term including P^μ is expressed as a linear combination of γ^μ and $\sigma^{\mu\nu}q_\nu$:

$$
\begin{aligned}
&\overline{u}(p', s_f)\sigma^{\mu\nu}q_\nu u(p, s_i) = \frac{i}{2}\overline{u}(p', s_f)[\gamma^\mu, q_\nu\gamma^\nu]u(p, s_i) \\
&= \frac{i}{2}\overline{u}(p', s_f)[\gamma^\mu, (p' - p)_\nu\gamma^\nu]u(p, s_i) = \frac{i}{2}\overline{u}(p', s_f)\left(\gamma^\mu(\not{p}' - m) - (m' - \not{p})\gamma^\mu\right)u(p, s_i) \\
&= \frac{i}{2}\overline{u}(p', s_f)\left((-\not{p}'\gamma^\mu + 2p^\mu - m\gamma^\mu\right) = i\,\overline{u}(p', s_f)\ \left[P^\mu - \gamma^\mu\left(m' + m\right)\right]\ u(p, s_i) \\
\Leftrightarrow\ & i\,\overline{u}(p', s_f)\ P^\mu\ u(p, s_i) = i\,\overline{u}(p', s_f)\ \left[\sigma^{\mu\nu}q_\nu + \gamma^\mu\left(m' + m\right)\right]\ u(p, s_i) \quad . \qquad (4.15)
\end{aligned}
$$

So choosing a linearly independent basis set, the operator can be reduced to

$$
J^\mu_{\mathrm{QE}} = e^2\left(F_1\gamma^\mu + \frac{i}{2m_N}F_2\sigma^{\mu\nu}q_\nu + F_3 q^\mu\right) \qquad (4.16)
$$

with the functions $F_1(q, P), F_2(q, P)$ and $F_3(q, P)$, the square of the elementary charge $e^2 = \alpha_{QED}/(4\pi)$ and the charge-averaged nucleon vacuum mass $m_N \simeq 0.938$ GeV. Charge conservation at the vertex, i.e. $q_\mu j^\mu = 0$, yields

$$
0 \ = \ \overline{u}(p', s_f)\left(F_1\not{q} + \frac{i}{2m_N}F_2\sigma^{\mu\nu}q_\nu q_\mu + F_3 q^2\right)u(p, s_i) \quad . \qquad (4.17)
$$

The term $\sigma^{\mu\nu}q_\nu q_\mu$ is antisymmetric in μ and ν and the implicit sum over ν and μ is therefore zero. Using

$$
\overline{u}(p', s_f)\not{q}u(p, s_i) = \overline{u}(p', s_f)(p - p')u(p, s_i) = \overline{u}(p', s_f)(m - m')u(p, s_i) \qquad (4.18)
$$

we get

$$
\begin{aligned}
0 \ &= \ \overline{u}(p', s_f)\left(F_1(m - m') + F_3 q^2\right)u(p, s_i) && (4.19) \\
\Rightarrow\ F_3 &= \frac{F_1(m' - m)}{q^2} \quad . && (4.20)
\end{aligned}
$$

Finally, we get

$$
J^\mu_{\mathrm{QE}} = e^2\left(F_1\gamma^\mu + \frac{i}{2m_N}F_2\sigma^{\mu\nu}q_\nu + \frac{F_1(m' - m)}{q^2}q^\mu\right) \quad , \qquad (4.21)
$$

which simplifies to

$$
J^\mu_{\mathrm{QE}} = e^2\left(F_1\gamma^\mu + \frac{i}{2m_N}F_2\sigma^{\mu\nu}q_\nu\right) \quad , \qquad (4.22)
$$

since $m' = m = m_N$. The form factors F_1 and F_2 are the standard *Dirac and Pauli form factors*[5]. There is only one independent Lorentz scalar in vacuum, such that both form factors can be chosen to be functions of Q^2.

---

[5] In some parts of the literature you will find another definition of F_2: $F_2 \rightarrow \kappa F_2$ with κ being the anomalous part of the magnetic moment of the nucleon (for the proton $\kappa = \mu_p - 1 = 1.793$, for the neutron $\kappa = \mu_n = -1.913$)

Evaluation of the hadronic tensor

The hadronic tensor for QE scattering is given by

$$
\begin{aligned}
H^{\mu\nu}_{\mathrm{QE}} &= \frac{1}{2}\sum_{s_i,s_f} \overline{u}(p',s_f)J^{\mu}_{\mathrm{QE}}u(p,s_i)\left(\overline{u}(p',s_f)J^{\nu}_{\mathrm{QE}}u(p,s_i)\right)^{\star} && (4.23)\\
&= \frac{1}{2}Tr\left[\frac{\not{p}'+m'}{2m'}J^{\mu}_{\mathrm{QE}}\frac{\not{p}+m}{2m}\gamma^0(J^{\nu}_{\mathrm{QE}})^{\dagger}\gamma^0\right] \quad . && (4.24)
\end{aligned}
$$

Using eq. 4.15, we transform the current operator defined in eq. 4.22 to

$$
J^{\mu}_{\mathrm{QE}} = \alpha\gamma^{\mu} + \beta^{\mu} \qquad (4.25)
$$

with the scalar α and the 4-vector β given by

$$
\begin{aligned}
\alpha &= e^2\left(F_1+F_2\right) \in \mathbb{R} \quad , && (4.26)\\
\beta^{\mu} &= -e^2\frac{F_2}{2m_N}\,P^{\mu} \in \mathbb{R}^4 \quad . && (4.27)
\end{aligned}
$$

In this notation, we get

$$
\begin{aligned}
8m'mH^{\mu\nu}_{\mathrm{QE}} &= Tr\left[(\not{p}'+m')J^{\mu}_{\mathrm{QE}}(\not{p}+m)\gamma^0(J^{\nu}_{\mathrm{QE}})^{\dagger}\gamma^0\right] && (4.28)\\
&= Tr\left[(\not{p}'+m')\left(\alpha\gamma^{\mu}+\beta^{\mu}\right)(\not{p}+m)\gamma^0\left(\alpha^{\star}\gamma^0\gamma^{\nu}\gamma^0+(\beta^{\nu})^{\star}\right)\gamma^0\right] && (4.29)\\
&= Tr\left[(\not{p}'+m')\left(\alpha\gamma^{\mu}+\beta^{\mu}\right)(\not{p}+m)\left(\alpha\gamma^{\nu}+\beta^{\nu}\right)\right] \; . && (4.30)
\end{aligned}
$$

The traces over the γ matrices can be evaluated using the following identities:

$$
\begin{aligned}
\mathrm{Tr}\left[1\right] &= 4 \quad , && (4.31)\\
\mathrm{Tr}[\gamma^{\mu}\gamma^{\nu}] &= 4g^{\mu\nu} \quad , && (4.32)\\
\mathrm{Tr}[\#\text{odd number of }\gamma\text{'s}] &= 0 \quad , && (4.33)\\
\mathrm{Tr}[\gamma^{\mu}\gamma^{\nu}\gamma^{\rho}\gamma^{\sigma}] &= 4(g^{\mu\nu}g^{\rho\sigma}-g^{\mu\rho}g^{\nu\sigma}+g^{\mu\sigma}g^{\mu\rho}) \quad . && (4.34)
\end{aligned}
$$

Thus we get

$$
\begin{aligned}
H^{\mu\nu}_{\mathrm{QE}} &= \frac{1}{8m'm}Tr\left[\alpha^2\not{p}'\gamma^{\mu}\not{p}\gamma^{\nu}+\alpha m\beta^{\nu}\not{p}'\gamma^{\mu}+\beta^{\mu}\beta^{\nu}\not{p}'\not{p}+\beta^{\mu}m\alpha\not{p}'\gamma^{\nu}\right.\\
&\quad \left.+m'\alpha\beta^{\nu}\gamma^{\mu}\not{p}+m'm\alpha^2\gamma^{\mu}\gamma^{\nu}+m'\beta^{\mu}\alpha\not{p}\gamma^{\nu}+\beta^{\mu}\beta^{\nu}m'm\right] && (4.35)\\
&= \frac{1}{2m'm}\left[\alpha^2(p'^{\mu}p^{\nu}+p'^{\nu}p^{\mu}-g^{\mu\nu}p'\cdot p)+\alpha m\beta^{\nu}p'^{\mu}+\beta^{\mu}\beta^{\nu}p'\cdot p+\beta^{\mu}m\alpha p'^{\nu}\right.\\
&\quad \left.+m'\alpha\beta^{\nu}p^{\mu}+m'm\alpha^2g^{\mu\nu}+m'\beta^{\mu}\alpha p^{\nu}+\beta^{\mu}\beta^{\nu}m'm\right] && (4.36)\\
&= \frac{1}{2m'm}\left[\alpha^2(p'^{\mu}p^{\nu}+p'^{\nu}p^{\mu}-g^{\mu\nu}p'\cdot p+m'mg^{\mu\nu})+\beta^{\mu}\beta^{\nu}(p'\cdot p+m'm)\right.\\
&\quad \left.+\alpha\beta^{\nu}(m'p^{\mu}+mp'^{\mu})+\alpha\beta^{\mu}(m'p^{\nu}+mp'^{\nu})\right] \quad , && (4.37)
\end{aligned}
$$

which simplifies again due to $m = m' = m_N$ to our final result

$$
\begin{aligned}
H^{\mu\nu}_{\mathrm{QE}} &= \frac{1}{2m_N^2}\left[\alpha^2(p'^{\mu}p^{\nu}+p'^{\nu}p^{\mu}-g^{\mu\nu}p'\cdot p+m_N^2g^{\mu\nu})+\beta^{\mu}\beta^{\nu}(p'\cdot p+m_N^2)\right.\\
&\quad \left.+m_N\alpha\left(\beta^{\nu}(p^{\mu}+p'^{\mu})+\beta^{\mu}(p^{\nu}+p'^{\nu})\right)\right] \quad . && (4.38)
\end{aligned}
$$

Form factors

The form factors F_1 and F_2 are connected to the so-called *Sachs form-factors* G_e and G_m, which have in the Breit-frame[6] an interpretation as charge form-factor and magnetic form-factor. Given

$$\begin{aligned} G_e(Q^2) &= F_1(Q^2) - \frac{Q^2}{4m_N^2} F_2(Q^2) \quad , & (4.39) \\ G_m(Q^2) &= F_1(Q^2) + F_2(Q^2) & (4.40) \end{aligned}$$

we obtain

$$\begin{aligned} F_1(Q^2) &= \frac{G_e(Q^2) + \frac{Q^2}{4m_N^2} G_m(Q^2)}{1 + \frac{Q^2}{4m_N^2}} \quad , & (4.41) \\ F_2(Q^2) &= \frac{G_m(Q^2) - G_e(Q^2)}{1 + \frac{Q^2}{4m_N^2}} \quad . & (4.42) \end{aligned}$$

The Sachs form factors have originally been determined using the so-called *Rosenbluth* method. This method relies on the OPE approximation, in which the cross section for electron scattering off a free nucleon is given by

$$\frac{d\sigma}{d\Omega_{l'}} = \sigma_{Mott} \left(G_E^2 + \frac{\tau}{\epsilon} G_M^2 \right) \frac{1}{1+\tau} \tag{4.43}$$

with $\tau = Q^2/(4m_N^2)$, $\epsilon = 1/(1 + 2(1+\tau)\tan((\theta_{l'}/2))$ and the Mott cross section σ_{Mott}. Plotting the measured cross section as a function of $1/\epsilon$ for a constant Q^2, one can extract the form factors by a linear fit to the resulting data points – the so-called *Rosenbluth-extraction* method.

Another, more modern, method relies on the polarization transfer to the recoiling nucleon. Within this method the ratio of the electric to the magnetic form factor is proportional to the ratio of transverse and longitudinal polarization of the final state nucleon

$$\frac{G_e}{G_m} \sim \frac{P_t}{P_l} \quad . \tag{4.44}$$

This ratio is considered to be a robust observable, since several systematic errors are expected to drop out in the ratio. As a great surprise, one noted in JLab experiments [Jon00], that the Rosenbluth method and the polarization method yield contradicting results. As has been mentioned in the introduction of this chapter, this puzzle is nowadays attributed to the influence of two-photon exchange processes which are now being studied with increasing interest [Kon06, Bra06, Arr07].

There exists a recent parametrization of the Sachs form-factors according to Bradford et al. [Bra06], the so-called *BBBA05 parametrization*, which does not include Rosenbluth data for $Q^2 > 1$ GeV^2. In their publication, the Rosenbluth data are referred to as unreliable. We will use this parametrization for all four Sachs form-factors (G_e^p, G_m^p, G_e^n, G_m^n), which are then given by

$$G_{e,m}^{n,p}(Q^2) = \frac{\sum_{k=0}^{2} a_k \tau^k}{1 + \sum_{k=1}^{4} b_k \tau^k} \tag{4.45}$$

with the constants a_k and b_k as given in table 4.1.

---

[6] The *Breit frame* (or *brick-wall frame*) is the frame in which $q^0 = 0$. For an elastic event, this corresponds to the CM-frame.

	a_0	a_1	a_2	b_1	b_2	b_3	b_4
G_e^p	1.	-0.0578	0.	11.1	13.6	33.	0.
G_m^p	1.	0.15	0.	11.1	19.6	7.54	0.
G_e^n	0.	1.25	1.3	-9.86	305.	-758.	802.
G_m^n	1.	1.81	0.	14.1	20.7	68.7	0.

Table 4.1: Parameters for the form factor parametrization according to eq. 4.45 deduced by Bradford et al. [Bra06].

4.4.2 Vacuum cross sections

In the following we treat only the vacuum case for which $m' = m = m_N$ – the evaluation of the in-medium cross section will be demonstrated in chapter 5.

Electron induced processes

In appendix D, different cross section formulas are derived for $eN \to eN$ scattering in vacuum (cf. eq. D.9 and eq. D.11). The cross section for fixed electron scattering angle $\theta_{l'}$ is given

$$\frac{d\sigma}{d\cos\theta_{l'}} = \frac{m_e^2\, m_N^2}{\pi(s - m_N^2)} \, \frac{|\vec{l}\,'|}{r_0 - |\vec{r}|\cos\theta_{l'}} \, |\mathcal{M}|^2 \Bigg|_{|\vec{l}\,'| = \frac{r^2 - m_N^2}{2(r_0 - |\vec{r}|\cos\theta_{l'})}} \quad . \tag{4.46}$$

with $r = p + q$ and

$$|\mathcal{M}|^2 = L_{\mu\nu} H^{\mu\nu}_{\mathrm{QE}} \, . \tag{4.47}$$

In fig. 4.3, the resulting cross section is compared to the experimental result obtained by Christy et al. [Chr04]. One observes excellent agreement which proves the correct numerical implementation of the quasi-elastic cross-section in our model.

Photon induced processes

The cross section for the in-vacuum $\gamma N \to N$ process is given by

$$\sigma_{\gamma N \to N} = \frac{4 m_N^2}{4\sqrt{(q_\alpha p^\alpha)^2}} \frac{dp'^4}{(2\pi)^4} \, 2\pi \mathcal{A}(p'^2 - m_N^2)\, |\mathcal{M}|^2 \, (2\pi)^4 \delta^4\left(p + q - p'\right) \tag{4.48}$$

$$= \frac{4 m_N^2}{4\sqrt{(q_\alpha p^\alpha)^2}} \, 2\pi \mathcal{A}(p'^2 - m_N^2)\, |\mathcal{M}|^2 \Bigg|_{p+q=p'} \quad . \tag{4.49}$$

The spectral function of the free nucleon is a δ function which peaks at its vacuum mass. Thus the absorption of a real photon by a nucleon is impossible due to kinematics, and the cross section vanishes

$$\sigma_{\gamma N \to N} = 0 \quad . \tag{4.50}$$

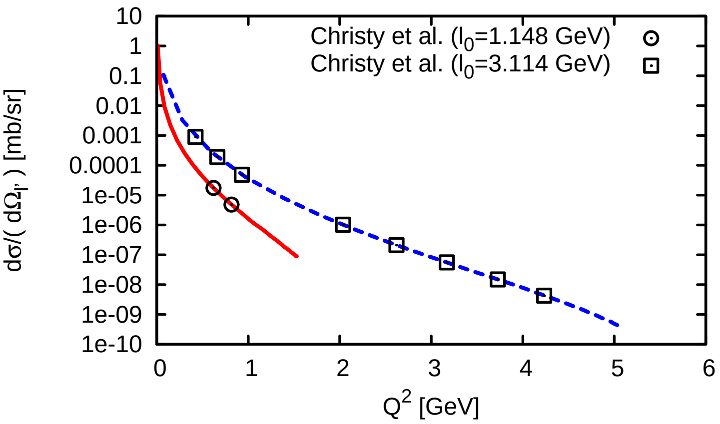

Figure 4.3: This figure shows $d\sigma/d\Omega$ for the elementary reaction $ep \rightarrow ep$ as a function of Q^2 for two different beam energies (dashed line: 3.114 GeV, solid line: 1.148 GeV) of the incoming electron. The data are taken from Christy et al. [Chr04].

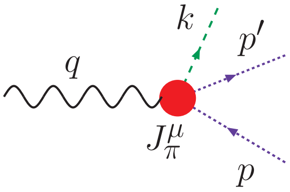

Figure 4.4: The upper panel shows the vertex for photon induced single pion production. We denote the photon momentum q, the in- and outgoing nucleon momenta p and p', the pion momentum k. The vertex functional J_π^μ is chosen according to an ansatz by Berends et al. [Ber67].

4.5 Single-pion production

Single pion production contributes to the total interaction probability of (virtual) photons and nucleons, as soon as the center of mass energy exceeds the sum of nucleon and pion mass ($\approx$ 1.076 GeV). A comprehensive review on this topic can, e.g., be found in [Dre92]. In the following paragraphs we primarily introduce the technical framework and emphasize on the structure and the explicit evaluation of the hadronic vertex. The ansatz used to parametrize the vertex structure is based on the work of Berends *et al.* [Ber67].

Our notation for single-pion production is chosen according to fig. 4.4: the nucleon momenta are denoted p and p', the photon momentum by q, the pion momentum k and the masses of the in- and outgoing nucleons m and m'. The electron mass is denoted m_e, the in- and outgoing lepton momenta are denoted l and l'. The hadronic vertex for pion production is parametrized by the vertex function J_π^μ. In principle, we get for each charge configuration of the in- and outgoing nucleons and the pion a different vertex function - this will later be absorbed into different sets of form-factors. Owing to the scalar nature of the outgoing pion field, the hadronic tensor is given in the same shape as in eq. 4.23 by

$$H_\pi^{\alpha\mu} = \frac{1}{2}\sum_{s_i,s_f} \overline{u}(p',s_f)J_\pi^\alpha u(p,s_i)\left(\overline{u}(p',s_f)J_\pi^\mu u(p,s_i)\right)^\star \quad . \tag{4.51}$$

4.5.1 Structure of the hadronic vertex

In the same spirit as Berends et al. [Ber67], but in the notation of MAID [Pas07], we parametrize the hadronic vertex by

$$J_\pi^\mu = \sum_{i=1}^{6} A_i M_i^\mu \tag{4.52}$$

with

$$\begin{aligned}
M_1^\mu &= \frac{-i}{2}\gamma^5(\gamma^\mu \slashed{q} - \slashed{q}\gamma^\mu) = -i\gamma^5(\gamma^\mu \slashed{q} - q^\mu) \quad , && (4.53)\\
M_2^\mu &= 2i\gamma^5(P^\mu q\cdot(k-\frac{q}{2}) - P\cdot q(k-\frac{q}{2})^\mu) \quad , && (4.54)\\
M_3^\mu &= -i\,\gamma^5(\gamma^\mu k\cdot q - \slashed{q}k^\mu) \quad , && (4.55)\\
M_4^\mu &= -2i\,\gamma^5(\gamma^\mu q\cdot P - \slashed{q}P^\mu) - 2m_N M_1^\mu \quad , && (4.56)\\
M_5^\mu &= i\,\gamma^5(q^\mu k\cdot q - q^2 k^\mu) \quad , && (4.57)\\
M_6^\mu &= -i\,\gamma^5(\slashed{q}q^\mu - q^2\gamma^\mu) && (4.58)
\end{aligned}$$

and

$$P = \frac{p' + p}{2} \quad . \tag{4.59}$$

The form factors $A_1, \ldots, A_6$, the so called *invariant amplitudes*, can be taken from a parametrization performed by the MAID group [MAI, Dre92]. These form factors are functions depending on all possible scalars which one can construct out of the available 4-vectors at the vertex. One can choose for a 2 → 2 vertex the Mandelstam variables s, t, u as a minimal set of scalars. L. Tiator supplied us with a parameter table[7] being prepared using the following set of variables

$$\begin{aligned}
W &= \sqrt{s} && (4.60)\\
Q^2 &= -q_\mu q^\mu && (4.61)
\end{aligned}$$

and the CM scattering angle θ between $\vec{q}$ and $\vec{k}$

$$\theta = \arccos\left(\frac{\vec{q}_{CM}\cdot\vec{k}_{CM}}{|\vec{q}_{CM}|\,|\vec{k}_{CM}|}\right) \quad . \tag{4.62}$$

4.5.2 Evaluation of the hadronic tensor

For the later numerical evaluation of the hadronic tensor, we sort the hadronic current according to the number of γ-matrices

$$J_\pi^\mu = i\gamma^5\left(\gamma^\mu \slashed{q} a + \gamma^\alpha b_\alpha^\mu + c^\mu\right) \tag{4.63}$$

with the following factors

$$\begin{aligned}
a &= -(A_1 - 2m_N A_4) \quad , && (4.64)\\
b_\alpha^\mu &= -A_3(g_\alpha^\mu k\cdot q - q_\alpha k^\mu) - 2A_4(g_\alpha^\mu q\cdot P - q_\alpha P^\mu) - A_6(q_\alpha q^\mu - g_\alpha^\mu q^2) && (4.65)\\
&= g_\alpha^\mu(-A_3 k\cdot q - 2A_4 q\cdot P + A_6 q^2) + q_\alpha(A_3 k^\mu + 2A_4 P^\mu - A_6 q^\mu) \quad , && (4.66)\\
c^\mu &= (A_1 - 2mA_4)q^\mu + 2A_2(P^\mu q\cdot(k-\frac{q}{2}) - P\cdot q(k-\frac{q}{2})^\mu) + A_5(q^\mu k\cdot q - q^2 k^\mu) \,, && (4.67)
\end{aligned}$$

---

[7] One finds these input files in the directory *buuinput/electronNucleon* of the GiBUU trunk.

A / B	$\not{q}\gamma^\nu\gamma^5$	$\gamma^\beta\gamma^5$	γ^5
$\gamma^5\gamma^\mu\not{q}$	$\mathcal{S}_1^{\mu\nu}$	$\mathcal{S}_2^{\mu\beta}$	$\mathcal{S}_3^{\mu}$
$\gamma^5\gamma^\alpha$	$\mathcal{S}_4^{\nu\alpha}$	$\mathcal{S}_5^{\alpha\beta}$	$\mathcal{S}_6^{\alpha}$
γ^5	$\mathcal{S}_7^{\nu}$	$\mathcal{S}_8^{\beta}$	$\mathcal{S}_9$

Table 4.2: Overview over all possible traces $Tr[(\not{p}'+m')A(\not{p}+m)B]$

which commute with the γ-matrices. *As for the QE-case, we will for later usage keep track of the in- and outgoing nucleon masses m and m', although they are identical in vacuum and given by $m = m' = m_N$*. In this notation, the hadronic tensor is given by

$$
\begin{aligned}
H_\pi^{\mu\nu} &= \frac{1}{2}\sum_{s_i,s_f}\overline{u}(p',s_f)J_\pi^\mu u(p,s_i)\ \left(\overline{u}(p',s_f)J_\pi^\nu u(p,s_i)\right)^\star && (4.68)\\
&= \frac{1}{2}\mathrm{Tr}\left[\frac{(\not{p}'+m')}{2m'}J_\pi^\mu\frac{(\not{p}+m)}{2m}\gamma^0(J_\pi^\nu)^\dagger\gamma^0\right] && (4.69)\\
&= \frac{1}{8\ m'm}\sum_{i=1}^{6}\sum_{j=1}^{6}\mathrm{Tr}\left[(\not{p}'+m')\left\{i\gamma^5\left(\gamma^\mu\not{q}a+\gamma^\alpha b_\alpha^\mu+c^\mu\right)\right\}(\not{p}+m)\right. && (4.70)\\
&\qquad \left.\gamma^0\left\{i\gamma^5\left(\gamma^\nu\not{q}a+\gamma^\beta b_\beta^\nu+c^\nu\right)\right\}^\dagger\gamma^0\right]\ . && (4.71)
\end{aligned}
$$

Using $(\gamma^5)^\dagger = \gamma^5$ and $(\gamma^\mu)^\dagger = \gamma^0\gamma^\mu\gamma^0$ we derive

$$
\begin{aligned}
H_\pi^{\mu\nu} &= \frac{1}{8\ m'm}\sum_{i=1}^{6}\sum_{j=1}^{6}\mathrm{Tr}\left[(\not{p}'+m')\left\{\gamma^5\left(\gamma^\mu\not{q}a+\gamma^\alpha b_\mu^\alpha+c^\mu\right)\right\}(\not{p}+m)\right. && (4.72)\\
&\qquad \left.\left\{\left(-\not{q}\gamma^\nu a^\star-\gamma^\beta(b_\beta^\nu)^\star-(c^\nu)^\star\right)\gamma^5\right\}\right]\ . && (4.73)
\end{aligned}
$$

Altogether, nine different traces have to be evaluated which will be named according to table 4.2. One obtains

$$
\begin{aligned}
\mathcal{S}_1^{\mu\nu} &= \mathrm{Tr}[(\not{p}'+m')\gamma^5\gamma^\mu\not{q}(\not{p}+m)\not{q}\gamma^\nu\gamma^5] = \mathrm{Tr}[(\not{p}'+m')\gamma^\mu\not{q}(-\not{p}+m)\not{q}\gamma^\nu]\\
&= -\mathrm{Tr}[\not{p}'\gamma^\mu\not{q}\not{p}\not{q}\gamma^\nu]+mm'\mathrm{Tr}[\gamma^\mu\not{q}\not{q}\gamma^\nu]\\
&= -\mathrm{Tr}[\not{p}'\gamma^\mu(-\not{p}\not{q}+2p\cdot q)\not{q}\gamma^\nu]+4mm'q^2g^{\mu\nu}\\
&= q^2\mathrm{Tr}[\not{p}'\gamma^\mu\not{p}\gamma^\nu]-2p\cdot q\mathrm{Tr}[\not{p}'\gamma^\mu\not{q}\gamma^\nu]+4mm'q^2g^{\mu\nu}\\
&= (q^2p'_\kappa p_\lambda-2p\cdot qp'_\kappa q_\lambda)\mathrm{Tr}[\gamma^\kappa\gamma^\mu\gamma^\lambda\gamma^\nu]+4mm'q^2g^{\mu\nu}\\
&= 4(q^2p'_\kappa p_\lambda-2p\cdot qp'_\kappa q_\lambda)(g^{\kappa\mu}g^{\lambda\nu}+g^{\kappa\nu}g^{\mu\lambda}-g^{\mu\nu}g^{\lambda\kappa})+4mm'q^2g^{\mu\nu}\\
&= 4q^2\left(p'^\mu p^\nu+p'^\nu p^\mu-g^{\mu\nu}p\cdot p'\right)-8p\cdot q(p'^\mu q^\nu+p'^\nu q^\mu-g^{\mu\nu}p'\cdot q)\\
&\quad +4mm'q^2g^{\mu\nu}\quad , && (4.74)
\end{aligned}
$$

$$
\begin{aligned}
\mathcal{S}_2^{\mu\beta} &= \mathrm{Tr}[(\not{p}'+m')\gamma^5\gamma^\mu\not{q}(\not{p}+m)\gamma^\beta\gamma^5] = \mathrm{Tr}[(\not{p}'+m')\gamma^\mu\not{q}(\not{p}-m)\gamma^\beta]\\
&= -m\mathrm{Tr}[\not{p}'\gamma^\mu\not{q}\gamma^\beta]+m'\mathrm{Tr}[\gamma^\mu\not{q}\not{p}\gamma^\beta]\\
&= -4m(p'^\mu q^\beta+q^\mu p'^\beta-g^{\mu\beta}p'\cdot q)+4m'(-p^\mu q^\beta+q^\mu p^\beta+g^{\mu\beta}p\cdot q)\quad , && (4.75)
\end{aligned}
$$

$$\begin{aligned}
\mathcal{S}_3^{\mu} &= \mathrm{Tr}[(\not{p}\,' + m\,')\gamma^5\gamma^\mu \not{q}(\not{p} + m)\gamma^5] = \mathrm{Tr}[(\not{p}\,' + m\,')\gamma^\mu \not{q}(-\not{p} + m)] \\
&= -\mathrm{Tr}[\not{p}\,'\gamma^\mu \not{q}\not{p}] + m\,'m\mathrm{Tr}[\gamma^\mu \not{q}] \\
&= -4\left[p\,'^\mu p\cdot q + q^\mu p\cdot p\,' - p^\mu p\,'\cdot q\right] + 4m\,'mq^\mu \quad , \qquad (4.76)
\end{aligned}$$

$$\begin{aligned}
\mathcal{S}_4^{\nu\alpha} &= \mathrm{Tr}[(\not{p}\,' + m\,')\gamma^5\gamma^\alpha(\not{p} + m)\not{q}\gamma^\nu\gamma^5] = \mathrm{Tr}[(\not{p}\,' + m\,')\gamma^\alpha(\not{p} - m)\not{q}\gamma^\nu] \\
&= m\,'\mathrm{Tr}[\gamma^\alpha \not{p}\not{q}\gamma^\nu] - m\mathrm{Tr}[\not{p}\,'\gamma^\alpha \not{q}\gamma^\nu] \\
&= 4m\,'(p^\alpha q^\nu + g^{\nu\alpha} p\cdot q - p^\nu q^\alpha) - 4m(p\,'^\alpha q^\nu - g^{\nu\alpha} p\,'\cdot q + p\,'^\nu q^\alpha) = \mathcal{S}_2^{\nu\alpha} \quad , \qquad (4.77)
\end{aligned}$$

$$\begin{aligned}
\mathcal{S}_5^{\alpha\beta} &= \mathrm{Tr}[(\not{p}\,' + m\,')\gamma^5\gamma^\alpha(\not{p} + m)\gamma^\beta\gamma^5] = \mathrm{Tr}[(\not{p}\,' + m\,')\gamma^\alpha(-\not{p} + m)\gamma^\beta] \\
&= 4mm\,'g^{\alpha\beta} - \mathrm{Tr}[(\not{p}\,'\gamma^\alpha \not{p}\gamma^\beta] \\
&= 4mm\,'g^{\alpha\beta} - 4(p\,'^\alpha p^\beta + p\,'^\beta p^\alpha - p\,'\cdot p g^{\alpha\beta}) \quad , \qquad (4.78)
\end{aligned}$$

$$\begin{aligned}
\mathcal{S}_6^{\alpha} &= \mathrm{Tr}[(\not{p}\,' + m\,')\gamma^5\gamma^\alpha(\not{p} + m)\gamma^5] = \mathrm{Tr}[(\not{p}\,' + m\,')\gamma^\alpha(\not{p} - m)] \\
&= 4mp^\alpha - 4mp\,'^\alpha \quad , \qquad (4.79)
\end{aligned}$$

$$\begin{aligned}
\mathcal{S}_7^{\nu} &= \mathrm{Tr}[(\not{p}\,' + m\,')\gamma^5(\not{p} + m)\not{q}\gamma^\nu\gamma^5] = \mathrm{Tr}[(\not{p}\,' + m\,')(-\not{p} + m)\not{q}\gamma^\nu] \\
&= 4mm\,'q^\nu - \mathrm{Tr}[(\not{p}\,'\not{p}\not{q}\gamma^\nu] \\
&= 4mm\,'q^\nu - 4(p\,'\cdot pq^\nu + q\cdot pp\,'^\nu - p\,'\cdot qp^\nu) = \mathcal{S}_3^{\nu} \quad , \qquad (4.80)
\end{aligned}$$

$$\begin{aligned}
\mathcal{S}_8^{\beta} &= \mathrm{Tr}[(\not{p}\,' + m\,')\gamma^5(\not{p} + m)\gamma^\beta\gamma^5] = \mathrm{Tr}[(\not{p}\,' + m\,')(\not{p} - m)\gamma^\beta] \\
&= -4mp\,'^\beta + 4mp^\beta = \mathcal{S}_6^{\beta} \quad , \qquad (4.81)
\end{aligned}$$

$$\begin{aligned}
\mathcal{S}_9 &= \mathrm{Tr}[(\not{p}\,' + m\,')\gamma^5(\not{p} + m)\gamma^5] = \mathrm{Tr}[(\not{p}\,' + m\,')(-\not{p} + m)] \\
&= 4m'm - 4p\,'\cdot p \quad . \qquad (4.82)
\end{aligned}$$

After having evaluated these traces, the hadronic tensor can now be rewritten and we obtain

$$\begin{aligned}
-8m\,'m\; H_\pi^{\mu\nu} &= aa^\star \mathcal{S}_1^{\mu\nu} + a(b_\beta^\nu)^\star \mathcal{S}_2^{\mu\beta} + a(c^\nu)^\star \mathcal{S}_3^{\mu} \\
&\quad + b_\alpha^\mu a^\star \mathcal{S}_4^{\nu\alpha} + b_\alpha^\mu (b_\beta^\nu)^\star \mathcal{S}_5^{\alpha\beta} + b_\alpha^\mu (c^\nu)^\star \mathcal{S}_6^{\alpha} \\
&\quad + c^\mu a^\star \mathcal{S}_7^{\nu} + c^\mu (b_\beta^\nu)^\star \mathcal{S}_8^{\beta} + c^\mu (c^\nu)^\star \mathcal{S}_9 \\
&= aa^\star \mathcal{S}_1^{\mu\nu} + a(b_\beta^\nu)^\star \mathcal{S}_2^{\mu\beta} + a(c^\nu)^\star \mathcal{S}_3^{\mu} \\
&\quad + b_\alpha^\mu a^\star \mathcal{S}_2^{\nu\alpha} + b_\alpha^\mu (b_\beta^\nu)^\star \mathcal{S}_5^{\alpha\beta} + b_\alpha^\mu (c^\nu)^\star \mathcal{S}_6^{\alpha} \\
&\quad + c^\mu a^\star \mathcal{S}_3^{\nu} + c^\mu (b_\beta^\nu)^\star \mathcal{S}_6^{\beta} + c^\mu (c^\nu)^\star \mathcal{S}_9 \quad . \qquad (4.83)
\end{aligned}$$

4.5.3 Vacuum cross sections

As for the quasi-elastic contribution, we postpone the more involved evaluation of the in-medium cross section to the next chapter (cf. sec. 5.3.2 for details). The following section treats the vacuum case in which $m' = m = m_N \approx 0.938$ GeV and $m_\pi \approx 0.138$ GeV, and compares our results to elementary data.

Electron induced events

According to Bjorken and Drell ([Bjo93], formula B.1), the cross section for the $e^- N \to e^- N\pi$ process in vacuum is given by

$$\begin{aligned} d\sigma^\pi &= \frac{1}{|v_e - v_N|}\frac{m_e}{l^0}\frac{m_N}{p^0}\frac{d\vec{k}}{2k^0(2\pi)^3}\frac{m_e}{l'^0}\frac{d\vec{l}'}{(2\pi)^3} \\ &\quad \frac{m_N}{p'^0}\frac{d\vec{p}'}{(2\pi)^3}\; L_{\mu\nu}H_\pi^{\mu\nu}\;(2\pi)^4\delta^4\left(l+p-\left(l'+k+p'\right)\right) \quad , \end{aligned} \tag{4.84}$$

where l, l' are the initial and final electron momenta, p and p' the nucleon momenta and k is the pion momentum. This reaction is usually described in the lab frame, where the nucleon is at rest ($p = (m_N, \vec{0})$). In this special frame, we get

$$\frac{1}{|v_e - v_N|} = \frac{l^0}{\left|\vec{l}\right|} \tag{4.85}$$

and

$$d\sigma^\pi = \frac{m_e^2\, m_N^2}{2\,(2\pi)^5}\frac{1}{\left|\vec{l}\right| p^0}\frac{d\vec{k}}{k^0}\frac{d\vec{l}'}{l'^0}\frac{d\vec{p}'}{p'^0}\; L_{\mu\nu}H_\pi^{\mu\nu}\;\delta^4\left(l+p-\left(l'+k+p'\right)\right) \quad .$$

Eventually we are aiming for an equation for $d\sigma^\pi/d\Omega_{\vec{k}}/d\vec{l}'$. First, we integrate out the $\vec{p}'$ dependence

$$\int d\vec{k}d\vec{p}'\;\delta^4\left(l+p-\left(l'+k+p'\right)\right)\ldots = \int \vec{k}^2\; d|\vec{k}|\; d\Omega_k\;\delta\left(l^0+p^0-\left(l'^0+k^0+p'^0\right)\right) \tag{4.86}$$

and transform the δ-function to

$$\begin{aligned} &\delta\left(l^0+p^0-\left(l'^0+k^0+p'^0\right)\right) = \delta\left(|\vec{k}|-\xi\right)\frac{1}{\left|\frac{d(k^0+p'^0)}{d|\vec{k}|}\right|_{|\vec{k}|=\xi}} \\ = \;& \delta\left(|\vec{k}|-\xi\right)\frac{1}{\left|\frac{d(\sqrt{|\vec{k}|^2+m_\pi^2}+\sqrt{|\vec{p}'|^2+m_N^2})}{d|\vec{k}|}\right|_{|\vec{k}|=\xi}} = \delta\left(|\vec{k}|-\xi\right)\frac{1}{\left|\frac{d(\sqrt{|\vec{k}|^2+m_\pi^2}+\sqrt{(\vec{q}-\vec{k})^2+m_N^2})}{d|\vec{k}|}\right|_{|\vec{k}|=\xi}} \\ = \;& \delta\left(|\vec{k}|-\xi\right)\frac{1}{\left|\frac{|\vec{k}|}{\sqrt{|\vec{k}|^2+m_\pi^2}}+\frac{|\vec{k}|-\vec{q}\vec{k}/|\vec{k}|}{\sqrt{(\vec{q}-\vec{k})^2+m_N^2)}}\right|_{|\vec{k}|=\xi}} = \delta\left(|\vec{k}|-\xi\right)\frac{1}{\left|\frac{|\vec{k}|}{k^0}+\frac{|\vec{k}|-\vec{q}\vec{k}/|\vec{k}|}{p'^0}\right|_{|\vec{k}|=\xi}} \quad , \end{aligned} \tag{4.87}$$

where ξ is the solution for $\left|\vec{k}\right|$ which solves the energy conservation condition

$$q^0 + p^0 = \sqrt{\left|\vec{k}\right|^2 + m_\pi^2} + \sqrt{(\vec{q}-\vec{k})^2 + m_N^2} \quad . \tag{4.88}$$

So we get

$$\int d\vec{k}d\vec{p}'\;\delta^4\left(l+p-\left(l'+k+p'\right)\right)\ldots = \int |\vec{k}|^2\; d\Omega_k\frac{1}{\left|\frac{|\vec{k}|}{k^0}+\frac{|\vec{k}|-\vec{q}\vec{k}/|\vec{k}|}{p'^0}\right|}\ldots\Bigg|_{|\vec{k}|=\xi} \quad , \tag{4.89}$$

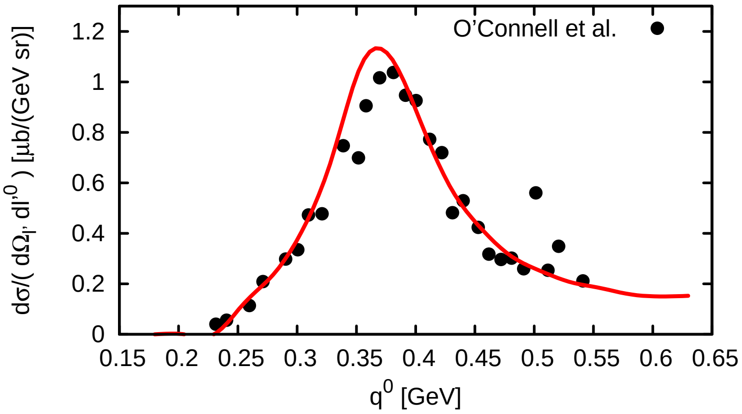

Figure 4.5: Electron scattering off a proton at an incoming electron energy of 730 MeV and an electron scattering angle of 37.1°. The plot shows a comparison of our elementary cross section to the experimental data obtained by O'Connell et al. [O'C84] in lab coordinates as a function of the virtual photon energy q^0. The statistical errors of the data points are negligible, therefore they have been omitted.

which leads to the desired result

$$\frac{d\sigma^\pi}{d\vec{l'}_f d\Omega_k} = \frac{m_e^2\ m_N^2}{2\ (2\pi)^5} \frac{1}{\left|\vec{l}\right|\ p^0\ k^0\ p'^0\ l^0} \frac{|\vec{k}|^2}{\left|\frac{|\vec{k}|}{k^0} + \frac{|\vec{k}| - \vec{q}\vec{k}/|\vec{k}|}{p'^0}\right|} L_{\mu\nu} H_\pi^{\mu\nu} \ . \tag{4.90}$$

Using

$$d\vec{l'} = \vec{l'}^2 d|\vec{l'}| d\Omega_{l'} \simeq (l'^0)^2 dl'^0 d\Omega_{l'} \ , \tag{4.91}$$

where we neglected the electron mass, we get together with $l^0 \simeq \left|\vec{l}\right|$ and $p^0 = m_N$

$$\frac{d\sigma^\pi}{dl'^0 d\Omega_{l'} d\Omega_k} = \frac{m_e^2\ m_N}{2\ (2\pi)^5} \frac{|\vec{k}|^2\ l'^0}{k^0\ p'^0\ l^0} \frac{1}{\left|\frac{|\vec{k}|}{k^0} + \frac{|\vec{k}| - \vec{q}\vec{k}/|\vec{k}|}{p'^0}\right|} L_{\mu\nu} H_\pi^{\mu\nu} \quad . \tag{4.92}$$

Fig. 4.5 shows a comparison of our result for $\sigma_{eN \to e'N'\pi}$ to the experimental data for $\sigma_{eN \to e'X}$ measured by O'Connell et al. [O'C84] at the Bates Linear Accelerator Center with an electron beam of 730 MeV. We observe very good agreement to the data, which makes us very confident in the successful implementation of the *MAID* form factors and the elementary cross sections for π production in our simulation[8]. Note that appendix F shows also how to evaluate the cross section using the so-called Hand convention, which becomes useful when comparing to other models.

---

[8] To compare this result obtained in the rest-frame of the initial nucleon to the results on the MAID website [MAI] one must keep in mind that MAID is calculating $\frac{d\sigma^\pi}{dl'^0 d\Omega_{l'} d\Omega_k^{CM}}$ with the pion angular element given in the CM frame of the hadronic vertex. To transform one exploits the Jacobian (derivation in [Byc73])

$$\frac{d\Omega_k^{CM}}{d\Omega_k} = \frac{W\vec{k}^2}{|\vec{k}|^{CM}(|\vec{k}|(m_N + q_0) - |\vec{q}| k_0 \cos(\theta_k))} \ . \tag{4.93}$$

with $W = \sqrt{(p+q)^\mu (p+q)_\mu}$.

Photon induced events

Assuming that the nucleon spectral function is given by a δ function, we get for the $\gamma N \to N\pi$ cross section

$$d\sigma_{\gamma N\to N\pi} = \frac{2m_N}{4\sqrt{(q_\alpha p^\alpha)^2}}\ |\mathcal{M}|^2\ \frac{1}{2k_0}\frac{d\vec{k}}{(2\pi)^3}\frac{m_N}{p'_0}\frac{d\vec{p}\,'}{(2\pi)^3}(2\pi)^4\delta^4(q+p-p'-k)\ . \quad (4.94)$$

Analogous to eq. 4.88 and 4.89 one derives

$$\int d\vec{k}d\vec{p}\,'\ \delta^4\left(q+p-\left(k+p'\right)\right)\ldots = \int |\vec{k}|^2\ d\Omega_k \frac{1}{\left|\frac{|\vec{k}|}{k^0}+\frac{|\vec{k}|-\vec{q}\vec{k}/|\vec{k}|}{p'^0}\right|}\ldots\Bigg|_{|\vec{k}|=\xi} \quad (4.95)$$

with ξ being a solution for $|\vec{k}|$ to

$$q^0+p^0=\sqrt{\left|\vec{k}\right|^2+m_\pi^2}+\sqrt{(\vec{q}-\vec{k})^2+m_N^2}\ . \quad (4.96)$$

Finally, we obtain

$$\frac{d\sigma_{\gamma N\to N\pi}}{d\Omega_k} = \frac{m_N^2}{4p'_0\ k_0\ \sqrt{(q_\alpha p^\alpha)^2}}\frac{1}{(2\pi)^2}\frac{|\vec{k}|^2}{\left|\frac{|\vec{k}|}{k^0}+\frac{|\vec{k}|-\vec{q}\vec{k}/|\vec{k}|}{p'^0}\right|}|\mathcal{M}|^2\Bigg|_{|\vec{k}|=\xi} \quad (4.97)$$

with

$$|\mathcal{M}|^2=-\frac{1}{2}H_\pi^{\mu\nu}g_{\mu\nu}\ . \quad (4.98)$$

In fig. 4.6, the total cross sections for photon-induced pion production is shown for both proton (left panel) and neutron targets (right panel). Let us first compare the sum of π^0 and π^+ production off the proton (solid line, left panel) to the experimental cross section for the inclusive reaction $\gamma p \to X$ (filled circles). We observe that the single-pion-production contribution makes up for the total cross section in the region below $E_\gamma < 0.5$ GeV. However, at higher energies also other channels can be populated, especially 2π channels, and the single-π contribution becomes less important. The open squares in the left panel represent the experimental findings of the *CB-ELSA TAPS collaboration* [Bar05] for the exclusive process $\gamma p \to p\pi^0$. We emphasize, that the perfect agreement of our result (dashed curve) to the latter data points proves the proper implementation of the *MAID* form factors in our model.

4.6 Resonance excitations

Resonance excitations play a dominant role in the spectrum of low-energy $\gamma^\star$N scattering (for a comprehensive review see, e.g., [Bof96]). Applying a partial wave analysis to the world data on photon and electron scattering, e.g. the MAID group [MAI] provides resonance information. An important result of such an analysis are the so-called helicity amplitudes, which give information about the possibility to excite a resonance at its pole mass. These helicity amplitudes can then be used to determine resonance form factors, as shown in appendix E. In the following we establish the framework for resonance excitations and discuss the hadronic tensors for different

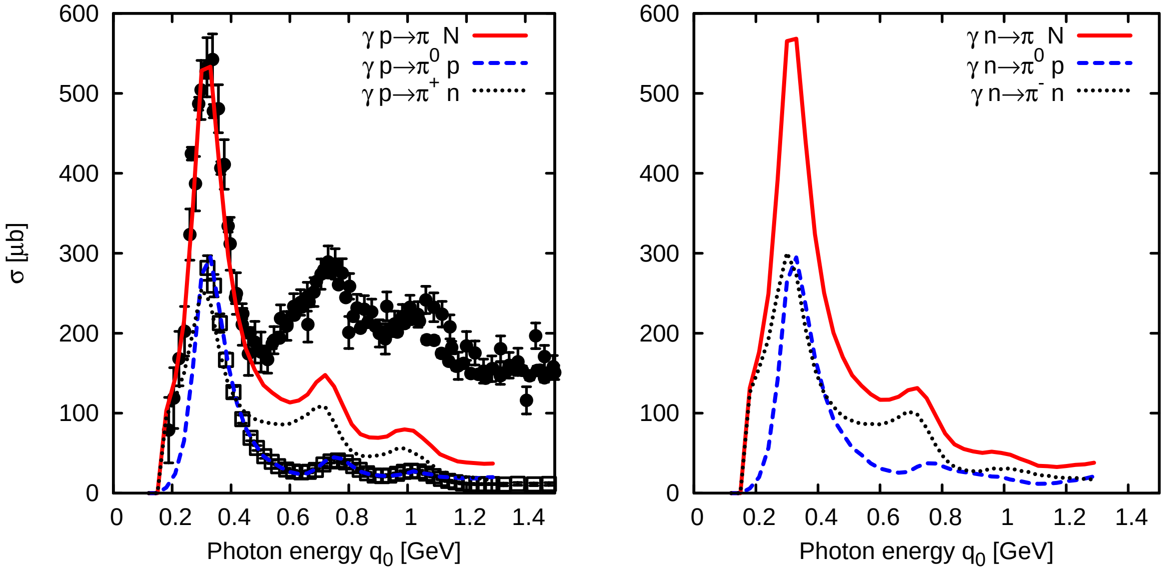

Figure 4.6: The upper plot shows photon induced pion production off proton (left panel) and neutron (right panel) as a function of the photon energy. The data in the left panel represent the experimental findings for $\gamma p \to p\pi^0$ of the *CB-ELSA TAPS collaboration* [Bar05] (open squares) and a compilation of data for the inclusive cross section $\sigma_{\gamma p \to X}$ [Yao06](filled circles). The dashed curves show our results for π^0 production, the dotted ones show $\pi^{\pm}$ production and the solid curves represent the sum of both charge channels.

name	spin	isospin	parity
$P_{33}(1232)$	3/2	3/2	+
$P_{11}(1440)$	1/2	1/2	+
$D_{13}(1520)$	3/2	1/2	-
$S_{11}(1535)$	1/2	1/2	-
$S_{31}(1620)$	1/2	3/2	-
$S_{11}(1650)$	1/2	1/2	-
$D_{15}(1675)$	5/2	1/2	-
$F_{15}(1680)$	5/2	1/2	+
$D_{33}(1700)$	3/2	3/2	-
$P_{13}(1720)$	3/2	1/2	+
$F_{35}(1905)$	5/2	3/2	+
$P_{31}(1910)$	1/2	3/2	+
$F_{37}(1950)$	7/2	3/2	+

Table 4.3: Resonances which are included in the MAID analysis [MAI].

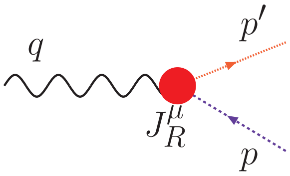

Figure 4.7: The upper Feynman diagram represents photon-induced resonance excitation and visualizes our notation. The photon momentum is denoted q, the incoming nucleon momentum p and the outgoing resonance momentum p'. The vertex is parametrized by the functional J^μ_{R}.

isospin and parity. We aim for an implementation of all those resonances in our model, which are also included in the present MAID analysis [MAI] – namely the ones given in table 4.3.

Our notation for (virtual) photon induced resonance excitation is chosen according to fig. 4.7. The photon momentum is denoted q, the incoming nucleon momentum p and the outgoing resonance momentum p'. In the following, the structure of the hadron tensor is discussed, which includes the hadronic vertex denoted J^μ_{R}.

4.6.1 Structure of the hadron tensors

Spin 1/2 resonances. The nucleon resonances with spin $S = 1/2$ are treated on the same footing as the nucleon itself. Only the notation for the form factors differs slightly, here we use instead of the Pauli and Dirac form-factors a similar notation as, e.g., Devenish *et al.* [Dev76]. The hadronic flux is defined by

$$j^\nu_{1/2} = \overline{\phi}(p', s_f) J^\nu_{\mathrm{R},1/2} u(p, s_i) \quad , \tag{4.99}$$

where u is the nucleon spinor and ϕ is the resonance spinor. The vertex operator is parametrized for positive-parity resonances by

$$(J^+_{\mathrm{R},1/2})^\nu = \frac{g_1}{(2m_N)^2}(Q^2\gamma^\nu + \not{q} q^\nu) + \frac{g_2}{2m_N} i\sigma^{\nu\rho} q_\rho \tag{4.100}$$

and for negative-parity ones by

$$(J^-_{\mathrm{R},1/2})^\nu = (J^+_{\mathrm{R},1/2})^\nu \gamma_5 \quad . \tag{4.101}$$

We assume that the form factors g_1 and g_2 depend solely on Q^2; and the form factors are fixed using the *MAID* helicity amplitudes as shown in appendix E.1. Analogous to eq. 4.23, the hadronic tensor is given by

$$H^{\mu\nu}_{\mathrm{R},1/2} = \frac{1}{2}\sum_{s_i, s_f} \overline{\phi}(p', s_f) J^\mu_{\mathrm{R},1/2} u(p, s_i) \left(\overline{\phi}(p', s_f) J^\nu_{\mathrm{R},1/2} u(p, s_i)\right)^\star \tag{4.102}$$

$$= \frac{1}{2} Tr\left[\frac{\not{p}' + m'}{2m'} J^\mu_{\mathrm{R},1/2} \frac{\not{p} + m_N}{2m_N} \gamma^0 (J^\nu_{\mathrm{R},1/2})^\dagger \gamma^0\right] \tag{4.103}$$

with the resonance mass $m' = \sqrt{p' \cdot p'}$ and the nucleon mass $m_N = \sqrt{p \cdot p}$.

Spin 3/2 resonances. The spin 3/2 resonances can be described using Rarita-Schwinger spinors ψ_α. Within this framework, the hadronic flux is given by

$$j^{\nu}_{1/2} = \overline{\psi}_\alpha(p', s_f) J^{\alpha\nu}_{\mathrm{R},3/2} u(p, s_i) \tag{4.104}$$

where u is the nucleon spinor and ψ_α is the resonance Rarita-Schwinger spinor. The vertex operator for negative-parity resonances can be parametrized by

$$(J^{-}_{\mathrm{R},3/2})^{\alpha\nu} = g^{\alpha\nu}\left(\frac{C_3}{m_N}\not{q} + \frac{C_4}{m_N^2} p' \cdot q + \frac{C_5}{m_N^2} p \cdot q\right) - q^{\alpha}\left(\frac{C_3}{m_N}\gamma^{\nu} + \frac{C_4}{m_N^2} p'^{\nu} + \frac{C_5}{m_N^2} p^{\nu}\right)$$

and for positive-parity ones by

$$(J^{+}_{\mathrm{R},3/2})^{\nu} = (J^{-}_{\mathrm{R},3/2})^{\nu}\gamma_5 \quad . \tag{4.105}$$

The constant $m_N = 0.938$ GeV denotes the charge-averaged nucleon mass. Again, we assume that the form factors C_3, C_4 and C_5 depend solely on Q^2; and these form factors are again fixed using helicity amplitudes (cf. appendix E.2 for details). The hadronic tensor is given by

$$\begin{aligned} H^{\mu\nu}_{\mathrm{R},3/2} &= \frac{1}{2}\sum_{s_i, s_f} \overline{\psi}_\alpha(p', s_f) J^{\alpha\mu}_{\mathrm{R},3/2} u(p, s_i) \left(\overline{\psi}_\beta(p', s_f) J^{\beta\nu}_{\mathrm{R},3/2} u(p, s_i)\right)^{\star} && (4.106) \\ &= \frac{1}{2} Tr\left[\frac{\Lambda_{\beta\alpha}}{2m'} J^{\alpha\mu}_{\mathrm{R},3/2} \frac{\not{p} + m_N}{2m_N} \gamma^0 (J^{\beta\nu}_{\mathrm{R},3/2})^{\dagger}\gamma^0\right] . && (4.107) \end{aligned}$$

In the equation above, we used the identity for the spin 3/2 projector

$$\sum_{s_f} \psi_\beta(p', s_f)\overline{\psi}_\alpha(p', s_f) = \frac{\Lambda_{\beta\alpha}}{2m'} \tag{4.108}$$

with

$$\Lambda_{\mu\nu}(p) = -(\not{p}' + m')\left(g^{\mu\nu} - \frac{2}{3}\frac{p'^{\mu}p'^{\nu}}{(m')^2} + \frac{1}{3}\frac{p'^{\mu}\gamma^{\nu} - p'^{\nu}\gamma^{\mu}}{m'} - \frac{1}{3}\gamma^{\mu}\gamma^{\nu}\right) \tag{4.109}$$

and the resonance mass is given by $m' = \sqrt{p' \cdot p'}$.

Resonances with spin $> 3/2$. The description of spinors with spin greater 3/2 within a Lagrange framework is highly complicated. As a simplifying assumption, we will treat all particles with spin greater than 3/2 within the spin 3/2 formalism.

4.6.2 Vacuum cross sections

Again, we first treat the vacuum case and postpone the in-medium treatment to chapter 5, as a consequence $m = m_N = 0.938$ GeV. Analogous to the nucleon case (cf. eq. D.1), the cross section to produce a specific resonance R is given by

$$\frac{d\sigma_{eN\to e'R}}{d\Omega_{l'}\, d|\vec{l'}|} = \frac{1}{\sqrt{(l_\alpha p^\alpha)^2}} \frac{m_e^2\, m_N\, m'}{2\pi^2} |\vec{l'}|\, \mathcal{A}_R(p'^2)\, |\mathcal{M}_R|^2 \, . \tag{4.110}$$

The matrix element

$$|\mathcal{M}_R|^2 = H^{\mu\nu}_{\mathrm{R}} L^{\mu\nu} \tag{4.111}$$

includes the leptonic tensor defined in eq. 4.5 and the hadron tensor is evaluated numerically[9]. Since the resonances are broad particles, the spectral function of the resonance $\mathcal{A}_R(p'^2)$ replaces the δ function of eq. D.1.

The in-vacuum cross section for $\gamma N \to R$ is given by

$$\begin{aligned}\sigma_{\gamma N\to R} &= \frac{2m_N}{4\sqrt{(q_\alpha p^\alpha)^2}} 2m' \frac{dp'^4}{(2\pi)^4}\, 2\pi\mathcal{A}_R(p'^2)\, |\mathcal{M}_R|^2\, (2\pi)^4\delta^4\left(p+q-p'\right) \\ &= \frac{2m_N\; 2m'}{4\sqrt{(q_\alpha p^\alpha)^2}}\, 2\pi\mathcal{A}_R(p'^2)\, |\mathcal{M}_R|^2 \Bigg|_{p+q=p'} \quad , \end{aligned} \tag{4.112}$$

where the squared matrix element is given by eq. 4.4 using the corresponding hadronic tensor.

4.7 Total cross section

For *electron induced* events, the total cross section contains all contributions which we elaborated on in the last sections: quasi-elastic scattering, resonance production and direct pion production. However, for the *photon induced* events only resonance excitation and pion production are relevant. There one may neglect the QE contribution since the outgoing nucleon has large off-shellness for $Q^2 = 0$.

For both cases, one must be careful to avoid double counting since also the resonances contribute to pion production. Thus one must subtract these resonance contributions from the direct pion production cross section. We interpret this subtracted contribution as a single-π background and denote it by σ_π^{BG}. With this prerequisite, we define the total cross sections for the electron

$$\frac{d\sigma_{e,\mathrm{tot}}}{d\Omega_{l'}\, d|\vec{l}\,'|} = \frac{d\sigma_{\mathrm{QE}}}{d\Omega_{l'}\, d|\vec{l}\,'|} + \frac{d\sigma_\pi^{\mathrm{BG}}}{d\Omega_{l'}\, d|\vec{l}\,'|} + \sum_R \frac{d\sigma_{\mathrm{R}}}{d\Omega_{l'}\, d|\vec{l}\,'|} \tag{4.113}$$

and for the photon

$$\sigma_{\gamma,\mathrm{tot}} = \sigma_\pi^{\mathrm{BG}} + \sum_R \sigma_{\mathrm{R}} \quad . \tag{4.114}$$

Note that the background terms σ_π^{BG} include all kind of interferences among the resonances and among resonance and background amplitudes.

Contribution of the resonances to pion production

In the following, the single-π background $d\sigma_\pi^{\mathrm{BG}}$, which was introduced in the preceding paragraph, is evaluated.

The MAID model (cf. sec. 4.5.3) fits its parameters to the world data on electron- and photon-induced pion production, hence it represents a physically motivated fit to the world data and can also be used as a parametrization of the world data. With the overall assumption of our model that the resonances do not interfere and using the single-pion production cross sections σ_π

---

[9] Note that the hadron tensors for single-π and QE scattering have been simplified by hand. For the resonance production, we evaluate the traces and matrix multiplications for the calculation of $H_{\mu\nu}$ numerically. This job is performed online during run-time by a set of routines being especially developed for this function (see in particular *minkowski.f90* and *matrix_module.f90* within the GiBUU code).

according to the MAID model (cf. sec. 4.5.3) as a parametrization of data, we get the following definition of the single-π background for the electron

$$\frac{d\sigma_\pi^{\mathrm{BG}}}{d\Omega_{l'}\ d|\vec{l}\,'|\ d\Omega_k} = \underbrace{\frac{d\sigma_\pi}{d\Omega_{l'}\ d|\vec{l}\,'|\ d\Omega_k}}_{\text{MAID input}} - \sum_R \frac{d\sigma_{eN\to eR\to eN\pi}}{d\Omega_{l'}\ d|\vec{l}\,'|\ |d\Omega_k} \tag{4.115}$$

and for the photon induced events

$$\frac{d\sigma_\pi^{\mathrm{BG}}}{d\Omega_k} = \underbrace{\frac{d\sigma_\pi}{d\Omega_k}}_{\text{MAID input}} - \sum_R \frac{d\sigma_{\gamma N\to N\pi}}{d\Omega_k} \quad , \tag{4.116}$$

with Ω_k denoting the solid angle of the pion (for notation see also fig. 4.4).

In our model, the resonances are assumed to decay isotropically in their rest-frames. This approximation is based upon the numerical result that the information contained in non-isotropic distributions is mostly lost during repeated rescatterings of the resonances or resonance decay products within the nuclear medium [Eng94]. Thus the resonance contributions are given by

$$\begin{aligned}\frac{d\sigma_{eN\to eR\to eN\pi}}{d\Omega_{l'}\ d|\vec{l}\,'|\ |d\Omega_k} &= \frac{d\sigma_{\mathrm{R}}}{d\Omega_{l'}\ d|\vec{l}\,'|}\frac{\Gamma_{R\to N\pi}}{\Gamma_R}\frac{1}{d\Omega_k^{\mathrm{CM}}} \\ &= \frac{d\sigma_{\mathrm{R}}}{d\Omega_{l'}\ d|\vec{l}\,'|}\frac{\Gamma_{R\to N\pi}}{\Gamma_R}\frac{1}{d\Omega_k}\frac{\sqrt{p'^{\mu}p'_{\mu}}\vec{k}^2}{|\vec{k}^{\mathrm{CM}}|\left(|\vec{k}|p'^{0}-|\vec{p}\,'|k_0\cos(\theta_k)\right)}\end{aligned} \tag{4.117}$$

and

$$\frac{d\sigma_{\gamma N\to R\to eN\pi}}{d\Omega_k} = \sigma_{\gamma N\to R}\frac{\Gamma_{R\to N\pi}}{\Gamma_R}\frac{1}{d\Omega_k}\frac{\sqrt{p'^{\mu}p'_{\mu}}\vec{k}^2}{|\vec{k}^{\mathrm{CM}}|\left(|\vec{k}|p'^{0}-|\vec{p}\,'|k_0\cos(\theta_k)\right)} \quad , \tag{4.118}$$

with $\theta_k = \measuredangle(\vec{k},\vec{p}\,')$ [10].

Note that there remains one subtle issue: the cross section $d\sigma_\pi^{\mathrm{BG}}/(d\Omega_{l'}\ d|\vec{l}\,'|\ d\Omega_k)$ or, respectively, $d\sigma_\pi^{\mathrm{BG}}/d\Omega_k$ can become negative at some value of $d\Omega_k$. The reason for this is given by the assumption of isotropic decays of the resonances and, most important, in the fact that our so-called background includes all kind of interferences among the resonances themselves and interferences among the resonances and the physical background processes (e.g. u- and t-channel processes). This feature is somewhat reduced for the integrated cross sections: the resonances of different partial waves do not interfere in the total cross section, and the information about the angular distribution of the resonance decay is integrated out. The fact that the background may become negative is no short-coming of our model. Rather it is a physical feature based on the way we divide our cross section into resonances and background. One must emphasize that it is natural that the background cross section may become negative, since the background explicitly includes all the interferences. Sec. 5.5 sketches the implementation of such negative cross sections in our GiBUU Monte-Carlo framework via negative weight factors.

---

[10] The Jacobian for the transformation from CM- to lab-frame has been derived, e.g., in [Byc73]:

$$\frac{d\Omega_k^{CM}}{d\Omega_k} = \frac{\sqrt{p'^{\mu}p'_{\mu}}\vec{k}^2}{|\vec{k}^{\mathrm{CM}}|\left(|\vec{k}|p'^{0}-|\vec{p}\,'|k_0\cos(\theta_k)\right)} \ . \tag{4.119}$$

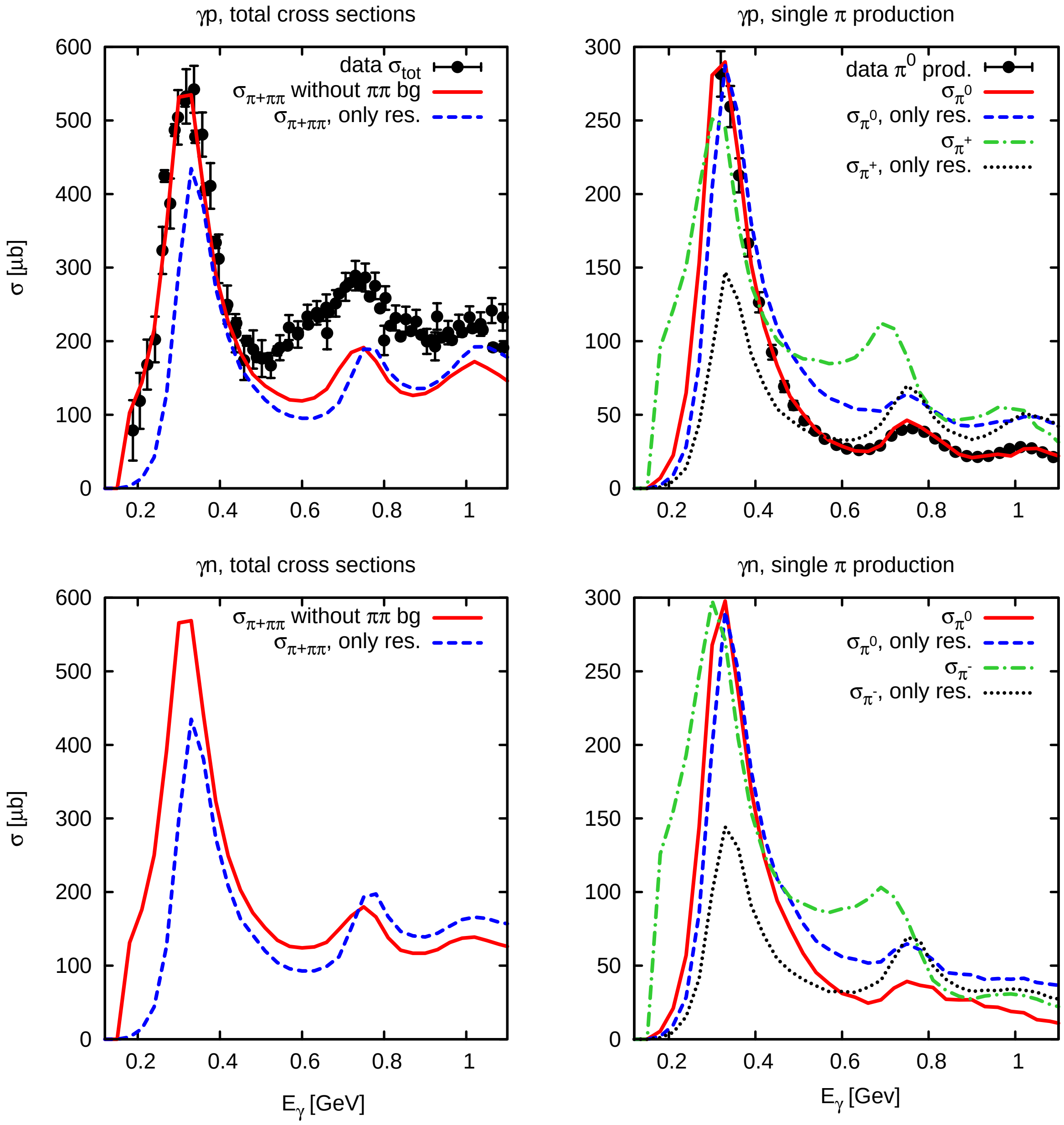

Figure 4.8: The upper figure shows photon induced reactions on the proton (upper panels) and the neutron (lower panels) as a function of the incoming photon energy without a 2π background cross section. The plots on the left panel show the total cross section (without $\pi\pi$ background) and the contribution of the resonances. The right hand plots detail the single pion production contributions: for the different outgoing pion charges, resonance contributions and total cross sections are given. The data are taken from [Yao06] and [Bar05].

Photon scattering The cross section for photon reactions with the proton and neutron are shown in fig. 4.8. Evidently, the ”non-interfering” resonance model alone describes the cross sections only qualitatively. Comparing the single-π^0 production cross sections off the proton (upper right panel of fig. 4.8) to the experimental data, it becomes evident that it is necessary to include the single-π backgrounds to achieve also quantitative agreement. Furthermore, the total cross section (cf. the upper left panel of fig. 4.8) is well described at low energies. However, there is some missing strength in the higher energy region, especially missing $\pi\pi$ strength. Thus we must also introduce an additional $\pi\pi$ background. Double pion production is addressed in detail in chapter 8. There, the total cross sections for all charge channels are defined and their uncertainties are discussed. Given parametrizations $\sigma^{\text{data}}_{\pi\pi}$ of the experimental data (cf. sec. 8.3 for details), we can define the 2π background by

$$\sigma^{BG}_{\pi\pi} = \sigma^{\text{data}}_{\pi\pi} - \sigma^{\text{Res}}_{\pi\pi} \ . \tag{4.120}$$

This subtraction must be done independently for all possible charge channels: $\pi^+\pi^-$,$\pi^0\pi^0$ and $\pi^0\pi^\pm$. Double pion production via resonances can only occur via the four channels

$$\begin{array}{ccccccc} \gamma N & \to & R & \to & \pi\Delta & \to & 2\pi N \ , \\ \gamma N & \to & R & \to & \pi P_{11}(1440) & \to & 2\pi N \ , \\ \gamma N & \to & R & \to & \rho N & \to & 2\pi N \ , \\ \gamma N & \to & R & \to & \sigma N & \to & 2\pi N \ . \end{array} \tag{4.121}$$

Given $\sigma_{\gamma N\to R}$, the evaluation of $\sigma_{\gamma N\to R\to N\pi\pi}$ involves a weighting with the partial decay widths into the channels listed above and the relevant isospin Clebsch-Gordan factors. The distribution of the final state momenta of the $\pi\pi$ background events are assumed to follow a phase space distribution[11]. The resulting 2π contributions are shown in fig. 4.9 for both proton and neutron targets. Obviously, the total cross section is now very well described and the resonance contribution to $\pi\pi$ is in fact small as compared to the total $\pi\pi$ production cross section, especially at energies below 600 MeV.

Electron scattering Furthermore, we show in fig. 4.10 the single-π production for electron induced reactions with and without background contributions. Also here, the background has a profound impact and must be taken into account. However, we can not introduce a sensible 2π background due to a lack of such data, and so we consider only a single-π background. This leads to a restriction of our model, such that we can not trust the model far above the $\pi\pi$ threshold.

---

[11] In chapter 8 we will also address a more involved model - however, the there derived momentum distribution is already including all resonances in the intermediate state and it is not possible to split the momentum distribution into a resonance like and background like part. Therefore, it is not possible to use this distribution for the background events.

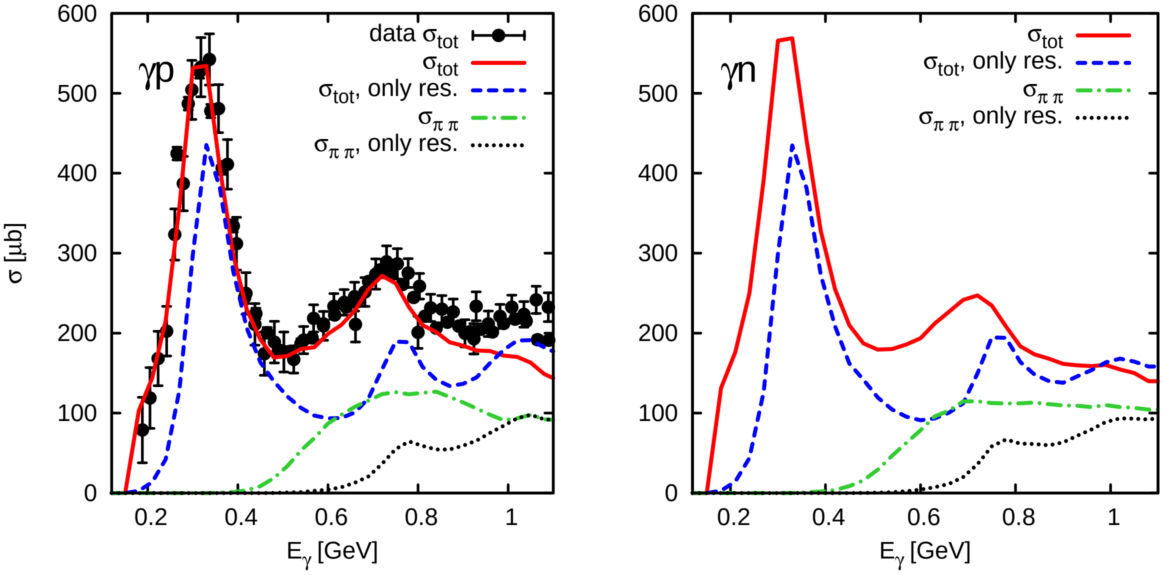

Figure 4.9: Photon induced reactions on proton (left panel) and neutron (right panel) as a function of the incoming photon energy including a 2π background. The solid line shows the result for σ_{tot} for the full model, the dashed line shows the result without single-π and $\pi\pi$ background contributions. The contribution of the resonances to double-π production is shown by the dotted line, the full 2π contribution is shown by the dashed-dotted line. The data are taken from [Yao06].

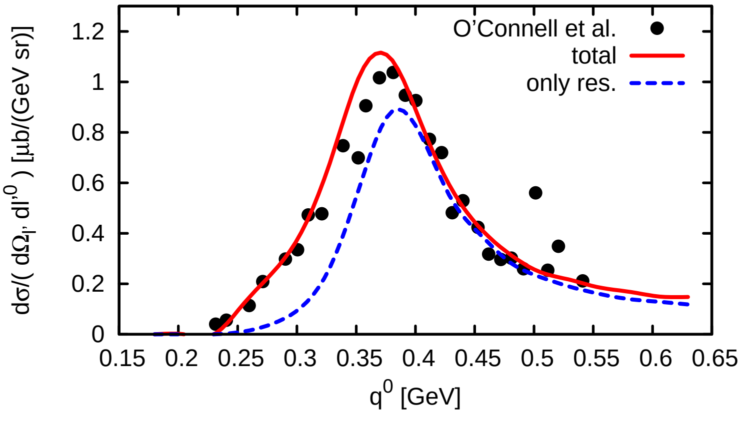

Figure 4.10: Electron scattering off a proton at an incoming electron energy of 730 MeV and an electron scattering angle of 37.1°. The plot shows a comparison of our elementary cross section with and without background to the experimental data obtained by O'Connell et al. [O'C84] in lab coordinates as a function of the virtual photon energy q^0. The statistical errors of the data points are negligible, therefore they have been omitted.

Chapter 5

Interaction of electrons and photons with nuclei

Overview: This chapter generalizes the elementary cross sections presented in chapter 4 to the case that the target nucleon is embedded in a nuclear medium. Therefore, the kinematics are revisited and the modeling of in-medium form factors is addressed. Finally, the nuclear cross sections and the implementation in the GiBUU framework are specified.

5.1 Introduction

In the previous chapter, we studied the interaction of photons and electrons with single nucleons. This is now generalized to the case that those probes scatter off an ensemble of nucleons, i.e. nuclei. Therefore, we must take nuclear effects into account: nucleons and resonances within a nuclear medium are bound by mean fields, which modify their dispersion relations (cf. sec. 3.4.2), and the finite density leads to Fermi motion among the nucleons (cf. sec. 3.8). First, the in-medium matrix elements are discussed and then the rather technical issue of in-medium-kinematics of the final state products. In the end of this chapter, we will then derive a formula for the electron- and photon-nucleus interaction cross-section.

To study the impact of mean-field potentials on the cross sections, let us first recall the structure of the hadronic potentials. They are defined in the so called *local rest-frame* (LRF) in which the baryon flux is identical to zero. For a nucleus in its ground state, this corresponds to the nucleus rest-frame, which we will from now on use as our calculation frame. As discussed in sec. 3.4.2, the four momenta of the initial- and final- state nucleons in the LRF are given by

$$p_{i,f} = \left(\sqrt{\vec{p}_{i,f}^{\,2} + m_N^2} + A_N^0(\vec{p}_{i,f}), \vec{p}_{i,f}\right) \quad , \tag{5.1}$$

where m_N denotes the bare mass of the baryon in vacuum and A^0 represents the mean-field potential, which is introduced in sec. 3.4.2 as the 0th component of a vector potential. The invariant mass of the incoming nucleon is given by

$$m^2 = p^\mu p_\mu = \left(\sqrt{\vec{p}^{\,2} + m_N^2} + A_N^0\left(\vec{p}\right)\right)^2 - \vec{p}^{\,2} = m_N^2 + 2\sqrt{\vec{p}^{\,2} + m_N^2}\, A_N^0(\vec{p}) + A_N^0(\vec{p})^2 \quad , \tag{5.2}$$

and in analogy the one of the outgoing nucleon by

$$m'^2 = m_N^2 + 2\sqrt{\vec{p}'^{\,2} + m_N^2}\, A_N^0(\vec{p}') + A_N^0(\vec{p}')^2 \quad . \tag{5.3}$$

The masses of outgoing resonances and pions are modified in the same manner. The matrix elements are calculated with the medium-modified 4-vectors and all masses are replaced by the in-medium masses. And those medium-modified 4-vectors must also be taken into account for energy and momentum conservation and the flux factor $1/|v_e - v_n|$ must be evaluated taking the real value of v_n in the medium into account.

The next two sections are devoted to the matrix elements in the medium and derivation of in-medium photon-nucleon and electron-nucleon cross sections. Thereafter, the nuclear cross sections are addressed.

5.2 Matrix elements in the medium

If one wants to evaluate the matrix elements in the medium, one must reconsider the structure of the hadronic currents in the medium.

5.2.1 Resonance excitations and quasi-elastic scattering

As detailed by Naus *et al.* [Nau90], the most general in-medium vertex for the quasi-elastic $\gamma^\star N \to N'$ process has in general 12 linearly independent Lorentz structures, which yields also 12 different form factors. These form factors may, unlike the vacuum ones, depend on all the possible independent Lorentz scalars - e.g. q^2, P^2 and $P \cdot q$ where $P = p + p'$. However, there is to my knowledge no feasible way to extract all these different form factors out of the available experimental data. Therefore, we model the in-medium nucleon-photon vertex in the same spirit as de Forest [DF83], which means that the in-medium vertex structure is assumed to be the same as the vacuum one. We only introduce for the QE contribution an additional charge-conserving term, which is motivated by eq. 4.21. Thus the in-medium vertex is given by

$$J^\mu_{\mathrm{QE}} = e^2 \left(F_1 \left\{ \gamma^\mu + \frac{\not{q}}{Q^2} q^\mu \right\} + \frac{i}{2m_N} F_2 \sigma^{\mu\nu} q_\nu \right) \quad . \tag{5.4}$$

The term $e^2 F_1 \frac{\not{q}}{Q^2} q^\mu$ is absent if the masses of in- and outgoing nucleons are equal; note that a very similar expression shows up for the resonance-production current, which was defined in eq. 4.100 according to Devenish *et al.* [Dev76].

Pollock *et al.* [Pol96] find that this extra term $F_1 \not{q}/Q^2 q^\mu$, which guarantees charge conservation at the vertex, can also be generated via a gauge transformation of the result obtained in Landau gauge to Feynman gauge. So they argue that the above term is no more than a gauge relict. Thus we checked the impact of the above extra term on our results, and found that it does not modify any of our results.

In fact there are several ways to conserve the charge at the vertex. De Forest [DF83], for example, does not include the last term of eq. 4.22, but proposes to replace the component of the hadronic current which is parallel to $\vec{q}$ by

$$J_{||} \to \frac{q_0 J_0}{|\vec{q}|} \quad . \tag{5.5}$$

Also using this scheme, charge is conserved ($q_\mu J^\mu = 0$) at the vertex. In de Forest's work [DF83] one finds an extensive discussion of different cross section models, i.e. off-shell extrapolations. He also concludes that at high electron energies and small angle $\sphericalangle(p', p)$ the ambiguities of most models tend to decrease.

Using different masses for the incoming and outgoing nucleons has the following consequences on α and β^μ presented in eq. 4.26 and 4.27

$$\begin{aligned}\alpha &= e^2\left(F_1 + \frac{1}{2m_N}F_2(m' + m)\right) \in \mathbb{R} \quad , & (5.6)\\ \beta^\mu &= e^2\left(F_1\frac{m'-m}{q^2}q^\mu - \frac{1}{2m_N}F_2\,P^\mu\right) \in \mathbb{R}^4 \quad . & (5.7)\end{aligned}$$

We fulfill for both resonance production and quasi-elastic scattering the condition $q^\mu J_\mu = 0$ which guarantees charge conservation at the vertex. Any further violation of gauge invariance due to the momentum dependent potentials has not been considered so far and should be studied in the near future.

5.2.2 Single pion production

According to section 4.5.1, the hadronic current for single-pion production in the vacuum depends on 6 complex valued functions depending on Q^2, W and θ. These functions are parametrized in elementary scattering processes. Again, we use the approximation, that the in-medium vertices are identical to the vacuum ones. However, we have to be careful since W can get modified in the medium since the momentum of a nucleon gets modified in a medium. In the medium, the full momentum of a nucleon is given by

$$k^\mu = p^\mu + A_N^\mu \quad , \tag{5.8}$$

where p is the bare (vacuum) momentum and A is the contribution due to potentials. One conventionally defines a fourth momentum

$$p_{\text{vac}} = (\sqrt{\vec{k}^2 + m_N^2}, \vec{k}) \quad , \tag{5.9}$$

which does not include the zeroth component of the potential, but still includes the 3-components of the potential. This momentum is then used to define

$$W^{\text{vac}} = \sqrt{(q + p^{\text{vac}})^\mu (q + p^{\text{vac}})_\mu}\ . \tag{5.10}$$

Since this quantity W^{vac} is frame-dependent due to the tricky definition of ${p_{\text{vac}}}^1$, we choose the CM-frame as our reference frame to evaluate it. Finally, the in-medium form-factors are assumed identical to the vacuum form-factors A_i, which are traditionally called *invariant amplitudes* [Ber67], evaluated at the vacuum point $\left(Q^2, W^{\text{vac}}, \theta\right)$:

$$A_i^{\text{medium}} = A_i(Q^2, W = W^{\text{vac}}, \theta) \quad . \tag{5.12}$$

The *medium* caption will be suppressed in the following. However, one should keep this replacement in mind.

5.3 Cross sections in the medium

5.3.1 Quasi-elastic scattering and resonance excitations

For the cross sections of processes with only one hadronic final state, e.g. resonance excitation or quasi-elastic scattering, the implementation of medium-modifications is straight-forward. The vacuum spectral function gets replaced by the in-medium one

$$\mathcal{A}_{\text{vac}} \to \mathcal{A}_{\text{medium}} \quad , \tag{5.13}$$

and the four-momentum p' of the outgoing hadronic particle is directly given by energy and momentum conservation. Thus the in-medium cross section for electron scattering is given by

$$d\sigma = \frac{1}{\sqrt{(l_\alpha p^\alpha)^2}} \frac{m_e^2 \; m \; m'}{2\pi^2} d\Omega_{l'} \; d|\vec{l}\,'| \; |\vec{l}\,'| \; \mathcal{A}(p'^2 - m'^2) \; |\mathcal{M}|^2 \tag{5.14}$$

and for photon absorption by

$$d\sigma = \frac{2mm'}{\sqrt{(q_\alpha p^\alpha)^2}} 2\pi \mathcal{A}(p'^2 - m'^2) \; |\mathcal{M}|^2 \quad . \tag{5.15}$$

---

[1] If p^{vac} was a proper 4-vector then W^{vac} would be frame independent. However, p^{vac} is no proper Lorentz 4-vector. This we want to show in the following.

For each Lorentz-4-vector a, its square $a^\mu a_\mu$ is a constant under Lorentz-boosts. However, the opposite statement that each vector b for which $b^\mu b_\mu$ is a Lorentz scalar must also be Lorentz-vector is *not* true. The vector b is only then a Lorentz-4-vector if it transforms under boosts like a 4-vector would do. Thus is the fact that we get by definition (eq. 5.9) $p_{\text{vac}}^2 = m_N^2$ *no* proof for p_{vac} being a Lorentz-4-vector! Let us rather investigate its transformation properties.

In the LRF we get $p^{\text{vac}} = k - A^N$ since $A^N = (A_0^N, \vec{0})$ in the LRF frame. If p^{vac} was a proper 4-momentum, then it should be in any frame given by

$$p^{\text{vac}} = k - A^N = (k_0 - A_0^N, \vec{k} - \vec{A}^N) \quad . \tag{5.11}$$

Let us now consider another frame where we have the boosted momenta k' and $A^{N\,\prime}$. According to its definition in eq. 5.9 we would get for p^{vac} in this frame

$$p^{\text{vac}\,\prime} = (\sqrt{(\vec{k}\,')^2 + m_N^2}, \vec{k}\,') \quad ,$$

which contradicts, however, eq. 5.11

$$p^{\text{vac}\,\prime} = (k_0' - A_0^{N\,\prime}, \vec{k}\,' - \vec{A}^{N\,\prime})$$

since $\vec{A}^{N\,\prime} \neq 0$ in the general case. Hence p^{vac} has no proper transformation properties, although $(p^{\text{vac}})^2$ is a Lorentz scalar. As a consequence, W^{vac} is frame dependent.

5.3.2 Single-pion production

Electron-induced processes

To describe electron-induced single-pion production in the medium, the results of eq. 4.87 must be generalized. The following notation for the momenta is used: l and l' denote initial and final lepton momenta, p and p' the ones for the nucleons, k is the pion momentum. Including a pion potential A^0_π, and considering momentum-dependent nucleon masses m according to eq. 5.2 and Fermi motion we get

$$\begin{aligned}
&\delta\left(l^0 + p^0 - \left(l'^0 + k^0 + p'^0\right)\right) \\
&= \delta\left(|\vec{k}| - x_0\right) \left(\left| \frac{d\left(\sqrt{|\vec{k}|^2 + m_\pi^2} + A^0_\pi(\vec{k}) + \sqrt{(\vec{p} + \vec{q} - \vec{k})^2 + m'^2}\right)}{d|\vec{k}|} \right|_{|\vec{k}|=x_0} \right)^{-1} \\
&= \delta\left(|\vec{k}| - x_0\right) \left(\left| \frac{|\vec{k}|}{\sqrt{|\vec{k}|^2 + m_\pi^2}} + \frac{dA^0_\pi(\vec{k})}{d|\vec{k}|} + \frac{|\vec{k}| - (\vec{q} + \vec{p})\vec{k}/|\vec{k}| + \frac{dm'^2}{d|\vec{k}|}}{p'^0} \right|_{|\vec{k}|=x_0} \right)^{-1} \qquad (5.16)
\end{aligned}$$

The derivative of the squared nucleon-mass with respect to the absolute pion momentum is given by

$$\begin{aligned}
\frac{dm'^2}{d|\vec{k}|} &= \frac{d\left(m_N^2 + 2\sqrt{\vec{p'}^2 + m_N^2}\; A^0_N(\vec{p'}) + A^0_N(\vec{p'})^2\right)}{d|\vec{k}|} \\
&= \frac{d\left(2\sqrt{\vec{p'}^2 + m_N^2}\; A^0_N(\vec{p'}) + A^0_N(\vec{p'})^2\right)}{d|\vec{k}|} \\
&= \left(2\frac{|\vec{p'}|\frac{d|\vec{p'}|}{d|\vec{k}|}}{\sqrt{\vec{p'}^2 + m_N^2}}\; A^0_N(\vec{p'}) + 2\sqrt{\vec{p'}^2 + m_N^2}\frac{dA^0_N(\vec{p'})}{d|\vec{p'}|}\frac{d|\vec{p'}|}{d|\vec{k}|} + 2A^0_N(\vec{p'})\frac{dA^0_N(\vec{p'})}{d|\vec{p'}|}\frac{d|\vec{p'}|}{d|\vec{k}|}\right) \\
&= 2\frac{|\vec{k}| - (\vec{q} + \vec{p'})\vec{k}/|\vec{k}|}{|\vec{p'}|} \\
&\quad \times \left(\frac{|\vec{p'}|}{\sqrt{\vec{p'}^2 + m_N^2}}\; A^0_N(\vec{p'}) + \sqrt{\vec{p'}^2 + m_N^2}\frac{dA^0_N(\vec{p'})}{d|\vec{p'}|} + A^0_N(\vec{p'})\frac{dA^0_N(\vec{p'})}{d|\vec{p'}|}\right) \quad . \qquad (5.17)
\end{aligned}$$

In the LRF, the mean field potential is only dependent on $|\vec{p}|$ and not on the direction of $\vec{p}$. Thus we get working in this frame $A^0_N(\vec{p'}) = A^0_N(|\vec{p'}|)$. The value x_0 in eq. 5.16 is the solution for $|\vec{k}|$ to the energy conservation condition

$$\begin{aligned}
q^0 + p_0 &= k^0 + p'^0 \\
&= \sqrt{|\vec{k}|^2 + m_\pi^2} + A^0_\pi(\vec{k}) + \sqrt{|\vec{p'}|^2 + \left[m'(\vec{p'})\right]^2} \\
&= \sqrt{|\vec{k}|^2 + m_\pi^2} + A^0_\pi(\vec{k}) + \sqrt{|\vec{p} + \vec{q} - \vec{k}|^2 + \left[m'(\vec{k})\right]^2} \quad , \qquad (5.18)
\end{aligned}$$

which is solved numerically using a Newton method. Finally, we get

$$
\begin{aligned}
\delta\left(l^0+p^0-\left(l'^0+k^0+p'^0\right)\right)=\delta\left(|\vec{k}|-x_0\right)\Bigg(&\left.\frac{|\vec{k}|}{\sqrt{|\vec{k}|^2+m_\pi^2}}+\frac{dA_\pi^0(\vec{k})}{d|\vec{k}|}\right.\\
&\left.+\frac{\left(|\vec{k}|-(\vec{q}+\vec{p})\vec{k}/|\vec{k}|\right)\left(1+\frac{2}{|\vec{p}\,'|}\left(\frac{|\vec{p}\,'|}{\sqrt{\vec{p}\,'^2+m_N^2}}A_N^0(|\vec{p}\,'|)+\sqrt{\vec{p}\,'^2+m_N^2}\,\frac{dA_N^0(|\vec{p}\,'|)}{d|\vec{p}\,'|}+A_N^0(|\vec{p}\,'|)\frac{dA_N^0(|\vec{p}\,'|)}{d|\vec{p}\,'|}\right)\right)}{p'^0}\right|_{|\vec{k}|=x_0}\Bigg)^{-1},
\end{aligned}
\tag{5.19}
$$

and the cross section for single-pion production in the medium is given by[2]

$$
\begin{aligned}
\frac{d\sigma^\pi}{dl'^0\,d\Omega_{l'}\,d\Omega_k}=\frac{1}{|v_e-v_n|}\frac{m_e^2\ m'\ m}{2\ (2\pi)^5}\frac{|\vec{k}|^2\ l'^0}{k^0\ p'^0\ l^0\ p^0}L_{\mu\nu}H_\pi^{\mu\nu}\Bigg(&\left.\frac{|\vec{k}|}{\sqrt{|\vec{k}|^2+m_\pi^2}}+\frac{dA_\pi^0(\vec{k})}{d|\vec{k}|}\right.\\
&\left.+\frac{\left(|\vec{k}|-(\vec{q}+\vec{p}_j)\vec{k}/|\vec{k}|\right)\left(1+\frac{2}{|\vec{p}\,'|}\left(\frac{|\vec{p}\,'|}{\sqrt{\vec{p}\,'^2+m_N^2}}A_N^0(|\vec{p}\,'|)+\sqrt{\vec{p}\,'^2+m_N^2}\,\frac{dA_N^0(|\vec{p}\,'|)}{d|\vec{p}\,'|}+A_N^0(|\vec{p}\,'|)\frac{dA_N^0(|\vec{p}\,'|)}{d|\vec{p}\,'|}\right)\right)}{p'^0}\right|_{|\vec{k}|=x_0}\Bigg)^{-1}.
\end{aligned}
\tag{5.20}
$$

Note that all the final state momenta and masses $|\vec{k}|$, p', m, m' depend on the momentum of the target nucleon. The structure of the hadron tensor $H_\pi^{\mu\nu}$ has been evaluated in sec. 4.5.2, the lepton tensor $L_{\mu\nu}$ is defined in eq. 4.5.

Photon-induced events

For photon-induced pion production we obtain in an analogous fashion as for the electron-induced process

$$
\begin{aligned}
\frac{d\sigma_{\gamma N\to N\pi}}{d\Omega_k}=\frac{m\ m'|\vec{k}|^2}{4p'_0\ k_0\ \sqrt{(q_\alpha p^\alpha)^2}}\frac{|\mathcal{M}|^2}{(2\pi)^2}\times\Bigg(&\left.\frac{|\vec{k}|}{\sqrt{|\vec{k}|^2+m_\pi^2}}+\frac{dA_\pi^0(\vec{k})}{d|\vec{k}|}\right.\\
&\left.+\frac{\left(|\vec{k}|-(\vec{q}+\vec{p})\vec{k}/|\vec{k}|\right)\left(1+\frac{2}{|\vec{p}\,'|}\left(\frac{|\vec{p}\,'|}{\sqrt{\vec{p}\,'^2+m_N^2}}A_N^0(|\vec{p}\,'|)+\sqrt{\vec{p}\,'^2+m_N^2}\,\frac{dA_N^0(|\vec{p}\,'|)}{d|\vec{p}\,'|}+A_N^0(|\vec{p}\,'|)\frac{dA_N^0(|\vec{p}\,'|)}{d|\vec{p}\,'|}\right)\right)}{p'^0}\right|_{|\vec{k}|=x_0}\Bigg)^{-1}
\end{aligned}
\tag{5.21}
$$

with

$$
|\mathcal{M}|^2=-\frac{1}{2}H_\pi^{\mu\nu}g_{\mu\nu}\quad . \tag{5.22}
$$

5.3.3 Single-pion production as background process

Let us now consider the case that the resonances are also included and contribute to single-pion production. Then the direct single pion production channel is treated as a background channel (cf. discussion in sec. 4.7). So we consider the single pion cross section as a parametrization of the vacuum data and the background is the difference of data and resonance contributions. Thus

---

[2] For numerical implementation of this cross section see electronPionProduction_medium.f90

we first construct the total single pion cross section using the MAID input and the contribution of the resonances to single-pion production using vacuum kinematics (no modifications besides Fermi motion, in particular no potentials, no Pauli blocking). Then we evaluate the difference of both cross sections using vacuum kinematics– this yields for electron induced events the background cross section $d\sigma_\pi^{\text{bg}}/d\Omega_\pi/dl_f$ and for photon induced events $d\sigma_\pi^{\text{bg}}/d\Omega_\pi$.

This background cross section is now assumed not to be influenced by the potentials, which means that in-medium background cross section is for electron scattering given by

$$\frac{d\sigma_\pi^{\text{bg, medium}}}{d\Omega_\pi dl_f}(p,q) = \frac{d\sigma_\pi^{\text{bg, vacuum}}}{d\Omega_\pi dl_f}(p_{\text{vac}},q) \tag{5.23}$$

and for photon-induced reactions by

$$\frac{d\sigma_\pi^{\text{bg, medium}}}{d\Omega_\pi}(p,q) = \frac{d\sigma_\pi^{\text{bg, vacuum}}}{d\Omega_\pi}(p_{\text{vac}},q) \quad , \tag{5.24}$$

where $p_{\text{vac}} = \left(\sqrt{m_N^2 + \vec{p}^2}, \vec{p}\right)$.

5.3.4 Double-pion production backgrounds

For the photon-induced reactions we introduced in sec. 4.7 a $\pi\pi$-production background. Unlike for the single-pion production, we do not use an underlying microscopic model for the total cross sections. The total cross section is parametrized in the nucleon rest-frame as a function of Mandelstam s. However, in the medium the nucleon is in motion so we must consider the boost of the cross section. Analogous to the single-pion background we neglect the impact of potentials on the background, such that

$$\sigma_{\pi\pi}^{\text{bg, medium}}(s) = \underbrace{\frac{\sqrt{p_{\text{vac}}^2}\;\left|\vec{q}^{\,\text{NRF}}\right|}{\left|\vec{p}_{\text{vac}}\, q^0 - p_{\text{vac}}^0 \vec{q}\right|}}_{\text{boost factor}} \sigma_{\pi\pi}^{\text{bg, vacuum}}(s_{\text{vac}}) \tag{5.25}$$

$$= \frac{m_N\;\left|\vec{q}^{\,\text{NRF}}\right|}{\left|\vec{p}_{\text{vac}}\, q^0 - p_{\text{vac}}^0 \vec{q}\right|} \sigma_{\pi\pi}^{\text{bg, vacuum}}(s_{\text{vac}}) \quad , \tag{5.26}$$

where $s_{\text{vac}} = (p_{\text{vac}} + q)^2$ with $p_{\text{vac}} = \left(\sqrt{m_N^2 + \vec{p}^2}, \vec{p}\right)$ and $\vec{q}^{\,\text{NRF}}$ is the photon momentum in the nucleon rest-frame (cf. appendix G.1 for details on the boost of the cross section).

5.4 Nuclear cross sections

Having established the eN and γN cross sections in the medium, let us now consider the nuclear cross sections. Assuming a small wavelength of the incoming photon, we will treat the whole problem in impulse approximation (IA). Hence the nuclear current operator is assumed to be a sum of one-body currents $J_A \to \sum_i J_i^\mu$. Furthermore, we assume that the nucleus is constructed out of a sum of single particle plane-wave states, for which the dispersion relations are modified due to the potentials. In Bjorken Drell notation, each plane wave state $|k,s\rangle$ (s denotes spin) has the normalization $1/\sqrt{2m(k)/(2E_k)}$. So the nuclear wave function is given by

$$\Psi(r) = \sum_{s=\pm\frac{1}{2}} \left(\int^{k_F(\text{protons})} \frac{d^3k}{(2\pi)^3} \sqrt{\frac{2m(k)}{2E_k}}\,|k,s\rangle + \int^{k_F(\text{neutrons})} \frac{d^3k}{(2\pi)^3} \sqrt{\frac{2m(k)}{2E_k}}\,|k,s\rangle \right) \quad ,(5.27)$$

which is normalized to the number of nucleons A

$$\int d^3r \Psi^\dagger(r)\Psi(r) = A\,. \tag{5.28}$$

Electron scattering. Within the above approximations, the matrix element for electron scattering off a nucleus with mass number A is given by a contraction of the lepton tensor with the sum of all hadronic currents generated by the A nucleons within the nucleus . In formulas, we get (cf. also [DF83, i.e. eq. 1-3])

$$|\mathcal{M}_A|^2 = L_{\mu\nu} \int d^3r H_A^{\mu\nu}(r) \quad , \tag{5.29}$$

where

$$\begin{aligned} H_A^{\mu\nu}(r) &= \frac{1}{2}\sum_{s,s',\ldots}\sum_{\alpha=p,n}\int^{p_f^\alpha(r)} \frac{d^3p}{(2\pi)^3}\sqrt{\frac{2m(p)}{2E_p}}\sqrt{\frac{2m(p')}{2E_{p'}}}\ldots \langle p',s';\ldots|\, J^\mu\, |p,s\rangle \\ &\quad \times\sqrt{\frac{2m(p)}{2E_p}}\sqrt{\frac{2m(p')}{2E_{p'}}}\ldots \left(\langle p',s';\ldots|\, J^\nu\, |p,s\rangle\right)^\star \\ &= \sum_{\alpha=p,n}\int^{p_f^\alpha(r)} \frac{d^3p}{(2\pi)^3}\frac{2m(p)}{2E_p}\frac{2m(p')}{2E_{p'}}\ldots \\ &\quad \underbrace{\times\frac{1}{2}\sum_{s,s',\ldots}\langle p',s';\ldots|\, J^\mu\, |p,s\rangle \left(\langle p',s';\ldots|\, J^\nu\, |p,s\rangle\right)^\star}_{H^{\mu\nu}} \quad . \end{aligned} \tag{5.30}$$

Note that the dots "…" should just remind us that there could be more than one final state particle. Obviously, the previous equation is just an integral over single particle hadronic currents $H^{\mu\nu}$, which were already evaluated in the last chapter. Thus the nuclear cross section is given by

$$\begin{aligned} d\sigma_A &= \sum_{\alpha=p,n}\frac{1}{v_\text{rel}}\frac{2m_e}{2l_0}\frac{2m_e}{2l_0'}L_{\mu\nu}\int d^3r\int^{p_f^\alpha(r)}\frac{d^3p}{(2\pi)^3}\int d\Phi_f\frac{2m(p)}{2E_p}\frac{2m(p')}{2E_{p'}}\times\ldots \\ &\quad \times H^{\mu\nu}(r,p,\Phi_f)\times(2\pi)^4\,\delta^4(p+l-l'-p'-\ldots)\times P_{PB}(\vec{r},\Phi_f) \end{aligned} \tag{5.31}$$

where $v_\text{rel} \simeq 1$ is the relative velocity of nucleus and electron. The variable Φ_f denotes the phase space of all the final state particles, which includes also p' and l'. The function $P_{PB}(\vec{r},\Phi_f)$ includes Pauli blocking of the final state fermions. Comparing to the single particle cross sections σ_N, one realizes that

$$d\sigma_A = \sum_{\alpha=p,n}\int d^3r\int^{p_f^\alpha(r)}\frac{d^3p}{(2\pi)^3}\frac{|v_N-v_E|}{v_\text{rel}}d\sigma_N \tag{5.32}$$

$$= \sum_{\alpha=p,n}\int d^3r\int^{p_f^\alpha(r)}\frac{d^3p}{(2\pi)^3}\frac{1}{v_\text{rel}}\frac{l_\mu p^\mu}{l_0p_0}d\sigma_N \quad . \tag{5.33}$$

The variable v_N denotes the single particle velocity due to the Fermi motion and v_e is the electron velocity. Note, that the Pauli blocking factor has been included in the single particle cross section.

Photon scattering. For photon induced reactions we get an analogous result

$$\begin{aligned} d\sigma_A &= \sum_{\alpha=p,n} \frac{1}{v_{\mathrm{rel}}} \frac{1}{2q_0} g_{\mu\nu} \int d^3r \int^{p_f^\alpha(r)} \frac{2m(p)}{2E_p} \frac{2m(p')}{2E_{p'}} \times \dots \\ &\times H^{\mu\nu}(r,p,\Phi_f) \frac{d^3p}{(2\pi)^3}\, P_{PB}(\vec{r},\Phi_f) d\Phi_f \quad , \end{aligned} \tag{5.34}$$

where $v_{\mathrm{rel}} \simeq 1$ is the relative velocity of nucleus and photon. Finally, we obtain

$$\begin{aligned} d\sigma_A &= \sum_{\alpha=p,n} \int d^3r \int^{p_f^\alpha(r)} \frac{d^3p}{(2\pi)^3} \frac{|v_N - v_\gamma|}{v_{\mathrm{rel}}} d\sigma_N \\ &= \sum_{\alpha=p,n} \int d^3r \int^{p_f^\alpha(r)} \frac{d^3p}{(2\pi)^3} \frac{1}{v_{\mathrm{rel}}} \frac{q_\mu p^\mu}{q_0 p_0} d\sigma_N \end{aligned} \tag{5.35}$$

with v_γ being the photon velocity. Again, we included the Pauli blocking probability in the single particle cross section.

5.5 Implementation in the BUU simulation

Eventually, we want to evaluate eq. 5.33 and eq. 5.35 within the GiBUU framework. There the electron-nucleus scattering process is assumed to be a two-step process. First, the electron scatters off a single nucleon and generates new particles, respectively excites a resonance – this is the so-called *initial state*. In the so-called *final state* process the produced particles are propagated out of the nucleus. This may, owing to rescattering effects, lead to a change in the final state particle multiplicities.

For the numerical implementation, the integrals of eq. 5.33 and eq. 5.35 are being solved using a Monte-Carlo sampling method. Therefore, let us rewrite these integrals in the test-particle representation of the nuclear ground state

$$\int d^3r \int^{p_f^\alpha(r)} \frac{d^3p}{(2\pi)^3} \dots = \int d^3r \frac{d^3p}{(2\pi)^3} \Theta(p_f - p) \dots \tag{5.36}$$

$$= \int d^3r \frac{d^3p}{(2\pi)^3} f(\vec{r},\vec{p},t=t_0) \dots \tag{5.37}$$

$$= \int d^3r \frac{d^4p}{(2\pi)^4} g^<(\vec{r},p,t=t_0) \dots \tag{5.38}$$

$$= \int d^3r d^4p \frac{1}{N} \sum_{i=1}^{N\times A} \delta^4(p-p_i)\delta^3(r-r_i) \dots \quad . \tag{5.39}$$

Note that $g^<$ includes only nucleons. Evaluating the δ-functions, we get for each nucleon test-particle a distinct contribution to the integrals. For instance for electron-scattering we get

$$d\sigma_A = \frac{1}{N} \sum_{i=1}^{N\times A} \frac{1}{v_{\mathrm{rel}}} \frac{l_\mu(p_i)^\mu}{l_0(p_i)_0} d\sigma_N(\vec{r}_i,p_i) \quad , \tag{5.40}$$

where $d\sigma_N(\vec{r}_i,p_i)$ is the cross section to scatter off the ith test-particle. Now $d\sigma_N(\vec{r}_i,p_i)$ is given by a sum of all contributing channels

$$d\sigma_N(\vec{r}_i,p_i) = \sum_{f\in\{N,\pi N,\pi\pi N,\Delta,P_{11}(1440),\dots\}} d\sigma_{N\to f}(\vec{r}_i,p_i) \quad . \tag{5.41}$$

For each of the channels above the final-state phase-space integral is now performed using just one random phase space point ϕ_f, which is a good approximation in the limit of large number of subsequent choices. Thereafter, one chooses by a Monte-Carlo decision which final-state channel to populate and propagate in the transport step. The kinematics of the propagated channel is given by the random point ϕ_f. If all partial cross sections are positive, then the probability $P(f)$ to choose a special channel f is simply given by the usual importance sampling algorithm

$$P(f) = \frac{d\sigma_{N\to f}}{d\sigma_N} \quad ; \tag{5.42}$$

and the chosen channel is attributed the Monte Carlo weight $w = d\sigma_N$.

As we pointed out in sec. 4.7, the background cross section for single pion production may become negative due to the fact that it implicitly includes all kind of interferences among the resonances and among resonance and background amplitudes. So the problem appears how to treat negative cross sections during the importance sampling procedure. We resolved this issue choosing the event according to a modified importance sampling algorithm in which

$$P(f) = \frac{|d\sigma_{N\to f}|}{\sum_{f\in\{N,\pi N,\pi\pi N,\Delta,P_{11}(1440),\ldots\}} |d\sigma_{N\to f}|} \quad . \tag{5.43}$$

and attribute to the event a Monte-Carlo weight which includes the sign of the partial cross section

$$w_i = \underbrace{\frac{d\sigma_{N\to f}}{|d\sigma_{N\to f}|}}_{=\mathrm{sign}(d\sigma_{N\to f})} \sum_{f\in\{N,\pi N,\pi\pi N,\Delta,P_{11}(1440),\ldots\}} |d\sigma_{N\to f}| \quad . \tag{5.44}$$

Within this scheme, the total cross section approaches its expectation value if large enough number of subsequent Monte-Carlo decisions are performed. To show this let us assume that we make n subsequent decisions where we populate n_i times the ith channel. Then we get in the limit $n \to \infty$ as a mean value for the total cross section

$$\begin{aligned} \langle d\sigma_N \rangle &= \lim_{n\to\infty} \frac{1}{n} \sum_i n_i w_i = \lim_{n\to\infty} \sum_i \frac{n_i}{n} w_i && (5.45)\\ &= \sum_i P(i) w_i = \sum_i d\sigma_{N\to i} = d\sigma_N \quad . && (5.46) \end{aligned}$$

Additionally, also each partial channel approaches its expectation value

$$\begin{aligned} \langle d\sigma_{N\to i} \rangle &= \lim_{n\to\infty} \frac{1}{n} n_i w_i && (5.47)\\ &= \sum_i P(i) w_i = d\sigma_{N\to i} \quad . && (5.48) \end{aligned}$$

The number of subsequent decisions is determined by the product of the number of ensembles times the number of subsequent simulation runs. To get a statistical meaningful result this product must be sufficiently large. In order to control the statistical fluctuations we estimate our statistical uncertainty by the standard deviation of the mean value of subsequent runs.

Since the final electron is assumed not to interact after the collision, we can neglect it in the final state step. Thus we only need to transport the hadronic test-particles. After the transport step, particle multiplicities and exclusive cross sections (e.g. pion production) can be evaluated.

5.5.1 Parallel ensembles, full ensembles and the perturbative mode

In the simulation, the whole problem is treated on an event-by-event basis: different events are assumed not to interfere during the propagation step. In sec. 2.5.2, the technique of full and parallel ensembles was introduced. In a *full ensemble run with real final state particles* one generates one event choosing a random test-particle i and $d\sigma_A$ is then approximated by

$$d\sigma_A \simeq A \times \frac{1}{v_{\text{rel}}} \frac{l_\mu(p_i)^\mu}{l_0(p_i)_0} d\sigma_N(\vec{r}_i, p_i) \quad . \tag{5.49}$$

This event is then propagated and several subsequent runs are needed to gain sufficient statistics.

For a *parallel ensemble run with real final state particles* the ensembles do not interfere and one can propagate one event per ensemble. So one initializes also one event per ensemble and we get

$$d\sigma_A \simeq \sum_{j=1}^{N} \frac{A}{N} \times \frac{1}{v_{\text{rel}}} \frac{l_\mu(p_{i(j)})^\mu}{l_0(p_{i(j)})_0} d\sigma_N(\vec{r}_{i(j)}, p_{i(j)}) \quad , \tag{5.50}$$

where $i(j)$ is a random test-particle in the jth ensemble. For a *parallel ensemble run with perturbative final state particles*[3], even the final state particles of one ensemble do not interfere. Thus for each test-particle an event can be generated and all events can be propagated in parallel. In this scheme one gets

$$d\sigma_A = \sum_{i=1}^{N \times A} \frac{1}{N} \times \frac{1}{v_{\text{rel}}} \frac{l_\mu(p_i)^\mu}{l_0(p_i)_0} d\sigma_N(\vec{r}_i, p_i) \quad . \tag{5.51}$$

After the propagation, each event must be analyzed independently. Each event is categorized by its multiplicities and the exclusive cross sections are generated - in principle, like the experimentalist would do. Several subsequent initialization and propagation steps have to performed to generate enough events for a statistical stable result. It is clear that one needs to perform more subsequent runs when using the full ensemble technique, since one generates only one event per run. Let us denote the number of runs necessary for a full-ensemble run by $\mathcal{R}$. To collect the same statistics within a parallel ensemble run, one only needs to perform $\mathcal{R}/N$ runs. Introducing additionally the concept of perturbative final-state particles, one gains an additional factor of A in the number of events per run – thus only $\mathcal{R}/(N \times A)$ runs have to performed. Almost all the precursor calculations [Eff99a, Leh03] have been performed within the computational fast "parallel & perturbative" approximation and it has proven to be a proper approximation.

---

[3] cf. appendix B.1 for an explanation of the perturbative method

Part II

Results: Scattering pions, photons and electrons off complex nuclei

Chapter 6

Pion induced reactions

Overview: Results on pion scattering off nuclei are presented. After discussing the pion mean free path within our model and comparing simulations for pion absorption to the data, we primarily address the double-charge exchange process, which serves as a strict model benchmark. In the course of this chapter we investigate numerical approximations to the collision term and evaluate their impact on the observables. Thereby it is shown that the full ensemble method is superior to the parallel ensemble method. We achieve good agreement with the available data in the regime of 30 − 200 MeV kinetic energy.

6.1 Introduction

The interaction of pions and nucleons is a crucial cornerstone of every hadronic transport approach. Both particle species are most abundant and, therefore, very important within the coupled channel calculations. To benchmark our pion-nucleon interaction model, we discuss in this chapter pion induced reactions. This will set the stage for the subsequent chapters, where we discuss single pion production in electron and photon induced processes as well as double-pion production in photon induced processes.

We especially aim for a description of low-energetic pions with kinetic energies down to 30 MeV. Hence we first need to establish whether it is meaningful to discuss pions with a long wave length in a semi-classical BUU picture. Especially for the analysis of the $\pi\pi$ production experiment performed by the TAPS collaboration [Mes02, Sch05, Sch06b, Sch06a], low-energy pions are crucial. For this experiment, it has already been shown using GiBUU [Mü04a, Bus05, Bus06c] that pion rescattering in the final state description of photon induced double-pion production produce a considerable modification of the $\pi\pi$ invariant mass distributions as observed by the TAPS collaboration. Moreover, neutrino-induced pion production, a source of background for neutrino oscillation experiments [Dra04], is very sensitive to pion final state interactions [Lei06a, Lei06b]. The BUU picture for low-energy pions is tested by comparison to quantum calculations and experimental data on πA scattering.

Already in earlier works of Salcedo et al. [Sal88], with a simulation of pion propagation in nuclear matter, and of Engel et al. [Eng94], with a precursor of our present simulation, pions with kinetic energies in the regime of 85 − 300 MeV have been investigated in transport models. As motivated above, we now investigate even less energetic pions. Therefore, we carefully account for Coulomb corrections in the initial channel of π-induced processes and improve the description of the threshold behavior of the cross sections in the model (cf. appendix A.3.1 for details on the implemented cross sections). Additionally, a momentum dependent hadronic pion potential has been implemented [Bus04]. This potential sketched in fig. 6.1 is based upon a low-energy result by Oset *et al.* [Nie93a] and a first order Δ-hole model calculation [Bus04]. Both models are

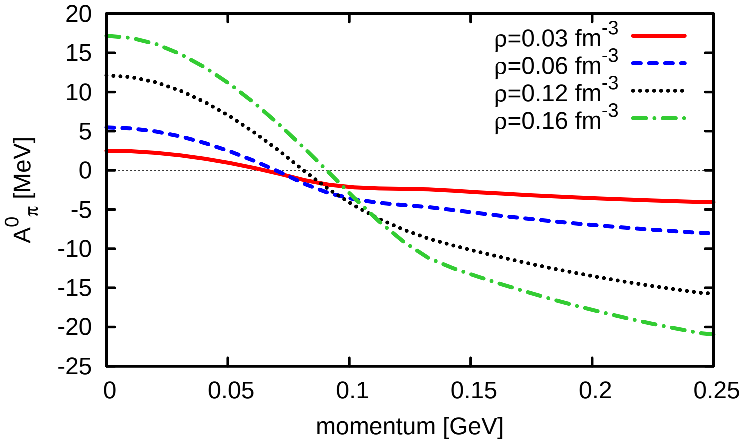

Figure 6.1: Hadronic potential A^0_π of the pion [Bus04] as a function of pion momentum for symmetric nuclear matter density at different densities.

matched using a cubic interpolation in the regime $p_\pi = 80 - 140$ MeV (for details confer [Bus04, sec. 5.3]). The potential shows a repulsive nature at low momenta which is due to S-wave interactions of pions and nucleons, whereas the P-wave Δ-hole excitations lead to an attractive contribution which dominates at higher momentum.

This chapter is structured in the following way. First we consider the pion mean free path in nuclear matter and discuss the consequences of medium modifications of the pion. Hereafter we compare our simulations to experimental results on pion scattering off complex nuclei to validate our model. Finally, we address - as a very stringent benchmark - double-charge exchange (DCX) of pions in πA collisions [1].

If not explicitly stated otherwise, all results have been obtained using the *mass-shift+Oset model* option for the baryon-baryon cross sections (cf. sec. 3.6.1 for details).

6.2 Pion properties in the medium

The simplest properties of the pion to investigate are its total width

$$\Gamma_{\text{tot}} = \ln\left(-\frac{d(\ln(N_\pi))}{dt}\right) ,$$

its velocity v and its mean free path $\lambda = v/\Gamma_{\text{tot}}$. In our model the loss of pions per time-step Δt is given by

$$\frac{1}{N_\pi}\frac{\Delta N_\pi(E,\rho_n,\rho_p)}{\Delta t} = -\sum_{N=n,p}\int d^3p_N e^{-\sigma_N(p_\pi,p_N)\rho_N\, v(p_\pi,\rho_p,\rho_n)\Delta t}$$
$$-\sum_{(N,M)\in\{(n,p),(n,n),(p,p)\}}\int d^3p_N\int d^3p_M e^{-\Gamma^{\text{BG}}(p_\pi,p_N,p_M,\rho_N,\rho_M)\Delta t} = -e^{-\Gamma_{tot}\Delta t} \quad , \qquad (6.1)$$

where v denotes the pion velocity in the medium, σ_N the πN scattering cross section and Γ^{BG} is the absorptive three-body width of the pion and Γ_{tot} the total width. For the cross sections

---

[1] Results presented in this chapter have also been published in [Bus06a, Bus06b, Bus06c, Bus07a].

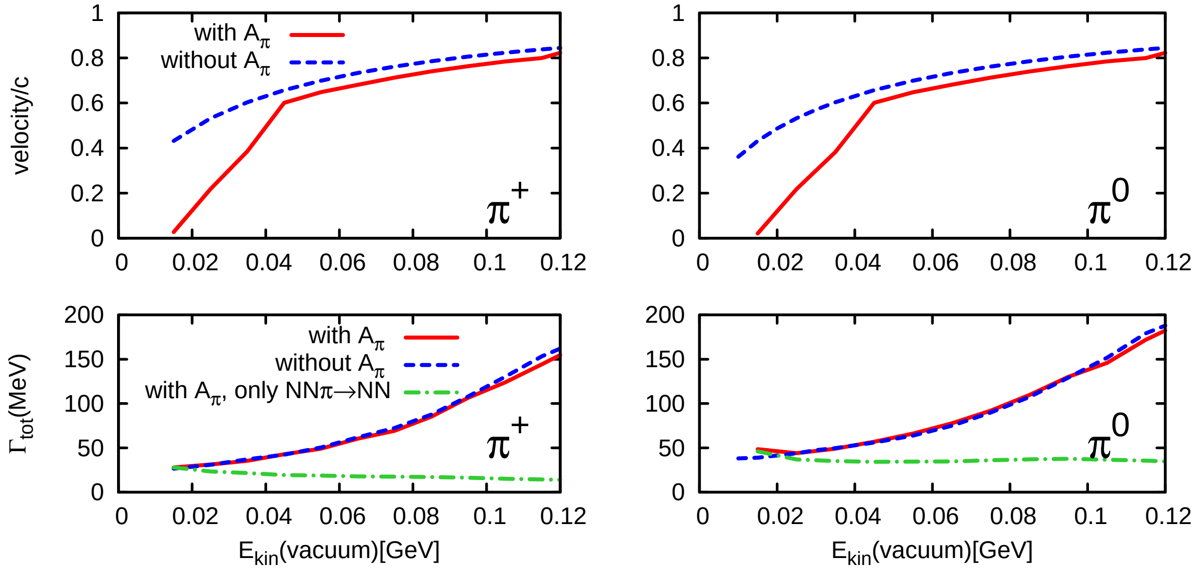

Figure 6.2: BUU results without electromagnetic forces inside symmetric nuclear matter at $\rho_0 = 0.168\ \mathrm{fm}^{-3}$. The results are shown without (dashed line) and with (solid line) hadronic pion potential. The upper panels show the velocity of the pions in nuclear matter, the lower ones visualize the full width of the pion. The lower curves in the lower panel denoted "only $NN\pi \rightarrow NN$" shows the strength of the direct *non-resonant* $NN\pi \rightarrow NN$ three-body absorption rate (cf. sec. 3.3.2 on page 36 for details), i.e. this rate does not include the resonant $\pi NN \rightarrow NR \rightarrow NN$ pion absorption mechanism.

and the width we include the medium modifications discussed earlier. The integrals above are performed over the Fermi spheres of neutrons and protons.

In practice, we obtain Γ_{tot} by performing a Monte-Carlo simulation with pions and nucleons initialized in a box with continuous boundary conditions within our BUU framework, including all the medium modifications and necessary collision rates.

The momentum p_π is calculated in the medium from the dispersion relation

$$E_{\mathrm{total}} \quad = \quad \sqrt{p_\pi^2 + m_\pi^2} + A_0^\pi(p) + V_C \tag{6.2}$$

with the hadronic potential A_0^π and the Coulomb potential V_C. Finally, Γ_{tot} and λ can be easily extracted by observing the time evolution of the pions. All results are shown as functions of the experimental observable

$$E_{\mathrm{kin}}^{\mathrm{Vacuum}} = E_{\mathrm{total}} - m_\pi \tag{6.3}$$

in the classically allowed region $E_{\mathrm{kin}}^{\mathrm{Vacuum}} \geq A_0^\pi(p) + V_C$.

Isospin dependence. To begin with, we study the case in which we omit all potentials. In the GiBUU-simulation we use the same mass of $m_\pi = 138$ MeV for all pions regardless of their charge. For both positive and negative pions the same data are used as input for the vacuum cross sections. Due to isospin symmetry the positive and negative charge states have the same properties in symmetric matter if electromagnetic forces are neglected. In fig. 6.2 we observe that the positive and neutral pions do actually have the same velocities, but not the same width in nuclear matter. The difference is quite small except for very low energies. The reason for this can be found in the elementary absorption and scattering processes. As mentioned before, we have used vacuum data to pin down the elementary reaction rates. Therefore the absorptive width of the charged pions is fixed by the elementary reactions

$$\begin{aligned} p\,p &\rightarrow p\,n\,\pi^+ \quad , && (6.4)\\ p\,n &\rightarrow p\,p\,\pi^- \quad , && (6.5)\end{aligned}$$

while the absorptive width of the π^0 is determined by

$$\begin{aligned} p\,p &\rightarrow p\,p\,\pi^0 \quad , && (6.6)\\ p\,n &\rightarrow p\,n\,\pi^0 && (6.7)\end{aligned}$$

through detailed balance. Fig. 3.1 of chapter 3 shows that the *non-resonant* three-body absorption rate for the neutral pions at low energies is higher than for the charged ones (cf. sec. 3.3.2 on page 36 for details on this rate). This explains the larger width of the π^0 near threshold. The kinks in the velocity at roughly 45 MeV come from the hadronic pion potential, which has been determined using two different models for low and high momentum matched in the momentum region of $p_\pi = 80 - 140$ MeV [Bus04, sec. 5.3.3]. This matching guarantees a continuous derivative of the pion potential, but not a continuous second derivative which explains the velocity kink.

Collisional width in the medium. Using the neutral pion as an example, we first discuss the lower right panel of fig. 6.2. At low energies there is practically no difference in the width between the simulation with (dashed lines) and without (solid lines) pion potential. Due to the absence of resonance contributions in this energy regime, the width of the pion is dominated by its absorption via the $NN\pi \rightarrow NN$ background. At higher energies a small difference in the two curves can be observed. Here the decay width is somewhat smaller if the pion potential is included.

This difference can be understood by investigating the resonance production process $N\pi \rightarrow \Delta$ in detail [Bus04]. At fixed pion energy, the attractive pion potential leads to a higher momentum of the pion and, therefore, also to a higher momentum of the produced Δ, resulting in a decrease of its mass. In the considered energy regime this mass is smaller than the pole mass. As a consequence, the production of the Δ resonance is less probable and the width of the pion decreases.

Pion velocity in the medium. The velocity of the pions is given by Hamilton's equation

$$\frac{\partial r_i}{\partial t} = \frac{\partial H}{\partial p_i} = \frac{\partial\left(\sqrt{p^2+m^2} + A_0^\pi + V_C\right)}{\partial p_i} = \frac{p_i}{\sqrt{p^2+m^2}} + \frac{\partial A_0^\pi}{\partial p_i} \quad . \tag{6.8}$$

The hadronic potential is repulsive for low values of E_{tot} and of the same order as E_{kin}. Therefore, in the first term of equation (6.8) the pion momentum is considerably smaller and, as shown in the upper panels of fig. 6.2, the velocity is strongly modified at low values of E_{kin}. The second term $\partial A_0^\pi/\partial p$ is always negative. It is large in absolute magnitude for low energies and small for energies greater than 80 MeV and leads to an overall reduction of the velocities.

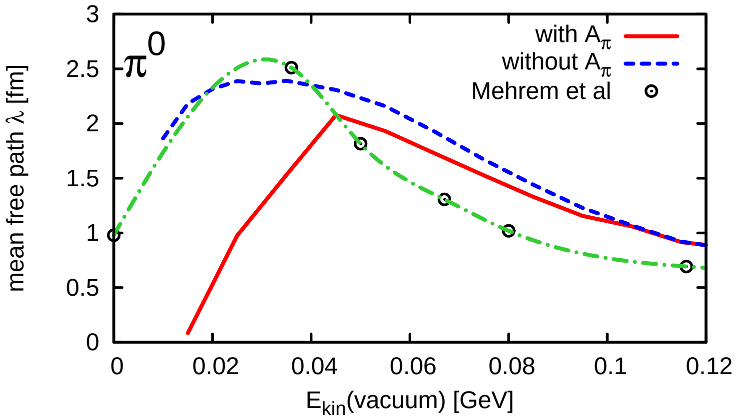

Figure 6.3: Mean free path of a neutral pion in symmetric nuclear matter at $\rho_0 = 0.168\ \mathrm{fm}^{-3}$. We show the result with (solid line) and without (dashed line) hadronic potential for the pion; all other standard medium modifications are included. For comparison, the result of Mehrem et al. [Meh84] is also shown (circles linked by a dashed-dotted interpolating line).

Results for the mean free path. After having extracted the width of the pion in the nuclear matter rest-frame directly from our numerical simulation, the mean free path is obtained by $\lambda = v/\Gamma$. Therefore we now consider the two effects discussed earlier in order to understand the changes in the mean free path: modification of the decay width Γ and modification of the velocity v due to the potentials. The effect of including the hadronic potential becomes visible in fig. 6.3, where the mean free path is plotted as a function of pion momentum. Especially at very low energies, the mean free path drops rapidly at low energies compared to the simulation without hadronic potential. This sharp decrease of the mean free path as a function of asymptotic kinetic energy stems from the velocity decrease at low energies when including the repulsive hadronic potential. At larger values of the kinetic energy the effect of width and velocity just compensate each other.

We have also studied the density dependence of the mean free path, choosing the π^0 as a showcase. The results are shown in fig. 6.4. It is important to note that the density dependence is highly nonlinear, contrary to the low-density limit. This non-linearity is generated by the $NN\pi \to NN$ process, which goes to quadratically with density, and by the implicit density dependence in the medium modifications.

Full and parallel ensembles. All previous results have been calculated using the *parallel ensembles technique* (cf. sec. 2.5.2 for details). However, this should not have any impact on the observables since we performed the calculations within a homogeneous box of nuclear matter. Due to the homogeneous density distribution, the locality of the scattering processes is not expected to play any role.

To check the consistency of the local and parallel techniques, we performed runs without a pion potential as a benchmark. In fig. 6.5 we observe good agreement between the results obtained in the different approximation methods[2].

---

[2] For the BUU specialist: Note that we expect at higher energies some differences. The local ensemble scheme does not use a maximal impact parameter b_{max} as cut-off, but the parallel ensemble scheme includes such a cut-off (e.g. $b_{max} = 2.52$ fm for baryon-meson collisions).

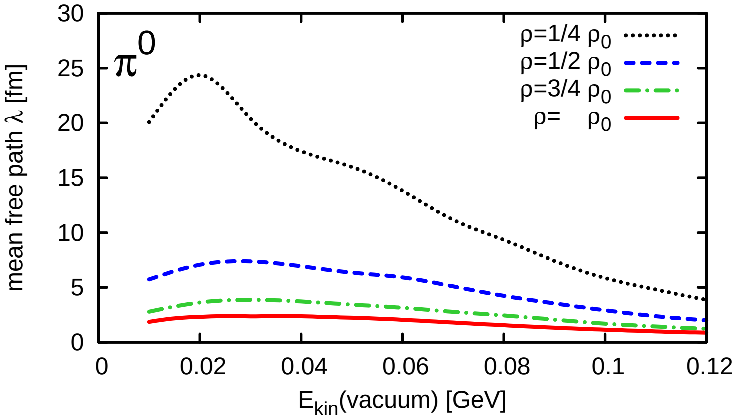

Figure 6.4: The mean free path of a π^0 meson investigated at different densities of the nuclear matter. The hadronic potential for the pion is not included.

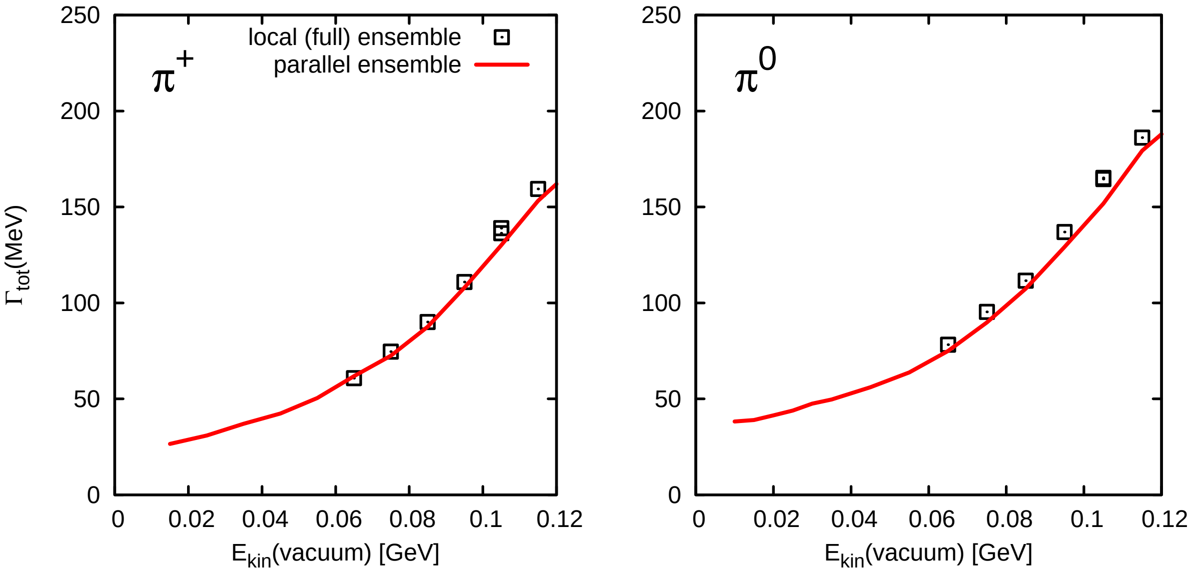

Figure 6.5: The width of π^+ and π^0 mesons within local (open squares) and parallel ensemble (solid line) technique at $\rho = 0.168$ fm^{-3} $(\rho_n = \rho_p)$.

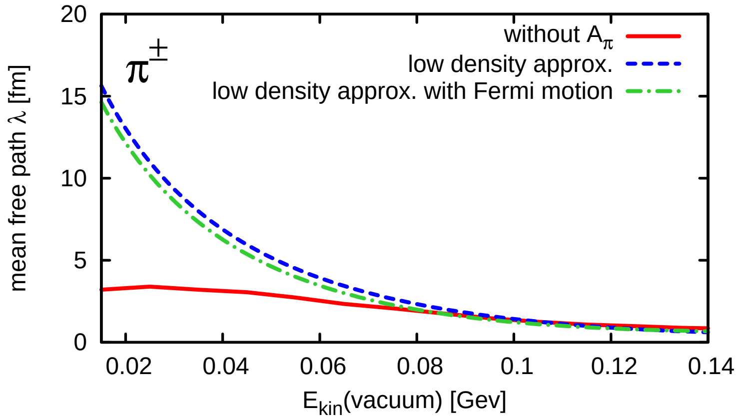

Figure 6.6: Mean free path of the charged pions in the naive low-density approximation. The inclusion of Fermi motion does not have a sizable impact. A BUU calculation without Coulomb forces and without hadronic potential for the pion is shown for comparison.

The vacuum approximation. We now compare our results to the low-density approximation, commonly found in the literature as, e.g., in [Eri88, Cas90]. In this approximation the mean free path is given by

$$\lambda = \frac{1}{2\,\Im(p)} = \frac{1}{\rho\ \sigma_{\mathrm{vac}}} \quad , \tag{6.9}$$

with σ_{vac} denoting the pion-nucleon scattering cross section in vacuum. In the equation above $\Im(p)$ denotes the imaginary part of the momentum. Using the total cross sections shown in fig. A.6, we can now evaluate the mean free path. Due to the lack of pion-neutron scattering data, we assume $\sigma_{\pi^- n\to X} = \sigma_{\pi^+ p\to X}$ and $\sigma_{\pi^+ n\to X} = \sigma_{\pi^- p\to X}$.

In the case of symmetric matter, we calculate σ_{vac} for the π^+ and π^- by averaging over the neutron and proton contribution to the cross section:

$$\sigma^{\pm}_{\mathrm{vac}} = \frac{1}{2}\left(\sigma_{\pi^\pm n\to X} + \sigma_{\pi^\pm p\to X}\right) = \frac{1}{2}\left(\sigma_{\pi^+ p\to X} + \sigma_{\pi^- p\to X}\right) \quad . \tag{6.10}$$

For charged pions the mean free path in this approximation is shown in fig. 6.6. Comparing it to a full BUU calculation, which considers the Pauli blocking of the final states, as well as the Fermi motion of the initial states and three-body interactions, we see a dramatic discrepancy at small energies.

For completeness we have also investigated the influence of Fermi-motion and calculated the mean free path by integrating over the interactions in the Fermi sea,

$$\lambda = \frac{1}{4 \underset{p_F}{\iiint} \sigma_{\mathrm{vac}}(\sqrt{s}) \frac{d^3p}{(2\pi)^3}} \quad . \tag{6.11}$$

The result can also be seen in fig. 6.6. The modifications of the mean free path due to the Fermi motion in the vacuum approximation are very small.

The low-density approximation does not consider any kind of many-body interactions at low energy. Only the two body πN interaction is allowed. In our model, the principle of detailed balance forced us to take the $NN\pi \to NN$ process into account since also its inverse

$NN \to NN\pi$ channel is included. In fig. 6.2 we see the large contribution of this process to the width at low energies. Such a three body $NN\pi$ interaction is not included in the vacuum approximation. At higher energies, especially above 120 MeV the low-density approximation coincides with our results, since there the dominant process is the two body process $N\pi \to \Delta$.

We conclude that the naive low-density approximation is qualitatively and quantitatively not reliable in the energy regime of $E_{\text{kin}} \lesssim 70$ MeV where multi-body collisions, potential effects and Pauli-blocking are important.

Comparison to optical model results. In [Hec81] Hecking published calculations of the pion mean-free-path based on two different types of phenomenological optical potentials V_{opt}. Starting from equation (6.9) one can calculate the imaginary part of the momentum using the dispersion relation $p^2 = E^2 - \left(m^2 + 2E\, V_{\text{opt}}(p,E)\right)$ approximating $\Pi = 2E\, V_{\text{opt}}$ by ignoring terms of the order $O\left(V_{\text{opt}}^2/m^2\right)$. Instead of solving the real and imaginary parts of the dispersion relation, Hecking approximates the real part of the dispersion relation by the vacuum solution $\Re\left[p^2\right] = E^2 - m^2$ and uses this approximation in the equation for the imaginary part $\Im\left[p^2\right] = -\Im\left[2E\ V_{\text{opt}}(p, E = \sqrt{p^2+m^2})\right]$. This last equation now defines also $\Im\left[p\right]$, which can be used in equation (6.9) to obtain the mean free path. Hecking's results [Hec81, fig. 1] show two solutions for the mean free path which give maximal values of 4 fm and 5.7 fm. Our result is not only at the peak position but over the full energy range lower than Hecking's. Eventually, the work performed by Mehrem et al. [Meh84] explains this discrepancy. Solving the full dispersion relation with an optical potential calculated by J. A. Carr[3], it [Meh84] reports a mean free path of the pion which is smaller than Hecking's result. Mehrem *et al.* attribute this discrepancy to Hecking's approximations described above.

As a benchmark for our model, the result of Mehrem *et al.* [Meh84] for the mean free path is shown in fig. 6.3 in comparison to our result obtained with the BUU simulation [4]. Including the hadronic potential in our model we notice that the mean free path decreases considerably at low pion kinetic energies. There the hadronic potential becomes repulsive with $V \gtrsim E_{kin}$ and the semi-classical model breaks down, as mentioned earlier. In contrast to this, quantum mechanics allows for tunneling, i.e. propagation, into such classically forbidden regions.

A proper discussion of the mean free path is obviously important in the analysis of experiments with final state pions being produced inside the nuclear medium. When working in a quantum mechanical framework, solving the full dispersion relation, as done e.g. by Mehrem et al., is very important. Ad hoc assumptions have a large effect on the pion mean free path and this has a dramatic effect on any final state analysis.

Since the mean free path is not directly observable, it is ultimately an open question whether transport gives a reasonable mean free path for the pion. This can only be answered by experiment. A test for our model assumptions will, therefore, be the absorption cross sections which we address in the next paragraph.

6.3 Pion absorption and quasi-elastic scattering

Low-energy pion scattering experiments have been studied extensively with elementary targets (e.g. [Car71, Dav72, Kri99, Sad04]). However, there exist only a few data points for pions

---

[3] The parameters are given in [Meh84]

[4] The real part of V_{opt}, which is used in Mehrem's work, is very strong at low energies with $V_{\text{opt}} \approx 48$ MeV at $E_{\text{kin}}^{\text{vac}} = 0$. A direct comparison by including this real part in our semi-classical model is, therefore, not possible.

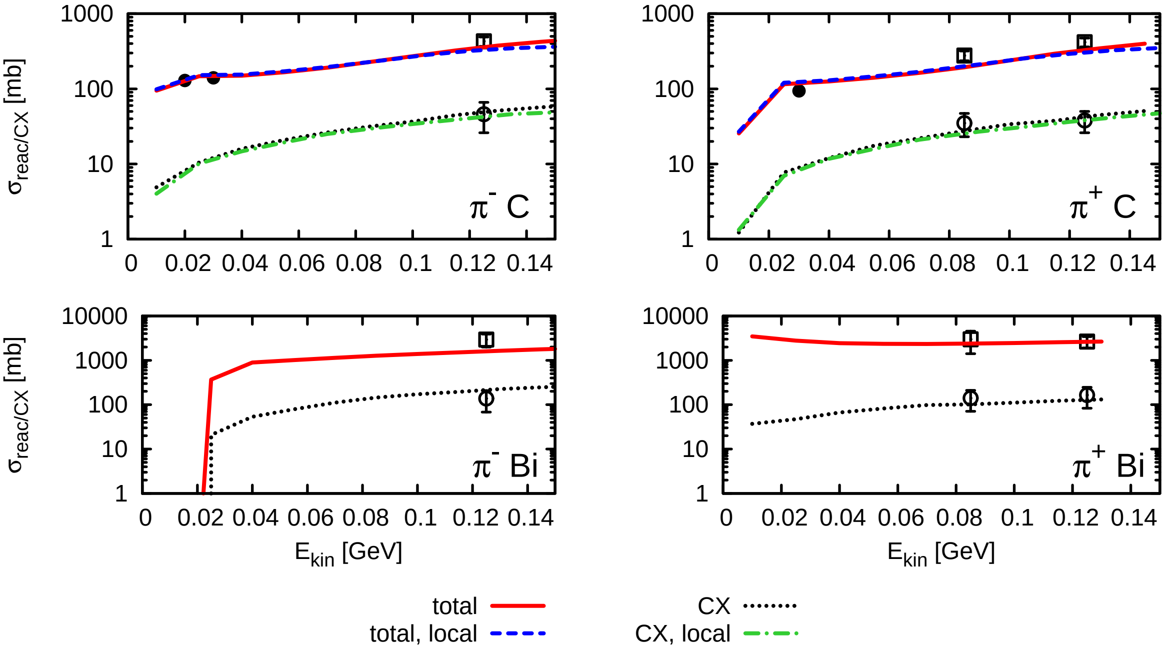

Figure 6.7: Reaction ("reac"; solid and dashed) and charge exchange ("CX"; dotted and dashed-dotted lines) cross sections for ^{12}C and ^{209}Bi. The data points are taken from [Ash81] (open squares: σ_{CX}, open circles: σ_{reac}) and [Fri91] (full circles: σ_{reac}).

scattering off complex nuclei [Car76b, Clo74, Wil73, Ash81, Fri91, Nak80, Byf52].

The total cross section [Car76b, Clo74, Wil73] includes the coherent contribution, which would have to be subtracted before comparing them to our results (for a discussion on this issue see e.g. [Ash81]). We study here solely reaction, charge exchange (CX) and absorption cross sections. In the considered energy regime, reaction and CX cross-section measurements are rare [Ash81, Fri91]. In fig. 6.7 we present our results for reaction and CX cross sections for ^{12}C and ^{209}Bi. The overall agreement with the few existing data points is good. Fortunately, the experimental situation for absorption cross sections [Ash81, Nak80, Byf52] is more promising. Therefore, we now will concentrate on this observable.

In a quantum mechanical approach one cannot calculate absorption cross sections in the general case. Such an absorption cross section can be obtained only at very low energies (e.g. [Nie93a]), where the quasi-elastic contribution to the total reaction cross section is negligible. One thus relies on eikonal approximations to split the reaction cross section into a quasi-elastic and absorptive part. On the contrary, in the BUU simulation the calculation of an absorption cross section is straightforward due to the semi-classical treatment.

In fig. 6.8 we show calculations for different nuclei as a function of the pion energy. Comparing the curves obtained without any potential (dotted) to those with the Coulomb potential included (dashed), we see that the Coulomb potential alone has only a small influence on light nuclei, but is very important at low energies for heavy nuclei. Its long range leads to a sizable deformation of the trajectories already long before the pions reach the nucleus. Therefore the negative pions can interact with the nucleus even if they have large impact parameter while the positive pions are deflected. In the presence of the Coulomb potential we see a reduction of the cross section for the π^+ and a large increase of the cross section for the π^- meson. This agrees to the findings of Nieves et al. [Nie93b], who pointed out the relevance of the Coulomb potential in their quantum

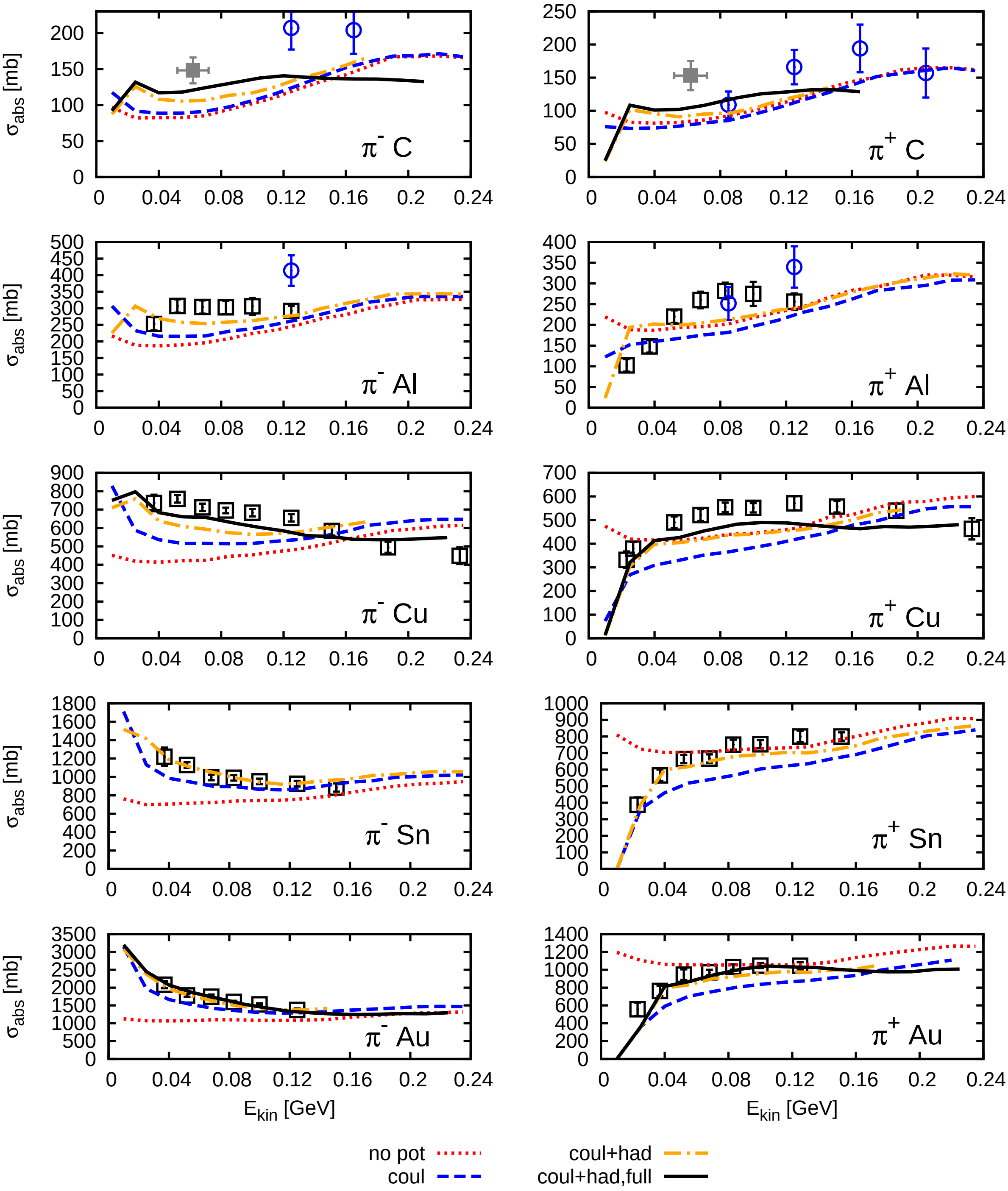

Figure 6.8: Absorption on light nuclei depending on the choice of potentials for the pion. The data points are taken from [Ash81] (open circles), [Nak80] (open squares) and [Byf52] (full squares) . In all plots the standard hadronic potentials for the nucleon and Δ resonance are used. The dotted line represents a calculation without Coulomb potential and hadronic potential for the pion such that the pion feels no potentials. All other lines are obtained with the Coulomb potential included. The dashed-dotted line additionally includes a hadronic potential for the pion. Finally, the solid line has been obtained using all potentials and, in contrast to the other results, in a full-ensemble calculation.

mechanical calculation of absorption and reaction cross sections.

When one includes the hadronic potential for the pion (dashed-dotted line), another overall effect sets in. Once the pion enters the nucleus it is influenced by the short-range hadronic potential, which amounts to -40 MeV at high momenta and to $+20$ MeV at low momenta, as well as the Coulomb potential which amounts to roughly ± 10 MeV in a medium size nucleus, and to roughly ± 20 MeV in the case of a ${}^{207}_{82}\mathrm{Pb}$ nucleus. At very low energies the two potentials nearly compensate for the negative pion, while they add up to a strongly repulsive potential in the caseof a π^+.

In fig. 6.8 we see qualitative agreement for ${}^{12}_{6}\mathrm{C}$ and ${}^{27}_{13}\mathrm{Al}$ nuclei with the data, when the hadronic potential is included. The heavier the nuclei, the better the calculations including a hadronic potential agree with the data. The curves which include a hadronic potential for the pion show a prominent kink structure at roughly 30 MeV (20 MeV) for the positive (negative) pion. This kink is caused by the repulsive character of the pion potential at low energies. On the one hand, the mean free path decreases rapidly at very low energies (compare fig. 6.3) and this causes the absorption cross section to rise. On the other hand, the repulsive potential pushes the pions out of the nucleus or even reflects them. Below the kink the repulsive feature is more prominent; above the kink the decreasing mean free path is more important.

Impact of the full ensemble scheme. All above discussed results have been obtained using the parallel ensemble scheme. The solid lines in the upper, middle and lower panels of fig. 6.8 show the result using the superior local ensemble scheme (box size=0.5 fm^3) with all previously discussed potentials being included. We observe deviations as compared to the dashed-dotted line, which shows the result using the same physics input in the parallel ensemble scheme. The local ensemble scheme produces at higher energies less absorption and at smaller energies more absorption. The overall agreement to the data is slightly improved. We expect two effects to be responsible for this. If the reactions are non-local then also pion test-particles which in a local interaction would just fly by the nucleus without interaction might be deflected during a reaction towards the nucleus. So the absorption cross section rises due to the non-locality - the difference to the local description should increase with rising 2-body cross section (i.e. rising energy). And as a second effect, pions might be deflected outward too early before reaching a region of higher nuclear density, which would be reached with a local collision criteria. This should counteract the increasing effect discussed before. We expect this decreasing influence to be quite constant in energy: as soon as there is a non-vanishing two-body strength, an incoming pion which would anyhow hit the nucleus can be deflected before it enters a region of higher density where the absorption probability is high. Overall, the time-consuming full ensemble scheme is expected to yield a more reliable result since it represents a better approximation of the underlying BUU equation.

Conclusions. As an overall conclusion, we find that it is critical to include Coulomb corrections. On top, the absorption cross sections are sensitive to the hadronic potential of the pion, in particular to the real part of the self energy in the medium. As we have already seen in fig. 6.3, the mean free path is quite insensitive to the hadronic potential except at very low energies. We thus conclude that the modification of the trajectories of the pion is the main effect of the hadronic potential. In its repulsive regime the hadronic potential pushes the pion outwards and the overall path of the pion inside the nucleus becomes shorter. The probability of absorption is therefore decreased. The attractive behavior at larger energies causes the opposite effect.

The overall agreement to the data is satisfactory in spite of some discrepancies, especially for the $^{12}_{6}$C and $^{27}_{13}$Al nuclei. Considering the fact that the pions have very large wave lengths at such low energies, the success of the semi-classical BUU model is quite astonishing. Due to the large wave length one expects also many-body correlations and quantum interference effects to be important. Many-body effects are partially included via the mean fields acting on pions and baryons and the modification of the Δ width. Besides this we included only $1 \leftrightarrow 2$, $2 \leftrightarrow 2$ and $2 \leftrightarrow 3$ body processes in the collision term. We take the success as an evidence that no higher order correlations than the latter ones are necessary to describe pion absorption.

In our earlier publication [Bus06c], we achieved a slightly better agreement with the data. At that stage, we also included the Oset model for the Δ width. However, we implemented it as a purely absorptive width. As outlined in appendix A.2.1, we now improved on this by dividing the width into quasi-elastic and absorptive contributions. As a consequence, we absorb less Δ's since the quasi-elastic contribution is no longer treated as an absorptive contribution. This explains why we achieved in [Bus06c] slightly higher ($\approx 15\%$ at $E_{kin} = 0.1$ GeV) absorption cross sections, especially at higher kinetic energies.

6.4 Double charge exchange

Pionic double charge-exchange (DCX) in πA scattering is a very interesting reaction – as a model benchmark but also concerning the underlying physics itself. The fact that DCX requires at least two nucleons to take place makes it a very sensitive benchmark for pion rescattering and absorption. This reaction received a considerable attention in the past (see for instance reference [Gib90] and references therein). The mechanism of two sequential single charge-exchanges has traditionally succeeded to explain the main features of this reaction [Bec70, Gib77] at low energies although the contribution of the $A(\pi, \pi\pi)X$ reaction becomes progressively important as the energy increases [Vic89, Alq02]. At higher (~ 1 GeV) energies, the sequential mechanism becomes insufficient to account for the reaction cross section [Abr03, Kru05]. Extensive experimental studies performed at LAMPF obtained high precision data for doubly differential cross sections on $^{4}_{3}$He [Yul97] and heavier nuclei ($^{16}_{8}$O, $^{40}_{20}$Ca, $^{207}_{82}$Pb) [Woo92] in the region of $E_{\text{kin}} = 120 - 270$ MeV.

Hüfner and Thies [Hüf79] explored for the first time the applicability of the Boltzmann equation in πN collisions and achieved qualitative agreement with data on single and double charge exchange. Their method to solve the Boltzmann equation was based upon an expansion of the pion one-body distribution function in the number of collisions. There, in contrast to our work, the Boltzmann equation is not solved with a test-particle ansatz, but by reformulating it into a set of coupled differential equations which can then be solved in an iterative manner. However, this approach was based on simplifying assumptions of averaged cross sections and averaged potentials. The work by Vicente et al. [Vic89] was based upon the cascade model described in [Sal88]. There, a microscopic model for πN scattering was used as input for the pion reaction rates in the simulation. In ref. [Vic89], pion DCX off $^{16}_{8}$O and $^{40}_{20}$Ca nuclei was explored and fair quantitative agreement with the data has achieved.

In our work, we explore DCX on heavier nuclei, comparing with the data measured by Wood et al. [Woo92]. We also address the scaling of the total cross section discussed by Gram et al. [Gra89]. To focus only on single-pion rescattering, we consider incoming pion energies below $E_{\text{kin}} = 180$ MeV; above this energy 2π production becomes prominent and DCX does not happen necessarily in a two-step process anymore. Due to the small mean free path of the incoming pions, the process is mostly sensitive to the surface of the nucleus. Therefore, we will discuss and compare two widely used numerical schemes for the solution of the Boltzmann equation: *parallel* *ensemble method* employed in the BUU models [Aic85, Bau86, Ber88, Cas90] and in the Vlasov-Uehling-Uhlenbeck model [Mol85]; and *full ensemble method* used in the Landau-Vlasov [Gre87], Boltzmann-Nordheim-Vlasov [Bon89, Bon94] and Relativistic BUU [Fuc96, Gai05] models. Both schemes are based on the test-particle representation of the single-particle phase space density, but they differ in the locality of the scattering processes (c.f. discussion in section 2.5.2). In the following, we first compare both schemes and, thereafter, point out the impact of neutron skins. Finally, the transport results are confronted with the experimental data obtained at LAMPF by Wood et al. [Woo92].

6.4.1 Comparison of full and parallel ensemble runs

The fact that the DCX reaction depends considerably on the spatial distributions of protons and neutrons implies that it is also sensitive to the degree of locality of the scattering processes. In the non-discretized version of the BUU equation, the interactions are strictly local in space-time. Utilizing the so called *test-particle ansatz* to solve the problem numerically, this is no longer the case. Therefore, we want to elaborate on this degree of locality of the scattering processes in our simulation. In section 2.5.2 we introduced the concept of the parallel ensemble approximation. For DCX, surface effects are expected to be important, so that the spatial resolution could be relevant in this context. Indeed, a major problem of the parallel ensemble scheme is that the interaction volume ΔV_{ij} can become very large. In the energy regime under consideration, the incoming pions interact strongly with the nucleons so that the total cross section can reach more than 200 mb. For a parallel ensemble run, the typical volume has therefore the size of 5 fm^3 for a typical time-step size $\Delta t = 0.25$ fm/c. Since it is not obvious that the parallel ensemble scheme should be reliable in this regime, we have decided to evaluate this approximation scheme by comparison to the full ensemble method.

In fig. 6.9, the results for $d\sigma/d\Omega$ at 180 MeV kinetic energy of the pion are presented for both methods. The error bars in fig. 6.9 show the statistical uncertainties of our results. As an improvement to our earlier publication [Bus06a], we resolve due to an improved error analysis a slight difference between the results using the full (solid lines) and the parallel (dashed lines) ensemble scheme. While the results are consistent with each other for the ${}^{40}_{20}$Canucleus and within the statistical uncertainties also more or less for ${}^{16}_{8}$O, we see some major discrepancy for the lower left panel which shows the $\pi^+ Pb \to \pi^- X$ reaction. As a consequence we decided to perform all calculations with both the parallel ensemble method and the full ensemble method to compare the results to the data. Note that in the present problem, in order to obtain a result at a given energy for one specific nucleus one CPU-day is required in the parallel ensemble scheme. In the full scheme this takes of the order of approximately 4 CPU-days for an acceptable statistics, as shown in fig. 6.9.

6.4.2 Influence of the density profile

The DCX is, due to the low pion mean free path in nuclear matter, very sensitive to the surface properties of the nuclei. Therefore, we compare the results with the present parametrization for ${}^{208}Pb$ according to [Nie93b], as described in section 3.8, to the results obtained with the one used in previous publications [Bus06c, Mü04a, Eff97b]. For ${}^{208}Pb$, both distributions are parametrized according to eq. 3.73 with the parameters given in table 6.1. However, neutron skins are very interesting because in these skins only π^+ mesons can undergo charge exchange reactions. For the positive pions this causes an enhancement of DCX processes at the surface, so the pions do not need to penetrate deeply for this reaction. Hence, the probability for their

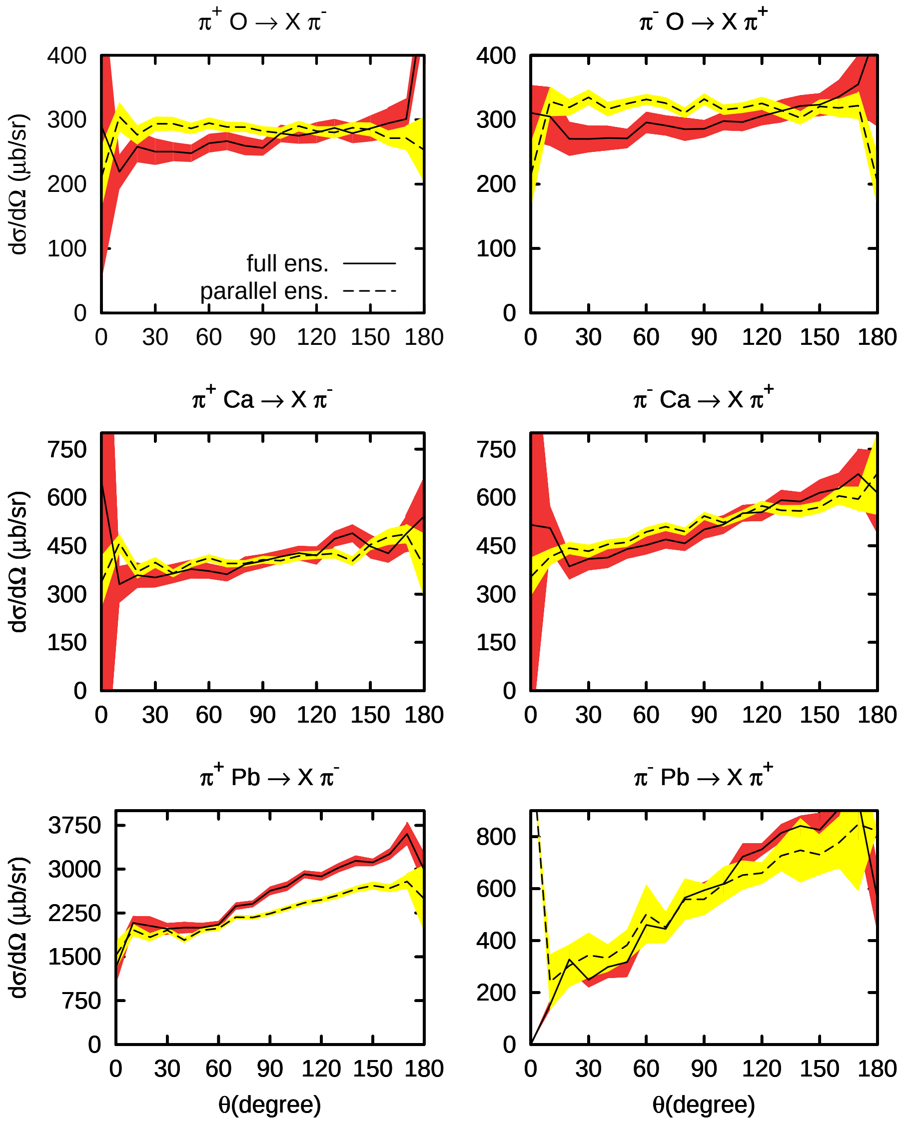

Figure 6.9: Comparison of the full (solid lines) and parallel (dashed lines) ensemble methods. The upper panels show angular distributions for the double-charge exchange process $\pi^{\pm}A \to \pi^{\mp}X$ at $E_{\text{kin}} = 180$ MeV. The yellow and red error bands denote the 1σ confidence level based upon our statistics.

	ρ_p^0 [fm^{-3}]	ρ_n^0 [fm^{-3}]	R_p [fm]	R_n [fm]	$a_p = a_n$ [fm]
default parametrization [Nie93b]	0.0631	0.0859	6.624	6.890	0.549
old parametrization [Bus06c]	0.0590	0.0900	6.826	6.826	0.476

Table 6.1: Parameters of the Woods-Saxon parametrizations for ${}^{207}_{82}$Pb.

absorption is reduced. In fig. 6.10 we present the results for $\pi^+\text{Pb} \rightarrow \pi^-\text{Pb}$ for an incoming pion energy of 180 MeV. Comparing the result obtained in a calculation including a neutron skin having the diameter of $R_n - R_p = 0.266$ to the one neglecting it, we conclude that the enhancement in the total cross section is roughly 35%.

The accurate determination of neutron skins is relevant for different areas of physics such as nuclear structure, neutron star properties, atomic parity violation (PV) and heavy ion collisions [Hor01, Hor06, Pie06]. The Parity Radius Experiment (PREX) at JLab [Mic] plans to measure the neutron radius with high precision (1%) using PV electron scattering. We have just shown that the DCX cross section is very sensitive to the size of the difference between the proton and the neutron radii of the $^{207}_{82}\text{Pb}$ nucleus. The effect is specially large (ca. a factor 2) at forward angles, where our model performs very well (see next section). Indeed, without neutron skin, due to strong pion absorption in the bulk of nuclear matter, the DCX cross section is small at forward angles. The presence of neutron skins favors DCX in peripheral reactions, where the pion propagates in practically pure neutron matter. This naturally enhances the DCX cross section at forward angles. Hence, a precise measurement of DCX at forward angles, combined with a realistic theoretical analysis could be a valuable source of information on the neutron skins complementary to the one obtained with PV electron scattering. Note that following similar arguments for the π^--lead reaction, we expect a reduction of the cross section.

6.4.3 Comparison to the data

To compare with the data measured at LAMPF by Wood et al. [Woo92], we discuss first the total cross section. Hereafter, we explore angular distributions and, finally, the double differential cross section is addressed as a function of both angles and energies of the outgoing pions.

In fig. 6.11 one can see the good quantitative agreement to the total cross section data at 120, 150 and 180 MeV for the $^{16}_{8}\text{O}$, $^{40}_{20}\text{Ca}$, $^{103}_{45}\text{Rh}$ and $^{207}_{82}\text{Pb}$ nuclei. Only for the $^{16}_{8}\text{O}$ nucleus and the low energy of 120 MeV we see statistically significant discrepancies. The difference of full and parallel ensemble runs is rather small. Notice that we reproduce the different A dependencies of both (π^+, π^-) and (π^-, π^+) reactions. This is due to the fact that, when A increases, the number of neutrons increases with respect to the number of protons, and this favors the π^+ induced reaction.

In [Gra89], Gram et al. discuss a scaling law of the total cross section. Their line of argument starts with the assumption that the first collision takes place predominantly at the surface and, therefore, the cross section should scale with $A^{2/3}$. Furthermore they assume that DCX is mainly a two-step process, and that a pion which undergoes an elastic process at the first collision will not contribute. This is reasonable because the incoming pions loose energy in the elastic process, and their cross section for a second charge-exchange reaction is hereafter very much reduced. For a negative pion the first charge exchange reaction occurs with a probability of Z/N where $Z(N)$ denotes the number of protons (neutrons). This is the case if the interaction is dominated by the Δ resonance, as it should be in this energy region. Finally, the second charge exchange process then takes place with the probability $(Z-1)/(A-1)$ since, in the isospin limit, the π^0 interacts equally well with protons and neutrons. Putting these considerations together and extending them to the π^+ case, the cross section for DCX is expected to scale according to

$$\sigma_{tot} \sim A^{2/3} \frac{Q}{A-Q} \frac{Q-1}{A-1} \quad , \tag{6.12}$$

where Q denotes the number of protons in the case of π^- induced and the number of neutrons in π^+ induced DCX.

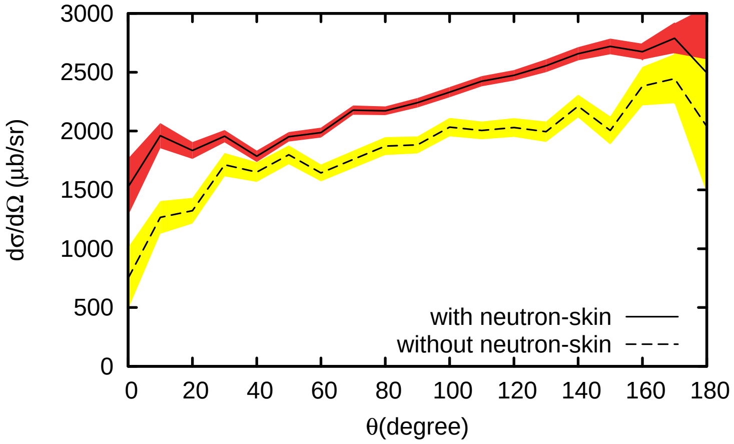

Figure 6.10: Influence of the density distribution on the angular distributions for the double charge exchange process $\pi^+ Pb \rightarrow \pi^- X$ at $E_{\text{kin}} = 180$ MeV within the parallel ensemble scheme. The solid line shows the result obtained with our present density distribution [Nie93b]; the dashed line was obtained with the previously used one [Bus06c, Mü04a, Eff97b], which contains no neutron skin. The yellow and red error bands denote the 1σ confidence level based upon our statistics.

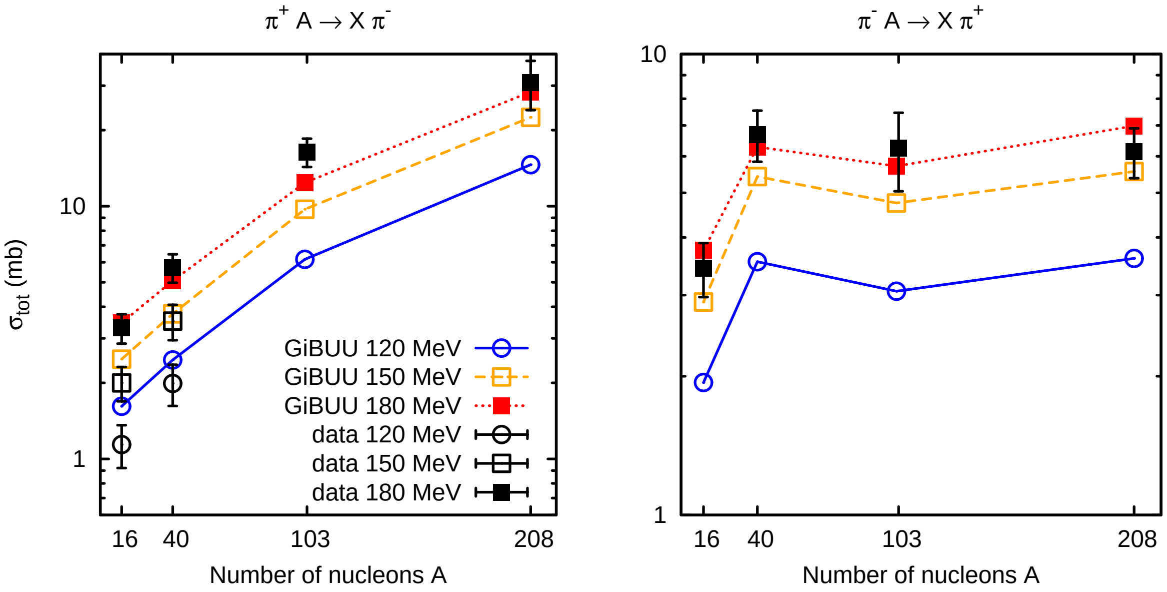

Figure 6.11: The inclusive double charge exchange total cross section as a function of the nuclear target mass at $E_{\text{kin}} = 120, 150$ and 180 MeV. The lines connecting our results are meant to guide the eye; the data are taken from Ref. [Woo92] (left panel: $E_{\text{kin}} = 120$ MeV (open circles), 150 MeV (open squares) and 180 MeV (full squares), right panel: only 180 MeV (full squares)).

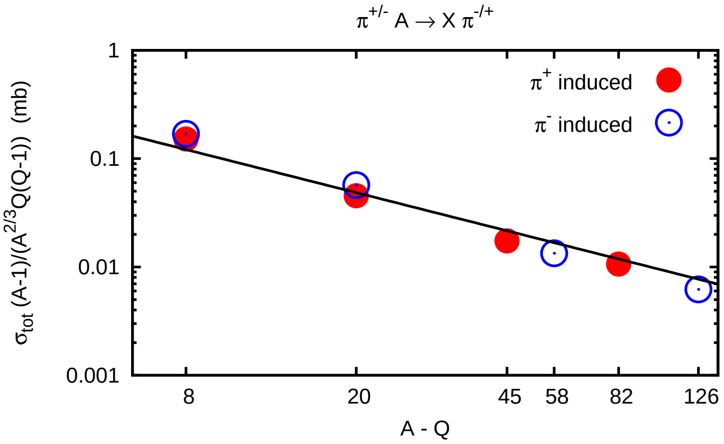

Figure 6.12: The scaling of the total charge exchange cross section according to eq. (6.12) is visualized by dividing σ_{tot} by the factor $A^{2/3}Q(Q-1)/(A-1)$ and plotting it as a function of $A-Q$. Q denotes the number of protons in the case of (π^-,π^+) and the number of neutrons in (π^+,π^-). The points are GiBUU results at pion kinetic energies of 180 MeV; the solid line denotes a function proportional $1/(A-Q)$, corresponding to the exact scaling.

Gram et al. [Gra89] found good agreement of this scaling law with experimental data. This scaling law is fulfilled also in the GiBUU simulations as can be seen in fig. 6.12, which shows the obtained results in comparison to the predicted scaling law. Nevertheless, one may wonder why this scaling law works in a process which is so sensitive to the neutron skin on heavy nuclei, as has been shown in fig. 6.10. Since the first collision takes place on the surface, a neutron skin causes an enhancement in the $A(\pi^+,\pi^-)X$ reaction while $A(\pi^-,\pi^+)X$ is suppressed. This effect leads to a deviation from the scaling. However there are also Coulomb forces which are not negligible. The Coulomb force enhances $A(\pi^-,\pi^+)X$ by attracting the negative projectiles and repelling the positive products, which therefore have a smaller path in the nucleus and undergo less absorption. And, due to similar arguments, the reaction $A(\pi^+,\pi^-)X$ is suppressed. We find that this effect counteracts the one from the neutron skin restoring the scaling. In any case, the approximate scaling exhibited by the cross section shows that the reaction is very much surface driven and can be very well understood in terms of a two-step process.

In fig. 6.13 we show $d\sigma/d\Omega$ for DCX at $E_{\text{kin}} = 120$ (lowest curves), 150 and 180 MeV (highest curves) on ${}^{16}_{8}$O, ${}^{40}_{20}$Ca and ${}^{207}_{82}$Pb as a function of the scattering angle θ in the laboratory frame for both the full (black curves) and parallel (gray curves) ensemble schemes. Our results (lines) are shown together with their statistical uncertainties (error bands). The uncertainties are well under control except at very small and very large angles, where statistics is very scarce. Again, there is a very good quantitative agreement for both ${}^{40}_{20}$Ca and ${}^{207}_{82}$Pb nuclei. For ${}^{16}_{8}$O, the data is somewhat overestimated for low kinetic energies of the pion.

Going into further details of the energy distribution of the produced pions, we show in figures 6.14, 6.15 and 6.16 the results for $d\sigma/(d\Omega\, dE_{\text{kin}})$ at different laboratory angles θ, as a function of the kinetic energy of the outgoing pion E_{kin}. The overall agreement is good, better at forward and transverse angles than at backward angles. Astonishingly, the discrepancy for the ${}^{16}_{8}$O data is less prominent than for the integrated cross sections. However, we observe an overall lack of pions with energies below $E_{\text{kin}}\simeq 30$ MeV. This feature becomes more prominent when going from O to Pb and is present for both incoming π^+ and π^-. The same problem also shows up

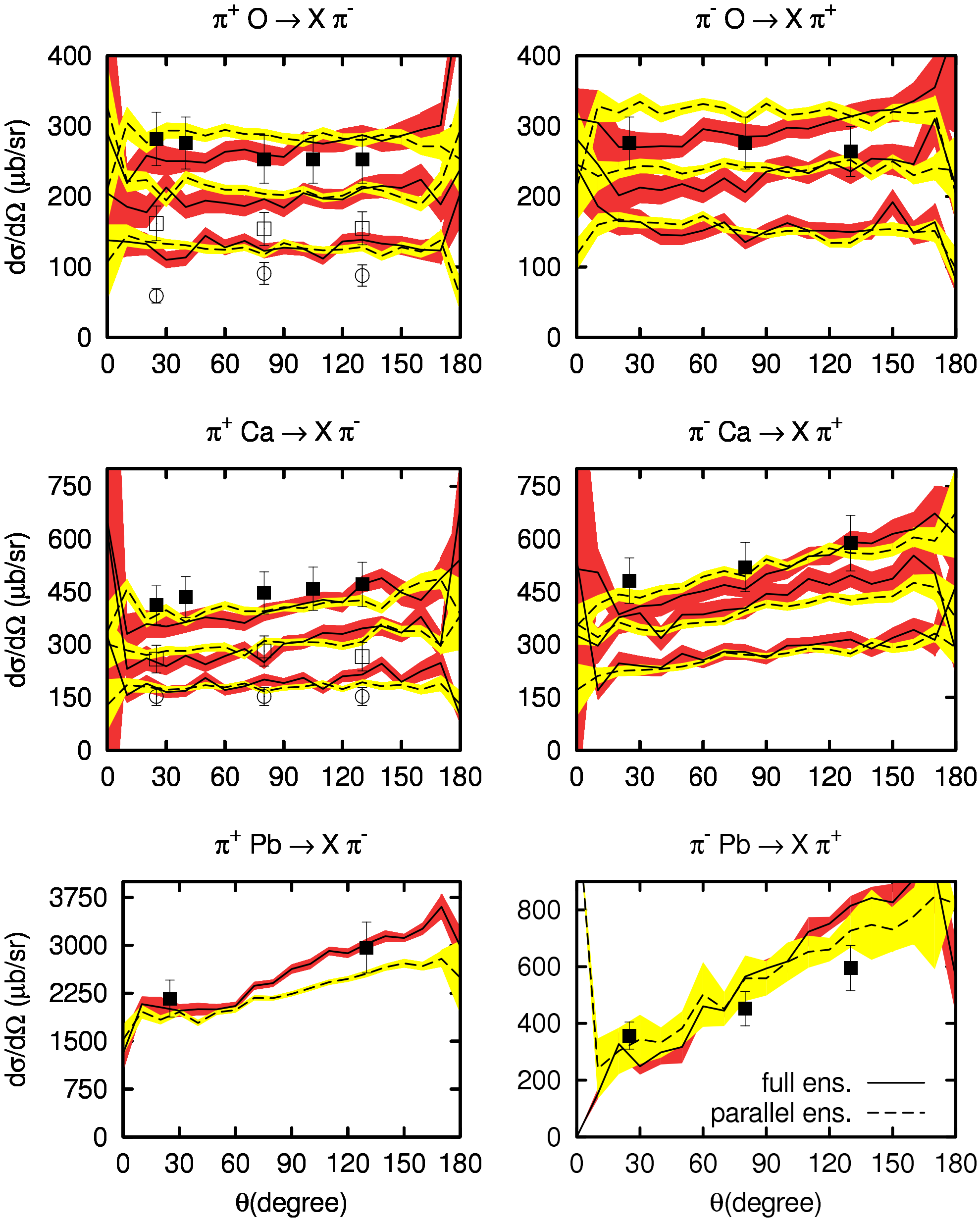

Figure 6.13: Angular distributions for the DCX process $\pi^{\pm}A \rightarrow \pi^{\mp}X$ at $E_{\text{kin}} = 120, 150$ and 180 MeV. The data points are taken from [Woo92]; only systematical errors are shown. The solid lines represent the GiBUU results obtained using the full ensemble scheme, the dashed ones the result for the parallel ensemble scheme. For ${}^{207}_{82}$Pb (lower panels) we only show the result and the corresponding experimental data for 180 MeV kinetic energy of the pion. For ${}^{16}_{8}$O (upper panels) and ${}^{40}_{20}$Ca (middle panels) we show the results for all three energies 120 MeV (experimental data: open circles), 150 MeV (open squares) and 180 MeV (full squares). The lowest curves of our results correspond to 120 MeV, the highest ones to 180 MeV. The yellow and red error bands denote the 1σ confidence level based upon our statistics.

in the work of Vicente et al. [Vic89] (see their fig. 9). An explanation of this feature is not clear. One may speculate whether quantum mechanical effects, which should be sizable for the low-energy pions with long wavelength, lead to the enhancement in the data compared to the semi-classical transport theory.

Summarizing this last section, we resolved small inaccuracies of the parallel ensemble scheme for the DCX reaction by comparing the results with those obtained in the more precise but time consuming full ensemble method. Henceforth, we suggest to use the full ensemble method for further studies. Furthermore, we compared the results of our model with the extensive set of data taken at LAMPF [Woo92], achieving a good agreement, not only for the total cross section, but also for angular distributions and double differential cross sections. Still, we miss some strength at backward angles and pion energies below $E_{\text{kin}} \approx 30$ MeV. The scaling of the total cross sections pointed out in [Gra89] could be reproduced. However, we found that the effects of neutron skins and Coulomb forces, which both break this scaling, compensate each other such that the scaling is restored in a non-trivial fashion. We have shown in section 6.4.2 that the DCX cross section is very sensitive to the size of the neutron skin. A precise measurement of DCX at forward angles combined with a theoretical analysis could bring quantitative results on the neutron skins of heavy nuclei.

6.5 Summary: "Is transport applicable for low energetic pions?"

In the beginning of this chapter, the key question arose "Is transport applicable for low energetic pions?". In pion absorption and charge exchange reaction we achieved agreement with the available experimental data. However, we also had to realize that the propagation of pions with too long wavelength ($E_{\text{kin}} < 30$ MeV) is not very meaningful and that the semi-classical treatment starts to break down in this energy regime. Finally, after addressing DCX we can conclude that the implementation of pion rescattering and absorption in the GiBUU transport model successfully passes the demanding test of describing DCX reactions. Thus our answer to the initial question is the following: the semi-classical approach is well suited to describe pion dynamics in nuclei for pion kinetic energies greater $E_{\text{kin}} \approx 30$ MeV on a level of $10 - 20\%$ accuracy.

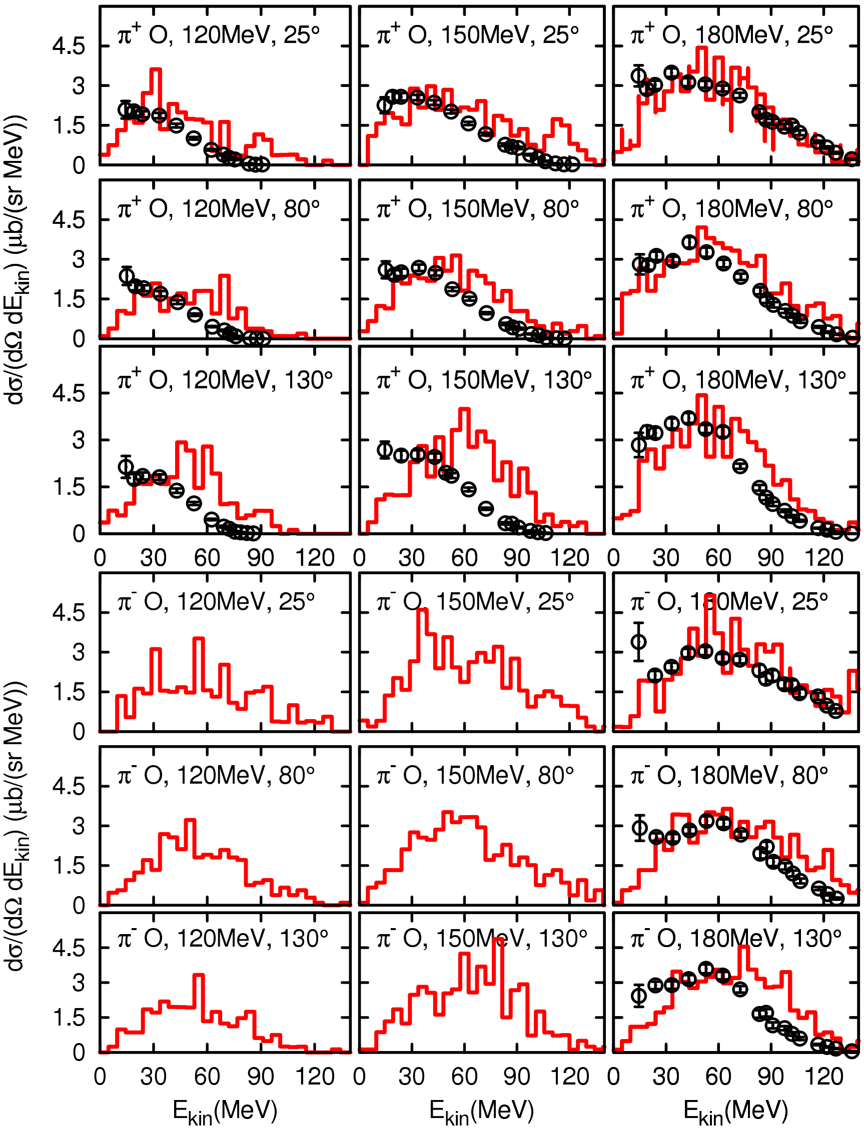

Figure 6.14: Double differential cross sections for the DCX process $\pi^{\pm}O \rightarrow \pi^{\mp}X$ at $E_{\mathrm{kin}} = 120, 150$ and 180 MeV obtained using the parallel ensemble scheme. The results at different angles are shown as functions of the kinetic energies of the produced pions. Data are taken from [Woo92]; only statistical errors are plotted. The GiBUU results are presented as histograms, where the fluctuations indicate the degree of statistical uncertainty.

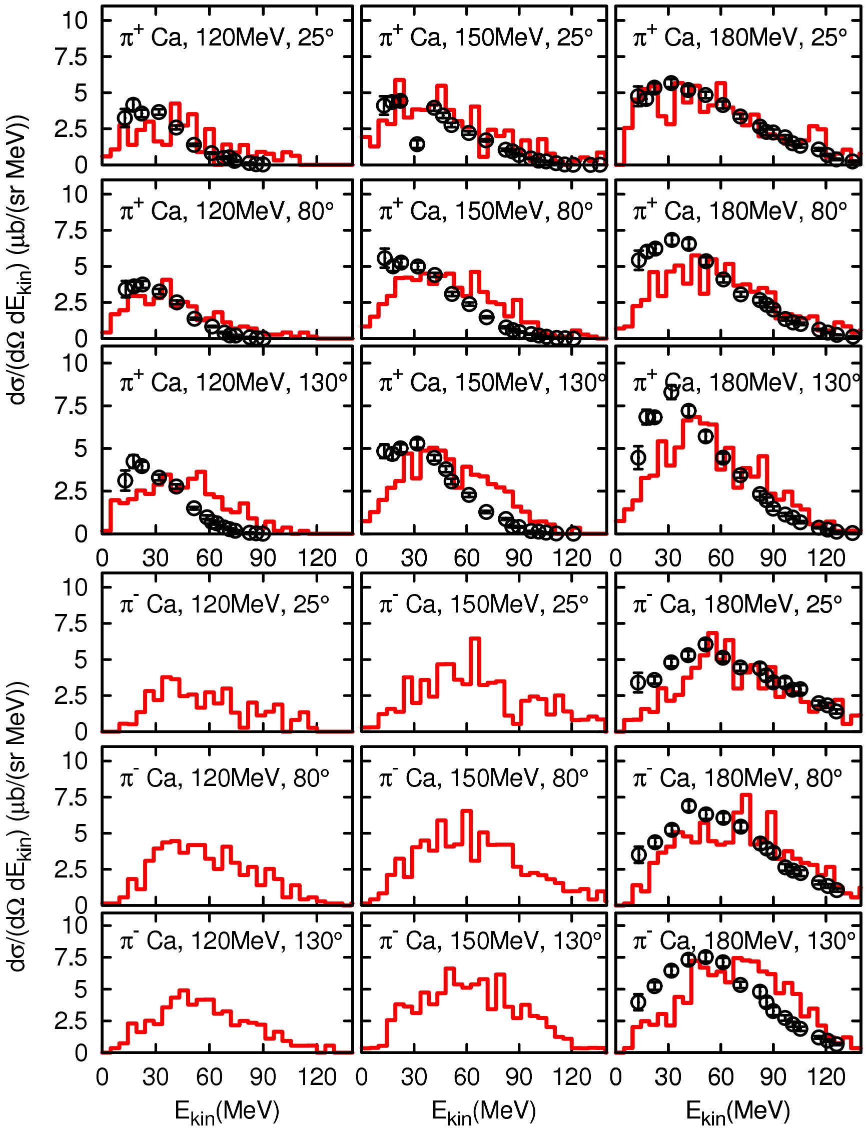

Figure 6.15: Same as fig. 6.14 for Ca.

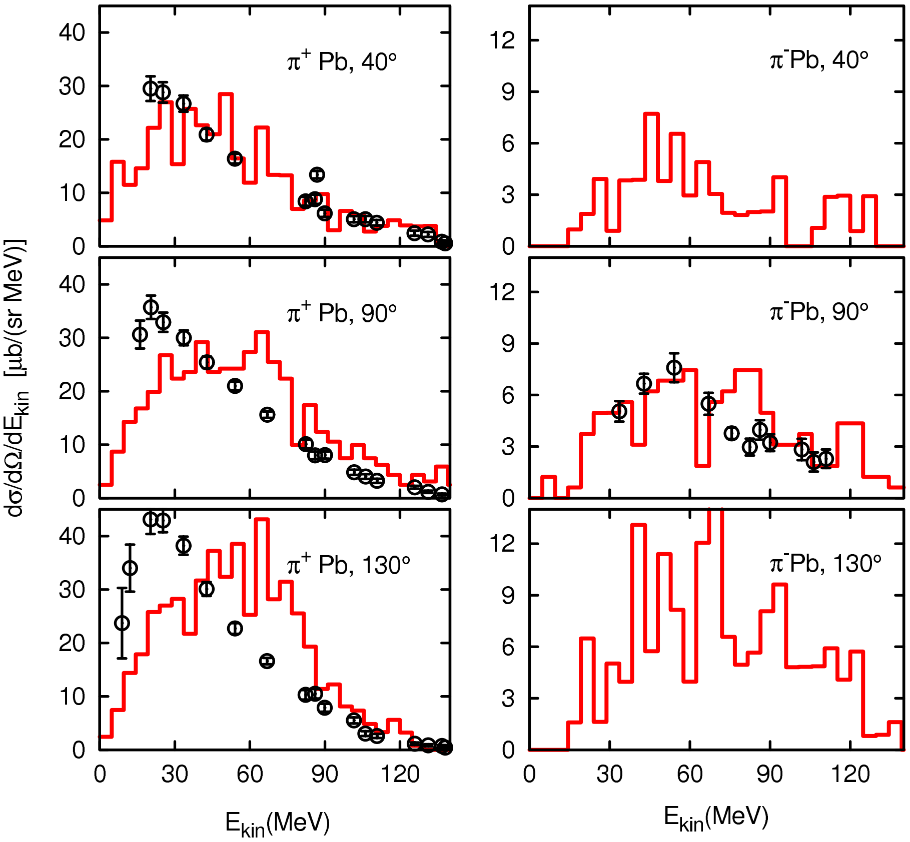

Figure 6.16: Same as fig. 6.14 for Pb at $E_{\text{kin}} = 180$ MeV.

Chapter 7

Electron and photon induced reactions

Overview: Inclusive electron and photon scattering off nuclei is addressed and a good description of existing data is obtained. The role of a momentum-dependent mean field is emphasized and the impact of different model ingredients is investigated. Finally, simulations for photon-induced pion production are presented.

7.1 Introduction

Scattering electrons and photons off the nucleon, a wealth of information on its properties such as, e.g., structure functions, charge radius, the distribution of its quark and gluon constituents and its excitation spectrum has been gathered. As a next step of sophistication one might wonder how these properties change when embedding the nucleon in a nuclear medium. In particular, the question arises whether its structure changes in the medium due to the interaction with the other nucleons, an effect which is now known as the EMC-effect[1] [Aub83]. Furthermore, the properties of the resonance excitations in the medium are under investigation. Both the resonances and the nucleon acquire complex self-energies within in the medium which may lead both to mass-shifts and modifications of the life-times. Calculating life-times and mass-shifts with a given interaction model and comparing such predictions to the measured quantities, one is testing our understanding of the hadronic many body problem. Such studies have first been performed via inclusive experiments with nuclear targets where only the outgoing electron was detected[2]. Studying exclusive processes in the intermediate energy regime with an energy transfer of $0.1-2$ GeV, one gains further sensitivity on in-medium changes of baryonic resonances and the nucleon since such modifications may also lead to unexpected final-state interaction patterns. A related hot topic is the modification of mesons such as, e.g., σ [Mes02] and ω [Trn05] within the medium due to chiral symmetry restoration and/or collisional broadening. Since those mesons decay also to pions, such modifications must result in a modified pion yield in the detectors. Here the quest is to gain first a proper understanding of the amount of pion production one would expect assuming no modifications. Only given this understanding, conclusions on chiral symmetry restoration may be drawn. In high energy reactions at center of mass energies greater than 2 GeV, one is trying to deduce information on the build-up of the wave-function of a hadron – in other words the formation of a hadron or simply hadronization – via the measurement of the attenuation of these hadrons within the medium[3]. Especially at large Q^2 one expects to observe the onset of color transparency.

There are three key issues in the theoretical understanding of photon- or electron-scattering off nuclei. First and foremost, one needs to model effectively the nuclear ground state and

---

[1] EMC=European Muon Collaboration

[2] For a recent review cf. [Ben08].

[3] For details cf. [Fal04c, Gal05] and references therein.

take into account the modification of the elementary lepton-nucleon vertex within the nuclear medium. Furthermore, the study of exclusive channels such as pion production or nucleon knockout demands for a proper description of final state interactions of the produced particles with the nuclear medium. The last-mentioned issue can ideally be addressed within our Giessen BUU (GiBUU) framework. In this work we focus on the intermediate energy regime, where the $\gamma^\star N$ cross-section is dominated by elastic scattering, resonance excitations and non-resonant meson production. We aim at a consistent treatment of the initial γN vertex and the final state processes. Applying a precursor version of our present transport model, Lehr *et al.* [Leh03] have already been studying π, η and nucleon production within the same energy region. However, their model for the $\gamma^\star N$ reaction was less complex. In particular, there was no direct consideration of in-medium kinematics for the cross sections. Additionally, we improved the physical input to the BUU collision-term and its numerical implementation.

Another rather closely related subject is the scattering of neutrinos and nucleons, where experiments propose to shed light on the nucleon axial form factor and its strange quark content. However, such an elementary experiment would need to have a very large tank containing several tons of liquid hydrogen as a target: with a small target the count rate would be too low due to the tiny interaction cross section. Since such an explosive target is considered to be a major security risk, there is no such experiment running or even planned. So all present neutrino experiments use nuclear targets [nui] and all the measured cross sections incorporate nuclear corrections to the underlying nucleon-neutrino interaction. To draw conclusion on the underlying νN process it is therefore necessary to master these corrections. The neutrino and electron scattering off the nucleon are interconnected via iso-spin symmetry and one can treat both processes within the same formalism. So the proper description of the electron nucleus interaction is for the neutrino community a necessary benchmark of their nuclear corrections. In this work we do not consider neutrino scattering off nuclei. However, Leitner *et al.* [Lei06b, Lei06a, Lei] have developed a model for this process which uses the here presented formalism for the $\gamma^\star N$ interaction to constrain the iso-vector part of the νN interaction. Furthermore, they apply the same nuclear model and in-medium modifications as presented here. So our work serves as a direct benchmark for the work of Leitner *et al.*

This chapter is organized as follows. First, we investigate the impact of different assumptions on the nuclear ground-state. Therefore, we will study inclusive $e^- A$ and γA scattering which is mostly sensitive to this aspect. Finally, we will also consider exclusive pion production and investigate the role of final state rescattering[4].

7.2 Inclusive electron scattering off complex nuclei

7.2.1 Introduction

Electron scattering off nuclei in the regime of energy transfers between 0.1 and 1 GeV^2 has been addressed by several experiments within the last two decades, for a recent review cf. [Ben08]. Comparing the measured nuclear cross sections to the nucleon cross sections, several modifications could be observed. First, the Fermi motion within the nuclei leads to a smearing of the peak structures such as the quasi-elastic and the Δ peak. Furthermore, one observed a quenching of the spectral strength in the region of the quasi-elastic peak which was also addressed as violation of the Coulomb sum-rule [Bar88, Day93, Zgh94]. In contrast to the quenching in the peak region one observed an enhancement in the so-called *dip-region* in between quasi-elastic

---

[4] Results presented in this chapter have also been published in [Bus07a, Bus07b, Lei07, Bus08].

and Δ peak. The peak position of the Δ resonance was found to be both A and Q^2 dependent [Bar83, Sea89]: a shift towards lower masses for $Q^2 \lesssim 0.1$ and a shift towards higher masses for higher Q^2 [O'C84, Sea89, Che91, Ang96]. There is a considerable amount of theoretical work aiming at a good description of the inclusive electron cross section; cf. the recent review given by Benhar *et al.* [Ben08] for an overview. Benhar and collaborators [Ben05] employ the impulse approximation with realistic spectral functions obtained from electron-induced proton knockout data and theoretical calculations based on nuclear many body theory (NMBT). With this model, they achieve impressive agreement in the quasi-elastic (QE) peak region; however, they underestimate the data in the Δ region. In [Ben06, Nak07] they improved on this and a good description of the data also in the single-pion production region could be reached. Also, Szczerbinska *et al.* [Szc07] use Benhar's spectral functions [Ben05] for the QE contribution, but in the Δ region they apply the dynamical Sato-Lee model developed to describe photo- and electron-induced pion-production off the nucleon. A different approach, which – as our model – yields a combined investigation of neutrino and electron interactions, makes use of the superscaling properties of the electron scattering data (cf. [Ama05] and references therein). More work has been done in the QE region. In particular the model by Gil *et al.* [Gil97] yielded a particular successful description of the dip region in between the QE and Δ peak.

7.2.2 Results

Scattering of Oxygen

In the following, the results of our model are compared to data and the impacts of the most prominent model ingredients are investigated. To start the discussion, we show in fig. 7.1 our results for the inclusive reaction ${}^{16}_{8}O\,(e^-,e^-)\,X$ for a beam energy of 700 MeV and different nucleon mean fields, in-medium changes to the width have been neglected. The solid curve denotes the result without potentials, including only Fermi motion and Pauli blocking. Including a momentum-independent potential (dashed curve) does not change anything to the QE peak ($q_0 = 0. - 0.15$ GeV). However, the single-pion region ($q_0 \gtrsim 0.2$ GeV) is modified. This is due to the effect that the Δ is less strongly bound than the nucleon. Therefore, more energy must be transferred by the photon such that this binding effect is compensated. When the momentum-dependent mean field is included (dashed-dotted curve), then the faster (on average) final state nucleons experience a shallower potential than the initial state nucleons. Also the resonance potential gets shallower towards higher momentum. Therefore, even more energy must be transferred by the photon. Hence, the QE peak is broadened towards a higher energy transfer q_0 and shifted by approximately 8 MeV; also the single pion spectrum is slightly shifted towards higher energies and broadened. A similar result has also been obtained within the Walecka model [Ros80]. There the nucleon mass becomes in the medium an effective mass $m^\star(\vec{r})$ and the energy of the nucleon is given by $E_{\vec{p}} = \sqrt{\vec{p}^{\,2} + m^\star(\vec{r})}$ which can be rewritten as $E_{\vec{p}} = \sqrt{\vec{p}^{\,2} + m} + V(\vec{r},\vec{p})$ with the momentum-dependent potential

$$V(\vec{r},\vec{p}) = \sqrt{\vec{p}^{\,2} + m^\star(\vec{r})} - \sqrt{\vec{p}^{\,2} + m}\,.$$

For small momenta ($|\vec{p}| \ll m^\star$, $|\vec{p}| \ll m$), one obtains a simple harmonic dependence of the potential on the momentum:

$$V(\vec{r},\vec{p}) \approx p^2 \frac{m - m^\star(\vec{r})}{2mm^\star(\vec{r})} + m^\star(\vec{r}) - m \quad .$$

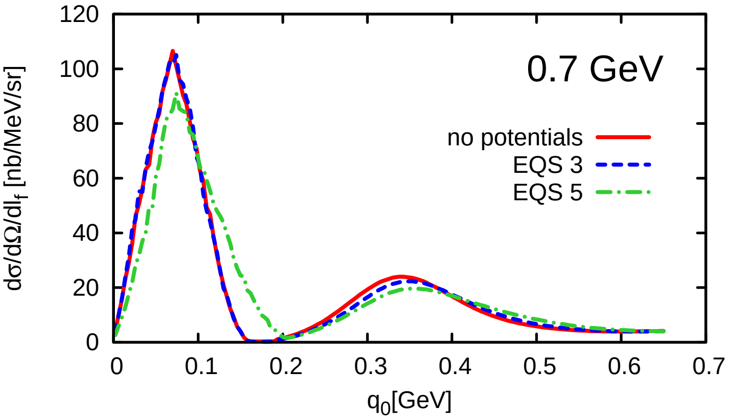

Figure 7.1: The inclusive electron cross section $d\sigma/(d\Omega dl_f)$ on ^{16}O as a function of the energy transfer q_0 for a beam energy of 0.7 GeV and a scattering angle of $\theta_{l_f} = 32°$. The graph shows the results for different nucleon potentials: no potential (solid line), momentum-independent potential EQS 3 (dashed line) and momentum-dependent potential EQS 5 (dashed-dotted line). The calculations do not include in-medium changes of the widths.

Rosenfelder [Ros80] shows that the value of $m^\star$ can then be used to fit the QE peak. We emphasize however, that we do not fit our potential to the electron data but the potential has been fixed before by nucleon-nucleus scattering [Tei97].

In fig. 7.2, we additionally included different scenarios for the in-medium width modifications which are named according to sec. 3.6.1. Obviously, all different scenarios for the in-medium width yield very similar results. Since the scenario including the Oset model (*mass-shift+Oset*) has yielded good results also for pion scattering in chapter 6, we use in the following this scenario for the in-medium width. Comparing the different in-medium width scenarios to the result obtained assuming no in-medium changes of width (dotted curve), we notice that the larger in-medium width leads to a broadening in both the QE- and pion-region.

Figure 7.3 shows the comparison of our model to the data measured by Anghinolfi *et al.* [Ang96]. From this figure we conclude that our model is considerably improved by including the in-medium width. One also notices a short-coming of our model for the QE-region in the upper left panel (beam energy=0.7 GeV). This problem could not yet been resolved. In the work of Kalok [Kal07] it was shown that the inclusion of short-range-correlations in our model lead to a lowering of the peak. These short-range correlations imply a modified momentum distribution of the ground state nucleus. However, also with Kalok's improvements [Kal07] no quantitative satisfactory result could be obtained. However, when going to larger beam energies (cf. fig. 7.3) then we see already at a slightly higher beam energy of 880 MeV very good agreement with the experimental data. The solid curves in fig. 7.3 represent our full result which agrees well with the available data. Especially the dip-region in between QE-region and single-pion region is well reproduced. At very high beam energies, a lack of $\pi\pi$ strength leads to a too low result at large photon energies. Overall, the in-medium width leads to an improvement of the model.

To analyze the problem at $E_{\text{beam}} = 0.7$ GeV more closely, we also compare our model to the experiment performed by O'Connell *et al.* [O'C84], which has very similar kinematical constraints ($E_{\text{beam}} = 0.737$ GeV, $\theta_{l_f} = 37.1°$) as the run performed by Anghinolfi *et al.* ($E_{\text{beam}} = 0.700$ GeV, $\theta_{l_f} = 32.0°$). To compare experiments one often defines the so-called Q^2 at the QE-peak. It corresponds to the Q^2 at which the center of mass energy at the hadronic

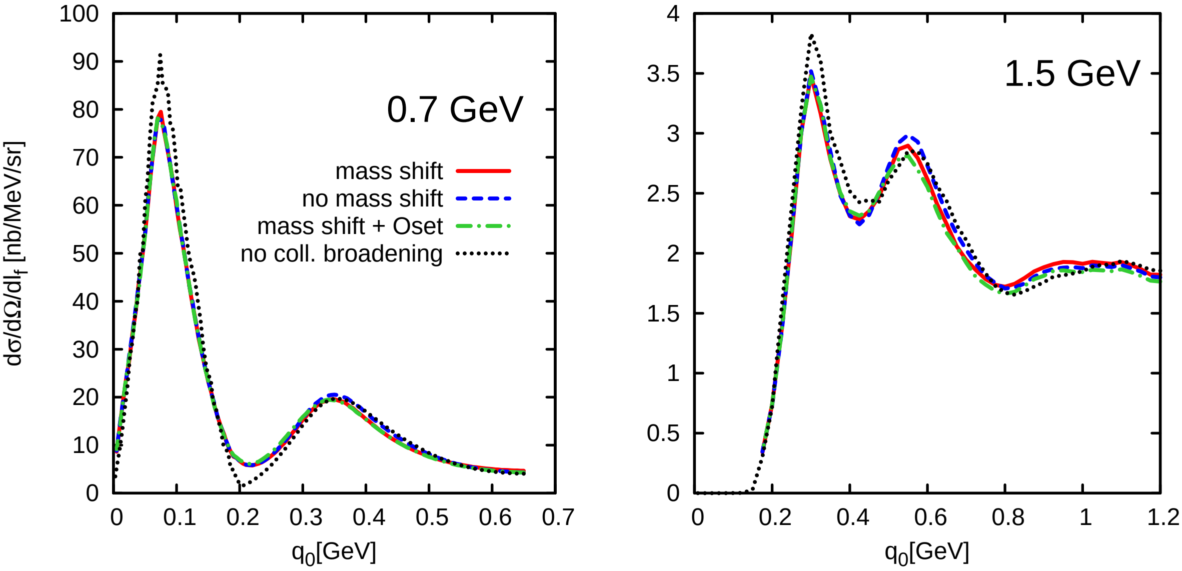

Figure 7.2: The inclusive electron cross section $d\sigma/(d\Omega dl_f)$ on ^{16}O as a function of the energy transfer q_0 for two beam energies of 0.7 GeV and 1.5 GeV and a scattering angle of $\theta_{l_f} = 32°$. All results include the momentum-dependent potential (EQS 5). The upper graph shows results for a variety of in-medium width scenarios: no modifications (dotted curve), collisional broadening via *mass-shift* scenario (solid line), via *no mass-shift* scenario (dashed line) and via *mass-shift + Oset* scenario. The data are taken from [Ang96, QEW08].

vertex equals the nucleon mass if one assumes a free nucleon target at rest. This parameter is determined by two conditions which relate Q^2 to the initial and final beam energy (E_{beam}, E_{final}) and to the scattering angle θ_{l_f}:

$$Q^2_{\text{QE-peak}} = 2m_N q_0 = 2m_N(E_{\text{beam}} - E_{\text{final}}) \quad , \tag{7.1}$$

$$Q^2_{\text{QE-peak}} = 2E_{\text{beam}}E_{\text{final}}(1-\cos\theta_{l_f}) \quad . \tag{7.2}$$

Solving these equations we get

$$Q^2_{\text{QE-peak}} = \frac{2E^2_{\text{beam}}(1-\cos\theta_{l_f})}{1+\frac{E_{\text{beam}}}{m_N}(1-\cos\theta_{l_f})} \quad . \tag{7.3}$$

This parameter does not include any in-medium input, but it gives a simple estimate on the real in-medium Q^2 at the QE-peak. The Anghinolfi and the O'Connell experiments differ slightly in this $Q^2_{\text{QE-peak}}$ value (Anghinolfi: $Q^2_{\text{QE-peak}} = 0.13$ GeV^2, O'Connell: $Q^2_{\text{QE-peak}} = 0.19$ GeV^2). Figure 7.4 shows that our model describes the O'Connell data quite well. This feature is quite astonishing and hints to some missing physics input at rather low Q^2.

In fig. 7.5, we show the contribution of the different production mechanisms to the total electron-nucleus cross section which we calculated including all in-medium modifications and in particular the in-medium changes of the width according to the *mass-shift+Oset* scenario. The dashed line shows the quasi-elastic contribution, the dashed-dotted the single-π and the dotted one the 2π contribution to the initial scattering process. One observes that going from low too high beam energies, the importance of single-π and 2π production mechanism gradually

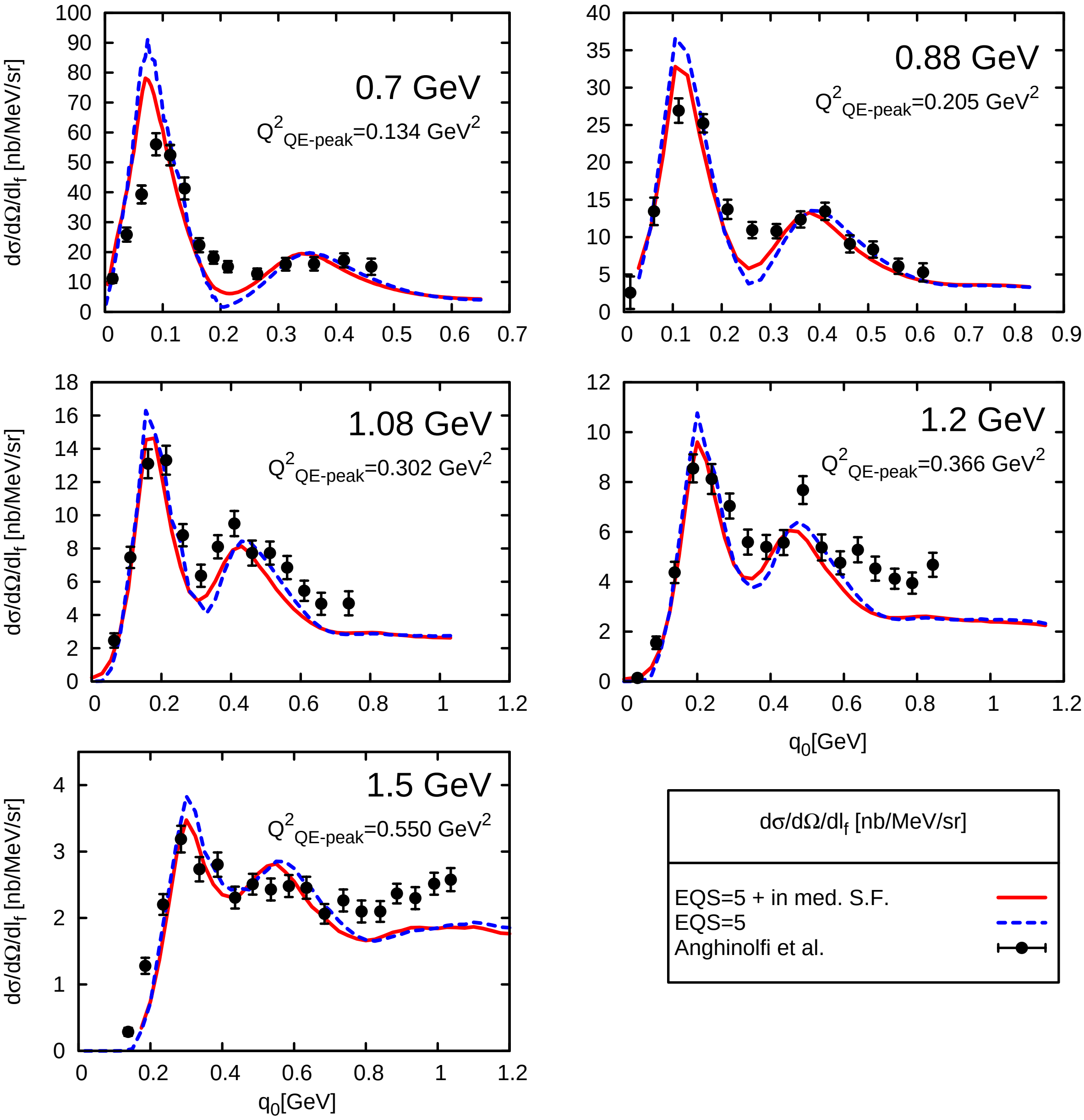

Figure 7.3: The inclusive electron cross section $d\sigma/(d\Omega dl_f)$ on ^{16}O as a function of the energy transfer q_0 at five distinct fixed electron energies (0.7, 0.88, 1.08, 1.2 and 1.5 GeV) and a scattering angle of $\theta_{l_f} = 32°$. The dashed line denotes our result, where we include all in-medium modifications besides collisional broadening. The solid line denotes the full calculation, which includes in-medium changes of the width according to the *mass-shift+Oset* scenario. The data are taken from [Ang96, QEW08] and the parameter $Q^2_{\text{QE-peak}}$ is evaluated according to eq. 7.3.

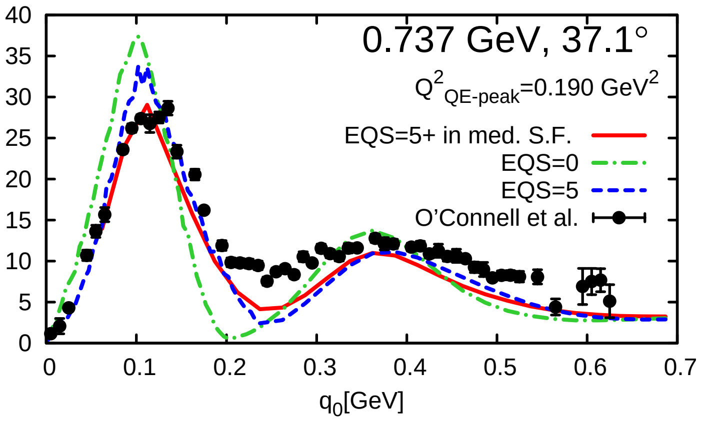

Figure 7.4: The inclusive electron cross section $d\sigma/(d\Omega dl_f)$ on ^{16}O as a function of the energy transfer q_0 for a beam energy of 0.737 GeV and a scattering angle of $\theta_{l_f} = 37.1°$ in comparison to the data measured by O'Connell *et al.* [O'C84]. The parameter $Q^2_{\text{QE-peak}}$ is evaluated according to eq. 7.3.

increases, whereas at low energies the quasi-elastic contribution is dominating. Note that this result does not yet include any FSI of the outgoing particles and the classification into different channels is solely based on the initial vertex and not on the final-state multiplicities.

Impact of the initial phase space distribution. In the following we want to compare results for two different phase space distributions of the target nucleons. As outlined in sec. 3.8, we assume for the nuclear ground state that the positions of the nucleons are distributed according to density parametrizations obtained from low-energy electron scattering and Hartree-Fock calculations. The momenta of the nucleons are distributed according to a local Thomas-Fermi (LTF) approximation, i.e. it is assumed that at each space-point $\vec{r}$ the nucleon momenta occupy a uniform sphere in momentum space with a radius given by the Fermi momentum $p_f(\vec{r})$. This gives phase space distributions for the ground-state protons and neutrons which are given by

$$f_{n,p}(\vec{r},t,\vec{p}) = \Theta\left(p_f^{n,p}(\vec{r}) - p\right) \tag{7.4}$$

with the Fermi momenta

$$p_f^{n,p}(\vec{r}) = \sqrt[3]{3\pi^2\rho^{n,p}(\vec{r})} \quad . \tag{7.5}$$

In the literature, one may also find a more simplistic model which we denote 'naive Fermi gas model' (FG). Here the Fermi momentum is a direct input parameter and the whole nucleus is assumed to have the same Fermi momentum. As a consequence the nuclear density becomes constant all over the nucleus and is given by

$$\rho_{FG} = \frac{2}{3\pi^2}p_f^3 \quad , \tag{7.6}$$

which means that the surface region of the nucleus is neglected. Especially for small nuclei, where the surface is large compared to the core, this approximation is questionable.

For a nucleon at rest, there is according to eq. G.28 only one photon energy (if the incoming beam energy and scattering angle are fixed)

$$q_0 = \frac{Q^2}{2m} = \frac{E^2_{\text{beam}}(1 - cos\theta_f)}{E_{\text{beam}}(1 - \cos\theta_f) + m} \quad , \tag{7.7}$$

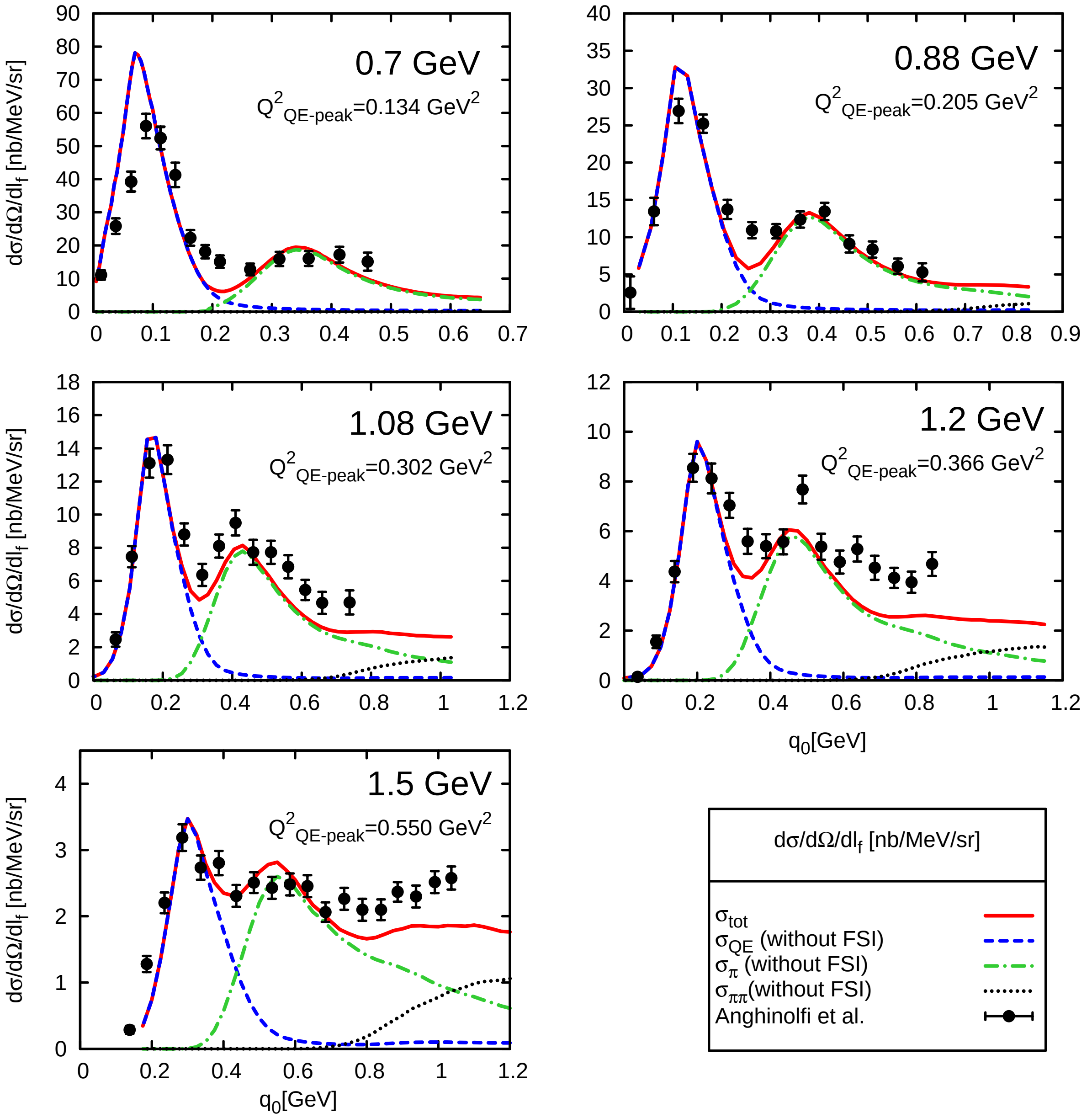

Figure 7.5: The inclusive electron cross section $d\sigma/(d\Omega dl_f)$ on ^{16}O as a function of the energy transfer q_0 at five distinct fixed electron energies (0.7, 0.88, 1.08, 1.2 and 1.5 GeV) and a scattering angle of $\theta_{l_f} = 32°$. The solid line denotes our full result, where we include all in-medium modifications and in particular in-medium changes of the width according to the *mass-shift+Oset* scenario. The data are taken from [Ang96, QEW08]. The dashed line shows the quasi-elastic contribution, the dashed-dotted the single-π and the dotted one the 2π contribution to the initial scattering process. This result does not yet include any FSI of the outgoing particles. The parameter $Q^2_{\text{QE-peak}}$ is evaluated according to eq. 7.3.

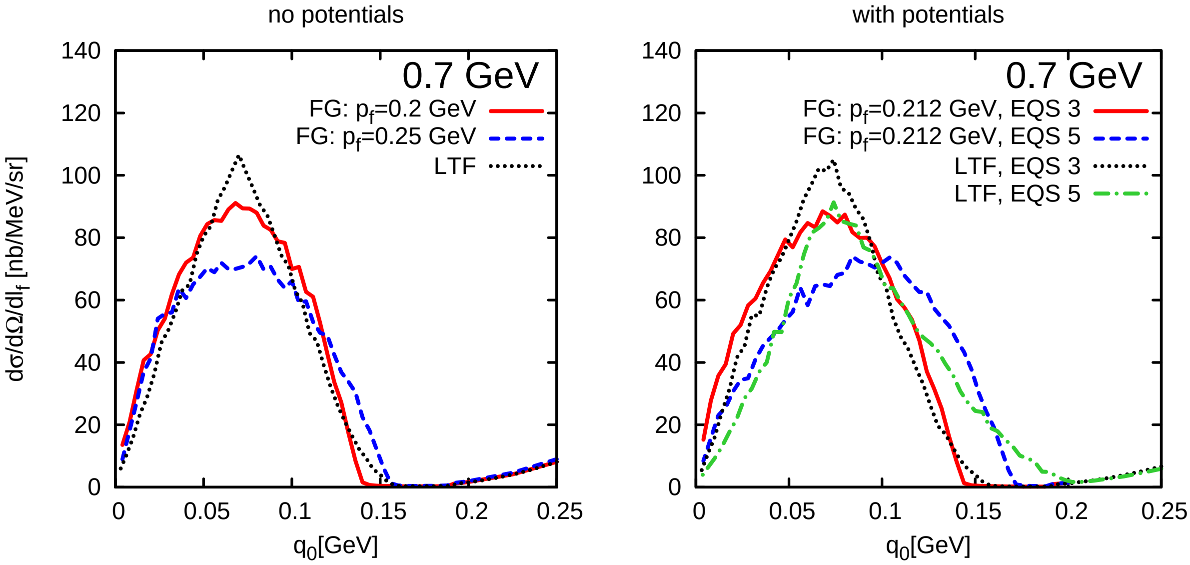

Figure 7.6: The inclusive electron cross section $d\sigma/(d\Omega dl_f)$ on ^{16}O as a function of the energy transfer q_0 for a beam energy of 0.7 GeV and a scattering angle of $\theta_{l_f} = 32°$. The graphs on the left panel show the results for a calculation where we neglected potentials and in-medium width modifications. The results for various assumptions concerning the momentum distribution of the target nucleons are shown: Fermi gas with Fermi momentum $p_f = 0.2$ GeV (solid line), Fermi gas with Fermi momentum $p_f = 0.25$ GeV (dashed line), momentum distribution according to local Thomas-Fermi (LTF) approximation (dashed-dotted line). The calculations shown on the right left panel include mean field potentials, but also no in-medium changes of the widths. The FG result on the right panels was obtained with a Fermi momentum of 212 MeV.

for which a quasi-elastic (QE) event is possible. In appendix sec. G.2.2 it is shown, that the finite target nucleon momenta within a Fermi gas lead to a finite range of possible q_0 centered roughly around $q_0 = \frac{Q^2}{2m}$, for which a QE-event can be realized. The size of this range is determined by the Fermi momentum: the larger the Fermi momentum the larger the possible range of q_0's. Thus going from a nucleon target to a Fermi gas target, the sharp δ-like QE-peak for the nucleon target gets replaced by a smeared structure with a peak at $q_0 \approx \frac{Q^2}{2m}$. The momentum distribution for the LTF scheme represents an integral of several different Fermi gases having different Fermi momenta. Thus one also expects for the LTF scheme a smearing of the QE-peak around $q_0 \approx \frac{Q^2}{2m}$.

To compare the LTF and FG schemes we use the very same physics input, in particular same potentials and widths, and vary only the initial $\vec{r}$ and $\vec{p}$ distributions focusing on the quasi-elastic peak.

On the left panel of fig. 7.6, we show the results for different input distributions neglecting all in-medium modifications besides Pauli blocking and Fermi motion. The dashed-dotted curve represents the result with our standard momentum distribution according to the local-Thomas-Fermi (LTF) ansatz. One observes, that using an initial distribution according to the FG scheme with a constant Fermi momentum of 0.2 GeV yields already a slightly lower and broader QE-peak compared to the LTF result. In correspondence to the result derived in eq. G.34 of

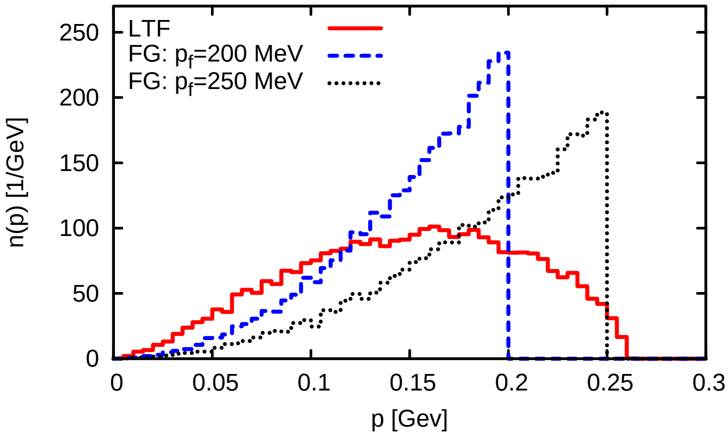

Figure 7.7: Momentum densities $n(p)$ for different phase-space distributions of the ground-state nucleons in $^{16}_{8}$O. The solid curve depicts the result for the LTF scheme, the dashed and dotted curves show the densities for a naive Fermi gas with $p_f = 200$ MeV and $p_f = 250$ MeV. The momentum density is normalized to $\int n(p)dp = A$.

appendix sec. G.2.2, we observe for $p_f = 200$ MeV a QE-contribution in the photon energy region of $0 - 140$ MeV, which corresponds to a final electron energy of $560 - 700$ MeV. Fig. 7.7 shows the momentum densities of the target nucleons for the LTF scheme (solid line) and the Fermi gas with $p_f = 200$ MeV. Both distributions have the same average value for the nucleon momentum of 150 MeV. However, within the LTF scheme there are more nucleons with low momenta which leads to more strength around the original QE-pole at $q_0 \approx \frac{Q^2}{2m}$. The surplus of high-momentum nucleons for the LTF compared to the FG scheme leads to a slightly higher maximal photon energy for LTF and to a slight broadening of the peak at low and high photon energies for LTF. With a further increase of the Fermi momentum to 0.25 GeV we conceive a further broadening of the QE peak, which leads to a prominent drop of the peak height. The peak position is however insensitive to the magnitude of the Fermi momentum. Thus one could fit the height of the QE-peak within the FG scheme by a variation of its free parameter, namely the Fermi momentum. Note that a Fermi momentum of 0.25 GeV is not very realistic: on the basis of a proper density profile for Oxygen (cf. sec. 3.8) one can not generate such a high average Fermi-momentum in LTF for the dilute Oxygen nucleus.

On the right panel of fig. 7.6, we additionally considered the impact of two different mean-field potentials for the nucleons and compare the LTF results to FG results with $p_f = 212$ MeV (this Fermi momentum gives a nuclear density of 0.84 fm^{-3} which is approximately the same as the average nuclear density of an $^{16}_{8}$O nucleus). For the FG scheme, the density is constant and therefore all nucleons are bound by a similar potential which only differs due to its momentum-dependence. For the LTF scheme, however, the nucleons feel quite different potentials depending on their position: in the surface the potential is weak whereas in the core the potential is strongly attractive. The solid and dotted curves on the right panel of fig. 7.6 show the results for a momentum-independent potential (EQS 3). Comparing our results with such a potential to the ones without potential (on the left panel) shows that a momentum independent potential has almost no visible impact on the results. This feature is based on the fact that the potentials for the incoming and outgoing nucleons are the same. Therefore, there is no change in the energy transfer to the nucleon. Also the slightly lower nucleon in-medium masses due to the

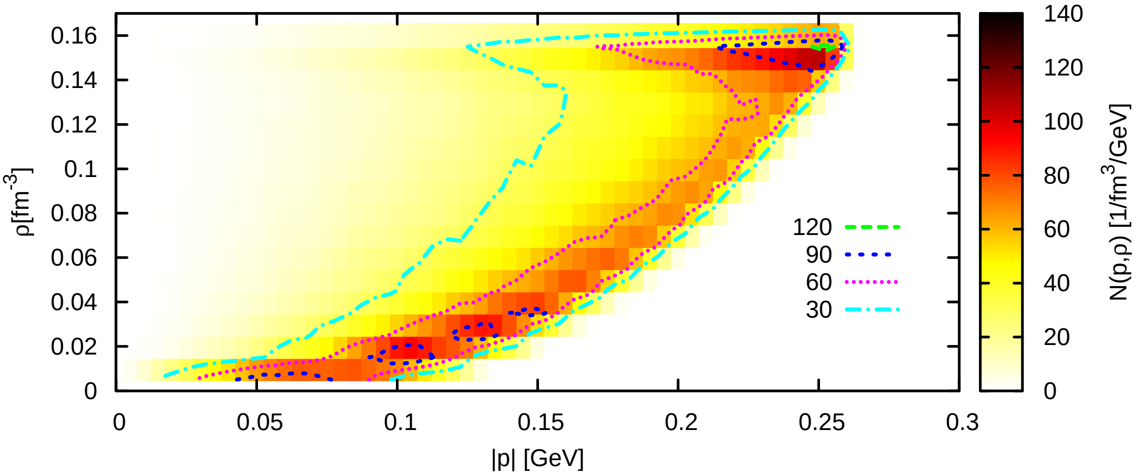

Figure 7.8: The upper graph shows for the LTF scheme the probability $N(|p|, \rho)$ to find a nucleon with absolute momentum $|p|$ at a position with nuclear matter density ρ within an $^{16}_{8}$O nucleus. The normalization condition is given by $\int d\rho d|p|\ N(|p|, \rho) = 1$.

mean-field potential do not lead to a sizable modification of the cross section. The dashed and dashed-dotted curves on the right panel of fig. 7.6 show the results for the FG and LTF schemes when including a momentum dependent potential. One observes in both cases a shift of strength towards higher photon energies. This shift comes from the potential difference of the slow and strongly bound target nucleon to the faster and less strongly bound final-state nucleon. However, there is a qualitative difference in the spectra for LTF and FG: the QE-peak for the FG scheme is shifted by roughly 25 MeV towards higher q_0 while it hardly shifts for the LTF scheme.

This astonishing feature comes from the fact that the LTF scheme yields a strong correlation of the initial nucleon momenta and the density at the position of the initial nucleon. This correlation is depicted in fig. 7.8, where the probability to find a nucleon within an $^{16}_{8}$O nucleus with a given momentum at a position with a given density is plotted. One observes that the probability to find a low-momentum nucleon is highly concentrated at low densities. Without potentials, the region close to the peak of the quasi-elastic contribution comes from scattering events with nucleons which have low-momentum. The larger the momentum of the nucleon, the more the necessary photon energy for a QE-event differs from the mean photon energy in a Fermi gas which is roughly the same as for the free nucleon $q_0 = Q^2/2m$ (cf. the discussion in appendix G.2.2). Including potentials the kinematics for those nucleons with low-momenta barely change in the LTF scheme, since they sit mostly in a low-density environment. Thus the region close to the original peak does not change very much. Those nucleons which have high momenta and which are mostly sitting within a high-density environment contributed without potentials to the regions to the left and to the right of the peak. In fact one observes in fig. 7.6 that the momentum-dependent potential modifies the overall spectrum quite considerably, due to the fact that the formerly off-peak strength is shifted due to the strong potentials at high densities. For the FG scheme, however, there is no such correlation of density and momentum since the density is constant all over the nucleus. Thus the peak is shifted in the same manner as the off-peak strength and one observes within the FG scheme also a large shift of the peak.

Impact of the collisional broadening of the resonances. In fig. 7.2, we have already observed that all different scenarios for the in-medium width yield very similar results. We discussed in

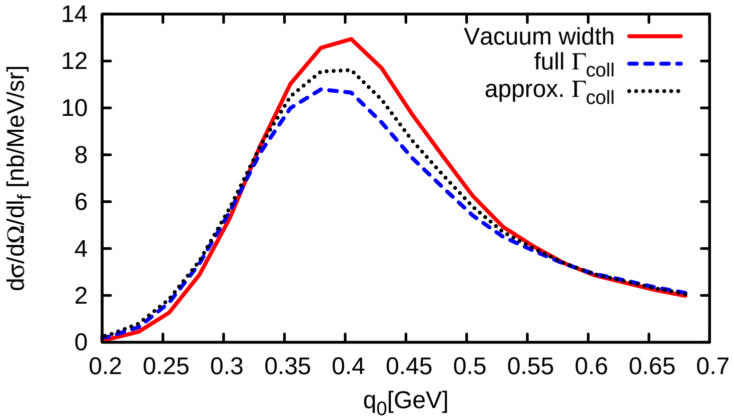

Figure 7.9: The Δ contribution to inclusive electron-oxygen cross section $d\sigma/(d\Omega dl_f)$ as a function of the energy transfer q_0 at a fixed electron energy of 0.88 GeV and a scattering angle of $\theta_{l_f} = 32°$. The solid line shows the result obtained with the vacuum width, for the dashed one we used the full in-medium width whereas we used for the dotted one an approximation according to eq. 7.11. Baryon potentials have been neglected.

sec. 3.6.1 the complicated numerical implementation of the collisional broadening using the full model. Thus the question remains, whether a very much simplified model for the collisional broadening could be implemented which reproduces the main features of the full model, but costs less computation time than the full model. Let us consider the Δ resonance as a showcase. In the mass-shift scenario the which is given by eq. 3.54:

$$\Gamma_{\text{coll}}(p,\vec{r},t) = \int_{\text{Fermi sea at } \vec{r}} \sigma(p,p')\ v_{\text{rel}}(p,p')\ \frac{d\vec{p}\,'}{(2\pi)^3} \quad , \tag{7.8}$$

with $\sigma = \sigma_{N\Delta\to N\Delta} + \sigma_{N\Delta\to NN} + \sigma_{N\Delta\to NR}$ (cf. appendix A.2 for details on the cross sections). Let us approximate this width using an constant total cross section $\hat{\sigma}$ which gives

$$\Gamma_{\text{coll}}(p,\vec{r},t) \approx \hat{\sigma}\rho\frac{|\vec{p}|}{p_0} \quad . \tag{7.9}$$

The free parameter $\hat{\sigma}$ must be estimated, we choose the value of the $p\Delta^+ \to X$ interaction cross section of a Δ^+ at its pole mass having a momentum $|\vec{p}| = 0.6$ GeV with a proton at rest. In our model this value is given by $\hat{\sigma} \approx 36$mb, so we get

$$\Gamma_{\text{coll}}(p,\vec{r},t) \approx 119 \text{ MeV}\frac{\rho}{\rho_0}\frac{|\vec{p}|}{p_0} \quad . \tag{7.10}$$

$$\Leftrightarrow \Gamma_{\text{coll,resonance r.f.}}(p,\vec{r},t) \approx 119 \text{ MeV}\frac{\rho}{\rho_0}\frac{|\vec{p}|}{\sqrt{p^\mu p_\mu}} \quad . \tag{7.11}$$

This formula for the width can now easily be implemented, even without the need to tabulate it. Fig. 7.9 shows the Δ contribution to the inclusive electron-oxygen scattering cross section at a fixed electron energy of 0.88 GeV and a scattering angle of $\theta_{l_f} = 32°$. We neglected the real part of the self energies and focused on the impact of the collisional broadening. The solid curve shows the result obtained with the vacuum width for the Δ, i.e. without collisional broadening.

The dashed curve has been obtained with the full in-medium width, whereas the dotted one has been obtained by setting

$$\Gamma_{\text{tot}}^{\text{med}} = \Gamma_{\text{vac}} + \Gamma_{\text{coll,resonance r.f.}} \tag{7.12}$$

with the approximation for $\Gamma_{\text{coll,resonance r.f.}}$ according to eq. 7.11. One sees that both the full width and the approximation lead to a broadening of the Δ peak. Tuning the value of $\hat{\sigma}$ one could even get a better agreement, however: *is this what we want*? The value of $\hat{\sigma}$ depends on the average Δ momentum during the reaction. At higher Q^2 the 3-momentum transfers at the Δ-peak are higher than at low Q^2, hence the average Δ momentum is higher. Thus one would need to consider different $\hat{\sigma}$ as input for different reactions, which is not very aesthetic. From the author's point of view, the tabulation of the width as a function of mass, $|\vec{p}|$ and density has the great advantage that one doesn't need to tune parameters such as $\hat{\sigma}$. Finally, we will anyhow mostly be interested in the simulation of exclusive events where the computation time used for the width tabulations is of the order of 10% (confer sec. B.3 for details on CPU time consumption). Hence using the full model for the width does not hinder us from performing calculations.

Impact of the normalization of the spectral functions. In sec. 3.7, we pointed out the importance of a proper real part of the self energies (Π) for the normalization of the resonance spectral functions. To study the impact of this normalization procedure, we want to study two different scenarios in which we include or neglect the dispersive contribution to Re[Π] while keeping the mean field contribution in both cases. In fig. 7.10, we show the results for a beam energy of 1080 MeV at the same electron scattering angle ($\theta_{l_f} = 32°$) as above. The solid lines in the figure denote the results including the dispersive contributions, the dashed one have been obtained neglecting these contributions. The left upper panel shows the sum of all resonance contributions for the e^-p reaction, i.e. $\sum_R d\sigma_{e^-p\to Re^-}/(d\Omega dl_f)$. Since the normalization of the spectral function was mostly too large without the dispersive contributions (cf. sec. 3.7), it is intuitive that including the dispersive contributions, which normalize the spectral function, yields smaller resonance contributions in e^-p-scattering. In the total e^-p-scattering cross-section, which is shown on the right upper panel of fig. 7.10, one can not observe any impact of the dispersive contributions. This becomes clear when recalling the definition of the background cross section for the dominating single-π production mechanism. By definition (cf. eq. 4.116) the sum of background cross section and resonances yield the MAID cross section, no matter how large the resonance contributions are. This means that including the dispersive contributions, i.e. restoring the normalization of the spectral functions, we simply move strength from the resonances to the background. This fact becomes important in the medium, since we only modify the resonance part of the cross section in the medium while the background cross section stays untouched. To evaluate this in-medium effect, we show in the lower panels of fig. 7.10 the same comparison with an Oxygen nucleus instead of a proton as target. Again, there is a difference in the resonance contribution which is almost fully compensated in the total cross section by the differing backgrounds. Note that the resonance cross sections are smaller when the dispersive contributions are included, however the total cross section is slightly larger for this case. We conclude that our background treatment, which basically absorbs the normalization error of the spectral functions into the absolute magnitude of the background, leads to the fact that including or neglecting the dispersive parts of the real parts of the self energies has almost no impact on inclusive electron-nucleus cross sections.

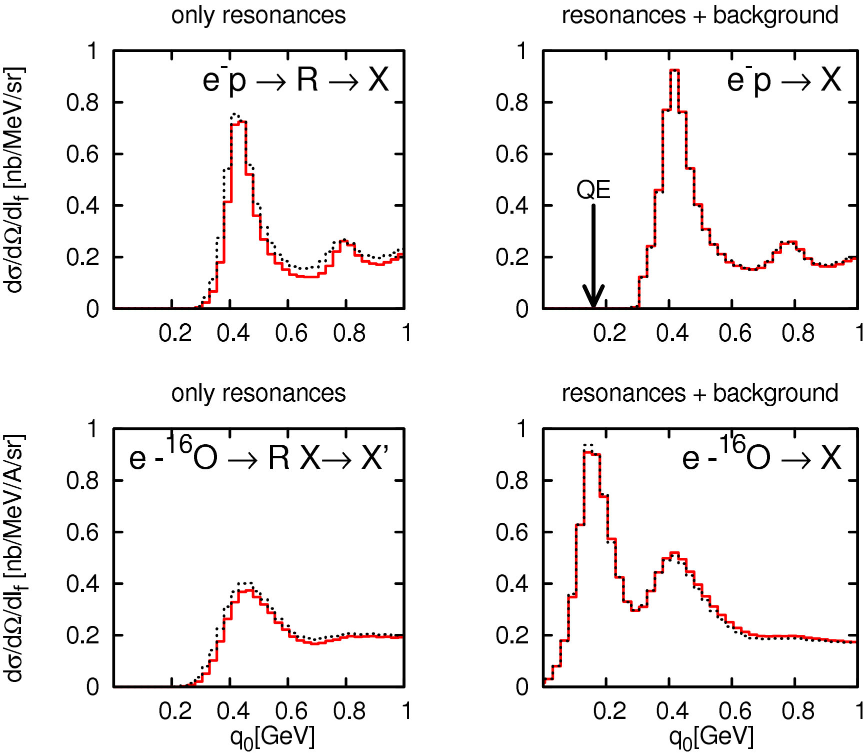

Figure 7.10: The inclusive electron-proton (upper panels) and electron-oxygen (lower panels) cross section $d\sigma/(d\Omega dl_f)$ as a function of the energy transfer q_0 at a fixed electron energy of 1.08 GeV and a scattering angle of $\theta_{l_f} = 32°$. The left panel shows the sum of all resonance contributions, the right one the total cross section. The dotted line denotes the resonance contributions neglecting the dispersive contributions to the real parts of the self energies, the solid one has been calculated including the dispersive contribution. The arrow in the upper right panel denotes the proper photon energy for quasi-elastic scattering, which gives for the proton target a δ-like contribution to $d\sigma/(d\Omega dl_f)$.

Scattering off Iron

We performed the same analysis as for the ${}^{16}_{8}$O target also for the heavier ${}^{56}_{2}$Fe target, which is one of the preferred target materials of many neutrino experiments. Our results for $d\sigma/(d\Omega dl_f)$ with $Q^2 = 0.09 - 0.13$ at the QE-peak, which is almost the same Q^2 as for the 700 GeV Oxygen run performed by Anghinolfi *et al.*, are shown in the upper four panels of fig. 7.11. Comparing these results to the data measured by Baran *et al.* [Bar88] exhibits the same features as for the low-Q^2 results for Oxygen: the quasi-elastic peak is considerably overestimated whereas the dip region is underestimated. In the lower panels of fig. 7.11 and in fig. 7.12 we again show the inclusive cross section – however, at different kinematical set-ups according to experiments performed by Sealock *et al.* [Sea89], Chen *et al.* [Che91] and Day *et al.* [Day93], which lead to higher Q^2 at the QE-peak. The data show a melting of the peak structures when going from those experiments with low Q^2 at the QE-peak to those with high Q^2. Altogether the agreement with data is at a satisfying level of 10-20% for most of the energy ranges. However, there is a tendency to underestimate strength at high energy transfer which is at high photon energies due to missing 2π strength, but at the QE-peak not yet understood.

Conclusions

We conclude, that the overall agreement to the data is improved by a calculation which in addition to a local Fermi gas momentum distribution also includes a mean field and in-medium spectral functions. Especially at low energies, a proper treatment of the nucleon spectral function is important. The increase of the energy loss due to a momentum-dependent nucleon potential reshapes the QE peak considerably. An additional modification of the nucleon width leads to further broadening and decrease of the QE peak height. In the single-π and Δ production region[5], we achieve a good description for all energies for the ${}^{16}_{8}$O-target – for the ${}^{56}_{26}$Fe target the description is not as good as for ${}^{16}_{8}$O. The in-medium modifications improve the overall correspondence with the data. In the dip region, which is conventionally attributed to 2N excitations, the description is considerably improved due to the previously discussed broadening of the QE peak. At higher beam energies, the data are underestimated at high photon energies q_0 due to the fact that 2π-production channels have not yet been included.

An impulse approximation calculation by Benhar *et al.* [Ben05] that uses nuclear many-body theory (NMBT) spectral functions yields in the QE-region a better result for the Anghinolfi [Ang96]-experiment at 700 MeV beam energy. However, already at a slightly higher beam energy of 1080 MeV our model and the NMBT one yield equally good results for the QE peak. We thus conclude, that our simple ansatz for the in-medium width (cf. eq. 3.54) and the inclusion of a proper potential incorporate the main features of the nucleon spectral function in the medium. The pion production in the NMBT calculation of Benhar *et al.* [Ben05] has lately been improved in [Nak07] using similar methods as in our calculations.

7.2.3 Tuning the mean field potential

In the previous sections we used a mean field potential according to eq. 3.29 with potential parameters which have been fixed by Teis [Tei96] using input from nucleon-nuclei scattering (cf. table 3.4 for the parameter values). However, the question arises how reliable these parameters are and whether our results could be improved by fine-tuning the parameters in a sensible manner.

---

[5] In the medium, the Δ has also pion-less decay modes and contributes, therefore, not only to single-π production.

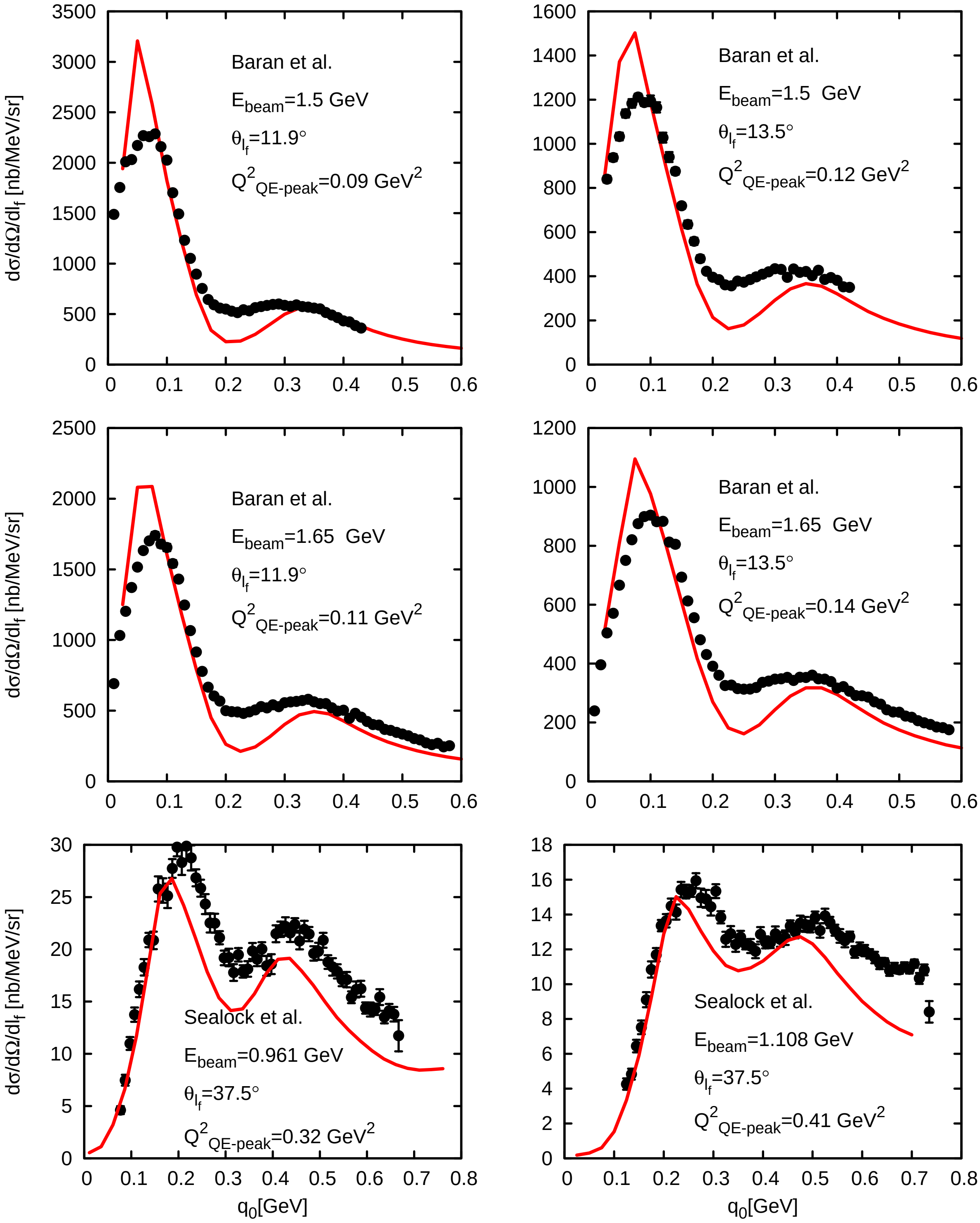

Figure 7.11: The inclusive electron cross section $d\sigma/(d\Omega dl_f)$ on ^{56}Fe as a function of the energy transfer q_0 for various electron beam energies E_{beam} and electron scattering angles θ_{l_f}. In each panel, the parameter $Q^2_{\text{QE-peak}}$ evaluated according to eq. 7.3 is given as an estimate of Q^2 at the quasi-elastic peak. The curves represent results obtained with our full model, i.e. both the momentum-dependent potentials and the in-medium broadening of the widths are included. The data are taken from [Sea89, Bar88] and the parameter $Q^2_{\text{QE-peak}}$ is evaluated according to eq. 7.3.

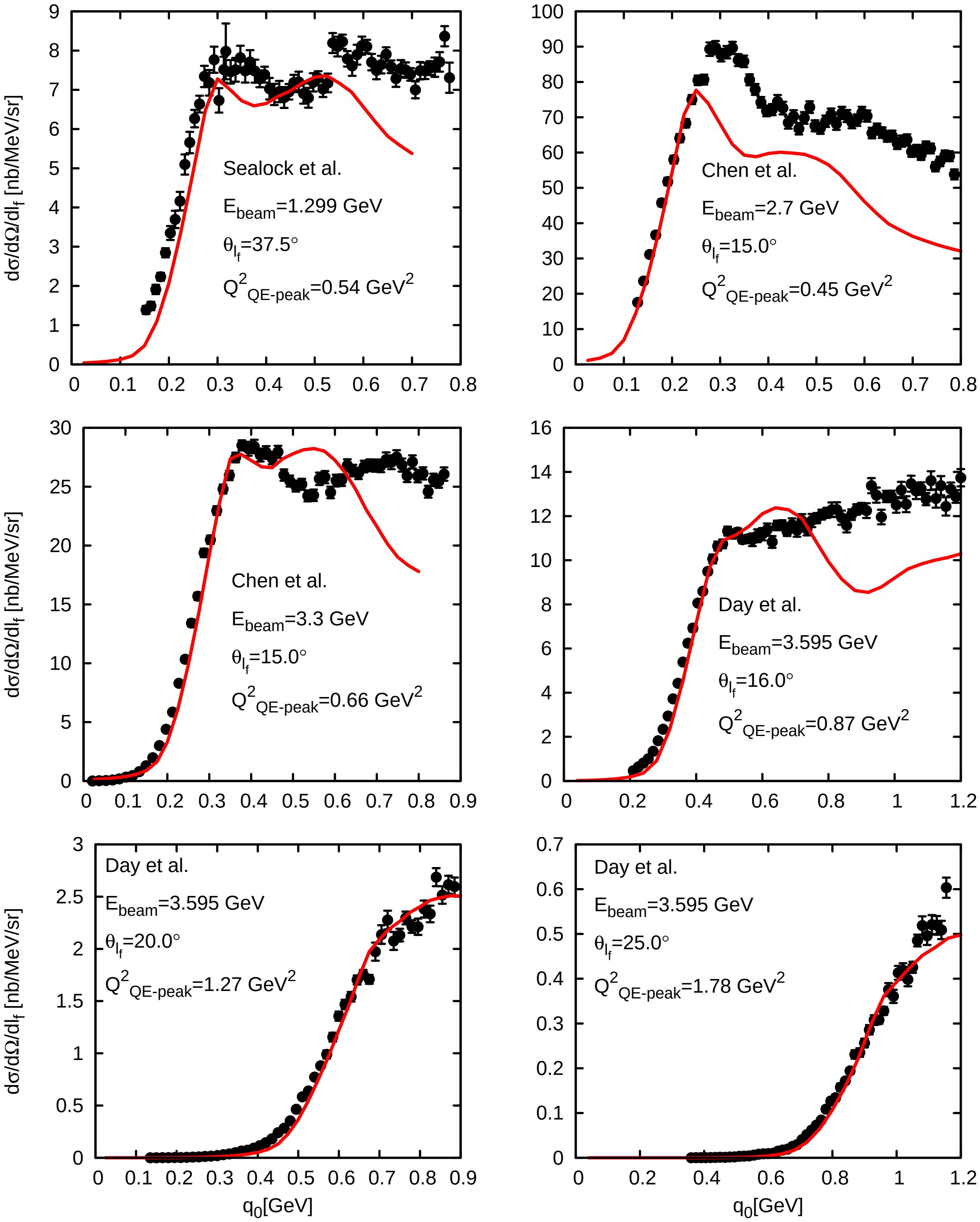

Figure 7.12: Same as fig. 7.11 for different electron kinematics. The data are taken from [Sea89, Che91, Day93].

Appendix A.4.1 details the fixing of the parameters which depends on five physical inputs: the nuclear matter saturation density ρ_0, the nuclear matter compressibility C, the nuclear matter binding energy E_{bind}, the depth U of the single particle potential A_N^0 for $\vec{p} = 0$ at saturation density and the momentum p_0 at which A_N^0 vanishes at saturation density.

In the following we choose

$$\begin{aligned} \rho_0 &= 0.16 \text{ fm}^{-3} \quad , & (7.13) \\ C &= 220 \text{ MeV} \quad , & (7.14) \\ E_{\text{bind}} &= 16 \text{ MeV} \quad . & (7.15) \end{aligned}$$

The choices for ρ_0 and for the compressibility C differ slightly from Teis' choice for those parameters. Teis used $\rho_0 = 0.168 \text{ fm}^{-3}$ which we replaced by a more up-to-date value. Both a compressibility of 290 MeV (EQS 5) and 220 MeV are in correspondence with data on transverse and longitudinal flow in high-energy heavy-ion reactions [Dan02]. However, the analysis by Danielwicz [Dan02] seems to prefer a lower value of C such as 220 MeV. For the determination of the parameter sets presented in table 3.4 the potential depth at saturation density and vanishing momentum was assumed to be $U = -75$ MeV. Additionally the momentum p_0 was set to 800 MeV. Those parameters have been estimated by Welke *et al.* [Wel88] based on a comparison of different optical model fits to nucleon-nuclei scattering. We consider those two parameters to be the most suited ones for our fine-tuning procedure, since the momentum dependence of the potential does have a prominent impact on the observed inclusive electron scattering cross section.

Let us first analyze our freedom in choosing p_0 and U. For this, fig. 7.13 shows all possible combinations of p_0 and U which fulfill the conditions stated in eq. A.77-A.81 with the choice of ρ_0, C and E_{bind} according to eq. 7.13-7.15. Obviously, there is wide range of possible (p_0, U)-combinations also if we restrict ourselves to solutions with $\tau < 2.5$. This limitation is meant to restrict the second term of eq. 3.29 to a mainly three-body interaction.

Fig. 7.14 shows the results for a, b, c, τ and Λ as a function of p_0 and U keeping ρ_0, C and E_{bind} fixed according to eq. 7.13-7.15. Decreasing the value of U must lead to shift of attractive strength from the non-momentum dependent part of the potential to the momentum dependent part. Consequently fig. 7.14 shows that the influence of the first two terms in eq. 3.29 decrease, i.e. a increases and b decreases, and the influence of the third term increases, i.e. c decreases, if U decreases. At low U ($U \lesssim -0.1$ GeV) the value of a becomes even positive. Thus the first term in eq. 3.29 starts counter-acting the third one. Both terms describe a pure two-body interaction: the first one describes a momentum independent short-range interaction while the second one depends on momenta, represents therefore a more long-ranged contribution to the nucleon force. In the panel showing the Λ parameter one observes that a more attractive potential at $p = 0$ leads to a lower value of λ, hence the Yukawa mass of the exchanged meson decreases, i.e. the interaction described by the third term becomes more long-ranged.

Now let us try to tune the potential to improve on the results presented in fig. 7.3. The two upper panels of fig. 7.3 show that the shift of the quasi-elastic peak is underestimated by roughly $20 - 30$ MeV at these Q^2 values. Around the nucleon QE-peak the three-momentum transfer of the photon amounts to roughly $300 - 400$ MeV. To shift the peak to a higher photon energy transfer one must generate a higher energy loss during the reaction, which is determined by the difference of the incoming to outgoing nucleon potentials. Thus we would get a larger shift, if our potential offered a larger momentum gradient at momenta in the range of $0 - 600$ MeV. To cure this problem one can decrease the value of U which has two major consequences: first of all the momentum dependent term becomes more important, i.e. $|c|$ increases, and as a second effect Λ

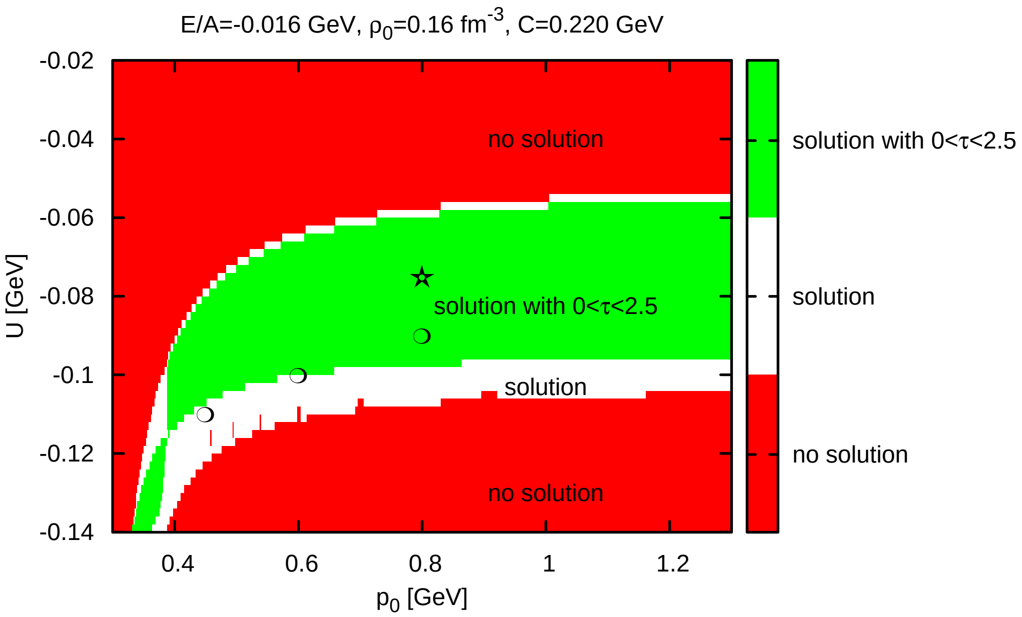

Figure 7.13: The upper figure depicts the possible parameter space for p_0 and U, if one sets ρ_0, C and E_{bind} according to eq. 7.13-7.15. The star at $p_0 = 0.8$ GeV and $U = 0.075$ GeV shows the (p_0, U)-combination chosen by Teis [Tei96]; the open circles depict the parameter sets chosen according to table 7.1.

	U_0[GeV]	p_0[GeV]	a[GeV]	b[GeV]	τ	c[GeV]	Λ[fm^{-1}]
Set #1	-0.09	0.8	-0.0229	0.0339	1.82	-0.102	0.960
Set #2	-0.1	0.6	0.00572	0.0136	2.61	-0.144	0.807
Set #3	-0.11	0.45	0.0567	0.00475	3.69	-0.145	1.180

Table 7.1: Different parameter sets a, b, τ, c and Λ for the nuclear mean field potential defined in eq. 3.29. The parameters sets differ in the potential depth U and the root momentum p_0 and share a common definition of ρ_0, C and E_{bind} according to eq. 7.13-7.15.

decreases and therefore the momentum dependence becomes stiffer. For our studies we choose three different sets for U and p_0 given in table 7.1 and the resulting single particle-potentials for the nucleon are depicted in fig. 7.15 in comparison to the EQS 5 potential used before. Fig. 7.15 shows the potential as a function of momentum for four distinct density cuts. It is very remarkable that at $\rho = 0.08$ fm^{-3}, which is close to the average nuclear density[6] in Oxygen of 0.085 fm^{-3}, set #1-3 produce a potential difference $A_N^0(p = 0 \text{ MeV}) - A_N^0(p = 400 \text{ MeV})$ of 30-40 MeV, while EQS 5 gives there only approximately 20 MeV. Additionally, this higher potential difference is visible for all density cuts. Hence the stiffer momentum dependence must also be visible in electron-scattering via a higher energy loss in the problematic regime of 400 MeV 3-momentum transfer.

The results obtained with the new potential parameter sets for the inclusive electron- ${}^{16}_{8}$O scattering cross-section are shown in fig. 7.16, where on observes a shift of strength towards higher energies for the new parameter sets but almost no shift in the peak position. The

---

[6] The average density is given by $\langle\rho\rangle = \frac{\int \rho(r)^2 d^3r}{\int \rho(r) d^3r}$.

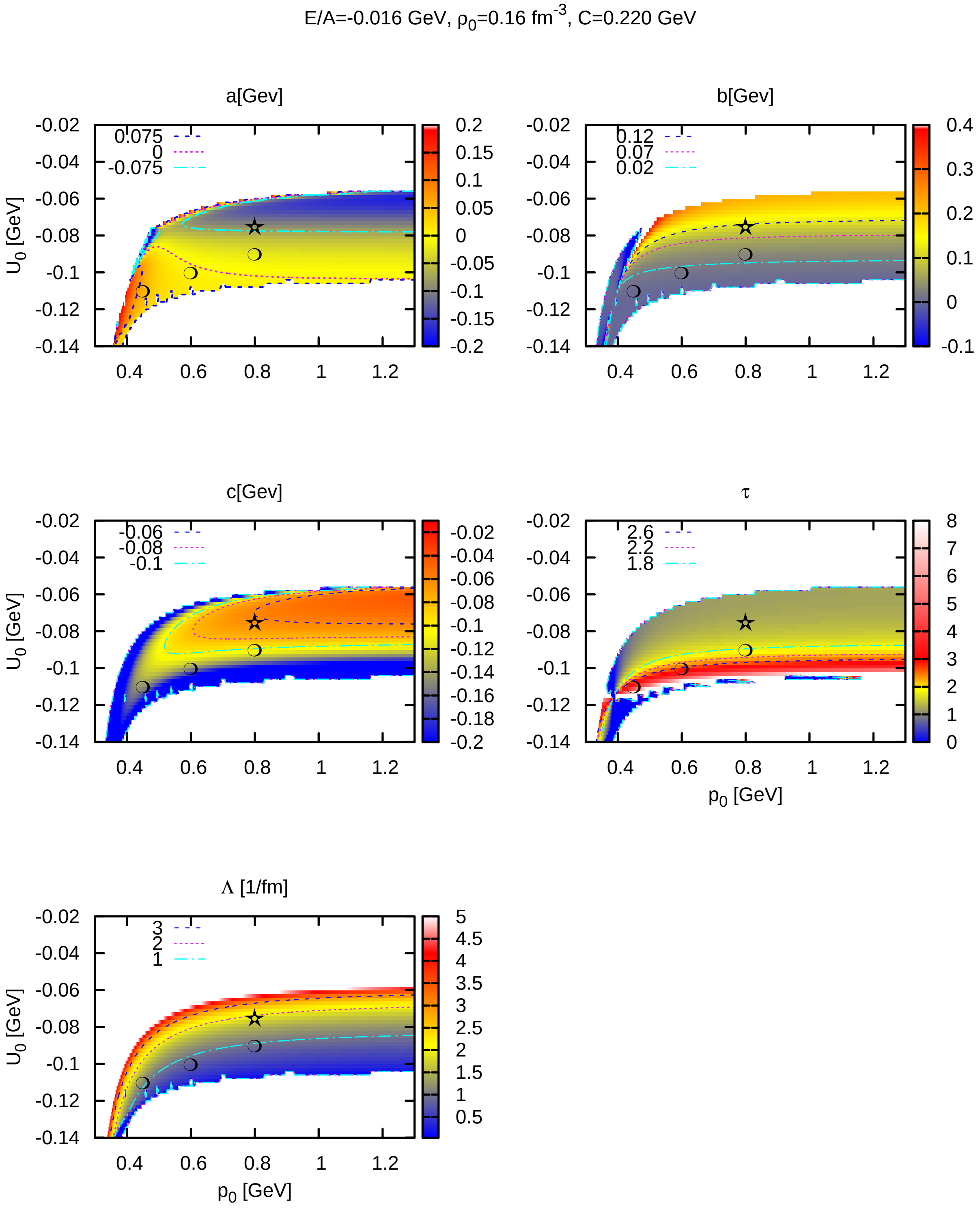

Figure 7.14: The upper figure shows the value of the potential parameters as a function of p_0 and U, if one sets ρ_0, C and E_{bind} according to eq. 7.13-7.15. The star in each panel at $p_0 = 0.8$ GeV and $U = 0.075$ GeV shows the (p_0, U)-combination chosen by Teis [Tei96]; the open circles depict the parameter sets chosen according to table 7.1.

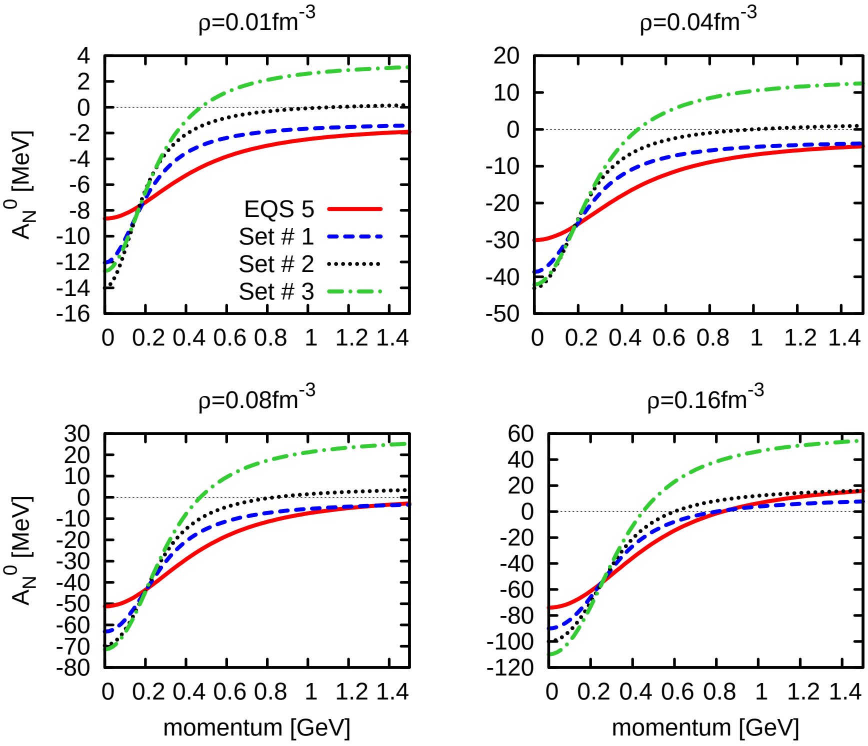

Figure 7.15: The upper panels shows the single-particle nucleon potential A_N^0 as a function of nucleon potential for different nuclear matter densities. The solid line represents the result according to the parameter set EQS 5 presented in table 3.4 ; the other three curves show the results for the three parameter sets given in table 7.1.

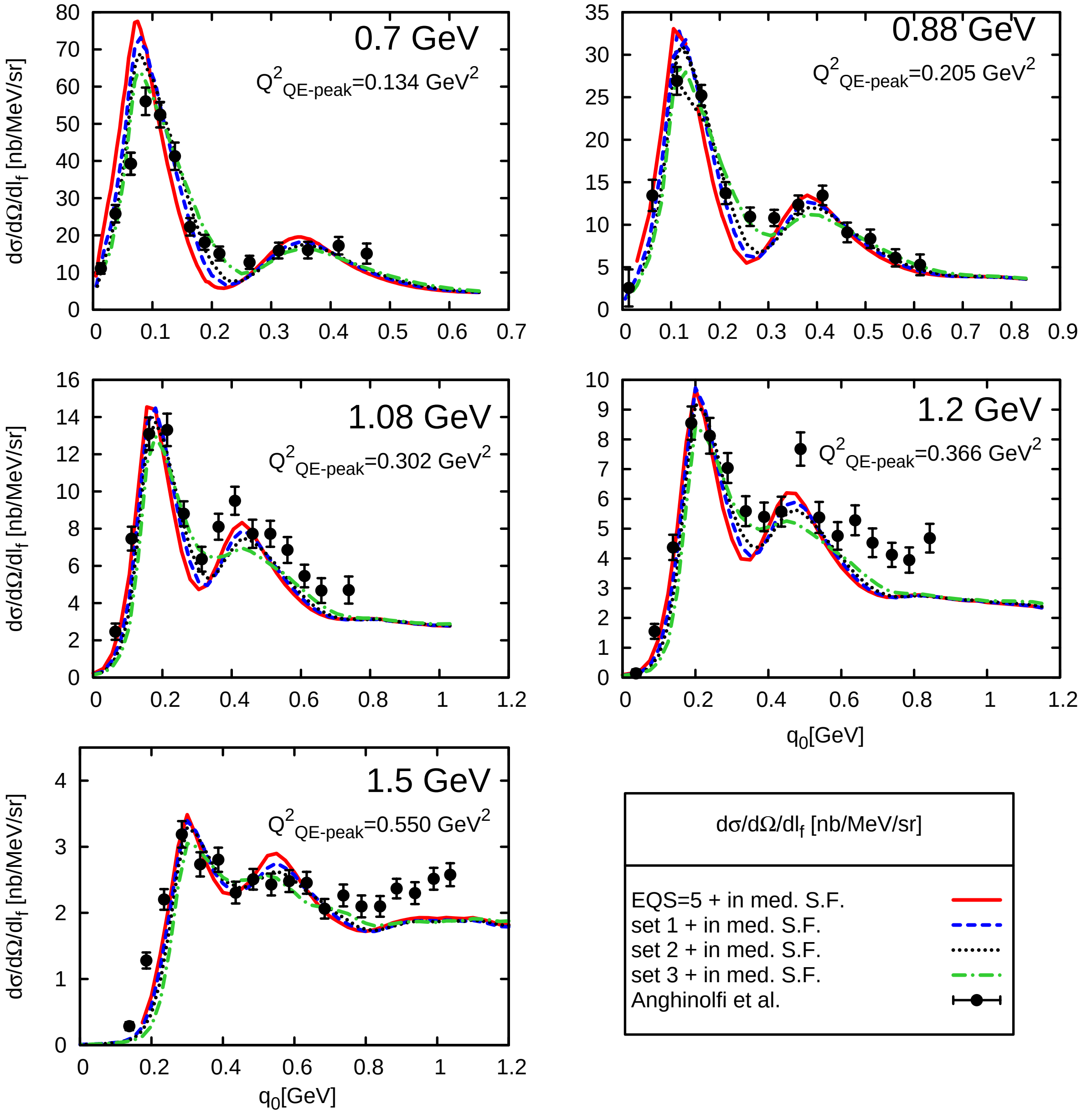

Figure 7.16: Impact of potential parameters p_0 and U on inclusive electron- ${}^{16}_{8}$O scattering cross sections. In each panel, we compare the inclusive electron cross section $d\sigma/(d\Omega dl_f)$ on ${}^{16}_{8}$O obtained with the standard potential EQS 5 (solid line) to the ones obtained with the parameter sets chosen according to table 7.1 (dashed curves=set 1, dotted= set 2, dashed-dotted = set 3). Each panel shows the result for one fixed electron beam energy (0.7, 0.88, 1.08, 1.2 and 1.5 GeV) and a scattering angle of $\theta_{l_f} = 32°$. The data are taken from [Ang96, QEW08] and the parameter $Q^2_{\text{QE-peak}}$ is evaluated according to eq. 7.3. All results have been obtained with the "mass-shift option" for the imaginary parts of the in-medium self-energies and include dispersive contributions to the real parts (cf. sec. 3.6.1 for details).

latter feature is caused by the initial phases space distribution of the target nucleons, which has been discussed in detail on page 137. Especially parameter set #1 describes the data well and especially better than the EQS 5 parameter set. However, a value of $p_0 = 450$ MeV is not in agreement with nuclear optical model fits and, therefore, parameter set #3 must be rejected. The more realistic sets 1 and 2 also describe the data better than EQS 5, however the improvement is rather moderate. We conclude that varying the potential parameters it is very well possible to improve the correspondence of our model with inclusive electron scattering data. However, the level of improvement is within a sensible p_0 window of 800 ± 50 MeV and for sensible $\tau \lesssim 2.5$ rather small.

7.3 Total photon absorption cross sections for complex nuclei

In the total photon absorption cross section on nucleons, one observes three major peaks, which are according to our present knowledge generated by several overlapping resonances. The most important ones are the $P_{33}(1232)$, $S_{11}(1535)$, $D_{13}(1520)$ and $F_{15}(1680)$ resonance states. To study the properties of those resonance states embedded in nuclear matter, one has investigated their photon-induced excitation in nuclei. First experiments using a tagged high-energy photon-beam ($E_\gamma = 0.3 - 2.6$ GeV), which offered sufficient energy to excite the second resonance region, were performed by the Yerevan group [Ara83, Ana87]. Following up this pioneering work, the photon absorption of photons on nuclei was measured at the *Mainz microton (MAMI) facility* [Fro92, Fro94] with a beam energy of $E_\gamma = 0.05 - 0.8$ GeV, with higher energy of $E_\gamma = 0.2 - 1.2$ GeV at the *Adone storage ring facility* (Frascati, Italy) [Bia93b, Bia93a, Bia93c, Bia94, Bia96], using the *SAPHIR tagged photon beam* of $E_\gamma = 0.5 - 2.67$ GeV at *ELSA* (Bonn, Germany) [Muc99] and at *Hall B* of the *Jefferson Laboratory* (Newport News, USA) [Cet00, Cet02] with a beam energy of $E_\gamma = 0.17 - 3.84$ GeV. In fact, some of the above experiments did not measure directly the photon absorption cross section but only the photo-fission cross section [Fro92, Fro94, Bia93c, Bia93b, Cet00, Cet02]. Contrary to earlier assumptions, it has been shown by Cetina *et al.* [Cet00, Cet02] that these two cross sections must not be identical. So we focus for our analysis on a comparison with the direct measurements of photon absorption as presented by Bianchi *et al.* [Bia94, Bia96] and Muccifora *et al.* [Muc99].

Let us briefly summarize the experimental findings. First, the Δ resonance region is also within the nucleus still exhibiting a peak like structure. However, one has observed a slight shift to higher energies and a broadening as compared to the vacuum structure. At higher energies, one has observed a more interesting and a somewhat unexpected effect. The experimental results show no structures in the second and third resonance region, often quoted as the disappearance of the resonances in the medium.

In the last two decades, various theoretical attempts have been performed to explain these data. The elaborate work of Carrasco *et al.* [Car92] showed in a microscopic model approach, that it is possible to describe the data in the Δ resonance region in a very satisfactory manner when including the Δ self-energy. This work emphasizes the importance of multi-body absorption channels. After the publication of the surprising results in the second resonance region, Kondratyuk *et al.* [Kon94] set up a baryon resonance model including the collisional widths of the resonances as free parameters. Then these parameters were fitted to the existing data and thereby the collisional widths of the resonances were extracted. However, these extracted widths were extraordinary large (ca. 320 MeV for the $S_{11}(1535)$, $D_{13}(1520)$ and $F_{15}(1680)$ resonance) and the whole analysis has offered several points for criticism (cf. pages 368-369 in [Eff97a]). Rapp *et al.* [Rap98] applied a vector-meson dominance (VMD) model to the problem.

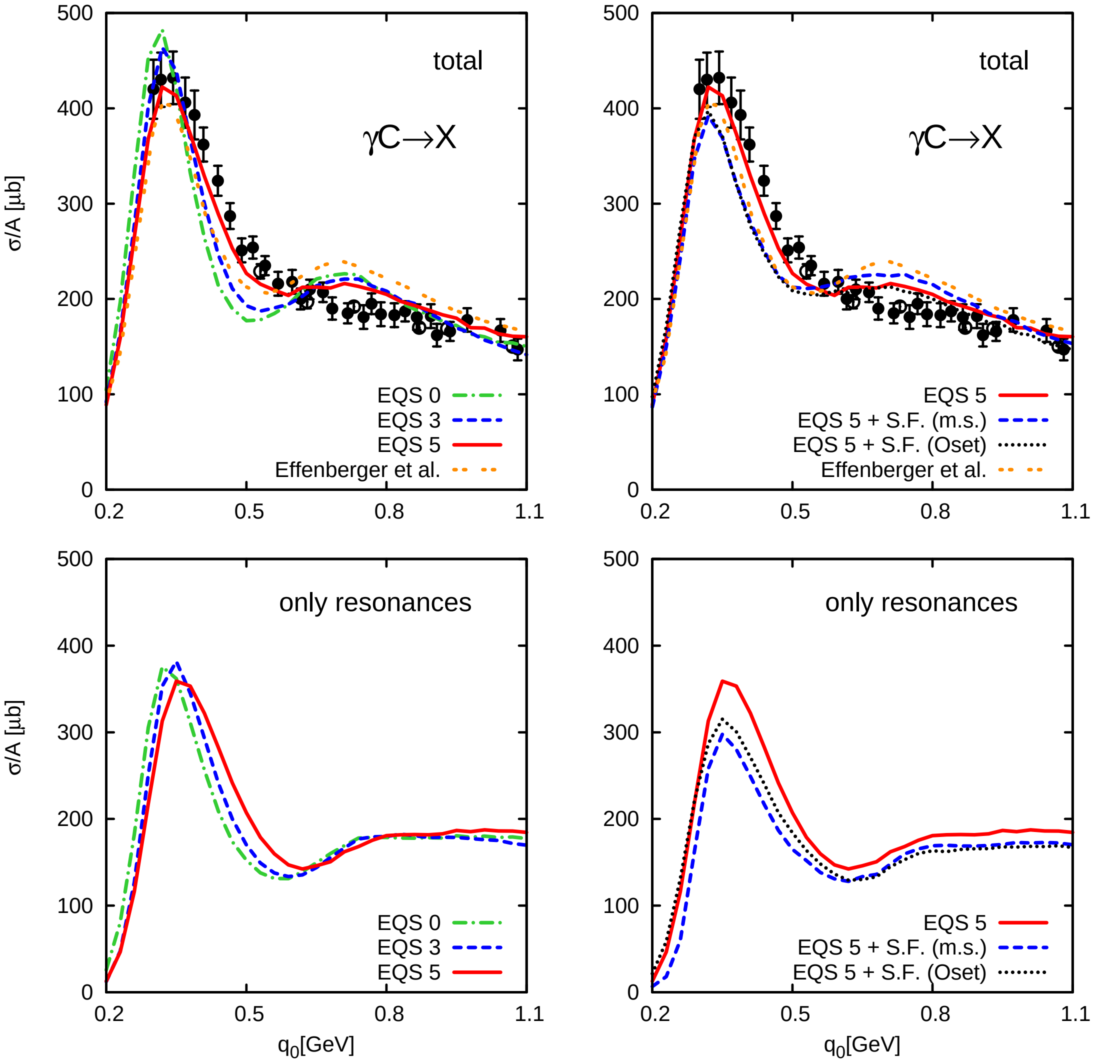

Figure 7.17: The photon absorption cross section for $^{12}_{6}$C. The upper panels show the full cross section including background contributions whereas the lower ones show only the resonance contribution. In the left panel we show the the impact of different assumptions on the baryon potential: the red solid line denotes the result with a momentum-dependent potential (EQS 5), the dashed blue one represents a calculation with a momentum-independent potential (EQS 3) and the green dashed-dotted a calculation where the baryon potentials have been neglected (EQS 0). In the right panels we keep the potential the same (EQS 5) and vary the modification of the in-medium self-energy: no modification (red solid curve), mass-shift option (blue dashed), mass-shift without dispersion relation analysis for the real part (green dashed-dotted) and the result using the Oset option for the Δ (black dotted). The data are taken from Bianchi *et al.* [Bia96] (full circles) and Muccifora *et al.* [Muc99] (open circles) , the error bars denote the sum of statistical and systematical errors.

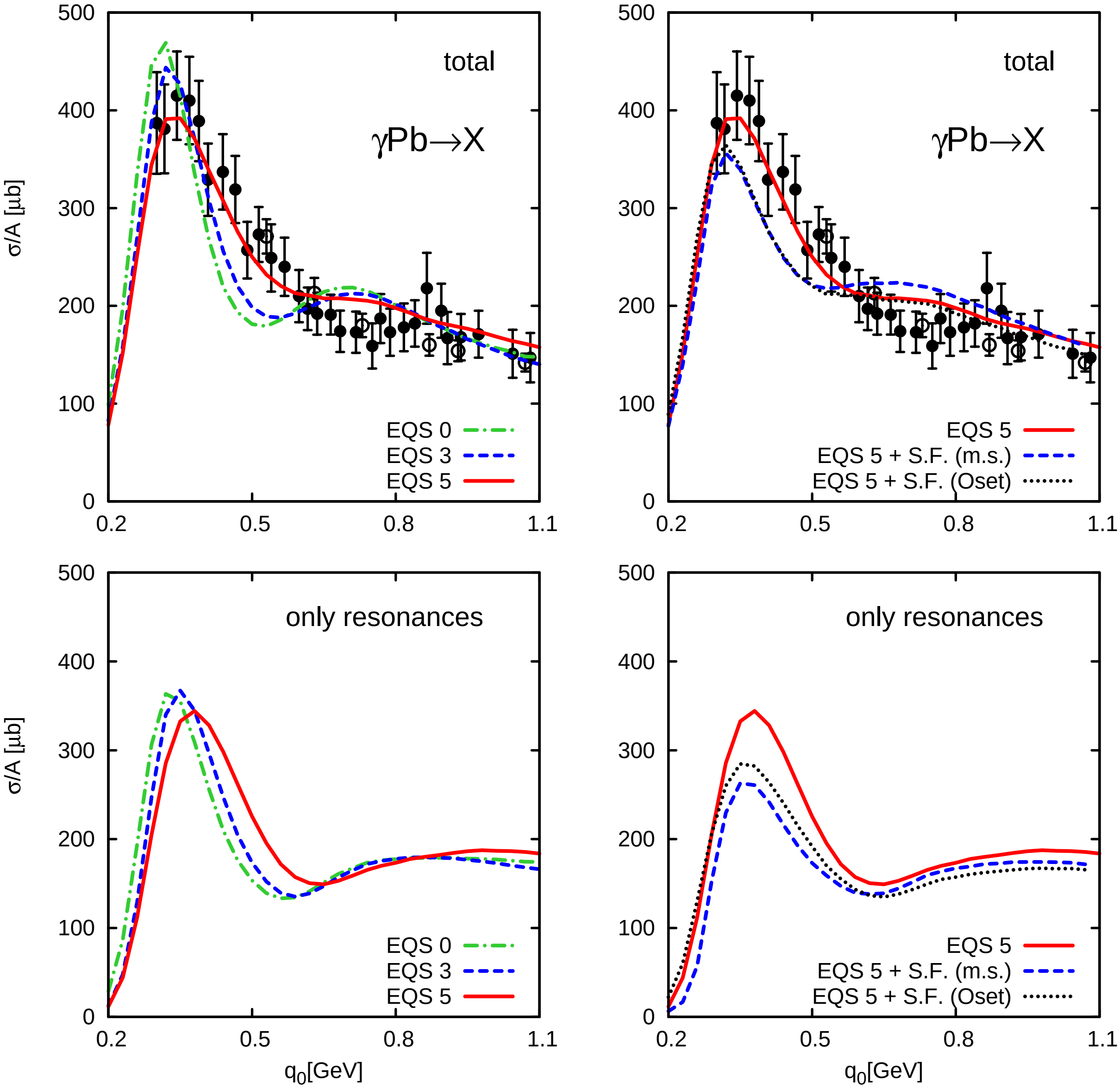

Figure 7.18: Same as fig. 7.17, but for a ${}^{207}_{82}$Pb absorber.

An energy-independent collisional broadening of the baryon resonances of 15 MeV for the Δ, 250 MeV for the D_{13} and 50 MeV for all other contributing resonances has been included by hand. The model fails to reproduce the elementary data on the proton in the region in-between Δ and second resonance region, but it describes the nuclear data in a satisfactory manner. The work of Hirata [Hir02] points out that according to their model the interference patterns among the resonances and the background change when going from vacuum to medium which is in then the driving force for the disappearance of the resonances. Iljinov *et al.* [Ili97] extended the *Dubna/Moscow INC* model, a hadronic transport model, such that it can be used for high photon energies up to 10 GeV. They achieved good correspondence with exclusive channels such as single-pion production. Based on the *Dubna/Moscow INC* model, the *RELDIS* code [Psh05] achieved good results for photo-absorption on large nuclei. Both the *INC* and *RELDIS* model include a phenomenological two-body absorption channel on top of single-particle absorption. Also the *LAQGSM* model [Mas05] is based on the *Dubna/Moscow INC* model, which also results in a good model for nuclear fissibilities. Deppman *et al.* [Dep02] have successfully applied the so-called *MCMC/MCEF* cascade model, to evaluate photon fission cross sections using the photon absorption cross section as given input. Complementary to this first work, Deppman achieved with the *CRISP* code [Dep04, Dep06], where the photon absorption is modeled via a microscopic resonance model, also satisfactory results for photon absorption.

Within a precursor version of our present model, also Effenberger *et al.* [Eff97a] tried to explain the experimental observation of resonance disappearance. A quite good description of the Δ peak was achieved, however the model failed explaining the data at higher energies: the results still showed a prominent structure in the second and third resonance region. Our present model, which was also used for the analysis of the inclusive electron scattering presented in the previous section, differs from Effenberger's one in four major aspects. First, we use the up-to-date input for the photon-nucleon interaction, in particular for the helicity amplitudes of the resonances and for the invariant amplitudes used to parametrize pion production (cf. chapter 4). Second, the single-pion background terms are treated differently: Effenberger *et al.* rescaled the resonance contributions to fit the single-pion data while we include a point-like single-pion production vertex which includes all background and interference terms. So in our case the background and interference terms are not modified in the medium, whereas in Effenberger's case those two terms are hidden in the resonance contributions and, therefore, they are modified in the same way as the resonances. Third, the absolute magnitude of the collisional width is different. While the "no-mass-shift scheme" almost reproduces the collisional broadening as presented by Effenberger, we get with the "mass-shift scheme" more collisional broadening due to a larger elastic cross section (cf. fig. 3.5-3.6 for the implemented width of the four most prominent resonances: $P_{33}(1232)$,$S_{11}(1535)$, $D_{13}(1520)$, $F_{15}(1680)$). This possibility of having a larger elastic cross sections was not discussed earlier, and increasing this elastic contribution might help to solve the problem of too prominent resonance structures in Effenberger's results. Finally, Effenberger neglected the real parts of the self energies which lead to non-normalized spectral functions.

Our results for photon absorption in Carbon are shown in fig. 7.17. For the calculations shown in the graphs on the left panel, the width of the resonances in the medium has not been modified and the dispersive contributions to the real part of the self energy have not been included. Again, as for the quasi-elastic peak in the electron-nucleus scattering, one observes a broadening of the spectra just due to the momentum-dependent mean field. The solid curve shows the result when including such a mean-field, which describes the data properly in the Δ region and overestimates the data slightly in the second resonance region. It is however remarkable, that the mean field smears the spectra so much that the second resonance peak is dissolved. Given this level of agreement with data on might now declare complete success. However, we know from pion absorption in nuclei and from pion scattering off nuclei that the broadening of the Δ resonance plays an essential role. Hence one must take such in-medium resonance broadenings into account.

The right panels show additionally to the result calculated with a momentum-dependent mean field (solid line), the results for which the in-medium width and the dispersive contributions to the real parts have been taken into account (dotted and dashed lines). The lower right panel shows that the resonance contributions are decreased due the dispersive contributions and the larger width in medium. Both features are well understood: a larger width leads to smearing of the peaks and therefore to a lowering of the resonance contributions, including the dispersive parts also leads to a lowering of the peaks as we have seen in sec. 3.7.2. The upper right panel shows the sum of the resonances and the background contributions. Note that the background contributions differ for all calculations which is caused by the inclusion of the dispersive parts. These dispersive parts basically shift strength from the resonances to the background. As for the elementary γp scattering shown in fig. 7.19, the background is smallest for the calculation without dispersive contributions (solid line), larger for the case that all resonances besides the Δ receive dispersive contributions to the self energy (dotted line, Oset option) and largest for the case that we account for the dispersive contributions of all resonances (dashed line, mass-shift option). Be reminded that one can not evaluate the real part of the self energy of the Δ based on a dispersion approach when using the Oset option for the imaginary part, since the imaginary part is simply not defined for large enough energies. The upper right panel shows that the Δ region is underestimated for both options for the in-medium width. The situation also does not improve in the second resonance region where a strong in-medium broadening, as in the mass-shift scenario (blue dashed curve), even leads to an enhancement of the peak structure due to a shift of Δ spectral strength towards higher masses as shown in fig. 3.12.

As a summary one must conclude that the full model describes the model worse than the model neglecting a modification of the in-medium width which hints either to a problem in our understanding of the in-medium broadening of the resonances or to a yet not included physical effect such as an in-medium modified background or in-medium modified resonance-background interferences.

Comparing to the former result by Effenberger (double dashed curves in the upper panels), we must state that both models describe the data equally well. In our approach it is however interesting to see, that the proper treatment of the medium-dependent potential leads all by itself to a smearing of the second resonance peak. As a consequence, it should be interesting to include the in-medium kinematics also in the background treatment, which was too involved for our approach since one would need a microscopic model for the background. For completeness, we show in fig. 7.18 also the photon absorption in Lead. Compared to the Carbon case we do not see a qualitative change of the picture. We observe the same level of correspondence with the experimental data as for the Carbon case.

Fig. 7.20 shows again the photon absorption in Carbon. To obtain the results shown in the latter graph, we have ignored the resonance model and have just used the in-medium modified $\gamma N \to N\pi$ process (cf. sec. 5.3.2) and added the 2π production channel. The Δ peak structure is in its magnitude well described by a calculation which includes both a pion and nucleon potential (red solid line). However, the width of the Δ peak is underestimated and the peak structure in the second resonance region is not present in the data. We conclude that the resonance model framework gives a far better description of the data at high photon energies q_0.

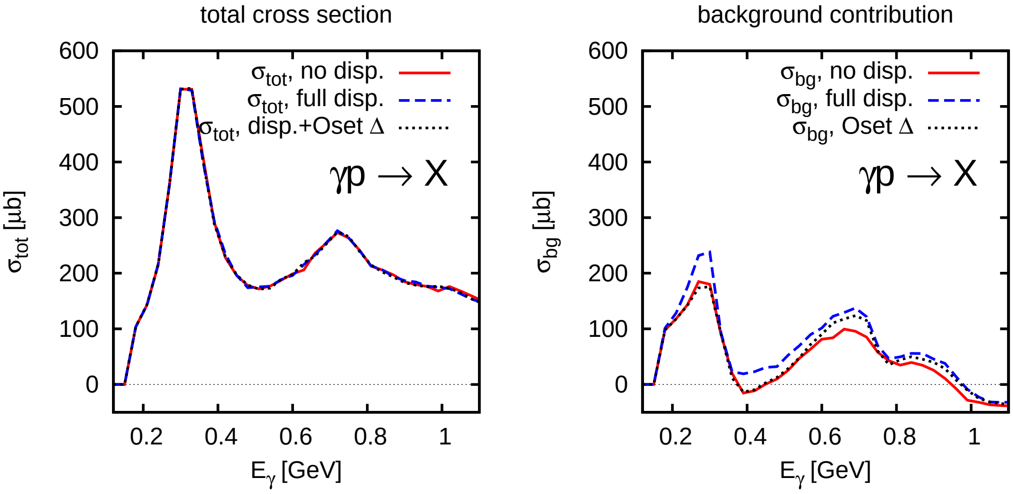

Figure 7.19: The upper figure shows photon scattering off the proton in vacuum as a function of the incoming photon energy for different choices on the treatment of the dispersive contributions for the real part of the self energy. The left panel shows the total cross section, the right panel shows only the non-resonant background contribution to the cross section. The full line depicts a scenario, where no dispersive contributions are included. The dashed line includes all dispersive contributions but the one for the Δ resonance. The dashed curve includes all dispersive contributions. Note that all curves in the right panel are identical by construction, and should only differ by the statistical uncertainties of the Monte-Carlo integration. The background contributions may become negative since they also include the interference terms.

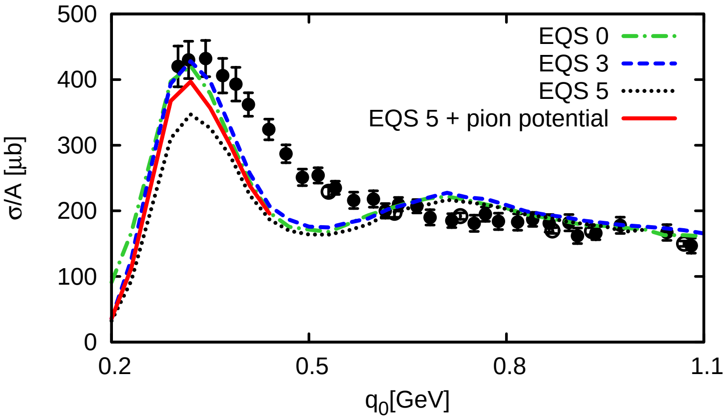

Figure 7.20: The photon absorption cross section for ^{12}C without resonances in the intermediate state. The curves in the upper panel represent calculation where we did not include resonances but treated the $\gamma N \to N\pi$ reaction as a point-like vertex. The red solid line denotes the result with a momentum-dependent potential (EQS 5) and a low-energy potential for the pion, the other curves have been obtained without a pion potential using different types of the nucleon potential: no potential (dot-dashed), a momentum independent potential (dashed) and a momentum dependent potential (dotted curve). The data are taken from Bianchi *et al.* [Bia96] (full circles) and Muccifora *et al.* [Muc99] (open circles) , the error bars denote the sum of statistical and systematical errors.

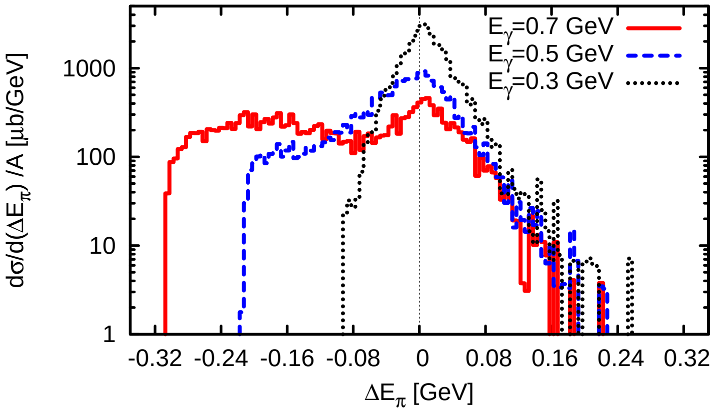

Figure 7.21: A typical plot for $d\sigma_{\pi^0,total}/d(\Delta E)$ for a $\gamma^{40}\text{Ca} \to \pi^0 X$ reaction at 0.5 GeV and 0.7 GeV right after production (*i.e. FSI effects are not included*). This result was obtained with a momentum dependent potential ($EQS = 5$) and the Oset choice for the self energies (400 ensembles).

7.4 Photon and electron induced meson production

The GiBUU transport model is explicitly designed to allow for the study of exclusive reactions, like pion production and nucleon knockout, taking into account rescattering effects leading to a change in the final state particle multiplicities and distributions. To my knowledge, there exist only few data for pion production in electron induced reactions in the resonance region. However for photon induced reactions, there exist high quality data on π^0-meson production measured by Krusche *et al.* [Kru04b, Kru04a] using the TAPS spectrometer, which has been installed at the MAMI facility in Mainz, and on π^+-meson production by Fissum *et al.* [Fis96] taken at the Saskatchewan Accelerator Laboratory. The Fissum data are taken in the very threshold region, where most of the produced pions have energies in the regime below 40 MeV, where our FSI model becomes unreliable. In the following we, therefore, consider only the experiment performed by Krusche.

7.4.1 π^0 production for $E_\gamma = 0.2 - 0.8$ GeV

For the π^0 production experiment performed by Krusche *et al.* [Kru04b, Kru04a], the MAMI facility delivered a photon beam of $200 - 800$ MeV energy on Deuterium, Carbon and Lead targets. Since the TAPS spectrometer did not have a charged-particle identification at that time, there are only data on neutral pion production. The experiment counted each produced neutral pion as a single event, therefore events with $2\pi^0$ in the final state are doubly counted. So the cross section for neutral pion production can be written as

$$\sigma_{\pi^0,\text{ total}} = \sigma_{\pi^0} + 2\sigma_{\pi^0\pi^0} + \sigma_{\pi^0\pi^+} + \sigma_{\pi^0\pi^-} + \beta\sigma_\eta$$

where $\beta \approx 1.2$ is the expected number of π^0's in the final state of a η decay.

In the experimental analysis one was trying to differentiate between quasi-free pion production and in-medium pion production. For the production of quasi-free pions one assumed that the energy of those should be similar to the energy of a pion being produced on a nucleon at rest.

This energy is in the πN CM-frame given by

$$E_\pi^{\text{free}} = \sqrt{|\vec{p}_{\text{CM}}|^2 + m_\pi^2} \tag{7.16}$$

with

$$|\vec{p}_{\text{CM}}| = \sqrt{\left(\frac{s - m_\pi^2 - m_N^2}{2m_N}\right)^2 - m_\pi^2} \quad , \tag{7.17}$$

where $s = (E_\gamma + m_N)^2 - E_\gamma^2 = m_N^2 + 2m_n E_\gamma$. The difference of the reconstructed energy in the πN CM-frame to that *quasi-free* energy is defined as ΔE_π (cf. also [Kru04a]):

$$\Delta E_\pi = E_\pi^{\pi N-\text{CM}} - E_\pi^{\text{free}}(E_\gamma) \quad .$$

A typical plot of such a distribution without final state interactions is shown in fig. 7.21. Indeed, one observes a peak at $\Delta E_\pi \approx 0$ but the peak is not sharp but rather smeared out due to potentials and Fermi motion. Additionally, there is a broad background at lower ΔE_π which stems from $\pi\pi$ production. Since this background leaks into the single-π peak, one has introduced an asymmetric cut and one has counted all those events for $\sigma_{\pi^0,\,\text{quasi-free}}$ which have positive ΔE_π. Note that there is no reason for this peak to be exactly at $\Delta E_\pi = 0$. For instance, let us consider the case that we include Fermi motion but no potentials. For this scenario, one gets a higher mean center-of-mass energy than in an elementary collision. In an elementary collision one gets

$$s_{\text{elementary}} = m_N^2 + 2q_0 m_n \tag{7.18}$$

and in a collision with a nucleus

$$\begin{aligned}
\overline{s}_{\text{nucleus}}(\vec{r}) &= m_N^2 + 2\frac{4}{\rho(\vec{r})}\int_0^{p_f(\vec{r})} \frac{d^3\vec{p}}{(2\pi)^3}\, p^\mu q_\mu && (7.19)\\
&= m_N^2 + 2q_0\frac{4}{\rho(\vec{r})}\int_0^{p_f(\vec{r})} \frac{d^3\vec{p}}{(2\pi)^3}\, p_0 && (7.20)\\
&= m_N^2 + 2q_0\frac{4}{\rho(\vec{r})}\int_0^{p_f(\vec{r})} \frac{d^3\vec{p}}{(2\pi)^3}\, \sqrt{m_N^2 + \vec{p}^2} && (7.21)\\
&> m_N^2 + 2q_0\frac{4}{\rho(\vec{r})}\frac{4\pi p_f^3}{3\,(2\pi)^3}\, m_N = m_N^2 + 2q_0 m_N = s_{\text{elementary}} \quad , && (7.22)
\end{aligned}$$

which gives

$$\overline{s}_{\text{nucleus}} > s_{\text{elementary}} \quad . \tag{7.23}$$

Since the average center-of-mass energy is higher for the Fermi sea case compared to the elementary case, also the average pion kinetic energy must be higher. This should translate into a slight positive shift of the ΔE_π spectrum right after production – a feature which is observable in fig. 7.21, although for this result also potentials have been included. However, since the particles have to transverse the medium before being detected, an additional energy loss of the particles has to be considered, which should result in an additional downward shift of the ΔE_π spectrum. Overall, it is important to realize that the spectrum must not be symmetric around $\Delta E_\pi = 0$.

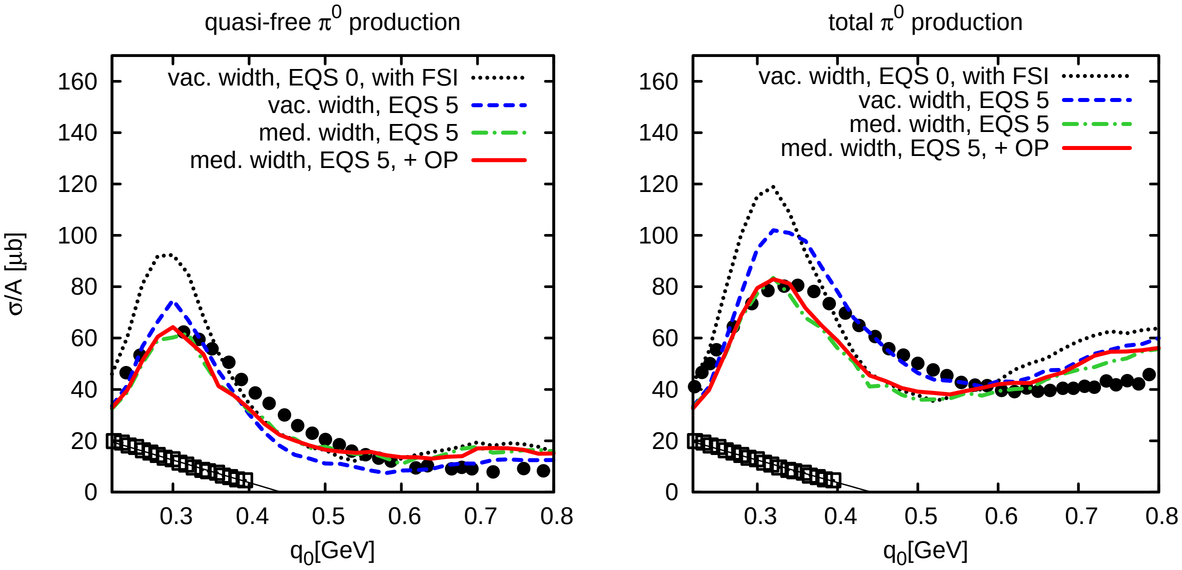

Figure 7.22: Quasi-free and total cross section for the $\gamma^{40}\mathrm{Ca} \rightarrow \pi^0 X$ reaction: the left panel shows the so-called *quasi-free* yield, whereas the right one depicts the total yield of π^0's. The statistical error bars of the data are negligible and have been omitted. The squares show the data for the coherent π^0 production cross section [Kru02] and the circles depict the data for the quasi-free, respectively total, cross section [Kru04a]. The dotted line represents a calculation without in-medium width and without potential (EQS 0), the dashed one includes also no in-medium widths but a momentum-dependent potential (EQS 5), both the dashed-dotted and the dotted curves have been obtained by a calculation which included in-medium widths and a momentum-dependent potential (EQS 5). Additionally, the off-shell potential (OP) has been included when calculating the solid curve while all other results do not include any OP. The thin solid line connecting the coherent data points (squares) represents our fit of these data, which is given in table 7.2.

For the analysis one approximated the spectrum as a symmetric one, such that the left-hand side of the quasi-free peak was assumed to equal the right-hand side which means

$$\sigma_{\pi^0,\text{ quasi-free}} = \frac{2\times\ \text{rate of events with } \Delta E_\pi > 0}{\text{photon flux} \times \text{density of targets}} \quad .$$

To compare to data, we will apply the very same counting and cutting scheme also in our analysis. Note that the sizable coherent contribution [Kru02] also contributes to $\sigma_{\pi^0,\text{quasi-free}}$ and $\sigma_{\pi^0,\text{ total}}$. However, our model just gives the incoherent contribution. So we fitted the data for the coherent process [Kru02], depicted in fig. 7.22 by open squares, by a polynomial

$$\sigma_{\text{coherent}}(E_\gamma) = \sum_{i=-1}^{2} a_i E_\gamma^i \quad , \tag{7.24}$$

where the fit parameters are given in table 7.2 and the fitted curve is also shown in fig. 7.22. This fit of the coherent data has then been added to our incoherent result. The resulting curves are shown in fig. 7.22, both for the quasi-free cross section $\sigma_{\pi^0,\text{ quasi-free}}$ on the left panel and for $\sigma_{\pi^0,\text{ total}}$ on the right panel. Including in-medium width and momentum-dependent potentials

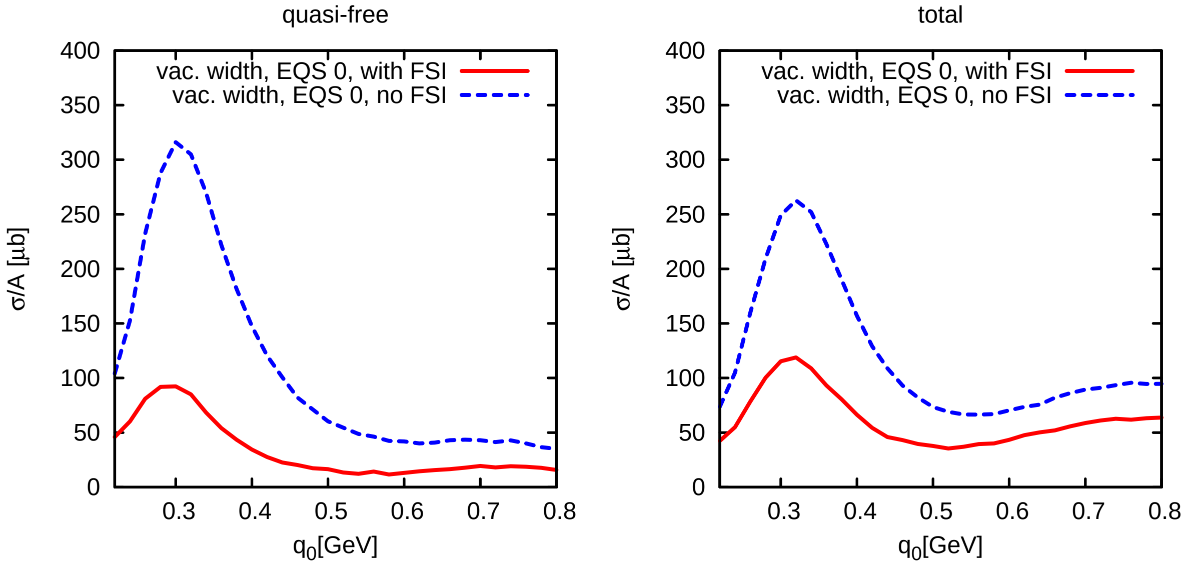

Figure 7.23: Quasi-free and total cross section for the $\gamma^{40}\mathrm{Ca} \to \pi^0 X$ reaction with and without final state interactions: the left panel shows the so-called *quasi-free* yield, whereas the right one depicts the total yield of π^0's. The lines represent calculations which have been performed neglecting the in-medium width and potentials. The dashed line does not include any FSI, whereas the solid line includes them. Note that without FSI the quasi-free yield is at low photon energies higher than the total yield. This is caused by the analysis procedure. Since the quasi-free peak is without FSI treatment slightly shifted towards positive ΔE_π (see fig. 7.21), we get $\sigma_{\text{quasi-free}} = 2\ \sigma|_{\Delta E_\pi > 0} > \sigma_{\text{tot}}$.

Target	a_{-1} [mb/GeV]	a_0 [mb/GeV]	a_1 [mb/GeV]	a_2 [mb/GeV]
Ca	-2.29696×10^4	279.07	-0.904315	9.0384×10^{-4}

Table 7.2: Parameters for the fit of $\sigma_{\text{coherent}}(E_\gamma) = \sum_{i=-1}^{2} a_i E_\gamma^i$ to the data of Krusche *et al.* [Kru02].

one retrieves the dashed-dotted curves, which give a quite good description of the quasi-free cross section. The influence of the off-shell potential, which has only been included when calculating the dashed curved, is rather minor. Considering the large slow-down of our simulations due to this off-shell potential (cf. sec. 3.9 on page 62ff), it is good news that neglecting this potential does not change our results in a significant manner.

For the total cross section we get no improvement of the description when comparing to earlier results by Lehr *et al.* [Leh03], although the model is much more advanced. Since the description of the quasi-free data is fine one might speculate whether there is a problem with the 2π contribution, which rises continuously from almost 0% at $q_0 = 0.45$ GeV to roughly 30% of the π^0 yield at $q_0 = 0.8$ GeV. An additional in-medium modification of the $\pi\pi$ background could, therefore, have a major impact on the spectra. Such a modification has not been included so far. One should also note that interference effects play a major role in single-π^0 production at the energy region of discrepancy (see also fig. 4.8). So one must conclude that it will be unavoidable to take both a dynamical model for the $\pi\pi$ and single-π background into account to improve on the present situation which is, however, out of the scope for the present work. Furthermore, there is major impact of FSI on the spectra. Fig. 7.23 shows that for a basic calculation which does not include any medium modifications of the self energies, i.e. no potentials or collisional broadening, there is an overall reduction of the pion yield by approximately a factor of 3 just due to FSI. Thus the accuracy of the FSI must be very high to achieve a proper agreement with the data. We tried to estimate the FSI accuracy performing the pion DCX and pion absorption analysis in chapter 6. Although the description of pion interaction with the nuclear medium was quite successful, we can in principle not rule out that we are still missing some effect which could help to improve the correspondence to data. However, the close agreement for the quasi-free case makes us confident on the FSI description.

Chapter 8

Double pion photo-production

Overview: This chapter is devoted to photon-induced $\pi\pi$ production off nucleons and nuclei. After a survey on the available data for the elementary reaction, we analyze the implications of nuclear corrections on the extraction of the neutron data from the deuteron data. It is concluded that only a minor impact of such corrections has to be expected. Finally, we address $\pi\pi$ production off complex nuclei and outline the dominant role of final-state interactions on the resulting spectra.

8.1 Introduction

In the limit of vanishing quark masses QCD incorporates chiral symmetry, which is spontaneously broken in vacuum. The order parameter $\langle \bar{q}q \rangle$ of this symmetry breaking is expected to decrease by about 30% already at normal nuclear matter density [Dru90, Coh92, Bro96]. Therefore, signals for partial chiral symmetry restoration should be observable in nuclear reaction experiments and, in particular, in photon induced processes, which are highly suited due to two key reasons. The reaction leaves the nucleus close to its ground state, so the reaction takes place under well defined conditions. Second, the photon penetrates deeply into the nucleus, giving rise to a high effective density. The modification of the so-called σ or $f_0(600)$ meson inside the nuclear medium was proposed as a signal for such a partial symmetry restoration. Theoretical models predict a shift of its spectral strength to lower masses and a more narrow width due to the onset of the restoration [Ber87, Hat99]. The σ-meson is a very short-lived state with a width of roughly $600 - 1000$ MeV [Hag02], decaying predominantly into a $\pi\pi$ final state in S-wave. Owing to its short life time, this decay occurs very close to its production place, i.e. in the medium. If there were no final-state interactions acting on the pionic decay products, then the mass of the σ-meson could be directly determined measuring the 4-momentum of the pions. So the experiments devoted to this topic have been focusing on $\pi\pi$ production in nuclei and studied the $\pi\pi$ production rate as a function of the total mass of the $\pi\pi$ pair. The major aim was to observe a modification of this signal when comparing the nuclear production rate to the vacuum rate. Using different nuclear targets one probes different effective densities, which allows for a detailed study of the density dependence of this production rate. Experiments on $\pi\pi$ production in nuclear matter have been performed with incident pions by the *CHAOS* collaboration [Bon96, Bon00] and with photons by the *TAPS* collaboration [Mes02, Blo07, Gre07]. Both experiments have shown an accumulation of strength near the $\pi\pi$ threshold in the decay channel of the σ in large nuclei. A possible interpretation of this effect is the in-medium modification of the σ resonance due to partial symmetry restoration. However, already in an earlier work [Mü04a] we have pointed out the importance of conventional final-state effects in the analysis of the experiment performed by the *TAPS* collaboration. In this chapter we want to improve on our early calculations using up-to-date input for the elementary rates and using an improved final-state model.

In [Mü04a], we have presented results on the double-pion photoproduction off nuclei using the transport approach. There the treatment of the pion final state differed from the treatment presented in the previous chapters. In order to compare to a work by Roca *et al.* [Roc02], we implemented there the same absorption probability for the pion as in their work. Therefore we did not propagate the resonances explicitly, but rather used experimental data to describe the quasi-elastic $N\pi \rightarrow N\pi$ scattering. We also used contributions to the imaginary part of the optical potential of [Nie93a] to model pion absorption. The aim there was to indicate the relevant role of conventional final-state interaction (FSI) effects in two-pion photoproduction in nuclei. The authors of [Roc02] achieved quite an impressive agreement with the experimental data, when studying double pion production in a many-body approach which allowed for pion-pion correlations. However their treatment of the pion FSI was based upon a purely absorptive Glauber damping-factor calculated along straight line trajectories. Additionally, the calculation was missing a factor 2 for the $\pi^0\pi^\pm$ channel.

Note that we need to consider pions with very low energy in nuclear matter to analyze the experiment performed by the *TAPS* collaboration [Mes02, Blo07, Gre07]. We have already shown in chapter 6 that our GiBUU transport model successfully describes pion absorption and rescattering off complex nuclei. Since there is no fully quantum description for the incoherent 2π reaction available, we utilize this semi-classical final state description to simulate the $\pi\pi$-photo production reaction.

This section is organized in the following way. First we present an overview on the existing data on double pion production. Thereafter, the modeling of the elementary reaction is discussed. Finally, our results for $\pi\pi$ production off complex targets are compared to experimental data [Mes02, Blo07, Gre07] [1].

8.2 Experimental evidence

8.2.1 Elementary data

Already in the 1960's and 70's, first extensive photo-induced $\pi\pi$ production experiments on elementary targets have been performed (cf. [Hau67, Aac68, Car76a] and references therein). More recently, the *TAPS*[2] [Har97b, Wol00, Kot04, Lan01, Kle00], *DAPHNE* [Zab97, Bra95], *GDH/A2* [Ahr03, Ahr05] and *GRAAL*[3] [Ass03] collaborations have been examining $\pi\pi$ production with high statistical accuracy. In fig. 8.1, we plotted as an overview over the regarded threshold region the most recent data sets. This plot shows only results of the second generation experiments save for the $\gamma n \rightarrow n\pi^+\pi^-$ channel, where there are only the old bubble-chamber data of Carbonara *et al.* [Car76a] available. In [Ahr03] (cf. page 178, first paragraph) it was pointed out, that there was a systematic error in the *DAPHNE* [Zab97, Bra95] analysis program. Henceforth, the original *DAPHNE* data are now superseded by the more accurate *TAPS* and *GDH/A2* experiments. Furthermore, there are data which are still preliminary and not yet published. *GDH/A2* [Ped07a, Ped07b] provided us preliminary data on $\gamma n \rightarrow p\pi^-\pi^0$ and $\gamma p \rightarrow p\pi^-\pi^+$ and Crystal Ball-*TAPS* (*CB-TAPS*) reported preliminary results on $\gamma n \rightarrow p\pi^0\pi^0$ and $\gamma p \rightarrow p\pi^0\pi^0$ [Jae07].

Taking *TAPS* and *GDH/A2* for granted, the proton channels are measured to a satisfying precision. However, the neutron channels (left panels of fig. 8.1) are still poorly know. In the

---

[1] Results presented in this chapter have also been published in [Mü04a, AR05, Bus05, Bus06b, Bus06c]

[2] Two Arm Photon Spectrometer [TAP08]

[3] Grenoble Anneau Accélérateur Laser [GRA08]

channel $\gamma n \to p\pi^0\pi^-$, Pedroni *et al.* [Ped07c] corrected the original *DAPHNE* data [Zab97] for their systematical error. The resulting corrected data are shown together with the original data, the Carbonara data [Car76a] and the preliminary *GDH/A2* data [Ped07b] in the lower right panel of fig. 8.1. In the latter channel, the discrepancies of Carbonara *et al.* and the corrected *DAPHNE* data raise also doubts concerning the quality of the Carbonara data, and as a consequence discredit also the $\gamma n \to n\pi^+\pi^-$ data of Carbonara. For the $\gamma n \to n\pi^0\pi^0$ reaction, which is depicted in the middle panel of the right row, new preliminary *TAPS* data (provided by Jaegele [Jae07]) hint to a somewhat larger cross section than estimated by Kleber *et al.* [Kle00]. To sum up, one must realize that the neutron data have still large uncertainties, whereas the proton data seem to be reliable after a period of contradiction between different experiments, in particular *TAPS* and *DAPHNE*.

8.2.2 Complex targets

For photon induced $\pi\pi$ production on complex targets such ^{12}C, ^{40}Ca and ^{208}Pb, there exist only data by the *TAPS* collaboration which performed two different independent measurements. The first pioneering measurement [Mes02, Sch05, Sch06b, Sch06a, Blo07] was performed 1999 at the MAMI-B accelerator. The *TAPS* detector covered roughly 40% of the solid angle in a setup being sketched in fig. 8.2.

Since the *TAPS* detector does not include a magnetic field, positively and negatively charged pions could not be distinguished. The uncharged pions are identified via the measurement of their two-photon decay channel. The most celebrated observable was the ratio of the mass-differential cross section per nucleon on Pb over the one on C

$$R = \frac{\left(\frac{1}{A}\frac{d\sigma}{dm_{\pi\pi}}\right)_{Pb}}{\left(\frac{1}{A}\frac{d\sigma}{dm_{\pi\pi}}\right)_{C}} \quad .$$

Figure 8.3 shows the first results, published in [Mes02], for this ratio for photon energies averaged over a $400-460$ MeV bin. The low photon-energy window was chosen to suppress the η production background and to enhance the production of low energetic pions, for which one assumed a very large mean free path. The experimental finding was that there is no modification of the $\pi^0\pi^\pm$ channel when going from Pb (high effective density) to C (low effective density), whereas the experiment found a strong modification in the $\pi^0\pi^0$ channel which was interpreted as an in-medium modification within the $I = J = 0$ channel of the initial $\gamma N \to N'\pi\pi$ reaction. Preliminary results for higher photon energies, in particular total cross sections, have also been presented in [Sch06a, Sch06b]. Recently, Bloch *et al.* [Blo07] published a final paper on this first campaign with the analysis of ^{40}Ca data. The authors show mass-differential cross sections for the energy bins $400-500$ MeV and $500-550$ MeV and total cross sections in the range of $E_\gamma \simeq 300-800$ MeV. In the latter paper, no significant difference in the $\pi^0\pi^0$ channel could be observed when comparing ^{12}C to ^{40}Ca [Blo07, sec. 6].

This first campaign was followed up by a second campaign of measurements with much more statistics and an considerably improved setup (for details cf. [Gre07]). It also took place at the MAMI accelerator facilities in Mainz. The detector setup consisted out of the *TAPS* detector as a forward wall and the Crystal Ball detector which surrounded the reaction chamber and lead to an almost 4π coverage in the solid angle. Within the Crystal Ball an additional particle identification detector and multi-wire proportional chambers enhanced the particle identification and especially charged particle reconstruction [Gre07, Lug07a].

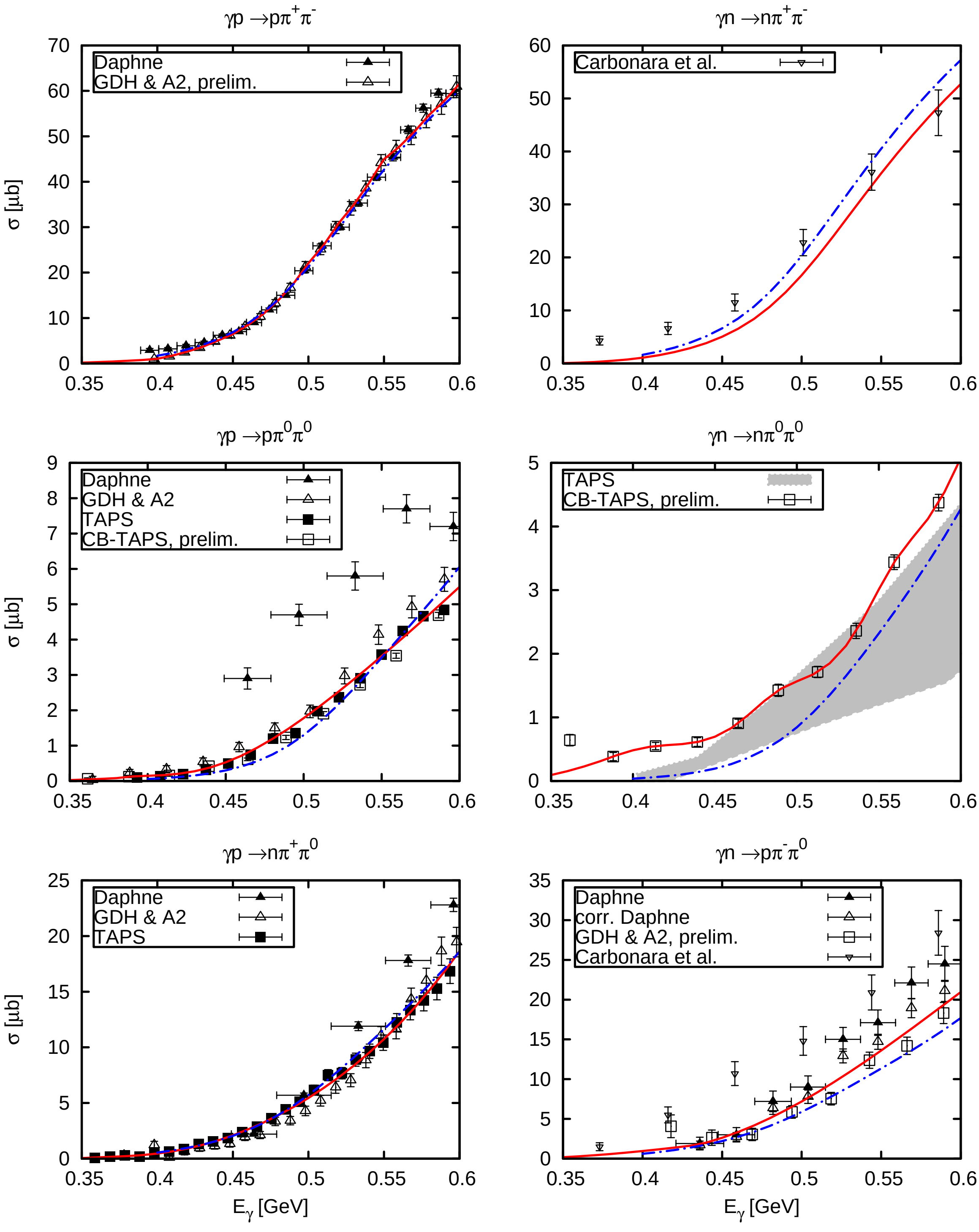

Figure 8.1: The upper figure shows the different isospin channels for the reaction $\gamma N \rightarrow N\pi\pi$. For the error bars we added in quadrature the systematical and statistical uncertainties ($\Delta = \sqrt{\Delta^2_{\text{stat}} + \Delta^2_{\text{sys}}}$) as quoted by the experiments. The data are taken from [Car76a, Zab97, Bra95, Har97b, Wol00, Kot04, Lan01, Kle00, Ahr03, Ahr05]; preliminary data were communicated by [Jae07, Ped07a, Ped07b]. In the panel representing $\gamma n \rightarrow n\pi^0\pi^0$, the shaded area shows the cross section measurement by [Kle00]. The solid line represents our parametrizations which we use as input for the nuclear targets. The dotted-dashed curves show the result obtained with the original model of Nacher *et al.* [Nac01, Alv05] based on Tejedor *et al.* [GT95, GT96].

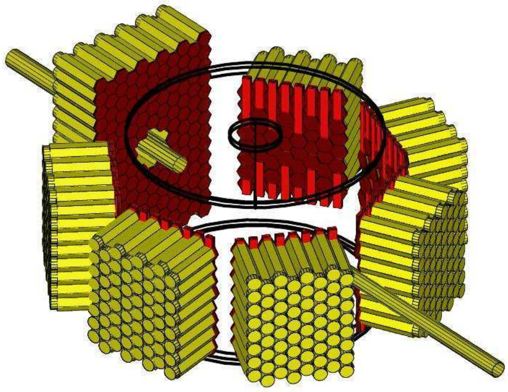

Figure 8.2: The setup of the TAPS detector in the experimental campaign at MAMI-B in 1999 [Jan02]. Each of the seven detector blocks (large forward wall and six smaller blocks) consists out of several hexagonal BaF_2 crystals, which is an inorganic scintillator. Particles transversing a crystal loose energy, which induces scintillation light in the crystal. This light signal is converted to an electron signal via the photo effect and finally amplified by photo multipliers.

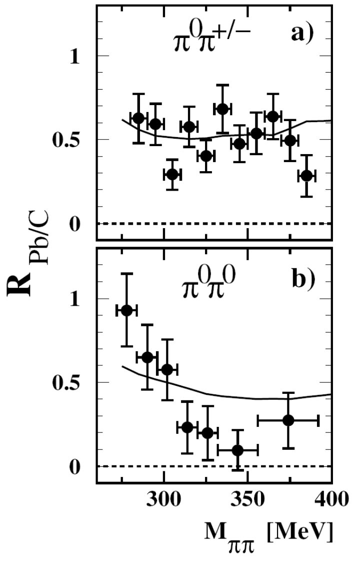

Figure 8.3: The upper figure shows the original plot of Messchendorp *et al.* [Mes02, fig. 4] for the ration $R = (d\sigma/dm_{\pi\pi}/A)_{Pb}/(d\sigma/dm_{\pi\pi}/A)_C$ and an incoming photon energy $E_\gamma = 400 - 460$ MeV. The solid lines show the result of Roca *et al.* [Roc02].

8.3 Model for the elementary reaction

In the following sections, γ-induced $\pi\pi$ in nuclei will be analyzed within the GiBUU framework. For the elementary two pion production process on the nucleon we apply the model of Nacher *et al.* [Nac01], which is an updated version of a model developed by Tejedor *et al.* [GT95, GT96]. This model provides a reliable input for the momentum distributions of the pions in the elementary process. It is based upon a set of tree level diagrams, which include the coupling of the nucleons, pions, photons and baryon resonances ($P_{33}(1232)$, $P_{11}(1440)$, $D_{13}(1520)$ and $P_{33}(1700)$).

The dotted-dashed curves in the panels of 8.1 show the result of this model for the total cross sections. Overall, the agreement of the model to data is satisfactory. However, we decided when possible to scale the total cross section to the available data such that we exploit as much as possible this experimental input before analyzing the reaction in complex targets. Hence, we use for all channels besides $\gamma N \to N\pi^+\pi^-$ directly the data measured by the *TAPS*, *DAPHNE* and the GDH & A2 collaborations [Zab97, Bra95, Har97b, Wol00, Kot04, Lan01, Kle00, Ahr03, Ahr05, Ped07a, Jae07, Ped07b] to normalize the calculated cross sections, while we take the decay mass distributions from theory. In the threshold regions of $\gamma p \to p\pi^0\pi^0$, $\gamma p \to p\pi^-\pi^+$, $\gamma n \to n\pi^0\pi^0$ and $\gamma n \to p\pi^0\pi^-$, where there are no data sets, we estimate the total cross section based on the three particle phase space structure. We assume the matrix element $\mathcal{M}$ to be constant in this region and get

$$\begin{aligned}\sigma_{\text{threshold}} &= \frac{(2\pi)^4}{4m_N q_0}|\mathcal{M}|^2 \int \frac{d\vec{k}_1}{2k_1^0(2\pi)^3}\frac{d\vec{k}_2}{2k_2^0(2\pi)^3}\frac{d\vec{p}\,'}{2p_0'(2\pi)^3}\delta^4\left(q+p-(p'+\sum_{i=1}^{2}k_i)\right) \\ &= \frac{(2\pi)^4}{4m_N q_0}|\mathcal{M}|^2 \times 16\,(2\pi)^7 \times \int \frac{dm_{12}^2 dm_{13}^2}{s} \qquad (8.1)\end{aligned}$$

where s is the Mandelstam s of the process; dm_{12}^2 and dm_{13}^2 are defined by[4]

$$m_{12} = (k_1+k_2)^2 \quad , \qquad (8.2)$$

$$m_{13} = (k_1+p\,')^2 \quad . \qquad (8.3)$$

The value of $|\mathcal{M}|^2$ is now fixed by the value of the lowest available data point

$$\sigma_{\text{threshold}}(\text{energy of lowest data point}) = \sigma(\text{lowest data point})\ .$$

Table 8.1 shows a compilation of those $|\mathcal{M}|^2$.

The solid line shown in the $\gamma n \to n\pi^+\pi^-$ panel shows the model result according to the implementation by Alvarez-Ruso which differs slightly from the original model by the choice of parameters. The other solid lines represent our fits and threshold estimates. Altogether, these six solid lines represent our elementary input cross sections.

8.4 Neutron data

The right hand side panels of fig. 8.1 show evidently, that the available data for neutron targets do not allow for a precise estimate of the total cross section. To determine the $\gamma N \to N'\pi\pi$ cross sections, one often measures the cross section on deuteron and subtracts the proton contribution. Also the *TAPS* collaboration [Lug07b] intends to apply this procedure to the already measured

---

[4] For details on this three-body phase-space confer [Hag02], i. e. chapter 38 *"Kinematics"*.

Channel	E_γ [MeV]	σ [μb]	$\lvert\mathcal{M}\rvert^2 \times (2\pi)^{11}$
$\gamma p \to p\pi^0\pi^0$	380	0.08128	4.871
$\gamma p \to p\pi^-\pi^+$	398	0.9083 [Ped07a]	34.74
$\gamma n \to n\pi^0\pi^0$	387.9	0.3840 [Jae07]	18.60
$\gamma n \to p\pi^0\pi^-$	435	1.752	34.96

Table 8.1: Parameters for the threshold estimation of the total cross section: For each channel, we show the lowest possible energy at which we can reliably estimate the cross section from experiment and the extracted cross section σ. The fourth column shows the corresponding value of the threshold matrix element $|\mathcal{M}|^2$.

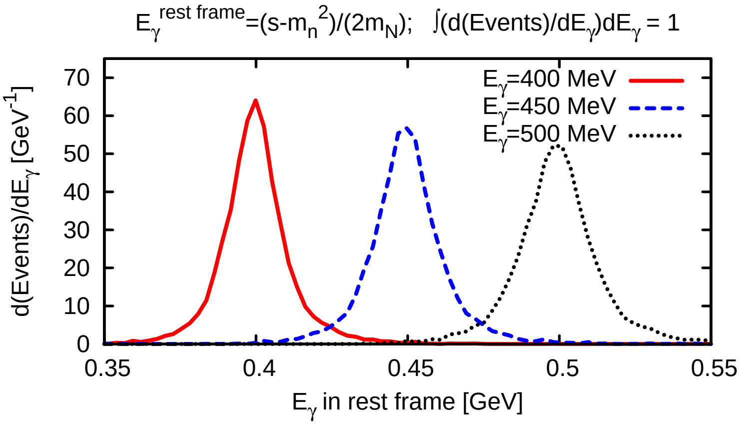

Figure 8.4: The upper figure shows the distribution of photon energies in the rest frame of the target nucleons E_γ^{RF} for three different laboratory photon energies $E_\gamma^{\text{lab}} = 400$, 450 and 500 MeV and a ^2H target.

high-precision deuteron data. However, this subtraction is non-trivial since the target nucleons are in motion within the deuteron. Henceforth, the photon energy in the single nucleon rest frames is different as compared to the nuclear rest frame. Thus one not only needs to subtract the proton contribution, but one also needs to account for this smearing due to Fermi motion to extract the proper energy dependence for the neutron cross section. In fig. 8.4, we show the distribution of the nucleon rest-frame energies

$$E_\gamma^{\text{rest frame}} = \frac{s - m_n^2}{2m_n}$$

for Deuteron (^{2}H) as a function of the photon energy in the nuclear rest frame. It is evident that already in ^{2}H, different regimes of E_γ get mixed due to Fermi motion. Furthermore, final state rescattering might play a role. However, there is no elementary neutron target and so there is no better method to extract the neutron data than measuring the cross section on the deuteron and subtracting the proton contribution. In the following, we want to estimate the model dependence on the extraction of the neutron cross section out of the deuteron data. Since the *TAPS* collaboration [Lug07b] is at present still working on the analysis of the deuteron cross section, the extraction of the neutron cross section could not yet be performed. To be prepared

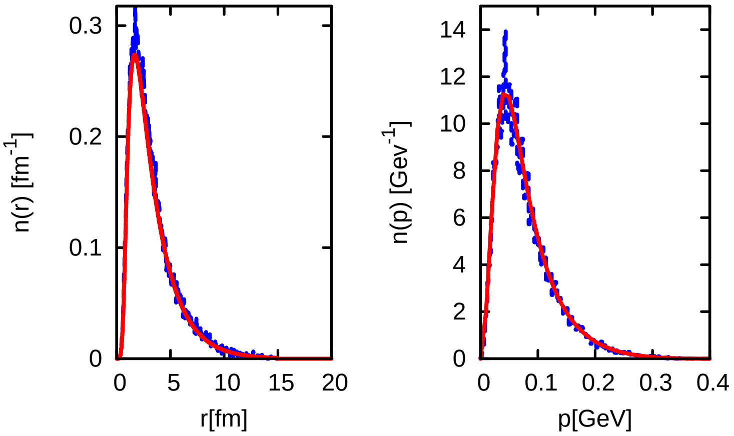

Figure 8.5: This figure shows the relative separation of the two nucleons both in position (upper plot) and momentum space (lower plot). Both distributions are normalized to one. The solid curves denote the result based on the underlying wave functions and the fluctuating step functions represent the Monte Carlo initialization (40.000 ensembles).

for the hopefully soon available data, the following subsections are devoted to this extraction and outlines the most relevant considerations in a simple model.

8.4.1 Deuteron target

The deuteron is a bound state of proton and neutron with total spin $S = 1$. It is not bound by a central potential alone, but by a sum of central potential, the tensor force and spin-spin interactions. The latter tensor force explains also the non-zero quadrupole moment of the deuteron. The experimental binding energy amounts to roughly 2.225 MeV.

For the density and momentum distribution of the nucleons in the ^{2}H target, we adopt the resulting position-space wave-functions (w.f.) $\Psi(r)$ and momentum-space w.f. $\Psi(p)$ of the so-called *Argonne V18 NN-potential*[5] model by Wiringa *et al.* [Wir95]. The deuteron wave function is given by a linear combination of S- and P-wave components, however we neglect for simplification the minor P-wave part. For the BUU-approach we need to define a classical phase-space density. Our choice will be

$$f(\vec{r}, \vec{p}) = |\Psi(r)|^2 \times |\Psi(p)|^2$$

where $\vec{r}$ ($\vec{p}$) is the relative distance of proton and neutron in position (momentum) space. The latter definition of the phase space density does not exhibit the quantum mechanical correlations among position and momentum space. Strictly speaking it is not even possible to write down a quantum mechanical phase space density due to the uncertainty relation. However, our choice yields when integrated over position or momentum the proper distribution functions in position, or respectively momentum, space. In the simulation, we sample the phase-space density by many ensembles ($\sim$ 40.000) of test-particle pairs. This is done on an event-by-event basis, which implies that test-particles of different ensembles do not interact with one another.

---

[5] Cf. [Arg08b, Arg08a] for recent information, deuteron wave function tabulations and the code, which returns the Argonne V18 potential.

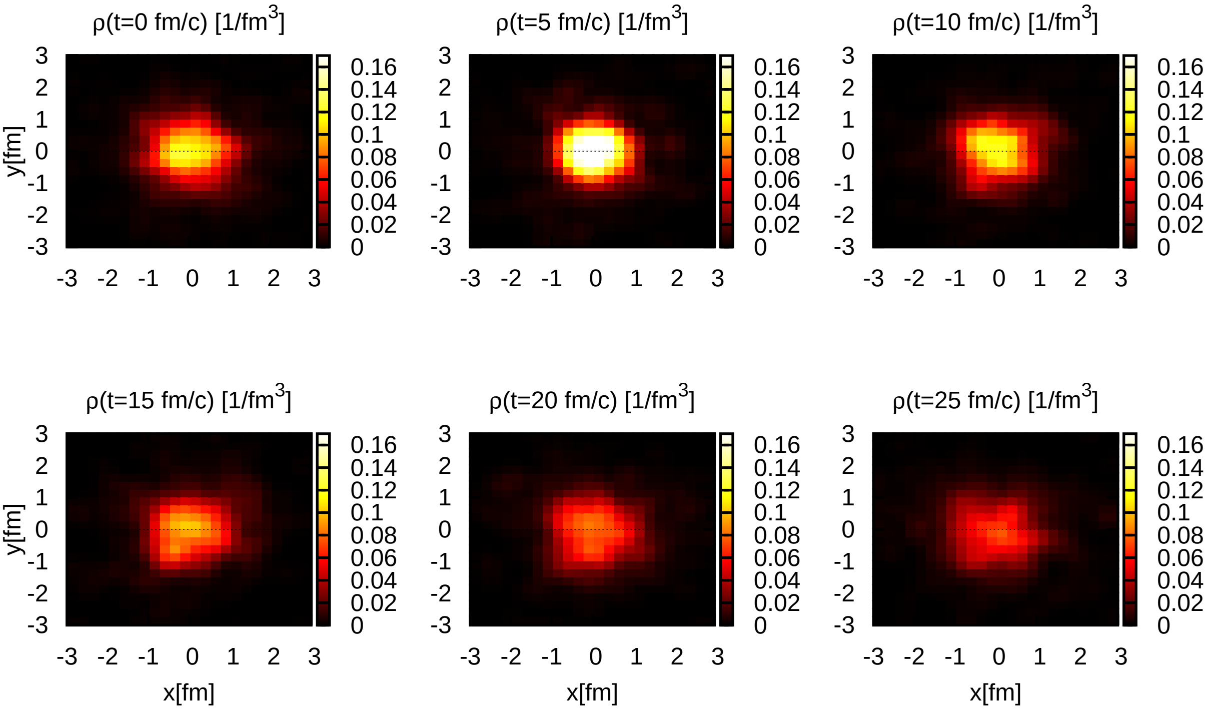

Figure 8.6: The density distribution of ^{2}H in the x-y plane is shown at different times (t=0,5,10,15,20,25 fm/c). The propagation in time was performed with the standard mean field potential *EQS 5*. (Time step size Δt=0.25 fm/c, 5000 ensembles, grid-size= $\sigma_{\text{smearing}} =$ 0.15 fm).

In fig. 8.5, the relative separation of the two nucleons is shown both with our Monte-Carlo initialization and in comparison with the result based on the underlying position and momentum-space wave functions. Within our test-particle realization, the deuteron target has a root-mean-square (RMS) radius of $r = 1.97 \pm 0.01$ fm (40.000 ensembles, grid-spacing= $\sigma_{\text{smearing}} = 0.15$ fm).

In fig. 8.6, we show the propagation of the initialized deuteron configuration according to [Wir95] under the influence of our standard mean field potential *EQS 5*. Evidently, the configuration is very unstable since the initialized distribution does not correspond to the ground state of the potential. To stabilize the initialized configuration in time, we must implement the Argonne V18 potential into our propagation. In this approach, the Hamiltonian for the nucleons in each ensemble is given by

$$H = \sqrt{p_1^2 + m_1^2} + \sqrt{p_2^2 + m_2^2} + V(|\vec{r_1} - \vec{r_2}|)$$

where p_1 and p_2 are the momenta of the two nucleons and V denotes the two-body potential, which depends only on the relative distance of both nucleons and is shown in fig. 8.7. Note, that there is no mean field anymore and that the different ensembles decouple entirely. The binding energy amounts to 1.68 ± 0.2 MeV (Experimental value $\cong 2.22$ MeV [Hag02]); the error of the calculation is based upon the Monte-Carlo sampling of the wave function with 40.000 ensembles.

The V18 potential has large space-derivatives close to the origin. Henceforth, the propagation must be performed with very small time step sizes and within the predictor-corrector scheme. In fig. 8.8, the binding energy is shown as a function of time for 2000 ensembles. From this

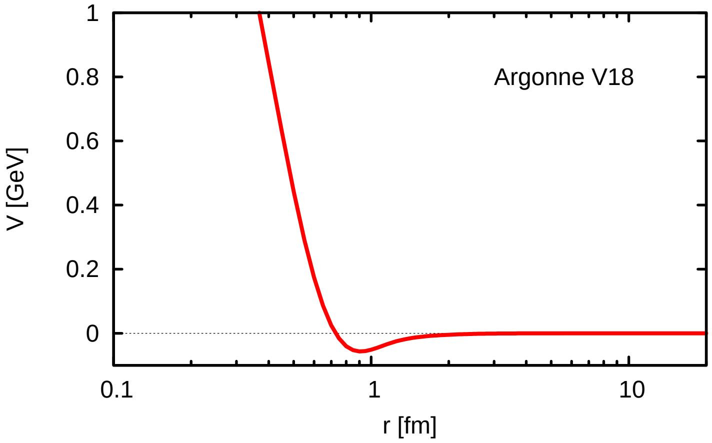

Figure 8.7: The Argonne V18 potential for total spin S=1, total isospin T=0, orbital angular momentum l=0 and total angular momentum J=1[Wir95, Arg08a].

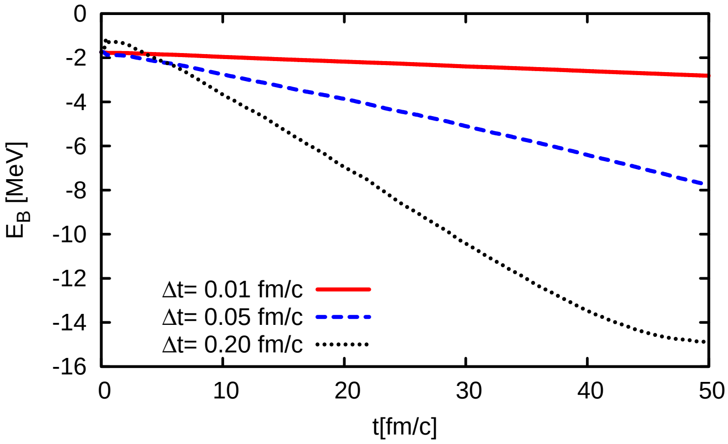

Figure 8.8: The time-evolution of the ^{2}H binding energy for three different time-step sizes $\Delta t =$ 0.01 (solid), 0.05 (long dashed), 0.2 (short dashed line) fm/c (predictor-corrector algorithm, 2000 ensembles).

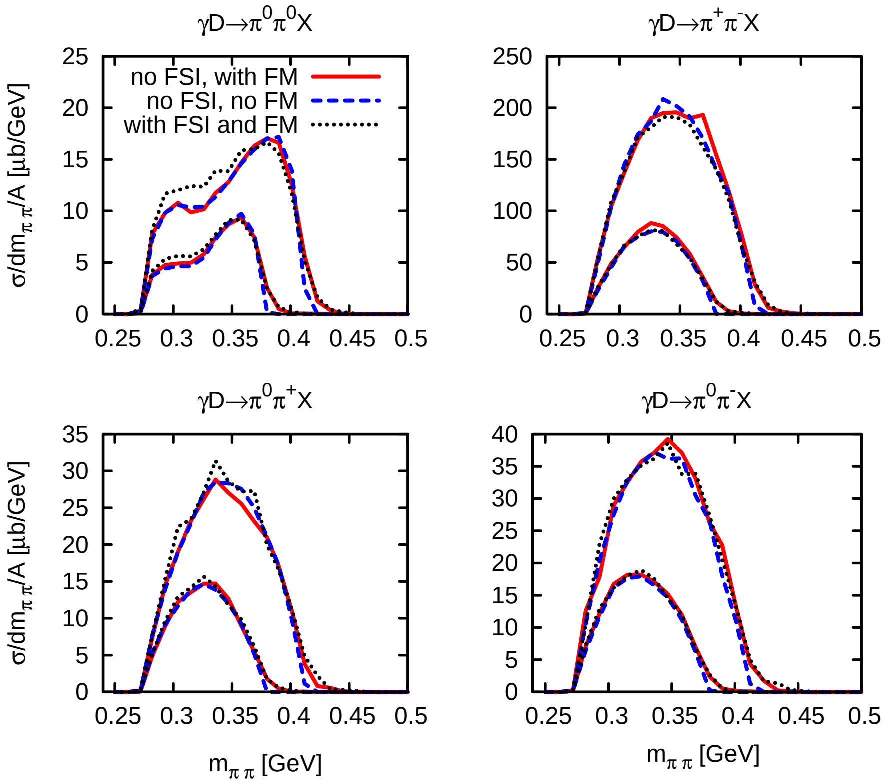

Figure 8.9: Mass differential cross sections for $\pi\pi$ production off the deuteron: for each possible charge channel there is a separate panel which shows the mass-differential cross section $d\sigma/dm_{\pi\pi}$ for two photon energies $E_\gamma = 450, 500$ MeV. The higher the photon energy the larger the cross sections. The solid lines denote the result with Fermi motion (FM) and without final state interactions (FSI); the dotted lines are calculated without both FM and FSI; the dashed lines have been obtained with both FM and FSI included.

figure, we conclude that a time-step size of 0.01 fm/c guarantees for a good description of the deuteron ground state over a period of 50 fm/c. For the latter 2π production simulations, we will choose the same time step size.

8.4.2 Double pion production off the deuteron

To estimate the importance of final state interaction (FSI) and Fermi motion (FM) in the deuteron, we performed three runs for photon energies ranging from 400 to 550 MeV: with both FM and FSI, with FM but without FSI and finally without both FM and FSI. We assumed for the neutron photon interaction total cross sections as shown by the solid line in the right panel of fig. 8.1.

The comparison of those three different types of calculations is shown in fig. 8.9 where the (solid, dotted, dashed) lines denote the result (with,without,with) Fermi motion (FM) an (without,without,with) final state interactions (FSI). From this figure, we first conclude that FM has very little impact. This can be understood if one realizes that the cross sections are roughly linear on intervals which equal the width of the Fermi smearing ($\sim$ 30 MeV, cf. fig. 8.4). Since the smearing is mostly symmetric in the photon energy, this finally leads to almost no FM-modification. Within our FSI model, the FSI effect is also negligible and is maximal in the

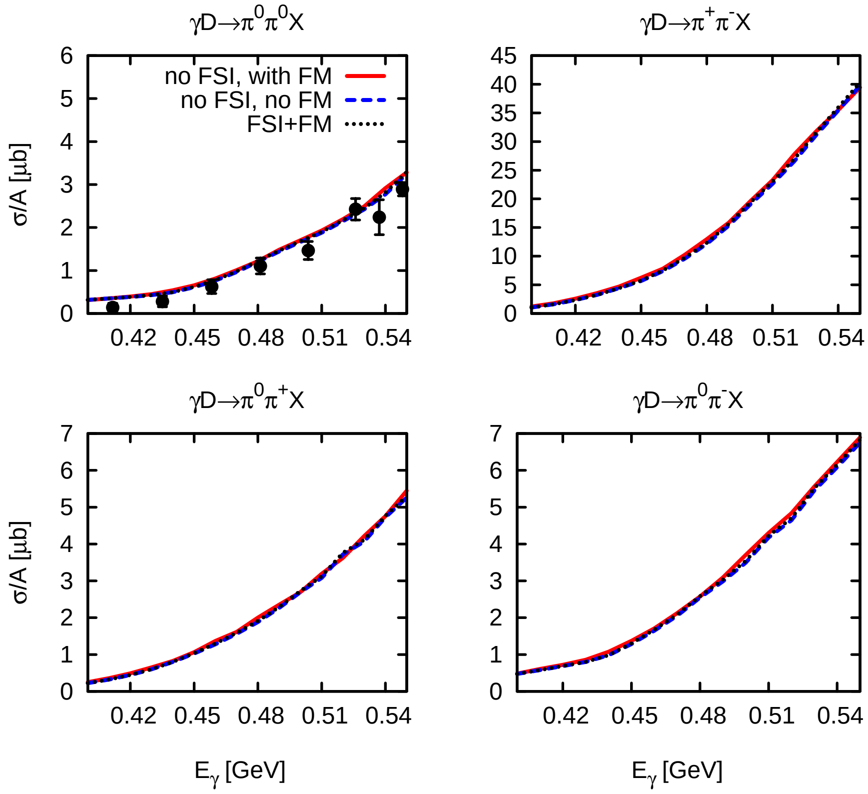

Figure 8.10: Total cross sections for $\pi\pi$ production off the deuteron: for each possible charge channel there is a separate panel. The dotted lines have been obtained with Fermi motion (FM) and without final state interactions (FSI), the solid lines without both FM and FSI and the dashed lines with both FM and FSI. All lines basically overlap. The data are taken from [Kle00].

$\pi^0\pi^0$ channel which profits most by side-feeding since it is the smallest one among the different charge channels. We estimate it to have a maximal impact of roughly 5%. Finally, we must conclude that it is a very good approximation to subtract simply the proton cross section from the deuteron cross section to gain the one on the neutron. According to our model, this should be good within a 5% uncertainty. Fix and Ahrenhövel [Fix05] have drawn very similar conclusions within a much more sophisticated model – especially in the energy region of 400 to 550 MeV, there is almost no FSI effect in their work [Fix05, fig. 10].

8.5 Double pion production off medium and heavy nuclei

Our results for $\pi\pi$ photoproduction off ${}^{40}_{20}\mathrm{Ca}$ and ${}^{207}_{82}\mathrm{Pb}$ nuclei are presented in fig. 8.11 for $E_\gamma = 0.4 - 0.46$ GeV and in fig. 8.12 for $E_\gamma = 0.4 - 0.5$ GeV; the two shown energy bins are the ones which are presently considered in the ongoing analysis by the TAPS group [Gre07]. The impact of a hadronic potential for the nucleon is rather minor, but the reduction of the cross section due to an in-medium modification of the resonance widths is sizable. These modifications according to the *Oset option* for the self energies (cf. sec. 3.6.1) includes a pion-less Δ decay contribution ($\Delta NN \rightarrow NNN$) [Ose87], which leads to a reduction of the final pion yield.

As already discussed in [Mü04a], we observe that absorption, elastic scattering and charge exchange processes cause a considerable change of the spectra with the peak of the mass distribution moving to lower masses due to rescattering. This effect is visualized in fig. 8.13: the dashed lines show our results for $\pi\pi$ production of ${}^{40}_{20}\mathrm{Ca}$ assuming no FSI, the solid lines have been obtained including FSI. One observes a reduction of the cross section by a factor of roughly 2-3 and a shift of the peaks towards lower masses due to FSI. There are two major effects, which lead to the modifications: absorption and rescattering. To point out the role of rescattering, fig. 8.13 shows a so-called *disturbed* (dashed-dotted curves) and *undisturbed* contribution (dotted curves) to the cross section. The undisturbed contribution includes all those pion pairs which do not undergo rescatterings and reach the detector mostly undisturbed; the *disturbed* contribution represents those pairs where at least one of the two pions scattered with the medium but was not absorbed. The total cross section is a sum of disturbed and undisturbed contribution. Obviously, the disturbed contribution is shifted more towards lower masses than the undisturbed one since the pions (on-average) loose energy in a scattering event. At low photon energies the disturbed contribution is small compared to the undisturbed one. Here the energies of the produced pions is small, such that FSI are dominated by the $NN\pi \rightarrow NNN$ process and the effect of $N\pi \rightarrow N\pi$ scattering is small. At higher photon energy (500 MeV) also the average pion energy is higher and, therefore, elastic and charge-exchange scatterings become more important. Thus the disturbed and undisturbed contributions are of the same magnitude for $E_\gamma = 500$ MeV.

To analyze the possible impact of additional in-medium modifications, such as e.g. chiral symmetry restoration, let us study the production points of those pion pairs which are not absorbed and which are, finally, observed. Fig. 8.14 shows the cross section for $\pi\pi$ production off ${}^{40}_{20}\mathrm{Ca}$ at 400 MeV and 500 MeV as function of those production points R_{prod}. The light-Gray areas in fig. 8.14 depict the R_{prod} region where the density is larger than 0.15 fm^{-3}, in the dark-Gray regions the density still reaches at least 0.075 fm^{-3}. Without FSI the distribution $d\sigma_{\pi^0\pi^0}/dR_{prod}$ is proportional to $\rho(R_{prod})R^2_{prod}$; including FSI the distribution is shifted towards higher radius and centered around 3.6 fm which corresponds to roughly $\rho = 0.075$ fm^{-3}. Most of the observed signal stems from a low-density region, which means that possible in-medium signals are expected to be rather weak. Also runs including a pion potential have been performed, only

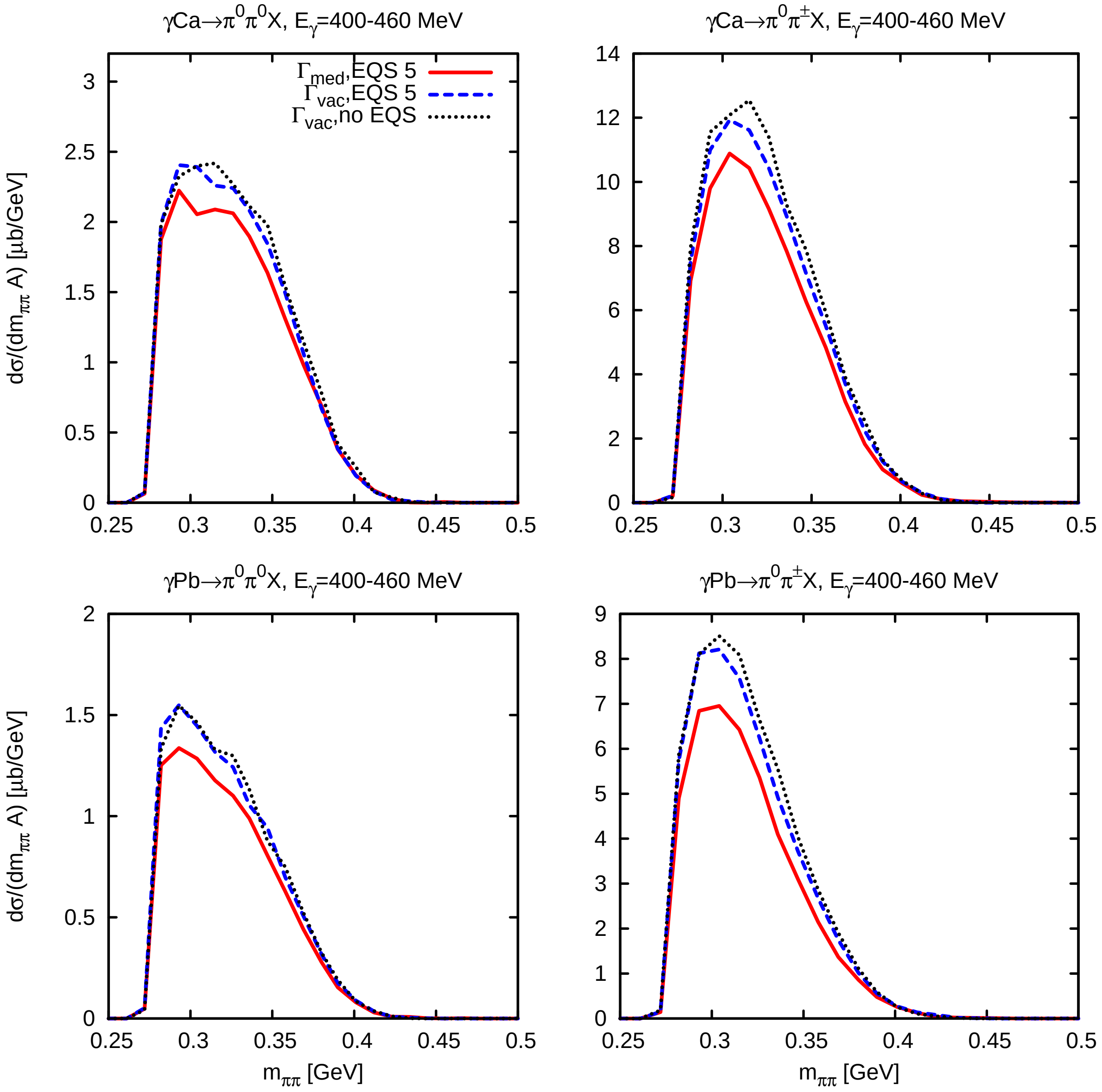

Figure 8.11: Two pion invariant mass distributions for $\pi^0\pi^0$ and $\pi^\pm\pi^0$ photoproduction off $^{40}_{20}$Ca and $^{207}_{82}$Pb for $E_\gamma = 0.4 - 0.460$ GeV. The uncharged $\pi^0\pi^0$ channel is plotted on the left, the charged channel $\pi^\pm\pi^0$ is presented on the right hand side. The solid line depicts the result including the in-medium width and a momentum-dependent mean field potential (EQS=5); the dashed line has been obtained using the vacuum width; the dotted one has been obtained using the vacuum width and assuming no mean field potential.

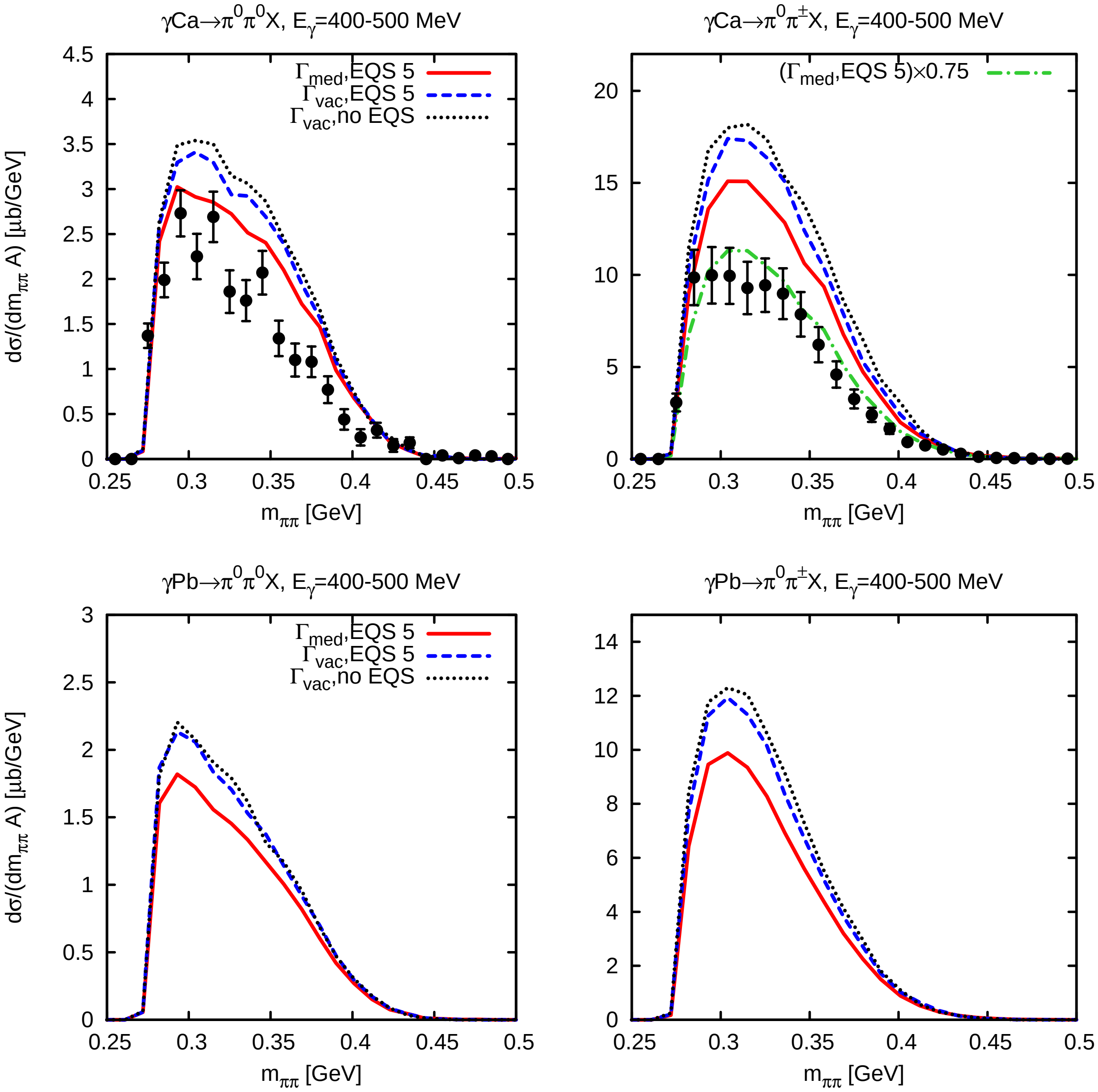

Figure 8.12: Same as fig. 8.11 for $E_\gamma = 0.4 - 0.5$ GeV. The dashed-dotted curve in the upper-left panel shows the result of the full model (Γ_{med} and momentum dependent potential) scaled by a factor 0.75.

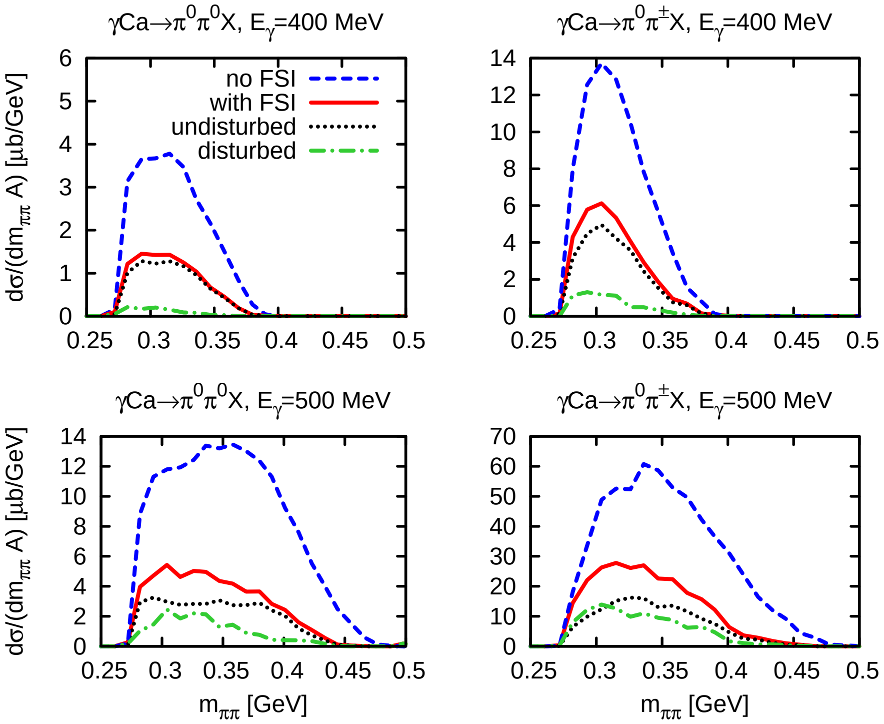

Figure 8.13: The upper figure visualizes the impact of final-state rescattering on the mass-differential cross section for $\pi\pi$ production in $^{40}_{20}$Ca. The dashed curve has been obtained neglecting final state interactions (FSI), while for the calculations represented by the solid, dotted and dashed-dotted curves the FSI have been included. The solid curve shows the total result including FSI; the dotted one represents the contribution of pions which left the medium without rescattering; one of the pions out of each pair contributing to the dashed-dotted "disturbed" contribution underwent at least one scattering event.

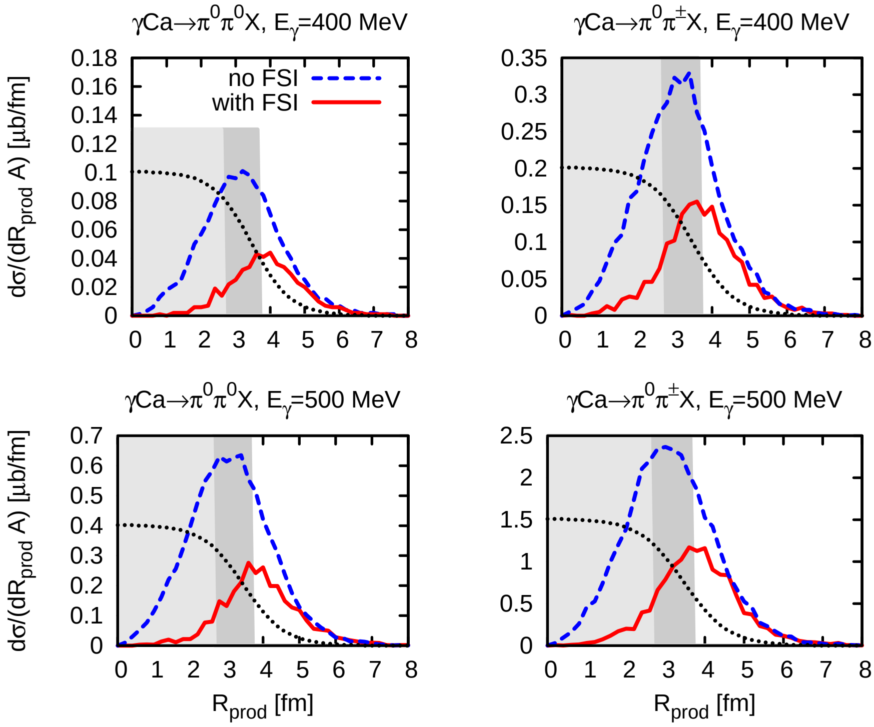

Figure 8.14: Cross section for $\pi\pi$ production in $^{40}_{20}$Ca as a function of the production radius $R_{prod} = (x^2_{prod} + y^2_{prod} + z^2_{prod})^{1/2}$: the solid curve depicts the result with final state interaction (FSI), the dashed one does not include FSI. Additionally, the dotted line depicts the density profile of the $^{40}_{20}$Ca nucleus; the light-gray areas show the R_{prod} region with $\rho \geq 0.15$ fm^{-3}, the dark shaded areas show the region with 0.15 fm$^{-3} \geq \rho \geq 0.075$ fm^{-3}.

a minor effect on the observed pions was found due to the low density at the initial production point.

First experimental results for $^{12}_{6}$C and $^{207}_{82}$Pb targets have been presented in [Mes02]. These data have been reanalyzed by the TAPS collaboration; preliminary results of this analysis can be found in [Sch06a, Sch06b], and a comparison of the former results to this new analysis is given in [Sch05]. Still the old analysis is being reevaluated, especially in the semi-charged channel. Hence we do not present these data sets here. At the moment, new sets of data, taken with a 4π setup with Crystal Ball and TAPS at MAMI, are being analyzed by R. Gregor [Gre07]. With these a meaningful comparison with experiment will be possible. Additionally, data for a $^{40}_{20}$Ca target have been taken [Blo07] during the same run time as the ones published in [Mes02]. However, they have been analyzed independently. In the upper panels of fig. 8.12, we show a comparison of our results to the latter data. One observes very good agreement in the $\pi^0\pi^0$ channel, both in the normalization and the shape of the spectrum. For the $\pi^\pm\pi^0$ channel the shape is also in a good agreement, but the overall normalization is off by a factor of 0.75 (dotted-dashed curve). Concerning the major impact of FSI, this result is already a major achievement. There are two dominant theoretical uncertainties in our calculation: pion reaction mechanism and initial production cross section. The pion FSI reaction mechanism incorporated in the model and its uncertainties have been discussed in the preceding sections. The influence of the uncertainty in the elementary cross sections is illustrated in fig. 8.1. In future, it will be essential to achieve better precision for the elementary neutron channels. Our normalization of the cross section on the nucleus depends directly on the magnitude of the elementary cross section. Thus the question whether our normalization error is a real issue can only be answered with improved experimental input.

To summarize we emphasize that final state interactions of the pions are strong and tend to shift the maximum of the $\pi\pi$ mass distribution in all channels towards lower masses. This effect considerably complicates drawing a link between the experimental data and a possible softening of the in-medium $I = 0$ channel. Any theory aiming to describe the observed effect on the basis of a partial chiral symmetry restoration or an in-medium modification of the $\pi\pi$ production process must take the final state effects into account. Upcoming experimental results on $\pi\pi$ production on the neutron [Lug07a] will improve the elementary input to our calculations. Given these data the normalization issue can be readdressed.

Chapter 9

Summary and Outlook

This study has been devoted to a transport approach to nuclear reactions induced by elementary probes. In the first part of this work, we have introduced the so-called Giessen-Boltzmann-Uehling-Uhlenbeck (GiBUU) transport model focusing both on its model ingredients and on its numerical implementation. The second part has addressed the topic of nuclear reactions induced by elementary probes, where we have applied the GiBUU model to photon-, electron- and pion-induced reactions with typical energy transfers to the nucleus in the range of 10 MeV−1000 MeV. Results obtained via GiBUU simulations have been compared to existing experimental data and predictions for future experiments have been presented.

In chapter 2, the numerical method to solve the Boltzmann-Uehling-Uhlenbeck (BUU) equation has been detailed. After introducing the so-called *test-particle ansatz*, the BUU equation has been rephrased in terms of such test-particles and the time-stepping algorithm has been derived. In the course of this derivation, the most important approximation scheme, the so-called *parallel-ensemble algorithm*, has been introduced and compared to the superior *full-ensemble* and *local-ensemble algorithms*.

While chapter 2 has given a rather general introduction to the BUU equation and its numerical solution, the following chapter 3 has focused on the application of the BUU equation to hadronic-matter transport. There the reader has been introduced to the so-called *GiBUU model* detailing its degrees of freedom and the included interaction mechanisms. The GiBUU model represents an improved version of a BUU model, which was developed by the Giessen theory group over the last two decades [Bau86, Cas90, Eng94, Hom98, Tei96, Eff99a, Lar05, Leh03, Fal04a, Gal05, Mü07]. One of the major improvements comprises a more consistent treatment of the baryonic self-energies. The imaginary parts have been consistently obtained from the underlying collision rates as a function of energy, momentum and density. Then we have applied an once-subtracted dispersion relation to derive the real parts from the imaginary parts, which has led to analytical self energies. Hence the normalization of the spectral functions has been guaranteed, which was not to the case within former treatments. The refined resonance model together with readjusted non-resonant background cross sections has also led to better elementary cross sections, which are needed as input for the BUU equations. As another major improvement, we have connected the region of high-energies, which is described in the model based on Pythia [pyt07], to the low-energy region, where the cross sections are based on the resonance model, by implementing event-mixing of both the string and the resonance model in a cross-over energy regime.

A major enhancement of the numerical realization of the model has been obtained via the implementation of the local-ensemble-algorithm [Lan93], such that the results presented in this work have mostly been obtained in a full-ensemble test-particle scheme which is superior to the parallel-ensemble approximation within earlier treatments. We have restructured and rewritten most of the model source code using FORTRAN 2003 instead of FORTRAN 77 and obtained a modularization of the source code, which has been facilitating the further development and debugging process. In the course of this effort we have introduced a completely new code management structure, with which it is now possible that the complete Giessen transport group[1] can work in parallel on the project source code. This feature has been boosting its development speed and its reliability. In April 2008, we have achieved a major landmark and published the first release of our model source code under the GPL license on the GiBUU website [GiB08b].

In chapter 4, our model for the interaction of electrons and photons with nucleons has been detailed. Based on the one-photon exchange approximation, in which the electron-nucleon scattering process is determined by the interaction of a single virtual photon with the nucleon, the electron-nucleon and photon-nucleon interaction have been treated in an unified picture. We have considered the quasi-elastic process ($\gamma^\star N \to N'$) using modern form factor inputs parametrized by Bradford *et al.* [Bra06]. Additionally, a single-π production process ($\gamma^\star N \to N'\pi$) and resonance production mechanisms ($\gamma^\star N \to R$) have been implemented based on the helicity amplitudes and the invariant amplitudes obtained by the MAID group [MAI]. For real photon-induced processes (i.e. $Q^2 = 0$) we have additionally considered a $\pi\pi$ production background. Since resonance production leads to both single-π and double-π production, we have had to split both processes in resonant and non-resonant contributions. The latter ones have been implemented as background terms and include within our approach also all interferences among resonances themselves and among resonances and non-resonant amplitudes. In Chapter 4 detailed formulas for the hadronic tensors have been given and our elementary input has been compared to electron and photon scattering data on the proton giving excellent correspondence. For real photons our elementary input is very reliable for center of mass energies in the range $m_N < W < 2$ GeV; for electron scattering the input is very good in W up to the 2π threshold, above it the model lacks at present a $\pi\pi$ background whereas the resonance contribution to $\pi\pi$ production is included. Concerning the virtuality of the exchanged photon, the model may be applied up to $Q^2 = 5$ GeV.

In chapter 5 we have focused on our description of the interaction of electrons and photons with nucleons embedded in a nuclear medium. The dispersion relations of the nucleons get modified in a nuclear medium due to hadronic potentials. Thus we account carefully for potentials when evaluating the hadronic tensors and calculate the cross sections taking the modified in-medium kinematics into account. For the form factors in the medium we have assumed, that they are unmodified compared to the vacuum form factors. In the end of this chapter we have derived the nuclear cross sections and we have detailed the implementation within the GiBUU transport model.

Chapter 6 has been devoted to the pion-nucleus interaction. The interaction of pions and nucleons is a crucial cornerstone of every hadronic transport approach since both particle species are most abundant and, therefore, very important within the coupled channel calculations. For our main goal, namely the treatment of electron and photon induced pion production, it is therefore essential to have the pion interactions with the medium well under control. We have benchmarked our pion-nucleon interaction model studying pion absorption, pion reaction and also pion double charge exchange (DCX) reactions in the pion kinetic energy regime of $10 - 200$ MeV. In simulations of pion absorption and charge exchange reactions we have achieved agreement with the available experimental data. However, we have also shown that the description of pions with too long wavelength ($E_{\text{kin}} < 30$ MeV) within a semi-classical treatment starts to break down. In our study of the DCX process we have found that the implementation of pion rescattering and absorption in the GiBUU transport model successfully passes the demanding test of describing DCX reactions. This process shows a high sensitivity on several model details and especially the high sensitivity on neutron skins of heavy nuclei has been discussed. This high sensitivity

---

[1] cf. our website [GiB08b] for a complete list of project members

could be utilized to extract the thickness of such skins indirectly from pion DCX. During our studies, we have also evaluated the parallel-ensemble approximation which was introduced in chapter 2 by comparing results obtained in this scheme to the full-ensemble result. Performing high statistics full ensemble runs, we found deviations to the results obtained in the parallel ensemble scheme. Thus we have concluded that it is favorable to use the full ensemble algorithm for further studies, especially since the performance advantage of the parallel ensemble scheme could be reduced by performing the full-ensemble simulations using the local ensemble algorithm [Lan93].

To summarize our study of pion-nucleus interactions using GiBUU, we have found out that in the kinetic energy region above $E_{\text{kin}} \approx 30$ MeV the semi-classical BUU approach is trustworthy. In this region we have described pion absorption, reaction and DCX data on a level of $10-20\%$ accuracy. This result has been setting the stage for the two following chapters, where we have shown results on inclusive cross sections and pion-production cross sections for electron and photon scattering off nuclei.

In chapter 7 we have first addressed inclusive cross sections to focus on the description of the initial $\gamma^{\star}N$ vertex. There we have outlined the importance of a momentum-dependent nucleon potential and the possibility to tune the included mean field potential has been discussed. Within proper limits on the mean field parameters given by optical model fits to nucleon-nuclei scattering, we have found only a decent improvement when comparing our results to experimental data on inclusive electron scattering off Oxygen [O'C84, Bar88, Sea89, Che91, Day93, Ang96]. Overall, we have achieved a quite good description of experimental data, comparable to state-of-the-art nuclear many-body calculations by Benhar *et al.* [Ben08]. We have also analyzed photon absorption in nuclei [Bia94, Bia96, Muc99], where we have found a good description of data when neglecting the in-medium modifications of the resonance spectral functions. Including the in-medium spectral functions the correspondence to data degraded. Since for the pion-nuclear reactions it is essential to have in-medium resonance modifications, in particular for the $\Delta(1232)$ resonance, this does not mean that there are no in-medium modifications of the resonances. It has rather been concluded that an important model ingredient has still been neglected, such as maybe two-nucleon absorption mechanisms which go beyond the standard impulse approximation. The success of the incomplete model, which neglected the in-medium broadening of the resonances, has been assumed to rather accidental.

For neutral pion production in the energy regime of $0.25-0.8$ GeV [Kru04b, Kru04a] we have achieved a proper description for the quasi-free production mechanism. For the total cross section we have not been able to improve on earlier results by Lehr *et al.* [Leh03], although our present model is much more advanced compared to Lehr's model. Since the description of the quasi-free data has been fine, we have speculated that there is a problem with the 2π contribution, which rises continuously from almost 0% at $q_0 = 0.45$ GeV to roughly 30% of the π^0 yield at $q_0 = 0.8$ GeV. An additional in-medium modification of the $\pi\pi$ background could, therefore, have a major impact on the spectra. Such a modification has not been included so far. We have also pointed out that interference effects play a major role in single-π^0 production at the energy region of discrepancy. Thus we have concluded that it will be unavoidable to take both a dynamical model for the $\pi\pi$ and single-π background into account to improve on the correspondence with data.

Beyond its general interest, the studies presented in chapter 7 have served as a benchmark for ν-induced processes, which are at present performed using the very same model basis by Leitner *et al.* [Lei06b, Lei06a]. We have found that the off-shell potential, which causes a dramatic slow-down of our simulations, has only a very minor impact on the presented results on exclusive pion production and could safely be neglected.

In chapter 8 we have addressed photon-induced $\pi\pi$-production off nuclei. First, we have investigated closely the present situation on the elementary data, before having analyzed the nuclear data. Since the *TAPS* collaboration [Lug07b] is at present still working on the analysis of the deuteron cross section, the data for the γ neutron $\to N\pi\pi$ reaction are still not very accurate. To be prepared for the hopefully soon available data for the deuteron, we have outlined the most relevant considerations for the extraction of the neutron data out of the deuteron data in a simplified model. We have concluded that it is a very good approximation to simply subtract the proton cross section from the deuteron cross section to gain the one on the neutron. According to our simple model, this should be good within a 5% uncertainty.

The modification of the so-called σ or $f_0(600)$ meson inside the nuclear medium was proposed as a signal for a partial restoration of chiral symmetry in nuclear matter. Theoretical models have predicted a shift of its spectral strength to lower masses and a more narrow width due to the onset of the restoration [Ber87, Hat99]. The experimental aim has been to find modifications of the σ state in its $\pi\pi$ decay products, in particular via the study of $\pi\pi$ production in finite nuclear systems close to threshold. Such experiments have been performed with incident pions by the CHAOS collaboration [Bon96, Bon00] and with photons by the TAPS collaboration [Mes02, Blo07]. Both experiments have shown an accumulation of strength near the $\pi\pi$ threshold in the decay channel of the σ in large nuclei. A possible interpretation of this effect is the in-medium modification of this resonance due to partial symmetry restoration, but also conventional final state interactions (FSI) must be treated properly. Lately new high-precision data for $\pi\pi$ production in complex nuclei have been taken by the TAPS collaboration [Gre07], but they are not yet completely analyzed.

We have shown and emphasized that for the $\gamma A \to \pi\pi A'$ reaction final state interactions of the pions are indeed strong and tend to shift the maximum of the $\pi\pi$ mass distribution in all channels towards lower masses. Thus this effect complicates considerably drawing a link between the experimental data and a possible softening of the in-medium $I = 0$ channel. We have emphasized that any theory aiming to describe the observed effect on the basis of a partial chiral symmetry restoration or an in-medium modification of the $\pi\pi$ production process must take final state effects into account. Our simulations have shown that most of the final pion pairs stem from the surface of the nucleus. Hence in-medium effects are expected to be rather weak due to the low effective density.

Finally, let us investigate possible future improvements or extensions of our model. Concerning the photon and electron induced reactions, the most needed improvement concerns the background treatment in $\gamma^\star N$ reactions. Here one must try to medium-modify the backgrounds like it has already been done for the resonance and quasi-elastic processes by implementing the in-medium kinematics and in-medium spectral functions into the background evaluation. A formidable task is, given an in-medium model for the background amplitudes, also the description of medium-modified interference patterns among resonances and background. Furthermore, a background for electron-induced $\pi\pi$ production must be added to improve on our elementary input for electron induced processes. In $\pi\pi$ production at $Q^2 = 0$ the data situation is still vague for the neutron targets. With more precise elementary data one could surely improve our predictions for the nuclear cross sections.

In the GiBUU transport simulations, we still neglect the impact of an in-medium modification of the final-state phase-spaces for the 2 and 3 particle final-states. Due to the density and momentum dependent potentials and spectral functions, one would need to integrate the final-state phase-spaces for each collision separately, since each collision takes place at another density and with a different total momentum. Given several possible final-state channels for each collision, this task can easily become demanding. Hence the main challenge is to develop an efficient treatment, which does not cost too much computation time. Another open issue is the ground state stability. At present our nucleus initialization has the problem, that the density parametrizations from experiment are not identical to the ground state of the applied mean field potential. Lately Steinmüller [Ste07] improved our description by deriving density distributions which are really consistent with a given mean field potential. However, he had to assume a momentum-independent mean-field potential which does not reproduce the peak-shifts seen in quasi-elastic electron-nucleus scattering. A future extension based on Steinmüller's work would be the derivation of a phase-space distribution which then gives the proper ground state for a momentum-dependent potential.

Looking further ahead, hardware trends seem to favor codes which are capable of running on several CPUs in parallel. The algorithms applied in the GiBUU model, in particular the local ensemble algorithm, are highly suited for such a task. Already today, it is possible to execute several identical jobs having different random seeds to work in parallel and one finally averages the results by hand or via shell scripts. Hereby the jobs do not communicate with each other, hence one can not really speak of one 'real' parallel job running on several nodes. Given a 'really' parallel implementation, collecting a lot of statistics could be facilitated and one could also think about working with higher numbers of ensembles than it is presently possible. This increase of ensembles would lead to better densities and an improved Pauli blocking procedure for the heavy-ion runs.

To infer hadronic in-medium properties from nuclear reactions is a formidable task, which however promises to reveal insights on the strong-coupling regime of QCD. Hereby transport models are still among the best suited tools to bridge the gap in between the experimental observables obtained in nuclear reactions and the underlying physics by differentiating profane final-state effects from the *interesting* effects caused by changes of hadronic in-medium properties.

Appendix

Appendix A

GiBUU - physical inputs

Overview: This appendix contains parameters and explicit details on the reaction rates implemented in the GiBUU collision term.

A.1 Decay channels of baryon and meson resonances

The decay channels of the implemented baryons and mesons are summarized in tables A.1 and A.2. For the baryons we list besides the strength of the individual channels at the pole mass of the resonance also the angular momenta of the outgoing states.

	Strength $\Gamma_{R\to AB}/\Gamma_{\text{tot}}$ at pole mass	Product A	Product B	Angular Momentum
Δ	1.0000	π	N	1
$P_{11}(1440)$	0.6900	π	N	1
	0.2200	π	Δ	1
	0.0900	σ	N	0
$S_{11}(1535)$	0.5100	π	N	0
	0.4300	η	N	0
	0.0300	ρ	N	0
	0.0100	σ	N	1
	0.0200	π	$P_{11}(1440)$	0
$S_{11}(1650)$	0.8900	π	N	0
	0.0300	η	N	0
	0.0200	π	Δ	2
	0.0300	ρ	N	0
	0.0200	σ	N	1
	0.0100	π	$P_{11}(1440)$	0
$S_{11}(2090)$	0.1000	π	N	0
	0.0600	π	Δ	2
	0.4900	ρ	N	0
	0.0500	σ	N	1
	0.3000	π	$P_{11}(1440)$	0
$D_{13}(1520)$	0.5900	π	N	2
	0.0500	π	Δ	0
	0.1500	π	Δ	2
	0.2100	ρ	N	0

	Strength $\Gamma_{R\to AB}/\Gamma_{\mathrm{tot}}$ at pole mass	Product A	Product B	Angular Momentum
$D_{13}(1700)$	0.0100	π	N	2
	0.0500	π	Δ	0
	0.7900	π	Δ	2
	0.1300	ρ	N	0
	0.0200	σ	N	1
$D_{13}(2080)$	0.2300	π	N	2
	0.0300	π	Δ	0
	0.2100	π	Δ	2
	0.2600	ρ	N	0
	0.2700	σ	N	1
$D_{15}(1675)$	0.4700	π	N	2
	0.5300	π	Δ	2
$G_{17}(2190)$	0.2200	π	N	4
	0.4900	ω	N	4
	0.2900	ρ	N	2
$P_{11}(1710)$	0.0900	π	N	1
	0.3700	K	Λ	1
	0.4900	π	Δ	1
	0.0300	ρ	N	1
	0.0200	σ	N	0
$P_{11}(2100)$	0.1500	π	N	1
	0.0200	K	Λ	1
	0.2400	π	Δ	1
	0.2700	ρ	N	1
	0.3200	σ	N	0
$P_{13}(1720)$	0.1300	π	N	1
	0.8700	ρ	N	1
P_{13}	0.2600	π	N	1
	0.3000	ω	N	1
	0.4400	ρ	N	1
$F_{15}(1680)$	0.7000	π	N	3
	0.1000	π	Δ	1
	0.0100	π	Δ	3
	0.0500	ρ	N	1
	0.0200	ρ	N	3
	0.1200	σ	N	2
$F_{15}(2000)$	0.0800	π	N	3
	0.1200	π	Δ	1
	0.6000	ρ	N	1
	0.1500	ρ	N	3
	0.0500	σ	N	2
$F_{17}(1990)$	0.0600	π	N	3

	Strength $\Gamma_{R\to AB}/\Gamma_{\text{tot}}$ at pole mass	Product A	Product B	Angular Momentum
	0.9400	η	N	3
$S_{31}(1620)$	0.0900	π	N	0
	0.6200	π	Δ	2
	0.2500	ρ	N	0
	0.0400	ρ	N	2
$S_{31}(1900)$	0.4000	π	N	0
	0.1600	π	Δ	2
	0.0500	ρ	N	0
	0.3300	ρ	N	2
	0.0600	π	$P_{11}(1440)$	0
$D_{33}(1700)$	0.1400	π	N	2
	0.7400	π	Δ	0
	0.0400	π	Δ	2
	0.0800	ρ	N	0
$D_{33}(1940)$	0.1800	π	N	2
	0.0700	π	Δ	0
	0.4000	π	Δ	2
	0.3500	ρ	N	0
$D_{35}(1930)$	0.1800	π	N	2
	0.8200	ρ	Δ	2
$D_{35}(2350)$	0.0200	π	N	2
	0.9800	ρ	Δ	2
P_{31}	0.0800	π	N	1
	0.2800	π	$P_{11}(1440)$	1
	0.6400	ρ	Δ	1
$P_{31}(1910)$	0.2300	π	N	1
	0.1000	ρ	N	1
	0.6700	π	$P_{11}(1440)$	1
$P_{33}(1600)$	0.1200	π	N	1
	0.6800	π	Δ	1
	0.2000	π	$P_{11}(1440)$	1
$P_{33}(1920)$	0.0200	π	N	1
	0.8300	π	Δ	1
	0.1500	π	$P_{11}(1440)$	1
F_{35}	0.0200	π	N	3
	0.2800	π	Δ	1
	0.4800	π	Δ	3
	0.2200	ρ	N	1
$F_{35}(1905)$	0.1200	π	N	3
	0.0100	π	Δ	1
	0.8700	ρ	N	1

	Strength $\Gamma_{R\to AB}/\Gamma_{\text{tot}}$ at pole mass	Product A	Product B	Angular Momentum
$F_{37}(1950)$	0.3800	π	N	3
	0.1800	π	Δ	3
	0.4400	ρ	Δ	3
$\Sigma(1385)$	0.8800	π	Λ	2
	0.1200	π	Σ	1
$\Lambda(1405)$	1.0000	π	Σ	0
$\Lambda(1520)$	0.4600	$\overline{K}$	N	2
	0.4300	π	Σ	2
	0.1100	π	$\Sigma(1385)$	2
$\Lambda(1600)$	0.3500	$\overline{K}$	N	1
	0.6500	π	Σ	1
$\Lambda(1670)$	0.2500	$\overline{K}$	N	0
	0.4500	π	Σ	0
	0.3000	η	Λ	1
$\Lambda(1690)$	0.2500	$\overline{K}$	N	2
	0.3000	π	Σ	2
	0.4500	π	$\Sigma(1385)$	2
$\Lambda(1810)$	0.3500	$\overline{K}$	N	1
	0.2000	π	Σ	1
	0.4500	$\overline{K}^*$	N	1
$\Lambda(1820)$	0.6000	$\overline{K}$	N	3
	0.1200	π	Σ	3
	0.2800	π	$\Sigma(1385)$	3
$\Lambda(1830)$	0.0500	$\overline{K}$	N	2
	0.6000	π	Σ	2
	0.3500	π	$\Sigma(1385)$	2
$\Sigma(1670)$	0.1500	π	Λ	1
	0.1500	$\overline{K}$	N	2
	0.7000	π	Σ	2
$\Sigma(1775)$	0.2000	π	Λ	3
	0.4500	$\overline{K}$	N	2
	0.0500	π	Σ	2
	0.1000	π	$\Sigma(1385)$	2
	0.2000	π	$\Lambda(1520$	3
$\Sigma(2030)$	0.2500	π	Λ	4
	0.2500	$\overline{K}$	N	3
	0.1000	π	Σ	3
	0.1500	π	$\Sigma(1385)$	3
	0.0500	$\overline{K}^*$	N	3
	0.2000	π	$\Lambda(1520$	4

	Strength $\Gamma_{R\to AB}/\Gamma_{\text{tot}}$ at pole mass	Product A	Product B	Angular Momentum
$\Lambda(1800)$	0.3500	$\overline{K}$	N	0
	0.3500	π	Σ	0
	0.3000	π	$\Sigma(1385)$	0
$\Lambda(1890)$	0.3000	$\overline{K}$	N	1
	0.1000	π	Σ	1
	0.3000	π	$\Sigma(1385)$	1
	0.3000	$\overline{K}^*$	N	1
$\Lambda(2100)$	0.3000	$\overline{K}$	N	4
	0.0500	π	Σ	4
	0.4500	π	$\Sigma(1385)$	4
	0.2000	$\overline{K}^*$	N	4
$\Lambda(2110)$	0.1500	$\overline{K}$	N	3
	0.3000	π	Σ	3
	0.5500	$\overline{K}^*$	N	3
$\Sigma(1660)$	0.4000	π	Λ	0
	0.2000	$\overline{K}$	N	1
	0.4000	π	Σ	1
$\Sigma(1750)$	0.1000	π	Λ	1
	0.3000	$\overline{K}$	N	0
	0.6000	π	Σ	0
$\Sigma(1915)$	0.4500	π	Λ	2
	0.1000	$\overline{K}$	N	3
	0.4500	π	Σ	3
Ξ^*	1.0000	π	Ξ	0
Σ_c^*	1.0000	π	Λ_c	0
Ξ_c^*	1.0000	π	Ξ_c	0

Table A.1: The resonance decay channels for baryons in the GiBUU model. The given strength corresponds to the value of the branching ratio at the resonance pole mass.

	Strength $\Gamma_{R\to AB(C)}/\Gamma_{\text{tot}}$ at pole mass	Product A	Product B	Product C
η	0.400	γ	γ	
	0.280	π^0	π^-	π^+
	0.320	π^0	π^0	π^0
ρ	1.000	π	π	
σ	1.000	π	π	
ω	0.020	π	π	
	0.090	π	γ	
	0.890	π^0	π^-	π^+
η'	0.310	ρ	γ	
	0.220	π^0	π^0	η
	0.470	π^+	π^-	η
ϕ	0.130	π	ρ	
	0.840	K	$\overline{K}$	
	0.030	π^0	π^-	π^+
$K^\star$	1.000	K	π	
$\overline{K}^\star$	1.000	$\overline{K}$	π	
$(D^\star)^0$	0.381	γ	D	
	0.619	π	D	
$(\overline{D}^\star)^0$	0.381	γ	$\overline{D}$	
	0.619	π	$\overline{D}$	
$(D^\star)^+$	0.016	γ	D	
	0.984	π	D	
$(\overline{D}^\star)^-$	0.016	γ	$\overline{D}$	
	0.984	π	$\overline{D}$	
$(D_s^\star)^+$	0.950	γ	D_s^+	
	0.050	π	D_s^+	
$(D_s^\star)^-$	0.950	γ	D_s^-	
	0.050	π	D_s^-	

Table A.2: The resonance decay channels for mesons in the GiBUU model. The given strength corresponds to the value of the branching ratio at the resonance pole mass. For two-body decay channels the branching into different charge states is not shown explicitly, it is governed by isospin symmetry.

A.2 Baryon-baryon cross sections

A.2.1 Low-energy baryon-baryon cross sections

$NN \leftrightarrow NN$

For elastic NN scattering we use a parametrization by A. Larionov for the low-energy region and Cugnon *et al.* [Cug96] for the higher-energy region. The elastic pn cross section is given by

$$\sigma = \begin{cases} 17.05\text{ mb GeV } m_N/(s-m_N^2) - 6.83\text{ mb} & \text{for } p_{\text{lab}} \leq 0.525\text{ GeV} \\ 33\text{ mb} + 196\text{ mb}\left|\frac{p_{\text{lab}}}{\text{GeV}} - 0.95\right|^{5/2} & \text{for } 0.525\text{ GeV } < p_{\text{lab}} \leq 0.8\text{ GeV} \\ 31\text{ mb }/\sqrt{\frac{p_{\text{lab}}}{\text{GeV}}} & \text{for } 0.8\text{ GeV} < p_{\text{lab}} \leq 2\text{ GeV} \\ 77\text{ mb }/\left(\frac{p_{\text{lab}}}{\text{GeV}} + 1.5\right) & \text{for } 2\text{ GeV} < p_{\text{lab}} \leq 6\text{ GeV} \end{cases} \quad , \tag{A.1}$$

where p_{lab} denotes the momentum in the target rest frame and $m_N = 0.938$ GeV the averaged nucleon mass. The cross section for nn and pp scattering is given by

$$\sigma = \begin{cases} 5.118\text{ mb GeV } m_N/(s-m_N^2) + 1.673\text{ mb} & \text{for } p_{\text{lab}} \leq 0.435\text{ GeV} \\ \left[23.5 + 1000(\frac{p_{\text{lab}}}{\text{GeV}} - 0.7)^4\right]\text{ mb} & \text{for } 0.435\text{ GeV } < p_{\text{lab}} \leq 0.8\text{ GeV} \\ \left[1250\ /(\frac{p_{\text{lab}}}{\text{GeV}} + 50) - 4(\frac{p_{\text{lab}}}{\text{GeV}} - 1.3)^2\right]\text{ mb} & \text{for } 0.8\text{ GeV} < p_{\text{lab}} \leq 2\text{ GeV} \\ 77\text{ mb}/\left(\frac{p_{\text{lab}}}{\text{GeV}} + 1.5\right) & \text{for } 2\text{ GeV} < p_{\text{lab}} \leq 6\text{ GeV} \end{cases} \quad . \tag{A.2}$$

$NN \leftrightarrow N\Delta$

For the description of the $NN \leftrightarrow N\Delta$ process, Effenberger[Eff96] adopted the successful model of Dmitriev*et al.* [Dmi86] for the Giessen BUU model. We include here for the sake of completeness also the derivations of the matrix elements. Within the Dmitriev model, the interaction between nucleons and Δ's is mediated via the exchange of pions. The interaction Lagrangian is given by

$$\mathcal{L} = \frac{f_\pi F(t)}{m_\pi} \bar{\Psi}\gamma_\mu\gamma_5\tau_a\Psi\partial^\mu\Pi_a + \frac{f_\pi^\star F(t)}{m_\pi}\bar{\Phi}_\mu T_a \Psi\partial^\mu\Pi_a \quad , \tag{A.3}$$

which includes the spin 3/2 spinor Φ_μ for the Δ, the spin 1/2 spinor for the nucleon, the isospin 1/2 matrices τ_a and the isospin 1/2 → 3/2 matrices T_a. The coupling constants are given by

$$f_\pi = 1.008 \quad , \tag{A.4}$$

$$f_\pi^\star = 2.202 \quad . \tag{A.5}$$

And the vertex form factor is chosen to be

$$F(t) = \frac{\Lambda^2 - m_\pi^2}{\Lambda^2 - t} \quad , \tag{A.6}$$

where t is the mass of the virtual pion and $\Lambda = 0.63$ GeV. For each $\Delta N\pi$ vertex one assumes an additional form factor $\sqrt{z}$ (cf. [Dmi86] for motivation), which is given by

$$z(t, m_\Delta) = \frac{p_{\text{cm}}^2(\sqrt{s} = m_\Delta, m_N, m_\pi = \sqrt{t}) + \kappa^2}{p_{\text{cm}}^2(\sqrt{s} = m_\Delta^{\text{pole}}, m_N, m_\pi = \sqrt{t}) + \kappa^2} \quad , \tag{A.7}$$

where $p_{\text{cm}}(\sqrt{s}, m_N, m_\pi)$ denotes the CM-momentum of a pion with mass m_π and a nucleon with mass m_n for a given center-of-mass energy $\sqrt{s}$. The parameter κ is set to 0.2 GeV.

Let us now consider Δ production as depicted in fig. A.1. The cross section for this process

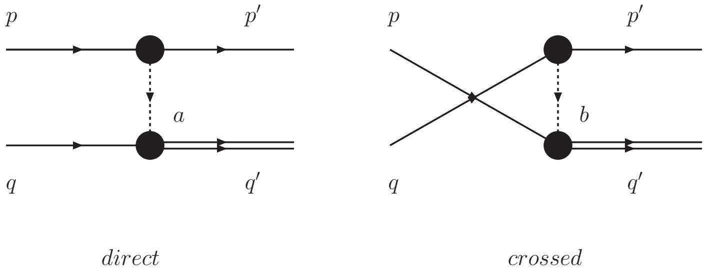

Figure A.1: The direct and crossed diagrams for the $NN \to N\Delta$ process.

	$\mathcal{I}_d$	$\mathcal{I}_c$
$pp \to n\Delta^{++}$	$\sqrt{2}$	$-\sqrt{2}$
$pp \to p\Delta^{+}$	$\sqrt{2/3}$	$-\sqrt{2/3}$
$np \to p\Delta^{0}$	$\sqrt{2/3}$	$-\sqrt{2/3}$.

Table A.3: Isospin factors for the $NN \to N\Delta$ process.

is given by

$$\frac{d\sigma}{d\Omega} = \int dM_\Delta^2 \frac{1}{64\pi^2 s} \frac{p'_{cm}}{p_{cm}} |\mathcal{M}^2| \mathcal{A}_\Delta(M_\Delta) \quad , \tag{A.8}$$

where p_{cm} and p'_{cm} are the initial and final CM momenta. Since the Δ is broad particle, we need to integrate over the spectral function $\mathcal{A}_\Delta$ of the resonance. The matrix element is given by a sum of the crossed and direct contribution

$$\begin{aligned}\mathcal{M} &= \mathcal{I}_d \underbrace{\frac{f_\pi f_\pi^\star F^2(a^2)}{m_\pi^2(a^2-m_\pi^2)} \bar{u}(p')\gamma_\mu\gamma_5(ia^\mu)u(p)\bar{\Phi}_\mu(q')(-ia^\mu)u(q)}_{=\mathcal{M}_d=\text{direct term}} \\ &\quad + \mathcal{I}_c \underbrace{\frac{f_\pi f_\pi^\star F^2(b^2)}{m_\pi^2(b^2-m_\pi^2)} \bar{u}(p')\gamma_\mu\gamma_5(ib^\mu)u(q)\bar{\Phi}_\mu(q')(-ib^\mu)u(p)}_{=\mathcal{M}_c=\text{crossed term}} \quad ,\end{aligned} \tag{A.9}$$

with the pion momenta

$$a = p - p' \quad , \tag{A.10}$$
$$b = q - p' \quad . \tag{A.11}$$

The isospin factors $\mathcal{I}_c$ and $\mathcal{I}_d$ are summarized in table A.3. In the following we will sum and average over the spins of the in- and outgoing particles. We get three terms in the squared matrix element: direct, crossed and interference

$$\mathcal{M}^2 = \frac{1}{4} \sum_{s_p, s_{p'}, s_q, s_{q'}} \mathcal{I}_d^2 |M_d|^2 + \mathcal{I}_c^2 |M_c|^2 + \mathcal{I}_d \mathcal{I}_c (M_d M_c^\star + M_d^\star M_c) \quad . \tag{A.12}$$

Direct contribution The direct contribution is given by

$$\begin{aligned}\sum_{s_p,s_{p'},s_q,s_{q'}} |M_d|^2 &= \left(\frac{f_\pi f_\pi^\star F^2(a^2)}{m_\pi^2(a^2-m_\pi^2)}\right)^2 z(\sqrt{a^2},m_\Delta) Tr\left[(\not{p}'+m)\not{a}\gamma_5(\not{p}'+m)\gamma_0\gamma_5\gamma_0\not{a}\gamma_0\gamma_0\right] \\ &\quad \times Tr\left[(\not{q}'+m)a_\mu a_\nu \Lambda^{\mu\nu}\right] \\ &= \left(\frac{f_\pi f_\pi^\star F^2(a^2)}{m_\pi^2(a^2-m_\pi^2)}\right)^2 z(\sqrt{a^2},m_\Delta) Tr\left[(\not{p}'+m)\not{a}(\not{p}'-m)\not{a}\right] \\ &\quad \times Tr\left[(\not{q}+m)a_\mu a_\nu \Lambda^{\mu\nu}(q')\right] \quad , \qquad \text{(A.13)}\end{aligned}$$

with $\Lambda^{\mu\nu}$ as defined in eq. 4.109. The first trace gives

$$\begin{aligned}Tr\left[(\not{p}'+m)\not{a}(\not{p}'-m)\not{a}\right] &= Tr[\not{p}'\not{a}\not{p}\not{a}] - m^2 Tr[\not{a}^2] \\ &= 4(2(p'a)(pa)-(p'p)a^2-m^2a^2) = -8m^2t \quad , \qquad \text{(A.14)}\end{aligned}$$

where we denoted $t = a^2$ and used $p'p = m^2 - \frac{t}{2}$. Our result for the second trace in the direct contribution is

$$\begin{aligned}Tr\left[(\not{q}+m)a_\mu a_\nu \Lambda^{\mu\nu}(q')\right] &= Tr\left[(\not{q}+m)a_\mu a_\nu(-1)(\not{q}'\,'+m_\Delta)\left(g^{\mu\nu}-\frac{2}{3}\frac{q'^\mu q'^\nu}{m_\Delta^2}\right.\right. \\ &\quad \left.\left.+\frac{1}{3}\frac{q'^\mu\gamma^\nu-q'^\nu\gamma^\mu}{m_\Delta}-\frac{1}{3}\gamma^\mu\gamma^\nu\right)\right] \\ &= -Tr\left[(\not{q}+m)(\not{q}'\,'+m_\Delta)\right]\left(\frac{2}{3}a^2-\frac{2}{3}\frac{(aq')^2}{m_\Delta}\right) \\ &= -\frac{8}{3}\left(qq'+mm_\Delta\right)\left(a^2-\frac{(aq')^2}{m_\Delta^2}\right) \\ &= -\frac{8}{6m_\Delta^2}\left(m_\Delta^2+m^2-t+2mm_\Delta\right)\left(m_\Delta^2 t-\frac{1}{4}(m^2-m_\Delta^2-t)^2\right) \\ &= -\frac{1}{3m_\Delta^2}\left((m_\Delta+m)^2-t\right)\left(2t(m^2+m_\Delta^2)-t^2-(m^2-m_\Delta^2)^2\right) \\ &= -\frac{1}{3m_\Delta^2}\left((m+m_\Delta)^2-t\right)^2\left((m-m_\Delta)^2-t\right) \quad , \qquad \text{(A.15)}\end{aligned}$$

where we used $qq' = \frac{1}{2}\left(m_\Delta^2+m^2-t\right)$.

Altogether we get

$$\sum_{s_p,s_{p'},s_q,s_{q'}} |M_d|^2 = z(t,m_\Delta)\left(\frac{f_\pi f_\pi^\star F^2(t)}{m_\pi^2(t-m_\pi^2)}\right)^2 \frac{8m^2t}{3m_\Delta^2}\left((m+m_\Delta)^2-t\right)^2\left((m-m_\Delta)^2-t\right) . \text{(A.16)}$$

Crossed contribution Replacing $t = a^2 \to u = b^2$ in the direct contribution, we get the crossed one.

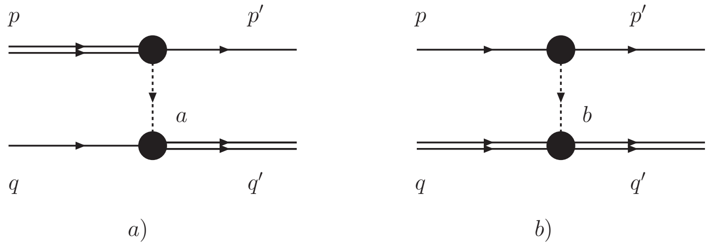

Figure A.2: The diagrams for the $N\Delta \to N\Delta$ process within a one-pion exchange model.

Interference contribution The interference term is given by

$$\begin{aligned}
&\sum_{s_p,s_{p'},s_q,s_{q'}} M_d M_c^\star + M_d^\star M_c = 2\mathrm{Re}\left(M_d M_c^\star\right) \\
&= \left(\frac{f_\pi f_\pi^\star F^2(t)}{m_\pi^2(t-m_\pi^2)}\right)\left(\frac{f_\pi f_\pi^\star F^2(u)}{m_\pi^2(u-m_\pi^2)}\right)\sqrt{z(t,m_\Delta)z(u,m_\Delta)} \\
&\quad\times 2\mathrm{Re}\left\{Tr\left[(\not{p}'-m)\not{a}(\not{p}+m)\Lambda^{\nu\mu}b_\nu a_\mu(\not{q}+m)\not{b}\right]\right\} \\
&= \left(\frac{f_\pi f_\pi^\star F^2(t)}{m_\pi^2(t-m_\pi^2)}\right)\left(\frac{f_\pi f_\pi^\star F^2(u)}{m_\pi^2(u-m_\pi^2)}\right)\frac{8m^2}{2m_\Delta^2}(tu+(m_\Delta^2-m^2)(t+u)-m_\Delta^4+m^4) \\
&\times(tu+m(m+m_\Delta)(m_\Delta^2-m^2)) - \frac{1}{3}(tu-(m_\Delta+m)^2(t+u)+(m+m_\Delta)^4) \\
&\times(tu-m(m_\Delta-m)(m_\Delta^2-m^2)) \quad . \qquad \text{(A.17)}
\end{aligned}$$

For a detailed comparison of these result with data we refer the reader to the work of Dmitriev *et al.* [Dmi86], where the authors demonstrate excellent agreement with data on $d\sigma/dm_\Delta$ and also for the measured angular distributions.

$N\Delta \to N\Delta$

Inspired by the successful description of the $NN \to N\Delta$ process within the one-pion exchange model, we also want to treat the elastic nucleon-Δ scattering within this approximation. The relevant Feynman diagrams are depicted in fig. A.2 where the diagram to the right includes also a $\Delta\Delta\pi$ interaction vertex. In [Eff96], a model based on Dönges *et al.* [Dö95] was applied to the $N\Delta \to N\Delta$ process. Diagram a) of fig. A.2 contains a divergence in case that the intermediate pions goes on on-shell. Effenberger argues that this dominant pole is already included in our model by the two step process of Δ decay and nucleon-pion scattering. Effenberger's result[1] [Eff96, eq. 3.45] for the elastic $N\Delta \to N\Delta$ process is

$$\begin{aligned}
\frac{d^2\sigma}{d\mu_f d\Omega} \quad = \quad & \mathcal{I}\frac{1}{8}\frac{1}{64\pi^2 s}\frac{p'_{\mathrm{cm}}}{p_{\mathrm{cm}}}\left(\frac{f_{NN\pi}f_{\Delta\Delta\pi}}{m_\pi^2}\right)^2\frac{F^4(t)}{(t-m_\pi^2)^2}\frac{16(\mu_i+\mu_f)^2m^2t}{9\mu_i^2\mu_f^2}\times \\
&\times(-\mu_i^2+2\mu_i\mu_f-\mu_f^2+t)(\mu_i^4-2\mu_i^3\mu_f+12\mu_i^2\mu_f^2-2\mu_i\mu_f^3+\mu_f^4-2\mu_i^2t \\
&+2\mu_i\mu_f t-2\mu_f^2t+t^2)\frac{2\mu_f}{\pi}\frac{\mu_f\Gamma_\Delta(\mu_f)}{(\mu_f^2-m_\Delta^2)+(\mu_f\Gamma_\Delta(\mu_f))^2} \quad , \qquad \text{(A.18)}
\end{aligned}$$

with the monopole form factor $F(t)$ as in eq. A.6 and the Dmitriev coupling $f_{NN\pi} = 1.008$. The isospin factor $\mathcal{I}$ is given in table A.4. μ_f and μ_i denote initial and final mass of the Δ,

---

[1] Be careful: the plot 3.16 in [Eff96] does not include isospin factors, although the label says so.

			$\mathcal{I}_{N\Delta\to N\Delta}$
$p\Delta^{++}$	$\to$	$p\Delta^{++}$	9/4
$p\Delta^{+}$	$\to$	$n\Delta^{++}$	3
$p\Delta^{+}$	$\to$	$p\Delta^{+}$	1/4
$p\Delta^{0}$	$\to$	$p\Delta^{0}$	1/4
$p\Delta^{0}$	$\to$	$n\Delta^{+}$	4
$p\Delta^{-}$	$\to$	$p\Delta^{-}$	9/4
$p\Delta^{-}$	$\to$	$n\Delta^{0}$	3

Table A.4: Isospin factors for the $N\Delta \to N\Delta$ process according to Effenberger [Eff96, table 3.6] including also the values for and $p\Delta^- \to n\Delta^0$ and $p\Delta^0 \to n\Delta^+$. For the neutron channels, the isospin factors follow by isospin inversion.

m_Δ is the Δ pole mass, m is the nucleon mass, $t = b^2$. Let us now consider the remaining free parameters of eq. A.18: $\Lambda_{\Delta\Delta\pi}$ and $f_{\Delta\Delta\pi}$. Effenberger uses $\Lambda_{\Delta\Delta\pi} = 1.2$ GeV and as a coupling constant $f_{\Delta\Delta\pi} = 4/5 f_{NN\pi}$ where he cites [Dö95] for. However, it might be more consistent to use $\Lambda_{\Delta\Delta\pi} = \Lambda_{NN\pi} = 0.6$ GeV which has also been used to describe the $NN \to ND$ process (cf. previous section) and extract $f_{\Delta\Delta\pi}$ using the large N_c limit which gives [Pas06]

$$f_{\Delta\Delta\pi} = 9/5 f_{NN\pi} \,. \tag{A.19}$$

In fig. A.3 we contrast both scenarios. There we show the cross section for $p\Delta^+ \to N\Delta$, as a function of the mass and momentum of an incoming Δ scattering off a resting nucleon target. Due to the larger $\Delta\Delta\pi$ coupling, we get in general larger results than Effenberger. However, also the cutoff parameter has a profound impact on the shape of the cross section and mostly counter-balances the effect of the larger coupling. Finally, one must state that the quality of the $N\Delta \to N\Delta$ cross section is hard to evaluate since there are no elementary Δ beams. So it stays a major uncertainty factor within our model.

Implementation of the Δ width based on the model of Oset et al.

For comparison to our usual collisional width for the Δ, we included a description of the Δ width which is based on the work of Oset *et al.* [Ose87]. As Effenberger [Eff99a, appendix A.6], we use the parametrization given in [Ose87] for the special kinematical situation that the Δ was created by a $N\pi$ collision. This is only an approximation since the real width depends both on energy and momentum of the Δ. As detailed in [Eff99a, appendix A.6], our implementation depends only on the Δ mass and is in principle only fully correct if the Δ was created by πN scattering. However, this excitation via pions is the most relevant excitation channel.

In former code versions (in particular in the codes of Effenberger and Lehr), the absorptive part of the collisional width according to Oset *et al.* was implemented and interpreted as an absorption probability for the Δ. For each time step, one decided based on this probability whether the Δ was to be absorbed or not. In case that it was chosen to be absorbed, then it was simply deleted and there was no final state created. One assumed that the final state nucleons would not be relevant for the final particle spectra. However, this is only true if one is solely interested in meson-production: the probability that such an outgoing nucleon recreates a pion is indeed small. But if we want to analyze nucleon spectra, then we need to consider the final state nucleons.

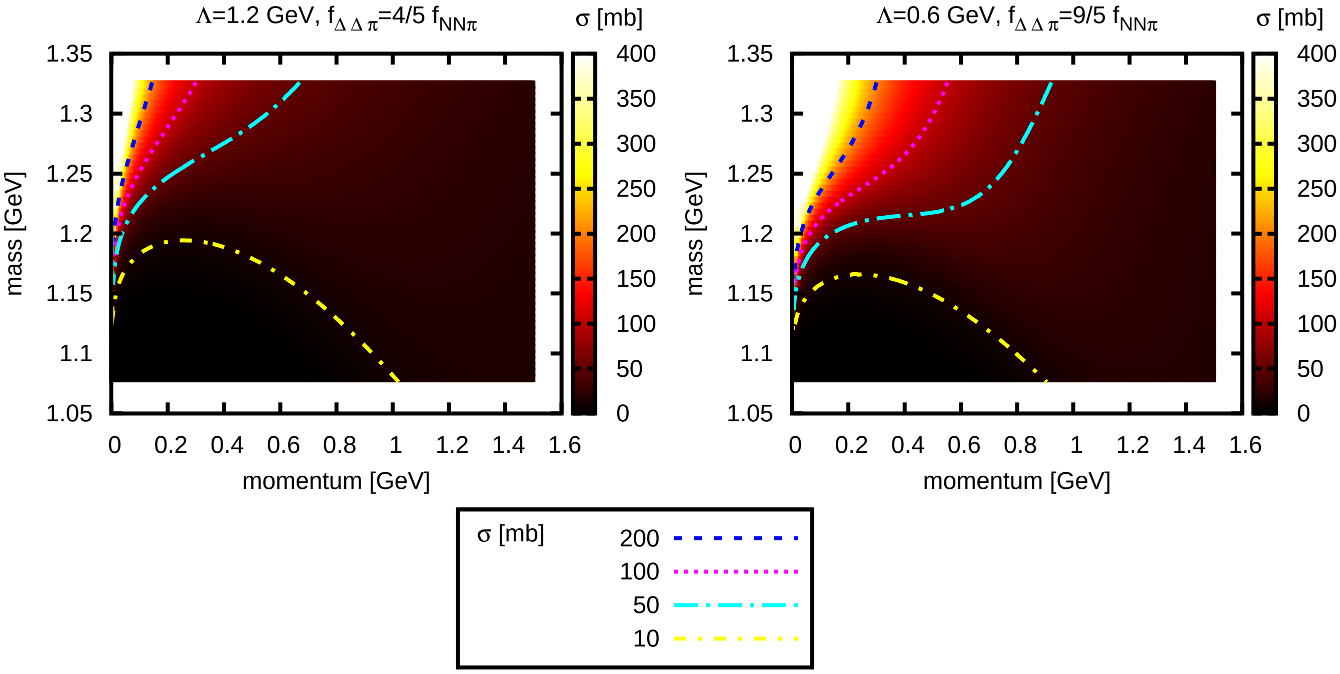

Figure A.3: The upper figure shows the total cross section for $\Delta^+ p \to \Delta N$ as a function of mass and momentum of the incoming Δ. The contours lines denote lines of constant cross section in units of mb. We summed over the final state charges and assumed a resting proton target. The left panel shows the result for $\Lambda = 1.2$ GeV and $f_{\Delta\Delta\pi} = 4/5 f_{NN\pi}$, the right one shows the outcome for $\Lambda = 0.6$ GeV and $f_{\Delta\Delta\pi} = 9/5 f_{NN\pi}$.

We improved on this in the following way. The absorptive part due to three-body processes is implemented as a three-body reaction rate in the collision term (cf. sec. 2.5.3 for details) - the Δ interacts with two random nucleons and we create according to phase-space a three-nucleon final state. The quasi-elastic width Γ_{QE} and the two-body absorption contribution $\Gamma_{\text{2-body abs}}$ are included as two-body reaction rates. Therefore, we define a $N\Delta \to NN$ and a $N\Delta \to N\Delta$ cross section based on these rates and implement them in our 2-body framework. We must demand that these cross sections fulfill

$$\Gamma_{\mathrm{QE}}(\rho, m_\Delta) = 4\int_{\text{Fermi sea}} \frac{d^3p}{(2\pi)^3}\, v_{\mathrm{rel}}\, \sigma_{\mathrm{QE}} \quad , \tag{A.20}$$

$$\Gamma_{\text{2-body abs}}(\rho, m_\Delta) = 4\int_{\text{Fermi sea}} \frac{d^3p}{(2\pi)^3}\, v_{\mathrm{rel}}\, \sigma_{\text{2-body abs}} \quad . \tag{A.21}$$

This means that the cross sections are chosen such that the original interaction rates Γ_{QE} and $\Gamma_{\text{2-body abs}}$ are retrieved when propagating the particle through nuclear matter in its ground state. Since we can not reconstruct the dependence of σ on the nucleon momentum out of the given parametrizations, we assume that σ is independent of this momentum. Finally, the cross sections to be implemented are given by

$$\sigma_{\mathrm{QE}} = \frac{\Gamma_{\mathrm{QE}}(\rho, m_\Delta)}{\bar{v}_{\mathrm{rel}}(p_\Delta)\rho} \quad , \tag{A.22}$$

$$\sigma_{\text{2-body abs}} = \frac{\Gamma_{\text{2-body abs}}(\rho, m_\Delta)}{\bar{v}_{\mathrm{rel}}(p_\Delta)\rho} \quad , \tag{A.23}$$

with the average relative velocity

$$\begin{aligned}
\bar{v}_{\mathrm{rel}}(q) &= \frac{4}{\rho}\int_{\text{Fermi sea}} \frac{d^3p}{(2\pi)^3}\, v_{\mathrm{rel}} = \frac{4}{\rho}\int_{\text{Fermi sea}} \frac{d^3p}{(2\pi)^3} \left| \frac{\vec{q}}{q_0} - \frac{\vec{p}}{p_0} \right| \\
&= \frac{4}{\rho}\int_{\text{Fermi sea}} \frac{d^3p}{(2\pi)^3} \sqrt{\frac{\vec{q}^2}{q_0^2} + \frac{\vec{p}^2}{p_0^2} - 2\frac{\vec{q}\vec{p}}{q_0 p_0}} \\
&= \frac{1}{\rho}\frac{4}{(2\pi)^3} 2\pi \int_0^{p_f} \int_{-1}^{1} d|\vec{p}||\vec{p}|^2 d\cos\theta \sqrt{\frac{\vec{q}^2}{q_0^2} + \frac{|\vec{p}|^2}{m^2+|\vec{p}|^2} - 2\frac{|\vec{q}||\vec{p}|\cos\theta}{q_0\sqrt{m^2+|\vec{p}|^2}}} \\
&= \frac{1}{\rho}\frac{4}{(2\pi)^3} 2\pi \int_0^{p_f} d|\vec{p}||\vec{p}|^2 \frac{2}{3} \left(-\frac{q_0\sqrt{m^2+|\vec{p}|^2}}{2|\vec{q}||\vec{p}|} \right) \left\{ \left(\frac{\vec{q}^2}{q_0^2} + \frac{|\vec{p}|^2}{m^2+|\vec{p}|^2} - 2\frac{|\vec{q}||\vec{p}|}{q_0\sqrt{m^2+|\vec{p}|^2}} \right)^{3/2} \right. \\
&\quad \left. - \left(\frac{\vec{q}^2}{q_0^2} + \frac{|\vec{p}|^2}{m^2+|\vec{p}|^2} + 2\frac{|\vec{q}||\vec{p}|}{q_0\sqrt{m^2+|\vec{p}|^2}} \right)^{3/2} \right\} . \\
&= \frac{1}{\rho}\frac{4}{(2\pi)^3} \frac{2\pi}{3} \frac{q_0}{|\vec{q}|} \int_0^{p_f} d|\vec{p}||\vec{p}| \sqrt{m^2+|\vec{p}|^2} \left\{ \left(\frac{\vec{q}^2}{q_0^2} + \frac{|\vec{p}|^2}{m^2+|\vec{p}|^2} + 2\frac{|\vec{q}||\vec{p}|}{q_0\sqrt{m^2+|\vec{p}|^2}} \right)^{3/2} \right. \\
&\quad \left. - \left(\frac{\vec{q}^2}{q_0^2} + \frac{|\vec{p}|^2}{m^2+|\vec{p}|^2} - 2\frac{|\vec{q}||\vec{p}|}{q_0\sqrt{m^2+|\vec{p}|^2}} \right)^{3/2} \right\} .
\end{aligned} \tag{A.24}$$

This last integral is solved numerically. The factor $\frac{4}{(2\pi)^3}$ comes from the 4-fold degeneracy of nucleons (spin+isospin) and the phase-space volume. A proof for the right implementation of

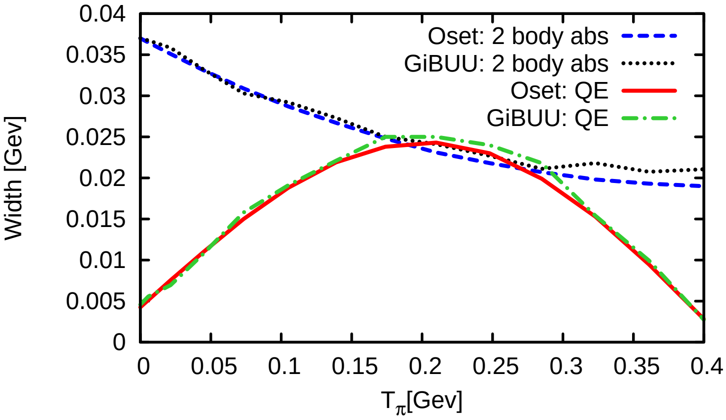

Figure A.4: The upper panel shows a comparison of the original Oset 2-body widths with the widths obtained from the GiBUU implementation. The solid line denotes the quasi-elastic width according to Oset *et al.* [Ose87], the dashed-dotted line the corresponding GiBUU implementation. For 2-body absorption the dashed (Oset *et al.*) and dotted (GiBUU) curves have to be compared. The width is shown as a function of the kinetic energy T_π of a pion which created the resonance in a scattering process with a nucleon out of the Fermi sea; for details confer also sec. 3.6.1.

the obtained cross sections is shown in fig. A.4. There, the width obtained with this GiBUU-implementation and the original Oset width are compared. We find good agreement within the statistical uncertainties.

$NN \leftrightarrow NR$, $NN \leftrightarrow \Delta\Delta$, $NR \leftrightarrow NR'$

We use the same cross sections as detailed in Appendix A1.2 of [Eff99a] based on the analysis presented by Teis [Tei96]. Note, that we have chosen the $NN \to NS_{11}(1535)$ matrix element to be $20 \times 16\pi$ mb GeV^2 (Effenberger has presented three different values in table A.1 of [Eff99a]).

$NR \leftrightarrow NR$

For all resonances besides the Δ, we assume

$$\sigma_{NR\to NR}(\sqrt{s}) = \sigma_{NN\to NN}(\sqrt{s} - m_R + m_N) \; . \tag{A.25}$$

$NN \leftrightarrow NN\pi$

For the $NN \leftrightarrow NN\pi$ process, we consider besides resonance processes, as e.g. $NN \to N\Delta \to NN\pi$, also a point-like background cross-section. The process $NN \to NN\pi$ has been extensively studied in several experiments over the last twenty years [Lan88, And88, Dau02, Har97a, Tsu88, Shi82, Bon95]. Hence we are in a position to define proper background cross sections on top of our resonance contributions for all possible isospin channels. In fig. A.5 we show the relevant cross sections.

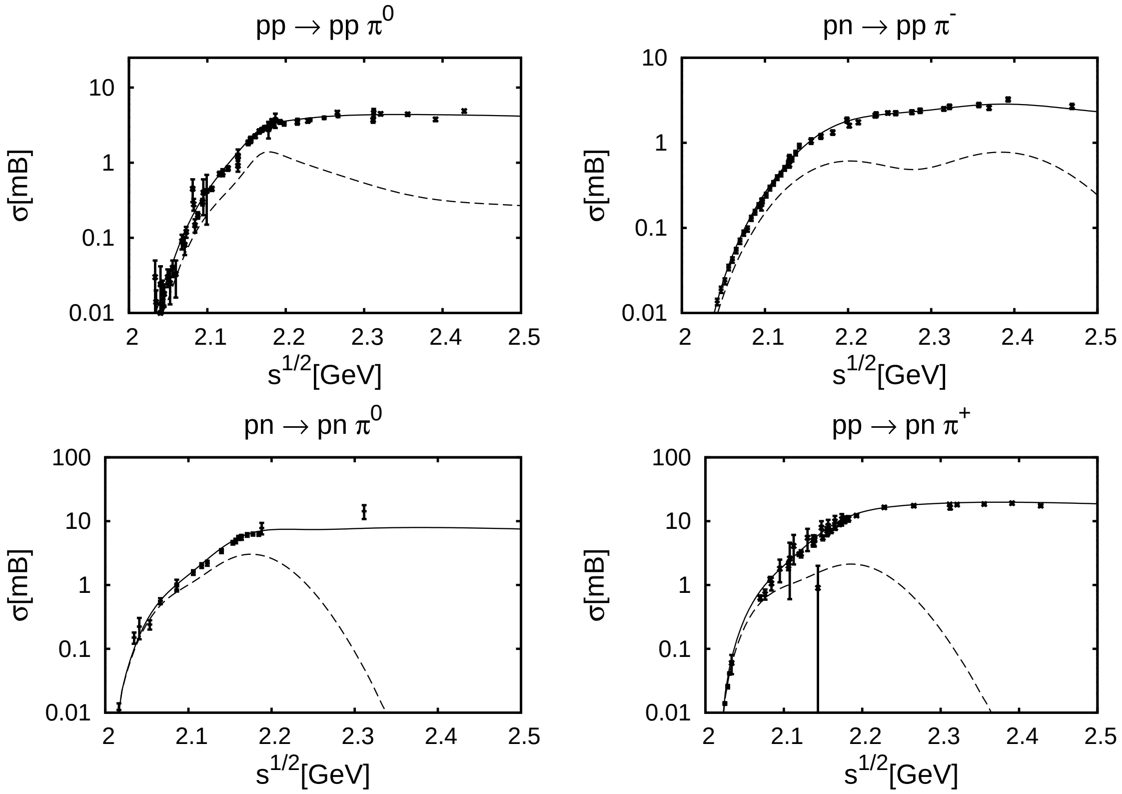

Figure A.5: Elementary cross sections for different $NN \rightarrow NN\pi$ isospin channels. The solid lines show the full cross section, whereas the dashed lines represent the non-resonant background contribution. The data are taken from [Lan88, And88, Dau02, Har97a, Tsu88, Shi82, Bon95].

A.2.2 High-energy baryon-baryon cross sections

For PYTHIA events we use for all baryon-baryon scattering events the same parametrization [Mon94] which is fitted to proton-proton data

$$\begin{aligned} \sigma_{\text{tot}} = & \left\{48.0 + 0.522 \left[\log\left(\frac{p_{\text{lab}}}{\text{GeV}}\right)\right]^2 - 4.51 \log\left(\frac{p_{\text{lab}}}{\text{GeV}}\right)\right\} \text{ mb} \quad , \qquad \text{(A.26)} \\ \sigma_{\text{elast}} = & \left\{11.9 + 26.9 \left(\frac{p_{\text{lab}}}{\text{GeV}}\right)^{-1.21} + 0.169 \left[\log\left(\frac{p_{\text{lab}}}{\text{GeV}}\right)\right]^2 \right. \\ & \left. -1.85 \log\left(\frac{p_{\text{lab}}}{\text{GeV}}\right)\right\} \text{ mb} \quad . \qquad \text{(A.27)} \end{aligned}$$

For $B\overline{B}$ scattering, the following parametrizations [Mon94] are implemented

$$\begin{aligned} \sigma_{\text{tot}} &= \max\left(0, 38.4 + 77.6 \left(\frac{p_{\text{lab}}}{\text{GeV}}\right)^{-0.64} + 0.26 \left(\log\left(\frac{p_{\text{lab}}}{\text{GeV}}\right)\right)^2 \right. \\ & \left. \quad -1.2 \log\left(\frac{p_{\text{lab}}}{\text{GeV}}\right)\right) \text{ mb} \quad , \qquad \text{(A.28)} \\ \sigma_{\text{elast}} &= \max\left(0, 10.2 + 52.7 \left(\frac{p_{\text{lab}}}{\text{GeV}}\right)^{-1.16} + 0.125 \left(\log\left(\frac{p_{\text{lab}}}{\text{GeV}}\right)\right)^2 \right. \\ & \left. \quad -1.28 \log\left(\frac{p_{\text{lab}}}{\text{GeV}}\right)\right) \text{ mb} \quad . \qquad \text{(A.29)} \end{aligned}$$

A.3 Baryon-meson cross sections: Non-resonant background cross sections in the resonance energy region

Besides the resonance cross sections, non-resonant cross section contributions have been implemented in the collision term. The background cross sections denoted by σ^{BG} are chosen in such a manner, that the elementary cross section data in the vacuum are reproduced. Background contributions are instantaneous in space-time, whereas the resonances propagate along their classical trajectories until they decay or interact with one or two nucleons in the nuclear medium.

For relevant channels, we introduce additional background terms due to non-propagated resonances[2], which are also not allowed to be produced in the collision term. To consider their contribution to the total cross section, we include their contribution to the cross section as a direct interaction. Denoting the contribution of all resonances $\sigma_{\text{All resonances}}$ and the one of the propagated ones by $\sigma_{\text{Propagated resonances}}$, we get the background definition

$$\sigma^{\text{BG}}_{res} = \sigma_{\text{All resonances}} - \sigma_{\text{Propagated resonances}} \; . \qquad \text{(A.30)}$$

A.3.1 $\pi N \to X$

$\pi N \to \pi N$

The cross section for quasi-elastic pion-nucleon scattering is in our model given by an incoherent sum of background σ^{BG} and resonance contributions

$$\sigma_{\pi N \to \pi N} \;\; = \;\; \sigma_{\pi N \to R \to \pi N} + \sigma^{\text{BG}}_{\pi N \to \pi N} \quad . \qquad \text{(A.31)}$$

---

[2] A reason for not propagating some resonances might, e.g., be to speed up the simulation.

There is a background due to non-propagated resonances. Additionally, we get a background term due to a lack of strength of the resonance cross sections (cf. sec. 3.3.1 for a definition of the resonance cross sections). Thus we define

$$\sigma^{\mathrm{BG}}_{low} = \max\left(\sigma_{exp} - \sigma_{\text{All resonances}}, 0\right) \quad . \tag{A.32}$$

Therefore the full direct cross section is given by

$$\sigma_{\pi N \longrightarrow \pi N} \quad = \quad \sigma^{\mathrm{BG}}_{low} + \sigma^{\mathrm{BG}}_{res} \, . \tag{A.33}$$

All different events in pion nucleon scattering can be categorized into four different isospin channels

$$\sigma_{\pi^- n \to \pi^- n} \quad = \quad \sigma_{\pi^+ p \to \pi^+ p} \quad , \tag{A.34}$$

$$\sigma_{\pi^- p \to \pi^0 n} \quad = \quad \sigma_{\pi^0 n \to \pi^- p} = \sigma_{\pi^+ n \to \pi^0 p} = \sigma_{\pi^0 p \to \pi^+ n} \quad , \tag{A.35}$$

$$\sigma_{\pi^- p \to \pi^- p} \quad = \quad \sigma_{\pi^+ n \to \pi^+ n} \quad , \tag{A.36}$$

$$\sigma_{\pi^0 n \to \pi^0 n} \quad = \quad \sigma_{\pi^0 p \to \pi^0 p} \quad . \tag{A.37}$$

The cross sections in the individual channels are either connected by time reversal or isospin symmetry. The first channel (eq. A.34) is a pure isospin $I = 3/2$ scattering process, whereas the other three channels are mixtures of $I = 1/2$ and $I = 3/2$. The cross section for the $I = 3/2$ channel $\sigma_{\pi\ N \to \Delta \to \pi\ N}$ is given explicitly in [Eff99a] based on the resonance analysis by Manley and Saleski [Man92].

There are good data sets for the first, second and third channel (eq. A.34-A.36)

$$\begin{aligned} \pi^+ p &\to \pi^+\ p \quad , \\ \pi^- p &\to \pi^-\ p \quad , \\ \pi^- p &\to \pi^0\ n \quad . \end{aligned}$$

down to very low energies. Hence, we introduce a background term on top of our resonance contributions for a better description of those channels. The last channel (eq. A.37) is inaccessible for experiment, therefore we can not introduce any background term. In this approach, we describe in a satisfying manner all available data as can be seen in fig. A.6. In this figure, the elastic (left panels) and total cross sections (right panels) for all pion proton channels are plotted. The solid lines depict the full cross section and the dashed lines show the background contributions.

The **cross sections on the neutron** follow by isospin inversion.

Angular distributions As an improvement in the earlier treatment [Bus06c, Eff97b, Eng94], we now included a more realistic angular distribution for the elastic scattering of the pions. Due to the P-wave nature of the $\Delta(1232)$ resonance, we assume for $\pi N \to \Delta \to \pi N$ in the resonance rest frame a distribution of the pion scattering angle θ [3] according to

$$f^{\Delta}(s, \theta) = \left(1 + 3\cos^2(\theta)\right) g(s, \theta) \quad , \tag{A.38}$$

which is peaked in forward and backward scattering angles. The function $g(s, \theta)$, depending on Mandelstam s, parametrizes the energy dependence of the πN angular distribution. In a

---

[3] The angle θ is spanned by the incoming and outgoing pion momenta. In the simulation, we must store for each Δ produced in a πN collision the momentum of the corresponding pion in the resonance rest frame.

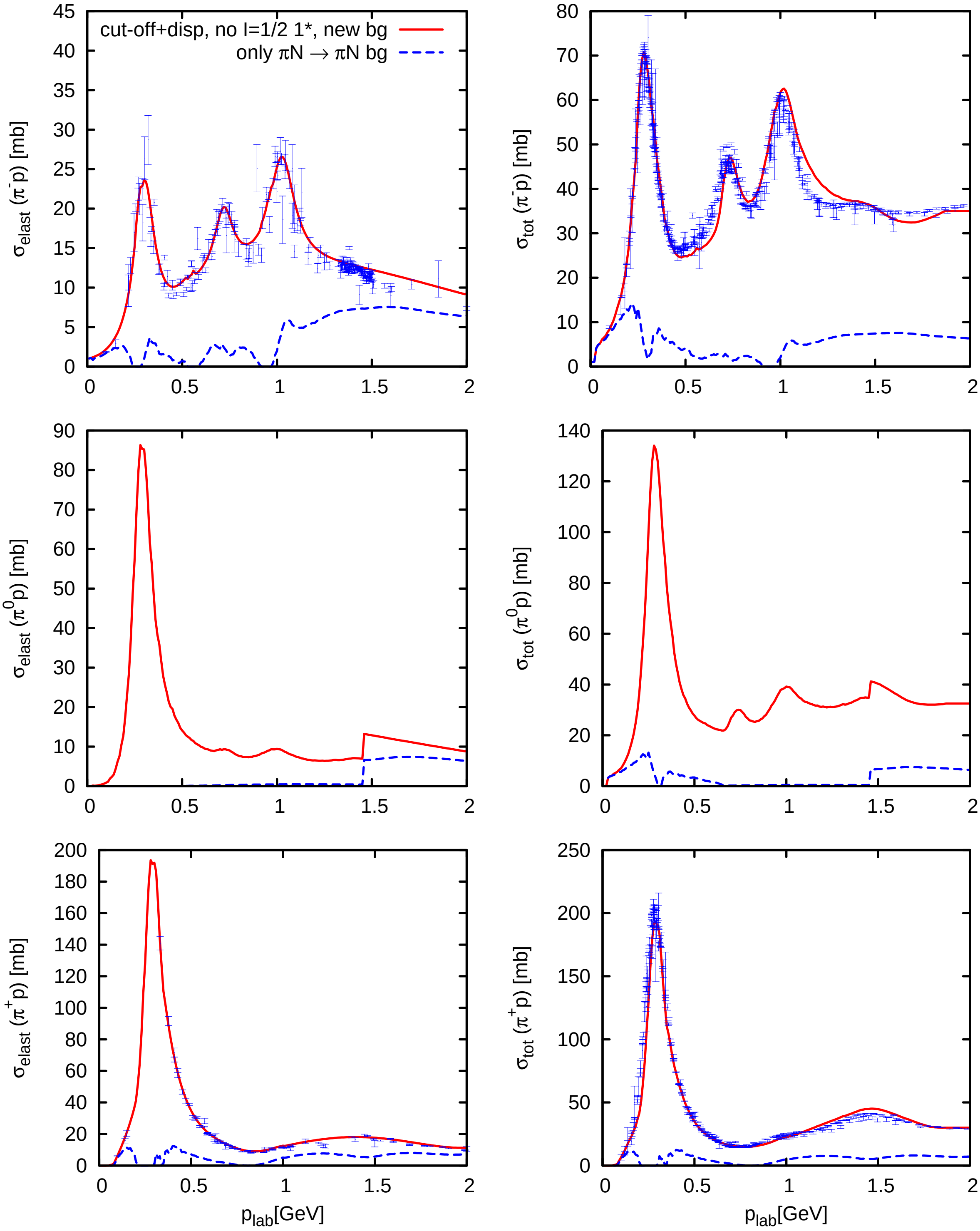

Figure A.6: Elastic (left panels) and total (right panels) cross sections for the scattering of pions and protons. The solid curves show the results with our default parameters: all resonances besides the $I = 1/2$ 1*-resonances are included, the real parts of the self energies are included in the propagators. The dashed curves show the background contributions. The data are taken from [Hag02].

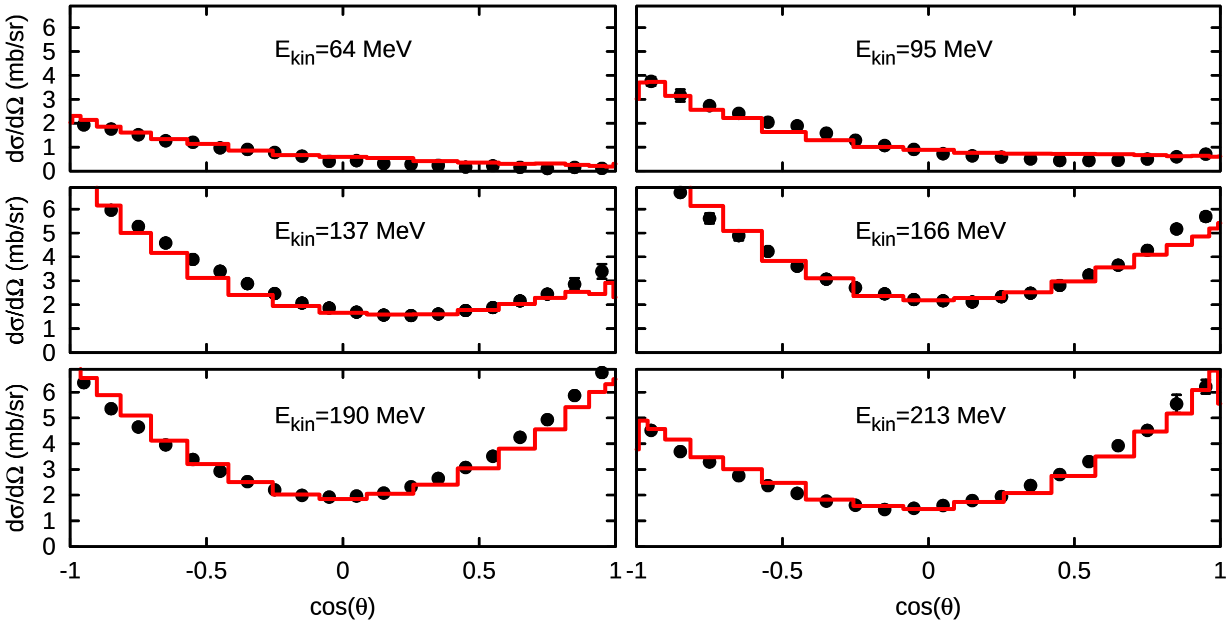

Figure A.7: The angular distributions for the charge exchange process $\pi^- p \to \pi^0 n$ in the CM-frame of pion and proton. The plots are labeled by the kinetic energies of the pions in the laboratory frame. The data are taken from ref. [Sad04].

coherent calculation the angular distribution is generated by interference effects, which can not be accomplished by our transport model. In our ansatz we need to split the cross section in an incoherent way to preserve our semi classical resonance picture. Therefore we take

$$g(s,\theta) = (\alpha - \cos(\theta))^{\beta\left(m_\Delta - \sqrt{s}\right)/m_\Delta} \tag{A.39}$$

with the Δ pole mass $m_\Delta = 1.232$ GeV. For the background events we assume

$$f^{\mathrm{BG}}(s,\theta) = g(s,\theta) \ . \tag{A.40}$$

The constants $\alpha = 1.9$ and $\beta = 26.5$ are fitted to the angular distributions measured by Crystal Ball [Sad04]; a comparison of our parametrization to this data is shown in fig. A.7.

$\pi N \to \pi\pi N$

The $\pi N \to \pi\pi N$ cross section is given by

$$\sigma_{\pi N \to N\pi\pi} = \sum_R \sigma_{\pi N \to R} \frac{\Gamma_{R \to N\pi\pi}}{\Gamma_{\mathrm{tot}}} \quad . \tag{A.41}$$

In A.8, we show the model results for all pion proton channels: $\pi^- p \to \pi^0\pi^0 n$, $\pi^- p \to \pi^+\pi^- n$, $\pi^- p \to \pi^0\pi^- pX$, $\pi^+ p \to \pi^+\pi^+ n$, $\pi^+ p \to \pi^+\pi^0 p$. The short-dashed curve denotes the result which was obtained with the former choice [Eff99a] of included resonances, which was neglecting all 1*-resonance of the Manley analysis. For the solid and long dashed curves, we included the $I = 3/2$ 1*-resonances and excluded only the $I = 1/2$ 1*-resonances. Obviously, this choice fits better the data, especially in the $\pi^+ p \to \pi^+\pi^+ n$ and $\pi^+ p \to \pi^+\pi^0 p$ channels. The difference between the solid and long dashed curve is given by the inclusion of the self energy real parts in the resonance propagators: the long-dashed line does not include it. However, there is only a modest impact of that real part. We conclude that the choice to exclude only the $I = 1/2$ 1*-resonances seems fits the data better than the former choice to exclude all 1*'s.

$\pi N \longrightarrow \eta\Delta$

This cross section is given by

$$\frac{d\sigma_{\pi N\to\eta\Delta}}{dm_\Delta} = \left\langle 1\,\frac{1}{2};q_N\,q_\pi\middle|\frac{3}{2}\,q_\Delta\right\rangle^2 |\mathcal{M}_{\pi N\to\eta\Delta}|^2\,\frac{p_{cm}^{\text{final}}(m_\Delta)}{s\;p_{cm}^{initial}}\mathcal{A}_\Delta(m_\Delta) \quad . \tag{A.42}$$

Assuming a constant matrix element $|\mathcal{M}_{\pi N\to\eta\Delta}|^2 = 7$ mB GeV^2 we can integrate over the mass of the Δ resonance and get

$$\sigma_{\pi N\to\eta\Delta} = \left\langle 1\,\frac{1}{2};q_N\,q_\pi\middle|\frac{3}{2}\,q_\Delta\right\rangle^2 |\mathcal{M}_{\pi N\to\eta\Delta}|^2\,\frac{1}{s\;p_{cm}^{initial}}\int p_{cm}^{\text{final}}(m_\Delta)\mathcal{A}_\Delta(m_\Delta)dm_\Delta \quad . \tag{A.43}$$

$\pi N \longrightarrow \phi N$

Using the result of Golubeva et al. [Gol97] for $\pi^- p \to \phi n$ we define

$$\sigma_{\pi^- p\to\phi n} = \sigma^{\text{Golubeva}}_{\pi^- p\to\phi n} \quad , \tag{A.44}$$

$$\sigma_{\pi^+ n\to\phi p} = \frac{\left\langle 1\,\frac{1}{2};1\,-\frac{1}{2}\middle|\frac{1}{2}\,\frac{1}{2}\right\rangle^2}{\left\langle 1\,\frac{1}{2};-1\,\frac{1}{2}\middle|\frac{1}{2}\,-\frac{1}{2}\right\rangle^2}\,\sigma^{\text{Golubeva}}_{\pi^- p\to\phi n} \quad , \tag{A.45}$$

$$\sigma_{\pi^0 p\to\phi p} = \frac{\left\langle 1\,\frac{1}{2};0\,\frac{1}{2}\middle|\frac{1}{2}\,\frac{1}{2}\right\rangle^2}{\left\langle 1\,\frac{1}{2};-1\,\frac{1}{2}\middle|\frac{1}{2}\,-\frac{1}{2}\right\rangle^2}\,\sigma^{\text{Golubeva}}_{\pi^- p\to\phi n} \quad , \tag{A.46}$$

$$\sigma_{\pi^0 n\to\phi n} = \frac{\left\langle 1\,\frac{1}{2};0\,-\frac{1}{2}\middle|\frac{1}{2}\,-\frac{1}{2}\right\rangle^2}{\left\langle 1\,\frac{1}{2};-1\,\frac{1}{2}\middle|\frac{1}{2}\,-\frac{1}{2}\right\rangle^2}\,\sigma^{\text{Golubeva}}_{\pi^- p\to\phi n} \quad . \tag{A.47}$$

$\pi N \longrightarrow \phi\pi\Delta$

As for the ϕ meson we utilize the model of Golubeva et al. [Gol97] and assume the cross section for different charge channels to be the same. Thus we define

$$\sigma_{\pi N\to\phi\pi N} = \sigma^{Golubeva} \quad . \tag{A.48}$$

$\pi N \longrightarrow \omega N$

Utilizing the result of Golubeva et al. [Gol97] for $\pi^- p \to \omega n$ we define

$$\sigma_{\pi^- p\to\omega n} = \sigma^{\text{Golubeva}}_{\pi^- p\to\omega n} \quad , \tag{A.49}$$

$$\sigma_{\pi^+ n\to\omega p} = \frac{\left\langle 1\,\frac{1}{2};1\,-\frac{1}{2}\middle|\frac{1}{2}\,\frac{1}{2}\right\rangle^2}{\left\langle 1\,\frac{1}{2};-1\,\frac{1}{2}\middle|\frac{1}{2}\,-\frac{1}{2}\right\rangle^2}\,\sigma^{\text{Golubeva}}_{\pi^- p\to\omega n} \quad , \tag{A.50}$$

$$\sigma_{\pi^0 p\to\omega p} = \frac{\left\langle 1\,\frac{1}{2};0\,\frac{1}{2}\middle|\frac{1}{2}\,\frac{1}{2}\right\rangle^2}{\left\langle 1\,\frac{1}{2};-1\,\frac{1}{2}\middle|\frac{1}{2}\,-\frac{1}{2}\right\rangle^2}\,\sigma^{\text{Golubeva}}_{\pi^- p\to\omega n} \quad , \tag{A.51}$$

$$\sigma_{\pi^0 n\to\omega n} = \frac{\left\langle 1\,\frac{1}{2};0\,-\frac{1}{2}\middle|\frac{1}{2}\,-\frac{1}{2}\right\rangle^2}{\left\langle 1\,\frac{1}{2};-1\,\frac{1}{2}\middle|\frac{1}{2}\,-\frac{1}{2}\right\rangle^2}\,\sigma^{\text{Golubeva}}_{\pi^- p\to\omega n} \quad . \tag{A.52}$$

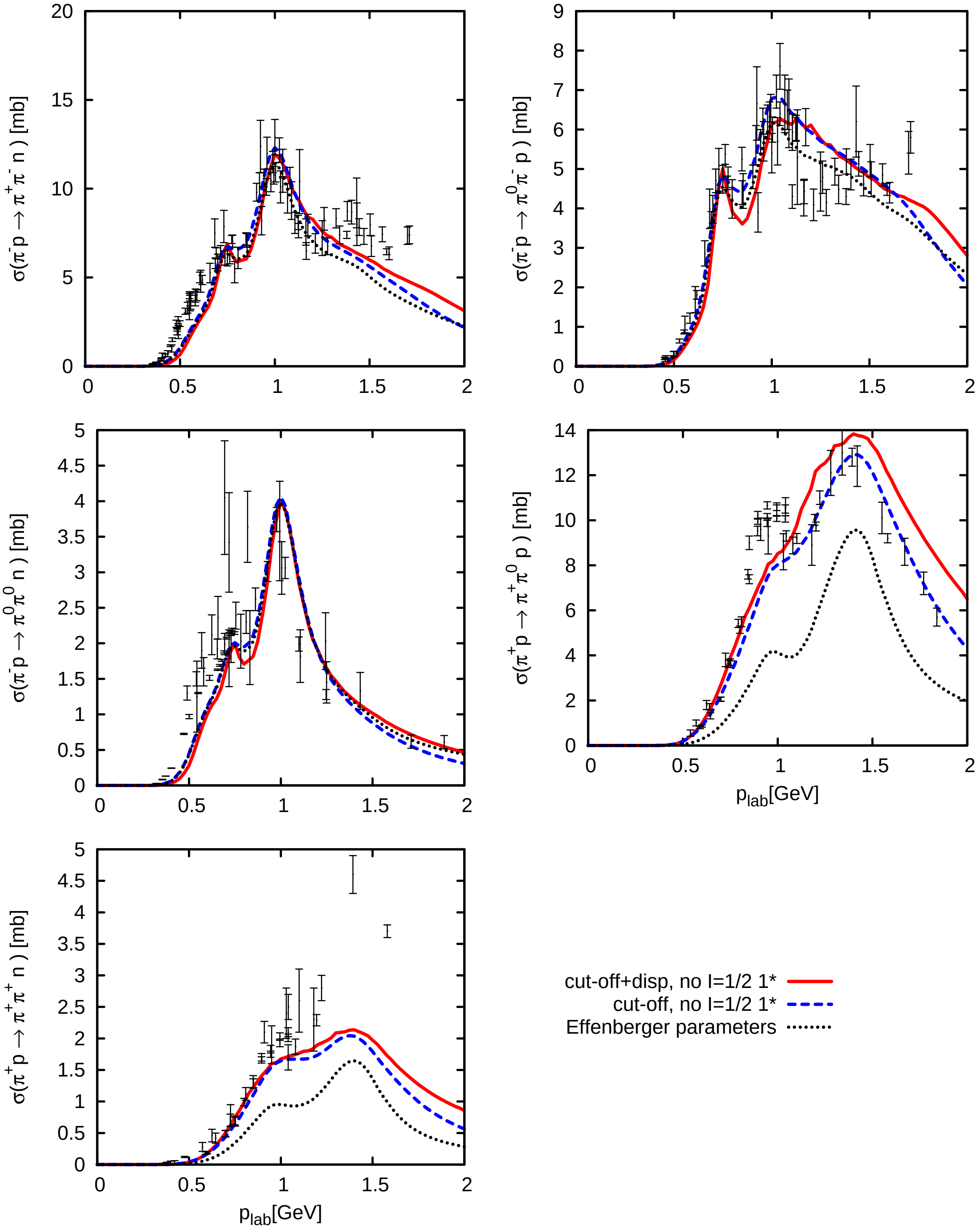

Figure A.8: Cross sections for $\pi^- p \to \pi^0 \pi^0 n$, $\pi^- p \to \pi^+ \pi^- n$, $\pi^- p \to \pi^0 \pi^- pX$, $\pi^+ p \to \pi^+ \pi^+ n$, $\pi^+ p \to \pi^+ \pi^0 p$. The solid line represents the full model in which only those 1*-resonances are not included which have isospin 1/2. The dashed curve neglects the effects of the dispersion relations and the dotted line represents the result according to the former choice of parameters [Eff99a].

$\pi N \longrightarrow \omega\pi N$

Here we utilize once again the results of Golubeva et al. [Gol97] and assume a constant cross sections for all channels and define

$$\sigma_{\pi N \to \omega \pi N} = \sigma^{Golubeva} . \tag{A.53}$$

$\pi N \longrightarrow \Sigma K$

As implemented in [Eff99a], we use a parametrization according to Tsushima et al [Tsu97] for

$$\begin{aligned}
\sigma_{\Sigma\, K}(1) &= \sigma_{\pi^+ p \to K^+ \Sigma^+} \quad , & \text{(A.54)}\\
\sigma_{\Sigma\, K}(2) &= \sigma_{\pi^0 p \to K^+ \Sigma^0} \quad , & \text{(A.55)}\\
\sigma_{\Sigma\, K}(3) &= \sigma_{\pi^- p \to K^0 \Sigma^0} \quad , & \text{(A.56)}\\
\sigma_{\Sigma\, K}(4) &= \sigma_{\pi^- p \to K^+ \Sigma^-} \quad . & \text{(A.57)}
\end{aligned}$$

Assuming isospin symmetry and isospin $I = \frac{1}{2}$ dominance, we get

$$\sigma_{\pi^0 p \to K^0 \Sigma^+} = \sigma_{\pi^- p \to K^0 \Sigma^0} = \sigma_{\Sigma\, K}(3) \ . \tag{A.58}$$

These last five cross sections (A.54) to (A.58) define all possible channels with a proton in the initial state. Channels with an initial neutron are defined by charge conjugation:

$$\begin{aligned}
\sigma_{\pi^- n \to K^0 \Sigma^-} &= \sigma_{\pi^+ p \to K^+ \Sigma^+} &= \sigma_{\Sigma\, K}(1) \quad , & \quad \text{(A.59)}\\
\sigma_{\pi^0 n \to K^0 \Sigma^0} &= \sigma_{\pi^0 p \to K^+ \Sigma^0} &= \sigma_{\Sigma\, K}(2) \quad , & \quad \text{(A.60)}\\
\sigma_{\pi^+ n \to K^+ \Sigma^0} &= \sigma_{\pi^- p \to K^0 \Sigma^0} &= \sigma_{\Sigma\, K}(3) \quad , & \quad \text{(A.61)}\\
\sigma_{\pi^+ n \to K^0 \Sigma^+} &= \sigma_{\pi^- p \to K^+ \Sigma^-} &= \sigma_{\Sigma\, K}(4) \quad , & \quad \text{(A.62)}\\
\sigma_{\pi^0 n \to K^+ \Sigma^-} &= \sigma_{\pi^- p \to K^0 \Sigma^0} &= \sigma_{\Sigma\, K}(3) \quad . & \quad \text{(A.63)}
\end{aligned}$$

$\pi N \longrightarrow \Lambda K$

As implemented in [Eff99a] we use a parametrization according to Tsushima et al [Tsu97] for $\pi^- p \to \Lambda K^0$. We define a $\pi N \longrightarrow \Lambda\, K$ background cross section by subtracting the resonance contributions.

$$\sigma^{\mathrm{BG}}_{\pi^- p \to \Lambda K^0} = \sigma^{\mathrm{Tsushima}}_{\pi^- p \to \Lambda K^0} - \sigma^{\mathrm{Resonances}}_{\pi^- p \to \Lambda K^0} . \tag{A.64}$$

The other channels follow by isospin considerations since all processes need to go through an isospin $I = \frac{1}{2}$ channel:

$$\begin{aligned}
\sigma^{\mathrm{BG}}_{\pi^+ n \to \Lambda K^+} &= \sigma^{\mathrm{BG}}_{\pi^- p \to \Lambda K^0} \quad , \\
\sigma^{\mathrm{BG}}_{\pi^0 p \to \Lambda K^+} &= \frac{\left\langle \frac{1}{2}\, 1; \frac{1}{2}\, 0 \middle| \frac{1}{2}\, \frac{1}{2} \right\rangle^2}{\left\langle \frac{1}{2}\, 1; \frac{1}{2}\, -1 \middle| \frac{1}{2}\, -\frac{1}{2} \right\rangle^2}\, \sigma^{\mathrm{BG}}_{\pi^- p \to \Lambda K^0} = \frac{1}{2}\, \sigma^{\mathrm{BG}}_{\pi^- p \to \Lambda K^0} \quad , \\
\sigma^{\mathrm{BG}}_{\pi^0 n \to \Lambda K^0} &= \frac{\left\langle \frac{1}{2}\, 1; -\frac{1}{2}\, 0 \middle| \frac{1}{2}\, -\frac{1}{2} \right\rangle^2}{\left\langle \frac{1}{2}\, 1; \frac{1}{2}\, -1 \middle| \frac{1}{2}\, -\frac{1}{2} \right\rangle^2} \sigma^{\mathrm{BG}}_{\pi^- p \to \Lambda K^0} = \frac{1}{2}\, \sigma^{\mathrm{BG}}_{\pi^- p \to \Lambda K^0} \quad .
\end{aligned}$$

$\pi N \to K\bar{K}N$

This cross section is parametrized according to Sibirtsev et al. [Sib97]. Details concerning the Clebsch-Gordan coefficients an be found in [Eff99a]. The cross-sections are given by

$$\sigma_{\pi^- p\to nK^0\bar{K}^0} = \sigma^{\text{Sibirtsev}} \qquad \sigma_{\pi^- p\to pK^0\bar{K}^-} = \tfrac{1}{2}\,\sigma^{\text{Sibirtsev}} \quad ,$$

$$\sigma_{\pi^- p\to nK^+\bar{K}^-} = \sigma^{\text{Sibirtsev}} \qquad \sigma_{\pi^0 p\to nK^+\bar{K}^0} = \sigma^{\text{Sibirtsev}} \quad ,$$

$$\sigma_{\pi^0 p\to pK^0\bar{K}^0} = \tfrac{1}{4}\,\sigma^{\text{Sibirtsev}} \qquad \sigma_{\pi^0 p\to pK^+\bar{K}^-} = \tfrac{1}{4}\,\sigma^{\text{Sibirtsev}} \quad ,$$

$$\sigma_{\pi^+ p\to pK^+\bar{K}^0} = \tfrac{1}{2}\,\sigma^{\text{Sibirtsev}} \quad ,$$

where

$$\sigma^{\text{Sibirtsev}} = 1.121\left(1-\frac{s_0}{s}\right)^{1.86}\left(\frac{s_0}{s}\right)^2 \text{ mB} \tag{A.65}$$

with $s_0 = (m_N + 2m_K)^2$. All channels with an incoming neutron are given by charge conjugation.

A.3.2 $\pi\Delta \to X$

Besides resonance production channels, backgrounds for ΛK and ΣK production are implemented according to [Tsu97].

A.3.3 $\rho N \to X$

Besides resonance production channels, a πN background is introduced to absorb missing inelasticities above $\sqrt{s} > 1.8$ GeV:

$$\sigma\rho N \to \pi N = \sigma_{\text{tot, data}} - \sigma_{\text{tot, resonances}} \;. \tag{A.66}$$

A.3.4 $\eta N \to X$

$\eta N \to \pi N$

Additionally to resonance production, a πN background is defined for $\sqrt{s} > 2$ GeV

$$\sigma\eta N \to \pi N = \sigma_{\text{tot, data}} - \sigma_{\text{tot, resonances}} \;. \tag{A.67}$$

In this approach, missing resonance strength is attributed to the πN channel.

A.3.5 $\eta\Delta \to X$

$\eta\Delta \to \pi N$

Due to detailed balance we get

$$\sigma\eta\Delta \to \pi N = \frac{1}{2}|\mathcal{M}_{\pi N\to\Delta\eta}|^2 \frac{p_f}{s\;p_i} \quad . \tag{A.68}$$

The factor 1/2 is due to (2j+1)-terms in the cross sections and different spins in initial and final state.

A.3.6 $\omega/\phi N \to X$

The results of Golubeva et al. [Gol97] are used for the background in ωN and ϕN scattering. Since we introduced $\pi N \leftrightarrow \omega/\phi N$ channels, we must introduces a corresponding reversed channel to conserve detailed balance. Additionally, an elastic background

$$\sigma\omega/\phi N \to \omega/\phi N = \sigma_{\text{elast,Golubeva}} - \sigma_{\text{elast, resonances}} \quad . \tag{A.69}$$

and a $\pi\pi N$ channel

$$\sigma\omega/\phi N \to \pi\pi N = \sigma_{\text{tot,Golubeva}} - \sigma_{\text{tot, resonances}} \quad , \tag{A.70}$$

is implemented. The latter one is attributed all the missing strength in the total cross section.

A.4 Nucleon mean field potential

The hadronic potentials have been introduced in sec. 3.4.2 as time-like components of vector potentials in the local rest-frame (LRF) (The *local rest frame* is defined to be the frame in which the baryonic currents vanish). This section is devoted to the fixing of the potential parameters a, b, c, τ and Λ, which have been introduced in eq. 3.29

$$A_N^0(\vec{r},\vec{p}) = a\frac{\rho(\vec{r})}{\rho_0} + b\left(\frac{\rho(\vec{r})}{\rho_0}\right)^{\tau} + \frac{2c}{\rho_0} g \int \frac{d^3p'}{(2\pi)^3} \frac{f(\vec{r},\vec{p}\,')}{1+\left(\frac{\vec{p}\,'-\vec{p}}{\Lambda}\right)^2} \quad . \tag{A.71}$$

The parameter $g = 4$ denotes the nucleon degeneracy factor. As we already pointed out in sec. 3.4.2, Teis [Tei96] fitted five distinct standard parameter sets (listed in table 3.4) to nuclear matter properties. By default, the parameter set *medium momentum-dependent* (EQS 5) is being used for all calculations. The aim of this section is to point out how these parameter sets have been fixed. This then opens the possibility to fine-tune the sets with the help of inclusive electron scattering data.

A.4.1 Fixing the potential parameters

The energy density of nuclear matter is given by

$$\epsilon(\vec{r}) = \underbrace{g\int \frac{d\vec{p}}{(2\pi)^3}\sqrt{\vec{p}^2+m_N^2}\, f(\vec{r},\vec{p})}_{\text{kinetic energy density}} + \underbrace{V_N(\rho(\vec{r}))}_{\text{potential energy density}} \quad . \tag{A.72}$$

Our parametrization for the above potential energy density V_N has been proposed by Welke [Wel88]

$$V_N(\rho) = \frac{a}{2}\frac{\rho^2}{\rho_0} + \frac{b}{\tau+1}\frac{\rho^{\tau+1}}{\rho_0^{\tau}} + \frac{c}{\rho_0} g^2 \int \frac{d\vec{p}\, d\vec{p}\,'}{(2\pi)^6} \frac{f(\vec{r},\vec{p}) f(\vec{r},\vec{p}\,')}{1+\frac{(\vec{p}-\vec{p}\,')^2}{\Lambda^2}} \quad . \tag{A.73}$$

Given this potential energy density, the single-particle potential A_N^0 can be derived via the relation

$$A_N^0 = \frac{(2\pi)^3}{g}\frac{\delta V_N}{\delta f} \quad . \tag{A.74}$$

Note that the momentum dependent term of the mean field potential corresponds to a potential resulting from Yukawa interaction. Additionally, one finds that the parameter Λ translates into the mass of the scalar exchange meson (cf. [Tei97, sec. 3.1] for derivation).

Let us assume infinite nuclear matter. There the phase space density is given by

$$f(\vec{r}, \vec{p} = \Theta(p_f - |\vec{p}|) \tag{A.75}$$

with the Fermi momentum

$$p_f = \sqrt[3]{\frac{3\pi^2}{2}\rho} \quad . \tag{A.76}$$

For this infinite nuclear matter, one formulates five conditions to fix the potential parameters

$$\begin{aligned}
&\text{Binding energy:} && \tfrac{E}{A}(\rho_0) = \tfrac{\epsilon}{\rho} - m_N && = E_{\text{bind}} \quad , && \text{(A.77)}\\
&\text{Compressibility:} && \left(9\rho^2 \tfrac{\partial^2}{\partial\rho^2}\tfrac{E}{A}(\rho)\right)_{\rho=\rho_0} && = C \quad , && \text{(A.78)}\\
&\text{Saturation point:} && \tfrac{\partial}{\partial\rho}\tfrac{E}{A}(\rho_0) && = 0 \quad , && \text{(A.79)}\\
&\text{Potential for } |\vec{p}| = 0\text{:} && A_N^0(\rho = \rho_0, |\vec{p}| = 0) && = U \quad , && \text{(A.80)}\\
&\text{Root of potential:} && A_N^0(\rho = \rho_0, |\vec{p}| = p_0) && = 0 \quad . && \text{(A.81)}
\end{aligned}$$

Within these five conditions we have introduced five constants: the nuclear matter saturation density ρ_0, the nuclear matter compressibility C, the nuclear matter binding energy E_{bind}, the depth U of the single particle potential A_N^0 for $\vec{p} = 0$ at saturation density and the momentum p_0 at which A_N^0 vanishes at saturation density. Now the problem is to relate the constants ρ_0, C, E_{bind}, U, p_0 to the potential parameters a, b, c, τ and Λ.

For this let us first solve the integrals showing up in the single-particle potential and in the energy density

$$\begin{aligned}
t_{\text{kin}}(\rho) &= g\int \frac{d\vec{p}}{(2\pi)^3}\sqrt{\vec{p}^2 + m_N^2}\, f(\vec{r}, \vec{p})\\
&= \frac{g\,4\pi}{(2\pi)^3}\left[\frac{p_f}{4}(p_f^2 + m_N^2)^{2/3}\right.\\
&\quad \left. -\frac{m_N^2}{8}\left(p_f\sqrt{p_f^2 + m_N^2} + m_N^2 \ln\left\{\frac{p_f + \sqrt{p_f^2 + m_N^2}}{m_N}\right\}\right)\right] \quad , \qquad \text{(A.82)}\\
f_1(\Lambda, \rho) &= g^2\int \frac{d\vec{p}\,d\vec{p}\,'}{(2\pi)^6}\frac{f(\vec{r}, \vec{p}) f(\vec{r}, \vec{p}\,')}{1 + \frac{(\vec{p} - \vec{p}\,')^2}{\Lambda^2}}\\
&= \frac{g^2}{(2\pi)^6}\frac{32\pi^2}{3}p_f^4\Lambda^2\left\{\frac{3}{8} - \frac{\Lambda}{2p_f}\arctan\left(\frac{2p_f}{\Lambda}\right) - \frac{\Lambda^2}{16p_f^2}\right.\\
&\quad \left. + \left(\frac{3}{16}\frac{\Lambda^2}{p_f^2} + \frac{1}{64}\frac{\Lambda^4}{p_f^4}\right)\ln\left(1 + \frac{4p_f^2}{\Lambda^2}\right)\right\} \quad , \qquad \text{(A.83)}\\
f_2(\Lambda, \rho, p) &= g\int \frac{d\vec{p}\,'}{(2\pi)^3}\frac{f(\vec{r}, \vec{p}\,')}{1 + \frac{(\vec{p} - \vec{p}\,')^2}{\Lambda^2}}\\
&= \frac{g}{(2\pi)^3}\pi\Lambda^3\left\{\frac{p_f^2 + \Lambda^2 - p^2}{2p\Lambda}\ln\left(\frac{(p + p_f)^2 + \Lambda^2}{(p - p_f)^2 + \Lambda^2}\right) + 2\frac{p_f}{\Lambda}\right.\\
&\quad \left. -2\left(\arctan\left(\frac{p + p_f}{\Lambda}\right) - \arctan\left(\frac{p - p_f}{\Lambda}\right)\right)\right\} \quad , \qquad \text{(A.84)}
\end{aligned}$$

and let us evaluate the binding energy and its derivatives at nuclear matter saturation density

$$\begin{aligned}
\frac{E}{A}(\rho_0) &= \frac{t_{\mathrm{kin}}(\rho_0)}{\rho_0} + \frac{a}{2} + \frac{b}{\tau+1} + \frac{c}{\rho_0^2} f_1(\Lambda,\rho_0) \quad , \qquad &(\mathrm{A.85})\\
\frac{\partial}{\partial\rho}\frac{E}{A}(\rho_0) &= -\frac{t_{\mathrm{kin}}(\rho_0)}{\rho_0^2} + \frac{1}{\rho_0}\frac{\partial}{\partial\rho} t_{\mathrm{kin}}(\rho_0) + \frac{a}{2\rho_0} + \frac{b\tau}{(\tau+1)\rho_0} \\
&\quad + \frac{c}{\rho_0^2} \underbrace{\left(-\frac{f_1(\Lambda,\rho_0)}{\rho_0} + \frac{\partial}{\partial\rho} f_1(\Lambda,\rho_0) \right)}_{=f_4(\Lambda,\rho_0)} \quad , &(\mathrm{A.86})\\
\frac{\partial^2}{\partial^2\rho}\frac{E}{A}(\rho_0) &= 2\frac{t_{\mathrm{kin}}(\rho_0)}{\rho_0^3} - 2\frac{1}{\rho_0^2}\frac{\partial}{\partial\rho} t_{\mathrm{kin}}(\rho_0) + \frac{1}{\rho_0}\frac{\partial^2}{\partial\rho^2} t_{\mathrm{kin}}(\rho_0) + \frac{b\tau(\tau-1)}{(\tau+1)\rho_0^2} \\
&\quad + \frac{c}{\rho_0^2} \underbrace{\left(\frac{2 f_1(\Lambda,\rho_0)}{\rho_0^2} - \frac{2}{\rho_0}\frac{\partial}{\partial\rho} f_1(\Lambda,\rho_0) + \frac{\partial^2}{\partial\rho^2} f_1(\Lambda,\rho_0) \right)}_{=f_3(\Lambda,\rho_0)} \quad . &(\mathrm{A.87})
\end{aligned}$$

Given these derivatives we can reformulate eq. A.77-A.81:

$$\begin{aligned}
\frac{a}{2} + \frac{b}{\tau+1} + \frac{c}{\rho_0^2} f_1(\Lambda,\rho_0) &= \underbrace{-\frac{t_{\mathrm{kin}}(\rho_0)}{\rho_0} + E_{\mathrm{bind}} + m_N}_{=C_1} \quad , &(\mathrm{A.88})\\
\frac{b\tau(\tau-1)}{(\tau+1)\rho_0^2} + \frac{c}{\rho_0^2} f_3(\Lambda,\rho_0) &= \underbrace{\frac{c}{9\rho_0^2} - \left(2\frac{t_{\mathrm{kin}}(\rho_0)}{\rho_0^3} - 2\frac{1}{\rho_0^2}\frac{\partial}{\partial\rho} t_{\mathrm{kin}}(\rho_0) + \frac{1}{\rho_0}\frac{\partial^2}{\partial\rho^2} t_{\mathrm{kin}}(\rho_0) \right)}_{=C_2} \quad , \\
& &(\mathrm{A.89})\\
\frac{a}{2\rho_0} + \frac{b\tau}{(\tau+1)\rho_0} + \frac{c}{\rho_0^2} f_4(\Lambda,\rho_0) &= \underbrace{\frac{t_{\mathrm{kin}}(\rho_0)}{\rho_0^2} - \frac{1}{\rho_0}\frac{\partial}{\partial\rho} t_{\mathrm{kin}}(\rho_0)}_{=C_3} \quad , &(\mathrm{A.90})\\
a + b + \frac{2c}{\rho_0} f_2(\Lambda,\vec{p}=0) &= U \quad , &(\mathrm{A.91})\\
a + b + \frac{2c}{\rho_0} f_2(\Lambda,\vec{p}=p_0) &= 0 \quad . &(\mathrm{A.92})
\end{aligned}$$

Using eq. A.92 we get

$$a = -b - \frac{2c}{\rho_0} f_2(\Lambda, p=p_0) \quad . \tag{A.93}$$

Inserting this in eq. A.88-A.91 gives

$$b\left(\frac{1}{\tau+1}-\frac{1}{2}\right)+\underbrace{c\left(\frac{f_1(\Lambda,\rho_0)}{\rho_0^2}-\frac{f_2(\Lambda,\rho_0,p=p_0)}{\rho_0}\right)}_{=f_5(\Lambda,\rho_0,p_0)} = C_1 \quad , \tag{A.94}$$

$$b\frac{\tau(\tau-1)}{\tau+1}\frac{1}{\rho_0^2}+c\frac{f_3(\Lambda,\rho_0)}{\rho_0^2} = C_2 \quad , \tag{A.95}$$

$$\frac{b}{\rho_0}\left(\frac{\tau}{\tau+1}-\frac{1}{2}\right)+\underbrace{c\left(\frac{f_4(\Lambda,\rho_0)}{\rho_0^2}-\frac{f_2(\Lambda,\rho_0,p=p_0)}{\rho_0^2}\right)}_{=f_6(\Lambda,\rho_0,p_0)} = C_3 \quad , \tag{A.96}$$

$$\underbrace{c\frac{2}{\rho_0}\left(f_2(\Lambda,\rho_0,p=0)-f_2(\Lambda,\rho_0,p=p_0)\right)}_{=f_7(\Lambda,\rho_0,p_0)} = U \quad . \tag{A.97}$$

Eq. A.97 yields

$$c=\frac{U}{f_7(\Lambda,\rho_0,p_0)} \quad , \tag{A.98}$$

which gives in A.96

$$b=\frac{\rho_0}{\frac{\tau}{\tau+1}-\frac{1}{2}}\left(C_3-U\frac{f_6(\Lambda,\rho_0,p_0)}{f_7(\Lambda,\rho_0,p_0)}\right) \quad . \tag{A.99}$$

Inserting our result for the parameters b and c in eq. A.95 gives τ as a function of Λ

$$\tau=\frac{1}{2}\frac{1}{C_3-U\frac{f_6(\Lambda,\rho_0,p_0)}{f_7(\Lambda,\rho_0,p_0)}}\left(C_2-\frac{U}{\rho_0^2}\frac{f_3(\Lambda,\rho_0,p_0)}{f_7(\Lambda,\rho_0,p_0)}\right) \quad . \tag{A.100}$$

Finally, eq. A.94 yields the equation to determine the final free parameter Λ

$$0=1+\frac{1}{\rho_0\left(C_3-U\frac{f_6(\Lambda,\rho_0,p_0)}{f_7(\Lambda,\rho_0,p_0)}\right)}\left(C_1-U\frac{f_5(\Lambda,\rho_0,p_0)}{f_7(\Lambda,\rho_0,p_0)}\right) \quad . \tag{A.101}$$

This final equation A.101 is highly non-linear and must be solved numerically. It may happen that there is a value Λ_0 such that the denominator vanishes

$$C_3-U\frac{f_6(\Lambda_0,\rho_0,p_0)}{f_7(\Lambda_0,\rho_0,p_0)}=0 \quad . \tag{A.102}$$

Therefore, we choose a bisection method with which we search a solution for Λ in the region $\Lambda \in (0, 30\ \text{fm}^{-1}]$. The upper cut-off is already so large that it relates to an exchange boson heavier than 5.9 GeV, which is already unrealistic. An even larger cut-off would not make sense concerning physics. If there is a pole Λ_0, then we divide the interval $(0, 30\ \text{fm}^{-1}]$ into two separate intervals $(0, \Lambda_0)$ and $(\Lambda_0, 30\ \text{fm}^{-1}]$ and perform separate root-searches in both intervals. Given reasonable values for the input parameters ρ_0, C, E_{bind}, U, p_0 we never found more than one solution for Λ within $(0, 30\ \text{fm}^{-1}]$. The numerical implementation of the full problem can be found in the FORTRAN module ”code/potential/skyrme/skyrme.f90”.

Appendix B

GiBUU - details on the numerics

Overview: This appendix introduces to special algorithms used for the GiBUU model. In particular, the concept of perturbative particles is explained and the final-state decision algorithm is detailed.

B.1 Real and perturbative test-particles

For some calculations, e.g. low-energetic πA or γA collision, it is a good assumption, that the target nucleus stays very close to its ground state. Henceforth, one keeps as an approximation the target nucleus constant in time. This basically means that the phase space density of the target is not allowed to change during the run. The test-particles which represent this constant target nucleus are called *real* test-particles. However, one also wants to consider the final state particles. Thus one defines another type of test-particles which are called *perturbative*. The perturbative test-particles are propagated and may collide with *real* ones, the products are perturbative particles again. However, perturbative particles may not scatter among each other. Furthermore, they are neglected in the calculation of the actual densities. One can simulate in this fashion the effects of the almost constant target on the outgoing nucleons without modifying the target. E.g. in πA collisions we initialize all initial state pions as perturbative test-particles. Thus the target stays automatically constant and all products of the collisions of pions and target nucleons are assigned to the perturbative regime.

Furthermore, since the perturbative particles do not react among each other or modify the real particles in a reaction, one can also split a perturbative particle in n pieces (several perturbative particles) during a run. Each piece is given a corresponding weight $1/n$ and one simulates like this n possible final state scenarios of the same perturbative particle during one run.

Using perturbative particles it is also possible to enhance rare particle production as sketched in [Eff99a]. One lets the real particles perform their collisions, but during these collisions one produces not only the real final state particles but also perturbative particles. For instance, let us consider Λ production in NN scattering. This process is very rare, such that the statistical information on this channel is very scarce in an usual run. However, one can also produce in each NN collision a $N\Lambda K$ final state (if the threshold condition is fulfilled) if one initializes them as perturbative particles and gives to each $N\Lambda K$ event a weight, which corresponds to its real production probability $\sigma_{N\Lambda K}/\sigma_{\text{tot}}$. Thus one achieves huge statistics - under the assumptions that these rare events do not lead to an overall change of particle flows.

B.2 Final State Decisions for hadron-hadron scattering events

The final state decision is straight forward in the case of resonance production. If there are two or three particles in the final state, the treatment is more involved. First, the treatment is discussed with vacuum in sec. B.2.2-B.2.3. Then the medium corrections are discussed.

B.2.1 Resonance Production

In the case of resonance production we get the final mass of the resonance by eq. (3.41), which completely fixes the kinematics.

B.2.2 Two body final states : $X \longrightarrow cd$ in the vacuum

The general definition of the cross section is given by (e.g. [Hag02])

$$d\sigma_{a\ b\to f_1,f_2,f_3,\ldots,f_n} = (2\pi)^4\, \mathcal{S}_{\text{final}} \frac{\mathcal{M}_{a\ b\to f_1,f_2,f_3,\ldots,f_n}}{j} d\Phi_n \quad , \tag{B.1}$$

where Φ_n denotes the n-particle phase space of the final-state particles, $\mathcal{S}_{\text{final}}$ stands for the symmetry factor of the final state and

$$j = 4\sqrt{(p_a p_b)^2 - m_a^2 m_b^2} \tag{B.2}$$

represents the flux factor of the particles a and b. This flux factor can be expressed in the center of mass system by

$$j = 4 p_{cm}\sqrt{s} \quad , \tag{B.3}$$

with the CM-momentum p_{cm} of the particles a and b. It can be shown, e.g. in [Leh03, cf. especially sec. 4.7][1], that one can express the cross section for the production of unstable particles c and d in the final state by

$$\frac{d\sigma_{ab\to cd}}{d\mu_c\, d\mu_d\, d\Omega}(s) = \frac{1}{64\pi^2\, s} \frac{p_{cd}}{p_{ab}} 2\mu_c \mathcal{A}_c(\mu_c, p_c(\mu_c,\Omega)) 2\mu_d \mathcal{A}_d(\mu_d, p_d(\mu_d,\Omega))\, |\mathcal{M}_{ab\to cd}(s)|^2 \quad , \tag{B.4}$$

with p_{ab} and p_{cd} denoting the CM momenta of the $a\,b$ and the $c\,d$-system. Here one needs to assume that the Matrix element is only dependent on s. The spectral functions depend only in the medium, which explicitly breaks Lorentz-invariance, on the four-momenta of the particles. Considering the vacuum-case they will only depend on the squares $\mu^2 = p^\nu p_\nu$.

We want to use a Monte-Carlo method to choose the final state. In eq. B.4, we note that the two-particle final state depends both on the masses of the outgoing particles and their directions of motion. The Mandelstam s and p_{ab} are determined by the initial state. So we choose the masses μ_c and μ_d at the same time as we choose Ω. The substitution

$$dy_i = \frac{\Gamma_0}{(\mu_i - M_i^0)^2 + \left(\frac{\Gamma_0}{2}\right)^2} d\mu_i \tag{B.5}$$

gives by integration the variable transformation

$$y_i(\mu_i) = 2\ \arctan\left[2\,\frac{\mu_i - M_i^0}{\Gamma_i^0}\right]; i \in \{c,d\} \quad , \tag{B.6}$$

---

[1] Note that Lehr uses a slightly different convention for the spectral function which differs by a factor $2m$ from the one used in this work.

with M_i^0 and Γ_i^0 being the values at the pole position in the vacuum. The function

$$\frac{dy_i}{d\mu_i} = \frac{\Gamma_0}{(\mu_i - M_i^0)^2 + \left(\frac{\Gamma_0}{2}\right)^2} \tag{B.7}$$

has a similar dependence on μ_i as $\mu_i \mathcal{A}_i$, which makes the function

$$\frac{d\sigma_{ab\to cd}}{dy_c\, dy_d\, d\Omega}(s) = \frac{1}{16\pi^2\, s}\frac{p_{cd}}{p_{ab}}\frac{\mu_c \mathcal{A}_c(\mu_c, p_c(\mu_c,\Omega))}{\frac{dy_c}{d\mu_c}}\frac{\mu_d \mathcal{A}_d(\mu_d, p_d(\mu_d,\Omega))}{\frac{dy_d}{d\mu_d}}\left|\mathcal{M}_{ab\to cd}(s)\right|^2 \quad , \tag{B.8}$$

smoother than the original function presented in eq. B.4 which is advantageous for the application of a rejection method. For this we choose y_c, y_d and Ω according to a flat distribution. The probability that a random ensemble (y_c, y_d, Ω) will be accepted is then given by

$$p_{\text{accept}}(y_c, y_d, \Omega) = \frac{p_{cd}\mu_c\mathcal{A}_c(\mu_c, p_c(\mu_c,\Omega))\mu_d\mathcal{A}_d(\mu_d, p_d(\mu_d,\Omega))\frac{d\mu_c}{dy_c}\frac{d\mu_d}{dy_d}}{\left(p_{cd}\mu_c\mathcal{A}_c\mu_d\mathcal{A}_d\frac{d\mu_c}{dy_c}\frac{d\mu_d}{dy_d}\right)_{\max}} \quad . \tag{B.9}$$

The maximal value $\left(p_{cd}\mu_c\mathcal{A}_c\mu_d\mathcal{A}_d\frac{d\mu_c}{dy_c}\frac{d\mu_d}{dy_d}\right)_{\max}$ is actually hard to find. We parametrize this maximal value by

$$\left(p_{cd}\mu_c\mathcal{A}_c\mu_d\mathcal{A}_d\frac{d\mu_c}{dy_c}\frac{d\mu_d}{dy_d}\right)_{\max} = Q_{cd} \times \max\{p_{cd}^{\text{vac}}\} \quad . \tag{B.10}$$

The dimensionless factor Q is of the order of 10 and depends on the outgoing particles. It has to be readjusted if one establishes new in-medium effects.

B.2.3 Three body final states : $X \to cde$ in the vacuum

For a three-particle final state one gets a more complicated structure

$$\begin{aligned}\frac{d\sigma_{ab\to cde}}{d\mu_c\, d\mu_d\, d\mu_e\; d|\vec{p}_c|\, d\Omega_c\, d|\vec{p}_d|\, d\phi_d}(s) &= \frac{1}{8\,(2\pi)^5}\frac{1}{p_{ab}\sqrt{s}}\frac{|\vec{p}_c|\,|\vec{p}_d|}{E_c E_d}2\mu_c\mathcal{A}_c(\mu_c, p_c)2\mu_d\mathcal{A}_d(\mu_d, p_d) \\ &\quad \times 2\mu_e\mathcal{A}_e(\mu_e, p_e)\left|\mathcal{M}_{ab\to cde}(s)\right|^2 \,. \end{aligned} \tag{B.11}$$

Here $\vec{p}_{c,d}$ denote the CM-momenta of the particles c and d. The CM-momentum of e is given by total momentum conservation

$$\vec{p}_c + \vec{p}_d + \vec{p}_e = 0 \quad . \tag{B.12}$$

In analogy to the two-particle final, we use the variable transformation

$$y_i(\mu_i) = 2\ \arctan\left[2\,\frac{\mu_i - M_i^0}{\Gamma_i^0}\right];\, i \in \{c, d\} \quad . \tag{B.13}$$

applied to eq. B.11. We obtain

$$\begin{aligned}\frac{d\sigma_{ab\to cde}}{dy_c\, dy_d\, dy_e\; d|\vec{p}_c|\, d\Omega_c\, d|\vec{p}_d|\, d\phi_d}(s) &= \frac{\mu_c\mu_d\mu_e}{(2\pi)^5}\frac{1}{p_{ab}\sqrt{s}}\frac{|\vec{p}_c|\,|\vec{p}_d|}{E_c E_d}\mathcal{A}_c(y_c, p_c)\mathcal{A}_d(y_d, p_d) \\ &\quad \times \mathcal{A}_e(y_e, p_e)\left|\mathcal{M}_{ab\to cde}(s)\right|^2 \frac{d\mu_c}{dy_c}\frac{d\mu_d}{dy_d}\frac{d\mu_e}{dy_e} \quad . \end{aligned} \tag{B.14}$$

Hence we need to choose $y_c, y_d, y_e, |\vec{p}_c|, \Omega_c, \phi_d$ and $|\vec{p}_d|$ independent of each other. The limits for the y_i are given by the smallest and largest possible masses. The absolute values of the momenta $|\vec{p}_i|$ are limited by the energy conservation. Evaluated in the CM-System

$$\sum_i E_i = \sum_i \sqrt{m_i^2 + p_i^2} = \sqrt{s} \tag{B.15}$$

this condition sets the limits to

$$|\vec{p}_i| < \sqrt{s} \quad . \tag{B.16}$$

The value of Ω_c is determined by choosing a random $\cos(\theta) \in [-1,1]$ and $\phi \in [0, 2\pi]$. Once we have chosen those parameters, the full kinematics is fixed. We can define a probability to accept such a configuration by

$$p_{\text{accept}} = \frac{\mu_c \mu_d \mu_e \frac{|\vec{p}_c||\vec{p}_d|}{E_c E_d} \mathcal{A}_c(y_c, p_c) \mathcal{A}_d(y_d, p_d) \mathcal{A}_e(y_e, p_e) \frac{d\mu_c}{dy_c} \frac{d\mu_d}{dy_d} \frac{d\mu_e}{dy_e}}{m} \tag{B.17}$$

where m is chosen such that it is larger than the maximum of the nominator. With a Monte-Carlo decision we now accept or reject this configuration. We evaluate different configurations until we get one which is accepted.

B.2.4 Medium Corrections

In the medium we have a more complicated dispersion relation. Therefore also the phase space factors differ from the ones used above. Already in [Eff99a] possibilities to implement the right phase-space factors for ΔN and NN scattering were discussed. Our treatment does not include such modifications, but preserves the energy in the medium for all collisions. We use the following algorithm:

1. Evaluate s_{vacuum}.
2. Do the final state decision with vacuum kinematics assuming $s = s_{\text{vacuum}}$.
3. Correct the final state by scaling the final state momenta by a factor x in the CM frame.

The last point needs special discussion. Therefore we go to the CM-frame of the final state. Here energy and momentum conservation in step 2 result in a solution for the momenta $\vec{p}_i$ which obeys

$$\begin{aligned} \sum_i \sqrt{\left(\vec{p}_i^{\,\text{CM}}\right)^2 + (m_i)^2} &= \sqrt{s_{\text{vacuum}}} \\ \sum_i \vec{p}_i^{\,\text{CM}} &= 0 \; . \end{aligned}$$

Now we want to define the four momenta in the medium. Let them be denoted by q_i. In the medium momentum and energy conservation demand

$$\sum_i q_i^0\left(\vec{q}_i\right) = \sqrt{s} \tag{B.18}$$

$$\sum_i \vec{q}_i = 0 \; . \tag{B.19}$$

The zeroth components of q_i are, due to the potentials, highly non-trivial functions of the vector components $\vec{q}_i$. Hence our recipe is the following: Using the vacuum result for $\vec{p}_i$ we choose

$$\vec{q}_i = x\, \vec{p}_i \, \forall\, i \quad , \tag{B.20}$$

where the scaling factor x is fixed by equation (B.18). Since all momenta are scaled by the same factor, momentum conservation is fulfilled trivially.

B.3 Time consumption

This section is devoted to the time consumption of the GiBUU code. For this the time consumption of different code modules is compared choosing two exemplary physics cases.

B.3.1 Inclusive electron scattering

First, let us consider the simulation of an inclusive electron-nucleus cross section as presented in fig. 7.3. We choose a fixed electron beam energy of 1.08 GeV and fixed final electron energies of 0.5 which corresponds to one single point in fig. 7.3; the scattering angle is chosen as in fig. 7.3 to be $\theta_{l_f} = 32°$. A full calculation is performed, which includes in-medium spectral functions according to the *mass-shift* scenario for the self-energy. Note that this physics case does not include the propagation of final states and almost the complete CPU-time is consumed by the initialization and analysis procedures. A calculation using 20 runs with 1000 ensembles/run takes 3644s ($\approx$ one hour). Fig. B.1 shows that most of the time ($\approx 75\%$) is used for the calculation of the resonance and single-pion background cross sections (σ_R and $\sigma_{\pi,\text{ bg}}$), which depend on the four-momentum of the target test-particle momenta. Therefore, we need to evaluate σ_R and $\sigma_{\pi,\text{ bg}}$ for each test-particle separetely. All other tasks (the resonance decays in the collision term, the analysis, the management of the particle arrays and anything else) consume less than 25% in total. The right columns in fig. B.1 show in detail where the computation time goes. To evaluate σ_R and $\sigma_{\pi,\text{bg}}$ one needs to evaluate hadron tensors for resonance excitation. In the code, the hadronic currents are defined using γ-matrices and form factors. To evaluate the spin-traces for the hadron tensors, one then needs to perform matrix multiplications and contractions during run time. To speed this procedure up, one could evaluate all the traces by hand as for the total single-pion production cross section presented in sec. 4.5.2. However, we will see for the next physics case that the initialization takes very little time compared to the full final-state treatment. Hence we did not focus on a speed-up of the resonance hadron-tensors yet.

B.3.2 π^0 production in a γ^{40}Ca $\rightarrow \pi^0 X$ reaction

As a second scenario we consider the simulation of π^0 production in a $\gamma^{40}\text{Ca} \rightarrow \pi^0 X$ reaction, which was presented in fig. 7.22. For this physics case all the final states must be propagated, which is done within the local-ensemble method (cf.sec. 2.5.2 for details). Again, we consider a full calculation which includes in-medium spectral functions and the off-shell potential (OP) presented in sec. 2.4. The photon energy is chosen to be $q_0 = 400$ MeV, which corresponds to one single point in fig. 7.22. For one point of the curves shown in fig. 7.22 the code needs roughly one CPU day using the full model. Fig. B.2 shows that most of the computation time is consumed by the propagation, but the initialization needs almost no time compared to all other tasks. During the propagation most of the time (35.5% of the total CPU time) is consumed for the evaluations of the gradients of the Hamilton functions. During the evaluation of the Hamilton functions, especially the interpolation for the baryon width is slow and consumes 11%

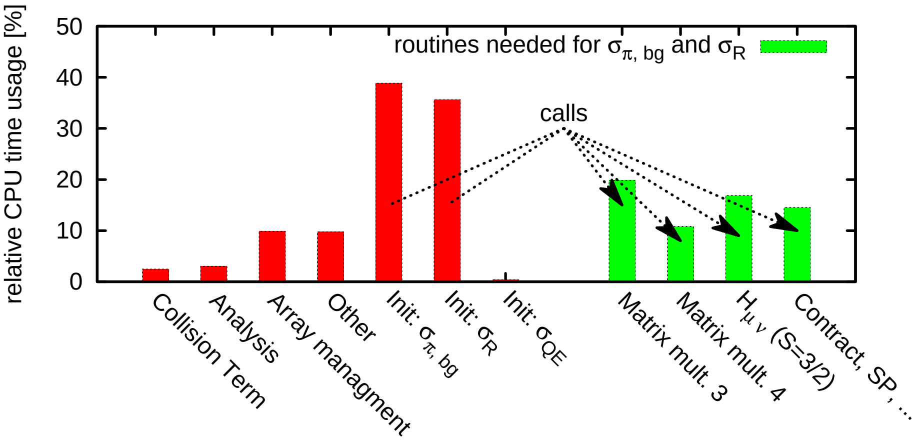

Figure B.1: Relative CPU time consumption for the calculation of an inclusive electron-nucleus cross section. The four right green (respectively brighter) columns represent routines which are called during the initialization of resonance and single-π background events: the multiplication of 3 complex matrices (matrix mult. 3), the multiplication of 4 complex matrices (matrix mult. 4), the hadron tensor for spin 3/2 resonances ($H_{\mu\nu}(3/2)$) and the entry “Contract, SP, …” represents the CPU time needed for routines which evaluate scalar products, contract vectors and γ matrices, return γ matrices, unit matrices or $\sigma_{\mu\nu}$.

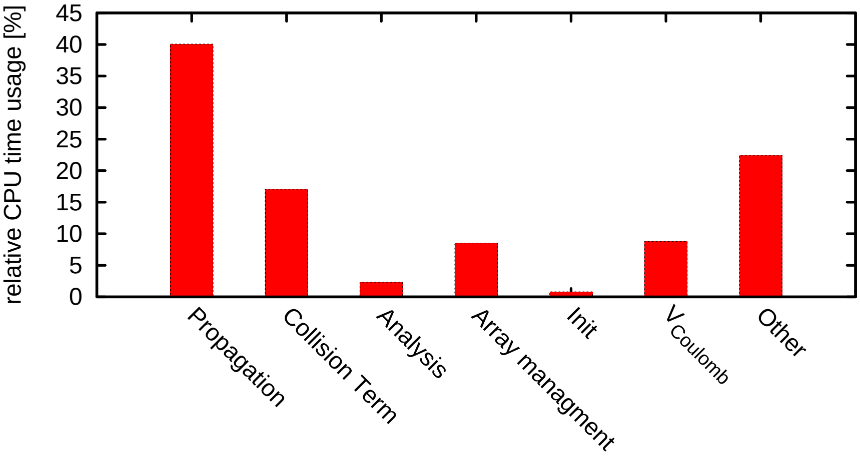

Figure B.2: CPU time consumption for π^0 production in a $\gamma^{40}\mathrm{Ca} \to \pi^0 X$ reaction.

of the complete computation time. Switching off the off-shell potential there are no gradients of the width to be calculated anymore, so the latter 11% can be saved. Additionally, one can increase the time-step size by almost a factor of 10 just by neglecting (i.e. switching off) the off-shell potential, which decreases the computation time of the propagation part by approximately the same factor.

Using the full model, i.e. including the off-shell potential and the in-medium baryon widths, there is not much potential to speed the code up. During run-time the baryon width must be interpolated, otherwise the gradients may have jumps which generate velocities larger than the speed of light. Additionally, there is no single routine consuming extraordinary much CPU time, but there are a lot of routines consuming small amounts of CPU time – a feature, which deters at the moment a further improvement on the performance.

B.3.3 Outlook

From the author's point of view, the present speed of the simulation is no severe issue except for high-statistics runs looking for rare observables. However, the algorithm is highly suited for a multi-threaded realization. Thus it might be an interesting option to convert the present implementation to a parallel code. Then one could use several slow and often unoccupied nodes of a computer cluster in parallel to perform a job which must at present be run on a very fast node.

Appendix C

GiBUU - Technical details concerning the code, code management and documentation

Overview: This appendix focuses on technical details of the GiBUU framework. The directory structure of the repository is outlined, the documentation and version control system is presented.

C.1 Directory structure

The GiBUU repository is structured into several directories and the source code itself is sorted into different topics. The following (incomplete) list outlines the directory structure. Within the base directory, one finds the sub-directories:

Documentation Includes the automatic documentation which is being generated by the ROBODOC documentation tool [rob07].

Documentation_Extra Includes all non-automatic documentation, e.g. supplementing pdf or tex-files.

TAGS Includes tex source-files for the published papers, diploma and phd theses. Furthermore, the job cards to relevant results should be included here and the revision of the code which was used for the relevant runs. With this prerequisite, the results can be fully reproduced at any later stage.

branches Includes copies of *workingCode* which are meant to be *non-permanent*. A branch opens the possibility for several users to work on a limited project which is later merged back into the *workingCode* directory. Additionally, the released versions are included in this directory.

workingCode The *workingCode* directory includes the main source code of the GiBUU project. The file *Makefile* steers the compilation process and is being documented in the file *README.Makefile.txt*. Furthermore, an example for the documentation usage is presented in *DemoFoRobodoc.f90*. The file *robodoc.css* includes the style sheets for the HTML documentation, and the ROBODOC configuration is included in the file *GenerateDoku.rc*. The file *Makefile.SUB* is distributed via *make renew* as a Makefile to all sub-directories within the *code* directory. Important sub-directories within *workingCode* are:

- **buuinput** Includes all input files to the code. Within the directory, the file *Makefile* is used to unzip large files and to prepare necessary input.
- **testRun** Here the executable "main.x" is found after successful compilation. The sub-directory *jobCards* includes sample job cards for different scenarios.

code This directory includes the full source code. The main steering program is called *main.f90*. Several sub-directories split the code into different topics:

- **analysis** Includes all analysis routines.
- **collisions** The collision term.
- **database** Includes particle ID's, particle properties and decay channels.
- **density** Density and Pauli blocking routines.
- **dilepton** Dilepton yields and analysis.
- **init** Initialization routines.
- **inMediumWidth** Includes the routines which are used to calculate the in-medium-width.
- **inputOutput** Includes the input module *input.f90* for the most important switches, such as e.g. the number of ensembles. Furthermore, this directory provides routines to generate output.
- **numerics** Includes numerical subroutines, includes also QUADPACK and CERNLIB fragments.
- **potential** Potential routines and energy determination routines.
- **propagation** Routines for propagating the test-particles in time.
- **run** Run-time check routines.
- **rmf** Relativistic mean field potential implementation.
- **spectralFunctions** Routines connected to self energies and spectral functions.
- **storage** Routines to generate histograms and to store information based on pointer lists.
- **typeDefinitions** Includes all underlying type definitions, e.g. the definition of the *particle* type.
- **width** Includes all kinds of routines which are connected to the width and spectral functions of the baryons and mesons.

C.2 Version control via Subversion

To work in parallel with several programmers on a software project, requires a proper version control management. Within the GiBUU project, this is presently realized with the *Subversion* package. For a detailed introduction into *Subversion*, I suggest the well-written manual [CS04], in particular the first chapters.

The so-called *repository* is basically a data bench which holds all the information about the present status of the code, all the changes to it in the past and the log-messages which go along with these changes. Each user checks out a copy of this repository and has then a local copy, his so-called *working copy*, of the code. After modifying files in that working copy, the user can submit changes to the repository.

A typical working cycle is sketched in fig. C.1. First, user A commits his changes of file X to the repository. Then user B simply updates his file X by retrieving the patches from the repository. However, it might also be possible that user A and B work on the same files. Such a situation is called a *conflict* and is sketched in fig. C.2. If they would both commit their changes to the repository without knowing about the changes of the co-worker, then the code could get corrupted. Therefore, *Subversion* forbids user B to commit his changes before he has not updated his code to the version of user A. After this update, user B must solve the conflict within his local working copy. Thereafter, he can commit the file back to the repository. User A retrieves the changes of user B by a simple update. Usually, conflicts appear rather seldom, since the code is modular and, therefore, users usually work on different files without disturbing each other. Only if a user does not update or commit his code for a long time, such a situation occurs with higher probability. Therefore, frequent updating and committing is a good strategy.

C.3 License issues - imported code fragments

The code includes at the present stage several imported subroutines which are not originally coded by any member of the GiBUU group. The following list gives an overview over the present situation (revision 2162):

Pythia The Pythia model [pyt07] is included as a high-energy event generator. It is under the *Gnu Public License (GPL)* and refers to the MCNET guidelines for event generators authors and users.

> Strictly speaking past Pythia versions have not come with a license, so you are not allowed to redistribute them AT ALL. You could only tell people that so-and-so a Pythia version is required and tell them to download it from the official Pythia web page. This has not been a consequence of deliberate policy, simply a lack of interest in such issues. It has been taken for granted that people can do minor modifications and appropriate redistributions in a responsible manner.
>
> The paradoxical consequence of the rise of the free software movement is that we now are forced to think much more about legal issues that we were used to. Only the last half year the newly started MCnet EU-funded network has tried to work out a common policy. We now have an agreement ”hot off the press” (maybe still with some i’s to be dotted). This policy primarily would apply to future versions, but if you were to apply them to the Pythia version then all would be well. To a large part they just encode a commonsense behavior of ”treating the code of other people with the respect that you would like others to treat your code”. For the rest we rely on GPL v. 2.
>
> *Torbjorn Sjostrand, e-mail conversation, June 14th, 2007*

Quadpack QUADPACK is a numerics library for estimating integrals [RP83]. According to my knowledge, there is no explicit statement about license issues on any QUADPACK website. However, the package is included in the Gnu Scientific Library (GSL) [gsl07]. Therefore, it is supposed to be published under GPL since GSL is under the GPL.

CERNLIB The CERN program library [cer07] is packaging several mathematical subroutines. The whole package is published under the GPL license.

MAID L. Tiator kindly allowed us to publish his source code for the MAID 2003 and 2005 helicity amplitudes together with the GiBUU code.

> Hallo Oliver,
>
> ist in Ordnung, diesen Programmcode könnt ihr weitergeben. Die Unterschiede zu Maid2007 sind nicht sehr groß und spielen für eure Anwendung wahrscheinlich keine Rolle.
>
> Beste Grüße
>
> Lothar

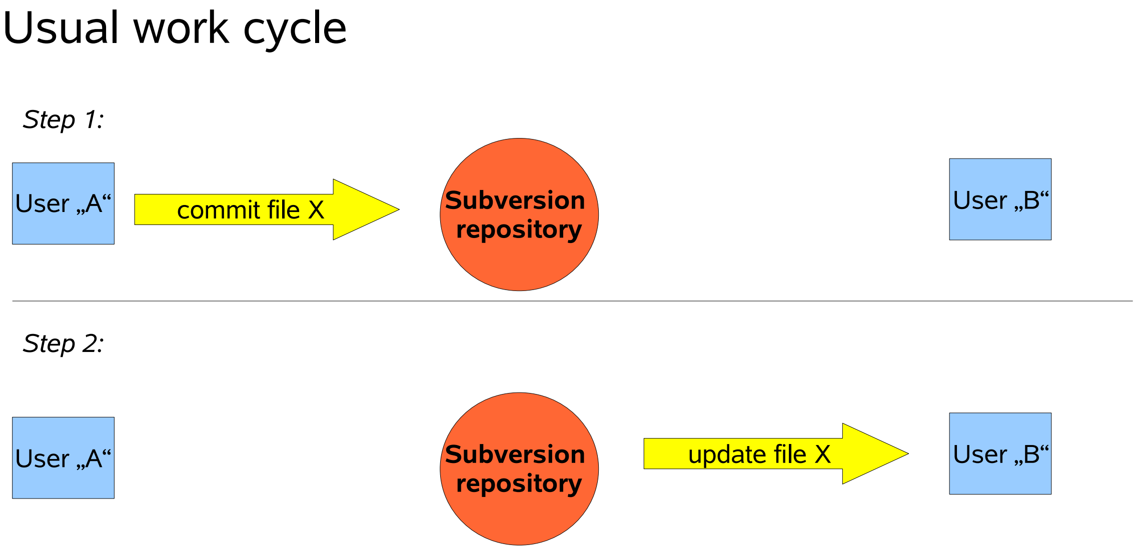

Figure C.1: A usual work cycle using Subversion version control management.

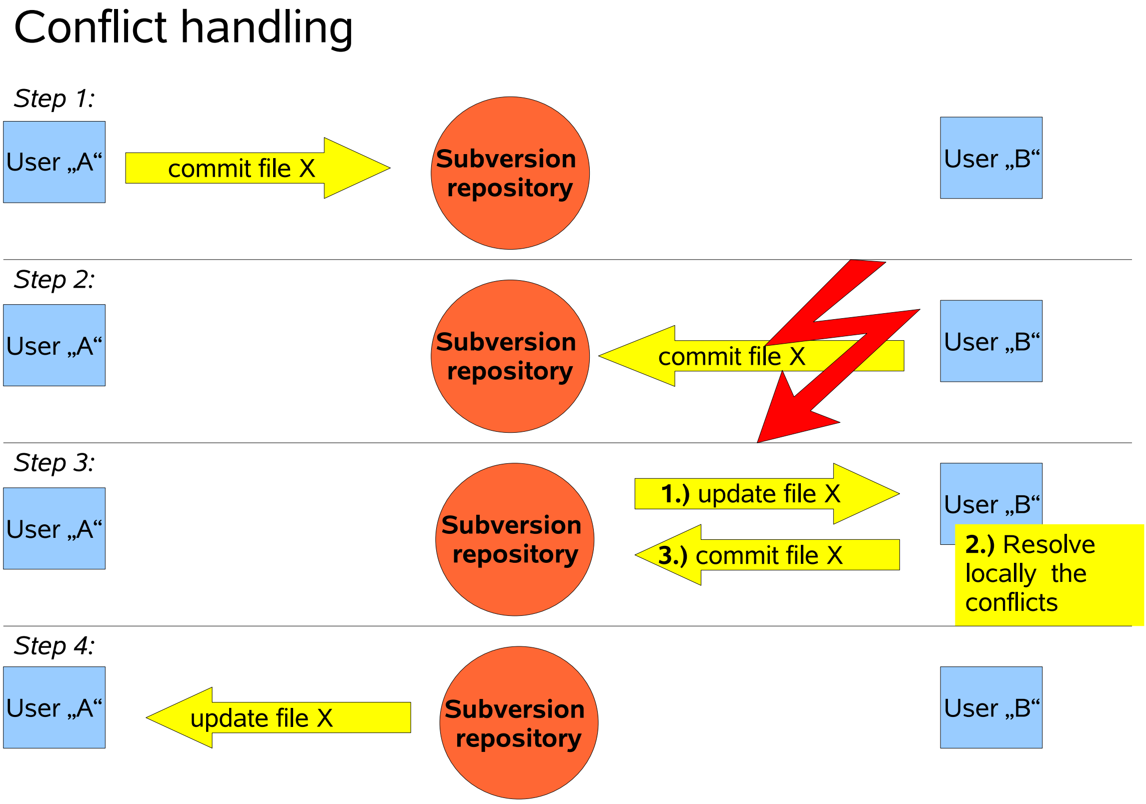

Figure C.2: Handling a conflict using Subversion version control management.

> Oliver Buss wrote:
> \> Hallo Lothar
> \>
> \> Im Anhang findet sich zum einen Dein Originalfile für MAID 2005 (”formfactors05.f”) und eine von uns adaptierte f90-Version (”helicityAmplitudes.f90”), die MAID 2005 und 2003 beinhaltet. Um die adaptierte Version ”helicityAmplitudes.f90” zu nutzen, muß man auch das Modul ”IdTable.f90” einbinden, welches unsere Teilchen-Ids beinhaltet.
> \>
> \> Viele Grüße, Oliver
> *E-mail conversation with Lothar Tiator in April 2008*

Fritiof The authors of Fritiof state:

> Licensing provisions: none.
> *Hong Pi [Pi92, page 1]*

Summarizing, all the imported code fragments are under the GPL license, or we are allowed to publish them in a package which is under the GPL license. The copy-left principle of GPL (cf. [gpl07] for details) implies, that any code, which includes GPL licensed fragments, must be published under GPL, too. Therefore, the GiBUU code may not be published under any other license than GPL as long as it includes GPL licensed fragments. Since a lot of GPL fragments have been customized, it would be very difficult to single out the used packages and to link them as external packages. **So the only feasible way to publish the code is to publish it under the GPL license.**

For the future code development, it will be very important not to include any proprietary software (e.g. Numerical Recipes (NR) or IMSL) in the project. This would spoil the possibility to publish the code. And it would diminish all our effort which we put in to clean the code from all the proprietary pieces (in particular the replacement of all *Numerical-Recipes* routines by *cernlib* routines).

C.4 Documentation system

> Document my code? Why do you think they call it ”code”?
> *unknown programmer*

The above quote reflects a very common line of thinking. Often, documentation is considered as too time consuming. However, for a long-term university project it is viable to document properly the source code. First and foremost, a lot of different programmers use the same pieces of code. And very often, the ”mother” or ”father” of a special module is no longer available since he has already left the institute. Second, the programs are usually rather involved and, therefore, hard to understand without proper guidance. Hence the GiBUU group agreed on a minimal set of necessary documentation which should be provided to modules, subroutines, functions, global variables and namelists. As a technical realization we decided for ROBODOC [rob07], which enables us to generate a set of web pages out of documentation which is provided within the source code. To generate and use the documentation, type *make doku* and *make showdoku* in the *workingCode* directory.

As a guideline, the following piece of code demonstrates the proper usage of the ROBODOC [rob07] keywords (e.g.: NAME, PURPOSE, INPUTS, NOTES, OUTPUT, SIDE

EFFECTS) and the necessary information which should be provided to guarantee a meaningful documentation. The syntax "!****m*" starts the documentation of a module, "!****s*" is for subroutines, "****f*" is for functions, "!****n*" is for namelists and "!****g*" for global module variables. The construct following this start syntax is given by "/moduleName" for module documentations and by "moduleName/componentName" for all other cases.

```
!***************************************************************************
!****m* /TemplateModule
! NAME
! module TemplateModule
!
! PURPOSE
! This module defines ...
!
! INPUTS
! The Namelist "TemplateModule_nl" in the Jobcard.
!
! NOTES
! In order to get best results from RoboDoc, you should respect the spelling
! of modules, subroutines, functions etc throughout all doku lines:
! usage of capital or small letters should be consistent all over the files!
!***************************************************************************

!***************************************************************************
!****n* TemplateModule/TemplateModule_nl
! NAME
! NAMELIST /TemplateModule_nl/
! PURPOSE
! This Namelist for module "TemplateModule" includes:
! * var1 -- The variable Nr1
! * var2 -- The variable Nr2
!***************************************************************************
module TemplateModule

  PRIVATE

  !*************************************************************************
  !****g* TemplateModule/var1
  ! SOURCE
  !
  integer, save :: var1
  ! PURPOSE
  ! The variable Nr1
  !
  ! This variable has the function ...
  !*************************************************************************

  PUBLIC :: Sub1, Fun1
```

```
contains

  !***********************************************************************
  !****s* TemplateModule/Sub1
  ! NAME
  ! subroutine Sub1(par1,par2,par3)
  !
  ! PURPOSE
  ! The first Subroutine.
  !
  ! This Subroutine calculates ...
  ! ...
  !
  ! INPUTS
  ! * integer :: par1 -- The parameter Nr1
  ! * real    :: par2 -- The parameter Nr2
  !
  ! OUTPUT
  ! * real    :: par2 -- The parameter Nr2
  !                      is modified according ...
  ! * integer :: par3 -- The parameter Nr3
  !
  ! * The global parameter PARAMETERNAME is set to .TRUE.
  !
  !***********************************************************************
  subroutine Sub1(par1,par2,par3)

    integer,     intent(in)    :: par1 ! please do not place any explanation
    real,        intent(inout) :: par2 ! here. do it in the header
    integer,     intent(out)   :: par3

    ! ...

  end subroutine Sub1


  !***********************************************************************
  !****f* TemplateModule/Fun1
  ! NAME
  ! real function Fun1()
  !
  ! PURPOSE
  ! The first Function
  !
  ! This Function calculates ...
  ! ...
  ! INPUTS
```

```
  ! (-- no input --)
  !
  ! OUTPUT
  ! Returns the function value of "functionName"
  !
  ! SIDE EFFECTS
  ! (-- no side effects --)
  !
  !***************************************************************************
  real function Fun1()
  end function Fun1

end module TemplateModule
```

Appendix D

The cross section for elastic electron-nucleon scattering

Overview: In this appendix several formulas for elastic electron-nucleon scattering are derived.

We consider a process, where an electron is scattering off a nucleon and creating a two body final state including a final state electron and a nucleon. Our notation for the $eN \to e'N'$ process is chosen according to fig. 4.2: the incoming nucleon momentum is denoted p and the outgoing nucleon momentum p', the incoming electron momentum is denoted l and the outgoing one l', the photon momentum is denoted q. The initial and final nucleon masses are given by m and m'. According to Bjorken and Drell ([Bjo93], formula B.1), the cross section is given by [1]

$$\begin{aligned} d\sigma &= \frac{2m_e 2m}{4\sqrt{(l_\alpha p^\alpha)^2 - \underbrace{m_e^2 m^2}_{\approx 0}}} \frac{m_e}{|\vec{l'}|} \frac{d\vec{l'}}{(2\pi)^3} 2m' \frac{dp'^4}{(2\pi)^4}\; 2\pi\delta(p'^2 - m'^2) \\ &\quad \times |\mathcal{M}|^2\; (2\pi)^4 \delta^4\left(r - \left(l' + p'\right)\right) \\ &= \frac{1}{\sqrt{(l_\alpha p^\alpha)^2}} \frac{m_e^2\; m\; m'}{2\pi^2} d\Omega_{l'}\; d|\vec{l'}|\; |\vec{l'}|\; \delta((r-l')^2 - m'^2)\; |\mathcal{M}|^2 \qquad \text{(D.1)} \end{aligned}$$

with $r = l + p$ being the total incoming 4-momentum.

D.1 Numerical realization

Let us consider an arbitrary momentum of the incoming nucleon. Starting with eq. D.1

$$d\sigma = \frac{1}{\sqrt{(l_\alpha p^\alpha)^2}} \frac{m_e^2\; m\; m'}{2\pi^2} d\Omega_{l'}\; d|\vec{l'}|\; |\vec{l'}|\; \delta((r-l')^2 - m'^2)\; |\mathcal{M}|^2 \quad ,$$

we represent in our numerical realization the δ function by a Breit-Wigner function of vanishing width

$$\delta((r-l')^2 - m'^2) = \frac{\delta(\sqrt{(r-l')^2} - m')}{2m'} = \frac{1}{2m'} \lim_{\Gamma\to 0} \left(\frac{1}{2\pi} \frac{\Gamma}{(\sqrt{(r-l')^2} - m')^2 + \Gamma^2/4} \right) . \text{(D.2)}$$

Thus we get

$$\frac{d\sigma}{d\Omega_l{}' dl'_0} = \frac{1}{\sqrt{(l_\alpha p^\alpha)^2}} \frac{m_e^2\; m}{4\pi^2}\; l'_0 \lim_{\Gamma\to 0} \left(\frac{1}{2\pi} \frac{\Gamma}{(\sqrt{(r-l')^2} - m')^2 + \Gamma^2/4} \right) |\mathcal{M}|^2 \quad . \qquad \text{(D.3)}$$

---

[1] We used for the flux factor $\frac{1}{4|v_e - v_n| l_0 p_0} = \frac{1}{4\sqrt{(l_\alpha p^\alpha)^2 - m_e^2 m^2}}$.

D.2 Including a broad spectral function

For the nucleon being a broad particle we must substitute

$$\delta((r-l\,')^2 - m\,'^2) \rightarrow \mathcal{A}(p\,'^2 - m\,'^2) \tag{D.4}$$

in the above formulas and we get

$$d\sigma \;=\; \frac{1}{\sqrt{(l_\alpha p^\alpha)^2}} \frac{m_e^2\; m\; m'}{2\pi^2} d\Omega_{l'}\; d|\vec{l}\,'|\; |\vec{l}\,'|\; \mathcal{A}((r-l\,')^2 - m\,'^2)\; |\mathcal{M}|^2 \quad . \tag{D.5}$$

D.3 Vacuum cross sections

In the following, we consider the vacuum case in which the masses are constant $m = m' = m_N$ and do not dependent on the momentum of the nucleon. Furthermore, let us consider the *lab frame* where the initial nucleon is at rest, i.e. $\vec{p} = 0$. In this frame we get

$$l_\alpha p^\alpha = l_0 p_0 = l_0 m_N = \frac{s - m_N^2}{2} \Rightarrow l_0 = \frac{s-m_N^2}{2m_N} \tag{D.6}$$

with the Mandelstam s

$$s = (l+p)^2 = (l_0 + m_N)^2 - \vec{l}\,'^2 = \underbrace{l_0^2 - \vec{l}\,'^2}_{=l\,'^2=0} + m_N^2 + 2l_0 m_N = m_N^2 + 2 l_0 m_N \; . \tag{D.7}$$

And furthermore

$$\begin{aligned}
d\sigma &= \frac{1}{\frac{s-m_N^2}{2}} \frac{m_e^2\; m_N^2}{2\pi^2} d\Omega_{l'}\; d|\vec{l}\,'|\; |\vec{l}\,'|\; \delta(r^2 + l\,'^2 - 2(\underbrace{l_0}_{=|\vec{l}\,'|} r_0 - \underbrace{\vec{l}\,'\vec{r}}_{=|\vec{l}\,'||\vec{r}|\cos\theta_{l\,'}}) - m_N^2)\; |\mathcal{M}|^2 \\
&= \frac{1}{\frac{s-m_N^2}{2}} \frac{m_e^2\; m_N^2}{2\pi^2} d\Omega_{l'}\; d|\vec{l}\,'|\; |\vec{l}\,'|\; \delta(|\vec{l}\,'| - x_0) \frac{1}{2(r_0 - |\vec{r}|\cos\theta_{l'})}\; |\mathcal{M}|^2 \Bigg|_{x_0 = \frac{r^2 - m_N^2}{2(r_0 - |\vec{r}|\cos\theta_{l\,'})}} \\
\Rightarrow \qquad \frac{d\sigma}{dl_0 d\cos\theta_{l'}} &= \frac{2\pi}{\frac{s-m_N^2}{2}} \frac{m_e^2\; m_N^2}{2\pi^2} |\vec{l}\,'|\; \delta(|\vec{l}\,'| - x_0) \frac{1}{2(r_0 - |\vec{r}|\cos\theta_{l'})}\; |\mathcal{M}|^2 \Bigg|_{x_0 = \frac{r^2 - m_N^2}{2(r_0 - |\vec{r}|\cos\theta_{l\,'})}} \\
&= \frac{m_e^2\; m_N^2}{\pi(s - m_N^2)}\; \frac{|\vec{l}\,'|}{r_0 - |\vec{r}|\cos\theta_{l'}}\; \delta(|\vec{l}\,'| - x_0)\; |\mathcal{M}|^2 \Bigg|_{x_0 = \frac{r^2 - m_N^2}{2(r_0 - |\vec{r}|\cos\theta_{l\,'})}}
\end{aligned} \tag{D.8}$$

with $\theta_{l'} = \angle(\vec{r}, \vec{l}\,') = \angle(\vec{l}, \vec{l}\,')$. Finally, we get

$$\begin{aligned}
\frac{d\sigma}{dl_0 d\cos\theta_{l'}} &= \frac{2\pi}{\frac{s-m_N^2}{2}} \frac{m_e^2\; m_N^2}{2\pi^2} |\vec{l}\,'|\; \delta(|\vec{l}\,'| - x_0) \frac{1}{2(r_0 - |\vec{r}|\cos\theta_{l'})}\; |\mathcal{M}|^2 \Bigg|_{x_0 = \frac{r^2 - m_N^2}{2(r_0 - |\vec{r}|\cos\theta_{l\,'})}} \\
&= \frac{m_e^2\; m_N^2}{\pi(s - m_N^2)}\; \frac{|\vec{l}\,'|}{r_0 - |\vec{r}|\cos\theta_{l'}}\; \delta(|\vec{l}\,'| - x_0)\; |\mathcal{M}|^2 \Bigg|_{x_0 = \frac{r^2 - m_N^2}{2(r_0 - |\vec{r}|\cos\theta_{l\,'})}} \\
\Rightarrow \frac{d\sigma}{d\cos\theta_{l'}} &= \frac{m_e^2\; m_N^2}{\pi(s - m_N^2)}\; \frac{|\vec{l}\,'|}{r_0 - |\vec{r}|\cos\theta_{l'}}\; |\mathcal{M}|^2 \Bigg|_{|\vec{l}\,'| = \frac{r^2 - m_N^2}{2(r_0 - |\vec{r}|\cos\theta_{l\,'})}} \qquad .
\end{aligned} \tag{D.9}$$

Hereafter, a transformation to invariant variables can be done using

$$
\begin{aligned}
\frac{dt}{d\cos\theta_{l'}} &= \frac{d\left((l-l')^2\right)}{d\cos\theta_{l'}} = \frac{d\,(-2ll')}{d\cos\theta_{l'}} \\
&= \frac{d\left(-2|\vec{l}||\vec{l}'|(1-\cos\theta_{l'})\right)}{d\cos\theta_{l'}} \\
&= -2|\vec{l}|\frac{d\left(\frac{r^2-m_N^2}{2(r_0-|\vec{r}|\cos\theta_{l'})}(1-\cos\theta_{l'})\right)}{d\cos\theta_{l'}} \\
&= -|\vec{l}|(r^2-m_N^2)\frac{-(r_0-|\vec{r}|\cos\theta_{l'})+(1-\cos\theta_{l'})|\vec{r}|}{(r_0-|\vec{r}|\cos\theta_{l'})^2} \\
&= 2|\vec{l}|\frac{r^2-m_N^2}{2(r_0-|\vec{r}|\cos\theta_{l'})}\,\frac{|\vec{r}|-r_0}{|\vec{r}|\cos\theta_{l'}-r_0} \\
&= 2|\vec{l}||\vec{l}'|\frac{r_0-|\vec{r}|}{r_0-|\vec{r}|\cos\theta_{l'}} \quad , \qquad \text{(D.10)}
\end{aligned}
$$

such that the formula is given in invariant form by[2]

$$
\begin{aligned}
\frac{d\sigma}{dt} &= \frac{2\pi}{\frac{s-m_N^2}{2}}\,\frac{m_e^2\,m_N^2}{2\pi^2}\,\frac{1}{2|\vec{l}|}\,\frac{1}{2(r_0-|\vec{r}|)}\,|\mathcal{M}|^2 \\
&= \frac{1}{\frac{s-m_N^2}{2}}\,\frac{m_e^2\,m_N^2}{\pi}\,\frac{1}{2\frac{s-m_N^2}{2m_N}}\,\frac{1}{2(m_N+|\vec{l}'|-|\vec{l}'|)}\,|\mathcal{M}|^2 \\
&= \frac{1}{(s-m_N^2)^2}\,\frac{m_e^2\,m_N^2}{\pi}\,|\mathcal{M}|^2\ . \qquad \text{(D.11)}
\end{aligned}
$$

---

[2] See also [Ell08], i.e. lecture 6, page 11 (Attention: Not "Bjorken & Drell" but "Peskin" notation.)

Appendix E

The resonance form factors: Fixing the form factors using helicity amplitudes

Overview: This appendix makes the connection between resonance form-factors and helicity amplitudes.

The resonance excitations play a dominant role in the spectrum of low-energy $\gamma^\star N$ scattering. Applying a partial wave analysis to the world data on photon and electron scattering, e.g., the MAID group [Dre92, MAI] provides information about resonance properties. An important result of such an analysis are the so-called helicity amplitudes, which can be used to fix the resonance form factors [AR98, AR03, Lal06] defined in sec. 4.6.1. Note that the results by Lalakulich *et al.* [Lal06] have been obtained in the lab-frame, whereas MAID defines its amplitudes in the CM frame ([Alv06]). Henceforth, the results of L. Alvarez-Ruso [Alv05] obtained in the CM-frame are the proper ones to be used and we summarize his findings in the following.

Let us assume that the photon momentum points in z-direction

$$q^\mu = (q^0, 0, 0, q^z) \quad . \tag{E.1}$$

The photon can have three different polarizations which all fulfill $\epsilon_\mu q^\mu = 0$:

$$\epsilon^\pm_\mu = \pm\tfrac{1}{\sqrt{2}}(0,1,\pm i,0) \quad \textit{transverse polarizations} \quad , \tag{E.2}$$

$$\epsilon^0_\mu = \tfrac{1}{\sqrt{Q^2}}(q^z,0,0,q^0) \quad \textit{longitudinal polarization} \quad . \tag{E.3}$$

The helicity amplitudes give the nucleon to resonance transition-probability dependent on the specific polarization of the incoming photon and the spin orientations of nucleon and resonance. The definition of the helicity amplitudes depends on spinor normalizations and may differ from on work to another. In the following, we work with a definition which is consistent with the MAID group (cf. especially [Tia04, eq. 16] using that $\rho = q_\mu J^\mu / q_0$ in their work [Dre92, eq. 5])

$$A_{1/2} = \sqrt{\frac{2\pi\alpha}{k_W}} \left\langle R, J_z = 1/2 | \epsilon^+_\mu J^\mu | N, J_z = -1/2 \right\rangle \quad , \tag{E.4}$$

$$A_{3/2} = \sqrt{\frac{2\pi\alpha}{k_W}} \left\langle R, J_z = 3/2 | \epsilon^+_\mu J^\mu | N, J_z = 1/2 \right\rangle \quad , \tag{E.5}$$

$$S_{1/2} = -\sqrt{\frac{2\pi\alpha}{k_W}} \left\langle R, J_z = 1/2 | \epsilon^0_\mu J^\mu | N, J_z = 1/2 \right\rangle \frac{|\vec{q}|}{\sqrt{Q^2}} \quad , \tag{E.6}$$

where $k_W = (W^2 - M^2)/(2W)$ and W denotes the CM energy.

E.1 Spin 1/2

E.1.1 Positive parity

$$A_{1/2} = \sqrt{\frac{2\pi\alpha}{M_N}\frac{(M_R - M_N)^2 + Q^2}{M_R^2 - M_N^2}}\left[\frac{Q^2}{4M_N^2}F_1^{p,n} + \frac{M_R + M_N}{2M_N}F_2^{p,n}\right] \tag{E.7}$$

and

$$S_{1/2} = -\sqrt{\frac{\pi\alpha}{M_N}\frac{(M_R + M_N)^2 + Q^2}{M_R^2 - M_N^2}}\frac{(M_R - M_N)^2 + Q^2}{4M_R M_N}\left[\frac{M_R + M_N}{2M_N}F_1^{p,n} - F_2^{p,n}\right]. \tag{E.8}$$

E.1.2 Negative parity

$$A_{1/2}^{p,n} = \sqrt{\frac{2\pi\alpha}{M_N}\frac{(M_R + M_N)^2 + Q^2}{M_R^2 - M_N^2}}\left[\frac{Q^2}{4M_N^2}F_1^{p,n} + \frac{M_R - M_N}{2M_N}F_2^{p,n}\right] \tag{E.9}$$

and

$$S_{1/2} = \sqrt{\frac{\pi\alpha}{M_N}\frac{(M_N - M_R)^2 + Q^2}{M_R^2 - M_N^2}}\frac{(M_R + M_N)^2 + Q^2}{4M_R M_N}\left[\frac{M_R - M_N}{2M_N}F_1^{p,n} - F_2^{p,n}\right]. \tag{E.10}$$

E.2 Spin 3/2

E.2.1 Positive parity

$$\begin{aligned}
A_{1/2} &= \sqrt{\frac{\pi\alpha}{3M_N}\frac{(M_R - M_N)^2 + Q^2}{M_R^2 - M_N^2}} \times \left[\frac{C_3^{p,n}}{M_N}\frac{M_N^2 + M_N M_R + Q^2}{M_R}\right. \\
&\quad \left. - \frac{C_4^{p,n}}{M_N^2}\frac{M_R^2 - M_N^2 - Q^2}{2} - \frac{C_5^{p,n}}{M_N^2}\frac{M_R^2 - M_N^2 + Q^2}{2}\right] \quad , \qquad \text{(E.11)} \\
A_{3/2} &= \sqrt{\frac{\pi\alpha}{M_N}\frac{(M_R - M_N)^2 + Q^2}{M_R^2 - M_N^2}} \\
&\quad \times \left[\frac{C_3^{p,n}}{M_N}(M_N + M_R) + \frac{C_4^{p,n}}{M_N^2}\frac{M_R^2 - M_N^2 - Q^2}{2} + \frac{C_5^{p,n}}{M_N^2}\frac{M_R^2 - M_N^2 + Q^2}{2}\right] \qquad \text{(E.12)}
\end{aligned}$$

and

$$\begin{aligned}
S_{1/2} &= \sqrt{\frac{\pi\alpha}{6M_N}\frac{(M_R - M_N)^2 + Q^2}{M_R^2 - M_N^2}}\frac{\sqrt{[(M_R - M_N)^2 + Q^2][(M_R + M_N)^2 + Q^2]}}{M_R^2} \\
&\quad \times \left[\frac{C_3^{p,n}}{M_N}M_R + \frac{C_4^{p,n}}{M_N^2}M_R^2 + \frac{C_5^{p,n}}{M_N^2}\frac{M_R^2 + M_N^2 + Q^2}{2}\right] \quad . \qquad \text{(E.13)}
\end{aligned}$$

E.2.2 Negative parity

$$\begin{aligned}
A_{1/2} &= \sqrt{\frac{\pi\alpha}{3M_N}\frac{(M_R+M_N)^2+Q^2}{M_R^2-M_N^2}} \times \left[\frac{C_3^{p,n}}{M_N}\frac{M_N^2-M_NM_R+Q^2}{M_R}- \right. \\
&\left. \frac{C_4^{p,n}}{M_N^2}\frac{M_R^2-M_N^2-Q^2}{2}-\frac{C_5^{p,n}}{M_N^2}\frac{M_R^2-M_N^2+Q^2}{2}\right], \qquad \text{(E.14)} \\
A_{3/2} &= \sqrt{\frac{\pi\alpha}{M_N}\frac{(M_R+M_N)^2+Q^2}{M_R^2-M_N^2}} \\
&\times \left[\frac{C_3^{p,n}}{M_N}(M_N-M_R)-\frac{C_4^{p,n}}{M_N^2}\frac{M_R^2-M_N^2-Q^2}{2}-\frac{C_5^{p,n}}{M_N^2}\frac{M_R^2-M_N^2+Q^2}{2}\right] \qquad \text{(E.15)}
\end{aligned}$$

and

$$\begin{aligned}
S_{1/2} &= -\sqrt{\frac{\pi\alpha}{6M_N}\frac{(M_R+M_N)^2+Q^2}{M_R^2-M_N^2}}\frac{\sqrt{[(M_R-M_N)^2+Q^2][(M_R+M_N)^2+Q^2]}}{M_R^2} \\
&\times \left[\frac{C_3^{p,n}}{M_N}M_R+\frac{C_4^{p,n}}{M_N^2}M_R^2+\frac{C_5^{p,n}}{M_N^2}\frac{M_R^2+M_N^2+Q^2}{2}\right] \quad . \qquad \text{(E.16)}
\end{aligned}$$

Appendix F

Virtual photon cross sections for pion production

Overview: This appendix makes the connection between virtual-photon cross-section for pion production and the underlying hadron tensor.

In the literature, e.g. [Dre92], the cross section for electron-induced pion production is often defined in terms of the so called *virtual photon cross sections* which has already been addressed in sec. 4.3. These virtual photon cross sections are widely used for pion production, so we shortly introduce the notation and show how this notation is connected to the underlying hadron tensor H_π as defined in sec. 4.5.2.

Our notation for single-pion production is chosen according to fig. 4.4: the nucleon momenta are denoted p and p', the photon momentum by q, the pion momentum k and the masses of the in- and outgoing nucleons m and m'. The electron mass is denoted m_e, the in- and outgoing lepton momenta are denoted l and l'.

In the lab-frame, the total cross section is parametrized by

$$\frac{d\sigma^\pi}{dl'^0 d\Omega_{l'} d\Omega_k} = \Gamma \frac{d\sigma_v^\pi}{d\Omega_k}$$

where

$$\Gamma = \frac{\alpha}{2\pi^2} \frac{l'^0}{l^0} \frac{k_\gamma}{Q^2} \frac{1}{1-\epsilon}$$

is the *flux of the virtual photon field.* The variable

$$k_\gamma = (W^2 - m^2)/(2m)$$

denotes the laboratory energy which is necessary to excite a hadronic system with CM-energy W and

$$\epsilon = \left(1 + 2\vec{q}^{\,2}/Q^2 \tan^2\left(\frac{\theta_k}{2}\right)\right)^{-1}$$

is called the *degree of transverse polarization.* Furthermore

$$\begin{aligned}\frac{d\sigma_v^\pi}{d\Omega_k} &= \frac{d\Omega_k^{CM}}{d\Omega_k}\frac{d\sigma_v^\pi}{d\Omega_k^{CM}} = \frac{d\Omega_k^{CM}}{d\Omega_k}\left(\frac{d\sigma_T^\pi}{d\Omega_k^{CM}} + \epsilon\frac{d\sigma_T^\pi}{d\Omega_k^{CM}}\right.\\ &\quad + \sqrt{2\epsilon(1+\epsilon)}\frac{d\sigma_{LT}^\pi}{d\Omega_k^{CM}}\cos(\phi_k) + \epsilon\frac{d\sigma_{TT}^\pi}{d\Omega_k^{CM}}\cos(2\phi_k)\\ &\quad \left. + h\sqrt{2\epsilon(1+\epsilon)}\frac{d\sigma_{LT'}^\pi}{d\Omega_k^{CM}}\sin(\phi_k) + h\sqrt{1-\epsilon^2}\frac{d\sigma_{TT'}^\pi}{d\Omega_k^{CM}}\right)\end{aligned}$$

with h denoting the electron polarization. Note that in the case of non-polarized electrons $h = 0$. The various cross sections in the equation above are now related to the hadronic tensor by

$$\begin{aligned}
\frac{d\sigma_T^\pi}{d\Omega_k^{CM}} &= c\ \left((H_\pi)_{xx} + (H_\pi)_{yy}\right)/2 \quad , && \text{(F.1)}\\
\frac{d\sigma_L^\pi}{d\Omega_k^{CM}} &= c\,(H_\pi)_{zz} \quad , && \text{(F.2)}\\
\frac{d\sigma_{LT}^\pi}{d\Omega_k^{CM}} &= -c\,\frac{1}{\cos(\phi_k)}\mathrm{Re}((H_\pi)_{xz}) \quad , && \text{(F.3)}\\
\frac{d\sigma_{TT}^\pi}{d\Omega_k^{CM}} &= c\,\frac{1}{\cos(2\phi_k)}\left((H_\pi)_{xx} - (H_\pi)_{yy}\right)/2 \quad , && \text{(F.4)}\\
\frac{d\sigma_{TL'}^\pi}{d\Omega_k^{CM}} &= c\,\frac{1}{\sin(\phi_k)}\mathrm{Im}((H_\pi)_{yz}) \quad , && \text{(F.5)}\\
\frac{d\sigma_{TT'}^\pi}{d\Omega_k^{CM}} &= c\,\mathrm{Im}((H_\pi)_{xy}) && \text{(F.6)}
\end{aligned}$$

with

$$c = \frac{|\vec{k}|}{\frac{m}{W}k_\gamma}\left(\frac{m}{4\pi W}\right)^2 \quad .$$

It is important to remember that equations F.1-F.6 are all defined in the CM-frame of the hadronic vertex, i.e. the πN rest-frame.

Appendix G

Miscellaneous

G.1 Boosting a cross section

In the following we derive how to transform a cross section under Lorentz boosts. This is done using vacuum kinematics neglecting potentials, since the effect of this boost is anyhow small and because we only need this boost for the $\gamma N \to N\pi\pi$ background cross section, where we anyhow assume that the whole cross section is not modified by the medium.

Let us consider particles A and B colliding. The cross section σ is usually defined in a frame where particle A or B is resting. Since σ is invariant against boosts parallel to the motion of the particles, the cross section must be the same in both rest frames and the same as in any frame where the particles have co-linear (i.e. parallel or anti-parallel) momenta. The cross section is defined as

$$\sigma = \frac{\frac{dN}{dt}}{\Phi} \quad , \tag{G.1}$$

where N is the number of events, t the time and Φ the flux. In a frame where A is the target and at rest we get

$$\Phi = \rho_B v_{\text{rel}} = \rho_B v_B = \rho_B \left|\vec{v}_B\right| = \rho_B \left|\frac{\vec{p}_B}{E_B}\right| \quad . \tag{G.2}$$

which yields

$$dN = \sigma dt \rho_B \left|\frac{\vec{p}_B}{E_B}\right| \quad . \tag{G.3}$$

Let us now consider an arbitrary frame F' where particles A and B have no co-linear momenta. Since the number of events is a Lorentz invariant, we get for the cross section σ' in that frame

$$\sigma' = \frac{\frac{dN}{dt'}}{\Phi'} \quad . \tag{G.4}$$

The flux is given by

$$\Phi' = \rho'_B v'_{\text{rel}} \quad , \tag{G.5}$$

where the relative velocity in frame F' is given by

$$v'_{\text{rel}} = \left|\vec{v}_A{}' - \vec{v}_B{}'\right| = \left|\frac{\vec{p}_A{}'}{E'_A} - \frac{\vec{p}_B{}'}{E'_B}\right| \quad . \tag{G.6}$$

So we get

$$\begin{aligned}\sigma' &= \frac{\frac{\sigma dt \rho_B \left|\frac{\vec{p}_B}{E_B}\right|}{dt'}}{\Phi'} && \text{(G.7)}\\ &= \sigma \frac{1}{\gamma} \frac{\rho_B \left|\frac{\vec{p}_B}{E_B}\right|}{\rho'_B \left|\frac{\vec{p}_A{}'}{E'_A} - \frac{\vec{p}_B{}'}{E'_B}\right|} \quad . && \text{(G.8)}\end{aligned}$$

Furthermore, we use that ρ/E is a Lorentz-invariant and the boost factor to the rest-frame of particle A is given by $\gamma = E'_A/m_A$. Finally, we obtain

$$\begin{aligned}\sigma' &= \sigma \frac{m_A}{E'_A} \frac{|\vec{p}_B|}{\left|\frac{\vec{p}_A{}' E'_B}{E'_A} - \vec{p}_B{}'\right|} && \text{(G.9)}\\ &= \sigma \frac{m_A |\vec{p}_B|}{\left|\vec{p}_A{}' E'_B - E'_A \vec{p}_B{}'\right|} \quad . && \text{(G.10)}\end{aligned}$$

G.2 Electron and photon kinematics

G.2.1 $E_f, \theta_f \leftrightarrow Q^2, W$

The following relations are useful to relate electron kinematics to the so-called *momentum transfer* Q^2 and the *center-of-mass energy at the hadronic vertex* W. Assuming a resting nucleon target with mass m_N and four-momentum

$$p = (m_N, \vec{0}) \quad ,$$

and initial and final electrons with momenta

$$\begin{aligned} l_i &= (E_i, 0, 0, E_i)^t \quad ,\\ l_f &= (E_f, E_f \sin(\theta_f), 0, E_f \cos(\theta_f))^t \quad ,\end{aligned}$$

the photon momentum is given by

$$q = (E_i - E_f, -E_f \sin(\theta_f), 0, E_i - E_f \cos(\theta_f))^t \quad . \tag{G.11}$$

Thus the square of the center of mass energy at the hadronic vertex is given by

$$W^2 = (q+p)^2 = q^2 + p^2 + 2qp = -Q^2 + m_N^2 + 2m_N(E_i - E_f) \quad . \tag{G.12}$$

Here we introduced the momentum transfer $Q^2 = -q^2$, which is in terms of E_f and $\cos(\theta_f)$ given by

$$\begin{aligned} Q^2 &= -q^2 = -(E_i - E_f)^2 + E_f^2 \sin^2(\theta_f) + (E_i - E_f \cos(\theta_f))^2 \\ &= 2E_i E_f (1 - \cos(\theta_f)) \, . && \text{(G.13)}\end{aligned}$$

Combining eq. G.12 and G.13 one gets the relations which connect the set of variables (Q^2, W) to the set (θ_f, E_f)

$$\begin{aligned} Q^2 &= 2E_i E_f (1 - \cos(\theta_f)) \quad , && \text{(G.14)}\\ W^2 &= -2E_i E_f (1 - \cos(\theta_f)) + m_N^2 + 2m_N(E_i - E_f) && \text{(G.15)}\end{aligned}$$

and

$$\begin{aligned} E_f &= \frac{1}{2m_N}\left(-W^2 - Q^2 + m_N^2 + 2m_N E_i\right) \quad , && \text{(G.16)} \\ \cos(\theta_f) &= 1 - \frac{Q^2}{2E_i E_f} = 1 - \frac{Q^2\ 2m_N}{2E_i\left(-W^2 - Q^2 + m_N^2 + 2m_N E_i\right)} \quad . && \text{(G.17)} \end{aligned}$$

Transformation matrix

Finally, we want to evaluate the Jacobian J for the transformation

$$d\cos(\theta_f) dE_f = |J| dQ^2 dW \quad . \qquad \text{(G.18)}$$

Therefore, we evaluate

$$\begin{aligned} \frac{d\cos(\theta_f)}{dQ^2} &= -\frac{2m_N}{2E_i\left(-W^2 - Q^2 + m_N^2 + 2m_N E_i\right)} - \frac{Q^2\ 2m_N}{2E_i\left(-W^2 - Q^2 + m_N^2 + 2m_N E_i\right)^2} \quad , \\ \frac{d\cos(\theta_f)}{dW} &= -\frac{Q^2\ 2m_N\ 2W}{2E_i\left(-W^2 - Q^2 + m_N^2 + 2m_N E_i\right)^2} \quad , \\ \frac{dE_f}{dQ^2} &= -\frac{1}{2m_N} \quad , \\ \frac{dE_f}{dW} &= -\frac{2W}{2m_N} \quad , \end{aligned}$$

which gives

$$\begin{aligned} |J| &= \left|\begin{pmatrix} \frac{d\cos(\theta_f)}{dQ^2} & \frac{d\cos(\theta_f)}{dW} \\ \frac{dE_f}{dQ^2} & \frac{dE_f}{dW} \end{pmatrix}\right| \\ &= \left|\frac{2W}{2E_i\left(-W^2 - Q^2 + m_N^2 + 2m_N E_i\right)} + \frac{Q^2\ 2W}{2E_i\left(-W^2 - Q^2 + m_N^2 + 2m_N E_i\right)^2}\right. \\ &\qquad \left. - \frac{Q^2\ 2W}{2E_i\left(-W^2 - Q^2 + m_N^2 + 2m_N E_i\right)^2}\right| \\ &= \left|\frac{W}{E_i\left(-W^2 - Q^2 + m_N^2 + 2m_N E_i\right)}\right| \quad . && \text{(G.19)} \end{aligned}$$

G.2.2 Q^2 at the quasi-elastic peak

This section is devoted to the kinematics of quasi-elastic electron-nucleon scattering in vacuum. For a nucleon at rest we get by setting $W = m_N$ in eq. G.16 that the final electron energy is determined by

$$E_f = \frac{1}{2m_N}\left(-Q^2 + 2m_N E_i\right) \quad . \qquad \text{(G.20)}$$

Hence the Q^2 for this reaction is in the nucleon rest-frame given by

$$Q^2_{QE} = 2m_N\left(E_i - E_f\right) = 2m_n q_0 \quad . \qquad \text{(G.21)}$$

Now let us consider a nucleon moving with arbitrary momentum p. Boosting to its rest frame F we get the boosted photon energy

$$q_0^F \quad = \quad \frac{q_0 - \frac{\vec{p}}{p_0}\vec{q}}{\sqrt{1-\left(\frac{\vec{p}}{p_0}\right)^2}} \quad . \tag{G.22}$$

Given this rest-frame photon energy, we can apply eq. G.21 which gives

$$\begin{aligned} Q^2_{QE} = 2m_N q_0^F &= 2m_N \frac{q_0 - \frac{\vec{p}}{p_0}\vec{q}}{\sqrt{1-\left(\frac{\vec{p}}{p_0}\right)^2}} & \text{(G.23)} \\ &= 2\left(p_0 q_0 - \vec{p}\vec{q}\right) = 2pq \quad . & \text{(G.24)} \end{aligned}$$

So the general result, which is valid in any frame, is given by

$$Q^2_{QE} = 2pq \quad . \tag{G.25}$$

An alternative derivation starts from $p' = q+p$ where p' is the final nucleon momentum. Squaring this identity we get

$$\begin{aligned} & p'^2 = (q+p)^2 = -Q^2_{QE} + 2pq + p^2 & \text{(G.26)} \\ \Leftrightarrow\ & Q^2_{QE} = 2pq + p^2 - p'^2 = 2pq + m_N^2 - m_N^2 = 2pq \quad . & \text{(G.27)} \end{aligned}$$

Average photon energy and possible Q^2 range for a Fermi gas

Let us study the implications of eq. G.25 for the scattering of electrons off a nucleon Fermi gas, where potentials are neglected.

Let us consider the scenario that we have a fixed electron beam energy E_i and a fixed electron scattering angle θ_f. Using $Q^2 = \vec{q}^{\,2} - q_0^2 = 2qp$ and our choice for $\vec{q}$ given in eq. G.11 we get

$$q^0_{QE} = \frac{p_x E_i \sin\theta_f - p_z E_i (1-\cos\theta_f) - E_i^2(1-cos\theta_f)}{p_x \sin\theta_f + p_z \cos\theta_f - E_i(1-\cos\theta_f) - p_0} \quad . \tag{G.28}$$

The mean value of all possible photon energies, which generate a QE-event in the gas is then given by

$$\langle q^0_{QE} \rangle \quad = \quad \frac{\int_{p_f} d^3p\, q^0_{QE}}{\int_{p_f} d^3p} \tag{G.29}$$

and plotted in fig. G.1 as a function of the Fermi momentum. For a Fermi momentum of $p_f = 0.2$ GeV representing approximately nuclear matter density, this gives $< q_0 > \approx 70.2$ MeV. We emphasize that this value shows only a 1.4% deviation from the result for a nucleon at rest, where the photon energy is given by 71.3 MeV. For $p_f = 0.25$ GeV the average is shifted to 69.6 MeV, which is also only a 2.4% shift.

The maximum and minimum Q^2_{QE}, which can be absorbed by a Fermi gas, are determined by those cases where $\vec{q}\vec{p} = \pm|\vec{q}||\vec{p}|$:

$$\begin{aligned} Q^2_{QE}(\text{min}) &= 2\left(\sqrt{p_f^2 + m_n^2}\,q_0 + |\vec{q}|p_f\right) \quad , & \text{(G.30)} \\ Q^2_{QE}(\text{max}) &= 2\left(\sqrt{p_f^2 + m_n^2}\,q_0 - |\vec{q}|p_f\right) \quad . & \text{(G.31)} \end{aligned}$$

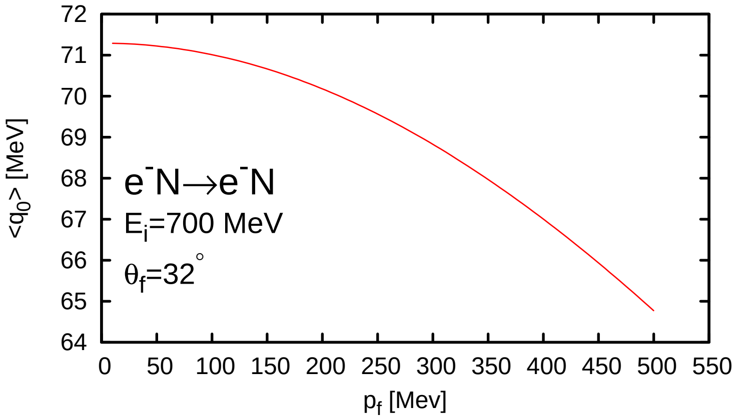

Figure G.1: The average photon energy $\langle q^0_{QE}\rangle$ at the QE-peak within a Fermi gas of nucleons having Fermi momentum p_f. The initial electron energy is fixed to 700 MeV and the scattering angle is given by 32°.

Again, let us keep the electron beam energy E_i and the electron scattering angle θ_f constant. Using eq. G.13, one gets the following equations for the final electron energy E_f at the minimal and maximal Q^2_{QE}

$$\begin{aligned}2E_iE_f(\max)(1-\cos\theta) &= 2\Big(\sqrt{p_f^2+m_n^2}(E_i-E_f(\max)) \\ &\quad +\sqrt{E_i^2+E_f(\max)^2-2E_iE_f(\max)\cos\theta}\,p_f\Big) \quad , \qquad \text{(G.32)}\\ 2E_iE_f(\min)(1-\cos\theta) &= 2\Big(\sqrt{p_f^2+m_n^2}(E_i-E_f(\min)) \\ &\quad -\sqrt{E_i^2+E_f(\min)^2-2E_iE_f(\min)\cos\theta}\,p_f\Big) \quad . \qquad \text{(G.33)}\end{aligned}$$

As an example, let us again consider a beam energy of $E_i = 700$ MeV, a scattering angle of 32° and a Fermi momentum of $p_f = 0.2$ GeV. Solving eq. G.32-G.33, we get for this scenario

$$560 \text{ MeV} \lesssim E_f \lesssim 700 \text{ MeV} \quad ,$$

which gives the following range of allowed Q^2's:

$$0.119 \text{ GeV}^2 \lesssim Q^2 \lesssim 0.149 \text{ GeV}^2 \quad . \qquad \text{(G.34)}$$

So the maximal spread within Q^2 is 20% which is quite considerable. We conclude that a Fermi sphere of nucleons can absorb photons having different Q^2 and we have shown with the preceding example that the allowed Q^2 range can become large compared to the mean Q^2.

Bibliography

[Aac68] Aachen-Berlin-Bonn-Hamburg-Heidelberg-Munich Collaboration. 'Photoproduction of meson and baryon resonances at energies up to 5.8-GeV.' *Phys. Rev.*, **175**:1669 (1968).

[Abr03] B. M. Abramov *et al.* 'Inclusive pion double charge exchange on O-16 at 0.6-GeV - 1.1-GeV.' *Nucl. Phys.*, **A723**:389 (2003). nucl-ex/0211016.

[Ahr03] J. Ahrens *et al.* 'Helicity dependence of the gamma(pol.) p(pol.) → n pi+ pi0 reaction in the second resonance region.' *Phys. Lett.*, **B551**:49 (2003).

[Ahr05] J. Ahrens *et al.* 'Intermediate resonance excitation in the gamma p → p pi0 pi0 reaction.' *Phys. Lett.*, **B624**:173 (2005).

[Aic85] J. Aichelin and G. Bertsch. 'Numerical simulation of medium energy heavy ion reactions.' *Phys. Rev.*, **C31**:1730 (1985).

[Ale07] C. Alexandrou. 'N to Δ electromagnetic and axial form factors in full QCD.' (2007). arXiv:0710.1202[hep-lat].

[Alq02] M. Alqadi and W. R. Gibbs. 'Pion double charge exchange on 4He.' *Phys. Rev.*, **C65**:044609 (2002). nucl-th/0112074.

[Alv05] L. Alvarez-Ruso (2005). Private communications.

[Alv06] L. Alvarez-Ruso and L. Tiator (2006). Private communications.

[Ama05] J. E. Amaro, M. B. Barbaro, J. A. Caballero, T. W. Donnelly, A. Molinari, and I. Sick. 'Using electron scattering superscaling to predict charge- changing neutrino cross sections in nuclei.' *Phys. Rev.*, **C71**:015501 (2005). nucl-th/0409078.

[Ana87] A. K. Ananikyan *et al.* 'Hadronic photoabsorption and coherent photoproduction of pi 0 mesons in be and c nuclei in the resonance energy region.' *Sov. J. Nucl. Phys.*, **46**:208 (1987).

[And88] V. P. Andreev *et al.* 'Measurement of the cross-section of the reaction $pp \to pp\pi^0$ in the region of dibaryon resonances.' *Z. Phys.*, **A329**:371 (1988).

[Ang96] M. Anghinolfi *et al.* 'Quasi-elastic and inelastic inclusive electron scattering from an oxygen jet target.' *Nucl. Phys.*, **A602**:405 (1996). nucl-th/9603001.

[AR98] L. Alvarez-Ruso, S. K. Singh, and M. J. Vicente Vacas. 'Charged current weak electroproduction of Delta resonance.' *Phys. Rev.*, **C57**:2693 (1998). nucl-th/9712058.

[AR03] L. Alvarez-Ruso, M. B. Barbaro, T. W. Donnelly, and A. Molinari. 'Nuclear response functions for the N - N*(1440) transition.' *Nucl. Phys.*, **A724**:157 (2003). nucl-th/0303027.

[AR05] L. Alvarez-Ruso, P. Muhlich, O. Buss, and U. Mosel. 'Low energy double-pion photoproduction in nuclei.' *Int. J. Mod. Phys.*, **A20**:578 (2005).

[Ara83] E. A. Arakelian *et al.* 'Measurement of total hadronic photoproduction cross- section in Be-9, C-12, O-16, Cu-64 nuclei in the photon energy range $E_\gamma = (0.25\text{ GeV} - 2.7\text{ GeV})$.' *Sov. J. Nucl. Phys.*, **38**:589 (1983).

[Arg08a] Argonne National Lab. 'Argonne V18 website.' (August 2008). http://www.phy.anl.gov/theory/research/forces.html.

[Arg08b] Argonne National Lab. 'Nuclear Forces and Nuclear Systems.' (August 2008). http://www.phy.anl.gov/theory/research/forces.html.

[Arr07] J. Arrington, W. Melnitchouk, and J. A. Tjon. 'Global analysis of proton elastic form factor data with two-photon exchange corrections.' *Phys. Rev.*, **C76**:035205 (2007). 0707.1861.

[Ash81] D. Ashery, I. Navon, G. Azuelos, H. K. Walter, H. J. Pfeiffer, and F. W. Schlepütz. 'True absorption and scattering of pions on nuclei.' *Phys. Rev.*, **C23**:2173 (1981).

[Ass03] Y. Assafiri *et al.* 'Double π^0 photoproduction on the proton at GRAAL.' *Phys. Rev. Lett.*, **90**:222001 (2003).

[Aub83] J. J. Aubert *et al.* 'The ratio of the nucleon structure functions $F2_n$ for iron and deuterium.' *Phys. Lett.*, **B123**:275 (1983).

[Bar83] P. Barreau *et al.* 'Deep-inelastic electron scattering from carbon.' *Nuclear Physics A*, **402**:515 (1983).

[Bar88] D. T. Baran, B. F. Filippone, D. Geesaman, M. Green, R. J. Holt, H. E. Jackson, J. Jourdan, R. D. McKeown, R. G. Milner, J. Morgenstern, D. H. Potterveld, R. E. Segel, P. Seidl, R. C. Walker, and B. Zeidman. 'Δ electroproduction and inelastic charge scattering from carbon and iron.' *Phys. Rev. Lett.*, **61(4)**:400 (Jul 1988).

[Bar05] O. Bartholomy *et al.* 'Neutral pion photoproduction off protons in the energy range 0.3 GeV < E (gamma) < 3 GeV.' *Phys. Rev. Lett.*, **94**:012003 (2005). hep-ex/0407022.

[Bas98] S. A. Bass *et al.* 'Microscopic models for ultrarelativistic heavy ion collisions.' *Prog. Part. Nucl. Phys.*, **41**:255 (1998). nucl-th/9803035.

[Bau86] W. Bauer, G. Bertsch, W. Cassing, and U. Mosel. *Phys. Rev. C*, **34**:2127 (1986).

[Bau89] W. Bauer and G. F. Bertsch. 'Production of energetic photons via excitation of the Delta resonance in heavy ion collisions.' *Phys. Lett.*, **B229**:16 (1989).

[Bec70] F. Becker and C. Schmit. 'Analysis of double charge exchange of pions on He-4.' *Nucl. Phys.*, **B18**:607 (1970).

[Ben05] O. Benhar, N. Farina, H. Nakamura, M. Sakuda, and R. Seki. 'Electron and neutrino nucleus scattering in the impulse approximation regime.' *Phys. Rev.*, **D72**:053005 (2005). hep-ph/0506116.

[Ben06] O. Benhar and D. Meloni. 'How well do we know the nucleon structure functions in the Delta production region?' *Phys. Rev. Lett.*, **97**:192301 (2006). hep-ph/0604071.

[Ben08] O. Benhar, D. Day, and I. Sick. 'Inclusive quasi-elastic electron-nucleus scattering.' *Rev. Mod. Phys.*, **80**:189 (2008). nucl-ex/0603029.

[Ber67] F. A. Berends, A. Donnachie, and D. L. Weaver. 'Photoproduction and electroproduction of pions. 1. Dispersion relation theory.' *Nucl. Phys.*, **B4**:1 (1967).

[Ber84] G. F. Bertsch and H. Kruse. 'Boltzmann equation for heavy ion collisions.' *Phys. Rev.*, **C29(2)**:673 (1984).

[Ber87] V. Bernard, U. G. Meissner, and I. Zahed. 'Properties of the scalar sigma meson at finite density.' *Phys. Rev. Lett.*, **59**:966 (1987).

[Ber88] G. F. Bertsch and S. D. Gupta. 'A guide to microscopic models for intermediate energy heavy ion collisions.' *Phys. Rep.*, **160(4)**:189 (1988).

[Bia93a] N. Bianchi *et al.* 'Absolute measurement of the total photoabsorption cross- section for carbon in the nucleon resonance region.' *Phys. Lett.*, **B309**:5 (1993).

[Bia93b] N. Bianchi *et al.* 'Measurement of the total cross-section for U-238 photofission in the nucleon resonance region.' *Phys. Lett.*, **B299**:219 (1993).

[Bia93c] N. Bianchi *et al.* 'Photofissility of Th-232 measured with tagged photons from 250-MeV to 1200-MeV.' *Phys. Rev.*, **C48**:1785 (1993).

[Bia94] N. Bianchi *et al.* 'Absolute total photoabsorption cross-sections on nuclei in the nucleon resonance region.' *Phys. Lett.*, **B325**:333 (1994).

[Bia96] N. Bianchi *et al.* 'Total hadronic photoabsorption cross-section on nuclei in the nucleon resonance region.' *Phys. Rev.*, **C54**:1688 (1996).

[Bjo93] J. Bjorken and S. Drell. *Relativistische Quantenfeldtheorie.* BI-Wissenschaftsverlag, Mannheim (1993).

[Blo07] F. Bloch *et al.* 'Double pion photoproduction off 40Ca.' *Eur. Phys. J.*, **A32**:219 (2007). nucl-ex/0703037.

[Bof96] S. Boffi, C. Guisti, F. D. Pacati, and M. Radici. *Electromagnetic response of atomic nuclei.* Clarendon Press, Oxford (1996).

[Bon89] A. Bonasera, G. Burgio, and M. D. Toro. *Phys. Lett. B*, **221**:233 (1989).

[Bon94] A. Bonasera, F. Gulminelli, and J. Molitoris. *Phys. Rep.*, **243**:1 (1994).

[Bon95] A. Bondar *et al.* 'The $pp \to pp\pi^0$ reaction near the kinematical threshold.' *Phys. Lett.*, **B356**:8 (1995).

[Bon96] F. Bonutti *et al.* 'A dependence of the $(\pi^\pm, \pi^+\pi^\pm)$ reaction near the $2m_\pi$ threshold.' *Phys. Rev. Lett.*, **77**:603 (1996).

[Bon00] F. Bonutti *et al.* 'The $\pi\pi$ interaction in nuclear matter from a study of the $\pi^+ A \to \pi^+\pi^\pm A'$ reactions.' *Nucl. Phys.*, **A677**:213 (2000).

[Bra95] A. Braghieri *et al.* 'Total cross-section measurement for the three double pion production channels on the proton.' *Phys. Lett.*, **B363**:46 (1995).

[Bra06] R. Bradford, A. Bodek, H. Budd, and J. Arrington. 'A new parameterization of the nucleon elastic form factors.' *Nucl. Phys. Proc. Suppl.*, **159**:127 (2006). hep-ex/0602017.

[Bro96] R. Brockmann and W. Weise. 'The chiral condensate in nuclear matter.' *Phys. Lett.*, **B367**:40 (1996).

[Bur05] V. D. Burkert. 'Electromagnetic excitations of baryon resonances.' *Prog. Part. Nucl. Phys.*, **55**:108 (2005).

[Bus04] O. Buss. *Low-energy pions in a Boltzmann-Uehling-Uhlenbeck transport simulation*, Diplomarbeit (Diploma thesis), JLU Giessen (March 2004).
http://theorie.physik.uni-giessen.de/documents/diplom/buss.pdf.

[Bus05] O. Buss, L. Alvarez-Ruso, P. Mühlich, U. Mosel, and R. Shyam. 'Low-energy pions in nuclear matter and $\pi\pi$ photoproduction within a BUU transport model.' (2005). nucl-th/0502031.

[Bus06a] O. Buss, L. Alvarez-Ruso, A. B. Larionov, and U. Mosel. 'Pion induced double charge exchange reactions in the Δ resonance region.' *Phys. Rev.*, **C74**:044610 (2006). nucl-th/0607016.

[Bus06b] O. Buss, L. Alvarez-Ruso, P. Mühlich, and U. Mosel. 'Low-energy pions and $\pi\pi$ photoproduction.' *Ricerca scientifica ed Educazione Permanente*, **Supplemento n.125** (2006). Proceedings of the XLIV international winter meeting on nuclear physics (Bormio, Italy).

[Bus06c] O. Buss, L. Alvarez-Ruso, P. Mühlich, and U. Mosel. 'Low-energy pions in nuclear matter and $\pi\pi$ photoproduction within a buu transport model.' *Eur. Phys. J.*, **A29**:189 (2006). nucl-th/0603003.

[Bus07a] O. Buss, L. Alvarez-Ruso, A. B. Larionov, and U. Mosel. 'Exciting pions in nuclei: DCX and Electroproduction in the resonance region.' *Ricerca scientifica ed Educazione Permanente*, **Supplemento n.127** (2007). Proceedings of the XLV international winter meeting on nuclear physics (Bormio, Italy), nucl-th/0703060.

[Bus07b] O. Buss, T. Leitner, U. Mosel, and L. Alvarez-Ruso. 'The influence of the nuclear medium on inclusive electron and neutrino scattering off nuclei.' *Phys. Rev.*, **C76**:035502 (2007). arXiv:0707.0232[nucl-th].

[Bus08] O. Buss, L. Alvarez-Ruso, T. Leitner, and U. Mosel. 'Inclusive results for electron and photon scattering in the resonance region.' *Ricerca scientifica ed Educazione Permanente*, **Supplemento n.129** (2008). Proceedings of the XLVI international winter meeting on nuclear physics (Bormio, Italy).

[Byc73] E. Byckling and K. Kajantie. *Particle Kinematics.* John Wiley &Sons (1973).

[Byf52] H. Byfield, J. Kessler, L. M. Lederman, *et al.* 'Scattering and absorption of Π-mesons in Carbon.' *Phys. Rev.*, **86(1)**:17 (April 1952).

[Car71] A. A. Carter, J. R. Williams, D. V. Bugg, P. J. Bussey, and D. R. Dance. 'The total cross-sections for pion-proton scattering between 70 MeV and 290 MeV.' *Nucl. Phys.*, **B26**:445 (1971).

[Car76a] F. Carbonara *et al.* ‘Analysis of $\gamma n \rightarrow n\pi^+\pi^-$ and $\gamma n \rightarrow p\pi^0\pi^-$ reactions from threshold up to 1 GeV.’ *Il nuovo cimento*, **Vol. 36A(3)**:229 (1976).

[Car76b] A. S. Carroll *et al.* ‘Pion - nucleus total cross-sections in the (3,3) resonance region.’ *Phys. Rev.*, **C14**:635 (1976).

[Car92] R. C. Carrasco and E. Oset. ‘INTERACTION OF REAL PHOTONS WITH NUCLEI FROM 100-MEV TO 500-MEV.’ *Nucl. Phys.*, **A536**:445 (1992).

[Cas90] W. Cassing, V. Metag, U. Mosel, and K. Niita. ‘Production of energetic particles in heavy ion collisions.’ *Phys. Rept.*, **188**:363 (1990).

[Cas99] W. Cassing and E. L. Bratkovskaya. ‘Hadronic and electromagnetic probes of hot and dense nuclear matter.’ *Phys. Rept.*, **308**:65 (1999).

[Cas00] W. Cassing and S. Juchem. ‘Semiclassical transport of particles with dynamical spectral functions.’ *Nucl. Phys.*, **A665**:377 (2000). nucl-th/9903070.

[CBM08] ‘The CBM experiment.’ (May 2008).
http://www.gsi.de/fair/experiments/CBM/1intro.html.

[cer07] ‘CERN program library website.’ (September 2007).
http://cernlib.web.cern.ch/cernlib/.

[Cet00] C. Cetina *et al.* ‘Photofission of heavy nuclei at energies up to 4-GeV.’ *Phys. Rev. Lett.*, **84**:5740 (2000). nucl-ex/0004004.

[Cet02] C. Cetina *et al.* ‘Photofission of heavy nuclei from 0.2 to 3.8 GeV.’ *Phys. Rev.*, **C65**:044622 (2002).

[Che91] J.-P. Chen *et al.* ‘Longitudinal and transverse response functions in Fe-56(e, e-prime) at momentum transfer near 1-GeV/c.’ *Phys. Rev. Lett.*, **66**:1283 (1991).

[Chr04] M. E. Christy *et al.* ‘Measurements of electron proton elastic cross sections for $0.4 - (\mathrm{GeV}/c)^2 < Q^2 < 5.5 - (\mathrm{GeV}/c)^2$.’ *Phys. Rev.*, **C70**:015206 (2004). nucl-ex/0401030.

[Clo74] A. S. Clough *et al.* ‘Pion - nucleus total cross-sections from 88-MeV to 860- MeV.’ *Nucl. Phys.*, **B76**:15 (1974).

[Coh73] E. G. D. Cohen, editor. *The Boltzmann Equation.* Springer Verlag, Wien (1973). Proceedings of the International Symposium ’100 years Boltzmann equation’ in Vienna 4th-8th September 1972.

[Coh92] T. D. Cohen, R. J. Furnstahl, and D. K. Griegel. ‘Quark and gluon condensates in nuclear matter.’ *Phys. Rev.*, **C45**:1881 (1992).

[CS04] B. Collins-Sussman, B. W. Fitzpatrick, and C. M. Pilato. *Version Control with Subversion.* O’Reilly (June 2004).

[Cug81] J. Cugnon, T. Mizutani, and J. Vandermeulen. ‘Equilibration in relativistic nuclear collisions. A Monte Carlo calculation.’ *Nucl. Phys.*, **A352**:505 (1981).

[Cug96] J. Cugnon, J. Vandermeulen, and D. L’Hote. ‘Simple parametrization of cross-sections for nuclear transport studies up to the GeV range.’ *Nucl. Instrum. Meth.*, **B111**:215 (1996).

[Dan02] P. Danielewicz, R. Lacey, and W. G. Lynch. ‘Determination of the equation of state of dense matter.’ *Science*, **298**:1592 (2002). nucl-th/0208016.

[Dau02] M. Daum *et al.* ‘The reaction $np \to pp\pi^-$ from threshold up to 570-MeV.’ *Eur. Phys. J.*, **C23**:43 (2002). nucl-ex/0108008.

[Dav72] D. Davidson, T. Bowen, P. K. Caldwell, E. W. Jenkins, R. M. Kalbach, D. V. Petersen, A. E. Pifer, and R. E. Rothschild. ‘Pion-nucleon total cross-sections from 0.4 to 0.90 GeV/c.’ *Phys. Rev.*, **D6**:1199 (1972).

[Day93] D. B. Day *et al.* ‘Inclusive electron nucleus scattering at high momentum transfer.’ *Phys. Rev.*, **C48**:1849 (1993).

[De 74] C. W. De Jager, H. De Vries, and C. De Vries. ‘Nuclear charge and magnetization density distribution parameters from elastic electron scattering.’ *Atom. Data Nucl. Data Tabl.*, **14**:479 (1974).

[Dep02] A. Deppman *et al.* ‘Photofissility of heavy nuclei at intermediate energies.’ *Phys. Rev.*, **C66**:067601 (2002).

[Dep04] A. Deppman *et al.* ‘The CRISP package for intermediate- and high-energy photonuclear reactions.’ *J. Phys.*, **G30**:1991 (2004).

[Dep06] A. Deppman *et al.* ‘Photofission and total photoabsorption cross sections in the energy range of shadowing effects.’ *Phys. Rev.*, **C73**:064607 (2006).

[Dev76] R. C. E. Devenish, T. S. Eisenschitz, and J. G. Körner. ‘Electromagnetic $n - n^*$ transition form factors.’ *Phys. Rev. D*, **14(11)**:3063 (Dec 1976).

[DF83] T. De Forest. ‘Off-Shell electron Nucleon Cross-Sections. The Impulse Approximation.’ *Nucl. Phys.*, **A392**:232 (1983).

[Dmi86] V. Dmitriev, O. Sushkov, and C. Gaarde. ‘Δ formation in the H-1 (He-3, H-3) Δ^{++} reaction at intermediate-energies.’ *Nucl. Phys.*, **A459**:503 (1986).

[Dra04] D. Drakoulakos *et al.* ‘Proposal to perform a high-statistics neutrino scattering experiment using a fine-grained detector in the NuMI beam.’ (2004). hep-ex/0405002.

[Dre92] D. Drechsel and L. Tiator. ‘Threshold pion photoproduction on nucleons.’ *J. Phys.*, **G18**:449 (1992).

[Dru90] E. G. Drukarev and E. M. Levin. ‘The QCD sum rules and nuclear matter. 2.’ *Nucl. Phys.*, **A511**:679 (1990).

[Dö95] H. C. Dönges, M. Schäfer, and U. Mosel. ‘Microscopic model of the timelike electromagnetic form- factor of the nucleon.’ *Phys. Rev.*, **C51**:950 (1995). nucl-th/9407012.

[Eff96] M. Effenberger. *Gammaabsorption an Kernen*, Diplomarbeit (Diploma thesis), JLU Giessen (1996).

[Eff97a] M. Effenberger, A. Hombach, S. Teis, and U. Mosel. ‘Photoabsorption on nuclei.’ *Nucl. Phys.*, **A613**:353 (1997). nucl-th/9607005.

[Eff97b] M. Effenberger, A. Hombach, S. Teis, and U. Mosel. 'Photoproduction of pions and etas in nuclei.' *Nucl. Phys.*, **A614**:501 (1997). nucl-th/9610022.

[Eff99a] M. Effenberger. *Eigenschaften von Hadronen in einem vereinheitlichten Transportmodell*, Ph.D. thesis, JLU Giessen, Institut für theoretisches Physik I (1999).

[Eff99b] M. Effenberger and U. Mosel. 'Off-shell effects on particle production.' *Phys. Rev.*, **C60**:051901 (1999). nucl-th/9906085.

[Ell08] S. Ellis. 'Physics 557-9, University of Washington.' (August 2008). http://courses.washington.edu/phys55x/.

[Eng94] A. Engel, W. Cassing, U. Mosel, M. Schafer, and G. Wolf. 'Pion - nucleus reactions in a microscopic transport model.' *Nucl. Phys.*, **A572**:657 (1994). nucl-th/9307008.

[Eri88] T. Ericson and W. Weise. *Pions and nuclei.* Clarendon Press,Oxford (1988).

[FAI08] 'FAIR - facility for antiproton and ion research.' (May 2008). http://www.gsi.de/fair/.

[Fal04a] T. Falter. *Nuclear reactions of high energy protons, photons, and leptons*, Ph.D. thesis, JLU Giessen (July 2004).

[Fal04b] T. Falter, W. Cassing, K. Gallmeister, and U. Mosel. 'Hadron attenuation in deep inelastic lepton nucleus scattering.' *Phys. Rev.*, **C70**:054609 (2004). nucl-th/0406023.

[Fal04c] T. Falter, W. Cassing, K. Gallmeister, and U. Mosel. 'Hadron formation and attenuation in deep inelastic lepton scattering off nuclei.' *Phys. Lett.*, **B594**:61 (2004). nucl-th/0303011.

[Fis96] K. G. Fissum *et al.* 'Inclusive positive pion photoproduction.' *Phys. Rev.*, **C53**:1278 (1996).

[Fix05] A. Fix and H. Arenhovel. 'Double pion photoproduction on nucleon and deuteron.' *Eur. Phys. J.*, **A25**:115 (2005). nucl-th/0503042.

[Fri91] E. Friedman, A. Goldring, R. R. Johnson, O. Meirav, D. Vetterli, P. Weber, and A. Altman. 'Total reaction cross-sections for 20-MeV - 30-MeV pions and the anomaly of pionic atoms.' *Phys. Lett.*, **B257**:17 (1991).

[Fro92] T. Frommhold *et al.* 'Total photofission cross-section for U-238 as a substitute for the photon absorption cross-section in the energy range of the first baryon resonances.' *Phys. Lett.*, **B295**:28 (1992).

[Fro94] T. Frommhold *et al.* 'Photofission of U-235 and U-238 at intermediate-energies: Absolute cross-sections and fragment mass distributions.' *Z. Phys.*, **A350**:249 (1994).

[Fro07] F. Froemel and S. Leupold. 'Short-range correlations in quark matter.' *Phys. Rev.*, **C76**:035207 (2007). nucl-th/0702017.

[Fuc96] C. Fuchs, T. Gaitanos, and H. Wolter. *Phys. Lett. B*, **381**:23 (1996).

[Gai05] T. Gaitanos, C. Fuchs, and H. Wolter. *Phys. Lett. B*, **609**:241 (2005).

[Gal05] K. Gallmeister and T. Falter. ‘Space-time picture of fragmentation in PYTHIA / JETSET for HERMES and RHIC.’ *Phys. Lett.*, **B630**:40 (2005). nucl-th/0502015.

[Gal07] K. Gallmeister (2007). Private communications.

[Gib77] W. R. Gibbs, B. F. Gibson, A. T. Hess, and G. J. Stephenson. ‘Pion double charge exchange on He-4.’ *Phys. Rev.*, **C15**:1384 (1977).

[Gib90] W. R. Gibbs and M. J. Leitch, editors. *Proceedings of the second LAMPF International Workshop on Pion-Nucleus Double Charge Exchange*. World Scientific (1990).

[GiB08a] GiBUU group. ‘GiBUU history.’ (August 2008). http://gibuu.physik.uni-giessen.de/GiBUU/wiki/GiBUU_Code_history.

[GiB08b] GiBUU group. ‘The GiBUU website.’ (August 2008). http://theorie.physik.uni-giessen.de/GiBUU.

[Gil97] A. Gil, J. Nieves, and E. Oset. ‘Many body approach to the inclusive (e,e’) reaction from the quasielastic to the Delta excitation region.’ *Nucl. Phys.*, **A627**:543 (1997). nucl-th/9711009.

[Gol97] Y. S. Golubeva, L. A. Kondratyuk, and W. Cassing. ‘Medium effects in the production and decay of vector mesons in pion nucleus reactions.’ *Nucl. Phys.*, **A625**:832 (1997). nucl-th/9710071.

[gpl07] ‘GPL website.’ (September 2007). http://www.gnu.org/copyleft/gpl.html.

[Gra89] P. A. M. Gram *et al.* ‘Dependence of the cross-section for inclusive pion double charge exchange on nuclear mass and charge.’ *Phys. Rev. Lett.*, **62**:1837 (1989).

[GRA08] ‘Graal website.’ (August 2008). http://www.lnf.infn.it/~levisand/graal/graal.html.

[Gre87] C. Gregoire, B. Remaud, F. Sebille, L. Vinet, and Y. Raffray. ‘Semi-classical dynamics of heavy-ion reactions.’ *Nucl. Phys. A*, **465**:317 (1987).

[Gre07] R. Gregor. *Modifikation von Pionenpaaren in Kernmaterie*, Ph.D. thesis, JLU Giessen (July 2007).

[gsl07] ‘GSL website.’ (September 2007). http://www.gnu.org/software/gsl/.

[GT95] J. A. Gomez Tejedor, M. J. Vicente-Vacas, and E. Oset. ‘Double pion photoproduction in nuclei.’ *Nucl. Phys.*, **A588**:819 (1995). nucl-th/9411029.

[GT96] J. A. Gomez Tejedor and E. Oset. ‘Double pion photoproduction on the nucleon: Study of the isospin channels.’ *Nucl. Phys.*, **A600**:413 (1996). hep-ph/9506209.

[Hag02] K. Hagiwara *et al.* ‘Review of Particle Physics.’ *Phys. Rev. D*, **66**:010001+ (2002).

[Han63] L. N. Hand. ‘Experimental investigation of pion electroproduction.’ *Phys. Rev.*, **129(4)**:1834 (Feb 1963).

[Har97a] J. G. Hardie *et al.* ‘Kinematically complete measurement of $pp \to pn\pi^+$ near threshold.’ *Phys. Rev.*, **C56**:20 (1997).

[Har97b] F. Harter *et al.* 'Two neutral pion photoproduction off the proton between threshold and 800-MeV.' *Phys. Lett.*, **B401**:229 (1997).

[Hat99] T. Hatsuda, T. Kunihiro, and H. Shimizu. 'Precursor of chiral symmetry restoration in the nuclear medium.' *Phys. Rev. Lett.*, **82**:2840 (1999).

[Hau67] M. G. Hauser. 'Photoproduction of Charged Pion Pairs and N*(1238)++ in Hydrogen from 0.9 to 1.3 GeV.' *Physical Review*, **160(5)**:1215 (August 1967).

[Hec81] P. Hecking. 'Pion mean free path in nuclear matter.' *Phys. Lett.*, **B103(6)**:401 (1981).

[Hir02] M. Hirata, N. Katagiri, K. Ochi, and T. Takaki. 'Nuclear photoabsorption at photon energies between 300-MeV and 850-MeV.' *Phys. Rev.*, **C66**:014612 (2002). nucl-th/0112079.

[Hom98] A. Hombach. *Kollektive Flußeffekte in relativistischen Schwerionenkollisionen bei SIS-Energien*, Ph.D. thesis, JLU Giessen, Institut für Theoretisches Physik I (1998).

[Hor01] C. J. Horowitz, S. J. Pollock, P. A. Souder, and R. Michaels. 'Parity violating measurements of neutron densities.' *Phys. Rev.*, **C63**:025501 (2001). nucl-th/9912038.

[Hor06] C. J. Horowitz. 'Links between heavy ion and astrophysics.' (2006). nucl-th/0602042.

[HSD08] HSD group. 'HSD website.' (August 2008).
http://th.physik.uni-frankfurt.de/~brat/hsd.html.

[Hüf79] J. Hüfner and M. Thies. 'Pion-nucleus scattering and absorption as a solution of the Boltzmann equation.' *Phys. Rev.*, **C20(1)**:273 (1979).

[Ili97] A. S. Ilinov *et al.* 'Extension of the intranuclear cascade model for photonuclear reactions at energies up to 10-GeV.' *Nucl. Phys.*, **A616**:575 (1997).

[Jae07] I. Jaegele (September 2007). Private communications, Igal.Jaegle@unibas.ch.

[Jan02] S. Janssen. *Doppel-Pionphotoproduktion an Blei*, Ph.D. thesis, JLU Giessen (Juni 2002).

[Jon00] M. K. Jones *et al.* 'G(E(p))/G(M(p)) ratio by polarization transfer in $e(pol.)p \rightarrow ep(pol.)$.' *Phys. Rev. Lett.*, **84**:1398 (2000). nucl-ex/9910005.

[Juc03] S. Juchem. *Nonequilibrium Quantum-Field Dynamics and Off-Shell Transport*, Ph.D. thesis, JLU Giessen (December 2003).

[Kad94] L. Kadanoff and G. Baym. *Quantum Statistical Mechanics.* Addison Wesley Publishing Company (November 1994).

[Kal07] D. Kalok. *The Influence of In-Medium Modifications on Quasi-Elastic Electron and Neutrino Scattering on Nuclei*, Diplomarbeit (Diploma thesis), JLU Giessen (July 2007).
http://theorie.physik.uni-giessen.de/documents/diplom/kalok.pdf.

[Kle00] V. Kleber *et al.* 'Double π^0 photoproduction from the deuteron.' *Eur. Phys. J.*, **A9**:1 (2000).

[Kon94] L. A. Kondratyuk, M. I. Krivoruchenko, N. Bianchi, E. De Sanctis, and V. Muccifora. ‘Suppression of nucleon resonances in the total photoabsorption on nuclei.’ *Nucl. Phys.*, **A579**:453 (1994).

[Kon06] S. Kondratyuk and P. G. Blunden. ‘Calculation of two-photon exchange effects for Δ production in electron proton collisions.’ *Nucl. Phys.*, **A778**:44 (2006). nucl-th/0601063.

[Kot04] M. Kotulla *et al.* ‘Double π^0 photoproduction off the proton at threshold.’ *Phys. Lett.*, **B578**:63 (2004). nucl-ex/0310031.

[Kri99] B. J. Kriss *et al.* ‘Pion proton integral cross sections at T(pi) = 40-MeV to 284-MeV.’ *Phys. Rev.*, **C59**:1480 (1999).

[Kru02] B. Krusche *et al.* ‘Coherent π^0-photoproduction from atomic nuclei.’ *Phys. Lett.*, **B526**:287 (2002). nucl-ex/0304006.

[Kru04a] B. Krusche *et al.* ‘Photoproduction of π^0-mesons from nuclei.’ *Eur. Phys. J.*, **A22**:277 (2004). nucl-ex/0406002.

[Kru04b] B. Krusche *et al.* ‘Surface and volume effects in the photoabsorption of nuclei.’ *Eur. Phys. J.*, **A22**:347 (2004). nucl-ex/0411009.

[Kru05] A. P. Krutenkova *et al.* ‘Inclusive pion double charge exchange on O-16 above the Delta resonance.’ *Phys. Rev.*, **C72**:037602 (2005). nucl-ex/0502017.

[Lal06] O. Lalakulich, E. A. Paschos, and G. Piranishvili. ‘Resonance production by neutrinos: The second resonance region.’ *Phys. Rev.*, **D74**:014009 (2006). hep-ph/0602210.

[Lan88] Landoldt and Boernstein, editor. *New Series*, volume 12. Springer Verlag, Berlin (1988).

[Lan93] A. Lang, H. Babovsky, W. Cassing, U. Mosel, H.-G. Reusch, and K. Weber. ‘A new treatment of boltzmann-like collision integrals in nuclear kinetic equations.’ *Journal of Comp. Phys.*, **106(2)**:391 (June 1993).

[Lan01] W. Langgartner *et al.* ‘Direct observation of a rho decay of the D(13)(1520) baryon resonance.’ *Phys. Rev. Lett.*, **87**:052001 (2001).

[Lar02] A. B. Larionov, M. Effenberger, S. Leupold, and U. Mosel. ‘Resonance life time in BUU: Observable consequences.’ *Phys. Rev.*, **C66**:054604 (2002). nucl-th/0107031.

[Lar03] A. B. Larionov and U. Mosel. ‘The N N → N Delta cross section in nuclear matter.’ *Nucl. Phys.*, **A728**:135 (2003). nucl-th/0307035.

[Lar05] A. B. Larionov and U. Mosel. ‘Kaon production and propagation at intermediate relativistic energies.’ *Phys. Rev.*, **C72**:014901 (2005).

[Lar07] A. B. Larionov, O. Buss, K. Gallmeister, and U. Mosel. ‘Three-body collisions in Boltzmann-Uehling-Uhlenbeck theory.’ *Phys. Rev.*, **C76**:044909 (2007). 0704.1785.

[Leh02] J. Lehr, H. Lenske, S. Leupold, and U. Mosel. ‘Nuclear Matter Spectral Functions by Transport Theory.’ *Nucl. Phys.*, **A703**:393 (2002). nucl-th/0108008.

[Leh03] J. Lehr. *In-Medium-Eigenschaften von Nukleonen und Nukleonresonanzen in einem semiklassischen Transportmodell*, Ph.D. thesis, JLU Giessen, Institut für theoretisches Physik I (2003).

[Lei] T. Leitner. PhD thesis, in preparation.

[Lei93] D. B. Leinweber, T. Draper, and R. M. Woloshyn. 'Baryon octet to decuplet electromagnetic transitions.' *Phys. Rev.*, **D48**:2230 (1993). hep-lat/9212016.

[Lei06a] T. Leitner, L. Alvarez-Ruso, and U. Mosel. 'Charged current neutrino nucleus interactions at intermediate energies.' *Phys. Rev.*, **C73**:065502 (2006). nucl-th/0601103.

[Lei06b] T. Leitner, L. Alvarez-Ruso, and U. Mosel. 'Neutral current neutrino nucleus interactions at intermediate energies.' *Phys. Rev.*, **C74**:065502 (2006). nucl-th/0606058.

[Lei07] T. Leitner, O. Buss, U. Mosel, and L. Alvarez-Ruso. 'Neutrino Interactions with Nuclei.' *AIP Conf. Proc.*, **967**:192 (2007). 0709.0244.

[Len05] H. Lenske (2005). Private communications.

[Leu00] S. Leupold. 'Towards a test particle description of transport processes for states with continuous mass spectra.' *Nucl. Phys.*, **A672**:475 (2000). nucl-th/9909080.

[Leu01] S. Leupold. 'Life time of resonances in transport simulations.' *Nucl. Phys.*, **A695**:377 (2001). nucl-th/0008036.

[Leu05] S. Leupold. 'Relativistic version of 'Towards a test particle description of transport processes for states with continuous mass spectra' .' (2005). Private communications.

[LHC08] 'The LHC facility.' (May 2008). http://lhc.web.cern.ch/lhc/.

[Lug07a] S. Lugert. *In-Medium Modification of Pion-Pairs on Deuterium*, Ph.D. thesis, JLU Giessen (October 2007).

[Lug07b] S. Lugert and M. Kotulla (2007). Private communications.

[MAI] 'MAID 2003 website.' http://www.kph.uni-mainz.de/MAID.

[Man92] D. M. Manley and E. M. Saleski. 'Multichannel resonance parametrization of pi n scattering amplitudes.' *Phys. Rev.*, **D45**:4002 (1992).

[Mas05] S. G. Mashnik, M. I. Baznat, K. K. Gudima, A. J. Sierk, and R. E. Prael. 'Extension of the CEM2k and LAQGSM codes to describe photo- nuclear reactions.' (2005). nucl-th/0503061.

[Meh84] R. A. Mehrem, H. M. A. Radi, and J. O. Rasmussen. 'Behavior of pions incident on a slab of uniform complex nuclear material.' *Phys. Rev.*, **C30**:301 (1984).

[Mes02] J. G. Messchendorp *et al.* 'In-medium modifications of the $\pi\pi$ interaction in photon-induced reactions.' *Phys. Rev. Lett.*, **89**:222302 (2002). nucl-ex/0205009.

[Mic] R. Michaels *et al.* '^{208}Pb Radius Experiment.' http://hallaweb.jlab.org/parity/prex/pbup2005.pdf.

[MK94] T. Mayer-Kuckuk. *Kernphysik*. Teubner Studienbücher, Stuttgart, 6th edition (1994).

[Mol85] J. J. Molitoris and H. Stoecker. ‘Further evidence for a stiff nuclear equation of state from a transverse momentum analysis of Ar (1800- MeV/nucleon) + KCl.’ *Phys. Rev.*, **C32**:346 (1985).

[Mon94] L. Montanet, K. Gieselmann, R. M. Barnett, D. E. Groom, T. G. Trippe, C. G. Wohl, B. Armstrong, G. S. Wagman, H. Murayama, J. Stone, J. J. Hernandez, F. C. Porter, R. J. Morrison, A. Manohar, M. Aguilar-Benitez, C. Caso, P. Lantero, R. L. Crawford, M. Roos, N. A. Törnqvist, K. G. Hayes, G. Höhler, S. Kawabata, D. M. Manley, K. Olive, R. E. Shrock, and S. Eidelman. ‘Review of Particle Properties.’ *Phys. Rev. D*, **50(3)**:1173 (Aug 1994).

[Muc99] V. Muccifora *et al.* ‘Photoabsorption on nuclei in the shadowing threshold region.’ *Phys. Rev.*, **C60**:064616 (1999). nucl-ex/9810015.

[Mü04a] P. Mühlich, L. Alvarez-Ruso, O. Buss, and U. Mosel. ‘Low-energy $\pi\pi$ photoproduction off nuclei.’ *Phys. Lett.*, **B595**:216 (2004). nucl-th/0401042.

[Mü04b] P. Mühlich, T. Falter, and U. Mosel. ‘Inclusive omega photoproduction off nuclei.’ *Eur. Phys. J.*, **A20**:499 (2004). nucl-th/0310067.

[Mü06a] P. Mühlich and U. Mosel. ‘Omega attenuation in nuclei.’ *Nucl. Phys.*, **A773**:156 (2006). nucl-th/0602054.

[Mü06b] P. Mühlich, V. Shklyar, S. Leupold, U. Mosel, and M. Post. ‘The spectral function of the omega meson in nuclear matter from a coupled-channel resonance model.’ *Nucl. Phys.*, **A780**:187 (2006). nucl-th/0607061.

[Mü07] P. Mühlich. *Mesons in Nuclei and Nuclear Reactions with Elementary Probes*, Ph.D. thesis, JLU Giessen, http://theorie.physik.uni-giessen.de/documents/dissertation/muehlich.pdf (April 2007).

[Nac01] J. C. Nacher, E. Oset, M. J. Vicente, and L. Roca. ‘The role of $\Delta(1700)$ excitation and ρ production in double pion photoproduction.’ *Nucl. Phys.*, **A695**:295 (2001). nucl-th/0012065.

[Nak80] K. Nakai, T. Kobayashi, T. Numao, T. A. Shibata, J. Chiba, and K. Masutani. ‘Measurements of cross-sections for pion absorption by nuclei.’ *Phys. Rev. Lett.*, **44**:1446 (1980).

[Nak07] H. Nakamura, M. Sakuda, T. Nasu, and O. Benhar. ‘Inclusive electron spectrum in the region of pion production in electron-nucleus scattering and the effect of the quasi-elastic interaction.’ (2007). arXiv:0705.3884[hep-ph].

[Nau90] H. W. L. Naus, S. J. Pollock, J. H. Koch, and U. Oelfke. ‘Electron scattering from a bound nucleon.’ *Nucl. Phys.*, **A509**:717 (1990).

[Nie93a] J. Nieves and E. Oset. ‘Many-body approach to low energy pion-nucleus scattering.’ *Nucl. Phys.*, **A554**:554 (1993).

[Nie93b] J. Nieves, E. Oset, and C. Garcia-Recio. ‘A theoretical approach to pionic atoms and the problem of anomalies.’ *Nucl. Phys.*, **A554**:509 (1993).

[nui] 'International Workshop On Neutrino-Nucleus Interactions In The Few-GeV Region (NuInt), conference series 2001-2007 , cf. e.g. http://conferences.fnal.gov/nuint07.'

[O'C84] J. S. O'Connell *et al.* 'Electron Scattering in the Excitation Region of the Delta Resonance on Nuclei with A=1 to 16.' *Phys. Rev. Lett.*, **53**:1627 (1984).

[Ose87] E. Oset and L. L. Salcedo. 'Delta self energy in nuclear matter.' *Nucl. Phys.*, **A468**:631 (1987).

[Pas06] V. Pascalutsa and M. Vanderhaeghen. 'The nucleon and Delta-resonance masses in relativistic chiral effective-field theory.' *Phys. Lett.*, **B636**:31 (2006). hep-ph/0511261.

[Pas07] B. Pasquini, D. Drechsel, and L. Tiator. 'Invariant amplitudes for pion electroproduction.' (2007). arXiv:0712.2327[hep-ph].

[Ped07a] P. Pedroni (April 2007). Private communications.

[Ped07b] P. Pedroni (September 2007). Private communications.

[Ped07c] P. Pedroni, A. Zabrodin, *et al.* (2007). Private communications.

[Pes] M. E. Peskin and D. V. Schroeder. *introduction to quantum field theory.* Addison-Wesley Pub. Co., Reading, Mass. ISBN 0201503972. Includes bibliographical references (p. 811-815) and index.

[Pet98] W. Peters, H. Lenske, and U. Mosel. 'Coherent photoproduction of pions on nuclei in a relativistic, non-local model.' *Nucl. Phys.*, **A640**:89 (1998). nucl-th/9803009.

[Pi92] H. Pi. 'An Event generator for interactions between hadrons and nuclei: FRITIOF version 7.0.' *Comput. Phys. Commun.*, **71**:173 (1992).

[Pie06] J. Piekarewicz. 'Parity violation, the neutron radius of lead, and neutron stars.' (2006). nucl-th/0608024.

[Pol96] S. Pollock, H. W. L. Naus, and J. H. Koch. 'The electron-nucleon cross section in $(e, e'p)$ reactions.' *Phys. Rev.*, **C53**:2304 (1996). nucl-th/9512043.

[Pos04] M. Post. *Hadronic Spectral Functions in Nuclear Matter*, Ph.D. thesis, JLU Giessen, Institut für theoretisches Physik I (2004).

[Pov99] Povh, Rith, Scholz, and Zetsche. *Teilchen und Kerne.* Springer, Berlin (1999).

[Psh05] I. A. Pshenichnov *et al.* 'Intranuclear-cascade model calculation of photofission probabilities for actinide nuclei.' *Eur. Phys. J.*, **A24**:69 (2005).

[pyt07] 'Pythia website.' (September 2007). http://www.thep.lu.se/~torbjorn/Pythia.html.

[QEW08] 'Quasielastic electron nucleus scattering archive.' (August 2008). http://faculty.virginia.edu/qes-archive/index.html.

[Rap98] R. Rapp, M. Urban, M. Buballa, and J. Wambach. 'A microscopic calculation of photoabsorption cross sections on protons and nuclei.' *Phys. Lett.*, **B417**:1 (1998). nucl-th/9709008.

[RHI08] 'The RHIC facility.' (May 2008). http://www.bnl.gov/rhic/.

[rob07] 'ROBODOC website.' (September 2007). http://sourceforge.net/projects/robodoc/.

[Roc02] L. Roca, E. Oset, and M. J. Vicente Vacas. 'The sigma meson in a nuclear medium through two pion photoproduction.' *Phys. Lett.*, **B541**:77 (2002). nucl-th/0201054.

[Ros80] R. Rosenfelder. 'Quasielastic electron scattering from nuclei.' *Annals Phys.*, **128**:188 (1980).

[RP83] C. U. Robert Piessens, Elise de Doncker-Kapenga and D. Kahaner. *QUADPACK: A Subroutine Package for Automatic Integration*. ISBN: 3540125531. Springer (1983). LC: QA299.3.Q36.

[Sad04] M. E. Sadler *et al.* 'Differential cross section of the pion nucleon charge- exchange reaction $\pi^- p \to \pi^0 n$ in the momentum range from 148-MeV/c to 323-MeV/c.' *Phys. Rev.*, **C69**:055206 (2004). nucl-ex/0403040.

[Sal88] L. L. Salcedo, E. Oset, M. J. Vicente-Vacas, and C. Garcia-Recio. 'Computer simulation of inclusive pion nuclear reactions.' *Nucl. Phys.*, **A484**:557 (1988).

[Sch05] S. Schadmand. 'Photoproduction from Nuclei in the Resonance Region.' (July 2005). Http://www.fz-juelich.de/ikp/copolt/susan/opusii.pdf. Habilitationsschrift.

[Sch06a] S. Schadmand. 'Double pion photoproduction from nuclei.' *Acta Phys. Hung.*, **A26**:159 (2006). nucl-ex/0504012.

[Sch06b] S. Schadmand. 'Two pion production in photon induced reactions.' *Pramana*, **66**:877 (2006). nucl-ex/0505023.

[Sea89] R. M. Sealock *et al.* 'Electroexcitation of the Delta(1232) in nuclei.' *Phys. Rev. Lett.*, **62**:1350 (1989).

[Shi82] F. Shimizu, Y. Kubota, H. Koiso, F. Sai, S. Sakamoto, and S. S. Yamamoto. 'Measurement of the p p cross-sections in the momentum range 0.9-GeV/c - 2.0-GeV/c.' *Nucl. Phys.*, **A386**:571 (1982).

[Sib97] A. A. Sibirtsev, W. Cassing, and C. M. Ko. 'Antikaon production in nucleon nucleon reactions near threshold.' *Z. Phys.*, **A358**:101 (1997). nucl-th/9612040.

[Ste07] B. Steinmüller. *Eine neue Initialisierung des Atomkerns für GiBUU*, Diplomarbeit (Diploma thesis), JLU Giessen (November 2007). http://theorie.physik.uni-giessen.de/documents/diplom/steinmueller.pdf.

[Szc07] B. Szczerbinska, T. Sato, K. Kubodera, and T. S. H. Lee. 'Neutrino nucleus reactions in the Δ resonance region.' *Phys. Lett.*, **B649**:132 (2007). nucl-th/0610093.

[TAP08] 'TAPS website.' (August 2008). http://pcweb.physik.uni-giessen.de/taps/.

[Tei96] S. Teis. *Transporttheoretische Beschreibung von relativistischen Schwerionenkollisionen bei SIS-Energien*, Ph.D. thesis, JLU Giessen, Institut für theoretisches Physik I (1996).

[Tei97] S. Teis, W. Cassing, M. Effenberger, A. Hombach, U. Mosel, and G. Wolf. 'Pionproduction in heavy-ion collisions at SIS energies.' *Z. Phys.*, **A356**:421 (1997). nucl-th/9609009.

[Tia04] L. Tiator *et al.* 'Electroproduction of nucleon resonances.' *Eur. Phys. J.*, **A19**:55 (2004). nucl-th/0310041.

[Trn05] D. Trnka *et al.* 'First observation of in-medium modifications of the omega meson.' *Phys. Rev. Lett.*, **94**:192303 (2005). nucl-ex/0504010.

[Tsu88] T. Tsuboyama, N. Katayama, F. Sai, and S. S. Yamamoto. 'Study of the $np \to pp\pi^-$ reaction in the incident neutron momentum range 1-GeV/c - 1.9-GeV/c.' *Nucl. Phys.*, **A486**:669 (1988).

[Tsu97] K. Tsushima, S. W. Huang, and A. Faessler. 'A study of the $\pi B \to YK$ reactions for kaon production in heavy ion collisions.' *Austral. J. Phys.*, **50**:35 (1997). nucl-th/9602005.

[Ueh33] E. A. Uehling and G. E. Uhlenbeck. 'Transport Phenomena in Einstein-Bose and Fermi-Dirac Gases. I.' *Phys. Rev.*, **43(7)**:552 (Apr 1933).

[URQ08] URQMD group. 'URQMD website.' (August 2008). http://th.physik.uni-frankfurt.de/~urqmd/.

[Vic89] M. J. Vicente, E. Oset, L. L. Salcedo, and C. Garcia-Recio. 'Inclusive pion nucleus double charge exchange.' *Phys. Rev.*, **C39**:209 (1989).

[Wag03] M. Wagner. *Kaon and Pion Production at CBM energies*, Diplomarbeit (Diploma thesis), JLU Giessen, Institut für theoretisches Physik I (2003). http://theorie.physik.uni-giessen.de/documents/diplom/wagner.pdf.

[Wag05] M. Wagner, A. B. Larionov, and U. Mosel. 'Kaon and pion production in relativistic heavy-ion collisions.' *Phys. Rev.*, **C71**:034910 (2005). nucl-th/0411010.

[Wei08a] J. Weil. *Dilepton Production in Elementary Nuclear Reactions within a BUU Transport Model*, Diplomarbeit (Diploma thesis), JLU Giessen (August 2008). http://www.uni-giessen.de/cms/resolveuid/4f64350f9d50d50f39161393ecb9cb97.

[Wei08b] W. Weise. 'Overview and Perspectives in Nuclear Physics.' (2008). 0801.1619.

[Wel88] G. M. Welke, M. Prakash, T. T. S. Kuo, S. D. Gupta, and C. Gale. 'Azimuthal distribution in heavy ion collisions and the nuclear equation of state.' *Phys. Rev.*, **C38(2101)** (1988).

[Wel89] G. Welke, R. Malfliet, C. Grégoire, M. Prakash, and E. Suraud. 'Collisional relaxation in simulations of heavy-ion collisions using Boltzmann-type equations.' *Phys. Rev. C*, **40(6)**:2611 (Dec 1989).

[Wig32] E. P. Wigner. 'On the quantum correction for thermodynamic equilibrium.' *Phys. Rev.*, **40**:749 (1932).

[Wil73] C. Wilkin *et al.* 'A comparison of π^+ and π^- total cross-sections of light nuclei near the 3-3 resonance.' *Nucl. Phys.*, **B62**:61 (1973).

[Wil07] F. Wilczek. 'Anticipating a New Golden Age.' (2007). 0708.4236.

[Wir95] R. B. Wiringa, V. G. J. Stoks, and R. Schiavilla. 'An accurate nucleon-nucleon potential with charge independence breaking.' *Phys. Rev.*, **C51**:38 (1995). nucl-th/9408016.

[Wol00] M. Wolf *et al.* 'Photoproduction of neutral pion pairs from the proton.' *Eur. Phys. J.*, **A9**:5 (2000).

[Woo92] S. A. Wood *et al.* 'Systematics of inclusive pion double charge exchange in the Delta resonance region.' *Phys. Rev.*, **C46**:1903 (1992).

[Yao06] W. M. Yao *et al.* 'Review of particle physics.' *J. Phys.*, **G33**:1 (2006). 2007 partial update for the 2008 edition.

[Yul97] M. Yuly *et al.* 'Pion double charge exchange and inelastic scattering on He- 3.' *Phys. Rev.*, **C55**:1848 (1997).

[Zab97] A. Zabrodin *et al.* 'Total cross section measurement of the $\gamma n \rightarrow p\pi^-\pi^0$ reaction.' *Phys. Rev.*, **C55**:1617 (1997).

[Zgh94] A. Zghiche *et al.* 'Longitudinal and transverse responses in quasi-elastic electron scattering from ^{208}Pb and ^{4}He.' *Nuclear Physics A*, **572**:513 (1994). Erratum in NPA 584 (1195), 757.

List of Tables

List of Figures

Deutsche Zusammenfassung

Einleitung und Motivation

Im letzten Jahrhundert änderte sich unser Bild der Materie drastisch aufgrund mehrerer revolutionärer Erkenntnisgewinne. Am Anfang des 20. Jahrhunderts glaubte man, dass Atome, welche die fundamentalen Bausteine der Festkörperphysik, Chemie und Biologie darstellen, aus einer homogenen Masse positiv geladener Teilchen mit darin eingebetteten Elektronen bestünden und ungefähr 10^{-10}m Durchmesser hätten. Dieses von Thomson 1903 vorgeschlagene Modell wurde auch als Rosinenkuchenmodell bekannt. Danach erfolgte im Jahr 1911 die Entdeckung des Atomkerns mittels der grundlegenden Experimente von E. Rutherford. Dadurch realisierten die Physiker zum ersten Mal, dass ein Stück Materie zu großen Teilen genauso leer ist wie das uns umgebende Weltall, denn der Atomkern besitzt lediglich eine Größe von 10^{-15}m.

Basierend auf innovativen Detektionsmethoden wie zum Beispiel der Blasenkammer kam es zur Entdeckung des Neutrons durch J. Chadwick (1932). Das Muon (1937 durch C.D. Anderson) und auch das Pion (1947 durch C.F. Powell) wurden danach in der kosmischen Strahlung nachgewiesen. Neuartige auf Beschleunigern basierende Experimente führten schließlich zur Entdeckung eines ganzen Zoos von Teilchen, welche wiederum als zusammengesetzte Objekte von sogenannten Quarks verstanden und kategorisiert werden konnten. Mesonen sind die leichtesten jener Objekte und bestehen aus einem Quark und einem Antiquark, wohingegen die schwereren Baryonen – darunter fallen zum Beispiel das Proton und das Neutron– aus drei Quarks zusammengesetzt sind. Diese Quarks wurden zuerst in hochenergetischer Elektronen-Proton-Streuung aufgelöst, wobei auch deren Multiplizität aus den Formfaktoren extrahieren konnte.

Heutzutage kennt man drei verschiedene elementare Bauteile der Materie. Zum einen sind es die *Quarks*, die allerdings fest in den Hadronen gebunden sind und nicht isoliert werden können. Die *Leptonen*, darunter fallen zum Beispiel das Elektron und das Neutrino, koppeln nicht an die starke Wechselwirkung, welche die Quarks bindet, und interagieren nur elektromagnetisch oder mittels der schwachen Kraft. Die Wechselwirkungen werden von *Eichbosonen* übertragen: die Starke durch Gluonen, die Schwache durch den Austausch von $W^{\pm}$- und Z^0-Bosonen und die elektromagnetische Wechselwirkung durch das Photon.

Das Standardmodell der Teilchenphysik erklärt alle bisher durchgeführten Messungen, um es mit den Worten des Nobelpreisträgers F. Wilczek zu sagen: „At present, the standard model of particle physics stands triumphant“ [Wil07]. Allerdings gibt es einige bisher ungelöste Probleme. Zum einen führten astrophysikalische Observationen zu den Schlussfolgerungen, dass nur ungefähr 4% der Energiedichte des Universums durch baryonische Materie gegeben ist und der Rest durch eine bisher unbekannte Materie- bzw. Energieform: dunkle Energie ($\approx$ 76%) und dunkle Materie ($\approx$ 20%) [Yao06]. Neben diesem Hauptproblem des Standardmodells, gibt es auch größere Unbekannte in dem baryonischen Sektor des Standardmodells.

Die starke Wechselwirkung der Quarks – den Bauteilen der Baryonen– wird im Standardmodell mittels der Theorie der Quantum-Chromo-Dynamik (QCD) beschrieben. Während die daraus resultierende Wechselwirkung für hohe Impulsüberträge schwach ist, wird sie sehr stark für kleine Impulsüberträge, so dass traditionelle Störungstheorie nicht zu einer erfolgreichen

Beschreibung verwendet werden kann. In den letzten Jahrzehnten eröffnete die ständige Verbesserung der Computerhardware eine Möglichkeit, jenes Regime der starken Wechselwirkung mittels der sogenannten Gitter-QCD (lattice QCD=LQCD), welche QCD-Erwartungswerte auf einem Raum-Zeit-Gitter auswertet, zu erforschen. Ein weiterer Zugang zum Regime der starken Wechselwirkung stellt Chirale Störungstheorie (χPT) dar, die für Niederimpulsprozesse angewendet werden kann. Zum Beispiel werden die Herkunft der Hadronmassen und der Ursprung der Nukleon-Nukleon-Wechselwirkung zur Zeit mittels dieser beiden Methoden untersucht[1].

Eine weitere wichtige Forschungsrichtung untersucht das QCD Phasendiagramm, welches in Abb. 1.1 auf Seite 2 dargestellt ist. Bei hohen Temperaturen erwartet man einen Phasenübergang von der hadronische Phase, in welcher die Quarks in Hadronen gebunden sind, zu einer Phase in welcher die Quarks sich frei in einem sogenannten Quark-Gluon-Plasma (QGP) bewegen können. Zur Erforschung jenes Phasenübergang bringt man zum Beispiel mit dem RHIC-Beschleuniger [RHI08] oder den zukünftigen LHC [LHC08] und FAIR [FAI08] Beschleunigeranlagen hochenergetische Schwerionen zur Kollision, um dadurch ein solch heißes und dichtes System aus hadronischer Materie zu erzeugen, welches schließlich in ein QGP übergeht. Allerdings erschwert die komplizierte zeitliche Entwicklung der Einteilchen-Phasenraumdichte die Trennung verschiedener Phänomene, wodurch der experimentelle Nachweis des QGP immer noch in der Diskussion steht. Neben dem Phasenübergang von gebundenen zu freien Quarks erwartet man in einem heißen und/oder dichten Medium auch die Wiederherstellung der Chiralen Symmetrie. Diese Symmetrie ist im Vakuum zum einen explizit durch die endlichen Quarkmassen verletzt, und wird zum anderen auch spontan aufgrund des nicht verschwindenden Erwartungswertes des $\bar{q}q$ Operators (dem sogenannten $\langle\bar{q}q\rangle$-Kondensat) gebrochen. Der Wert des $\langle\bar{q}q\rangle$-Kondensats stellt einen Ordnungsparameter der spontanen Symmetriebrechung dar und man erwartet, dass er bereits bei normalen Kernmateriedichte um circa 30% abgesenkt wird [Dru90, Coh92, Bro96]. Darum sollte man bereits in normalen Kernreaktionen Signale einer Symmetriewiederherstellung beobachten können – dafür sollten speziell auch photoninduzierte Reaktionen aufgrund zweier Hauptargumente bestens geeignet sein. Erstens bleibt die Kernkonfiguration während der Reaktion nahe am Grundzustand, so dass die Reaktion unter wohldefinierten Bedingungen stattfindet. Zweitens dringt das Photon tief in den Kern ein, wodurch die effektive Dichte, bei der die Reaktion stattfindet, relativ groß wird.

Besonders die Modifikation des σ-Mesons (auch bekannt als $f_0(600)$-Meson) in Kernmaterie wurde als eine Signal einer solchen partiellen Symmetriewiederherstellung vorgeschlagen. Theoretische Modelle sagen basierend auf jenem Effekt eine Verschiebung seiner spektralen Stärke zu niedrigeren Massen und eine schmälere Breite der Spektralfunktion voraus [Ber87, Hat99]. Das σ-Meson ist ein sehr kurzlebiger Zustand mit einer Breite von $600 - 1000$ MeV [Yao06], der primär in eine $\pi\pi$ S-Welle zerfällt. Darum bestand das experimentelle Bestreben darin, Modifikationen jenes Zustand in $\pi\pi$ Produktionsreaktionen in endlicher Kernmaterie nahe an der kinematischen Schwelle nachzuweisen. Solche Experimente wurden mit Pionen im Eingangskanal von der CHAOS Kollaboration [Bon96, Bon00] und mit Photonen von der TAPS Kollaboration [Mes02, Blo07] durchgeführt. Beide Experimente zeigten für schwere Kerne eine Anreicherung spektraler Stärke nahe der $\pi\pi$-Schwelle im Zerfallskanal des σ-Mesons. Eine mögliche Interpretation dieses Effekts stellt die Modifikation dieser Resonanz im Medium aufgrund der partiellen Symmetriewiederherstellung dar, aber auch konventionelle Endzustandswechselwirkungen (final state interactions = FSI) müssen vorsichtig berücksichtigt werden. Generell spielen FSI eine große Rolle in Kernreaktionen. Teilchen, die in Kernen produziert werden (z.B. mittels einer $\gamma A \to \pi A'$ Reaktion), durchdringen das nukleare Medium bevor sie möglicherweise im De-

---

[1] Details dazu finden sich zum Beispiel in dem aktuellen Übersichtsartikel von W. Weise [Wei08b].

tektor beobachtet werden. Aufgrund der großen Interaktionsraten mit dem Medium kommt es zu Störungen der Teilchentrajektorien, Ladungsaustauschreaktionen und Teilchenabsorption, so dass das beobachtete Spektrum verglichen zum ursprünglichen Spektrum ohne FSI stark verzerrt werden kann.

Mit den exakten QCD-Näherungen LQCD und χPT ist es momentan nicht möglich komplexe Vielteilchenreaktionen wie z.B. $\pi\pi$-Produktion in Kernen zu untersuchen. Diese Tatsache eröffnet eine Spielwiese für Modellbauer. Generell muss man zwischen Prozessen mit einer simplen Zeitentwicklung der Phasenraumverteilung (z.B. γA-Reaktionen bei niedrigen Energien) und Prozessen mit einer sich zeitlich schnell entwickelnden Phasenraumverteilung unterscheiden (z.B. Schwerionenkollisionen). Die erste Reaktionsklasse können auch mit komplett quantenmechanische Methoden angenähert werden (z.B. „distorted-wave“(DWIA) oder „plain-wave“-Impulsnäherung (PWIA)) , obwohl jene Modelle oft keine gekoppelten Kanäle berücksichtigen können. Speziell die oft verwendeten DWIA- und PWIA-Methoden berücksichtigen keine gekoppelten Kanäle aufgrund der komplexen Implementierung.

Als Beispiel für eine Reaktion innerhalb der zweiten Reaktionsklasse zeigt Abb. 1.2 (Seite 4) den Plot einer typischen Zeitentwicklung einer fast zentralen, hoch-energetischen (40 A GeV) Kalzium-Kalzium-Kollision. Neben der Produktion von vielen neuen Teilchen kommt es dabei auch zum Aufbruch beider Atomkerne. Für solche Reaktionen mit sich rapide ändernden Phasenraumverteilungen weit entfernt vom thermodynamischen Gleichgewicht wird die allgemeinste Beschreibung im Rahmen der Quantenfeldtheorie durch die sogenannte *Kadanoff-Baym-Gleichung* [Kad94] gegeben. Diese Gleichung vereinfacht sich unter gewissen Annahmen (speziell: kleine, langsam variierende Störungen und Born-Näherung für die Selbstenergien) zur sogenannten *Boltzmann-Uehling-Uhlenbeck(BUU)*-Gleichung. [Kad94, speziell Kapitel 9.2]. Die BUU-Gleichung ist semiklassischer Natur und beschreibt die Zeitentwicklung der sogenannten Wigner-Transformierten [Wig32], welche eine generalisierte Phasenraumdichte darstellt. Mittels der Simulation der BUU-Gleichung erhält man somit ein komplettes Bild der Raum-Zeit-Entwicklung der Phasenraumverteilung aller an der Reaktion beteiligten Teilchenarten. Die ersten BUU-Modelle zur Simulation von Schwerionenkollisionen wurden in den Anfängen der 1980er entwickelt [Ber84, Ber88]. Parallel dazu haben sich auch Quantum-Molekular-Dynamik(QMD)-Modelle etabliert, welche die Teilchen basierend auf Zwei- und Dreiteilchenkräften propagieren, anstatt mittlere Felder wie in BUU einzuführen. Heutzutage entwickeln, bzw. verbessern, etliche rege Gruppen anerkannte und hochkomplexe Transportmodelle. Einige der prominenteren Modelle sind zum Beispiel *Dubna/Moscow INC* [Ili97], *HSD* [Cas99, HSD08], *LAQGSM* [Mas05], *MCMC/MCEF* [Dep02], *RELDIS* [Psh05], *RQMD* [Fuc96, Gai05] und *URQMD* [Bas98, URQ08]. Die Modelle unterscheiden sich in den enthaltenen Reaktionsmechanismen, in der Vielfältigkeit der enthaltenen Teilchenspezien und vor allem auch in der numerische Realisation.

Im Jahr 1986 begann die Gießener Theoriegruppe mit der Entwicklung des ersten BUU-Modells. Basierend auf einer Neufassung des originalen *Bertsch-Codes* [Ber88], wurde die Rate für Photonproduktion in Schwerionenkollisionen vorhergesagt [Bau86, Bau89]. Ursprünglich wurde der Code zwar zur Beschreibung von Schwerionenkollisionen konzipiert [Cas90, Tei96, Hom98, Lar05], aber dann wurde er im letzten Jahrzehnt auch zu einem kompetitiven Modell zur Beschreibung von elektron- und photoninduzierten Reaktionen weiterentwickelt [Eff99a, Leh03, Fal04a, Gal05, Mü07]. In der Beschreibung solcher Reaktionen muss sich ein solches Modell der Konkurrenz von DWIA- und PWIA-Modellen stellen, wobei es den Vorteil bietet, die gekoppelten Kanaleffekte der FSI vollständig simulieren zu können. Während der Weiterentwicklung des Transportmodells wurde ein universales Anwendungsgebiet als Hauptziel ausgegeben und die Tatsache, dass es sowohl für hoch-energetische Reaktionen (z.B. [Lar05, Fal04c, Gal05]) also auch für nieder-energetische Reaktionen (z.B. [Eng94, Mü04a]) geeignet war, machte es zu einem hervorragenden Modell. Unglücklicherweise wurde die schnelle Entwicklung des Modells nicht von einer Änderung der Code-Infrastruktur begleitet. Dadurch existierten im Jahr 2004 mehrere parallele Zweige des Quellcodes und die Quellcodestruktur war sehr verwinkelt geworden, was eine weiterführende Entwicklung erschwerte. Als Konsequenz dieser Entwicklung haben wir 2004 das *GiBUU-Projekt* ins Leben gerufen, um den Code umzustrukturieren und um den Quellcode in einer Multi-User-Umgebung weiterentwickeln zu können. Unabdingbar waren dabei die Einführung einer Versionskontrolle, welche einen einheitlichen Hauptzweig des Quellcodes garantiert, und eine vernünftige Dokumentation, sowie Kompatibilität mit den wichtigsten Compilern.

Ergebnisse

Diese Doktorarbeit ist der Studie von Kernreaktionen mittels eines Transportzugangs gewidmet, wobei wir im Speziellen Kernreaktionen untersuchten, die von elementaren Teilchen induziert wurden. Im ersten Teil dieser Arbeit wird das Gießen-Boltzmann-Uehling-Uhlenbeck(GiBUU)-Transportmodell erläutert, wobei der Fokus auf den Modellannahmen und -parametern sowie dessen numerischer Implementation beruht. Der zweite Teil der Arbeit befasst sich mit dem Hauptthema, nämlich der Beschreibung von pion-, photon- und elektroninduzierten Kernreaktionen. Die Resultate dafür wurden mittels GiBUU-Simulationen gewonnen und mit existierenden experimentellen Daten verglichen, bzw. es wurden Vorhersagen für zukünftige Experimente getätigt.

In Kapitel 2 werden die numerischen Methoden zur Lösung der Boltzmann-Uehling-Uhlenbeck(BUU)-Gleichung detailliert dargelegt. Dabei führen wir den sogenannten *Testteilchenansatz* ein, schreiben die BUU-Gleichung in die Testteilchenrepräsentation um und leiten den Zeitentwicklunsalgorithmus her. Im Zuge dieser Herleitung wird das wichtigste Näherungsschema, der sogenannte *Parallelensemble-Algorithmus*, eingeführt und mit den exakteren *Vollensemble-* und *Lokalensemble-Algorithmen* verglichen.

Während Kapitel 2 eine eher generelle Einführung zur BUU-Gleichung und deren numerischer Lösung gibt, spezialisiert sich das darauf folgende Kapitel 3 auf die Anwendung der BUU-Gleichung auf die Beschreibung von hadronischem Materietransport. Dort wird der Leser in das *GiBUU Modell* eingeführt, wobei speziell dessen Freiheitsgrade und die enthaltenen Wechselwirkungsmechanismen detailliert dargestellt werden. Das GiBUU-Modell stellt eine verbesserte Version desjenigen BUU-Modells dar, welches von der Gießener Transportgruppe seit über 20 Jahren entwickelt wurde [Bau86, Cas90, Eng94, Hom98, Tei96, Eff99a, Lar05, Leh03, Fal04a, Gal05, Mü07]. Eine der Hauptverbesserungen stellt eine konsistentere Behandlung der Selbstenergien der Baryonen dar. Die Imaginärteile der Selbstenergie werden als Funktion von Energie, Impuls und Dichte aus dem zugrunde liegenden Kollisionsterm abgeleitet. Danach wird eine Dispersionsrelation verwendet, um den Realteil aus dem Imaginärteil zu gewinnen, was zu analytischen Selbstenergien führt. Dadurch wird die Normalisierung der Spektralfunktionen garantiert, was in früheren Behandlungen nicht der Fall war. Die Verbesserung des Resonanzmodells führte zusammen mit neu adjustierten Hintergrundtermen auch zu einer verbesserten Beschreibung der elementaren Querschnitte, welche als Input für die BUU-Gleichung dienen. Eine zweite wichtigere Verbesserung betrifft den Übergang von niedrigen zu hohen Energien im Kollisionsterm. Dabei wurde die Hochenergieregion, welche im Modell mittels Pythia [pyt07] beschrieben wird, an die Niederenergieregion, wo die Querschnitte auf dem Resonanzmodell basieren, mittels einem Verfahren angeglichen, bei dem in einer Übergangsregion die resultierenden Events beider Modelle gemischt werden.

Eine wichtige Verbesserung der numerischen Realisierung konnte durch die Einführung des Lokalensemble-Algorithmus [Lan93] erzielt werden, wodurch die Resultate in dieser Arbeit nicht mehr auf der Parallelensemble-Näherung basieren. Der Quellcode wurde restrukturiert und ein sehr großer Teil des Quellcodes in FORTRAN 2003 neu geschrieben (die Vorgängerversion basierte auf FORTRAN 77). Dadurch erzielten wir eine Modularisierung des Quellcodes, was die Weiterentwicklung und eventuelle Fehlersuchen vereinfacht. Im Zuge dieser Entwicklung haben wir eine auf Subversion [CS04] basierende Code-Management-Struktur eingeführt, wodurch jetzt die komplette Gießener Transportgruppe[2] parallel am Quellcode arbeiten kann. Dies hat unsere Entwicklungsgeschwindigkeit positiv beeinflusst und vor allem auch die Zuverlässigkeit des Quellcodes. Im April 2008 erreichten wir dann einen wichtigen Meilenstein, indem wir die erste Releaseversion des Quellcodes unter GPL-Lizenz [gpl07] auf unserer Website [GiB08b] publizierten.

In Kapitel 4 wird unser Modell zur Interaktion von Elektronen und Photonen mit Nukleonen detailliert dargelegt. Auf der Ein-Photon-Austausch-Näherung basierend, welche den Elektron-Nukleon-Streuprozess durch die Interaktion eines einzelnen virtuellen Photons mit dem Nukleon annähert, wird die Elektron-Nukleon- und die Photon-Nukleon-Interaktion in einem einheitlichen Verfahren behandelt. Der quasielastische Prozess ($\gamma^\star N \to N'$) wird mit Hilfe moderner Formfaktoren [Bra06] beschrieben. Zusätzlich werden auch der 1-π-Produktionsprozess ($\gamma^\star N \to N'\pi$) und Resonanzproduktionsmechanismen ($\gamma^\star N \to R$) implementiert, wobei wir die Helizitätsamplituden und invarianten Amplituden der MAID-Analyse [MAI] verwenden. Für Prozesse, die von reellen Photonen (d.h. $Q^2 = 0$) induziert werden, haben wir zusätzlich einen $\pi\pi$-Produktionshintergrund eingeführt. Da die Resonanzproduktion zu π- und $\pi\pi$-Produktion führt, gibt es für beide Prozesse einen resonanten und nicht-resonanten Querschnitt. Den letzteren betrachten wir als Hintergrundterm, welcher auch alle Interferenzen zwischen Resonanzen und zwischen Resonanzen und Hintergrund beinhaltet. Im Kapitel 4 werden detaillierte Formeln für den hadronischen Tensor angegeben und unsere elementaren Querschnitte werden mit Daten verglichen. Dabei ergibt sich exzellente Übereinstimmung. Für reelle Photonen ist unser Input in einem Schwerpunktsenergiebereich von $m_N < W < 2$ GeV sehr zuverlässig; für Elektronenstreuung ist der Input sehr gut bis zur 2π-Schwelle, darüber ist ein Resonanzanteil zur $\pi\pi$-Produktion berücksichtigt, aber ein $\pi\pi$-Hintergrundterm fehlt. Das Modell kann für alle Virtualitäten des Photons bis zu $Q^2 = 5$ GeV verwendet werden.

In Kapitel 5 adressieren wir die Beschreibung der Interaktion von Elektronen und Photonen mit Nukleonen, welche in einem nuklearen Medium eingebettet sind. Im Medium kommt es zu Modifikationen der Dispersionrelationen aufgrund der hadronischen Potentiale. Wir berücksichtigen darum jene Potentiale bei der Berechnung der hadronischen Tensoren und berechnen die Wirkungsquerschnitte unter Berücksichtigung der vollen In-Medium-Kinematik. Wir nehmen allerdings an, dass sich die Formfaktoren im Medium nicht ändern. Am Ende dieses Kapitels wird eine Formel für den Elektron-Kern-Wirkungsquerschnitt hergeleitet und die Implementation in das GiBUU-Transportmodell erläutert.

Kapitel 6 widmet sich der Pion-Kern-Interaktion. Die Wechselwirkung von Nukleonen und Pionen ist ein wichtiger Eckpfeiler eines jeden hadronischen Transportansatzes, da diese beiden Teilchenspezien in Reaktionen die höchsten Dichten erreichen und deshalb auch sehr wichtig für die gekoppelten-Kanal-Effekte sind. Auch für unser Hauptziel, nämlich der Beschreibung der elektron- und photoninduzierten Pionproduktion, ist es unabdingbar die Pioninteraktion mit dem Medium unter Kontrolle zu haben. Wir evaluieren die Pion-Nukleon-Interaktion in unserem Modell durch die Simulation von Wirkungsquerschnitten zur Pionabsorption, Pionreaktion

---

[2] Eine Liste mit allen ehemaligen und derzeitigen Projektmitgliedern findet sich auf unserer Website [GiB08b].

und zum Pion-Doppel-Ladungsaustausch (pion double charge exchange (DCX)) in der kinetischen Energieregion von $10 - 200$ MeV. Wir erreichen für Pionabsorption und Pionreaktion gute Übereinstimmung mit den Daten. Allerdings zeigen wir auch, dass die Beschreibung von Pionen mit extrem langen Wellenlängen ($E_{\text{kin}} < 30$ MeV) in einem semiklassischen Transportmodell problematisch ist. Das Transportmodell beschreibt auch erfolgreich den DCX-Prozess. Wir zeigen in den Studien zu DCX, dass dieser Prozess eine hohe Sensitivität bezüglich Modelldetails besitzt, besonders sensitiv ist er bezüglich dem Durchmesser der Neutronenhäute von schweren Atomkernen. Mittels dieser hohen Sensitivität könnte man DCX verwenden um die Neutronenhäute indirekt zu vermessen.

Zusammenfassend kann man über unsere Studien zur Pion-Kern-Interaktion sagen, dass wir jene Region bestimmen ($E_{\text{kin}} > 30$ MeV) für die das semiklassische BUU-Modell anwendbar ist. Dort beschreiben wir Pionabsorption, Pionreaktion und DCX mit $10 - 20\%$ Genauigkeit. Dieses Resultat stellt eine wichtige Aussage für die folgenden Kapitel dar, wo es sich um die Pionproduktion in elektron- und photoninduzierten Reaktion dreht.

Im Kapitel 7 behandeln wir zunächst inklusive Wirkungsquerschnitten um auf den $\gamma^\star N$-Eingangsvertex zu fokussieren. Wir betonen die Wichtigkeit impulsabhängiger Potentiale und diskutieren die Möglichkeit das verwendete Potential zu verbessern. Innerhalb vernünftiger Schranken für die Potentialparameter, welche durch Fits von optischen Potentialen an die Nukleon-Kern-Streuung gegeben sind, konnten wir allerdings nur eine leichte Verbesserung unsere Resultate zur Elektron-Sauerstoff-Streuung [O'C84, Bar88, Sea89, Che91, Day93, Ang96] erreichen. Insgesamt erreichen wir eine gute Übereinstimmung mit den Daten – vergleichbar zu modernen Kern-Vielteilchen-Rechnungen von Benhar *et al.* [Ben08]. Wir haben ebenfalls Photonabsorption in Kernen [Bia94, Bia96, Muc99] studiert, wobei wir eine gute Beschreibung der Daten erreichen, falls wir die In-Medium-Breiten vernachlässigen. Eine Berücksichtigung jener Breiten verschlechtert die Übereinstimmung mit den Daten. Da wir allerdings wissen, dass die Verbreiterung der $\Delta(1232)$-Resonanz essentiell zur Beschreibung der Pion-Kern-Wechselwirkung beiträgt, kann dieses Resultat nicht bedeuten dass es keine In-Medium-Verbreiterung der Resonanzen. Sondern es wird vermutet, dass ein wichtiger Modellbestandteil, wie z. B. die Zwei-Nukleon-Absorption, bisher vernachlässigt wird und die Übereinstimmung der Rechnung ohne In-Medium-Breite wird eher als zufällig angesehen.

Bezüglich der Produktion von neutralen Pionen im Energiebereich von $0.25 - 0.8$ GeV [Kru04b, Kru04a] erreichen wir gute Übereinstimmung für den quasi-freien Reaktionsquerschnitt. Unser Resultat für den totalen Querschnitt zeigt leider keine Verbesserung verglichen zu früheren Rechnungen von Lehr *et al.* [Leh03], obwohl unser Modell verglichen mit dem Lehr'schen Modell stark verbessert wurde. Da die Beschreibung der quasi-freien Daten vernünftig ist, spekulieren wir, dass es eine Problem mit den 2π-Beiträgen gibt. Eine zusätzliche In-Medium-Modifikation des $\pi\pi$-Hintergrunds könnte einen Einfluss auf die Daten haben. Wir betonen ebenfalls, dass Interferenzen in der π^0-Produktion einen wichtige Rolle spielen und deren In-Medium-Modifikation bisher auch noch nicht berücksichtigt werden konnte.

Diese Studien dienen auch als Benchmark für neutrinoinduzierte Prozesse, welche mit Hilfe des gleichen Modells von Leitner *et al.* [Lei06b, Lei06a] untersucht werden.

Kapitel 8 bezieht sich auf photoninduzierte $\pi\pi$-Produktion in Atomkernen. Zuerst wir die momentane Datenlage zur elementaren Reaktionen dargelegt, und danach werden Kerndaten simuliert. Da die *TAPS*-Kollaboration [Lug07b] momentan noch mit der Auswertung der Deuterondaten beschäftigt ist, ist die Datenlage für die γ Neutron $\rightarrow N\pi\pi$ Reaktion leider noch unbefriedigend. Um die Extraktion der Neutron- aus den Deuterondaten zu unterstützen, erläutern wir die wichtigsten Effekte, die dabei zu berücksichtigen sind. In einem vereinfachten Modell kommen wir zu dem Ergebnis, dass man in einer Genauigkeit von ca. 5% den Neutronenquerschnitt erhält, indem man einfach den Protonenquerschnitt vom Deuteronquerschnitt subtrahiert.

Für die $\gamma A \to \pi\pi A'$ Reaktion zeigen wir, dass Endzustandswechselwirkungen essentiell sind und dazu beitragen, dass Maximum der $\pi\pi$-Massenverteilung in allen Kanälen zu niedrigen Massen hin zu verschieben. Dadurch wird es schwierig eine Verbindung zwischen den experimentellen Ergebnissen und einer möglichen Veränderung des Isospin $I = 0$ Kanals zu ziehen. Wir betonen, dass jedes theoretische Modell, dass den beobachteten Effekt der Massenabsenkung mit partieller Chiraler Symmetriewiederherstellung in Verbindung bringen möchte, auch Endzustandswechselwirkungen berücksichtigen muss. Unsere Simulationen zeigen, dass die meisten Pionen aus der Oberfläche des Kerns kommen, wodurch die möglicherweise beobachtbaren In-Medium-Effekte schwach sein sollten.

Hadronische In-Medium-Eigenschaften aus Kernreaktionen abzuleiten, ist eine schwierige Aufgabe, welche allerdings Einsichten in das stark wechselwirkende Regime der QCD verspricht. Für diese Herausforderung stellen Transportmodelle gute Werkzeuge dar, um den Graben zwischen experimentellen Observablen und der zugrunde liegenden In-Medium-Physik zu überbrücken. Vor allem erlauben sie profane, auf Endzustandswechselwirkungen beruhende, Effekte von den wirklich interessanten Effekten, welche auf einer Änderung hadronischer In-Medium-Eigenschaften basieren, zu trennen.

Oliver Buß

Photon- and Pion-induced Nuclear Reactions in a Transport Approach

Addendum

April 6, 2009

Contents

1 Errata to Chapter 7.2: Inclusive electron scattering off complex nuclei

In revision 2483 (cf. especially `http://gibuu/GiBUU/changeset/2483#file1`) , we corrected for a numerical mistake in the single-π background which influences some of the results published in section 7.2 of my thesis [Bus08].

In the following we want to outline the issue and investigate its impact on results published in section 7.2 of [Bus08]. We use the same notation as in [Bus08]: the pion momentum is k, the in- and outgoing electron momenta are l and l', the in- and outgoing nucleon momenta are p and p' and q denotes the photon momentum. The z-axis is chosen in direction of $\vec{l}$.

To compute the single-π background, we use (cf. [Bus08, pages 87 ff.]):

$$\frac{d\sigma_\pi^{\mathrm{BG}}}{d\Omega_{l'}\, d|\vec{l'}|\, d\Omega_k} = \underbrace{\frac{d\sigma_\pi}{d\Omega_{l'}\, d|\vec{l'}|\, d\Omega_k}}_{\text{MAID input}} - \sum_R \frac{d\sigma_{eN\to eR\to eN\pi}}{d\Omega_{l'}\, d|\vec{l'}|\, |d\Omega_k} \quad . \tag{1}$$

Since the resonances are assumed to decay isotropically in their rest-frames, the resonance contributions are given by

$$\begin{aligned} \frac{d\sigma_{eN\to eR\to eN\pi}}{d\Omega_{l'}\, d|\vec{l'}\ |d\Omega_k^{CM}} &= \frac{d\sigma_{\mathrm{R}}}{d\Omega_{l'}\, d|\vec{l'}|}\frac{\Gamma_{R\to N\pi}}{\Gamma_R}\frac{1}{4\pi} \\ \Rightarrow \frac{d\sigma_{eN\to eR\to eN\pi}}{d\Omega_{l'}\, d|\vec{l'}\ |d\Omega_k} &= \underbrace{\frac{d\sigma_{\mathrm{R}}}{d\Omega_{l'}\, d|\vec{l'}|}\frac{\Gamma_{R\to N\pi}}{\Gamma_R}}_{=A}\underbrace{\frac{1}{4\pi}\frac{d\Omega_k^{CM}}{d\Omega_k}}_{=B} \end{aligned} \tag{2}$$

with [Byc73]

$$\frac{d\Omega_k^{CM}}{d\Omega_k} = \frac{\sqrt{p'^\mu p'_\mu}\,\vec{k}^2}{|\vec{k}^{\mathrm{CM}}|\left(|\vec{k}|p'^0 - |\vec{p}'|k_0\cos(\theta_k)\right)} \quad . \tag{3}$$

The mistake resolved in revision 2483 concerned only the evaluation of $(d\sigma_{eN\to eR\to eN\pi})/(d\Omega_{l'}\, d|\vec{l'}\ |d\Omega_k)$, and is somewhat subtle. In eq. 2, we have split this contribution in a term named A and another one named B. Term A does not depend on k and can be computed independently from B. The problem was now, that A was computed using

$$\vec{l}\,' = (l_0' \sin\theta_{l'}, 0, l_0' \cos\theta_{l'}) \tag{4}$$

while B was computed using

$$\vec{l}\,' = (-l_0' \sin\theta_{l'}, 0, l_0' \cos\theta_{l'}) \quad , \tag{5}$$

such that the two l' differed by a π-rotation in $\phi_{l'}$. Given a resting nucleon target, this does not cause any problems since there is a $\phi_{l'}$ rotational symmetry. The code was tested by comparing the cross sections obtained for a resting nucleon to the ones predicted by MAID, and perfect agreement was obtained.

But for a moving nucleon ($\vec{p} \neq 0$), the $\phi_{l'}$ symmetry is broken! This case was not tested against data or other models. Fortunately, for small photon momenta the term B is anyhow close to 1 since the boost is small. Hence this mistake does not have any visible effect on any results obtained at low energies. Only at higher photon momenta the boost becomes sizable, and the difference in the definition of the l''s becomes important. After spotting this issue, we resolved it in revision 2483 (cf. especially http://gibuu.physik.uni-giessen.de/GiBUU/changeset/2483#file1), and the relevant patch is given by (the "+" and "-" signs show the relevant changes):

```
Index: workingCode/code/init/lowElectron/resonanceProduction.f90
===================================================================
--- a/workingCode/code/init/lowElectron/resonanceProduction.f90
+++ b/workingCode/code/init/lowElectron/resonanceProduction.f90
@@ -87,11 +92,11 @@
     lin(3)=e_in
     lin(1:2)=0.

     !lepton: Assume phi=0.
     lout(0)=E_out
-    lout(1)=E_out*sin(radian(theta_lepton_out))
+    lout(1)=-E_out*sin(radian(theta_lepton_out))
     lout(2)=0.
     lout(3)=E_out*cos(radian(theta_lepton_out))
```

Comparison to former results

In the following we want to compare the results presented in my thesis to the ones obtained with the present revision 2856. Changes in the results are only due to the issue described above. All the model inputs are otherwise identical: same self energies for the baryon resonances; only QE-scattering, resonance excitation and single-π background are included; same MAID form factors.

A comparison of the present and former results for the inclusive cross sections $d\sigma/(d\Omega_l dl_f)$ are shown for oxygen in fig. 1 and for iron in fig. 2 and fig. 3. The solid lines denote the results presented in my thesis, the dashed ones the present outcome. First, one notes that both results agree very well for low beam energies (upper panels in fig. 1 and fig. 2). Especially for ${}^{16}_{8}$O there are no major changes, except for the beam energy of 1500 MeV. So all low-energy statements in [Bus08] stay unchanged.

However, there is an increasing discrepancy for higher electron beam energies and especially for ${}^{56}_{26}$Fe, where also Fermi momentum plays a more important role. This discrepancy can be back-traced to the l' issue! **So only figures 7.11-7.12 of [Bus08] should be replaced by figures 2 and 3 of this addendum.** In 3 one observes for both results a missing strength not only in the $\pi\pi$ production region, but also at lower q_0. As already stated in [Bus08], this feature is still not understood.

Note that our latest papers, especially [Lei08], already include the revision 2483 bug fix. Hence its results are not influences by this problem.

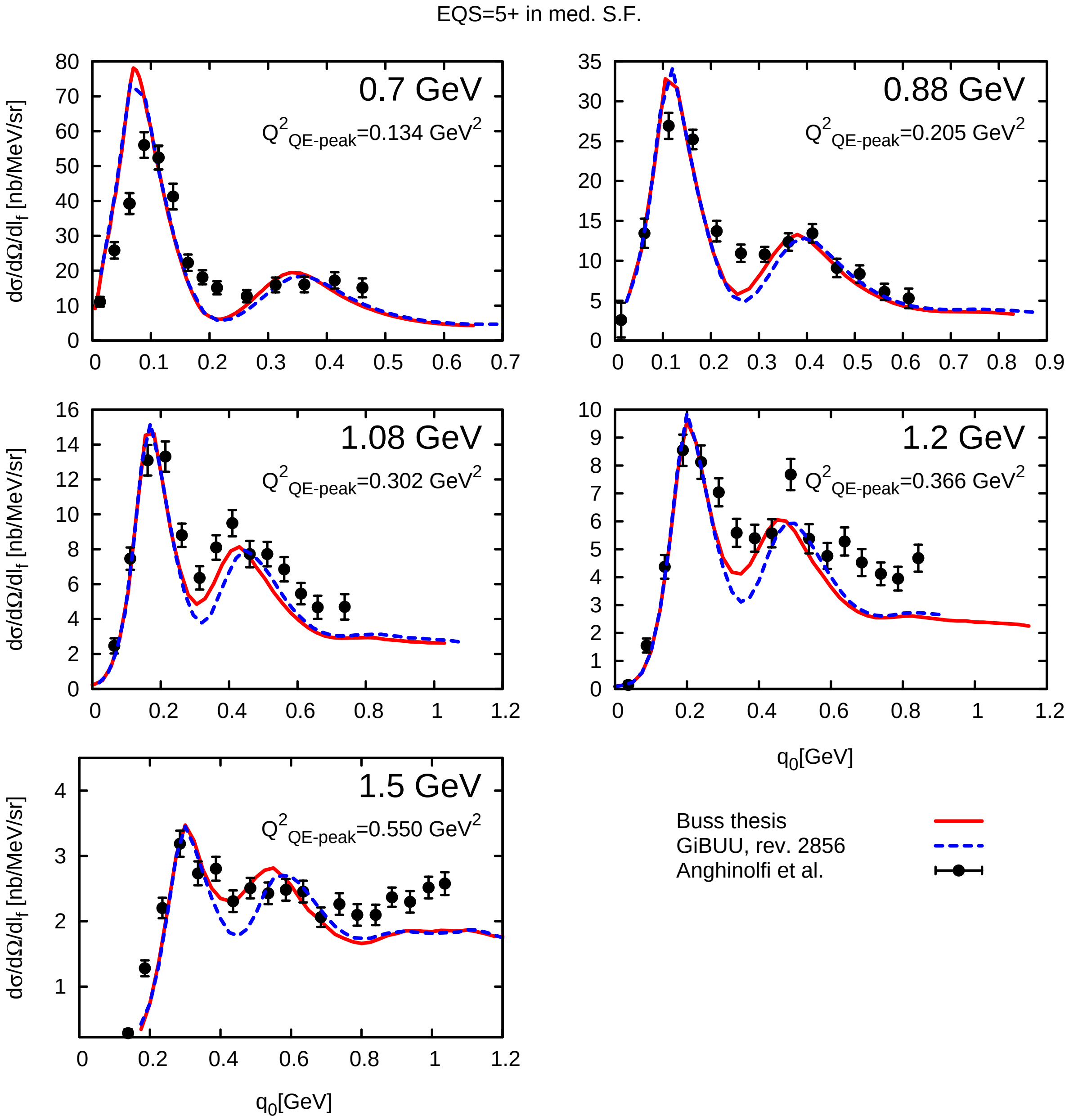

Figure 1: The inclusive electron cross section $d\sigma/(d\Omega dl_f)$ on ^{16}O as a function of the energy transfer q_0 at five distinct fixed electron energies (0.7, 0.88, 1.08, 1.2 and 1.5 GeV) and a scattering angle of $\theta_{l_f} = 32°$. The curves have been obtained using all in-medium modifications and in particular in-medium changes of the width according to the *mass-shift* scenario. The solid curve shows the result published in [Bus08], the dashed one has been obtained with revision 2856. No $\pi\pi$ or DIS background have been taken into account. The data are taken from [Ang96, QEW08]. In each panel, the parameter $Q^2_{\text{QE-peak}}$ (evaluated according to [Bus08, eq. 7.3]) is given as an estimate of Q^2 at the quasi-elastic peak.

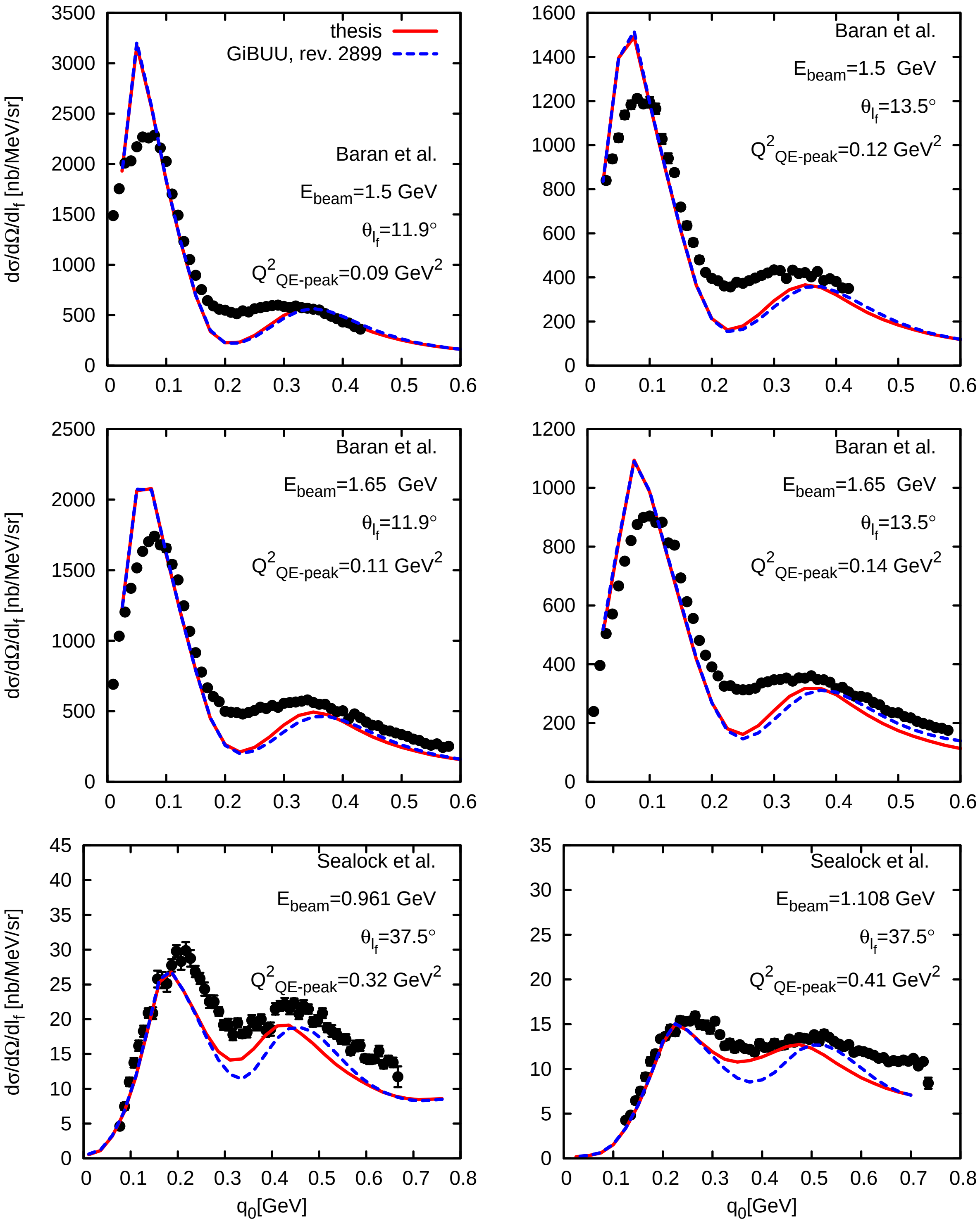

Figure 2: Same as fig. 1 for an ${}^{56}_{26}$Fe nucleus. Data are taken from [Sea89, Bar88].

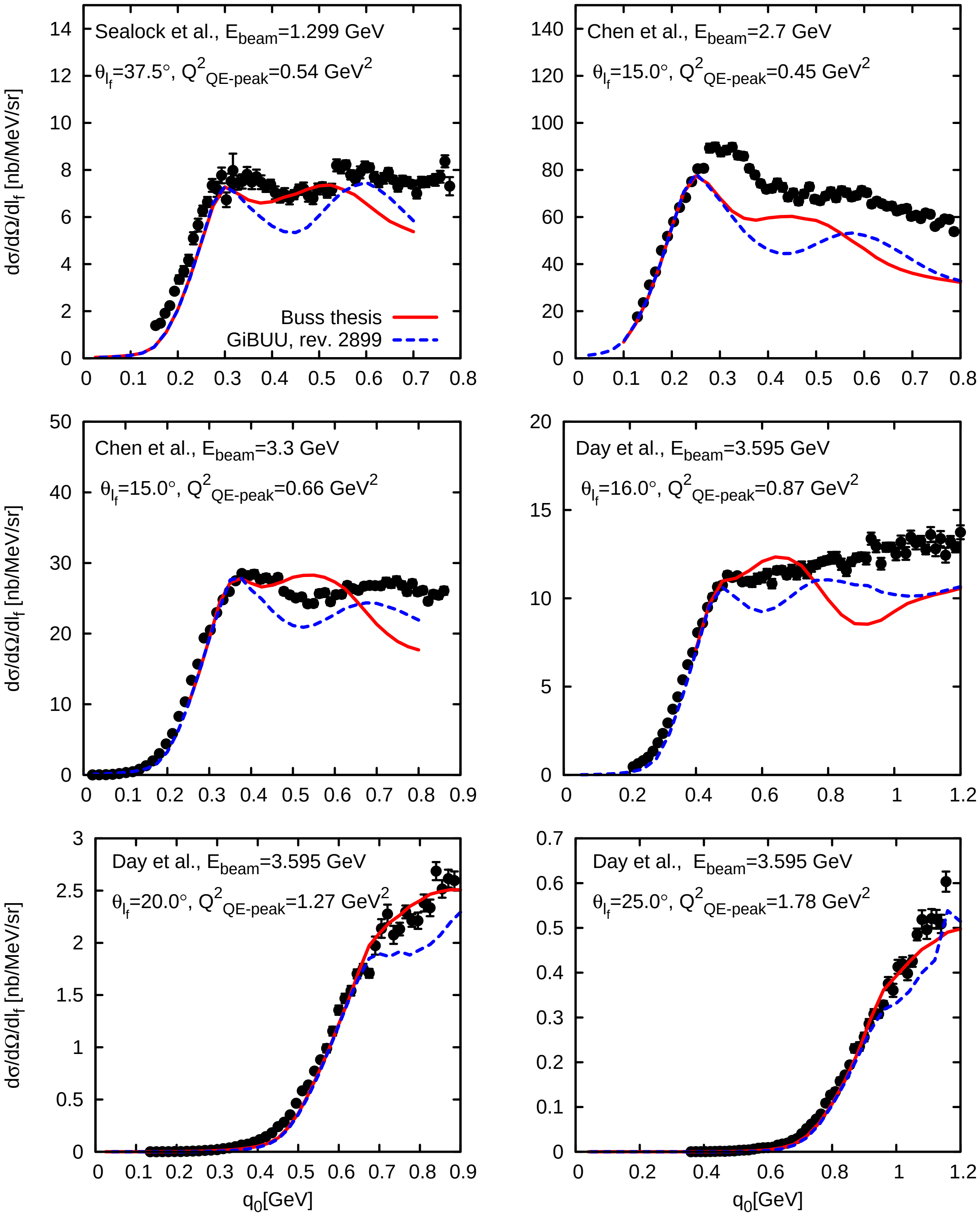

Figure 3: Same as fig. 2 for different electron kinematics. The data are taken from [Sea89, Che91, Day93].

References

[Ang96] M. Anghinolfi *et al.* 'Quasi-elastic and inelastic inclusive electron scattering from an oxygen jet target.' *Nucl. Phys.*, **A602**:405 (1996). nucl-th/9603001.

[Bar88] D. T. Baran, B. F. Filippone, D. Geesaman, M. Green, R. J. Holt, H. E. Jackson, J. Jourdan, R. D. McKeown, R. G. Milner, J. Morgenstern, D. H. Potterveld, R. E. Segel, P. Seidl, R. C. Walker, and B. Zeidman. 'Δ electroproduction and inelastic charge scattering from carbon and iron.' *Phys. Rev. Lett.*, **61(4)**:400 (Jul 1988).

[Bus08] O. Buss. *Photon- and Pion-induced Nuclear Reactions in a Transport Approach*, Ph.D. thesis, JLU Giessen, Institut für theoretisches Physik I (2008).

[Byc73] E. Byckling and K. Kajantie. *Particle Kinematics.* John Wiley &Sons (1973).

[Che91] J.-P. Chen *et al.* 'Longitudinal and transverse response functions in Fe-56(e, e-prime) at momentum transfer near 1-GeV/c.' *Phys. Rev. Lett.*, **66**:1283 (1991).

[Day93] D. B. Day *et al.* 'Inclusive electron nucleus scattering at high momentum transfer.' *Phys. Rev.*, **C48**:1849 (1993).

[Lei08] T. Leitner, O. Buss, L. Alvarez-Ruso, and U. Mosel. 'Electron- and neutrino-nucleus scattering from the quasielastic to the resonance region.' (2008). 0812.0587.

[QEW08] 'Quasielastic electron nucleus scattering archive.' (August 2008). http://faculty.virginia.edu/qes-archive/index.html.

[Sea89] R. M. Sealock *et al.* 'Electroexcitation of the Delta(1232) in nuclei.' *Phys. Rev. Lett.*, **62**:1350 (1989).